nature

THE INTERNATIONAL WEEKLY JOURNAL OF SCIENCE

FUTURE GENERATIONS

What kind of world will we pass on? PAGE 397

ASTROPHYSICS

FAST RADIO BURST LOCATED

FRB 150418 source is an elliptical galaxy

PAGES 427 & 453

SOCIAL EVOLUTION

TRUST AND PUNISHMENT

Explaining a unique aspect of human society

PAGE 473

PALAEONTOLOGY

DOWN IN THE MOUTH

Evolution of smaller human teeth follows a simple rule

PAGES 425 & 477

NATURE.COM/NATURE
25 February 2016 £10
Vol 530, No. 7591

THIS WEEK

EDITORIALS

HOT SEATS All change at the top of the UN climate body **p.382**

WORLD VIEW We must remember that the future will forget **p.383**

NANOMACHINE Tiny DNA rotor spins round and round **p.385**

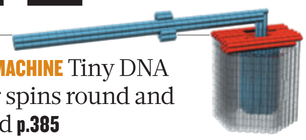

Safety first

It is worrying that US government departments are unable to divulge basic data on research projects involving human subjects. Such data should be publicly available to ensure volunteers' safety.

"Your safety is our priority." It's difficult to visit a sports stadium, travel on an aircraft or even head to the cinema these days without being told that someone, somewhere, is watching out for you. So why do some systems that are set up to protect the volunteers who participate in scientific research seem so inadequate?

It's not as if we haven't been warned about what can happen when supervision and scrutiny are lax. In 2010, the US Presidential Commission for the Study of Bioethical Issues was tasked with a sobering mission. A series of horrifying medical experiments on Guatemalan citizens — some intentionally infected with syphilis — in the 1940s had recently come to light. President Barack Obama asked the commission to determine whether such an atrocity could still happen today, and to evaluate the protections in place for all who participate in human-subject research funded by the US government.

The commission soon ran into a problem: a portrait of the current system was difficult to paint. Some government departments did not have ready access to essential data for identifying and tallying federally funded projects involving human subjects. More than six months after the commission asked for them, some departments were still unable to provide basic information, such as a list of all such projects, the number of participants involved and the location of the work.

When it reported its findings in 2011, the commission concluded that current regulations probably protect research participants from unethical treatment. But it could not say so with certainty: "Because of the currently limited ability of some governmental agencies to identify basic information about all of their human subjects research, the Commission cannot say that all federally funded research provides optimal protections," the report concluded.

To improve the situation, and to help to secure the protection of all involved, the commission made a simple request. Any federal department or agency that supports human-subject research should make a core set of data publicly available, listing the research title, investigator, location and funding. The Department of Defense quickly complied, but some agencies still have not. That is not good enough. Although the bioethics commission cannot compel agencies to collate and gather this information, if these agencies are to preserve public trust and ensure future research, then they should all do so.

The system that oversees human-subject research in the United States is already secretive at too many levels. For example, the ethics committees that assess risk and approve projects — institutional review boards — deliberate in private. Although there are guidelines on the types of expert who should sit on the boards, the guidelines are toothless because there is no independent system to check that they are followed. In 2009, investigators from the Government Accountability Office reported that they had been able to register a bogus ethics committee with the Department of Health and Human Services.

It is true that many federally funded medical trials are logged on the ClinicalTrials.gov website. But sponsors are not forced to register early, phase I studies, and the database extends to non-medical projects.

Officials and government agencies are keen to talk up the benefits of gathering big data. Well, now they need to cough up some information themselves. And there is more to providing these details than mere box-ticking. A reliable map of where research is taking place and what projects are under way allows researchers — and members of the public — to identify gaps and redundancies. It could flag up populations of research participants who are being under- or over-sampled, and studies that are being conducted on populations that may not receive the benefit of the results.

"The system that oversees US research on human subjects is secretive at too many levels."

Despite the struggle to obtain useful data, the bioethics commission's report was able to estimate that the government funded more than 55,000 projects involving human subjects in fiscal year 2010. Most of those were medical studies.

It's time for the system to give a little back to the many thousands of volunteers who help researchers to advance these studies, sometimes at risk to themselves — by lifting the veil of secrecy that limits oversight of such risks. Making the effort to fulfil the commission's recommendation is a good way for those in charge to start. ■

Generation game

A Nature *special issue takes on the world of tomorrow — and the decisions shaping it today.*

How do we get to the future? As the old joke goes: well, I wouldn't start from here. Perhaps the greatest trick that the film director George Lucas ever pulled was to set his Star Wars series not in the future, but a long time ago. Lucas's emblematic take on once-upon-a-time introduced each film as entirely unconnected in space and time to the present day. Everybody on screen was long dead. Their lives and troubles and loves and hates were dust. The tales of heroism and noble deeds were essentially myths.

Much science fiction does the opposite. It takes what we have now and spins it forward. Or it picks a destination and charts a course. Occasionally, the two narrative devices collide awkwardly, and present-day humans discover some futuristic technology, which they use to change their own path. But most of the time, even tales of aliens and interplanetary travel are presented as a consequence

of a plausible series of likely events.

Technologists will tell you that the future is already here, it is just unevenly distributed. But there is one factor that defies such a simplistic vision: humans. One day, in the not too distant future, everybody alive today will be dead. The planet will be inherited by people who had zero input into how Earth — their only home — was farmed, fished, burned, polluted, shaped and exhausted. Perhaps some of them are reading this.

If so, the people of the future — those born in the late twenty-first century and beyond — may well scan this special issue of *Nature* with bewilderment or mocking nostalgia. In a series of articles starting on page 397, we tackle the ethics and opportunities of early-twenty-first-century science and technology and its impact on our future generations (see nature.com/futuregenerations). Gene editing, nuclear waste, climate change, the march of computers and population growth — decisions and paths embarked on today will resonate well into the future.

Nature has long taken an interest in the fate of future generations and how science can improve — and endanger — them. Back in March 1870, an issue in the first volume of this journal carried a review of the book *Hereditary Genius* (Macmillan, 1869) by Francis Galton, who spawned the field of eugenics (see A. R. Wallace *Nature* **1,** 501–503; 1870). His book introduced claimed scientific concepts into what had previously been an economic and social debate about the relationship between present and future people. In Britain, this came during the era of friendly societies, groups of like-minded people who — before welfare and insurance — would pay subscriptions while young, and (they hoped) receive benefits in old age, sickness and death. (In reality, and in a stark example of the pressures that still squeeze pension provision, many of these societies paid out more to older members than they could take from healthy young workers, and so went bust.)

FUTURE GENERATIONS
A *Nature* special issue
nature.com/futuregenerations

The concept of intergenerational equity in popular debate has since focused on finance, with environmental stability and sustainability tacked onto discussions only in the past few decades. The younger generations might feel, quite legitimately, that they are getting a raw deal. Just as many of the people who paid into friendly societies never got a penny back, so the generation born around the turn of the millennium must look at the home-owning and financially secure baby-boomers and curse the timing of their births. Yet these are the young people who will, as they mature, be asked to make monumental decisions that affect not just one or two generations to come, but hundreds.

"How do we best serve tomorrow's people?"

As tools emerge that could eradicate the genetic basis for ill health, should they be used? When do nations abandon the (already shaky) attempts at collective action on climate change and make explicit their pursuit of pure self-interest? Just how do we dispose of drums of toxic waste that could remain hazardous for a million years? If the future starts tomorrow, then how do we best serve tomorrow's people?

Perhaps there is a lesson in science fiction? Taking what we have and spinning it forward raises questions about the direction we head in — some of which are addressed in this special issue. And the best way to answer those questions is to work out, as best we can, where we, they — or if you are reading this in the future, you — want to end up. We start from here. ■

Climate changes

The loss of three key facilitators must not impede progress on emissions mitigation.

Christiana Figueres has charmed the world. As executive secretary of the United Nations Framework Convention on Climate Change, she helped to lead a remarkable transition from nearly collapsed climate negotiations in Copenhagen in 2009, to an agreement between the world's governments in Paris last year. She transcended her once-thankless — and largely powerless — post as facilitator-in-chief to become a popular and influential advocate for action on global warming. Figueres has now announced that she will be stepping down in July. She will leave on a high note, but whoever fills her shoes will have to deal with significant head winds.

Figueres's departure, which became public knowledge on 19 February, is part of a larger shake-up in the UN climate shop. On the same day, Héla Cheikhrouhou, executive director of the Green Climate Fund, which was created to help developing countries to reduce emissions and adapt to climate change, announced that she will leave her post at the end of her term in September. And on 15 February, former French foreign minister Laurent Fabius, who skilfully guided the negotiations to a smooth conclusion in December, announced that he is stepping down as president of the climate talks. French environment minister Ségolène Royal will take his place until November, when the leadership transitions to Morocco at the next major meeting, in Marrakesh.

In her letter to governments, Figueres lauded the Paris agreement as a historic achievement and said that the world is now transitioning into a phase of "urgent implementation". From a political perspective, it is certainly true that the Paris agreement was historic. After all, there was no guarantee going into the meeting that anything at all would come out of it, let alone the formal agreement that will be opened up for ratification on 22 April, Earth Day, this year.

Both Figueres and Fabius deserve credit for making that happen, but their successors have plenty of work ahead. It is no secret that the actions that governments have committed to thus far fall well short of those needed to limit warming to 2 °C, let alone to 1.5 °C, which is the stated goal of the agreement. Nor is it clear that the world is urgently moving forward.

The Green Climate Fund, which was created more than five years ago and has approved just eight projects, is still trying to collect the money promised by nations. The US Supreme Court has put US President Barack Obama's regulations for power-plant emissions on ice, pending a legal challenge. Policymakers in the United Kingdom are still debating how to proceed in the wake of a government decision last November — just before the climate talks got under way — to pull the plug on a programme supporting the development of carbon capture and sequestration technologies. And in another branch of the UN, the International Civil Aviation Organization has proposed a rule on aircraft emissions that is so weak as to be irrelevant.

Nor is the Paris agreement a done deal: crucial details about the framework for monitoring commitments must still be negotiated. For instance, countries have yet to agree on precisely what kind of information they should submit to the UN. To track progress, build confidence and hopefully pave the way for more ambitious policies, scientists, environmentalists and governments need these data to be solid. Given that this objective is the only thing resembling accountability in an otherwise voluntary agreement, negotiations on this point could determine whether the Paris agreement is indeed a success.

Figueres was optimistic about the work to come. "The journey that lies ahead will require continued determination, ingenuity and, above all, our collective sense of humanity and purpose," she wrote to government officials. "I know that together you will again rise to the task." Let us hope that she is right. ■

➲ NATURE.COM
To comment online, click on Editorials at:
go.nature.com/xhunqv

Can today's decisions really be future-proofed?

The impact of long-term policies on future generations will differ over time, and policymaking should take this into account, argues **Céline Kermisch**.

The concept of 'future generations' is common in research and policymaking in fields that take a long view, such as energy and the environment. It is typically used to invoke an ethical dimension. But to whom do we refer when we speak about future generations? This question is not often asked, and even less often answered.

We need to define future generations carefully. Failure to do so leads to severe and potentially damaging shortcuts in deciding the legacy we choose to leave and debating its potential effects.

A good example is the discussion of radioactive-waste management. Here, future generations are considered as a unified group of people: every generation that follows ours, with no attempt to constrain them by time. So, in talking about nuclear waste, the consideration of future generations mandates us to plan for the entire period that the material will be harmful — up to a million years, according to some estimates.

That timeframe includes our grandchildren and those people — or other forms of life — who will share our planet hundreds of thousands of years from now. From an ethical point of view, it is meaningless to pretend that this is a homogeneous group for which nuclear-waste policies will have the same impact. And trying to treat it as such distorts policy.

One of the most important decisions to make when we plan what to do with our nuclear waste is whether we give people in the future the ability to overrule our decision and choose their own strategy. In a few thousand years, for example, a perfectly safe solution could be available. That argument demands that we put the waste somewhere from whence it can be retrieved. So, if we choose — as most nations have — to dispose of it in underground facilities, the ethical attitude towards future generations implies that we should not permanently seal off these disposal sites.

At first glance, this strategy respects the autonomy of future generations and so is ethical. Take a closer look, however, and there is a point in the future when this ability of our successors to choose their own option becomes irrelevant. That autonomy benefits only those who know and remember that the waste is down there. Given that we struggle to answer questions about lost human civilizations from just a few thousand years ago, humility demands that we assume that knowledge of the location of disposed-of radioactive waste, and how to handle it, could be lost some time in the next million years.

The French nuclear-safety authority assumes that this memory loss will not happen for at least 500 years. But clearly, much could happen between the years 2500 and 1002000. Some advocates of retrievable waste options claim that future generations will simply seal off the disposal before the memory is lost. Even if this is true — and we have no way of knowing — it does not solve the ethical problem of assuming that all future generations can be treated in the same way. In this case, the advantages of retrievability are relevant only to those generations alive before the disposal site is sealed.

This example shows that it makes no sense to talk of 'future generations'. We should instead refer to two groups: 'close future generations' and 'remote future generations'. How we define these groups depends on the problem being assessed. For radioactive-waste management, remote generations are defined as those that have forgotten that the waste is there. The exact time in the future at which the memory is lost is not a relevant question here. We assume it will happen, and plan accordingly.

IT MAKES NO SENSE TO TALK OF 'FUTURE GENERATIONS'.

Addressing impacts on future generations in this way questions another claimed benefit of keeping nuclear waste retrievable — that the ability to monitor and maintain disposal sites is keeping them safe. But, given that it applies only to close future generations, the number of people protected by this policy is much smaller than is generally assumed.

The same is true when talking about the security of the waste. Sealing off disposed radioactive material so that nobody — including terrorists — could access it protects fewer people than we might imagine. For remote future generations, the security risk evaporates — everybody, including those who would use it for malevolent reasons, has forgotten that it is there.

Just as there are intergenerational trade-offs between us and future generations, so there are similar conflicts between close and remote future generations. This applies to a range of long-term issues with impacts that vary with time. For instance, when analysing the funding of nuclear-waste management from an ethical perspective, it is relevant to distinguish between generations that benefit from nuclear technologies and those that do not.

This distinction could also be used to inform ethical debate on other long-term problems, including climate change. Remote future generations could be, for example, those that live in a world in which the average temperature increase has surpassed 3 °C and sea levels have risen by a set amount. Their needs are then clearly framed as different from those of close future generations, which could remain fixated on trying to prevent a 2 °C rise — or persist in arguing about whether the threat of global warming is real. ■

Céline Kermisch *works on the philosophy and ethics of risk at the Université Libre de Bruxelles, Brussels.*
e-mail: Celine.Kermisch@ulb.ac.be

RESEARCH HIGHLIGHTS

Selections from the scientific literature

CANCER BIOLOGY

How exercise helps to combat cancer

Mice that take exercise have fewer tumours than those that do not — thanks to more cancer-fighting immune cells finding their way into tumours.

Studies in humans have linked the effects of taking regular exercise to a reduced risk of developing cancer. To investigate the underlying molecular mechanisms, Pernille Hojman of the University of Copenhagen in Denmark and her colleagues compared tumour growth in sedentary mice and in those that had access to an exercise wheel over four weeks.

Animals that ran had about 60% fewer tumours, which were also smaller in size. Exercise was associated with an increase in the number of a particular type of immune cell — the natural killer cell — found in the tumours. An exercise-induced surge in the hormone adrenaline mobilized these cells.

Cell Metab. **http://doi.org/bcnk (2016)**

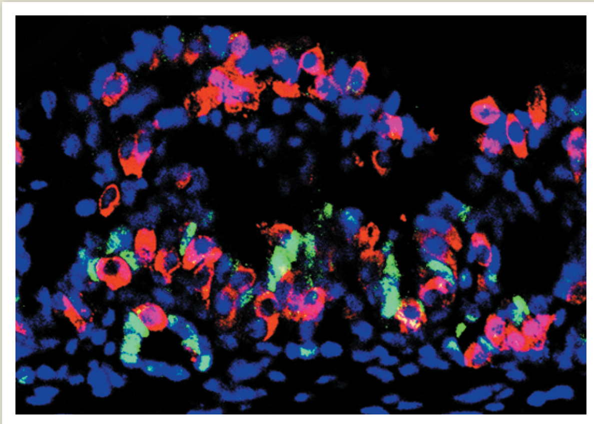

CHAIYABOOT ARIYACHET

REGENERATIVE BIOLOGY

Insulin from mini stomach

Stomach tissue can be reprogrammed to mimic insulin-producing pancreatic cells and control diabetes when implanted into mice.

A certain type of cell in one part of the stomach has similar gene-expression patterns to β-cells, which make insulin in the pancreas. Qiao Zhou at Harvard University in Cambridge, Massachusetts, and his colleagues reprogrammed these cells using a mix of key DNA-binding proteins, and found that more than 40% formed insulin-producing cells. The reprogrammed cells developed into stomach mini-organs (pictured) that, when transplanted into mice lacking β-cells, prevented spikes in blood sugar levels and kept animals alive for 6 months compared to untreated mice, which died within 8 weeks.

The results suggest that the stomach could serve as a renewable source of β-cells to treat diabetes, the authors say.

Cell Stem Cell **http://doi.org/bcqc (2016)**

MATERIALS

Shells spark strong graphene fibre

A composite thread with a structure inspired by nacre — the iridescent material found inside many seashells — is the strongest graphene-based fibre ever made.

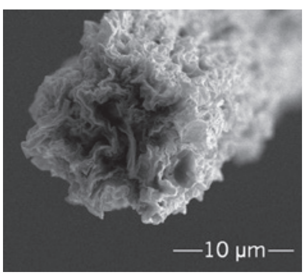

ADV. MATER.

Such fibres are typically produced by spinning together nanometre-thick sheets of graphene oxide. But they often have poor tensile strength, probably owing to weak interactions between the nanosheets. To strengthen the threads, Qunfeng Cheng of Beihang University in Beijing and his colleagues added two more ingredients: calcium ions and a flexible carbon compound called PCDO. These help to bind the nanosheets together, mimicking the strong interactions in nacre. The team produced a fibre roughly 20 micrometres wide (**pictured**) that could be tied in a knot without fracturing and could support a 2-gram weight.

The fibres also conduct electricity, making them a promising material for flexible electrodes or artificial muscles.

Adv. Mater. **http://doi.org/f3k23w (2016)**

PALAEOECOLOGY

Habitats of ancient humans revealed

Some hominins may have preferred to live in shady glades near fresh water nearly 2 million years ago.

Clayton Magill at the Swiss Federal Institute of Technology in Zurich and his colleagues took samples from a layer of soil in Olduvai Gorge, Tanzania, where fossil remains for early *Homo* and *Paranthropus boisei* hominins have been found. This 1.8-million-year-old soil was covered by a layer of volcanic ash, which preserved the distinctive chemical signatures left behind by ancient plants. By analysing these 'biomarkers', the team was able to distinguish aquatic from terrestrial plants, grasses from non-grasses, and woody plants from herbaceous ones.

The biomarker analysis and fossil remains suggest that the hominins favoured a small wooded area near a freshwater wetland, presumably because it offered drinking water, edible plants and shade. The presence of fossilized butchered animal remains also implies that the hominins brought food back to their woodland home from the larger grassland area.

Proc. Natl Acad. Sci. USA **http://dx.doi.org/10.1073/pnas.1507055113 (2016)**

MICROBIOLOGY

Gut microbes help malnutrition

Manipulating the gut microbes of undernourished children could help them to gain weight, three laboratory studies in mice and pigs suggest.

Malnourished children can struggle to gain weight even on high-nutrient diets, and studies have suggested that under-nutrition stops their gut microbiomes from maturing. A team led by Jeffrey Gordon at Washington University in St. Louis, Missouri, transplanted gut microbes from undernourished and healthy children from Malawi into germ-free mice, and found

KETTERER *ET AL.*/DIETZ LAB/TUM

that mice given microbes from healthy children gained more weight and muscle than did mice with the malnourished microbiomes. The team identified microbial species associated with these gains, and delivering two species to the guts of mice that had malnourished microbiomes boosted the animals' growth.

Martin Schwarzer and François Leulier at the University of Lyons, France, and their team found that giving malnourished mice a strain of *Lactobacillus plantarum* bacteria helped the mice to gain weight by restoring their growth hormone production. In a third study, Gordon and his colleagues identified a sugar in breast milk that promoted growth in mice and piglets harbouring microbes from a malnourished child.

Science **http://doi.org/bcnr (2016);** ***Science*** **351, 854–857 (2016);** ***Cell*** **http://doi.org/bcqd (2016)**

ANIMAL COGNITION

Horses read human emotions

Horses can differentiate between happy and angry human faces.

Researchers previously showed that dogs can identify emotions from human faces. To find out whether horses share this ability, Amy Smith, Karen McComb and their colleagues at the University of Sussex in Brighton, UK, tested the response of domestic horses (*Equus caballus*; **pictured**) to photographs of human faces with happy or angry expressions. Horses tended to view angry faces with their left eyes — a sign that they were processing the image using the brain's right hemisphere, which is thought to handle negative stimuli. The animals' heart rates also increased more rapidly in response to angry faces than to happy ones.

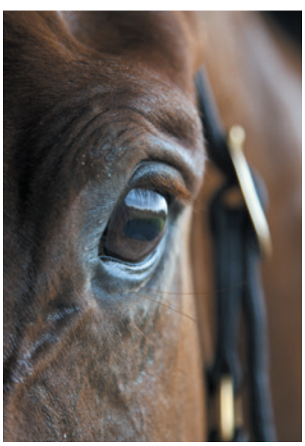

ALEX SHARP/GETTY

The ability of horses to recognize human expressions could have evolved during domestication, the authors say. They add that the animals probably also refine this skill during their lifetimes.

Biol. Lett. **12, 20150907 (2016)**

PLANETARY SCIENCE

First super-Earth atmosphere

The first gases to be identified around an exoplanet that is slightly larger than Earth show that its atmosphere is probably rich in hydrogen and carbon.

Angelos Tsiaras of University College London and his colleagues used a camera on the Hubble Space Telescope to probe the planet 55 Cancri e, which has a radius twice that of Earth, lies 12 parsecs (about 40 light years) away and orbits close to its host star.

The team found that the planet's atmosphere contains no water vapour but does have hydrogen, probably in the form of hydrogen cyanide, which is an indicator of carbon-rich atmospheres. The high level of carbon suggests exotic chemistry around the planet.

Astrophys. J. **in the press; preprint at http://arxiv.org/abs/1511.08901v2 (2016)**

CLIMATE CHANGE

Climate risks of low-carbon power

A transition to power plants that capture and store carbon could increase water use, probably leading to shortages in a major UK river basin as early as the 2030s.

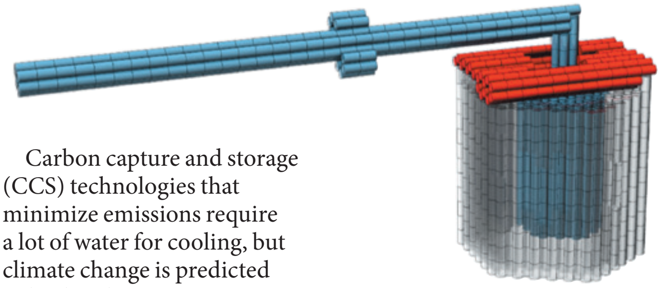

Carbon capture and storage (CCS) technologies that minimize emissions require a lot of water for cooling, but climate change is predicted to lead to drier summers in the United Kingdom. Edward Byers of Newcastle University, UK, and his colleagues used climate and hydrology models to analyse scenarios in which electricity production rises by 55% by 2040 as CCS technologies are fully adopted in the River Trent basin — the largest UK inland source of cooling water for power generation. The team projected declining river flows alongside rising demand for water from the power sector.

The researchers found that CCS power plants might become less reliable in the future when the river runs low, unless the most water-efficient technologies are used.

Environ. Res. Lett. **11, 024011 (2016)**

NANOSCIENCE

Nanorotor made of DNA

Researchers have made a nanometre-scale rotor out of 3D fragments of DNA.

Hendrik Dietz and his colleagues at the Technical University of Munich, Germany, designed the fragments to self-assemble into a rotor that looks like a helicopter blade (**pictured**). It spins around on an axle and is clamped in place by two other DNA units. To stop the blade from rotating freely, the team used docking sites on the inside of the clamp units so that the rotor was held in place. When the ion concentration of the solution containing the rotor changed, the rotor was released and could spin owing to Brownian motion.

The researchers say this action mimics that of an enzyme in the body that acts like a rotary machine, and claim that their nanomachine is more structurally complex than previous ones.

Sci. Adv. **2, e1501209 (2016)**

ROBOTICS

Microbots dance in the light

Tiny soft robots can swim, spin and make other complex motions in response to light.

Microbots — micrometre-scale robots — could one day be used to deliver medicines or to collect data inside the body. But most microbots are made of rigid materials, which limit them to simple back-and-forth motions, usually in response to chemical or magnetic forces. To develop microbots that are capable of more-versatile movement, Peer Fischer at the Max Planck Institute for Intelligent Systems in Stuttgart, Germany, and his colleagues designed soft, flexible ones using a liquid-crystal elastomer that was both rubbery and responsive to light.

By sweeping bands of light across disc- and rod-shaped microbots, the team induced wave-like swimming motions similar to those used by single-celled organisms. Different patterns of light also made the disc-shaped microbots spin, reverse their spinning direction or move around a path in the shape of a square.

Nature Mater. **http://doi.org/bcjk (2016)**

NATURE.COM
For the latest research published by *Nature* visit:
www.nature.com/latestresearch

SEVEN DAYS *The news in brief*

EVENTS

Earthquake action

Citing a sharp spike in earthquake activity, a US environmental group has filed a federal lawsuit seeking to curb the injection of wastewater from hydraulic fracturing (fracking) and oil activities in Oklahoma. The California-based Sierra Club, working with law firm Public Justice, filed the lawsuit against 3 energy companies on 16 February, 3 days after a magnitude-5.1 earthquake shook the state. There were 907 earthquakes of magnitude 3 or larger in 2015, compared with 109 in 2013. Scientists have linked the earthquakes to the injection of wastewater, a by-product of fracking.

ExxonMobil anger

More than 100 scientists have signed a letter urging the American Geophysical Union (AGU) to reject sponsorship from US oil and gas giant ExxonMobil. Following news reports in late 2015 that indicated that ExxonMobil scientists knew about the threat of global warming decades ago, the letter says that ExxonMobil's complicity in spreading "climate denial and misinformation" has been well documented. "By allowing Exxon to appropriate AGU's institutional social license to help legitimize the company's climate misinformation, AGU is undermining its stated values as well as the work of many of its own members," the 22 February letter states.

January heats up

Last month was the world's hottest January since records began in 1880, and the ninth month in a row to break a global monthly temperature record, the US National Oceanic and Atmospheric Administration reported on 17 February. The average global temperature was 1.04 °C above the twentieth-century average for January, beating the previous record, from 2007, by 0.16 °C. In the Arctic, which was remarkably warm for the time of year, sea ice was at its lowest January extent since records began in 1979, according to the US National Snow and Ice Data Center.

STEPHANE CORVAJA/ESA

Sentinel-3A launches to monitor Earth

The European Space Agency successfully launched the Earth-observing satellite Sentinel-3A on 16 February. The launch, from Plesetsk, Russia, carried a suite of four Earth-observing instruments into orbit as part of Europe's Copernicus programme. Sentinel-3A is one of two identical satellites, the second of which will launch in 2017. Over the oceans, they will measure sea surface temperatures and sea-ice thickness, and over land they will map how land is used, the extent of vegetation and the height of rivers and lakes. Two other Sentinel satellites launched in 2014 and 2015.

PEOPLE

New NAS president

Geophysicist Marcia McNutt has been elected president of the US National Academy of Sciences (NAS) by its members, the society announced on 16 February. McNutt is currently editor-in-chief of *Science* and its family of journals. She begins her six-year term at the NAS on 1 July, replacing atmospheric scientist Ralph Cicerone, who has served the maximum two terms. McNutt was director of the US Geological Survey from 2009 to 2013.

FDA vote due

As *Nature* went to press, the US Senate was poised to vote on the nominee to head the US Food and Drug Administration (FDA), clinical-trials expert Robert Califf. On 22 February, lawmakers voted to limit debate on Califf's nomination, setting the stage for a final vote that will determine whether he will become FDA commissioner. President Barack Obama nominated Califf last September, but some lawmakers delayed consideration of the nomination over concerns about the FDA's recent approval of genetically engineered salmon for use as food and the agency's handling of an ongoing opioid-approval crisis. See go.nature.com/mfdn9u for more.

Italy research chief

Physicist Massimo Inguscio took office on 22 February as president of Italy's National Research Council (CNR). Inguscio, who comes to the post from the University of Florence, will need to ensure that research in the 103 CNR institutes can stay on track without significant institutional funds — salaries and general expenses absorb most of the CNR's budget. He will also need to maintain the organization's

commitment to research integrity: the CNR is currently working its way through several cases of potential misconduct in papers co-published by its scientists.

More KI fallout

Heads continue to roll in the scandal rocking the Karolinska Institute (KI) in Stockholm: Hans-Gustaf Ljunggren resigned as dean of research on 22 February. He had participated in the decision to clear surgeon Paolo Macchiarini of allegations of misconduct in carrying out experimental transplants of artificial windpipes into patients. Earlier this month, two other KI professors resigned as vice-chancellor of the university and as secretary-general of the Nobel Assembly that chooses the Nobel physiology or medicine prize. The KI and its hospital have opened new investigations into Macchiarini, and Swedish health authorities have referred the matter to the police.

Figueres bows out

AREND KUESTER/CC BY-NC 2.0

Christiana Figueres (**pictured**) will step down in July after her six-year term at the helm of the United Nations Framework Convention on Climate Change comes to an end. The Costa Rican diplomat had a key role in international climate negotiations, which culminated in the landmark emissions-reduction agreement reached at the Paris climate talks in December last year. Figueres's yet-to-be-named successor will be charged with overseeing the implementation of the agreement, details of which are to be discussed at the UN Conference of the Parties in Morocco in November. See page 382 for more.

BUSINESS

Stem-cell leader

Stem-cell biologist Robert Lanza announced on 22 February that he will be the head of global regenerative medicine for Astellas Pharma, the Tokyo-based firm that acquired Lanza's company Ocata Therapeutics earlier this month. Lanza is the chief scientific officer for Ocata, based in Marlborough, Massachusetts, which has been a leader in developing stem-cell therapies, despite financial troubles and management changes over the past 15 years (see *Nature* **481,** 130–133; 2012). Ocata is running clinical trials to test stem-cell-derived retinal cells on vision-loss disorders. Lanza says that those trials and other ongoing Ocata research programmes will continue under Astellas.

FACILITIES

LIGO-India is go

India's cabinet approved plans to build a gravitational-wave detector on 17 February. The machine, LIGO-India, will be a copy of two LIGO (Laser Interferometer Gravitational-Wave Observatory) machines in the United States, which this month reported the first direct detection of these long-sought ripples in space-time. Having a third machine on the other side of Earth should help physicists to pinpoint the sources of gravitational waves. The site for the 12.6-billion-rupee (US$183-million) project has yet to be selected, but it could be operational by 2023.

Space panorama

NASA is officially moving ahead with its next flagship astrophysics observatory, the Wide Field Infrared Survey Telescope (WFIRST), the agency stated on 18 February. Set to launch in the mid-2020s, WFIRST will use a 2.4-metre telescope repurposed from the US National Reconnaissance Office to capture the sky in infrared wavelengths. With its wide-range view, it will be able to measure light from one billion galaxies and illuminate the nature of the dark energy thought to be accelerating the expansion of the Universe.

POLICY

Poor policy stances

Of more than 200 institutions that have produced public policy statements on animal research, most do not meet the highest standards of openness, according to the group Speaking of Research, which campaigns to improve understanding of animal work. The group analysed policy statements from institutions in Europe, North America and Australia and rated them on the level of detail provided, such as welfare information and images. Only ten institutions got full marks, the group said on 22 February.

COMING UP

25–26 FEBRUARY
Potential marine World Heritage sites in the Arctic will be discussed at UNESCO headquarters in Paris.
go.nature.com/crvleg

26–28 FEBRUARY
Mumbai in India hosts the American Association for Cancer Research's conference on new ideas in cancer.
go.nature.com/9mf9wt

29 FEB–2 MARCH
NASA invites the astrophysics community to Pasadena, California, to discuss the science that can be done with the Wide Field Infrared Survey Telescope, which will study the nature of dark energy and search for exoplanets.
go.nature.com/chvjtq

TREND WATCH

Only 36% of clinical trials completed in 2007–10 at 51 leading US institutions were published or reported on ClinicalTrials.gov within 2 years of the trials finishing, according to an analysis in the *BMJ* (R. Chen *et al. Br. Med J.* http://doi.org/bcqf; 2016). The University of Minnesota, which ranked 15th in terms of number of trials, was most prompt at reporting results, with 55% of trials reported within two years. See go.nature.com/9cwl9a for more.

THE TRIAL-PUBLISHING PROBLEM
Results from many clinical trials completed in 2007–10 at US institutions were unpublished or unreported two years after the studies had finished. (Top ten institutions listed by number of trials.)

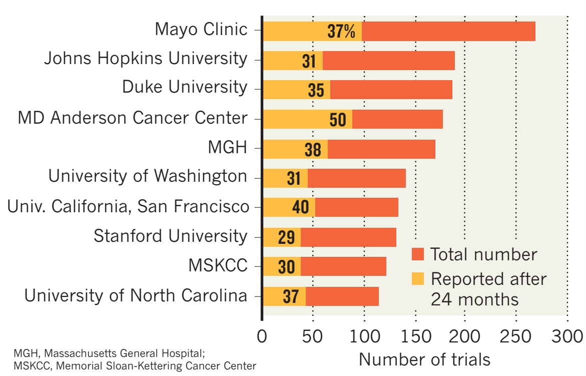

SOURCE: R. CHEN *ET AL. BMJ* HTTP://DOI.ORG/BCQF (2016)

NATURE.COM
For daily news updates see:
www.nature.com/news

NEWS IN FOCUS

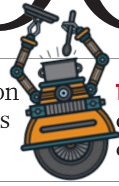

BIOMEDICINE US Cancer Institute rejuvenates cell line repository p.391

DEFORESTATION Satellite system to raise alarm hours after tree loss detected p.392

PSYCHOLOGY Modern take on iconic experiment shows power of authority p.394

TECHNOLOGY Why the world of 2020 will be dramatically different from that of today p.398

WILLIAM DANIELS/PANOS

The plant *Artemisia annua* (pictured being harvested in Tanzania) was the only source of artemisinin before biochemists invented a synthetic route.

PUBLIC HEALTH

Synthetic malaria drug meets market resistance

First commercial deployment of synthetic biology for medicine has modest impact.

BY MARK PEPLOW

When Paris-based pharmaceutical giant Sanofi started to sell malaria drugs made with the help of genetically engineered yeast in 2014, the move was hailed as a triumph for synthetic biology. The yeast was fermented in a vat to produce a chemical that Sanofi converted into artemisinin, which is used to make leading malaria treatments called artemisinin-based combination therapies (ACTs). Many hoped that the process would offer a cheap and plentiful supply of drugs to tackle a disease that claims almost half a million lives worldwide every year.

Yet Sanofi produced no 'semi-synthetic' artemisinin (SSA) at all in 2015, *Nature* has learned. And the company is now selling the manufacturing site in Garessio, Italy, where it made its SSA.

That such celebrated drugmaking technology — developed with the help of US$64 million from the Bill & Melinda Gates Foundation — stands idle illustrates the complicated web of economic forces that affects the market for malaria drugs. "This is a perfect example of how a new manufacturing process becomes extremely hard to scale up when there is a complex ecosystem of players," says Prashant Yadav, a health-policy researcher ▶

FREDERIC J. BROWN/GETTY

Artemisinin-based combination therapy pills (shown here in China) are leading treatments for malaria.

at the William Davidson Institute at the University of Michigan, Ann Arbor, who studies the ACT market.

Before the advent of SSA, the only source of artemisinin was the sweet wormwood plant (*Artemisia annua*), the discovery of which won Chinese scientist Youyou Tu a share of the 2015 Nobel Prize in Physiology or Medicine. But the agricultural supply has been erratic. Shortages of *A. annua* send prices soaring, which attracts more farmers to plant it; their produce then swamps the market, depressing prices and triggering fresh shortages (see 'A stable artemisinin market?').

SUPPLEMENT OR SAVIOUR?

The synthetic-biology route promised to end this rollercoaster by providing a stable and reliable source of artemisinin. Sanofi developed the capacity to produce almost 60 tonnes of the chemical per year — about one-third of global need — and the company hoped to supply other ACT manufacturers with the raw materials.

"In reality, that has not happened," says Yadav. Sanofi has so far used its SSA to make more than 39 million treatments of its own version of ACT — representing about 10% of global ACT demand — but has not sold the chemical to other drugmakers.

That is partly because of a glut in agricultural artemisinin. For the past two years, the naturally derived chemical has sold for less than \$250 per kilogram — below Sanofi's 'no profit–no loss' margin of around \$350–400 per kilogram. "If that price is already very low and there's a bumper crop, there's no reason to fire up a fermenter," says Jay Keasling of the University of California, Berkeley, who led the team that first developed the yeast strain.

But ACT manufacturers such as China's Guilin Pharma and India's Cipla are also reluctant to buy their drug ingredients from Sanofi, says Yadav, because the company is a direct competitor in the ACT market.

And Sanofi has not found it worthwhile to increase production of its own ACT because demand has plateaued. This is in part the result of growing efforts to diagnose malaria before doling out medicine: malaria treatments are often taken by people with fevers who do not actually have malaria, so more-accurate diagnoses help to reduce the number of treatments needed. Whether demand will rise again will depend on how international efforts to tackle malaria develop in the future, and how much funding will be available to purchase ACTs.

By July, Sanofi will complete the sale of its Garessio manufacturing plant to Bulgarian company Huvepharma, a contract manufacturer responsible for fermenting the engineered yeast in vats to make artemisinic acid — the precursor to artemisinin — for Sanofi.

Nicola de Risi, a manager for Huvepharma in Rome who will head the firm's Italian division, hopes that by gaining control of the entire SSA production process (from yeast to final product), the company will be able to lower costs and make sales to other ACT manufacturers. But Huvepharma will switch to using plant-derived artemisinin if it cannot make SSA cost-competitive, de Risi says.

PATH, a global-health organization based in Seattle, Washington, which coordinated the development of SSA, says that it still considers the project a success. "Since SSA entered the market, we have observed better price stability, and there has been adequate supply of artemisinin," it said in a statement.

"There is merit to the argument that SSA has contributed somewhat to stabilizing prices," says Yadav. But the main causes of price stability, he adds, are the recent steady demand for ACTs and long-term purchasing contracts with ACT manufacturers, set up by the Global Fund to Fight AIDS, Tuberculosis and Malaria.

PATH and Keasling say that SSA was always intended to be a supplemental source to fill gaps in agricultural production, or to cope with spikes in demand. But Claire Marris, a sociologist of science at City University London who previously worked at the Centre for Synthetic Biology and Innovation at Imperial College London, says that in her experience, SSA is often portrayed by those working in the field as simply a low-cost, high-volume substitute for agricultural artemisinin. "It was constantly talked about," she says. Now, Marris worries that unrealistic expectations for SSA's achievements could damage public trust in synthetic biology.

When the Gates Foundation awarded the first of its grants for the SSA project in 2004, it explicitly aimed to lower the cost of each ACT treatment from \$2.40 to "well under a dollar". But the median price of Sanofi's ACT had already dipped to \$0.92 per adult treatment by 2012, well before the introduction of SSA, and it has changed little since then.

De Risi says that SSA production will restart later this year so that Sanofi can produce its own ACT treatment. "I think it's good for synthetic artemisinin," says Yadav, who points out that other ACT producers may be more willing to buy artemisinin from Huvepharma because it is not an ACT producer itself — and therefore not a direct competitor.

Meanwhile, Guilin Pharma and Cipla are making plans to develop their own SSA, and Keasling hopes that more research and development work could make the synthetic process cheaper in the long term. "I'd like to see SSA take over as the dominant form, and some day I think it will," says Keasling. "But we have to be patient." ■

A STABLE ARTEMISININ MARKET?

After a decade of instability, prices of the malaria drug artemisinin have dropped and demand has stopped rising.

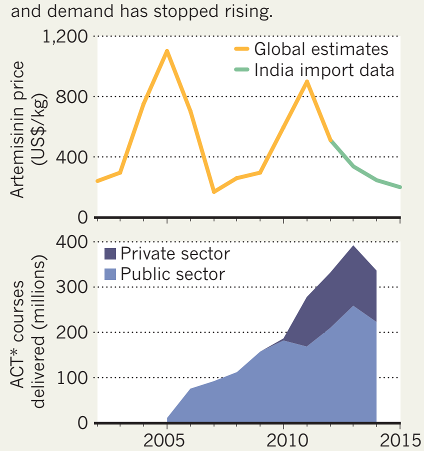

*Artemisinin-based combination therapies

SOURCE: WHO WORLD MALARIA REPORT 2015/A2S2/WILLIAM DAVIDSON

THE LIGHTHOUSE/UNIVERSAL IMAGES GROUP/REX SHUTTERSTOCK

New cancer models could help scientists to devise better treatments.

BIOMEDICAL SCIENCE

US cancer institute overhauls cell lines

Veteran cells to be replaced by human tumours grown in mice.

BY HEIDI LEDFORD

After more than 25 years of heavy use by researchers around the world, the US National Cancer Institute (NCI) has decided to stop screening most drugs using the NCI-60, its panel of 60 human cancer cell lines grown in culture. In late spring of this year, the institute will launch a rejuvenated repository of cancer models that are derived from fresh patient samples and tagged with details about their clinical past.

The NCI action responds to a widespread push for cancer models with a closer link to the patients they are intended to help. On 11 February, cancer researchers gathered in New Orleans, Louisiana, for a meeting hosted by the American Association for Cancer Research that focused on the creation of new models from clinical samples.

Since 1990, industry and academia have screened more than 100,000 compounds using the NCI-60, in order to study the molecular details of cancers.

When the NCI-60 was established, researchers had a very different conception of cancer, says James Doroshow, director of the Division of Cancer Treatment and Diagnosis at the NCI in Bethesda, Maryland. “Thirty years ago, the idea was that if you found a drug that worked on six breast cancer cell lines, then you could use it to treat breast cancer,” he says. “Well, it doesn’t work that way.”

Since then, breast cancer has been broken down into subcategories that are based on genetic mutations — and each category may respond differently to treatment.

The NCI-60 cell lines have also lived for thousands of generations in culture. Over time, this has altered their genetic make-up and behaviour.

The NCI will continue to supply the NCI-60 lines to researchers, but will eventually refocus its drug screening on newer models. It is developing hundreds of ‘patient-derived xenografts’ (PDXs) by implanting small chunks of human tumours in mice — an environment that better mimics the human body. The tumours can then be harvested and reimplanted in other mice, allowing researchers to study a given tumour in multiple animals. The NCI will distribute cells from those PDXs, plus data on each tumour’s genome sequence and gene-expression patterns, and the donor’s treatment history.

The institute will also make cell lines from the samples for use in more-detailed biochemical studies and in drug screening. And it is developing cell cultures and xenografts from tumour cells that are circulating in the blood to model tumours that are difficult for surgeons to biopsy. Doroshow estimates that his team will have 75 models ready for public distribution when the repository opens; the group aims to produce 1,000 in the first phase.

The NCI effort reflects a wider trend. Sixteen European institutions have formed EurOPDX, a consortium that boasts 1,500 PDXs. The Jackson Laboratory, a non-profit company in Bar Harbor, Maine, has 450 PDXs, and another 100 in development. Many more reside in pharmaceutical companies: last year, the Swiss pharma giant Novartis published a drug screen using 1,000 PDXs (H. Gao *et al. Nature Med.* **21,** 1318–1325; 2015).

PDXs have also garnered attention as models to guide treatment of individual patients: mice bearing PDXs could serve as ‘avatars’ to allow physicians to screen for the most-effective treatment regimen. But the process of generating a PDX is often too slow to benefit the donor, says Edison Liu, chief executive of the Jackson Laboratory. Instead, Liu sees Novartis’s approach — studying large collections of PDXs to help future patients — as more promising.

Such models can capture the genetic complexity of human cancers better than old cell cultures or genetically engineered mice, but PDXs also have shortcomings. Most are generated in mice that lack normal immune responses, to prevent rejection of the human cells. Efforts are under way to engineer mice with aspects of the human immune system, but no mouse fully captures the complexity of the system.

Despite the limitations, some researchers have translated PDX results into clinical gains. Livio Trusolino, a cancer researcher at the University of Turin in Italy, and his colleagues mined their collection of 600 colorectal cancer PDXs. They found that PDXs from some drug-resistant tumours responded better to a combination of treatments normally used against breast cancer — a result that was then borne out in a small clinical trial, Trusolino announced at the meeting in New Orleans.

”For the first time in my life, my results have been translated into a benefit for patients,” Trusolino says. “It is very rewarding.” ■

SPARKY BOOKER AND DEBORAH YOUNGS

MORE ONLINE

Q&A

A competition showcases how scientists capture the beauty of their work go.nature.com/azqijd

MORE NEWS

- Evidence tallies trysts in ancient human species go.nature.com/adgatx
- Academics fall short in reporting of clinical trials go.nature.com/9cwl9a
- New cause for Lyme disease complicates already-murky diagnosis go.nature.com/jla26z

NATURE PODCAST

Future-proofing our decisions — and should we edit the genomes of future generations? nature.com/nature/podcast

RICARDO FUNARI/BRAZIL PHOTOS/LIGHTROCKET/GETTY

Logging in the Brazilian Amazon has decreased in the past decade, but is still a problem.

CONSERVATION

Satellite alerts track deforestation in real time

System uses Landsat data to issue warnings just hours after tree loss is detected.

BY GABRIEL POPKIN

A satellite-based alert system could prove a potent weapon in the fight against deforestation. As few as eight hours after it detects that trees are being cut down, the system will send out e-mails warning that an area is endangered. That rapid response could enable environmental managers to catch illegal loggers before they damage large swathes of forest.

"It's going to be very, very helpful," says Brian Zutta Salazar, a remote-sensing scientist at the Peruvian Ministry of the Environment in Lima.

Satellites are already valuable tools for monitoring deforestation; in recent decades, they have delivered consistent data on forest change over large and often remote areas. One such effort, the Real Time System for Detection of Deforestation, or DETER, has helped Brazil's government to reduce its deforestation rate by almost 80% since 2004, by alerting the country's environmental police to large-scale forest clearing.

But DETER and other existing alert systems can be relatively slow to yield useful information. They use data from the Moderate Resolution Imaging Spectroradiometer (MODIS) on

Site of deforestation in Peru as detected using MODIS data (top) and Landsat data (bottom).

IMAGE: GOOGLE EARTH BASEMAP; DATA: WRI/UMD/GOOGLE/NASA/USGS VIA GLOBAL FOREST WATCH

NASA's Terra satellite, which at its top resolution produces images with pixels covering an area 250 metres on each side, roughly equivalent to 10 football pitches. This is too big to spot small changes in land cover, so it can take computer programs that process MODIS data weeks or even months to detect that a forest is being cleared. "By the time MODIS picks up on it, it's almost too late," says Peter Ellis, a forest-carbon scientist at the Nature Conservancy, a conservation group in Arlington, Virginia.

Seeking to provide a sharper view, geographer Matthew Hansen of the University of Maryland in College Park and his colleagues published maps showing year-to-year changes in global forest cover from 2000 to 2012 (M. C. Hansen *et al. Science* **342,** 850–853; 2013). The researchers relied on data from NASA's two active Landsat satellites, which together photograph every spot on Earth every eight days. Each pixel in a Landsat image is 30 metres on each side — roughly the size of a baseball diamond. This means that an area covered by just one MODIS pixel is captured in roughly 70 smaller Landsat pixels.

Hansen and his team wrote data-processing software that can use these higher-resolution images to recognize a disturbance as small as a road snaking its way through a previously untouched forest, something that often appears before clear-cutting begins. "It's much more advantageous to detect a smaller clearing first, and to figure out what that is, compared to finding something large," says Salazar.

Using this system, Hansen and his

colleagues plan to start updating the forest-change maps on their website more frequently — just hours after new deforestation is detected. A paper detailing the team's methodology has been accepted for publication in *Environmental Research Letters*.

The World Resources Institute, an environmental group in Washington DC, will provide access to the deforestation alerts on its Global Forest Watch website, beginning in early March. When trees disappear between successive Landsat passes, a pixel representing that location on an online map will turn red. Users will also be able to sign up to receive e-mails when land cover changes in a specific area, such as a park, an indigenous territory or a privately owned forest, which could facilitate rapid responses to small-scale deforestation.

But the alert system is limited in some important ways. Landsat detects only visible light and short-wave infrared, so it cannot see through clouds. This means that in the planet's cloudiest areas — such as many tropical rainforests — the satellites could go months without collecting images of the underlying land. Nor can the probes reliably detect damage from activities that leave the forest canopy intact, such as selective logging and the gathering of wood for fuel.

Because such forest degradation can yield carbon emissions that approach half those from all-out deforestation, tracking this damage is important in understanding the role of forests in climate change, says Alessandro Baccini, a remote-sensing expert at the Woods Hole Research Center in Falmouth, Massachusetts.

And then there is the difficulty of ensuring that deforestation alerts reach not only government officials, but also people who live in or near affected forests. "We will have faster detection, but OK, so what, what do you do next?" says Carlos Souza, a research scientist at Imazon, an environmental research institute in Belém, Brazil. He would like to see residents of remote forests trained to check the veracity of satellite-driven alerts on the ground. That could also help countries to improve their estimates of greenhouse-gas emissions from tree loss.

In the meantime, the Landsat-based alerts represent a significant step forward for the fight against deforestation, says Frances Seymour, a senior fellow at the Center for Global Development, a think tank in Washington DC. "In the context of law enforcement, timeliness is everything," she says. "A couple weeks later, not only is the forest gone, but so is the equipment and all the evidence you might be able to use for a successful prosecution." ■

RAYMOND GEHMAN/CORBIS

European bison in Białowieża Forest, where Poland's government is considering increased logging.

POLAND

Pristine forest at risk

Researchers suspect motives for a logging proposal are commercial, but forest administration cites pest control.

BY QUIRIN SCHIERMEIER

A Polish proposal to increase logging in the ancient Białowieża Forest is drawing fresh criticism from scientists. They suspect that the motives are partly commercial, and dispute claims that an outbreak of bark beetle threatens the forest. The Polish Ministry of the Environment says that there is no commercial benefit to the proposed logging and insists that it is needed for pest control.

The 1,500-square-kilometre forest, which straddles the Poland–Belarus border, has remained largely unchanged for centuries, making it a matchless stomping ground for researchers tracing the behaviour and ecology of insects, birds and mammals, including the largest population of European bison (*Bison bonasus*).

It is also a source of ecological measurements, for example on regeneration after disturbances, that inform forest management elsewhere, says Rafał Kowalczyk, director of the Polish Academy of Sciences' Mammal Research Institute in the village of Białowieża.

A Białowieża management plan limits logging in the forest to 48,000 cubic metres of wood per year — enough to allow locals to gather firewood. But on 10 November, the local forest administration proposed an amendment that would allow large-scale logging in sections outside the central 17% of the forest that is a national park. They cited an outbreak of the bark beetle pest (*Ips typographus*) in Białowieża's Norway spruce (*Picea abies*). In one forest district where logging is currently limited to 6,000 m^3 per year, the allowable yearly volume would increase to 53,000 m^3.

On 18 November, scientists with Poland's State Council for Nature Conservation condemned the proposal; public protests have followed. This week in *Nature*, Polish biologists express other concerns in two Correspondence articles (P. Chylarecki and N. Selva *Nature* **530,** 419; 2016; P. Michalak *Nature* **530,** 419; 2016).

Conservation council member and Correspondence author Przemysław Chylarecki, who is an ornithologist at the Museum and Institute of Zoology in Warsaw, suspects that commercial considerations, not just pest control, are behind the plan. Poland's government was elected in October — and the environment minister referred to the wasted commercial potential of unlogged trees in his election campaign, notes Chylarecki.

But an environment ministry spokesman, Jacek Krzemiński, says that there is no commercial incentive because the wood is only good for firewood, and the costs of logging and transport make it unprofitable to sell the wood on.

Kowalczyk, who also opposes the logging proposal, says that the pest-control argument is misguided. Recurring bark-beetle outbreaks do not endanger the forest at large because more-resilient tree species spread and replace spruce, he says. "That's a perfectly natural process and endlessly preferable to cutting down trees." But Jarosław Krawczyk, spokesman for the regional state forest directorate in Białystok, says that the current outbreak is unprecedented in scale and has already begun to attack other tree species.

A detailed assessment of forest health is under way, says Krzemiński. Earlier this month, a regional environment agency suggested that the amount of extra logging be reduced to half of the volume proposed in the new management plan, whereas Poland's national forest authority has yet to weigh in. Depending on its opinion, the ministry will decide on the amendment later this year, Krzemiński told *Nature*. ■

AUSTRALIA

Scientists oppose monkey import ban

Rush of protests against proposed Australian bill.

BY BIANCA NOGRADY

A bill calling for a ban on the import of non-human primates for medical research in Australia almost slipped under scientists' radar — but researchers have now rushed to argue against the proposal.

A Senate committee is considering the bill and will report in early March, before a possible debate and vote by the full Senate. That it is now publicly opposed by several scientific institutions worldwide is largely down to the efforts of neuroscientist Nicholas Price, who says that he was shocked to hear about it in late January.

Researchers had missed the legislative proposal when it was introduced in September 2015 as an amendment to Australia's federal Environment Protection and Biodiversity Conservation Act. This was because the committee that deals with this legislation is not usually of interest to those in the medical-research community, says Price, who uses marmosets and macaques in experiments at Monash University's Biomedicine Discovery Institute in Melbourne. By the time he heard about the proposed ban, from another researcher, the window for public comment was days away from closing (although it was later extended). Price and his Monash colleagues James Bourne and Marcello Rosa began e-mailing researchers around the world, and institutions rushed to submit statements of opposition.

Senator Lee Rhiannon, a member of the Greens party who trained as a zoologist and introduced the proposal, told *Nature* that her party is not calling for a ban on non-human primates in research. The bill is a "modest" way to improve the welfare of research animals, she says. But Price and Bourne say that cutting off access to the genetic diversity required to maintain Australia's three main breeding colonies would eventually lead to inbreeding, health problems and the end of the country's research on non-human primates.

Australia's Parliament may be dissolved for a general election before the bill makes it to a vote — as happened to a similar bill that Rhiannon introduced in 2012. Price says that the events have convinced him of a need to be more public about the importance of his work. "We feel that the majority of the public would be very supportive," he says. ■

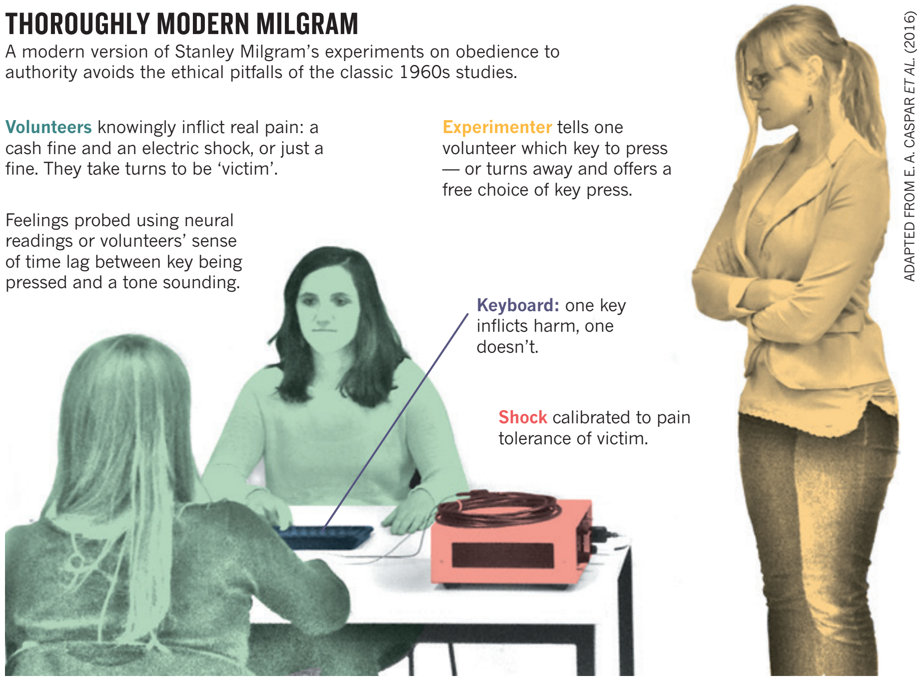

THOROUGHLY MODERN MILGRAM
A modern version of Stanley Milgram's experiments on obedience to authority avoids the ethical pitfalls of the classic 1960s studies.

ADAPTED FROM E. A. CASPAR *ET AL.* (2016)

PSYCHOLOGY

How the brain reacts to orders

Modern spin on iconic Milgram experiments suggests that people obeying commands feel less responsible for actions.

BY ALISON ABBOTT

More than 50 years after a controversial psychologist shocked the world with studies that revealed people's willingness to harm others on order, a team of cognitive scientists has carried out an updated version of these iconic 'Milgram experiments'.

The findings may offer some explanation for Stanley Milgram's uncomfortable revelations. When following commands, the team says, people genuinely feel less responsibility for their actions — whether they are told to do something evil or benign.

"If others can replicate this, then it is giving us a big message," says neuroethicist Walter Sinnot-Armstrong of Duke University in Durham, North Carolina, who was not involved in the work. "It may be the beginning of an insight into why people can harm others if coerced: they don't see it as their own action."

The study may feed into a long-running legal debate about the balance of personal responsibility between someone acting under instruction and their instructor, says Patrick Haggard, a cognitive neuroscientist at University College London, who led the work, published on 18 February (E. A. Caspar *et al. Curr. Biol.* http://doi.org/bcnj; 2016).

Milgram's work in the 1960s was motivated by the trial of Adolf Eichmann, a Nazi who argued that he was 'just following orders' when he sent Jews to their deaths. The latest findings don't legitimize harmful actions, Haggard emphasizes, but do suggest that the excuse of 'obeying orders' betrays a truth about how a person feels when acting under command.

In his experiments, Milgram told participants that a man was being trained to learn word pairs in a neighbouring room. The participants had to press a button to deliver an electric shock of escalating strength to the learner when he made an error; when they did so, they heard his cries of pain. In reality, the learner was an actor, and no shock was ever delivered. Milgram's aim was to see how far people would go when they were ordered to step up the voltage.

Routinely, an alarming two-thirds of participants continued to step up shocks, even after the learner was apparently rendered unconscious. But Milgram did not assess his

participants' subjective feelings as they were coerced into doing something unpleasant. And his experiments have been criticized for the deception that they involved — not just because participants may have been traumatized, but also because some may have guessed that the pain wasn't real.

Modern teams have conducted partial and less ethically complicated replications of Milgram's work. But Haggard and his colleagues wanted to find out what participants were feeling. They designed a study in which volunteers knowingly inflicted real pain on each other, and were completely aware of the experiment's aims.

Because Milgram's experiments were so controversial, Haggard says that he took "quite a deep breath before deciding to do the study". But he says that the question of who bears personal responsibility is so important that he thought it was "worth trying to do some good experiments to get to the heart of the matter."

In his experiments, the volunteers (all were female, as were the experimenters, to avoid gender effects) were given £20 (US$29). In pairs, they sat facing each other across a table, with a keyboard between them (see 'Thoroughly modern Milgram'). A participant designated the 'agent' could press one of two keys; one did nothing. But for some pairs, the other key would transfer 5p to the agent from the other participant, the 'victim'; for others, the key would also deliver an electric shock to the victim's arm. (The shock was calibrated to the participant, so that it was painful but bearable.) In one experiment, an experimenter stood next to the agent and told her which key to press. In another, the experimenter looked away and gave the agent a free choice about which key to press.

Whichever key was chosen, a tone sounded after a few hundred milliseconds, and both volunteers were asked to judge how long this took. Psychologists have established that people perceive the interval between an action and its outcome as shorter when they act of their own free will, for example to move their arm, than when the action is passive — having their arm moved by someone else. As a result, the time that the participant thinks has elapsed between the key press and the tone acts as a measure of their sense of being responsible for their actions.

When they were ordered to press a key, the participants perceived the time to the tone as longer than when they had free choice — as if their action had been passive.

In a separate experiment, volunteers followed similar protocols while electrodes on their heads recorded their neural activity through EEG (electroencephalography). When ordered to press a key, their EEG recordings were quieter — suggesting, says Haggard, that their brains were not processing the outcome of their action. Some participants later reported feeling reduced responsibility for their action.

Unexpectedly, giving the order to press the key was enough to cause the effects, even when the keystroke led to no physical or financial harm. "It seems like your sense of responsibility is reduced whenever someone orders you to do something — whatever it is they are telling you to do," says Haggard.

The study might inform legal debate, but it also has wider relevance to other domains of society, says Sinnot-Armstrong. For example, companies that want to create — or avoid — a feeling of personal responsibility among their employees could take its lessons on board. ■

CORRECTIONS

The News story 'Scientists probe Zika link to birth defects' (*Nature* **530,** 142–143; 2016) wrongly stated that at least seven countries have shown abnormal rates of microcephaly; this has happened only in Brazil. In addition, the article implied that 404 confirmed cases of microcepahly in Brazil could be linked to Zika virus — only 17 of those 404 have been linked so far. Finally, the correction note for the Editorial 'Blue future' (*Nature* **529,** 255–256; 2016) omitted to say that the carbon sequestration in question was by living organisms in the oceans.

SPECIAL ISSUE

A special issue examines whether researchers today consider the world of tomorrow — and why they should.

FUTURE GENERATIONS

The effects on distant tomorrows of the decisions we make today have never been greater. As we change our planet, ourselves and, potentially, our descendants, in ever more dramatic ways, this issue of *Nature* takes stock: do we have the brains and the tools to understand and account for the future and, if not, what should be done?

Technology experts foresee a world just a few decades away that is so radically different from today that it is hard to comprehend. The exponential rate of progress in a suite of enabling technologies, ranging from computer-processing power to communication, could drive drastic changes in artificial intelligence, robotics, molecular biology and more (see page 398).

Some think that the people who inhabit this world might also be irrevocably altered, for the first time, by genetic engineering. The arrival of the powerful genome-editing technology CRISPR–Cas9 might prevent children from being born with some deadly disorders or disabilities, and a feature on page 402 discusses the extent to which this is possible and desirable.

Forecasting is hard and fraught with bias. For example, as Nicholas Stern warns on page 407, current models of climate economics implicitly assume that lives in the future are less important than those today — a value judgement that is rarely scrutinized and difficult to defend. And, as Celine Kermisch writes on page 383, near and remote future generations have very different needs. Hundreds of social-science studies highlight the tensions between our tendencies to care about the well-being of others yet to favour current benefits over future ones. Therefore, on page 413, behavioural economists Helga Fehr-Duda and Ernst Fehr call for the design of sustainable-development policies and schemes that exploit these evolved behaviours.

Finally, John Bongaarts expresses the view on page 409 that the best thing we could do now for future generations is to ensure that there are fewer of them, by doubling the aid spent on family planning.

The only certainties are that tomorrow's world is difficult to predict, is heading straight for us, and that billions more people will inhabit it. How we account for future impacts in today's decisions should preoccupy researchers and policymakers more than it does now. ■

FUTURE GENERATIONS
A *Nature* special issue
nature.com/futuregenerations

ILLUSTRATION BY ANNA PARINI

TOMORROW'S

TECHNOLOGICAL CHANGE IS ACCELERATING TODAY AT AN UNPRECEDENTED SPEED AND COULD CREATE A WORLD WE CAN BARELY BEGIN TO IMAGINE.

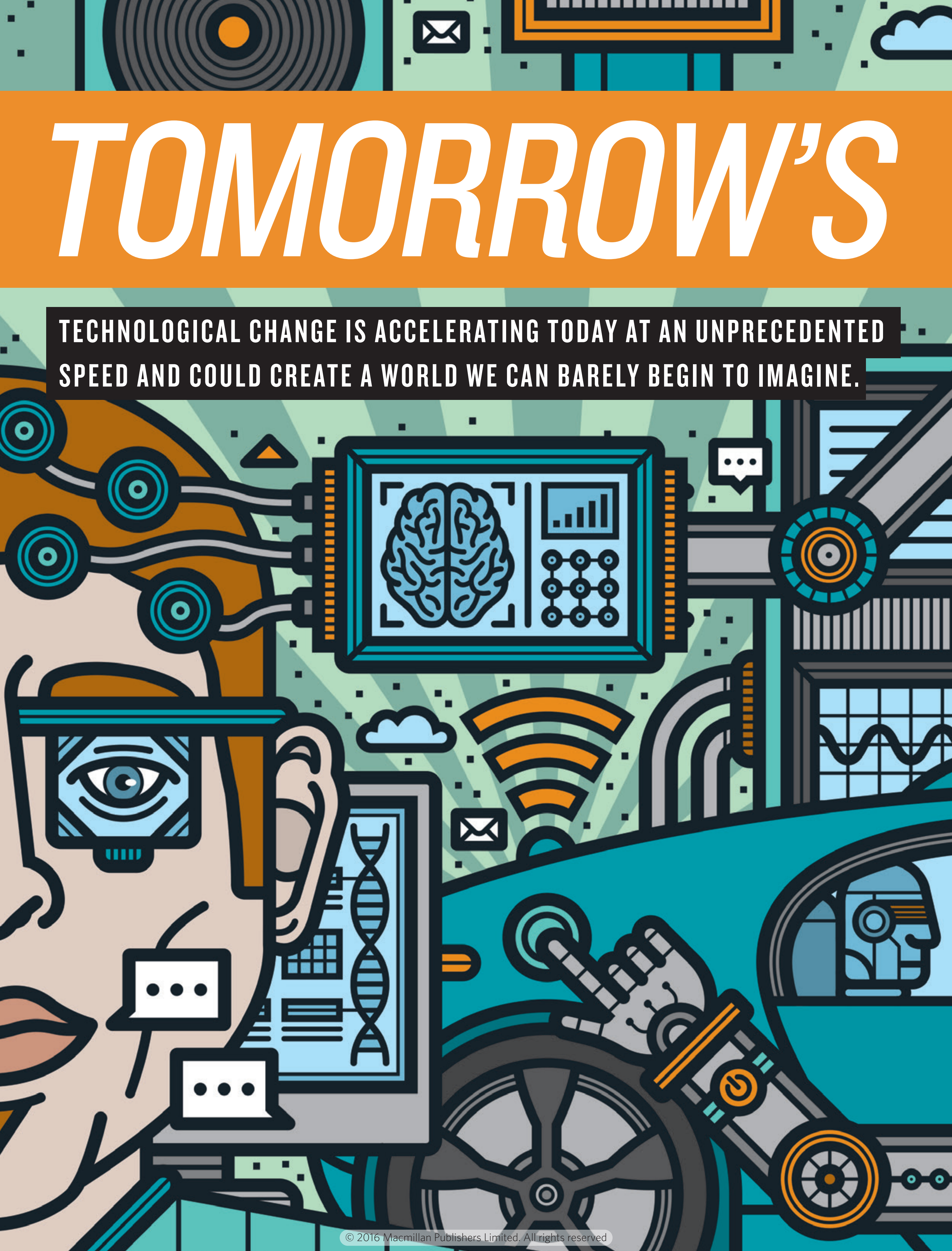

WORLD

BY DECLAN BUTLER

In March 2001, futurist Ray Kurzweil published an essay arguing that humans found it hard to comprehend their own future. It was clear from history, he argued, that technological change is exponential — even though most of us are unable to see it — and that in a few decades, the world would be unrecognizably different. "We won't experience 100 years of progress in the 21st century — it will be more like 20,000 years of progress (at today's rate)," he wrote, in 'The Law of Accelerating Returns'.

Fifteen years on, Kurzweil is a director of engineering at Google and his essay has acquired a cult following among futurists. Some of its predictions are outlandish or overhyped — but technology experts say that its basic tenets often hold. The evidence, they say, lies in the exponential advances in a suite of enabling technologies ranging from computing power to data storage, to the scale and performance of the Internet (see 'Onwards and upwards'). These advances are creating tipping points — moments at which technologies such as robotics, artificial intelligence (AI), biology, nanotechnology and 3D printing cross a threshold and trigger sudden and significant change. "We live in a mind-blowingly different world than our grandparents," says Fei-Fei Li, head of the Stanford Artificial Intelligence Laboratory in California, and this will be all the more true for our children and grandchildren.

WE LIVE IN A MIND-BLOWINGLY DIFFERENT WORLD THAN OUR GRANDPARENTS.

Kurzweil and others have argued that people find this pace of change almost impossible to grasp, because it is human nature to perceive rates of progress as linear, not exponential — much as when one zooms in on a small part of a circle and it appears as an almost straight line. People tend to focus on the past few years, but pulling back reveals a much more dramatic change. Many things that society now takes for granted would have seemed like futuristic nonsense just a few decades ago. We can search across billions of pages, images and videos on the web; mobile phones have become ubiquitous; billions of connected smart sensors monitor in real time everything from the state of the planet to our heartbeats, sleep and steps; and drones and satellites the size of shoeboxes roam the skies.

If the pace of change is exponentially speeding up, all those advances could begin to look trivial within a few years. Take 'deep learning', a form of artificial intelligence that uses powerful microprocessor chips and algorithms to simulate neural networks that train and learn through experience, using massive data sets. Last month, the Google-owned AI company DeepMind used deep learning to enable a computer to beat for the first time a human professional at the game of Go, long considered one of the grand challenges of AI. Researchers told *Nature* that they foresee a future just 20 years from now — or even sooner — in which robots with AI are as common as cars or phones and are integrated into families, offices and factories. The "disruptive exponentials" of technological change will create "a world where everybody can have a robot and robots are pervasively integrated in the fabric of life", says Daniela Rus, head of the Computer Science and Artificial Intelligence Laboratory at the Massachusetts Institute of Technology in Cambridge.

After decades in development, applications of AI are moving into the real world, says Li, with the arrival of self-driving cars, virtual reality and more. Progress in AI and robotics is likely to accelerate rapidly as deep-pocketed companies such as Google, Apple, Facebook and Microsoft pour billions of dollars into these fields. Gill Pratt, former head of the US Defense Advanced Research Projects Agency's Robotics Challenge, asked last year whether robotics is about to undergo a 'Cambrian explosion' — a period of rapid machine diversification (G. A. Pratt *J. Econ. Perspect.* **29,** 51–60; 2015). Although a single robot cannot yet match the learning ability of a toddler, Pratt pointed out that robots have one huge advantage: humans can communicate with each other at only 10 bits per second — whereas robots can communicate through the Internet at speeds 100 million times faster. This could, he said, result in multitides of robots building on each other's learning experiences at lightning speed. Pratt was hired last September to head the Toyota Research Institute, a new US$1-billion AI and robotics research venture headquartered in Palo Alto, California.

Many researchers say that it is important to prepare for this new world. "We need to become much more responsible in terms of designing and operating these robots as they become more powerful," says Li. In January 2015, a group including Elon Musk, Bill Gates and Stephen Hawking penned an open letter calling for extensive research to maximize the benefits of AI and avoid its potential pitfalls. The letter has now been signed by more than 8,000 people.

Yet predicting the future can be a fool's game — and not everyone is convinced that technological change will hit humanity quite so fast. Ken Goldberg, an engineer at the University of California, Berkeley, questions the idea that technologies advance exponentially across the board, or that those that do will continue indefinitely. "The danger of overly optimistic exuberance is that it could set unrealistic expectations and trigger the next AI winter," he says, alluding to periods in AI's history where hype gave way to disappointment followed by steep cuts in funding. Goldberg says that recent warnings that AI and robots risk surpassing human intelligence are "greatly exaggerated".

And Stuart Russell, a computer scientist at the University of California, Berkeley, questions the notion that exponential advances in technology necessarily lead to transformative leaps. "If we had computers a trillion times faster we wouldn't have human-level AI; half in jest, one might say we'd just get wrong answers a trillion times sooner," he says. "What matters are real conceptual and algorithmic breakthroughs, which are very hard to predict."

Russell did sign the Hawking letter — and says it is important not to ignore the ways that technologies could be taken in potentially harmful directions with profound results. "We made this mistake with fossil-fuel technologies 100 years ago — now it's probably too late." ■

Declan Butler **is a senior reporter for** Nature.

ILLUSTRATION BY GREYGOUAR

DRIVERS

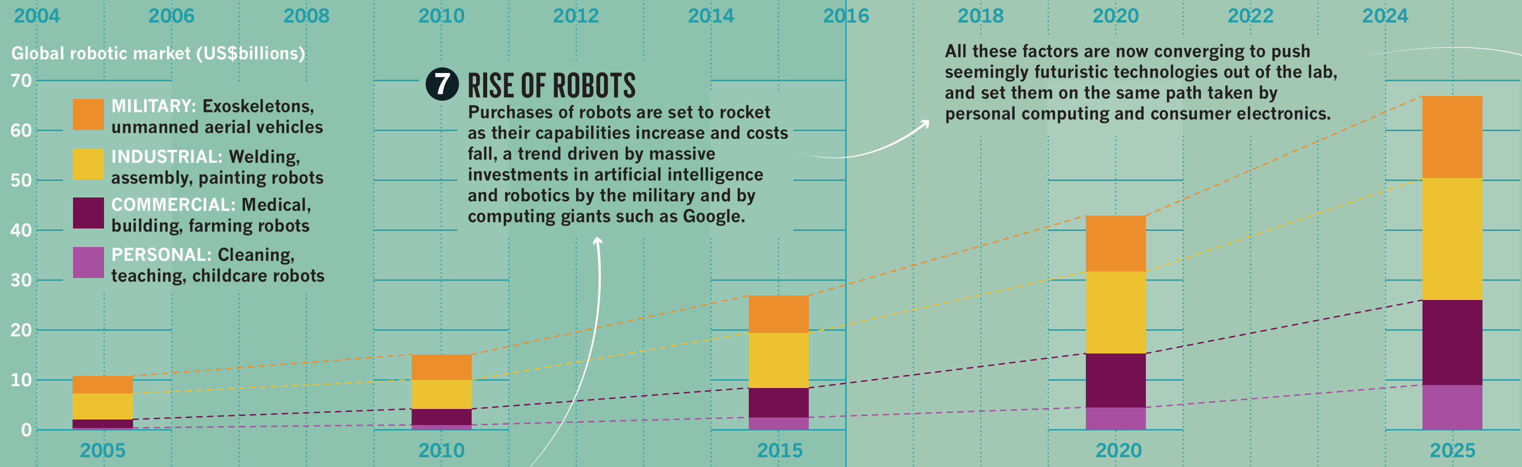

7 RISE OF ROBOTS

Purchases of robots are set to rocket as their capabilities increase and costs fall, a trend driven by massive investments in artificial intelligence and robotics by the military and by computing giants such as Google.

All these factors are now converging to push seemingly futuristic technologies out of the lab, and set them on the same path taken by personal computing and consumer electronics.

6 LIKE IT, PRINT IT

3D printing is becoming cheaper and quicker — one factor that could disrupt manufacturing and allow once-pricey robotics to be mass produced.

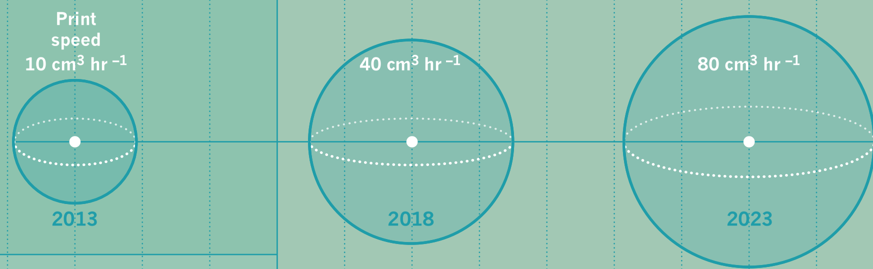

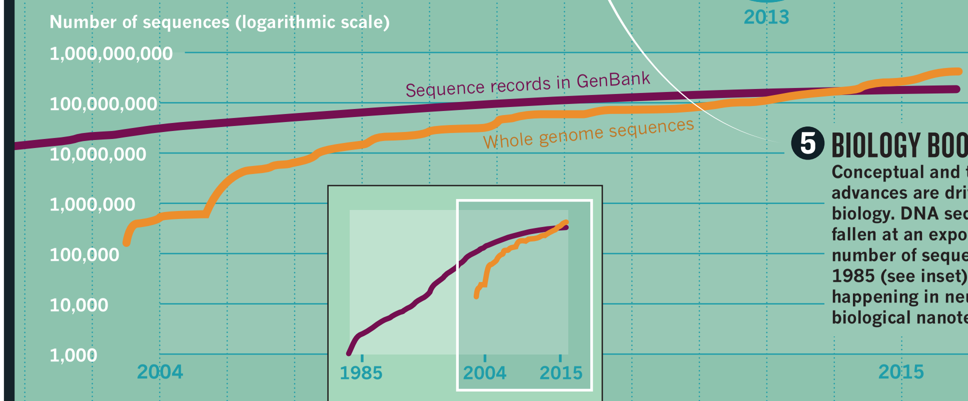

5 BIOLOGY BOOMS

Conceptual and technological advances are driving progress in biology. DNA sequencing costs have fallen at an exponential rate and the number of sequences has soared since 1985 (see inset). Similar advances are happening in neuroscience and biological nanotechnology.

4 TALKING DEVICES

By 2020, the number of connected sensors and devices in buildings, cities and farms — the 'Internet of Things' — will be twice that of the human population.

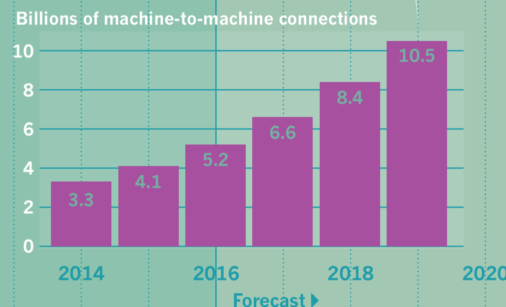

FUTURE FOCUS

Expert predictions

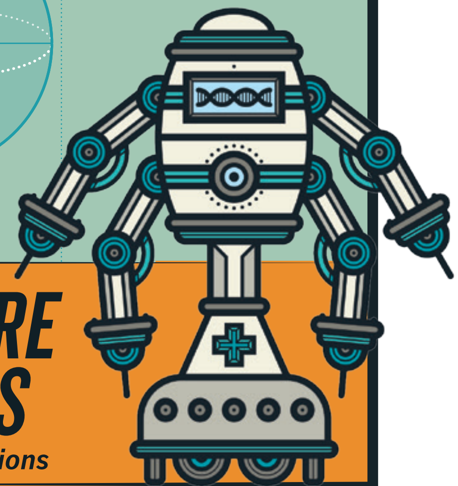

A possible 'Cambrian explosion' in robotics with a rapid period of incredible machine diversification. Robots communicating with each other at speeds that are 100 million times faster than humans might allow swarms of robots to build on each other's learning experiences at lightning speed.

GILL PRATT
Head of the Toyota Research Institute, Palo Alto, California

SOURCES: 4. CISCO VNI GLOBAL IP TRAFFIC FORECAST, 2014–2019; 5. NCBI; 6. EPSRC; DIRECT MANUFACTURING RESEARCH CENTER; ROLAND BERGER; 7. INTERNATIONAL FEDERATION OF ROBOTICS, JAPAN ROBOT ASSOCIATION; JAPAN MINISTRY OF ECONOMY, TRADE & INDUSTRY; EUROBOTICS; BCG.

ONWARDS & UPWARDS

BY DECLAN BUTLER / DESIGN BY WES FERNANDES

Exponential advances in enabling technologies have reached the point at which they could trigger disruptive change in sectors from artificial intelligence to robotics to medicine. As a result, many experts argue that tomorrow's world will be unrecognizable from that of today.

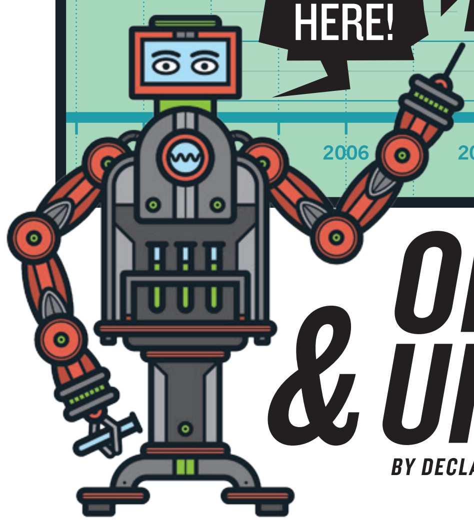

START HERE! ▸ ENABLERS

1 COMPUTING POWER
The exponential growth in supercomputing performance is one indicator of dizzying advances across computing.

Supercomputers in 2020 are likely to be 30 times more powerful than those of today.

2 REALLY BIG DATA
The amount of data worldwide is predicted to reach a whopping 44 zettabytes (10^{21} bytes) by 2020 — nearly as many digital bits as there are stars in the Universe. This gives more raw material for artificial-intelligence machines to learn from.

3 COMMUNICATION SPEED
Meanwhile, the performance and scale of the Internet improves. Broadband and WiFi speeds are increasing, and Internet data traffic will exceed a zettabyte this year and double by 2019.

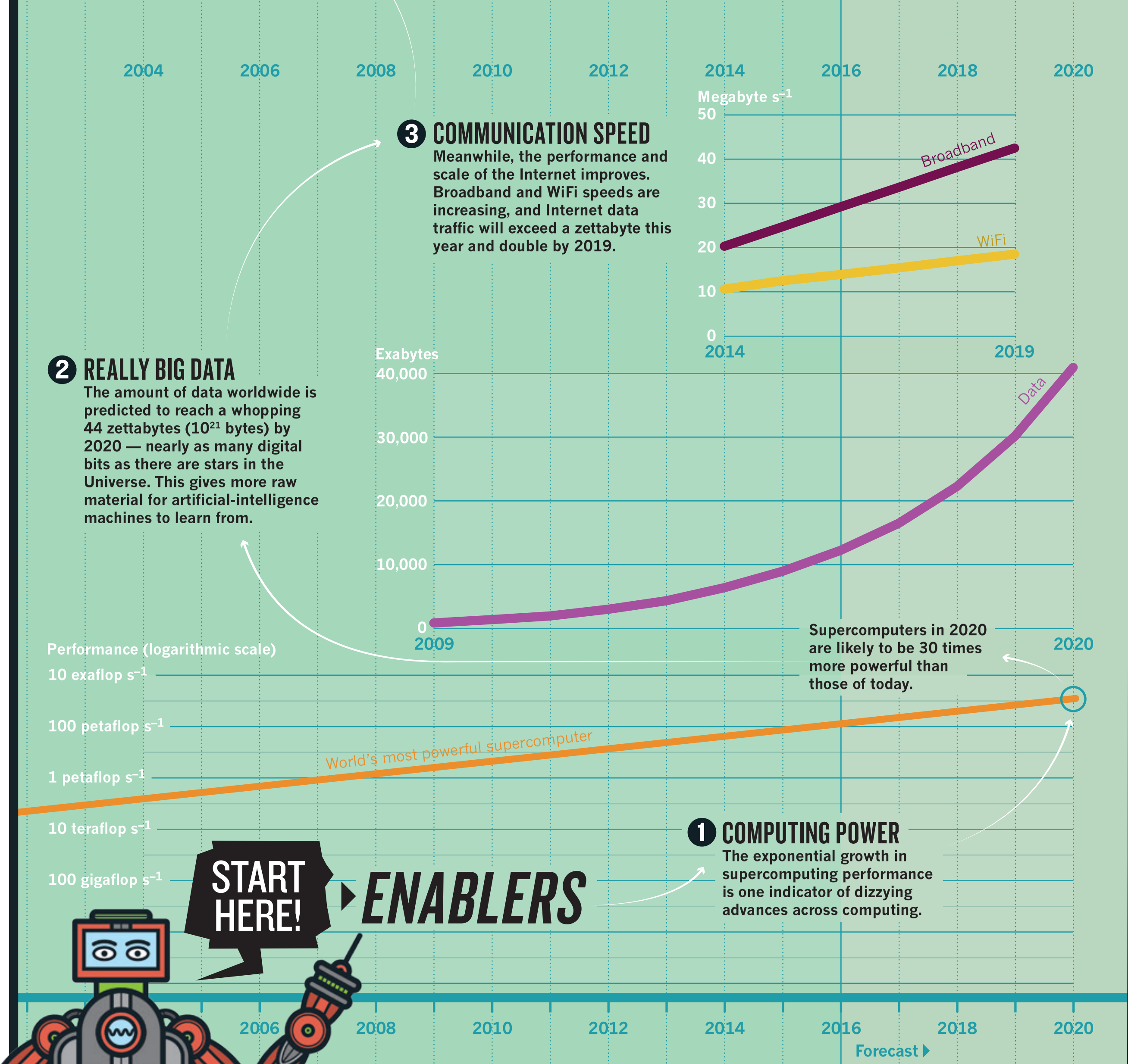

A full brain-activity map and connectome by 2020 and by 2040 it will be routine to read and write data to billions of neurons. By 2040, 1 billion people will have their whole genome sequenced and get constant updates of their immunomes and microbiomes.

GEORGE CHURCH
Geneticist at Harvard Medical School, Cambridge, Massachusetts

The promise for the future is a world where robots are as common as cars and phones, a world where everybody can have a robot and robots are pervasively integrated in the fabric of life.

DANIELA RUS
Head of the Computer Science and Artificial Intelligence Laboratory at the Massachusetts Institute of Technology, Cambridge

In the next couple of generations, we will see the first phase of true personal, assistive robots in the home and other human environments. There will be a huge opportunity to better the quality of life, for example by freeing up people from work.

FEI-FEI LI
Head of the Stanford Artificial Intelligence Laboratory, California

Tomorrow's scientists will have armies of virtual graduate students, doing lab work, statistical analysis, literature search and even paper-writing for them.

PEDRO DOMINGOS
Machine-learning researcher, University of Washington, Seattle

END HERE!

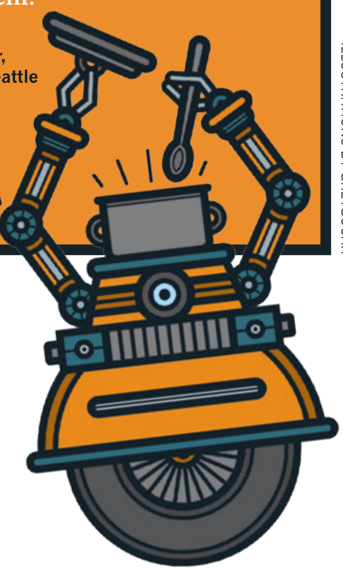

ILLUSTRATIONS BY GREYGOUAR

SOURCES: 1. TOP500; 2. IDC DIGITAL UNIVERSE STUDY, 2012; 3. CISCO VISUAL NETWORK INDEX (VNI), 2015.

Tomorrow's children

What would genome editing really mean for future generations?

BY ERIKA CHECK HAYDEN

Ruthie Weiss's basketball team seemed to be minutes away from its fourth straight loss. But even as she stood on the sidelines for a brief rest, the nine-year-old had not given up. She convinced the coach to put her back in the game. Then, she charged out onto the court, caught a pass from a teammate and drove straight to the basket. Swish! Ruthie scored a quick two points, putting her team in the lead. As the game clock wound down, she scored again, clinching the victory. The team had earned its first win of the season, and celebrated as if it had just taken the national championship. A couple of parents from the opposing team even stopped by to congratulate Ruthie, who had scored all of her team's 13 points: "Wow, she's unbelievable!" they told her mum and dad.

What makes Ruthie's performance even more extraordinary is her DNA. Because of a misspelling in one of her genes, she has albinism: her body produces very little of the pigment melanin, which means that her skin and hair are fair, and that she is legally blind. Her visual acuity is ten times worse than average. She is still learning to read

PRESTON GANNAWAY

Ruthie Weiss walks home from playing basketball with her father (centre) and uncle. Her sight problems have not prevented her from excelling at sport.

and will probably never be able to drive a car, but she can make out the basket and her teammates well enough to shoot, pass and play.

In January, Ruthie's dad Ethan asked her whether she wished that her parents had corrected the gene responsible for her blindness before she was born. Ruthie didn't hesitate before answering — no. Would she ever consider editing the genes of her own future children to help them to see? Again, Ruthie didn't blink — no.

The answer made Ethan Weiss, a physician–scientist at the University of California, San Francisco, think. Weiss is well aware of the rapid developments in gene-editing technologies — techniques that could, theoretically, prevent children from being born with deadly disorders or with disabilities such as Ruthie's. And he believes that if he had had the option to edit blindness out of Ruthie's genes before she was born, he and his wife would have jumped at the chance. But now he thinks that would have been a mistake: doing so might have erased some of the things that make Ruthie special — her determination, for instance. Last season, when Ruthie had been the worst player on her basketball team, she had decided on her own to improve, and unbeknownst to her parents had been practising at every opportunity. Changing her disability, he suspects, "would have made us and her different in a way that we would have regretted", he says. "That's scary."

Ethan and Ruthie are not the only people pondering these kinds of questions. The emergence of a powerful gene-editing technology, known as CRISPR–Cas9, has elicited furious debate about whether and how it might be used to modify the genomes of human embryos. The changes to their genomes would almost certainly be passed down to subsequent generations, breaching an ethical line that has typically been considered uncrossable.

But emerging technologies are already testing the margins of what people deem acceptable. Parents today have unprecedented control over what they pass on to their children: they can use prenatal genetic screening to check for conditions such as Down's syndrome, and choose whether or not to carry a fetus to term. Preimplantation genetic diagnosis allows couples undergoing *in vitro* fertilization to select embryos that do not have certain disease-causing mutations. Even altering the heritable genome — as might be done if CRISPR were used to edit embryos — is acceptable to some. Mitochondrial replacement therapy, which replaces a very small number of genes that a mother passes on with those from a donor, was approved last year in the United Kingdom for people who are at risk of certain genetic disorders.

Many safety, technical and legal barriers still stand in the way of editing DNA in human embryos. But some scientists and ethicists say that it is important to think through the implications of embryo editing now — before these practical hurdles are overcome. What sort of world would these procedures create for those currently living with disease and for future generations?

So far, little has been heard from the people who could be first affected by the technology — but speaking with these communities reveals a diverse set of views. Some are impatient, and say that there is a duty to use genome editing quickly to eliminate serious, potentially fatal conditions. Some doubt that society will embrace it to the degree that many have feared, or hoped. Above all, people such as Ethan Weiss caution that if policymakers do not consult people with disabilities and their families, the technology could be used unthinkingly, in ways that harm patients and society, today and in the future.

"Hearing the voices of people who live with these conditions is really important," says Tom Shakespeare, a medical sociologist at the University of East Anglia in Norwich, UK.

THE CASES FOR

John Sabine, now 60, was once described as one of the brightest legal minds of his generation in England. Now, he is in the advanced stages of Huntington's disease: he cannot walk or talk, is incontinent and requires constant care. Charles Sabine, his younger brother, carries the same genetic glitch that causes Huntington's disease, and therefore knows that, like his brother and his father before him, he is destined to undergo the same deterioration of brain and body.

Charles and his brother have five children between them, each of whom as a 50% chance of having inherited the mutation that causes Huntington's disease. To Charles — and to many others who live with the mutation that causes Huntington's — there is no legitimate ethical argument about whether gene editing should be used, either to treat people living with the condition now or to spare their children from it.

"Anyone who has to actually face the reality of one of these diseases is not going to have a remote compunction about thinking that there is any moral issue at all," Sabine says. "If there was a room somewhere where someone said, 'Look, you can go in there and have your DNA changed,' I would be there breaking the door down."

Matt Wilsey, a technology entrepreneur in San Francisco, would be there too. His daughter Grace was one of the first people in the world to be diagnosed with a disease caused by a mutation in the gene *NGLY1*, which makes it difficult for her cells to get rid of misshapen proteins. Grace, now six years old, has severe movement and developmental disabilities.

FUTURE GENERATIONS
A *Nature* special issue
nature.com/futuregenerations

She can barely walk and cannot talk. Because her condition is new to medicine, doctors cannot even predict how long she might live.

Wilsey is bullish on CRISPR. He says that if he had had the chance to detect and fix the mutation in Grace's genome before she was born, he would have. But he is frustrated that the debate over editing embryos seems to have monopolized discussions about the technology. He is hopeful that a gene-therapy-like approach using CRISPR, which would be free of the ethical concerns about altering the genes she passes on, could help Grace within several years. And he wonders whether a temporary moratorium on embryo editing might allow the field to focus on such approaches sooner.

"As a parent with an incredibly sick child, what are we supposed to do — sit by on the sidelines while my child dies? There's zero chance of that," Wilsey says. "CRISPR is a bullet train that has left the station — there's no stopping it, so how can we harness it for good?"

A meeting convened in December 2015 by the US national academies of sciences and medicine, the Chinese Academy of Sciences and the Royal Society of London recommended such a moratorium in light of multiple safety and ethical concerns. Still, many bioethicists and scientists have argued that if defects in single genes causing fatal and debilitating conditions could be corrected in an embryo, then they should be. Shakespeare notes that embryo editing for conditions that cause major disability and death are likely to raise less concern and criticism in the long term. But, he says: "As soon as you get away from the archetypal terrible condition, then you've got a debate about whether a condition makes life unbearably hard."

"These kinds of interactions significantly change our attitudes about what kinds of people matter in the world."

SOCIAL CONSEQUENCES

Many people are concerned about where that line would be drawn. Although it may seem now that only a few, very severe conditions should be subject to gene editing, disability activists point out that the list of conditions considered as illnesses, and possibly subject to medical treatment, is expanding. "More and more, people think of obesity or predisposition to alcoholism as disease," says Carol Padden, a linguist at the University of California, San Diego. She herself is deaf, and points out that many deaf people do not consider it a disability. This stance has led to controversy when, for instance, deaf parents decline technologies such as cochlear implants for their children, or even go so far as to select, through processes such as preimplantation genetic diagnosis, children who will be deaf.

Like Padden, some disability-studies researchers do not oppose the idea of gene editing, but do think that society needs to understand that it is not possible to eliminate all disability, and that humans might lose something important if they try to do so.

Padden points out that accommodations originally intended for people with disabilities often end up benefiting everyone. For example, the development of closed captioning — subtitles for the hearing-impaired on television — required major advocacy from the deaf community and legislative action to get off the ground in the United States in the 1970s. Today, people rely on it in ways that no one could have foreseen, such as in noisy airports and sports bars. Some people use it to learn to read or to learn a language.

Rosemarie Garland-Thomson, a literature scholar and co-director of the Disability Studies Initiative at Emory University in Atlanta, Georgia, adds that legislative mandates, such as the 1990 Americans with Disabilities Act in the United States, have helped to integrate people with disabilities into society — in workplaces, schools and other public spaces. As a result, the world is much more humane for everyone, says Garland-Thomson. "These kinds of interactions significantly change our attitudes about what kinds of people matter in the world."

The idea that parents should edit out characteristics that are considered debilitating goes against this drive towards inclusion, Garland-Thomson warns, and could create a harsher social climate for everyone. The experience of disability, she adds, is universal; all people inevitably experience sickness, accidents and age-related decline. "At our peril, we are right now trying to decide what ways of being in the world ought to be eliminated," she says.

Padden says that ethicists, patients and disabilities-studies researchers must work urgently to make a broad societal case in favour of greater acceptance of diversity. This has been a long-fought battle, and many see evidence of progress — for instance, in the 'neurodiversity' movement, which champions the idea that medical conditions such as autism are part of the spectrum of human variation. "We do have to start coming up with more arguments for diversity, and quickly, because CRISPR is coming upon us faster than some of us are thinking about this issue," she says.

MAKING CHOICES

The prospect of editing the genome of a human embryo is still in its early stages, but the ability to prevent the inheritance of some conditions already exists. Prenatal screening, which has advanced to the point that doctors can sample a developing fetus's DNA through its mother's blood, has given parents the option to terminate pregnancies when a disease or disability is diagnosed. This has already started to show limited effects on the population.

In Europe, for example, the prevalence of a Down's syndrome diagnosis during pregnancy has risen from 20 cases per 10,000 in 1990 to 23 cases per 10,000 today, as the average age of women having babies has increased. But the number of children born with the syndrome has stayed level at about 11 per 10,000, because many women whose fetuses are diagnosed with the condition terminate their pregnancies. In the United States, pregnancies in which a Down's syndrome diagnosis is made are terminated in 67–85% of cases.

By surveying women whose fetuses and babies are diagnosed with Down's syndrome, and by compiling similar surveys from around the world, medical geneticist Brian Skotko of the Massachusetts General Hospital in Boston has found that doctors sometimes advise women to terminate or give up for adoption babies diagnosed prenatally with Down's syndrome. They can influence the decision by using phrases such as "I'm sorry", or "I have some bad news to share"[1]. For instance, 34% of 71 Dutch women who terminated their pregnancy after a Down's syndrome diagnosis said that their doctors did not even mention the possibility of carrying the pregnancy to term when discussing their options[2].

Mark Leach, a lawyer in Louisville, Kentucky, whose 11-year-old daughter has Down's syndrome, says that he and his wife have been asked many times — especially when his wife was pregnant with their second child — whether they "knew beforehand" that Juliet would be born with Down's. (They didn't.) Some people are simply curious, Leach says, but for others, there's judgement in that question. "The ability to do something beforehand imposes a sense of, 'You should do not only what's right for you, but what's right for society'," Leach says. It bothers him, he says, that although government and private health insurers routinely pay for prenatal diagnosis, he recently learned that his school system is discontinuing support for the learning specialist who had been helping Juliet to thrive in mathematics and reading.

Dorothy Roberts, a professor of law and sociology at the University of Pennsylvania in Philadelphia, says that this kind of pressure is troubling and that it could get worse if embryo editing were to become readily available. "Women should not be given the responsibility of ensuring the genetic fitness of their children based on lack of support for children with disabilities."

Leach knows that children with disabilities can live rich lives. Juliet likes ballet dancing and horse-riding, and she is especially attuned to the names of people and animals whom she knows. And Leach says that she helps to remind other people how to care for others. "The main

thing that would be lost if Down's syndrome continues to diminish is a diminishment in the amount of compassion that is shown in this world," he says.

Even among people who already have life-threatening conditions, many choose not to interfere with the way the genetic cards are dealt. Edward Wild, a neurologist who cares for people with Huntington's disease at University College London, estimates that fewer than 5% of patients in the United Kingdom use preimplantation genetic screening to select embryos that lack the disease-causing mutation and so avoid passing it to their children. Some people do not know that they have the mutation; some decide against screening because of the costs or risks involved; some have personal or moral objections to the technique; and some just have a sense that 50–50 odds of passing down the disease are not so bad.

"Having kids the fun way is still much more popular than having kids the science way, even though the latter is how you guarantee the kid is free of Huntington's disease," Wild says.

Even if gene editing were safe, effective and everyone opted to use it, it would not eliminate genetic diseases, because researchers still have a long way to go to understand the genes involved. Even Huntington's, which is fairly well characterized, is no easy target. The glitch that causes it is a repeat of a particular genetic sequence; the more repeats, the more severe the symptoms, and repeats are added with each successive generation. New families are diagnosed with Huntington's all the time, either because the disease is misdiagnosed in older generations or because symptoms worsen, and become recognizable, in subsequent generations. Although he is working on genetic techniques to treat Huntingon's, Wild doesn't hold out high hopes for a future free of the disease. "Although it's nice to think about, it's little more than a dream," he says.

"Prediction: my grandchildren will be embryo-screened, germline-edited. Won't 'change what it means to be human'. It'll be like vaccination."

Human biology can complicate things in other ways. Padden notes, for instance, that some mutations that predispose to genetic disease, such as the sickle-cell mutation, confer population-level benefits, such as resistance to malaria. So editing out one disease could backfire by increasing the risk of another. She argues that very little is known about the potential benefits of other mutations associated with disease, and applying genome editing too freely could have unintended consequences.

And if it were adopted, the technology would almost certainly be applied unevenly around the world. Aleksa Owen, a sociologist at the University of Illinois at Chicago, predicts that genome editing would be used first in countries that approve of and support assisted reproductive technologies, such as the United Kingdom, some other European Union countries, China and Israel. But it would probably be too expensive for many people in developing countries.

UNEVEN ACCESS

Still, some scientists predict that editing human embryos could have transformative effects. During the National Academies' summit on gene editing in December, Harvard University geneticist Dan MacArthur tweeted, "Prediction: my grandchildren will be embryo-screened, germline-edited. Won't 'change what it means to be human'. It'll be like vaccination."

Sandy Sufian, a historian of medicine and disability at the University of Illinois, agrees with MacArthur that CRISPR has the potential to become widely adopted, both because of the perception that it would save money that would otherwise be spent caring for disabled people and because of people's fear of disability. But she questions the idea that eliminating such conditions will necessarily improve human life. Sufian has cystic fibrosis, a disease caused by mutations that render her lung cells more vulnerable to infection and disease. She spends 40 hours a week inhaling medicine to clear her lungs of mucus, exercising and undergoing physical therapy; others have to quit their jobs to make sufficient time for treatments. Yet given the option to edit cystic fibrosis out of her bloodline, Sufian wouldn't do it. "There are some great things that come from having a genetic illness," she says.

Garland-Thomson echoes that sentiment; she has one and a half arms and six fingers because of a condition called limb-reduction disorder. She says that she values traits in herself that she may have developed as adaptations to the condition: she is very sociable and wonders if that is because she's had to learn to work hard to make others feel comfortable around her. "Any kinds of restrictions or limitations have created the opportunity for me to develop work-arounds," Garland-Thomson says.

Shakespeare, who has achondroplasia, a genetic condition that causes shorter than average stature, says that people with disabilities are just as able to attain life satisfaction as others. "I have achieved everything I hoped for in life, despite having restricted growth: career, children, friendship and love." He wouldn't want to have altered his own genes to be taller, he says.

DISABILITY RIGHTS

People without disabilities consistently underestimate the life satisfaction of those with them. Although people with disabilities report a slightly lower overall quality of life than those without, the difference is small. One study[3] found that half of people with serious disabilities ranked their quality of life as 'good' or 'excellent'.

People also overestimate how severely health affects their happiness compared with other factors, such as economic or social support. One 1978 study[4], for instance, compared people who had recently become paralysed as a result of accidents with people who had recently won between US$50,000 and $1 million in a state lottery. Although people who had had accidents ranked their happiness lower than lottery winners, both groups predicted that their future happiness would be roughly equal, and people who had accidents derived more pleasure from everyday activities, such as eating breakfast or talking to a friend.

"A lot of this terrific science and technology has to take into account that the assumption of what life is like for people who are different is based on prejudice against disability," says Lennard Davis, a disability-studies researcher at the University of Illinois, who was raised by two deaf parents.

There is a common saying among people in the disability-rights community: "Nothing about us without us." People with disabilities argue that scientists, policymakers and bioethicists should take steps to ensure that the CRISPR debate reflects what is best for patients and their families, to ensure its most humane use now and for future generations.

At a minimum, they say, the investment in developing CRISPR should be matched by investments in innovations to help people who are already living with conditions that cause disability. And it is essential that people with the conditions that are up for consideration as possible CRISPR targets should be included in the decision-making processes.

For their part, Ruthie Weiss and her dad have already made up their minds. Ruthie must work harder than her classmates to do some routine activities. But when she is dominating the basketball court, or practising the piano, or skiing down a mountain, Ethan Weiss doesn't see a child with a disability. He sees his daughter making the most of her life, given all her strengths and challenges. And he knows that he wouldn't change a thing. ■

Erika Check Hayden *writes for* Nature *from San Francisco.*

1. Skotko, B. G. *et al. Am. J. Med. Genet.* **149A,** 2361–2367 (2009).
2. Korenromp, M. J., Page-Christiaens, G. C., van den Bout, J., Mulder, E. J. & Visser, G. H. *Am. J. Obstet. Gynecol.* **196,** 149.e1–149.e11 (2007).
3. Albrecht, G. L. & Devlieger, P. J. *Soc. Sci. Med.* **48,** 977–988 (1999).
4. Brickman, P., Coates, D. & Janoff-Bulman, R. *J. Pers. Soc. Psychol.* **36,** 917–927 (1978).

COMMENT

DEVELOPMENT Why minimizing population growth is the best investment in the future **p.409**

SUSTAINABILITY Tips for policymakers from behavioural economics **p.413**

LAW The US case that put eugenics on the map **p.418**

CONSERVATION Logging threatens Poland's primeval forest **p.419**

JONAS BENDIKSEN/MAGNUM

Sathkira District, Bangladesh, still flooded a year after 2009's Cyclone Aila.

Current climate models are grossly misleading

Nicholas Stern calls on scientists, engineers and economists to help policymakers by better modelling the immense risks to future generations, and the potential for action.

The twin defining challenges of our century are overcoming poverty and managing climate change. If we can tackle these issues together, we will create a secure and prosperous world for generations to come. If we don't, the future is at grave risk.

Researchers across a range of disciplines must work together to help decision-makers in the public, private and non-profit sectors to rise to these challenges. Economists, in particular, need more help from scientists and engineers to devise models that provide better guidance about what will happen if we succeed or if we fail.

As the 2015 Paris agreement on climate change made clear, we must achieve a net-zero carbon economy this century. Doing so will require policies that drive innovation, investment and entrepreneurship. The political will to make the necessary decisions depends partly on improving the analysis and estimates of the economics of climate change. Then the consequences of unmanaged global warming can be weighed much more transparently against the investments and innovations necessary to mitigate it.

Current economic models tend to underestimate seriously both the potential impacts of dangerous climate change and the ▶

FUTURE GENERATIONS
A *Nature* special issue
nature.com/futuregenerations

wider benefits of a transition to low-carbon growth. There is an urgent need for a new generation of models that give a more accurate picture.

DARK IMPACTS

The Fifth Assessment Report of the Intergovernmental Panel on Climate Change (IPCC), published in 2013 and 2014, provided a comprehensive overview of the literature on the costs of action and inaction. But the assessment understated the limitations of the research done so far. Essentially, it reported on a body of literature that had systematically and grossly underestimated the risks of unmanaged climate change. Furthermore, that literature had failed to capture the learning processes and economies of scale involved in radical structural and technical change, and the benefits of reducing fossil-fuel pollution, protecting biodiversity and forests, and so on.

The IPCC pointed out[1] that estimates of losses resulting from a 2 °C increase in mean global temperature above pre-industrial levels ranged from 0.2% to 2% of global gross domestic product. It admitted that the global economic impacts are "difficult to estimate" and that attempts depend on a large number of "disputable" assumptions. Moreover, many estimates do not account for factors such as catastrophic changes and tipping points.

It is these hard-to-predict impacts that are the most troubling potential consequences of inaction. The next IPCC report needs to be based on a much more robust body of economics literature, which we must create now. It could make a crucial difference.

Many estimates of economic losses are based on the outputs of integrated assessment models (IAMs). These models attempt to combine the key elements of biophysical and economic systems. This is a worthy endeavour. Sadly, most IAMs struggle to incorporate the scale of the scientific risks, such as the thawing of permafrost, release of methane, and other potential tipping points. Furthermore, many of the largest potential impacts are omitted, such as widespread conflict as a result of large-scale human migration to escape the worst-affected areas.

For instance, there is evidence that temperature increases of 1.5 °C and 2 °C would lead to differing extents of sea-level rise and extreme weather events[2], with obvious implications for small island states and coastal communities. These differences are simply not represented in the flawed estimates of economic losses.

IAMs are also used to calculate the social cost of carbon (SCC). They attempt to model the incremental change in, or damage to, global economic output resulting from 1 tonne of anthropogenic carbon dioxide emissions or equivalent. These SCC estimates are used by policymakers in cost–benefit analyses of climate-change-mitigation policies.

Because the IAMs omit so many of the big risks, SCC estimates are often way too low. As a first step, the consequences being assessed should include the damages to human well-being and loss of life beyond simply reduced economic output. And the very large uncertainty, usually involving downward bias, in SCC estimates should always be made explicit.

As the IPCC acknowledged[2], published SCC estimates "lie between a few dollars and several hundreds of dollars". These values often depend crucially on the 'discounting' used to translate future costs to current dollars. The high discount rates that predominate essentially assume that benefits to people in the future are much less important than benefits today.

"Discount rates are central to any discussion of our hand in the fate of future generations."

These discount rates are central to any discussion of our hand in the fate of future generations. Most current models of climate-change impacts make two flawed assumptions: that people will be much wealthier in the future and that lives in the future are less important than lives now.

The former assumption ignores the great risks of severe damage and disruption to livelihoods from climate change. The latter assumption is 'discrimination by date of birth'. It is a value judgement that is rarely scrutinized, difficult to defend and in conflict with most moral codes.

COSTING TRANSITION

The other role of IAMs — to estimate the costs of climate-change mitigation — also suffers from major shortcomings.

The IPCC's mitigation assessment[3] concluded from its review of IAM outputs that the reduction in emissions needed to provide a 66% chance of achieving the 2°C goal would cut overall global consumption by between 2.9% and 11.4% in 2100. This was measured relative to a 'business as usual' scenario. Clearly, growth itself can be derailed by climate change from business-as-usual emissions.

So the business-as-usual baseline, against which costs of action are measured, conveys a profoundly misleading message to policymakers that there is an alternative option in which fossil fuels are consumed in ever greater quantities without any negative consequences to growth itself.

Crucially, IAMs generally omit the potentially huge costs of air pollution from fossil fuels — which are saved if alternative fuels are used[4]. IAMs struggle to describe developments in alternative energy. They fail, in general, to capture the feedback loops in the innovation process that interact across the economy, prompting institutional and behavioural change, possible discoveries and economies of scale. There is empirical evidence, for example, that the geographical location of researchers and inventors can affect whether a firm chooses to do clean or dirty innovation.

The initial investment required to catalyse the transition to a low-carbon pathway might lead to great economic benefits in the long run. These could go well beyond avoided climate risks[5]. The knowledge spillover from low-carbon innovation into the wider economy — for instance, a battery developed for electric vehicles being used in wheelchairs — seems to be greater overall than that from high-carbon-energy technologies[6].

As engineers learn how to install, connect and repair technology cheaply, unit costs fall faster for many new technologies than for existing ones. This has already allowed solar-photovoltaic and onshore-wind technologies to become competitive with natural gas and coal in several locations, even without emissions taxation.

Also influential will be the emergence of new networks, such as the integration of electric-vehicle-energy storage into smart grids, as well as rapid technical progress. And these steps can be accelerated if, for example, consumers change behaviour and demand support for resource efficiency, recycling and pedestrianization. It is clear that much will depend on urban management and design; as cities grow rapidly, damaging infrastructure can become 'locked in'.

WHAT'S NEEDED?

There is much that can be done to make the assumptions in standard IAMs more realistic with respect to the scale and nature of damages[7,4]. But to give policymakers the reliable information that they need when implementing the Paris agreement, incremental improvements[7,8] to the present generation of IAMs may not be enough.

A comprehensive review of the problems of using IAMs in climate economics[5] called for the research community to develop a "third wave" of models. The authors identify various types of model that might offer advances. Two are: dynamic stochastic computable general equilibrium (DSGE) models, and agent-based models (ABMs).

Like current IAMs, DSGE models can explicitly account for uncertainty about the future through the introduction of shocks, for instance, to economic output, consumption or climate damages[9]. ABMs, by contrast,

seek to provide more-realistic representations of socio-economics by simulating the economy through the interactions of a large number of different agents, on the basis of specific rules. ABMs are widely used in finance, but have yet to be seriously applied to climate change. These are promising developments.

Now, a concerted effort is required by the research community to explore as many potential avenues as possible to better estimate the costs of action and inaction on climate change. The IPCC should distil what policymakers need to inform their decision-making. Learned societies and national academies must bring together researchers from a wide range of relevant disciplines to focus attention on improving economic modelling quickly.

Bangladeshi farmers and Cairo city-dwellers are at severe risk of flooding and storms; southern Europe and parts of Africa and the Americas are threatened by desertification. Perhaps hundreds of millions of people may need to migrate as a result, posing an immense risk of conflict.

There is huge potential in future technologies that can drive change. These are omitted or badly underestimated in our current climate modelling — deeply damaging our guidance for policymaking. The well-being and prosperity of future generations are worth more. ■

Nicholas Stern *is chair of the Grantham Research Institute on Climate Change and the Environment at the London School of Economics and Political Science (LSE), and president of the British Academy.*
e-mail: n.stern@lse.ac.uk

1. IPCC. *Climate Change 2014: Impacts, Adaptation, and Vulnerability. Contribution of Working Group II to the Fifth Assessment Report of the Intergovernmental Panel on Climate Change* (Cambridge Univ. Press, (2014).
2. Schaeffer, M. *et al. Nature Clim. Change* **2,** 867–870 (2012).
3. IPCC. *Climate Change 2014: Mitigation of Climate Change. Contribution of Working Group III to the Fifth Assessment Report of the Intergovernmental Panel on Climate Change* (Cambridge Univ. Press, 2014).
4. Stern, N. *Why are We Waiting?: The Logic, Urgency, and Promise of Tackling Climate Change* (MIT Press, 2015).
5. Aghion, P. *et al. Path Dependence, Innovation and the Economics of Climate Change* (Grantham Research Inst., 2014).
6. Dechezleprêtre, A., Martin, R. & Mohnen, M. *Knowledge Spillovers from Clean and Dirty Technologies: A Patent Citation Analysis* (Grantham Research Inst., 2013).
7. Dietz, S. & Stern, N. *Econ. J.* **583,** 574–620 (2015).
8. Gillingham, K. *et al.* National Bureau of Economic Research Working Paper No. 21637 (2015); available at http://dx.doi.org/10.3386/w21637
9. Golosov, M. *et al. Econometrica* **82,** 41–88 (2014).

GEORGE OSODI/PANOS

Oshodi market in Lagos.

Slow down population growth

Within a decade, women everywhere should have access to quality contraceptive services, argues **John Bongaarts**.

In 2100, our planet is expected to be home to 11.2 billion people. That's a more than 50% increase on today's 7.3 billion[1]. This expansion of humanity is likely to be spread unevenly across the world. In the most developed regions, we expect declines (such as in Europe and east Asia) or little further growth (as in the Americas; see 'Bulges, gaps and shifts'). Substantial further growth is anticipated in the least developed regions of south and west Asia (including in India and Pakistan) and north Africa (for example, in Egypt). By far the largest increase is projected in sub-Saharan Africa with a quadrupling of population — from just shy of 1 billion currently to 3.9 billion.

This potential addition of 4 billion people to the poorest regions of the globe is an obstacle to development that makes it difficult to be optimistic about their futures. Rapid population growth, with attendant consumption and waste, has pervasive adverse effects on societies ▶

and the world's ecosystems (see 'Four ways population rise takes its toll'). Many countries would be better off with lower population growth and birth rates. This is exemplified by the east Asian 'tiger' economies, including South Korea and Taiwan, that in recent decades have seen rapid increases in per capita incomes as birth rates declined. The boost to economic growth that follows a decline in fertility is referred to as the 'demographic dividend'[2].

So, how can the population juggernaut be stopped, or at least slowed?

WHAT CAN BE DONE

Since the 1960s, the main policy response to rapid population growth, alongside investments to improve education and health, has been the implementation of voluntary family-planning programmes[3]. To make contraception accessible, these programmes train staff, subsidize costs and develop distribution schemes — for example, clinics, drug stores and other delivery systems. Equally important, they provide education about the health and the socio-economic benefits of using contraception and having smaller families. The key reason for these programmes is to address the substantial level of unwanted and unplanned pregnancy, as well as an unsatisfied demand for contraception. About 74 million unplanned pregnancies occur each year in the developing world (39% of annual developing-world pregnancies). About half of these end in induced abortions[4].

Among the reasons for unwanted and unplanned pregnancies are low levels of female education, a lack of knowledge about and access to contraception, insufficient supplies and services, cost and fear of side effects. Just as problematic are opposition from spouses and other family members and traditional gender roles that support a desire for large families. To reduce unintended pregnancies, family-planning programmes must go beyond simply providing supplies and services; they must also reduce or eliminate these other obstacles.

The most persuasive evidence that such programmes work comes from field experiments, such as the one that began in 1977 in the Matlab region of Bangladesh[5]. A control area of Matlab received the same limited family-planning services as the rest of the country. An experimental area was provided with free services and supplies, home visits by well-trained female family-planning workers, and comprehensive media communication. Outreach to husbands, village leaders and religious leaders addressed potential social and familial objections.

> *"In particular, education of girls is a powerful brake on fertility."*

The results were clear-cut. Contraceptive use jumped from 5% to 33% among married women of reproductive age in the experimental area. In the control area, little changed. As a result, fertility declined rapidly in the experimental area. A difference of about 1.5 births per woman between the experimental and control areas was observed until 1990, and a smaller difference continued beyond 1996, when the experiment ended. Among the long-term consequences of this difference were the children in the experimental area being educated to higher levels, families having greater household assets, and the greater use of preventive health services. The experiment demonstrated that family-planning programmes can succeed even in highly traditional societies.

Contemporary evidence is fully consistent with the Matlab record. For example, countries that have suddenly implemented comprehensive family-planning programmes (such as Iran in 1989 and Rwanda in the mid-2000s) have seen rapid subsequent changes in reproductive behaviour.

Iran's fertility declined at an extraordinary pace from 5.6 births per woman in the late 1980s to 2.6 a decade later[6]. In Rwanda, fertility dropped from 6.1 in 2005 to 4.6 in 2010, and the proportion of married women using contraception jumped from 17% to 52%[7]. Both countries' information programmes shifted norms by including messages about the benefits of smaller families, raising the demand for family-planning services.

Any acceleration of fertility decline changes the trajectory of future population growth. This impact can be large, as demonstrated by a comparison of alternative United Nations population projections[1] for sub-Saharan Africa. With major investments in family planning, the fertility trajectory could easily be reduced by 0.5 births per woman within a few years after the start of the intervention. This would lead to a population of 2.8 billion in sub-Saharan Africa by 2100 (see 'Where will we be?'). That is around 1 billion fewer people than in the business-as-usual projection.

Family-planning programmes are most effective where socio-economic conditions

WHERE WILL WE BE?

By 2100, our planet is expected to be home to 11.2 billion people — over 50% more than in 2015.

SOURCE: REF. 1

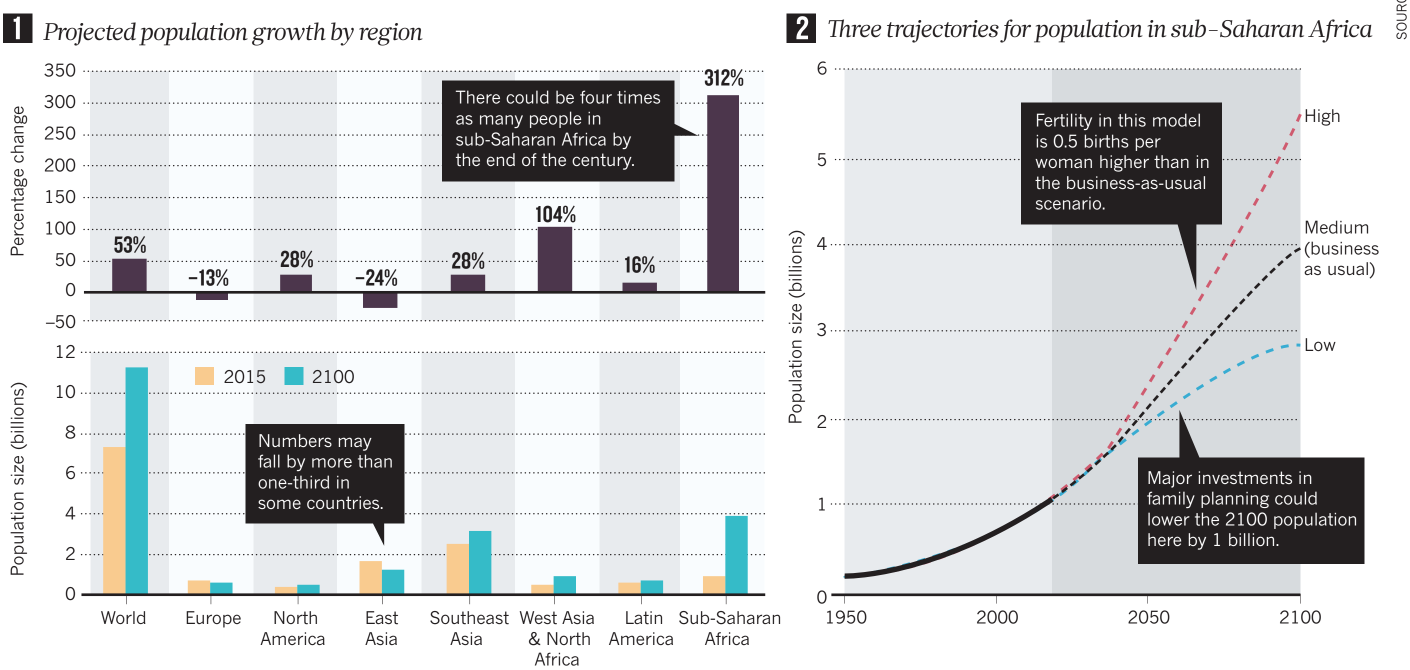

are improving. In particular, education of girls is a powerful brake on fertility. Educated women marry later, tend to want smaller families (in part, because the opportunity costs of childbearing are higher for these women) and are more capable of overcoming obstacles to their use of family planning. However, educated women must have access to contraception to act on their reproductive preferences. Family planning, education (of women and men) and socio-economic development are mutually reinforcing, and should be pursued together.

EVOLUTION OF SUPPORT

Family-planning programmes have been controversial, and support for them has fluctuated widely over the past half-century[3]. An initial surge of investment was made in the 1960s and early 1970s, as the UN and donor countries urged developing countries to address high fertility and rapid population growth. Several such countries accused the industrialized nations of making neo-colonial and imperialistic efforts to keep them weak and impoverished.

The Catholic Church, long opposed to artificial birth control and abortion, took an increasingly aggressive stance in opposition to government-sponsored family planning programmes worldwide. And when Republicans have occupied the White House, US lawmakers have also generally been unsupportive of international family-planning programmes — reducing funding and adding onerous restrictions.

Nonetheless, contraceptive use rose steadily in Asia and Latin America during the 1980s (see go.nature.com/r2oqrl). Then, in the 1990s, aid for family planning was diverted to fight the AIDS epidemic in Africa and elsewhere. Moreover, the fertility declines in Asia and Latin America led to optimism that population growth in Africa would soon slow.

Political and religious opponents were able to draw support for their views from a disagreement stirring in the academic literature: some economists argued that voluntary family-planning programmes are ineffective[8]. Conventional economic theory considers parents as people who want to maximize utility, and, who — within their budget — choose the number of children that they have in the same way that they might choose how many televisions or bicycles to buy.

An obvious problem with this reasoning is that durable goods require an active purchase, whereas pregnancies occur unless an effort is made to avoid them. Furthermore, economic theories also typically assume that the cost (monetary, social and practical) of contraception is sufficiently low so as not to influence decision-making. From this academic perspective, the occurrence of unwanted pregnancies should be as rare as people having unwanted new televisions; thus family-planning schemes should not be given priority.

Needless to say, that is not how things work in the real world. Avoiding unintended pregnancies is difficult even for women who use relatively effective methods and as a result, tens of millions of such pregnancies occur each year. Happily, the accumulating evidence of plummeting birth rates in a few countries (such as Ethiopia and Rwanda) has now largely persuaded policymakers of the cost-effectiveness of these programmes[9]. Religious and political opposition persists.

WHAT NOW?

To reduce rapid population growth and high birth rates, it is essential to start with a clear objective: within a decade, women everywhere should have access to quality

CARLOS CAZALIS/CORBIS

Over-65s make up more than one-quarter of Japan's population.

DEMOGRAPHIC TRENDS

Bulges, gaps and shifts

Ageing. The median age of populations is rising, especially in the developed world, as a consequence of lower birth rates and rising lifespans. Europe and Japan now host the highest proportion of people aged over 65. Further increase in this proportion is expected, putting enormous pressure on pension and health-care systems, and slowing economic growth.

Migration. The flow of people from poor and war-torn countries and continents to nearby developed ones (for example, from Africa and the Middle East to Europe) is rising. The tension this creates will grow as populations in poor countries rise, and while the economic disparities between sending and receiving countries remain large.

Low birth rate. In most developed countries and in a growing number of Asian and Latin American nations, women are having fewer than two children each — the level needed for long-term population stability. This causes population ageing and decline (for example, the populations of Eastern Europe and Japan will probably shrink by more than one-third by 2100). The near-absence of children to provide support will make life difficult for the elderly in countries where societal safety nets are weak (such as China).

Missing women. There are 100 million fewer women than naturally expected owing to sex-selective abortion and greater female mortality throughout life (for example, from female infanticide). In the past two decades, the number of such abortions has risen to about 1.5 million per year as a result of increased availability of low-cost ultrasound and genetic screening (to determine fetus sex), and greater access to methods for terminating pregnancies in countries that have strong cultural preferences for boys. These statistics document the widespread gender discrimination that still exists in many countries. An excess of single men may lead to social unrest and trafficking in women and girls.

GROWING PAINS

Four ways population rise takes its toll

Environmental degradation. Unprecedented global threats such as climate change and decreasing biodiversity have been building and will become more severe as populations, economies and consumption grow. Crucial local environmental problems — including shortages of fresh water and arable land, mounting waste, and air, water and soil pollution — adversely affect health and threaten the expansion of food production required to feed more people a better diet.

Economic stagnation. In poor societies, populations often double in size in two or three decades. Industries, offices, housing, schools, health clinics and infrastructure must be built at least at the same rate. Many communities are unable to keep up — as is evident from high unemployment rates, explosive growth of slum populations, overcrowded schools and health facilities and dilapidated public infrastructure (such as roads, sewage systems and power grids). Furthermore, in rapidly growing regions, about half[1] of the population is aged under 20. The low ratio of workers to dependents depresses living standards and makes it more difficult to invest in the physical and human capital needed. The size of the formal labour force is also limited when women remain at home to care for large families.

Maternal mortality. High birth rates mean frequent childbearing. Each pregnancy is associated with a risk of death or disability, and this is highest in countries with weak health-care systems. For example, in the poorest countries of West Africa, a woman's risk of dying in childbirth before the end of her reproductive years is about 1 in 20.

Political unrest. Youth unemployment becomes widespread when economies are unable to provide jobs. Vigorous competition for few jobs leads to low wages, which in turn contribute to poverty. Large numbers of unemployed and frustrated young men, in particular, fuel socio-economic tensions, high crime rates and political instability.

contraceptive services. Even in rural areas of poor countries, women should have the choice of multiple contraceptive methods — including not only pills, injectables and barrier methods, but also long-acting methods such as intrauterine devices and systems (IUDs and IUSs), implants and sterilization. Where legal, safe abortion services should be made available. Other obstacles to contraceptive use, such as incorrect rumours about side effects and conservative social attitudes, should be addressed by the education of women and men, media campaigns and collaboration with community leaders.

These efforts can be led by governments but better results are obtained when services are distributed through multiple channels, including private commercial providers and non-governmental organizations. Importantly, coercion of any kind should be ruled out. Women and men have the right to decide freely on the number, timing and spacing of children, and on the means to achieve their reproductive goals.

Achieving these aims requires substantially more resources than are available now. Funds are needed to build and equip clinics, to train and pay providers and to subsidize the direct cost of methods and services that are out of the reach of too many poor people. Over the past decade, investments in the developing world have risen, especially after the 2012 London Summit on Family Planning, at which many donors and governments renewed or increased their commitments.

Still, only 1% of all overseas development assistance (ODA) is now allocated to family planning[10]. This amount is inadequate; in too many countries, programmes remain weak and political commitment is lacking.

"Importantly, coercion of any kind should be ruled out."

The proportion of ODA allocated to family planning should be raised to 2% and developing-countries governments should expand their funding by an equivalent proportion. Such a doubling of funding will be more than repaid by savings in other sectors such as education and health care in future years.

FROM THE TOP

The final, crucial ingredient for success is political will and a commitment to family planning at the highest levels of national and international policymaking. A fundamental reason for the low priority assigned to the issue is that it is considered a health and human-rights problem.

Hence, family planning is part of the health budgets of donors and the responsibility for family-planning programmes is assigned to ministers of health throughout the developing world. Most poor countries are battling a range of diseases, and family planning is often not seen as a high health priority. From a broader development perspective, the low priority is nonsensical.

Several actions would remedy this situation. At the international level, development agencies and donors should hire more population experts (the World Bank, for example, employs thousands of economists but only a few demographers). These organizations write hundreds of reports on every dimension of development, yet only a fraction comment on population trends. Such reports should include a discussion of the role of demographic shifts in relevant sectors, of the development benefits of reduced birth rates and of the options available to change these trends.

At the national level, similar changes are needed. Typically, population trends are noted in government plans but are considered immutable and therefore of little interest. Ministries of finance or planning commissions often make detailed projections for specific sectors but rarely examine alternative population trajectories. They should. Economists at the Copenhagen Consensus Center, a think tank, last year ranked family planning as one of the most cost-effective development interventions (see go.nature.com/fumoop).

Family planning must be reclassified as a development intervention (as well as being a health and human-rights intervention) to give it the high national and global priority it deserves. This would lead to a more cost-effective use of scarce development resources, and to more rapid growth in living standards in poor countries. ■

John Bongaarts *is vice-president and distinguished scholar at the Population Council, New York City, New York, USA.*
e-mail: jbongaarts@popcouncil.org

1. United Nations Department of Economic and Social Affairs. *World Population Prospects: The 2015 Revision* (United Nations, 2015).
2. Bloom, D. E., Canning, D. & Sevilla, J. *The Demographic Dividend* (RAND Corporation, 2003).
3. May, J. F. *World Population Policies: Their Origin, Evolution, and Impact* (Springer, 2012).
4. Singh, S., Darroch, J. E. & Ashford, L. S. *Adding It Up: The Costs and Benefits of Investing in Sexual and Reproductive Health* (Guttmacher Institute, 2014).
5. Cleland, J., Phillips, J. F., Amin, S. & Kamal, G. M. *The Determinants of Reproductive Change in Bangladesh: Success in a Challenging Environment* (World Bank, 1994).
6. Abbasi-Shavazia, M. J. & McDonald, P. *Asian Pop. Stud.* **2,** 217–237 (2006).
7. Westoff, C. F., *Popul. Dev. Rev.* **38** (suppl. 1), 169–178 (2013).
8. Pritchett, L. *Popul. Dev. Rev.* **20,** 1–55 (1994).
9. Bongaarts, J., Cleland, J., Townsend, J., Bertrand, J. & Das Gupta, M. *Family Planning Programs for the 21st Century: Rationale and Design* (Population Council, 2012).
10. Wexler, A. & Kates, J. *Donor Government Assistance for Family Planning in 2014* (Kaiser Family Foundation, 2015).

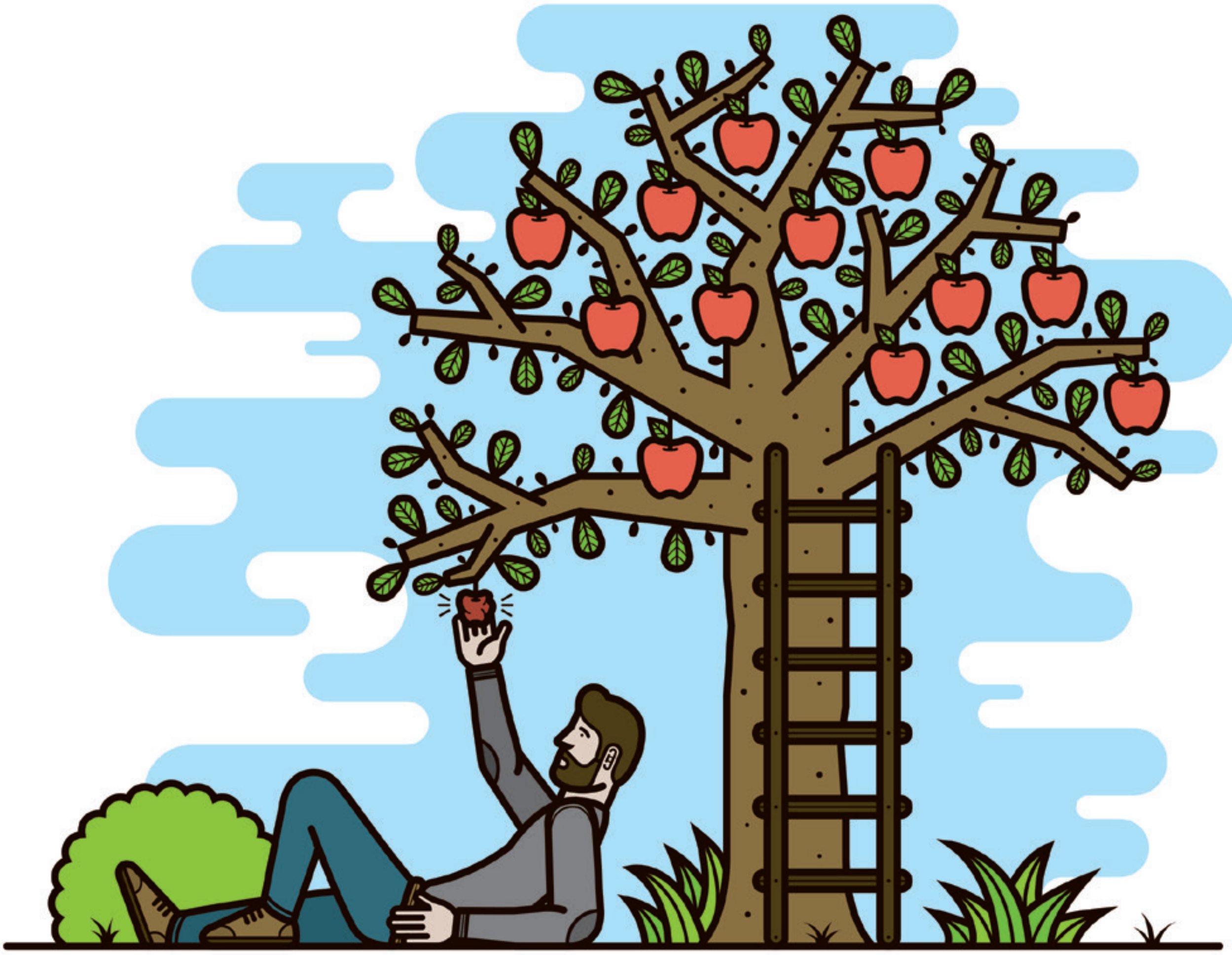

ILLUSTRATION BY GREYGOUAR

Game human nature

Finding ways to adapt natural tendencies and nudge collective action is central to the well-being of future generations, say **Helga Fehr-Duda** and **Ernst Fehr**.

Hundreds of studies in behavioural economics and other social sciences, conducted over the past few decades, have established that people often make choices that take into account the well-being of others. This contradicts an assumption held over centuries that people exclusively pursue their own material well-being. It also offers hope for the prospect of developing public goods (see 'Glossary: behavioural economics') that will benefit future generations.

However, another body of evidence, gathered over the past two or three decades, indicates that people display an array of other tendencies, such as giving excessive weight to current benefits over future ones. These could hamper policies and initiatives aimed at building or sustaining public goods.

The message emerging is that sustainable development will require the design of policies and schemes that specifically take advantage of some of our natural tendencies, and mitigate others.

SIX TENDENCIES

What does it mean to care about future generations? We posit that, by and large, future generations should be able to live as comfortably as do current generations in the developed world. This goal requires economic growth, at least in developing countries. It also requires current generations to hand down high-quality 'capital stock' — natural resources, scientific knowledge, infrastructure and sophisticated economic, legal and educational institutions. All of these types of stock are effectively public goods: everyone can enjoy them without necessarily having paid directly for them.

When it comes to the likelihood that investments in public goods will materialize, six behavioural tendencies come into play.

Other-regarding preferences. Public-goods experiments generally involve giving individuals in a group small sums of money that they can either keep for themselves or spend for the benefit of the group. Numerous such experiments, as well as field studies in real-world settings, have shown that many people have 'other-regarding preferences': their choices indicate that they care about things besides themselves, including the well-being of other people and the environment.

People with other-regarding preferences are often willing to share the burden of providing public goods as long as others do the same: they are 'conditional cooperators'[1]. Such people often care about social norms

and are willing to punish those who violate them[2]. They also tend to be concerned about what others might think of them. For instance, often the threat of being named publicly (within the group) as a defector is enough to keep such people cooperating in experiments.

There is considerable potential to leverage these tendencies for the benefit of future generations. The effect of social norms and conditional cooperation has been demonstrated by one of the largest-scale field experiments ever conducted. Since 2008, a US company called Opower has sent letters to customers of energy utilities, showing them how their electricity use compares with that of their neighbours. (Currently, 15 million households in 9 countries receive such letters.) This intervention generated a 2% reduction in energy consumption. A study of the company's three longest-running programmes shows persisting effects after mailings stop, but the energy savings decrease by 10–20% per year[3].

The emergence of smoking bans similarly provides a powerful example of what can be achieved through norm-altering collective action. Fifty years ago, smoking in public places was ubiquitous in Western countries. When it became clear that smoking causes serious cardiovascular and respiratory diseases in non-smokers as well as smokers, a new social norm emerged. About 20 years ago, many countries began to prohibit smoking in indoor public spaces, and even in outdoor ones.

Self-regarding preferences. Studies have also shown that there will always be some people who free-ride on the contributions of others. In public-goods experiments, for instance, some participants will stop contributing to the public good, but continue to reap the rewards from everyone else's contributions. Ultimately, the cooperation seen in these experiments tends to break down unless defectors can be punished by being made to pay money back to the experimenter[2].

Such detrimental effects of free-riding on the common good are demonstrated by the frequently frustrated attempts of individual political activists to overcome dictatorships. In these cases, free-riders might refrain from joining the opposition because (if the activists are successful), they stand to benefit without bearing the costs of fighting for political freedom.

Thus, although other-regarding preferences are a prerequisite for achieving sustainable development, uncoordinated changes to individuals' behaviours will not be sufficient. Political activists, for instance, will succeed only if they are able to turn their protests into a coordinated mass movement — as occurred in Tunisia in 2010 when civil resistance eventually led to the ousting of the country's president.

Delay-dependent risk tolerance. Other experiments have revealed that when evaluating the costs and benefits of a decision, people tend to be more tolerant of risk if their decision affects the future rather than the present[4] (see 'Time warp'). For instance, if people are given the choice of receiving \$100, or either \$0 or \$200 (with a 50% chance of receiving either), many will select the \$100 if they are told that they will receive the money immediately, but the more risky option if they will receive the money in a year's time.

Delay-dependent risk tolerance can account for why, globally, insurance coverage for natural disasters — perceived to occur in the distant future — is low relative to what is needed to prevent serious damage to a country or region's future economic growth. Between 1960 and 2011, nearly 60% of 'major natural catastrophes', those causing at least 100 fatalities and/or US\$250 million in direct losses (in 2011 dollars), were uninsured[5]. Even in high-income countries, only 50% of the damage resulting from catastrophes, such as earthquakes, tsunamis, floods and so on, were covered by insurance contracts[5].

These findings contrast sharply with the popularity of short-term accidental-death insurance policies sold at airports, which cover flight-related accidents, with the policy typically ending on completion of the flight. In the late 1950s and early 1960s, when such policies were still available at US airports, one group of underwriters insured potential losses of roughly \$651 billion (in 2015 dollars) from selling such policies, with a profit margin of almost 60%.

> *"Many people tend to be excessively impatient in the short term."*

This high tolerance of future risks and adversity to short-term risk suggests that investment in public goods that are relevant to climate change — such as tax increases to finance a shift to green-energy sources — will meet strong opposition from voters because the impact of such efforts is likely to be invisible for a long time, and the precise benefits are uncertain.

Feedback-dependent risk aversion. Experiments also indicate that people become more averse to risk if they expect to observe the outcomes of their decisions over the course of time. For instance, in one classic study[6], participants were asked to allocate 100 shares to two assets, one more risky than the other. Different groups of participants — informed about the performance of their shares either often or infrequently — could reallocate their shares on the basis of the feedback they had received.

Participants who received information more frequently invested nearly 60% of their shares in the less risky asset in the final round of reallocation, whereas those receiving information less often invested only about 30% of their shares in the lower-risk asset. In this case, the people following asset prices more closely are more likely to observe losses, and so tend to shy away from the riskier investments.

Such findings indicate that information that makes the costs of inaction visible — for instance, that global warming increases the occurrence of extreme weather events and the likelihood of wars — could significantly influence people's behaviour.

Short-term impatience. Numerous studies in behavioural economics and psychology have demonstrated that many people tend to be excessively impatient in the short term and give disproportionate weight to current benefits compared with future ones. For instance, if people are given the choice of receiving \$10 today but \$11 tomorrow, or \$10 in 100 days versus \$11 in 101 days, many will choose the smaller reward for the more immediate payment, but wait an extra

GLOSSARY: BEHAVIOURAL ECONOMICS

- A **public good** is a resource such as the atmosphere that individuals cannot be effectively excluded from using, and for which use by one person doesn't reduce the availability of the good to others.
- People who care about the well-being of others have **other-regarding preferences**.
- People who care only about their own material well-being have **self-regarding preferences**.
- **Conditional cooperators** will share the burden of providing public goods or comply with social norms that benefit the group as long as others do the same.
- People whose tolerance of risk depends on when in the future the consequences of their decisions will materialize show **delay-dependent risk tolerance**.
- People who become more cautious as a result of observing the outcomes of their decisions over time show **feedback-dependent risk aversion**.
- **Short-term impatience** is giving disproportionate weight to current benefits compared to future ones.

day for the larger reward in the second scenario. People also tend to be more averse to losses in the short term: current costs loom large, whereas future potential benefits have little bearing on today's decisions. Such behavioural tendencies explain why nearly one-third of people working in the United States have no retirement savings or pension, as found by a 2013 survey by the Federal Reserve's governors (see go.nature.com/kozp8q).

One way to deal with this bias is to shift benefits and costs across time. In the case of pensions, 'save more tomorrow'[7] or 'automatic escalation' plans commit employees to save a percentage of their incomes in the future. The pioneers of these schemes, economists Richard Thaler and Shlomo Benartzi, have reported that about 4.1 million people were participating in such plans in 2011, saving an extra $7.6 billion per year by 2014.

The basic principle of committing to a policy today but delaying the consequences is routinely used by politicians, for instance to increase retirement age without losing voters. This idea could be transferred to other arenas. For instance, policymakers and governments could commit some percentage of future increases in gross domestic product — and the associated tax hikes — to investments that benefit future generations. Although dependent on future economic growth, this would potentially increase the political acceptability of such investments by reducing the immediate burdens on the current generation.

The feasibility of this idea in relation to climate change has already been demonstrated. In 2008, people in Zurich, Switzerland, voted overwhelmingly to restrict their energy use to the levels of the 1960s by 2050 (a concept known as the 2,000-watt society). Today, Zurich residents use less energy than the average person in Switzerland, who in turn uses only about half of that used by most US residents.

Failure to carry through on intentions. A final insight from behavioural experiments and psychology studies is that people often fail to act on their intentions, be it because of inertia, inattention or the complexity of the task at hand. Take, for example, investments in energy-efficient appliances. Often, such investments provide net benefits to consumers because reduced operating costs more than offset higher purchase prices. However, worldwide, there is still a considerable gap between people's actual energy use and what it could be if they relied on the most efficient technology available to them — probably because people undervalue future cost savings. The consulting firm McKinsey estimates that, in the United States, $1.2 trillion could be saved by 2020 through use of more efficient technologies.

One way to address this 'resistance to switch' would be to convey information in a form that motivates people to change their behaviours. In most developed nations, energy labels showing information on running costs and efficiency are now provided on household appliances. Several small-scale field experiments suggest that labelling products with such information increases the likelihood that people will purchase a more efficient product. However, effects are small and may depend on the format of the information disclosed.

People's inertia could prove advantageous if, in a set of choices, the option favouring the public good requires no action. In many countries, the uptake of green-energy contracts has been 1% or less, even though in opinion polls, typically 50–90% of respondents say that they would use green energy if presented with a choice. A different picture has emerged in certain areas of Germany supplied by the utility company Energiedienst. In the Black Forest town of Schönau and in several communities in the south, green electricity is offered as the default option. And this is what customers use unless they take active steps to find a new supplier or choose a different contract. A 2008 study revealed that, in these communities, more than 90% of people were using energy from renewable sources such as solar or wind[8], even though in the short-term this is more costly than using electricity from coal, oil or gas.

In other words, people's unwillingness or inability to find and evaluate different options can be harnessed for the public good, while still protecting their freedom of choice.

TIME WARP

When people are told that they could get $0 (worst possible outcome) or $200 (best possible outcome) with varying probabilities now (yellow) or in a year's time (blue), they overestimate the likelihood of the best future outcome and underestimate the probability of the worst.

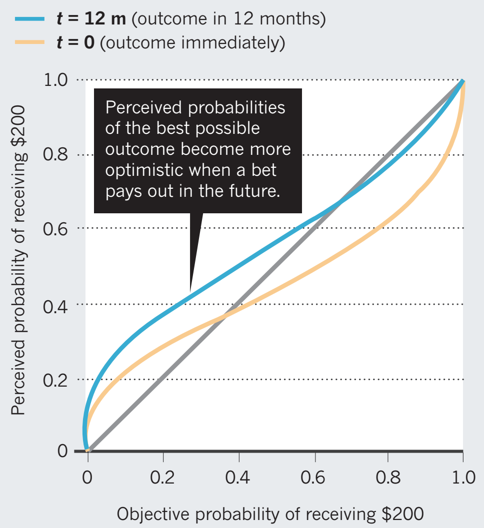

SOURCE: REF. 4

NURTURE OUR NATURE

The picture from behavioural and social science is clear. Nudges — such as commitments to save or invest future income increases — will be crucial to changing behaviour, and should complement conventional policies.

In the case of climate change, there are three principal take-home messages. First, conventional policy tools — such as taxing greenhouse-gas emissions — will be essential. Second, because people cooperate over the long term only if most others do as well, all key nations must be on board in international agreements[1]. Third, institutions for measuring and enforcing compliance — such as measures to monitor emissions and to verify national reports — will be needed[9].

Self-interest is a powerful force in human behaviour. But it is also part of our nature to care for others, including people who have not yet been born. Many examples in human history — from the abolition of slavery and the removal of dictatorships to the historical decline in violence and enforcement of human rights — demonstrate that it is possible to mobilize the better angels of our nature[10] to improve the human condition. ■

Helga Fehr-Duda *is professor of decision theory and experimental decision research at the University of Zurich, Switzerland.* **Ernst Fehr** *is professor of microeconomics and experimental economics at the University of Zurich, Switzerland.*
e-mail: helga.fehr@bf.uzh.ch

1. Fischbacher, U., Gächter, S. & Fehr, E. *Econ. Lett.* **71,** 397–404 (2001).
2. Fehr, E. & Gächter, S. *Am. Econ. Rev.* **90,** 980–994 (2000).
3. Allcott, H. & Rogers, T. *Am. Econ. Rev.* **104,** 3003–3037 (2014).
4. Fehr-Duda, H. & Epper, T. *The Missing Link: Unifying Risk Taking and Time Discounting* Working Paper No. 96 (Univ. Zurich Dept Econ., 2012).
5. vonPeter, G., vonDahlen, S. & Saxena, S. *Unmitigated Disasters? New Evidence on the Macroeconomic Cost of Natural Catastrophes* Working Paper No. 394 (Bank for International Settlements, 2012).
6. Thaler, R. H., Tversky, A., Kahneman, D. & Schwartz, A. *Q. J. Econ.* **112,** 647–661 (1997).
7. Thaler, R. H. & Benartzi, S. *J. Polit. Econ.* **112,** S164–S187 (2004).
8. Pichert, D. & Katsikopoulos, K. V. *J. Environ. Psychol.* **28,** 63–73 (2008).
9. Gollier, C. & Tirole, J. *Econ. Energy Environ. Policy* **4,** 5–27 (2015).
10. Pinker, S. *The Better Angels of Our Nature: Why Violence has Declined* (Penguin, 2011).

A hyena hunting flamingoes in Kenya.

EVOLUTION

Doing the locomotion

Kevin Padian assesses a study on how animals came to fly, wade, creep and glide.

It would be hard to find a more companionable guide to the marvels of locomotory evolution than Matt Wilkinson. In *Restless Creatures*, the zoologist and writer rehearses twice-told tales of animals becoming bilateral, exiting the sea for the land and evolving flight, but makes them fresh. These are wonderfully adept and informed explanations of locomotory modes — whether in birds, gliding snakes, eels, sharks or a host of fossil vertebrates — and there is not a single vignette that I failed to learn something from. His prose is knowing and wonky enough to sound as if it comes from the reincarnation of that senior lecturer you had who knew too much for most of the undergraduates, but was hip and amusing out of class.

Wilkinson's thesis is that locomotion drives the evolution of all other features. This is laid out in his introductory chapter, which begins by insulting most people with religious sensibilities: "Righteousness apparently requires that we take everything for granted." He then immediately takes natural selection for granted, declaring that "living things are as they are largely as a result of the process of adaptation". But he provides no demonstration of this, making it seem as if the only difference between the world views of science and religion is taste, because the believers of neither feel a need to test it.

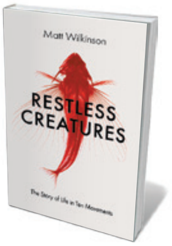

Restless Creatures: The Story of Life in Ten Movements
MATT WILKINSON
Basic: 2016.

Wilkinson does modify the claim that natural selection answers all questions about life by writing that it is only "sort of true", because it neglects the effects of mutations and the environment. But this is a 1960s view of evolution, of the kind propounded by Ernst Mayr. Yes, natural selection, mutation and environment are important. But there are also the inherited constraints of development, material properties and other functions of organisms, such as metabolism and reproduction, which are not necessarily optimized by natural selection. Sometimes they even work against it. The peacock's tail, for example, has long been thought (perhaps erroneously) to be a disadvantage in escaping predators quickly. The idea that the need for some form of locomotion has driven the whole evolution of plants and animals is a risky conceit.

But a deeper problem pervades *Restless Creatures*. About 40 years ago, evolutionary biologists such as Niles Eldredge and Joel Cracraft began to set hypotheses about the evolution of major features in phylogenetic context. Defining and dissecting an adaptation's components and then mapping them on an independently derived tree of relationships help us to visualize the sequence in which these traits arose, and therefore to test ideas of how functions evolved. We know that to fly, an animal does not need hollow bones or a perching foot. But it does need a wing capable of generating a specific kind of stroke, and the energetic and neuromuscular capacity to sustain flight. If you can work out in what sequence these traits appeared on a phylogenetic tree of the first members of a group, then your ideas about how flight evolved can become more explicit and testable.

But none of this is in Wilkinson's book. The older and ultimately unsatisfactory approach that he uses involves modelling (or

DENIS-HUOT/NATUREPL.COM

➲ NATURE.COM
For more on science in culture see:
nature.com/booksandarts

assuming) the functional efficiency of a structure in a single animal, and then imagining how natural selection would have shaped it. This is a good approach up to a point, but how do you know if you are wrong? One way is to check whether your hypothesis matches the phylogenetic pattern. But there is not a single phylogeny in this book to provide an independent test, even though that would provide a pictorial 'flow chart' to clarify the proposed direction of evolutionary change.

In the chapter on flight, on which he has published original research, Wilkinson begins by discussing some of the physical parameters (such as lift and drag) that constrain flight. This is straightforward and well written, although he does not sufficiently distinguish the kinematic and aerodynamic differences between gliding, flapping and other modes of flight. He assumes that all flying animals had gliding ancestors. But gliders such as the colugo and flyers such as bats are on completely different branches of the vertebrate tree — and their ecologies are completely different. Moreover, no one has convincingly shown how to transform a gliding wing into a flapping one, or that this ever happened. It cannot be assumed that stiff-limbed, quadrupedal gliders evolved the specialized flight stroke. This is why phylogeny matters.

Wilkinson acknowledges that opinion differs on the evolution of feathers, but he ignores the literature that has placed early feather types and their inferred functions — insulation, colour, brooding, inclined running and flight — in phylogenetic order (see R. O. Prum and A. H. Brush *Sci. Am.* **288,** 84–93; 2003). He does not explain the anatomy and functional morphology of flying animals, and pays little attention to kinematic studies of living animals that describe the uses of forelimbs and feathers (see, for example, K. P. Dial *et al. Nature* **451,** 985–990; 2008).

Restless Creatures runs the gamut from microorganisms to climbing primates (anthropoids, not clerics), although these are presented in no particular order. Wilkinson shows how locomotion is intimately related to breathing, metabolic rates, habitat and developmental genetics in a variety of groups. I was pleased that he also discusses the locomotion of pollen and seeds, because animal biologists so often ignore plants (see I. T. Baldwin *Nature* **522,** 282–283; 2015), even though they provide an alternate universe of evolutionary possibilities. There is a great deal in this book that is enjoyable and informative, but ultimately, I found it a less than satisfying guide to the evolutionary biology of locomotory studies. ■

Kevin Padian *is in the Department of Integrative Biology and the Museum of Paleontology of the University of California, Berkeley.*
e-mail: kpadian@berkeley.edu

Books in brief

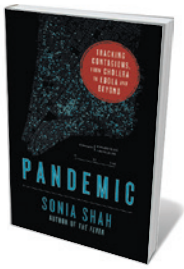

Pandemic: Tracking Contagions, from Cholera to Ebola and Beyond
Sonia Shah Sarah Crichton *(2016)*
Cholera — the acute bacterial infection that can kill in hours — serves as a lens on new pandemics in this grounded, bracingly intelligent study. As science journalist Sonia Shah reveals, more than 300 infectious diseases have emerged or re-emerged in the past half-century, and epidemiologists predict a catastrophic pandemic in the next. Shah lucidly layers history into a tour of transmission hotspots, from incubators of 'spillover' animal-borne illnesses such as China's wild-animal markets to globalized transport and hyperdense cities.

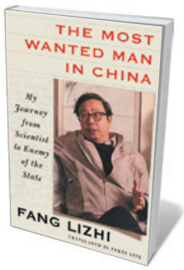

The Most Wanted Man in China: My Journey from Scientist to Enemy of the State
Fang Lizhi, translated by Perry Link Henry Holt *(2016)*
This memoir by late Chinese astrophysicist and dissident Fang Lizhi is a trenchant explication of science under siege. Fang learned English partly by studying Paul Dirac's 1930 *Principles of Quantum Mechanics*, and carved out a career at the University of Science and Technology of China. Although his youthful love for Communism withered during the forced labour and expulsions of the Cultural Revolution and beyond, Fang's "awe at the colossal thing called the universe" never waned, surviving surveillance and exile. Inspiring.

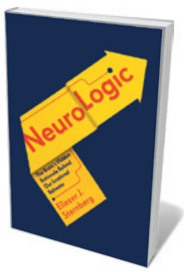

NeuroLogic
Eliezer J. Sternberg Pantheon *(2016)*
A man stumbling around in a brightly lit room insists it is dark. When a scan shows damage to his brain's visual monitoring as well as its processing system, his internal 'logic' is revealed. This case study is just one of many marshalled by neurologist Eliezer Sternberg for his research-rich study of the neurological circuitry behind the narratives we use to make sense of things. Sternberg cracks open the brain's "black box" to examine its parallel conscious and unconscious systems, and explores states from dreaming and acts on 'autopilot' to memory, hallucinations and trauma.

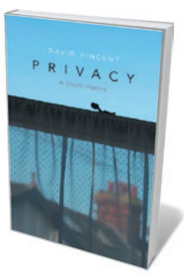

Privacy: A Short History
David Vincent Polity *(2016)*
Have the reports of privacy's demise been greatly exaggerated, or is it the dodo of our digitized world? Social historian David Vincent examines that question in this deft study of privacy in houses, cities, correspondence and surveillance, from 1300 to today. We peer into the "fugitive spaces" where medievals scratched epistles; the Victorian dichotomy of fortress-like abode and sociable public transport; and today's paranoia-soaked debates over digital media. Whether linked to ideas of sanctuary, secrecy or intimacy, privacy is a flashpoint in the charged relationship of individual to society.

Snowball in a Blizzard: A Physician's Notes on Uncertainty in Medicine
Steven C. Hatch Basic *(2016)*
How do you pinpoint a tumour in a mammogram? About as easily as you find a snowball in a blizzard, writes medical academic Steven Hatch in this penetrating examination of uncertainty in diagnoses and treatment. It is both constant, he shows, and ignored by physicians at their, and their patients', peril. He also shows why, looking in turn at issues such as false positives, mammography, hypertension treatments, drug trials and media reportage. **Barbara Kiser**

HISTORY OF SCIENCE

When eugenics became law

Victoria Nourse reviews a study on a historic US misuse of biology, the case of *Buck* v. *Bell*.

Eugenics is a well-known low point in the modern history of science. In the United States, from the late nineteenth century to the 1940s, credence was given to this pseudoscience focused on the notional 'improvement' of human populations by halting the reproduction of supposedly lesser genes. Less well known is the story of how US law rendered eugenics intellectually respectable across the world, supporting programmes from Canada to Sweden. Ultimately, this egregious failing led to the enforced sterilization of at least 60,000 US citizens, and was used by the Nazi regime to justify its own programme of sterilization and, later, extermination.

Adam Cohen's *Imbeciles* relates a key chapter in this story, the 1927 US Supreme Court case known as *Buck* v. *Bell*. The case began in September 1924, when Albert Priddy, head of the Virginia State Colony for Epileptics and Feebleminded, an asylum near Lynchburg, asserted that Carrie Buck, a teenage mother who had entered the asylum that June, was an "imbecile" — a term used at the time to signify intellectual disability. Priddy petitioned the asylum's board of directors to sterilize Buck.

Priddy's petition relied on a Virginia sterilization law that had become effective months earlier, and that Priddy himself had advocated for. At the time, almost half of US states had eugenics laws, but sterilization was considered dubious constitutionally. When Priddy died, his successor, John Hendren Bell, lent his name to the case. In 1927, the statute's constitutionality was affirmed by the Supreme Court, effectively reviving laws that even eugenicists had believed were unenforceable. Justice Oliver Wendell Holmes, in writing the decision, penned the now-famous phrase "three generations of imbeciles are enough", referring to Buck, her daughter and her mother. All three had been erroneously 'diagnosed' with mental disabilities; Buck's mother was also in the asylum.

Imbeciles is lively, accessible and, inevitably, often heart-wrenching. To historians of eugenics, much of the background and some of the characters will be well known. Eugenics champion Harry Laughlin (author of a tome on US eugenics law) and his fellow researcher Arthur Estabrook, who testified at Buck's trial, are two of them. Others include Priddy and Aubrey Strode, the lawyer and legislator who wrote the Virginia sterilization law.

Cohen is at his best when writing about Buck. Priddy claimed that she was a sexual 'degenerate' and 'feebleminded'. In fact, she was in the asylum because she had been raped and made pregnant by a relative of her foster parents. Thanks to research by evolutionary biologist Stephen Jay Gould and historian Paul Lombardo, author of *Three Generations, No Imbeciles* (Johns Hopkins University Press, 2008), we know that she had no disability. She was a poor, isolated victim of a social system that branded unmarried mothers as dangerous, and a punitive legal system.

Carrie Buck (left) and her mother Emma in 1924.

ARTHUR ESTABROOK PAPERS/SPECIAL COLLECTIONS AND ARCHIVES/UNIV. ALBANY SUNY

Cohen's account of the Supreme Court trial is illuminating. The law had been written to require fair legal procedures for the person sterilized, but Buck's hearing was entirely one-sided. Ludicrous testimony was admitted about Buck's child, then less than a year old. Cohen shows how Buck's lawyer, Irving Whitehead, was a fraud and imposter by today's standards, failing to ask questions that would help his client or to call witnesses on her behalf.

Buck was no match for Holmes, one of the most famous members of the 'Boston Brahmin' elite of the day. His pithy legal opinion reflected his personal enthusiasm for eugenics as a science. Sterilization, he implied, was consistent with liberty. It freed asylum inhabitants; otherwise, they would be interned all their lives to prevent them from procreating. As the fallacious thinking went, a sexually active, disabled individual would (in Holmes's words) sap the "strength of the state" by creating a lineage of disabled descendants.

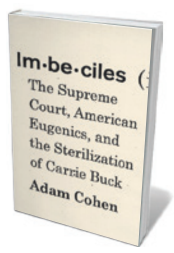

Imbeciles: The Supreme Court, American Eugenics, and the Sterilization of Carrie Buck
ADAM COHEN
Penguin: 2016.

Before *Buck* v. *Bell*, eugenic sterilization had been advocated for decades by US reformers and scientists, including prominent biologist Charles Davenport, but it had been used only sporadically because of fears that it was illegal. Eugenics itself was born in Britain in the late nineteenth century, nurtured by polymath Francis Galton, a half-cousin of Charles Darwin. The concept resonated with contemporary interpretations of 'social Darwinism', which hinged on engineering the 'survival of the fittest' — a gross caricature of Darwin's idea.

By 1928, a total of 375 US universities and colleges were teaching eugenics, and 70% of high-school biology textbooks endorsed the pseudoscience in some form. Eugenics was also endorsed by presidents including Theodore Roosevelt, funded by philanthropic organizations including the Carnegie Institution, and touted by award-winning scientists such as biologist Edwin Grant Conklin and the Nobel laureate Hermann Muller, discoverer of X-ray mutagenesis, as well as prominent inventors such as Alexander Graham Bell. Eugenics came to be seen as the solution to everything from hearing loss to criminality. In Britain, advocates tended to focus on segregation and voluntary sterilization. Major British eugenicists included left-leaning scientists J. B. S. Haldane and Havelock Ellis, and supporters included the economist John Maynard Keynes, social reformers Sidney and Beatrice Webb, and writer H. G. Wells.

In 1927, a month after her sterilization, Buck was released from the asylum as hired help, on a kind of parole. Later, she married. Her sister Doris was also sterilized; interviews suggest that she thought the operation an appendectomy. *Imbeciles* traces their later life in detail, noting one of the most poignant aspects of the case — Buck's letters to the asylum about her relatives and probationary status. These, Cohen notes, revealed Buck to be intelligent and diligent in trying to contact and protect her mother and child, who lived with a foster family: a testament to one of the most spectacular miscarriages of justice in US history. To this day, the Supreme Court has never officially overruled *Buck* v. *Bell*. ■

Victoria Nourse *is professor of law at Georgetown University, Washington DC.*
e-mail: vfn@law.georgetown.edu

Correspondence

Starlings' patterns are not spontaneous

You incorrectly use the flocking of starlings in murmurations to illustrate the concept of 'active matter' in determining the physics of life (*Nature* **529,** 16–18; 2016). This behaviour depends on information conveyed from individuals beyond a bird's immediate neighbours — unlike the spontaneous patterns formed in active matter from independently moving units.

In addition to information about the flight of their near neighbours, starlings use their location in the flock to adjust their murmuration behaviour (D. J. G. Pearce *et al. Proc. Natl Acad. Sci. USA* **111,** 10422–10426; 2014). The flock provides this information by projecting a 'shadow' of its surrounding density on each bird's retina. This lets the starling know whether it is on the edge of the flock or not, and safe or not from predators.

The starlings' behaviour is more akin to the idea of reflexivity (see G. Soros *J. Econ. Methodol.* **20,** 309–329; 2013). In reflexivity, individuals act in response both to the behaviour of those immediately around them and to the sociological effect of interacting as a collective entity — in this case, the flock. Like humans, a group of starlings seems to interact by using non-local sociological information to shape individual behaviour.

John Skoyles *University College London, UK.*
j.skoyles@ucl.ac.uk

Ancient forest: spare it from clearance

The Białowieża Forest on the borders of Poland and Belarus is the last lowland primeval forest in Europe that is still governed by natural processes. It is now under threat from logging on an unprecedented scale, proposed by the new Polish government ostensibly to halt an outbreak of European spruce bark beetle (*Ips typographus*). We argue strongly for Białowieża's preservation: it provides a much-needed ecological blueprint for restoring ancient forests, and a unique laboratory for investigating the effects of global change.

The government's proposed measures are to be included as an update to Poland's 10-year forest management plan, which in 2012 set timber extraction at 48,000 cubic metres annually. This limit was enough to meet the needs of local communities and to maintain spontaneous ecological processes.

The planned large-scale felling and salvage logging of infested trees ignores the bark beetle's keystone role in shaping the long-term dynamics and structure of forests (see B. Beudert *et al. Conserv. Lett.* **8,** 272–281; 2015). Moreover, to contain the outbreak, it would be necessary to log 80% of infested trees (L. Fahse and M. Heurich *Ecol. Model.* **222,** 1833–1846; 2011), which would mean violating the 35% of forest area that is protected. It is notable that only 57% of the stipulated harvest refers to spruce, the bark beetle's host tree species.

Przemysław Chylarecki *Museum and Institute of Zoology, Polish Academy of Sciences, Warsaw, Poland.*
Nuria Selva *Institute of Nature Conservation, Polish Academy of Sciences, Kraków, Poland.*
pch@miiz.waw.pl

Ancient forest: keep the logging ban

Poland's new conservative government is planning to lift a moratorium on the logging of old-growth trees in the primeval Białowieża Forest, amid mounting opposition from the Polish Academy of Sciences, ecologists and activists.

Divided between Belarus and Poland, the 1,500-square-kilometre forest is the largest remaining part of a vast, 8,000-year-old temperate forest that blanketed the European lowland (see *Nature* **455,** 277–280; 2008), and is a World Heritage Site.

The forest supports the largest population of European bison (*Bison bonasus*), as well as wolves, lynxes and some 120 species of breeding bird, including the lesser-spotted eagle (*Clanga pomarina*) and the three-toed woodpecker (*Picoides tridactylus*).

Poland's new environment minister, Jan Szyszko, backed by the logging lobby from Poland's state forests (see go.nature.com/dcjp2x; in Polish), claims that the forest is "rotting away". He proposes a 33-fold increase in logging.

Although the changes do not affect the small Białowieża National Park directly, the forest's remaining old growth will disappear from the buffer zones within a couple of years and jeopardize this unique ecosystem's sustainability.

Pawel Michalak *Virginia Polytechnic Institute and State University, Blacksburg, USA.*
pawel@vbi.vt.edu

Cochrane reviews expose bias too

Cochrane is an international network of health professionals, patients and others who summarize data from research studies in systematic reviews to help users to make informed decisions about disease treatment, prevention and screening (go.nature.com/z5w5ah). The model we use to accomplish this in the Cochrane Eyes and Vision (CEV) US group can also expose errors of the type noted by David Allison and colleagues (*Nature* **530,** 27–29; 2016).

In this group, clinician authors partner with a methodology 'hub' of experts who check data and apply validated methods in conducting the systematic review. These experts are trained to identify potential biases and statistical errors in reviews, and to expose what seem to be deliberate reporting biases or manipulation of outcomes.

The experts can identify errors in primary studies and draw attention to them, but cannot correct existing errors. Content experts need to collaborate with methodologists to eliminate mistakes at the outset, by designing and doing studies at a low risk of bias. Journal editors should insist that authors adhere to reporting standards. And the public must demand that health-care decisions are underpinned by conclusive scientific evidence.

Kay Dickersin, Tianjing Li *Johns Hopkins Bloomberg School of Public Health, Baltimore, Maryland, USA.*
kdicker3@jhu.edu
Competing financial interests declared (see go.nature.com/31fu47).

That's quite a collection

Your caption under the photo of testy entomologist Harrison Dyar that accompanies the review of Marc Epstein's biography (*Nature* **529,** 152–153; 2016) credits Dyar with having collected "500,000 different kinds of mosquitoes over his career". Given that there are still only about 3,000 species of mosquito known worldwide today, this seems a bit of a stretch.

Dyar may have collected 500,000 specimens, but not 500,000 different kinds.

Rick Borchelt *College Park, Maryland, USA.*
rborchelt@gmail.com

CORRECTION

The Correspondence 'No myth: benefits of breast screening' (*Nature* **529,** 283; 2016) omitted a declaration of competing interests. This has been added to the online version.

AUTOIMMUNITY

Antigen-specific immunotherapy

Nanoparticles coated with fragments of the body's own proteins are shown to induce T cells of the immune system to adopt regulatory functions that suppress autoimmune reactions involving these self-antigens. SEE ARTICLE P.434

DAVID WRAITH

Autoimmune diseases arise when our immune system attacks our own tissues. The immune cells of affected individuals are insufficiently tolerant towards certain 'self' proteins and attack them as if they were foreign. Helper T cells (T_H cells) play a central part in autoimmune diseases because they orchestrate the function of other cells in the immune system, including B cells, cytotoxic T cells and macrophages. Current treatments for autoimmune diseases tend to suppress the whole immune system or, at best, inhibit the movement or function of T cells; such approaches inevitably increase the risk of infection and cancer. The ideal treatment for autoimmune diseases would convert the function of T_H cells from disease-causing to disease-regulating without affecting the rest of the immune system. In this issue, Clemente-Casares *et al.*[1] (page 434) describe coated nanoparticles that mediate this conversion by binding to receptors on potentially self-reactive T cells.

The authors' approach can be considered as a type of antigen-specific immunotherapy. Antigens are the molecular structures that induce the activation of T or B cells; for T cells these are generally small fragments of proteins (peptides). Each T cell can express a different surface receptor, thereby allowing our immune system to respond to countless different antigens, including self-antigens. Antigen-specific immunotherapy is designed to dampen the immune response to a particular antigen or set of closely associated antigens. This concept has been used to treat allergies for more than a century[2], but specific immunotherapy for autoimmune diseases lagged behind until the discovery that T_H cells are activated by peptides bound to MHC class II proteins. This led to the design of peptides that selectively target T_H cells without risking the activation of self-reactive cytotoxic T cells or B cells[3].

How can exposure to a peptide known to stimulate self-reactive T_H cells switch off the disease they cause? This is best explained by the 'two-signal' rule of T-cell activation[4,5]. All antigens, whether self or foreign, must be broken down into peptides, which must then bind MHC class II proteins and be displayed at the surface of antigen-presenting cells (APCs) to activate T_H cells. This is referred to as signal 1. The APC must also upregulate co-stimulatory molecules, such as CD80 and CD86, to provide the second signal required for T_H-cell survival and proliferation.

What happens when T_H cells receive signal 1, but not signal 2? Historically, this was thought to induce a state of unresponsiveness known as anergy[6]. Now, Clemente-Casares *et al.* show that treating T_H cells with nanoparticles coated with a peptide bound to MHC class II proteins (pMHC-NP treatment) triggers signal 1 alone. But rather than simply inducing anergy, the treatment drives the T_H cells to differentiate into cells that have characteristics of regulatory T cells; these act to dampen immune responses.

The resulting regulatory cells exert their function by secreting the anti-inflammatory proteins IL-10 and TGF-β. Furthermore, the cells express the transcription factor T-bet and make the cytokine signalling molecule IFN-γ during their differentiation. These characteristics imply that they derive from cells of the T_H1 subset of T_H cells (Fig. 1). The differentiation of IL-10-secreting T cells — referred to here as T_R1-like cells — from T_H1 cells is an immunoregulatory mechanism known to prevent excessive immune responses to a range of infections[7–9]. These cells mediate a negative feedback mechanism involving suppression of co-stimulatory molecules on APCs and a reduction in the inflammatory proteins secreted by APCs[10].

What are the downstream effects of the

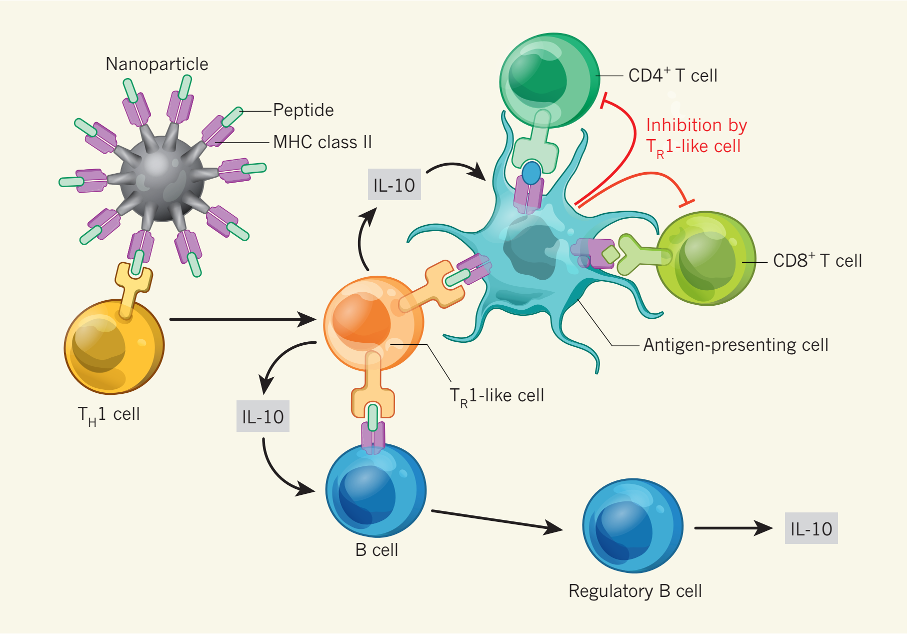

Figure 1 | Coated nanoparticles induce differentiation of regulatory T cells. Clemente-Casares *et al.*[1] produced nanoparticles coated with peptide fragments of the body's own proteins that are associated with autoimmune disease, bound to MHC class II proteins. They show that treating mice with these nanoparticles modifies the function of T_H1 cells that have receptors specific for that particular peptide: instead of inducing an immune response against the self-protein, the T_H1 cells differentiate into regulatory (T_R1-like) T cells that secrete the anti-inflammatory protein IL-10. The IL-10 promotes the differentiation of B cells into IL-10-secreting regulatory B cells, and also modifies the ability of antigen-presenting cells (APCs) to present the specific peptide to immune cells. Furthermore, the T_R1-like cells can inhibit the activation of helper ($CD4^+$) and cytotoxic ($CD8^+$) T cells that are specific for other peptides presented by the same APC, and thus mediate bystander suppression. In this way, T_R1-like cells can target APCs in tissues affected by autoimmune reactions and thereby suppress the inflammation associated with the disease.

T_R1-like cells induced by pMHC-NP treatment? Clemente-Casares *et al.* show that the cells suppress the function of APCs and reinforce immune regulation by promoting IL-10 production by B cells (Fig. 1). The authors verify the specificity of their approach by using different experimental models of autoimmune disease. pMHC-NPs carrying peptides from collagen, an antigen derived from joints, suppressed disease in a mouse model of rheumatoid arthritis, but not in mice with experimental autoimmune encephalitis (EAE), a model of multiple sclerosis. Conversely, pMHC-NPs carrying peptides of antigens from the central nervous system controlled EAE but not collagen-induced arthritis. This confirms that the immune regulation induced by pMHC-NP treatment is specific to the antigen and tissue, and so to the disease.

Furthermore, the pMHC-NPs did not need to target T cells specific for all peptides in the affected organ. Even peptides from sub-dominant antigens (weaker antigens that do not trigger disease in the first place) were able to induce T_R1-like cells that suppressed helper and cytotoxic T cells with activity against other antigens (Fig. 1). Thus, although this treatment is highly antigen-specific at the induction phase, it can influence other arms of the immune response locally, through induction of regulatory B-cell activity and suppression of helper and cytotoxic T cells specific for different antigens. This requires that the peptide fragment from the inducing antigen and the other antigens are presented by the same APC.

Is it possible that such bystander suppression could lead to systemic immune suppression by switching off cells not involved in the autoimmune response, thereby increasing the risk of infection or cancer? No: bystander suppression will be limited to lymph nodes associated with the affected organ and will influence only those APCs presenting the relevant self-antigen. Such specificity is clearly demonstrated by Clemente-Casares and colleagues — mice treated with pMHC-NPs are protected against the relevant autoimmune disease, yet show undiminished responses to infections and foreign antigens.

The experimental treatments in this study use well-characterized models of autoimmune disease. But is this work just another therapeutic approach that works in mice but will never work in humans? It seems not: the authors show that pMHC-NP treatment leads to differentiation and proliferation of human T_R1-like cells in immunodeficient mice transplanted with human T and B cells, demonstrating that pMHC-NP treatment works on human cells. The team's work also suggests that treatment with pMHC-NPs is more effective than with monomers of MHC-bound peptides at an equivalent dose. Furthermore, pMHC-NP treatment seems to be more suppressive than the application of peptide alone; however, the doses and routes of administration in these tests were not comparable.

> ***"The treatment drives the T_H cell to differentiate into cells with characteristics of regulatory T cells; these act to dampen immune responses."***

There is overwhelming evidence that peptide antigens can induce T_R1-like cells[11] and suppress autoimmune diseases in both mice and humans[9]. The fact that pMHC-NP treatment induces T_R1-like cells similar to those seen after the administration of peptide alone suggests that pMHC-NPs mimic the APC to which therapeutic peptides bind *in vivo*. The challenge with each of these approaches will be to find the optimal dose and route of administration for treating people. As these options progress towards clinical trials, it is vital that their mechanism of action is investigated in detail so that patients can benefit fully from antigen-specific immunotherapy for autoimmune disease. ■

David Wraith *is at the School of Cellular and Molecular Medicine, University of Bristol, Bristol BS8 1TD, UK.*
e-mail: d.c.wraith@bristol.ac.uk

1. Clemente-Casares, X. *et al. Nature* **530,** 434–440 (2016).
2. Noon, L. *Lancet* **i,** 1572–1573 (1911).
3. Larché, M. & Wraith, D. C. *Nature Med.* **11,** S69–S76 (2005).
4. Lafferty, K. J. & Cunningham, A. J. *Aust. J. Exp. Biol. Med. Sci.* **53,** 27–42 (1975).
5. Baxter, A. G. & Hodgkin, P. D. *Nature Rev. Immunol.* **2,** 439–446 (2002).
6. Schwartz, R. H. *Annu. Rev. Immunol.* **21,** 305–334 (2003).
7. O'Garra, A., Vieira, P. L., Vieira, P. & Goldfeld, A. E. *J. Clin. Invest.* **114,** 1372–1378 (2004).
8. Trinchieri, G. *J. Exp. Med.* **204,** 239–243 (2007).
9. Sabatos-Peyton, C. A., Verhagen, J. & Wraith, D. C. *Curr. Opin. Immunol.* **22,** 609–615 (2010).
10. Gabryšová, L. *et al. J. Exp. Med.* **206,** 1755–1767 (2009).
11. Burton, B. R. *et al. Nature Commun.* **5,** 4741 (2014).

The author declares competing financial interests. See go.nature.com/ukjrkv for details.

This article was published online on 17 February 2016.

EPIGENETICS

A new methyl mark on messengers

The presence of an N^1 methyl group on adenine bases in DNA and RNA was thought to be a form of damage. Results now show that it also occurs at specific sites in messenger RNAs, where it affects protein expression. SEE ARTICLE P.441

ANNA M. KIETRYS & ERIC T. KOOL

The fact that chemical modifications to DNA bases can alter gene expression without changing the nucleic-acid sequence has been known for more than a decade. But the key regulatory function of many such epigenetic modifications to messenger RNA molecules has been recognized only recently[1–3]. A simple mark — the methyl group — is widely observed in DNA and its associated histone proteins, and has been studied in mRNA in the forms of 5-methylcytosine and N^6-methyladenosine. On page 441 of this issue, Dominissini *et al.*[4] present a new member of the mRNA methyl-marked family, N^1-methyladenosine, and propose that its presence in mRNAs has an influence on biological processes. What is surprising about this modification is that it has previously been described as a form of cellular damage[5].

N^1-methyladenosine (m^1A) is unusual in having a positive charge at physiological pH (other bases are uncharged) and a methyl group that blocks the Watson–Crick base-pairing edge of adenine. The modification was previously documented in transfer RNA molecules, where it plays a crucial part in the formation of tertiary RNA structure. The methyl group forces the m^1A base to pair with a non-Watson–Crick configuration[6], and the positive charge has also been hypothesized to exert an electrostatic influence on protein interactions[7]. Dominissini *et al.* propose that this base modification may have similar biophysical effects in mRNAs: it could affect base-pairing interactions close to the site at which protein translation starts, and might alter RNA folding and electrostatic interactions.

m^1A was previously known to be formed by the exposure of RNA molecules to alkylating agents, and under alkaline conditions it is converted to N^6-methyladenosine (m^6A) through the Dimroth rearrangement[8] (Fig. 1). This is potentially a big problem in analysis,

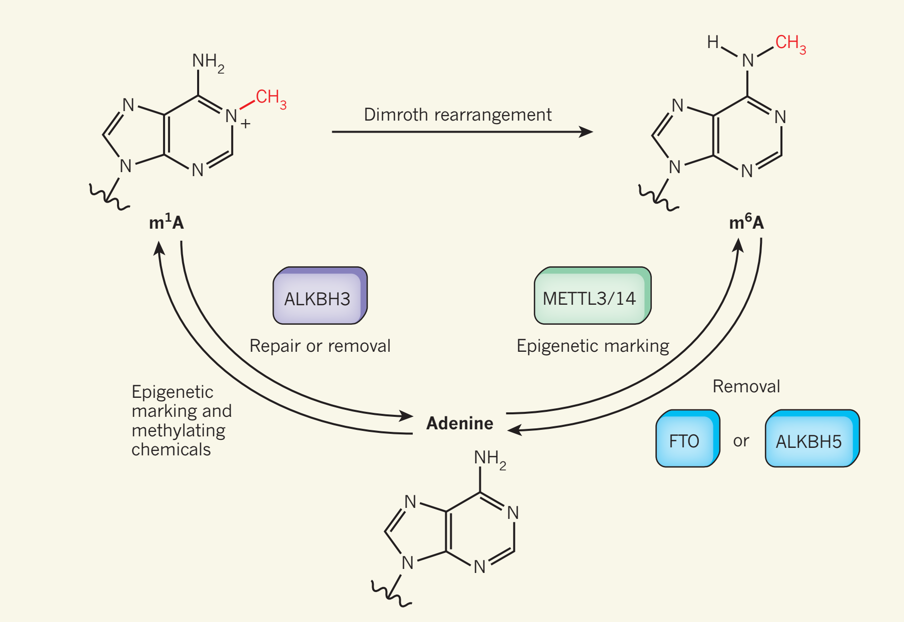

Figure 1 | Dynamic methylation of adenine. Methylation at the N^1 position of the base adenine generates the N^1-methyladenosine (m^1A) modification in RNA molecules, and occurs as a result of damage by chemical methylating agents[9]. Dominissini *et al.*[4] report the presence of m^1A in undamaged messenger RNA molecules, and propose that it represents a cellular epigenetic mark. In response to damage, the repair enzyme ALKBH3 can remove this methyl group to repair the base, but it is not clear if this or other enzymes function to remove the mark in an epigenetic context, nor how this mark is added[11]. Another form of methylated adenine, m^6A, is also recognized as an epigenetic mark in mRNA, added by the enzyme METTL3/14 and removed by FTO or ALKBH5. Under alkaline conditions, m^1A is converted to m^6A through the Dimroth rearrangement.

because m^6A is a considerably more abundant modification in mRNA, and thus obscures the rarer m^1A. Dominissini *et al.* found methods to suppress this confounding chemical instability of m^1A. Through carefully controlled sample preparation, they reduced the incidence of the m^1A-to-m^6A rearrangement to less than 10%, and the use of an isotopically labelled internal control during mass-spectrometry analysis allowed them to accurately quantify m^1A. These techniques enabled the researchers to identify the overall amounts of the modification in cells, and to map its locations in mRNAs.

The authors find that, although the N^1 methylation of adenine occurs several times less often than N^6 methylation, it is still found in thousands of mRNAs. They note an enrichment of m^1A signals near the translational start site of these mRNAs, and most of the molecules analysed were methylated only once, suggesting that the group has a single role in a given RNA. In the same region, they found sequences rich in the bases guanine and cytosine; such GC-rich motifs correlate with thermodynamically stable secondary RNA structure, which could be involved in directing the placement of m^1A. Moreover, the authors' mapping of m^1A across all RNA transcripts in the cell (the transcriptome) revealed that the modification in mRNAs is associated with higher levels of proteins.

What role does m^1A have in the cell? Dominissini *et al.* found that the fraction of mRNAs containing m^1A correlates positively with the level of gene expression, and may affect changes in cellular metabolism. The data also suggest the presence of a greater number of alternative translation initiation sites in the methylated RNAs than in RNAs lacking this modification. Most notable was the finding that m^1A-modified RNAs produced 1.7-fold higher protein levels than did non-methylated ones. Deeper analysis of the translation process led the authors to suggest that m^1A is involved in the processes by which pre-mRNA molecules are 'spliced' to form mature mRNAs. Thus, influencing protein expression seems to be one of the strongest effects of this methyl mark.

Importantly, the m^1A pattern in yeast RNAs differed from that in human and mouse RNAs: in yeast, the mark was distributed across the coding sequence without preferred locations, suggesting that more-sophisticated organisms have evolved m^1A marking as a distinct pathway. Comparing mouse and human mRNAs, the authors observed that the positions of m^1A modification showed 33% conservation, and that N^1-methylation in 5′-untranslated regions and close to the start site exhibited even higher conservation. The researchers also demonstrated that the m^1A level varies significantly between different mouse tissues. Furthermore, exposing cultured cells to different stress conditions resulted in changes in the m^1A level, which suggests that m^1A is a dynamic modification with a role in cellular stress responses and signalling processes.

A key question raised by these findings is how the cell differentiates between damage and intentional, stable cellular markers. When is m^1A a 'bug', and when is it a useful feature? Methylation of adenine at position 1 is well documented to arise from exposure to chemical methylating agents[9] (Fig. 1), and thus 1-methyladenine has been widely studied as a form of damage in DNA and RNA. At least one enzyme (ALKBH3) has been documented to remove this lesion and reduce its cytotoxicity[10]. A recent study that also documents m^1A in non-damaged mRNAs shows explicitly that this 'repair' enzyme can remove much of this methyl mark[11]. It will be important to determine how the stable m^1A mark is recognized as being distinct from that resulting from alkylation damage, and thus protected from immediate repair. And if m^1A is truly dynamic, in the sense of being specifically placed and removed from existing RNA as a cellular switch, then what methylase enzyme puts the mark in place, and what enzymes — ALKBH3 or other — remove it?

Dominissini and colleagues' findings represent an intriguing step for epitranscriptomics. More work is needed to understand the mechanism by which m^1A influences translation initiation and regulation, as well as the changes in its levels in stress responses. It will be exciting to see how this modification affects, and is affected by, RNA structure. Moreover, we need to know about the hypothesized proteins that are 'writers', 'readers' and 'erasers' of m^1A and thus take part in the dynamics of its regulation. Finally, as yet another modified base has been identified in mRNAs, one wonders how many more exist: is this the final one, or are we just seeing the tip of the epitranscriptome iceberg? ■

Anna M. Kietrys *and* **Eric T. Kool** *are in the Department of Chemistry, Stanford University, Stanford, California 94305, USA.*
e-mails: akietrys@stanford.edu; kool@stanford.edu

1. Meyer, K. D. & Jaffrey, S. R. *Nature Rev. Mol. Cell Biol.* **15,** 313–326 (2014).
2. Fu, Y., Dominissini, D., Rechavi, G. & He, C. *Nature Rev. Genet.* **15,** 293–306 (2014).
3. Edelheit, S., Schwartz, S., Mumbach, M. R., Wurtzel, O. & Sorek, R. *PLoS Genet.* **9,** e1003602 (2013).
4. Dominissini, D. *et al. Nature* **530,** 441–446 (2016).
5. Mishima, E. *et al. J. Am. Soc. Nephrol.* **25,** 2316–2326 (2014).
6. Helm, M., Giegé, R. & Florentz, C. *Biochemistry* **38,** 13338–13346 (1999).
7. He, C. *et al. Mol. Cell* **20,** 117–129 (2005).
8. Macon, J. B. & Wolfenden, R. *Biochemistry* **7,** 3453–3458 (1968).
9. Singer, B. & Grunberger, D. *Molecular Biology of Mutagens and Carcinogens* (Plenum, 1983).
10. Aas, P. A. *et al. Nature* **421,** 859–863 (2003).
11. Li, X. *et al. Nature Chem. Biol.* http://dx.doi.org/10.1038/nchembio.2040 (2016).

PALAEOANTHROPOLOGY

What teeth tell us

Models based on developmental mechanisms described in mice and shared by most mammals are shown to accurately predict tooth size in extinct hominins, and can explain the small third molars in our species. See Letter p.477

AIDA GÓMEZ-ROBLES

The third molars of modern humans — those often-troublesome molars we sometimes call wisdom teeth — are frequently very small or do not even develop. By contrast, the third molars of other hominin species in our evolutionary tree were huge, with chewing surfaces that were two to four times larger than those in an average modern human. This profound change in tooth proportions is usually explained by dietary and cultural changes considered to be unique to our species. But on page 477 of this issue, Evans *et al.*[1] offer an explanation that may make us feel rather less special. The authors propose that the evolution of our small third molars may be explained by basic developmental mechanisms that we share with most mammals.

In 2007, researchers proposed an inhibitory-cascade model of dental development on the basis of experimental studies in mice[2]. According to this model, dental proportions are established by the relative amount of inhibitory and activatory molecules that are expressed as one tooth develops after another (the greater the net inhibition exerted by an earlier tooth, the smaller the size of the later-developing tooth). Since then, researchers have explored the extent to which this model can explain tooth proportions in other mammalian species. Evans and colleagues, alongside others[3], have extended the application of this model to hominins.

Evans *et al.* focused on the lower primary postcanine teeth (lower milk molars and permanent molars). Their results show that variation in tooth size and proportions follows a remarkably simple rule that differs slightly between two major hominin groups. In australopiths, the group of African early hominins that includes, in this study, the genera *Ardipithecus*, *Australopithecus* and *Paranthropus*, teeth tend to get bigger towards the back of the primary molar row (up to the second or third permanent molar), with proportions that are constant irrespective of overall dental size. However, in the *Homo* genus, the proportional size of teeth varies with their overall size: smaller dentitions have disproportionately small third molars and tend to decrease in size from the first to the third molar.

The beauty of this model is that these simple relationships have an astonishing predictive power: by knowing only the size of a single tooth and the group to which it belongs — australopith or *Homo* — it is possible to infer with considerable accuracy the size of the remaining primary teeth. The model does not always correctly predict the location of the largest tooth, but predicted molar sizes are impressively close to observed values (Fig. 1). Dental anthropologists will be happy about this finding, but why should others care?

Size and proportions are but one aspect of the variation in dental anatomy, which can be studied using morphometric traits (measurable size and shape) and non-metric traits (such as the presence or absence of particular cusps and crests). Together with cranial features, dental traits are the bread and butter of hominin evolutionary studies, because they are thought to contain genetically coded information from which species relationships can be reconstructed. However, it is increasingly recognized that dental anatomy can vary in complex scenarios in which natural selection interacts with developmental and functional constraints[4]; this complexity may make teeth less useful for inferring phylogenies than we tend to recognize. For example, it is still debated whether the megadontia (extremely large dental size) observed in the genus *Paranthropus* is indicative of the evolutionary cohesion of this group, as is usually assumed, or whether it represents a convergent trend that was driven by similar ecological and developmental contexts[5].

At the other extreme of the dental-size spectrum, fossils from the Sima de los Huesos site in Atapuerca, Spain, which are dated to more than 400,000 years old and are considered to be closely related to Neanderthals[6], show an extreme degree of third-molar reduction[7]. The small third molars of these hominins are surprising for a taxon that is ancestral to classic Neanderthals, who had larger third molars. However, Evans and colleagues' model exactly predicts the strong third-molar reduction of Sima de los Huesos hominins as a result of their small overall postcanine dental size[8] (Fig. 1). It remains to be understood why these hominins had such small teeth without an equivalent reduction of their faces and jaws. It is to be hoped that future experimental work will help to unveil models of the interaction between teeth and jaws that will explain this apparent paradox.

Because of the paucity of hominin fossils, Evans and colleagues simplified their analysis by using species mean values. However,

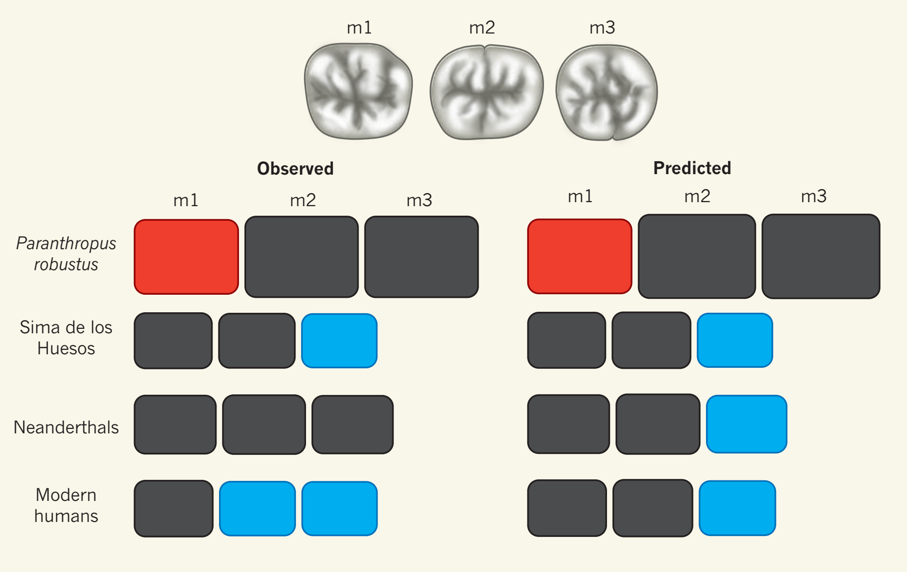

Figure 1 | Predicting molar size. Evans *et al.*[1] present a model that can use the measurement of a single tooth of a hominin (humans and other members of the human clade since the split from chimpanzees) to predict the sizes of its other lower primary postcanine teeth (milk and permanent molars). Depicted is a to-scale comparison of observed and predicted permanent-molar sizes in *Paranthropus robustus*, hominins from the Sima de los Huesos site, Neanderthals and modern humans (m1, first molar; m2, second molar; m3, third molar). Observed values are from refs 8 and 10, with updated values for Sima de los Huesos from ref. 11; predicted values were calculated from the observed m1 size using Evans and colleagues' model (see Supplementary Spreadsheet 1). Following their conventions, red is used for australopith hominins and blue for members of the *Homo* genus; the largest tooth in each series is filled in black, along with all teeth that are more than 95% of its size. (Tooth drawings are of modern human molars, and not to scale with boxes.)

activation and inhibition levels are expected to be individual-specific, which may result in tooth proportions that differ between individuals of the same species. It is therefore possible that the rule they describe would not be so simple had interindividual variation been included in the model.

Despite this limitation, Evans and colleagues' paper advances palaeoanthropology in three fundamental ways. First, it draws on experimental data from mice, which are the most common model organism, to explain the variation observed in the hominin fossil record. Second, it develops a rigorous quantitative framework to formally test hypotheses related to that model. And finally, it improves our understanding of the human fossil record by identifying evolutionary changes that are developmentally linked.

More importantly, Evans and colleagues' results are relevant beyond the study of fossil teeth. Many of the developmental constraints that influence dental evolution are shared by other systems formed by the repetition of serially homologous components, such as vertebrae, ribs, limbs and digits. Teeth can therefore be useful in identifying developmental mechanisms operating in these other systems[9]. By extension, the authors' model has the potential to help us understand the evolution of human traits that are associated with serially homologous structures, including our upright posture (which is influenced by vertebral anatomy), bipedal locomotion (which is linked to limb anatomy) and precision grip (which depends on the anatomy of digits). As with third-molar reduction, we tend to consider these traits the result of human-specific selective pressures, but their evolution is also fundamentally channelled by general developmental rules that humans have not escaped. ■

Aida Gómez-Robles *is in the Center for the Advanced Study of Human Paleobiology, Department of Anthropology, The George Washington University, Washington DC 20052, USA.*
e-mail: agomezrobles@gwu.edu

1. Evans, A. R. *et al. Nature* **530,** 477–480 (2016).
2. Kavanagh, K. D., Evans, A. R. & Jernvall, J. *Nature* **449,** 427–432 (2007).
3. Schroer, K. & Wood, B. *J. Anat.* **226,** 150–162 (2015).
4. Gómez-Robles, A. & Polly, P. D. *Evolution* **66,** 1024–1043 (2012).
5. Wood, B. & Constantino, P. *Yearb. Phys. Anthropol.* **50,** 106–132 (2007).
6. Arsuaga, J. L. *et al. Science* **344,** 1358–1363 (2014).
7. Gómez-Robles, A., Bermúdez de Castro, J. M., Martinón-Torres, M., Prado-Simón, L. & Arsuaga, J. L. *J. Hum. Evol.* **82,** 34–50 (2015).
8. Bermúdez de Castro, J. M. & Nicolas, M. E. *Am. J. Phys. Anthropol.* **96,** 335–356 (1995).
9. Young, N. M., Winslow, B., Takkellapati, S. & Kavanagh, K. *Nature Commun.* **6,** 6690 (2015).
10. Wood, B. A. & Abbott, S. A. *J. Anat.* **136,** 197–219 (1983).
11. Martinón-Torres, M., Bermúdez de Castro, J. M., Gómez-Robles, A., Prado-Simón, L. & Arsuaga, J. L. *J. Hum. Evol.* **62,** 7–58 (2012).

CLIMATE SCIENCE

Hidden trends in the ocean carbon sink

Simulations of the flux of atmospheric carbon dioxide into the ocean show that changes in flux associated with human activities are currently masked by natural climate variations, but will be evident in the near future. SEE LETTER P.469

TATIANA ILYINA

The world ocean has absorbed about one-third of the carbon released by humans[1], and therefore has a key role in moderating climate change. Observations[2] of the ocean interior confirm that increases in carbon dioxide emissions from fossil-fuel burning are accompanied by an increase in carbon content in the upper ocean. But, surprising as it may seem, McKinley *et al.*[3] report on page 469 that, in many ocean regions, changes in the uptake of CO_2 induced by human activities are currently indistinguishable from changes driven by natural climate variations. So, are anthropogenic trends in the ocean carbon sink concealed by Earth's own variability?

As atmospheric CO_2 levels increase, the ocean takes up this gas at a rate proportional to the difference of the partial pressure of CO_2 (a measure of CO_2 concentration in a mixture of gases) between the air and sea[2]. The strength of the ocean carbon sink is determined by chemical reactions in seawater, biological processes such as photosynthesis and respiration, and physical processes, including ocean circulation and vertical mixing[4]. But even though these key mechanisms are known, there are considerable uncertainties regarding their year-to-year (interannual) and decadal variations[5]. These variations are tightly linked to modes of internal variability in the climate system — such as the El Niño–Southern Oscillation (ENSO) — that have regional to worldwide effects on weather and climate, and thereby modulate air–sea CO_2 fluxes and ocean biogeochemical cycles.

Advances in observations and models have shed light on how internal climate variability controls the ocean carbon sink. Modern Earth-system models (ESMs) that were analysed in the fifth Coupled Model Intercomparison Project (CMIP5, which compared the output of

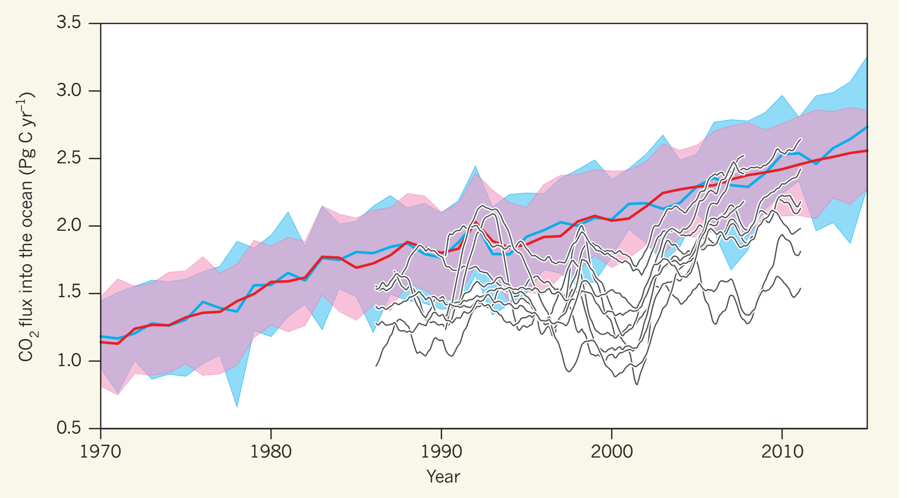

Figure 1 | Fluxes of carbon dioxide from the atmosphere into the ocean. These graphs compare the temporal evolution of the mean annual flux of CO_2 into the world ocean (in petagrams of carbon per year; 1 Pg is 10^{15} grams) predicted by different model simulations, and from observations. Although the models and observations reveal a similar trajectory for the global change of flux, the plotted values vary considerably because of uncertainties in models and gaps in observations. The model predictions are from the fifth Coupled Model Intercomparison Project (CMIP5; blue) and from an ensemble of 100 simulations made using the Max Planck Institute Earth System Model (MPI-ESM; red). Solid lines show the average of an ensemble of model data; shaded areas show the upper and the lower boundaries of the ensemble data. Findings based on observational data[7] are in black. McKinley *et al.*[3] report simulations suggesting that anthropogenic changes in the air–sea carbon flux are currently obscured by naturally occurring flux variations. (CO_2 fluxes into the ocean in CMIP5 models and in the MPI-ESM were calculated by Hongmei Li.)

models in which components of Earth's system are coupled) consistently predict that ocean carbon uptake increases in line with rises in fossil-fuel carbon emissions. But these ESMs poorly capture natural climate variability. Furthermore, CMIP5 projections generate a large spread in estimates of the ocean carbon sink because the models have different numerical schemes, process descriptions and spatial resolutions[6].

Further complications arise because there is a large spread in observed variations of CO_2 fluxes, due to both the use of different mapping procedures and gaps in the observational record[7]. This spread of variation from observational data is at least as large as the spread from the CMIP5 ensemble of models (Fig. 1). Estimates of the internal variability of the ocean carbon sink therefore remain unconstrained, impeding the detection and attribution of changes in air–sea CO_2 fluxes.

McKinley and co-workers report a crucial step towards detecting changes in the ocean carbon sink — they have generated a large ensemble of simulations based on an ESM. The authors repeated their model runs 32 times over the same time interval, spanning the years 1920 to 2100. The model follows historical climate evolution until the end of 2005, and then a climate-change scenario (known as RCP8.5) that projects high levels of atmospheric CO_2. Few modelling centres are able to perform so many runs because doing so is computationally expensive, but the value of using ensembles with a high number of simulations is increasingly being recognized.

External forcing factors such as the concentrations of atmospheric greenhouse gases and aerosols, volcanic eruptions and solar variability were identical across all simulations. The only difference between the ensemble members was their climate state at initialization: each simulation started with a different state generated by a small perturbation of the air temperature. As a result, individual ensemble members were not identical to each other, even though the model variables for each member followed the same general trajectory.

The authors considered two outcomes from the simulations: the forced trend, which is the average trend in model variables across all ensemble members produced under specified external forcing, and the internal trend, which is the difference between each member's trend and the forced trend, caused by the model's internal variability. They observed that the forced trends in ocean carbon uptake are indistinguishable from internal model variability in vast ocean regions between 1990 and 1999. When the period between 1990 and 2019 is considered, the forced trends become statistically significant in many more areas than during 1990 to 1999, and emerge almost everywhere in the ocean. This suggests that the predicted increase in oceanic carbon uptake is attributable to anthropogenic forcing. These trends intensify as atmospheric CO_2 levels increase, and so become detectable ocean-wide when the period from 1990 to 2089 is considered.

The researchers confirm that the spatial pattern in which trends emerge seems to be closely linked to the internal variability of the climate system. For instance, the largest internal variations are in the equatorial Pacific Ocean, a region known to be affected by ENSO. In regions such as this that exhibit strong seasonal and interannual variability, it is difficult to detect anthropogenic changes in CO_2 uptake. By contrast, anthropogenic trends emerge early in the subpolar North Atlantic and equatorial Atlantic oceans and in some regions of the Southern Ocean. A similar pattern has been reported[8] for several ocean biogeochemical parameters modelled in the CMIP5 ensemble.

McKinley and colleagues conclude that forced trends should be detectable in observations once they have emerged and become statistically significant. However, although internal model variability can give an indication of the chaotic behaviour of some natural processes, it is not equivalent to Earth's natural climate variability. Furthermore, predictions of the time of emergence are model-dependent[8,9], and may change if a different model or ensemble size is considered (Fig. 1).

Nevertheless, the current study makes a valuable contribution to the quantification of internal variability in the rates of change of the ocean carbon sink. Changes driven by human activities are undoubtedly there, but may be concealed by natural variations in many ocean regions because of the slow timescales on which ocean processes occur. Future work based on coordinated observational frameworks and large ensemble simulations using ESMs should enable the natural variability reported in this study to be verified. ■

Tatiana Ilyina *is at the Max Planck Institute for Meteorology, 20146 Hamburg, Germany.*
e-mail: tatiana.ilyina@mpimet.mpg.de

1. Le Quéré, C. *et al. Earth Syst. Sci. Data* **7,** 349–396 (2015).
2. IPCC. *Climate Change 2013: The Physical Science Basis. Contribution of Working Group I to the Fifth Assessment Report of the Intergovernmental Panel on Climate Change* (eds Stocker, T. F. *et al.*) (Cambridge Univ. Press, 2013).
3. McKinley, G. A. *et al. Nature* **530,** 469–472 (2015).
4. Heinze, C. *et al. Earth Syst. Dynam.* **6,** 327–358 (2015).
5. Marotzke, J. & Forster, P. M. *Nature* **517,** 565–570 (2015).
6. Bopp, L. *et al. Biogeosciences* **10,** 6225–6245 (2013).
7. Rödenbeck, C. *et al. Biogeosciences* **12,** 7251–7278 (2015).
8. Keller, K. M., Joos, F. & Raible, C. C. *Biogeosciences* **11,** 3647–3659 (2014).
9. Dobrynin, M., Murawski, J., Baehr, J. & Ilyina, T. *J. Clim.* **28,** 1578–1591 (2015).

COSMOLOGY

Home of a fast radio burst

Our understanding of fast radio bursts — intense pulses of radio waves — and their use as cosmic probes promises to be transformed now that one burst has been associated with a galaxy of known distance from Earth. See Letter p.453

DUNCAN LORIMER

Fast radio bursts (FRBs) are bright pulses of radio waves that last only milliseconds and originate from random locations on the sky. Although the physical processes that cause these pulses are unknown, FRBs hold great promise as probes of the cosmic web, a major constituent of the large-scale structure of the Universe. On page 453 of this issue, Keane *et al.*[1] report the discovery of a fading radio source associated with an FRB (FRB 150418) that was found on 18 April 2015. From observations with various telescopes, they show that FRB 150418 and its fading counterpart come from an elliptical galaxy some 1.9 billion parsecs (6 billion light years) away. Just as happened with γ-ray bursts almost 20 years ago, knowing both the location of origin and the distance of that location from Earth will help to reveal the physical nature of the event that caused the FRB.

A group that I led discovered[2] the first FRB while searching archival data taken with the 64-metre Parkes radio telescope in New South Wales, Australia. That burst, now known as FRB 010724, showed a clear dependence of pulse arrival time on frequency, with the highest-frequency signals travelling fastest through the ionized interstellar medium and arriving earlier than their lower-frequency counterparts. This well-known dispersion effect has allowed astronomers to map out the ionized material in the interstellar medium, and has helped us to understand the distribution of matter in the Milky Way[3]. For FRB 010724, however, the amount of dispersion observed is roughly ten times greater than

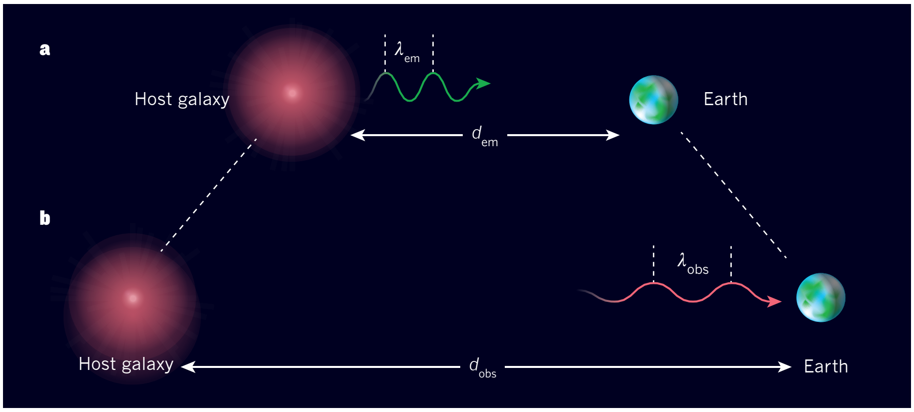

Figure 1 | Redshift of a fast radio burst (FRB). Light increases in wavelength (redshifts) as it travels across long distances. **a**, Here, light leaves a galaxy with an emitted wavelength λ_{em}. The distance between Earth and the galaxy at this time is d_{em}. **b**, When the signal subsequently reaches Earth, the expansion of the Universe will have caused the wavelength to redshift by a factor d_{obs}/d_{em}, where d_{obs} is the current distance to the galaxy; the new wavelength is λ_{obs}. From a measurement of λ_{obs} of the host galaxy for FRB 150418 (a bright pulse of radio waves that lasted only milliseconds), Keane *et al.*[1] determine its redshift and conclude that it was emitted when the Universe was about two-thirds of its current size (6 billion years ago).

that produced by the Milky Way, indicating that it is probably of extragalactic origin. Using models of intergalactic dispersion, we speculated[2] that FRB 010724 originated around 0.5 billion parsecs away, and was the first of a new population of sources that could act as cosmological probes.

On the basis of the amount of sky coverage and time spent by various radio telescopes scanning the sky, thousands of FRBs could be visible each day[4]. However, the limited fields of view of most radio telescopes mean that the pace of subsequent discoveries has been less rapid than expected. Currently, 17 FRBs are known[5], including FRB 150418, but none of the distances travelled by them has been directly measured. The energy budget of FRBs is therefore not well known, and there are currently more ideas about the nature of FRB sources than there are FRBs themselves. Among the possible theories[6] are that they are collapsing neutron stars, evaporating black holes or even non-stellar phenomena such as cosmic strings.

Unlike the FRB discoveries made in archival data, FRB 150418 was detected seconds after it reached the telescope. Keane *et al*. could therefore carry out follow-up observations of the burst's location on the sky using telescopes spanning the electromagnetic spectrum. Although almost all of these later observations yielded null results, one source was found in multiple images obtained at frequencies of 5.5 and 7.5 gigahertz using the Australia Telescope Compact Array. This transient radio source faded over six days to a level consistent with radio emission from a distant galaxy.

The authors' statistical analysis shows that there is only a tiny probability (less than 0.2%) that this source is unrelated to FRB 150418. Observations with the Subaru telescope on Mauna Kea, Hawaii, revealed an elliptical galaxy with a spectrum of optical light that originated predominantly from very old stars in the Galaxy. By analysing the redshift of these lines (the increase in wavelength due to the expansion of the Universe), the authors conclude that the distance to the galaxy and the source of FRB 150418 is 1.8 billion parsecs (Fig. 1).

Knowing the source location of an FRB and its distance from Earth provides new constraints on the FRB's emission process. Keane *et al.* find that the total energy released by the FRB is 8×10^{31} joules. This is comparable to the energy released by the Sun in two days, despite the much shorter duration of FRB 150418. The measured pulse width of 0.8 ms is only an upper bound on the intrinsic pulse duration, because the pulse broadens as it travels the long distance through different amounts of ionized material along the line of sight. As a result, the luminosity of the FRB is at least 10^{35} watts, or about one billion times that of the Sun.

These properties, together with the fading counterpart source and the FRB's location in an elliptical galaxy, strongly suggest models of the nature of the source population that involve old stellar populations found in elliptical galaxies, rather than much younger spiral galaxies such as the Milky Way. Keane *et al.* argue that FRB 150418 originated from the merger of two compact stars. I speculate that it represents the electromagnetic emission released when a binary neutron-star system coalesces[7]. Such a system would emit a large fraction of its energy in the form of gravitational waves, which are produced by accelerating bodies, according to Einstein's general theory of relativity.

Because gravitational waves result from the motion of objects, they carry information that is complementary to that conveyed by electromagnetic waves (light). The search for gravitational waves is a major goal of the Laser Interferometer Gravitational-Wave Observatory[8] (LIGO), which has just announced[9] the first detection of waves produced by the inspiralling and merger of two black holes. Although the source of FRB 150418 is too distant to be detectable by LIGO, closer FRB sources might be discovered in the future that could emit detectable gravitational-wave signals.

Perhaps the most important of Keane and co-workers' results is their demonstration that FRB 150418 can be used as a cosmological probe. The measurement of the pulse's dispersion (the frequency-dependent delay of the incoming radio waves) and the source's redshift provide an exact count of the number of free electrons along the line of sight stretching back in cosmic time to the source of FRB 150418. The authors show that the density of ionized material solves the 'missing baryon' problem[10] — the fact that the amount of baryonic (non-dark) matter in galaxies is well below that required to explain star formation rates, even after accounting for dark matter and dark energy. The measurement provided by FRB 150418 shows, for the first time, that the baryonic density is entirely consistent with the predictions from standard cosmological models.

There are good reasons to think that our understanding of FRBs will increase dramatically in the near future. New telescopes, including the Canadian Hydrogen Intensity Mapping Experiment and the Five-hundred-meter Aperture Spherical Telescope in China, should discover many FRBs. It is reasonable to expect many hundreds of observed FRBs by the end of the decade. A large census of FRBs will not only add to our understanding of their population, but also map out the cosmic web in great detail[11], provide stringent tests of general relativity[12] and even yield new constraints on the nature of dark energy[13]. ■

Duncan Lorimer *is in the Department of Physics and Astronomy, West Virginia University, Morgantown, West Virginia 26506, USA.*
e-mail: duncan.lorimer@mail.wvu.edu

1. Keane, E. F. *et al. Nature* **530,** 453–456 (2016).
2. Lorimer, D. R., Bailes, M., McLaughlin, M. A., Narkevic, D. J. & Crawford, F. *Science* **318,** 777–780 (2007).
3. Cordes, J. M., Weisberg, J. M., Frail, D. A., Spangler, S. R. & Ryan, M. *Nature* **354,** 121–124 (1991).
4. Thornton, D. *et al. Science* **341,** 53–56 (2013).
5. Petroff, E. *et al.* Preprint at http://arxiv.org/abs/1601.03547 (2016).
6. Kulkarni, S. R., Ofek, E. O., Neill, J. D., Zheng, Z. & Juric, M. *Astrophys. J.* **797,** 70 (2014).
7. Hansen, B. M. S. & Lyutikov, M. *Mon. Not. R. Astron. Soc.* **322,** 695–701 (2001).
8. Abramovici, A. *et al. Science* **256,** 325–333 (1992).
9. Abbott, B. P. *et al.* (LIGO Scientific Collaboration and the Virgo Collaboration) *Phys. Rev. Lett.* **116,** 061102 (2016).
10. Cen, R. & Ostriker, J. P. *Astrophys. J.* **514,** 1–6 (1999).
11. Masui, K. W. & Sigurdson, K. *Phys. Rev. Lett.* **115,** 121301 (2015).
12. Wei, J.-J., Gao, H., Wu, X.-F. & Mészáros, P. *Phys. Rev. Lett.* **115,** 261101 (2015).
13. Zhou, B., Li, X., Wang, T., Fan, Y.-Z. & Wei, D.-M. *Phys. Rev. D* **89,** 107303 (2014).

doi:10.1038/nature16544

Ancient gene flow from early modern humans into Eastern Neanderthals

Martin Kuhlwilm[1]*, Ilan Gronau[2]*, Melissa J. Hubisz[3], Cesare de Filippo[1], Javier Prado-Martinez[4], Martin Kircher[1,5], Qiaomei Fu[1,6,7], Hernán A. Burbano[1,8], Carles Lalueza-Fox[4], Marco de la Rasilla[9], Antonio Rosas[10], Pavao Rudan[11], Dejana Brajkovic[12], Željko Kucan[11], Ivan Gušic[11], Tomas Marques-Bonet[4,13,14], Aida M. Andrés[1], Bence Viola[15,16], Svante Pääbo[1], Matthias Meyer[1], Adam Siepel[3,17] & Sergi Castellano[1]

It has been shown that Neanderthals contributed genetically to modern humans outside Africa 47,000–65,000 years ago. Here we analyse the genomes of a Neanderthal and a Denisovan from the Altai Mountains in Siberia together with the sequences of chromosome 21 of two Neanderthals from Spain and Croatia. We find that a population that diverged early from other modern humans in Africa contributed genetically to the ancestors of Neanderthals from the Altai Mountains roughly 100,000 years ago. By contrast, we do not detect such a genetic contribution in the Denisovan or the two European Neanderthals. We conclude that in addition to later interbreeding events, the ancestors of Neanderthals from the Altai Mountains and early modern humans met and interbred, possibly in the Near East, many thousands of years earlier than previously thought.

Based on the fossil record, Neanderthals diverged from modern humans at least 430,000 years ago[1], and the analysis of a Neanderthal genome from a cave in the Altai Mountains in Siberia suggests they diverged 550,000–765,000 years ago[2]. The analysis of a Denisovan genome from the same cave in the Altai Mountains further suggests that Neanderthals and Denisovans diverged 381,000–473,000 years ago[2]. This divergence was followed by admixture among archaic and modern human populations, including gene flow from Neanderthals into modern humans outside Africa[2–5], Denisovan gene flow into the ancestors of present-day humans in Oceania and mainland Asia[6,7], gene flow into the Denisovans from Neanderthals[2] and, possibly, gene flow into the Denisovans from an unknown archaic group that diverged from the other lineages more than one million years ago[2]. Genetic evidence of gene flow from modern humans into Neanderthals or Denisovans, however, remains elusive.

Divergence and heterozygosity in the archaic genomes

The Altai Neanderthal genome shares 5.4% more derived alleles with present-day Africans than does the Denisovan genome. This excess is particularly pronounced for derived alleles found at >0.9 frequency in Africans (Extended Data Table 1). These observations have been interpreted as evidence of gene flow from an unknown and more deeply diverged archaic hominin into the Denisovan lineage[2]. Here we examine whether gene flow from modern humans into the ancestors of the Altai Neanderthal may also have occurred.

Noting that regions in the Denisovan genome introgressed from a deeply divergent archaic hominin should have unusually high divergence to present-day Africans, and that regions of the Altai Neanderthal genome introgressed from modern humans should have unusually low divergence to them, we examined the divergence of these archaic genomes to 504 African genomes[8] in 15,881 sequence windows of 100 kb (Supplementary Information section 9). Archaic alleles brought into Africa by Eurasians about 3,000 years ago[9,10] were excluded from these windows by using only derived alleles at >0.9 frequency in the combined African genomes. In the absence of information about the phase of the alleles in the two archaic genomes, we calculated their divergence to Africans using the archaic alleles in each window that give the minimum number of differences, to allow introgressed segments from modern humans to be more easily identified, if they exist. Noting also that introgressed regions in the Denisovan or Altai Neanderthal genome should have unusually high divergence to the other archaic genome, we calculated the divergence between the archaic genomes in the same windows by using the alleles that give the maximum number of differences.

We find that windows of the Denisovan genome with high divergence to Africans also have a high divergence to the Altai Neanderthal, whereas windows in the Altai Neanderthal genome with high divergence to Africans do not tend to have a high divergence to the Denisovan (Fig. 1a), consistent with gene flow from a deeply diverged hominin into the Denisovan ancestors. On the other hand, we find that windows of the Altai Neanderthal genome with low divergence to Africans have higher divergence to the Denisovan than Denisovan windows with low divergence to Africans (Fig. 1a). These windows in the Altai Neanderthal genome have higher heterozygosity than in the Denisovan genome (Fig. 1b), and 40.7% of their heterozygous sites share a derived allele with Africans, whereas 24.2% do so in the Denisovan. These observations raise the possibility of gene flow from modern humans into Neanderthals.

[1]Department of Evolutionary Genetics, Max Planck Institute for Evolutionary Anthropology, 04103 Leipzig, Germany. [2]Efi Arazi School of Computer Science, Herzliya Interdisciplinary Center (IDC), Herzliya 46150, Israel. [3]Department of Biological Statistics and Computational Biology, Cornell University, Ithaca, New York 14850, USA. [4]Institute of Evolutionary Biology (UPF-CSIC), 08003 Barcelona, Spain. [5]Department of Genome Sciences, University of Washington, Seattle, Washington 98195, USA. [6]Department of Genetics, Harvard Medical School, Boston, Massachusetts 02115, USA. [7]Key Laboratory of Vertebrate Evolution and Human Origins of Chinese Academy of Sciences, IVPP, CAS, Beijing 100044, China. [8]Department of Molecular Biology, Max Planck Institute for Developmental Biology, 72076 Tübingen, Germany. [9]Área de Prehistoria, Departamento de Historia, Universidad de Oviedo, 33011 Oviedo, Spain. [10]Departamento de Paleobiología, Museo Nacional de Ciencias Naturales, CSIC, 28006 Madrid, Spain. [11]Anthropology Center of the Croatian Academy of Sciences and Arts, 10000 Zagreb, Croatia. [12]Croatian Academy of Sciences and Arts, Institute for Quaternary Paleontology and Geology, 10000 Zagreb, Croatia. [13]Catalan Institution of Research and Advanced Studies (ICREA), 08010 Barcelona, Spain. [14]Centro Nacional de Análisis Genómico (CRG-CNAG), 08028 Barcelona, Spain. [15]Department of Anthropology, University of Toronto, Toronto, Ontario M5S 2S2, Canada. [16]Department of Human Evolution, Max Planck Institute for Evolutionary Anthropology, 04103 Leipzig, Germany. [17]Simons Center for Quantitative Biology, Cold Spring Harbor Laboratory, Cold Spring Harbor, New York 11724, USA.
*These authors contributed equally to this work.

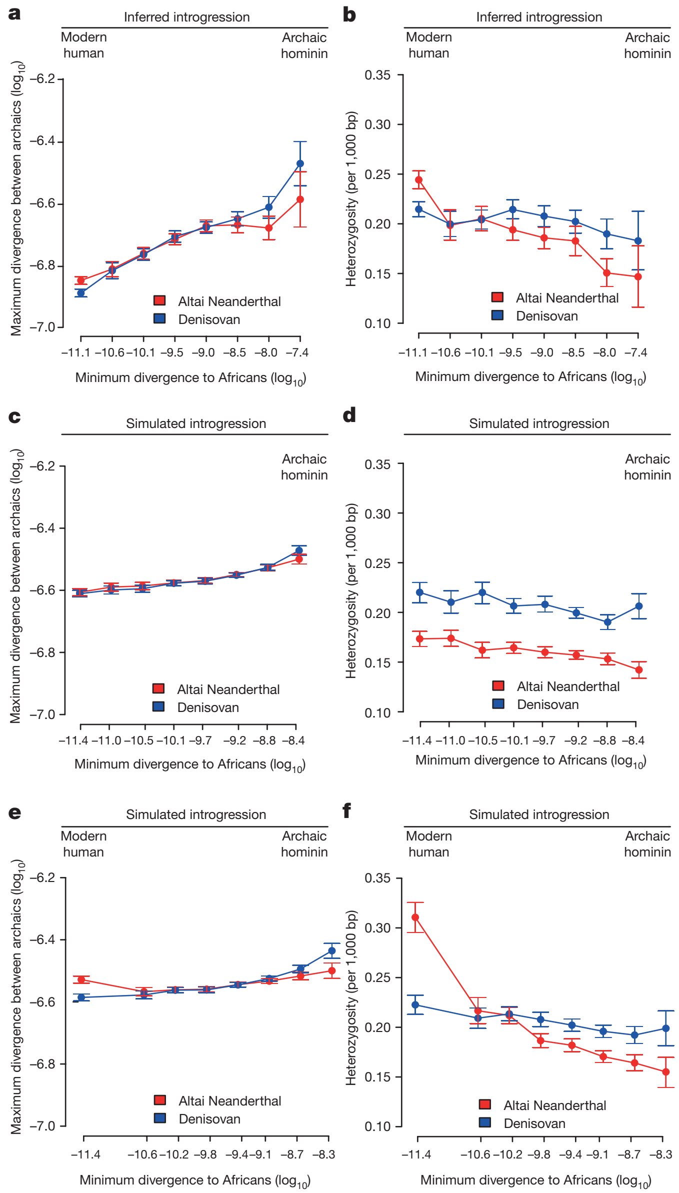

Figure 1 | Divergence and heterozygosity in the Altai Neanderthal and Denisovan genomes. a, The maximum divergence between windows in the two archaic genomes versus their minimum divergence to Africans. Error bars represent the 95% confidence intervals from 1,000 bootstrap replicates. Regions previously described as inbred in the Altai Neanderthal genome[2] were excluded. **b**, Heterozygosity (per 1,000 bp) in windows of each archaic genome versus their minimum divergence to Africans. **c**, **d**, Simulation of a model with gene flow into the Denisovan lineage from both the Altai Neanderthal (0.65%, 50,000 years ago) and an unknown archaic hominin (1%, 200,000 years ago) that diverged from other hominins 1.5 million years ago. The constant mutation rate used makes the slope of the simulated curves less steep than in the actual genomes, where mutation rate varies among windows. **e**, **f**, Simulation of a model that also includes modern human gene flow into the Altai Neanderthal lineage (3.55%, 100,000 years ago).

Model-based inferences of gene flow

We assessed the possibility of modern human gene flow into the Altai Neanderthal lineage using the Generalized Phylogenetic Coalescent Sampler (G-PhoCS)[11], a Bayesian method for inferring divergence times, effective population sizes and rates of gene flow from genome sequences. We applied G-PhoCS in five separate analyses, each considering the Altai Neanderthal and Denisovan genomes and two present-day human genomes from an African, European or Asian population (Supplementary Information section 8). We modelled gene flow among modern and archaic populations, including gene flow from an unknown deeply divergent archaic population, while accounting for the uncertainty in the ages of the archaic individuals.

The inferred demographic model confirms and provides quantitative estimates of previously inferred gene flow events among modern and archaic humans[2,3] (Extended Data Fig. 1). These include Neanderthal gene flow into modern humans outside Africa (3.3–5.8%) and gene flow from an unknown archaic hominin into the ancestors of Denisovans (0.0–0.5%). Interestingly, we also detect a signal of gene flow from modern humans into the ancestors of the Altai Neanderthal (1.0–7.1%). The precise source of this gene flow is unclear, but it appears to come from a population that either split from the ancestors of all present-day Africans or from one of the early African lineages, as significant admixture rates are estimated from San as well as Yoruba individuals. This introgression thus occurred in the opposite direction from the previously reported gene flow from Neanderthals to modern humans outside Africa[2,3,12].

Simulation of modern human gene flow

We used simulations to test if G-PhoCS correctly infers modern human gene flow into the Altai Neanderthal lineage (Extended Data Figs 2 and 3) and whether the patterns of divergence and heterozygosity observed in the Altai Neanderthal genome are expected from our inferred demographic model (Extended Data Fig. 1). Using parameters compatible with this model, we simulated windows of 100 kb for a model with gene flow into the Denisovan lineage from both the Altai Neanderthal and a deeply divergent archaic hominin[2], and a model including these admixture events together with modern human gene flow into the Altai Neanderthal lineage. Both models reproduced the observed patterns in windows most divergent to Africans (Fig. 1c and d), but only the model with modern human gene flow into the ancestors of the Altai Neanderthal reproduced the observed divergence and heterozygosity patterns in windows of the Altai Neanderthal least divergent to Africans (Fig. 1e and f).

Present-day human contamination among the DNA fragments from the Altai Neanderthal and Denisovan is around 1% (Table 1). After genotype calling, which is unaffected by low levels of error, these genomes should be largely free from contamination[2,7]. Even so, substituting gene flow from modern humans for present-day human contamination as high as 5% in the genotypes of the Altai Neanderthal fails to explain the observed sequence patterns (Extended Data Fig. 4).

Estimated ages of the introgressed haplotypes

The majority of haplotypes shared between present-day humans and an archaic genome should result from incomplete lineage sorting in the population ancestral to them and, thus, be old and short. However, if modern human introgression into the Altai Neanderthal lineage occurred after its separation from the Denisovan lineage we would expect a fraction of these shared haplotypes to be younger and longer in the Altai Neanderthal than in the Denisovan genome.

We examined these shared haplotypes making use of ARGweaver[13], a new computational method for sampling full genealogies and corresponding recombination events (ancestral recombination graphs) consistent with a collection of genome sequences (Supplementary Information section 10). We applied this method to six African genomes from three different populations (San, Mbuti, and Yoruba) and the two archaic genomes, and estimated the ages of haplotypes for which one archaic genome coalesces within the subtree of the African genomes more recently than it coalesces with the other archaic genome (Fig. 2a, inset). When we compare the age distribution of such 'African' haplotypes ($\geq$50 kb), we find that the Altai Neanderthal genome has more young 'African' haplotypes (Fig. 2a, left) than the Denisovan genome ($P < 0.01$; fraction of MCMC replicates). The majority of

Table 1 | The archaic individuals analysed in this work

		Altai Neanderthal[2]	Denisovan[7]	El Sidrón Neanderthal	Vindija Neanderthal
Age (years old)		>50,000	>50,000	~49,000	~44,000
mtDNA contamination (%)		0.78	0.35	0.40	1.08
Nuclear contamination (%)		0.80	0.22	0.000023	1.12
Genome					
Average coverage		52.7-fold	30.9-fold	–	–
Heterozygosity (per kb)		0.19	0.22	–	–
Chromosome 21					
DNA enrichment		–	–	320-fold	120-fold
Average coverage		53.7-fold	31.1-fold	14.1-fold	35.9-fold
Heterozygosity (per kb)		0.13	0.21	0.24	0.26
Cumulative length of homozygous segments (Mb)	10–100 kb	9.68	22.60	20.50	20.50
	>100 kb	19	4.80	5.10	5.10

Radiocarbon dates (uncalibrated), mean contamination estimates for the DNA fragments sequenced and summary statistics for the genomes and chromosome 21 sequences. mtDNA, mitochondrial DNA.

these young haplotypes are estimated to coalesce with the African genomes 100,000–230,000 years ago, suggesting that they entered into the ancestors of the Altai Neanderthal well before the reported gene flow from Neanderthals into modern humans outside Africa 47,000–65,000 years ago[12]. Both the cumulative and average length of the young 'African' haplotypes is longer in the Altai Neanderthal genome than in the Denisovan genome.

The introgression from a deeply divergent archaic population into the Denisovan lineage is a potential confounding factor in this analysis. However, this introgression event should affect older haplotypes in the Denisovan genome, rather than the young haplotypes examined above. Indeed, we find that the number of haplotypes in one archaic genome that coalesce outside Africans and the other archaic genome (Fig. 2b, inset) is higher in the Denisovan than in the Altai Neanderthal (Fig. 2b, right). Furthermore, the young 'African' haplotypes in the Altai Neanderthal genome do not significantly overlap with the older haplotypes in the Denisovan genome and in simulations ARGweaver only infers them under a model with modern human gene flow into the Altai Neanderthal lineage (Extended Data Fig. 5).

Inference of gene flow in European Neanderthals

To investigate possible differences among Neanderthal populations with respect to introgression from modern humans, we designed oligonucleotide probes[14] based on the human reference sequence of chromosome 21, and used them to capture[15] this chromosome in a Neanderthal from Spain (El Sidrón Cave) and a Neanderthal from Croatia (Vindija Cave). We estimated their present-day human contamination to be around 1% (Table 1).

We find that the chromosome 21 of the Altai Neanderthal shares more derived alleles with Africans than the chromosome 21 of El Sidrón (3.5% more) and Vindija (4.9% more) Neanderthals, with the European Neanderthals sharing more derived alleles with Africans than the chromosome 21 of the Denisovan (9.8% more for El Sidrón, 8.8% more for Vindija). A comparison of the distribution of haplotype ages is not possible with the European Neanderthals, owing to insufficient amounts of data, but we compared the cumulative length of haplotypes coalescing within the African subtree for each Neanderthal lineage. This length is significantly greater for the Altai Neanderthal than for the European Neanderthals ($P < 0.01$; fraction of MCMC replicates), consistent with introgression from modern humans primarily into this Neanderthal lineage.

When we refine our estimates of gene flow by adding the chromosome 21 sequences of the European Neanderthals to our genome-wide data, G-PhoCS infers significant rates of gene flow from Neanderthals into modern humans outside Africa only for El Sidrón and Vindija Neanderthals (0.3–2.6%) (Fig. 3a), suggesting that Neanderthals from Europe are more closely related than the Altai Neanderthal to the population that interbred with modern humans outside Africa 47,000–65,000 years ago[12]. Conversely, significant rates of gene flow from modern humans into Neanderthals are inferred only into the ancestors of the Altai Neanderthal (0.1–2.1%) (Extended Data Figs 6 and 7). This suggests that modern human introgression into Neanderthals occurred mainly after the divergence of the Altai Neanderthal from El Sidrón and Vindija lineages 110,000 (68,000–167,000) years ago (Fig. 3b). However, it is possible that the lack of complete genomes from the European Neanderthals currently precludes the identification of modern human gene flow into them.

To explore the source of the modern human gene flow among the African populations, we simulated three scenarios in which the source of the gene flow into the Altai Neanderthal lineage was alternately an unknown population diverging from the ancestors of all

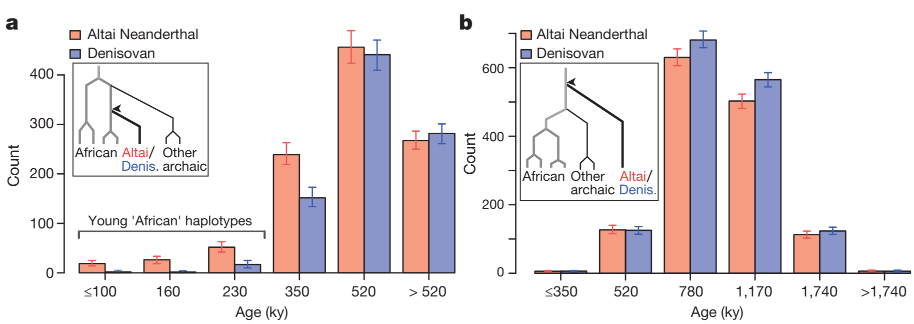

Figure 2 | Distinguishing between two scenarios of introgression into archaic humans. a, The age distribution of 'African' haplotypes (≥50 kb) in the Altai Neanderthal and the Denisovan genomes as inferred by ARGweaver. Error bars represent the 95% credible intervals from 302 Markov chain Monte Carlo (MCMC) replicates. An 'African' haplotype coalesces within the African subtree before coalescing with the other archaic individual (inset), and its age is inferred as that coalescent time (arrowhead). The majority of the young 'African' haplotypes in the Altai Neanderthal genome are estimated to coalesce 100,000–230,000 years ago, with just a few estimated to coalesce less than 100,000 years ago (Supplementary Information section 10). **b**, The age distribution of 'deep ancestral' haplotypes (≥50 kb) in the Altai Neanderthal and Denisovan genomes. A 'deep ancestral' haplotype coalesces above the African subtree and the other archaic lineage (inset), and its age is inferred as that coalescent time (arrowhead). ky, thousand years.

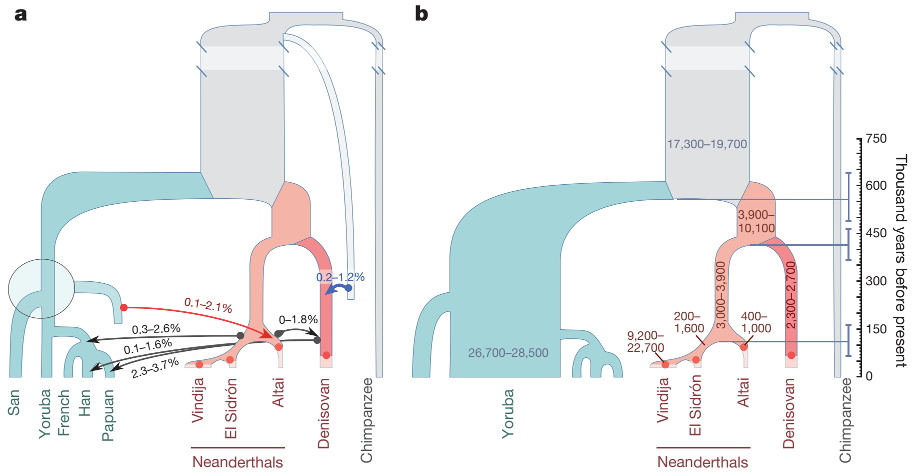

Figure 3 | Refined demography of archaic and modern humans. a, Total migration rates of six gene flow events inferred by G-PhoCS. The ranges correspond to 95% Bayesian credible intervals aggregated across runs. Five gene flow events have been previously reported, including gene flow from an unknown archaic group into Denisovans (blue arrow). In addition, we infer gene flow from a population related to modern humans into a population ancestral to the Altai Neanderthal (red arrow). It appears to come from a population that either split from the ancestors of present-day Africans or separated fairly early in the history of African populations (shaded circle). **b**, Effective population sizes and divergence times inferred by G-PhoCS. The ranges correspond to 95% Bayesian credible intervals aggregated across runs. The horizontal bars indicate posterior mean estimates for divergence times. Archaic samples (dots) are located at their estimated ages.

present-day Africans, of the San or of Yoruba lineage (Supplementary Information section 8). The G-PhoCS estimates from these three models are all similar and consistent with those in Fig. 3, and thus we cannot distinguish among them. However, it is clear that the source of the gene flow is a population equally related to present-day Africans and non-Africans (Extended Data Fig. 3). We conclude that the introgressing population diverged from other modern human populations before or shortly after the split between the ancestors of San and other Africans (Fig. 3a), which occurred approximately 200,000 years ago[11]. In agreement, the San, Mbuti and Yoruba genomes contribute equally to the young 'African' haplotypes in the Altai Neanderthal genome (Supplementary Information section 10).

Introgressed segments in the Altai Neanderthal

To shed light on possible functional implications of modern human gene flow into Neanderthals, we identified 163 putatively introgressed segments (≥50 kb) in the Altai Neanderthal genome (Supplementary Information section 9). These segments have no clear affinity to any present-day African population (Extended Data Fig. 8), and they overlap with 225 genes. Seven segments exceed 200 kb (Table 2) and the longest one (309 kb) overlaps with a region suspected to have been under positive selection in modern humans[3]. This region has a transcription factor gene (*NR5A2*) involved in liver development[16]. One segment of 150 kb is located within the *FOXP2* gene (Table 2), which encodes a transcription factor that may be relevant for language acquisition[17].

The number of putatively introgressed segments in the Altai Neanderthal decreases in regions of the genome under strong purifying selection (measured via background selection at linked sites[18]), and it is lower in the X chromosome compared to the autosomes. Because purifying selection purges deleterious alleles and the efficacy of purifying selection is higher on the X chromosome[19], this may indicate that modern human and Neanderthal[20] alleles were often not tolerated in each other's genetic background.

Population size in Neanderthals and Denisovans

Our demographic model suggests a long-term decline in the effective population size of Neanderthals and Denisovans since their divergence from the ancestors of present-day humans 484,000–640,000 years ago. However, the population ancestral to the Vindija Neanderthal appears to have expanded (Fig. 3b). In addition, the length distribution of homozygous stretches in the European Neanderthals resembles that of the Denisovan, who lacks a signal of recent inbreeding[7], and not that of the Altai Neanderthal, whose parents were related at the level of half-siblings[2] (Table 1). Still, the European Neanderthals and the Denisovan exhibit signs of a history of mating in small populations[21], with a larger cumulative length of homozygous segments of 10–100 kb than present-day humans and great apes (Fig. 4). In agreement with purifying selection being less efficient in small populations, regulatory and conserved[22] regions in Neanderthals have a larger proportion of putatively deleterious alleles than present-day humans (Extended Data Fig. 9), as shown previously for their protein-coding genes[23].

Discussion

Our integrated demographic analysis of multiple archaic and present-day human genomes suggests a scenario of long-term decline in the populations of Neanderthals and Denisovans, with the consistently small Altai Neanderthal population perhaps reflecting a long period of isolation in the Altai Mountains. In addition, we provide evidence

Table 2 | Introgressed segments from modern humans into the Altai Neanderthal

Genomic region	SNPs	Sequence length (bp)	Genetic length (cM)	Genes in the region
Chr1: 199,707,795–200,016,460	161	308,665	0.047	*NR5A2*; *RNU6-609P*; *RNU6-716P*; *RNU6-778P*
Chr13: 49,532,446–49,790,867	103	258,421	0.040	*COX7CP1*; *FNDC3A*; *OGFOD1P1*; *RAD17P2*; *RNU6-60P*; *RNY3P2*
Chr2: 88,815,371–89,061,977	116	246,606	0.023	*EIF2AK3*; *RPIA*; *TEX37*
Chr3: 89,790,776–90,031,537	70	240,761	0.017	–
Chr3: 30,590,736–30,816,806	100	226,070	0.547	*GADL1*; *TGFBR2*
Chr6: 42,492,777–42,713,223	67	220,446	0.088	*ATP6V0CP3*; *PRPH2*; *RNU6-890P*; *TBCC*; *UBR2*
Chr8: 93,809,505–94,011,334	122	201,829	0.070	*IRF5P1*; *TRIQK*
Chr7: 113,813,987–113,963,584	37	149,597	0.055	*FOXP2*

The seven segments (≥200 kb) in the Altai Neanderthal genome that are enriched in heterozygous sites with derived alleles at high-frequency in Africans. These sites are homozygous ancestral in the Denisovan. The segment overlapping the *FOXP2* gene is also shown.

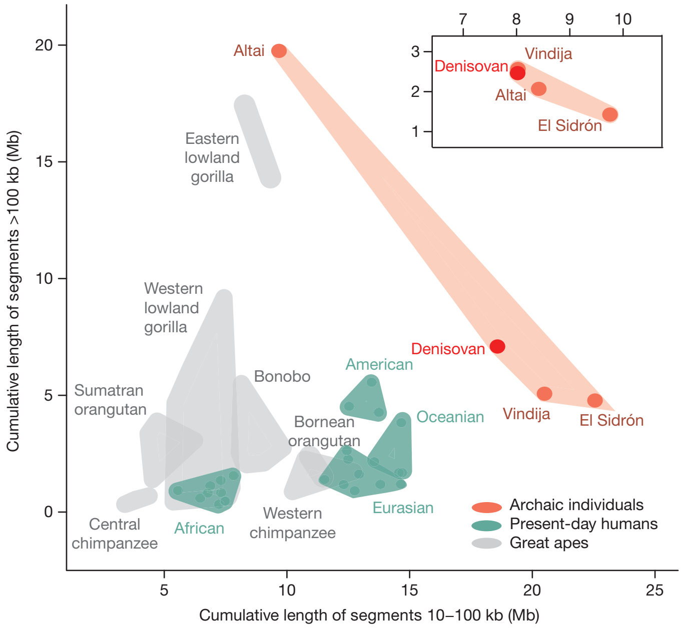

Figure 4 | Homozygous segments on chromosome 21. The range of the cumulative length (Mb) of homozygous segments is shown as the surface of a polygon, with individuals at the extremes of each group's range serving as vertices. Dots represent human individuals, archaic or otherwise, whereas great apes are not depicted individually. The Altai Neanderthal clusters with the other archaic individuals (inset) when recently inbred genomic regions are excluded.

for modern human introgression into the ancestors of this population of Neanderthals, and no such evidence in the European Neanderthals. These modern humans may represent a population that diverged early from other modern humans in Africa and later met the ancestors of the Altai Neanderthal. The finding of 'African' haplotypes as young as 100,000 years old in the Altai Neanderthal genome is consistent with interbreeding around that age.

Hublin[24] has proposed that Neanderthals expanded eastward from Europe during an interglacial period about 125,000 years ago (Oxygen Isotope Stage 5e). The presence of modern humans (at Skhul and Qafzeh) and Neanderthals (at Tabun) in the Levant as early as 120,000 years ago[25,26] provides one place where gene flow from early modern humans into Neanderthals could have occurred. Another place is Southern Arabia and the area around the Persian Gulf, where modern humans may have also settled early[27] and Neanderthals are likely to have been present[28]. The recent demonstration that modern humans may have been in China as early as 120,000 years ago[29] also suggests that modern humans migrated early out of Africa. Thus, early modern humans may have had the opportunity to admix with archaic hominins before the migration of the modern human ancestors of present-day non-Africans.

Online Content Methods, along with any additional Extended Data display items and Source Data, are available in the online version of the paper; references unique to these sections appear only in the online paper.

Received 28 July; accepted 17 December 2015.
Published online 17 February 2016.

1. Arsuaga, J. L. *et al.* Neandertal roots: Cranial and chronological evidence from Sima de los Huesos. *Science* **344,** 1358–1363 (2014).
2. Prüfer, K. *et al.* The complete genome sequence of a Neanderthal from the Altai Mountains. *Nature* **505,** 43–49 (2014).
3. Green, R. E. *et al.* A draft sequence of the Neandertal genome. *Science* **328,** 710–722 (2010).
4. Fu, Q. *et al.* Genome sequence of a 45,000-year-old modern human from western Siberia. *Nature* **514,** 445–449 (2014).
5. Fu, Q. *et al.* An early modern human from Romania with a recent Neanderthal ancestor. *Nature* (2015).
6. Reich, D. *et al.* Genetic history of an archaic hominin group from Denisova Cave in Siberia. *Nature* **468,** 1053–1060 (2010).
7. Meyer, M. *et al.* A high-coverage genome sequence from an archaic Denisovan individual. *Science* **338,** 222–226 (2012).
8. The 1000 Genomes Project Consortium. A global reference for human genetic variation. *Nature* **526,** 68–74 (2015).
9. Pickrell, J. K. *et al.* Ancient west Eurasian ancestry in southern and eastern Africa. *Proc. Natl Acad. Sci. USA* **111,** 2632–2637 (2014).
10. Llorente, M. G. *et al.* Ancient Ethiopian genome reveals extensive Eurasian admixture throughout the African continent. *Science* **350,** 820–822 (2015).
11. Gronau, I., Hubisz, M. J., Gulko, B., Danko, C. G. & Siepel, A. Bayesian inference of ancient human demography from individual genome sequences. *Nature Genet.* **43,** 1031–1034 (2011).
12. Sankararaman, S., Patterson, N., Li, H., Paabo, S. & Reich, D. The date of interbreeding between Neandertals and modern humans. *PLoS Genet.* **8,** e1002947 (2012).
13. Rasmussen, M. D., Hubisz, M. J., Gronau, I. & Siepel, A. Genome-wide inference of ancestral recombination graphs. *PLoS Genet.* **10,** e1004342 (2014).
14. Burbano, H. A. *et al.* Targeted investigation of the Neandertal genome by array-based sequence capture. *Science* **328,** 723–725 (2010).
15. Fu, Q. *et al.* DNA analysis of an early modern human from Tianyuan Cave, China. *Proc. Natl Acad. Sci. USA* **110,** 2223–2227 (2013).
16. Rausa, F. M., Galarneau, L., Bélanger, L. & Costa, R. H. The nuclear receptor fetoprotein transcription factor is coexpressed with its target gene HNF-3β in the developing murine liver intestine and pancreas. *Mech. Dev.* **89,** 185–188 (1999).
17. Enard, W. FOXP2 and the role of cortico-basal ganglia circuits in speech and language evolution. *Curr. Opin. Neurobiol.* **21,** 415–424 (2011).
18. McVicker, G., Gordon, D., Davis, C. & Green, P. Widespread genomic signatures of natural selection in hominid evolution. *PLoS Genet.* **5,** e1000471 (2009).
19. Veeramah, K. R., Gutenkunst, R. N., Woerner, A. E., Watkins, J. C. & Hammer, M. F. Evidence for increased levels of positive and negative selection on the X chromosome versus autosomes in humans. *Mol. Biol. Evol.* **31,** 2267–2282 (2014).
20. Sankararaman, S. *et al.* The genomic landscape of Neanderthal ancestry in present-day humans. *Nature* **507,** 354–357 (2014).
21. Pemberton, T. J. *et al.* Genomic patterns of homozygosity in worldwide human populations. *Am. J. Hum. Genet.* **91,** 275–292 (2012).
22. Siepel, A. *et al.* Evolutionarily conserved elements in vertebrate, insect, worm, and yeast genomes. *Genome Res.* **15,** 1034–1050 (2005).
23. Castellano, S. *et al.* Patterns of coding variation in the complete exomes of three Neandertals. *Proc. Natl Acad. Sciences USA* **111,** 6666–6671 (2014).
24. Hublin, J. J. in *Neandertals and Modern Humans in Western Asia* (eds Akazawa, T., Aoki, K. & Bar-Yosef, O.) (Kluwer Academic Publishers, 1998).
25. Mercier, N. H. V., Bar-Yosef, O., Vandermeersch B., Stringer, C. & Joron, J.-L. Thermoluminescence date for the Mousterian burial site of Es-Skhul, Mt. Carmel. *J. Archaeol. Sci.* **20,** 169–174 (1993).
26. Grün, R. *et al.* U-series and ESR analyses of bones and teeth relating to the human burials from Skhul. *J. Hum. Evol.* **49,** 316–334 (2005).
27. Armitage, S. J. *et al.* The southern route "Out of Africa": evidence for an early expansion of modern humans into Arabia. *Science* **331,** 453–456 (2011).
28. Rose, J. I. A. & Marks, A. E. "Out of Arabia" and the Middle–Upper Palaeolithic transition in the southern Levant. *Quartär* **61,** 49–85 (2014).
29. Liu, W. *et al.* The earliest unequivocally modern humans in southern China. *Nature* **526,** 696–699 (2015).

Supplementary Information is available in the online version of the paper.

Acknowledgements We thank M. Slatkin, F. Racimo, J. Kelso, K. Prüfer, M. Stoneking and D. Reich for comments; the MPI-EVA sequencing group, B. Nickel and R. Schultz for technical support; A. Heinze, S. Sawyer and J. Dabney for sequencing library preparation; U. Stenzel and G. Renaud for help with sequence processing. M.J.H. was supported by the National Science Foundation Graduate Research Fellowship under grant DGE-1144153. Q.F. was funded in part by the Special Foundation of the President of the Chinese Academy of Sciences. T.M-B. was supported by ICREA, EMBO YIP 2013 and Fundació Barcelona Zoo. The Max Planck Society, the Krekeler Foundation, MINECO (grants BFU2014-55090-P FEDER, BFU2015-7116-ERC and BFU2015-6215-ERC to T.M-B. and BFU2012-34157 FEDER to C.L.-F.) and the US National Institutes of Health (grant GM102192 to A.S. and U01 MH106874 to T.M-B.) provided financial support.

Author Contributions M.M. and Q.F. performed experiments; M.Ku., I.Gr., M.J.H., C.d.F., J.P.-M., M.Ki, Q.F., H.A.B., T.M.-B., A.M.A., S.P., M.M., A.S. and S.C. analysed genetic data; C.L.-F., M.d.I.R., A.R., P.R., D.B., Ž.,K., I.Gu. and B.V. analysed anthropological data; M.Ku., I.Gr., M.J.H., B.V., S.P., A.S. and S.C. wrote the manuscript.

Author Information Sequence data are available in the European Nucleotide Archive (ENA) under accession number PRJEB11828. Reprints and permissions information is available at www.nature.com/reprints. The authors declare no competing financial interests. Readers are welcome to comment on the online version of the paper. Correspondence and requests for materials should be addressed to A.S. (asiepel@cshl.edu) or S.C. (sergi.castellano@eva.mpg.de).

METHODS

Data reporting. No statistical methods were used to predetermine sample size. The investigators were not blinded to allocation during experiments and outcome assessment.

DNA extraction and library preparation. We prepared DNA extracts from two Neanderthal bones, SD1253 from El Sidrón Cave and Vi33.15 from Vindija Cave, as described in Rohland *et al.*[30] (Supplementary Table 1), and prepared DNA sequencing libraries containing a special 4 base pair (bp) clean-room tag sequence to avoid contamination in later steps[31,32]. During library preparation, we used a uracil-DNA-glycosylase (UDG) and endonuclease VIII mix to remove uracils resulting from cytosine deaminations[33].

Chromosome 21 capture experiment. We used a strategy previously described[15] that uses oligonucleotides synthesized on arrays to construct amplified probe libraries. We produced a probe library with a tile density of 3 nucleotides across the 29.8 Mb of non-repetitive sequences in chromosome 21 (GRCh37/hg19), with biotinylated probes similar to those described by Gnirke *et al.*[34]. We used this probe library, as previously described[23], to generate libraries from El Sidrón and Vindija Neanderthals. All libraries were subjected to a second round of amplification, followed by two rounds of hybridization capture. Capture eluates were amplified, barcoded with two indexes[32], pooled, and sequenced on the Genome Analyzer IIx (Illumina).

Contamination estimates. Estimates of present-day human mtDNA contamination in El Sidrón and Vindija libraries were previously reported in Castellano *et al.*[23]. These contamination estimates were calculated using diagnostic positions at which archaic mitochondrial genomes differed from sequences in a panel of 311 present-day human mitochondrial genomes. Nuclear DNA contamination estimates were calculated using a previously described maximum likelihood approach[7] that co-estimates the contamination and sequence error in the autosomes.

Computational correction of cytosine deaminations. Sequences may carry residual cytosine deaminations in the first positions of the 5′ end and in the last positions of the 3′ end in spite of the UDG treatment[33] (Supplementary Fig. 1). These bases are read as thymine and adenosine, respectively. As similarly described for the Altai Neanderthal genome[2], we decreased the quality to 2 of any 'T' base occurring within the first five bases or any 'A' base within the last five positions in El Sidrón and Vindija sequences.

Variation discovery. We called Neanderthal genotypes with GATK[35] and applied a previously described set of filters[23] (Supplementary Information section 3) to obtain high-quality sites for subsequent analyses. We obtained such calls for 17,014,623 and 20,582,399 sites for El Sidrón and Vindija chromosome 21, respectively. Genotypes in the Altai Neanderthal, Denisovan and present-day human genomes were similarly obtained (Supplementary Table 6), and a combined file for all individuals was created and annotated as in Meyer *et al.*[7]. Because multiple contaminated DNA fragments are needed for a contaminated genotype to be called, the proportion of contaminated genotypes is likely to be smaller than the reported contamination of 1% among DNA fragments.

Capture bias. In order to understand capture bias, we captured the chromosome 21 of the Altai Neanderthal to an average coverage of 46.9-fold. We then downsampled these sequences to assess capture bias at a wider range of average coverage from 8.1-fold to 35.7-fold, and did the same for the Altai Neanderthal shotgun sequences. The mean reference allele frequency is shifted from 0.52 in the shotgun sequences to 0.54–0.55, similar to the observed frequencies in the other archaic captured individuals (Supplementary Fig. 4). The mutation spectra after filtering do not change with coverage (Supplementary Fig. 2), and differences in allele frequency at heterozygous sites in the shotgun sequences are small (Supplementary Fig. 5). We observed that 3.8–5.2% of heterozygous sites in the shotgun sequences of chromosome 21 in the Altai Neanderthal are homozygous in the capture experiment at coverage from 14-fold to 46.9-fold (Supplementary Table 7). However, 22.3–45.4% of these heterozygous sites are filtered out, mainly due to low coverage in the capture sequences. The same is true for sites that are heterozygous in the capture experiment at 46.9-fold coverage, but homozygous (4.9–5.9%) or missing (14.1–21.6%) in the shotgun data at 15.1–53.7-fold coverage. In addition, the distribution of homozygosity stretches does not differ between the capture and the shotgun sequences (Supplementary Fig. 9). We conclude that capture bias does not distort our results in a systematic way.

Sequence patterns. Our analysis of the divergence of the archaic genomes to Africans and to each other sought to uncover the patterns that distinguish modern human gene flow into the Altai Neanderthal lineage from archaic gene flow into the Denisovan lineage. To do this, we analysed 15,881 sequence windows of 100 kb in length across the genomes of the two archaic individuals. These windows were required to have high-quality genotypes (as described in Supplementary Information section 3) in at least 50% of its length in both archaic genomes. Because the phase of the archaic alleles is unknown, the divergence of the archaic genomes to Africans was calculated using the archaic alleles in each window that give the minimum number of differences to derived alleles at >0.9 frequency in 504 individuals from five African present-day populations (Yoruba, Mende, Luhya, Gambian, and Esan)[8]. Using the minimum divergence to Africans allows introgressed segments from modern humans to be more easily identified. In contrast, the divergence between the archaic genomes was calculated using the archaic alleles in each window that give the maximum number of differences. Using the maximum divergence between the archaic windows allows introgressed segments in either of the two archaic individuals to be more easily identified. Derived alleles were determined using the inferred ancestral base in the EPO six-primate alignments[36] and the minimum and maximum number of differences in a sequence window was divided by its number of high-quality genotypes. Regions of the genome described as inbred in the Altai Neanderthal[2] were excluded from this analysis. These are 103 regions >2.5 cM depleted in heterozygous sites. In this way, heterozygosity in Fig. 1b could be calculated from the same 15,881 sequence windows of 100 kb in Fig. 1a.

We used the program ms[37] to simulate 15,881 sequence windows of 100 kb in length, using parameters that are consistent with the G-PhoCS estimates (Supplementary Information section 8). We simulated scenarios with and without modern human gene flow into the Altai Neanderthal lineage (Supplementary Information section 9). The mutation rate of 0.5×10^{-9} mutations per bp and year[4,38] and an average generation time of 29 years[39] (as assumed in the G-PhoCS inferences) were also used. The number of chromosomes simulated were 1,008 for the Africans, two for the Neanderthal, two for the Denisovan, one for the unknown archaic, and one for the chimpanzee.

Alignments at neutral loci. Multiple sequence alignments were obtained for our main demography inference using G-PhoCS. Following the guidelines established in previous studies[11,40], we extracted multiple sequence alignments of the Altai Neanderthal, the Denisovan and multiple present-day humans at 13,753 loci, 1 kb long, selected to minimize influence of direct selection, linkage between loci, and missing data. Among these, 2,960 loci were selected from chromosome 21, for which sequence data was available from El Sidrón and Vindija Neanderthals.

Demography inference. Our demography inference is based on five main G-PhoCS runs, each one containing the Altai Neanderthal, the Denisovan, the chimpanzee outgroup (panTro2), and two present day humans from a particular population. We considered populations from Africa (Yoruba and San), Europe (French), East Asia (China), and Oceania (Papuan). In five additional runs we added sequences from chromosome 21 of El Sidrón and Vindija Neanderthals. To account for the fact that different individuals lived at different times, we modified the algorithm to sample the times of the archaic individuals as four additional free parameters (Supplementary Information section 8). To validate the robustness of our estimates, we conducted additional inferences using subsets of the archaic individuals, different subsets of the loci, and allowing for gene flow from an unsampled (unknown) divergent human group, and explicitly modelling the source population of modern introgression into the ancestors of the Altai Neanderthal as an unsampled population branching off from the modern human population.

G-PhoCS setup. In each G-PhoCS run, we ran the Markov chain Monte Carlo (MCMC) sampler for 100,000 burn-in iterations and 200,000 subsequent sampling iterations, and checked manually for convergence of the Markov Chain. The samples were used to estimate a posterior mean and 95% Bayesian credible interval for each demographic parameter. For parameters common to the five runs with different present-day humans, we combined the five parameter traces to obtain aggregated estimates. Estimates of population divergence time and effective population size were calibrated by assuming an average mutation rate of 0.5×10^{-9} per base pair per year[4,38] and an average generation time of 29 years[39]. Estimates under different assumptions on mutation rate and generation time are obtained by simple scaling of the reported estimates. Gene flow is measured using the total migration rate, which is the estimated per-generation rate times the number of generations that migration is allowed in the model.

Simulations. To validate the G-PhoCS inferences we simulated, using ms[37], 10,000 loci of 1 kb of length for the Altai Neanderthal, Denisovan, three present-day humans from San, Yoruba, and European populations and the chimpanzee outgroup. Demographic parameters were set according to the ones inferred on the genomic sequences, with parameters describing divergence times of modern populations and growth of the European population taken from recent studies[11,41]. For these individuals, sequences were simulated under different scenarios for modern human introgression into the Altai Neanderthal population: (1) no introgression; (2) introgression from a population that diverged from present-day humans before the San divergence; (3) introgression from a population that diverged from the population ancestral only to Yoruba and Europeans; (4) introgression from a population that diverged from the population ancestral only to the San; and (5) introgression from a population ancestral only to Europeans. These five scenarios also included simulated gene flow from the Altai Neanderthal and an unsampled archaic population into the Denisovan population. G-PhoCS was run under

each scenario three times (one for each present-day individual) with the same settings used in the analysis of the actual genomes.

ARGweaver analysis. ARGweaver was run using the Altai Neanderthal and Denisovan genomes, six modern human genomes (two Yoruba, two San, and two Mbuti; Supplementary Table 2), and the chimpanzee reference genome (panTro4). Filters were applied to mask regions with uncertain genotype calls. The genome was divided into roughly 5 Mb blocks with 1 Mb overlap between adjacent blocks. A new method to integrate over genotype phase was used on the archaic and present-day human genomes (Supplementary Information section 10). Other settings, such as the recombination and mutation rate map, and the population size ($n = 11,534$), were the same as previously reported[13]. ARGweaver was run for 5,000 MCMC iterations, with an ancestral recombination graph sampled every 20 iterations starting at iteration 2,000. ARGweaver was run similarly with El Sidrón and Vindija chromosome 21 included. 'African' and 'deep ancestral' haplotypes were determined in each sampled ancestral recombination graph using only a single lineage from each archaic genome to avoid differences in power between them due to different levels of heterozygosity and inbreeding.

Screen for introgressed segments. A screen for modern human introgressed segments was performed using the frequency in Africans of derived alleles in sites that are heterozygous in one archaic genome (Altai Neanderthal or Denisovan) and homozygous ancestral in the other archaic genome. This allows us to identify segments that carry an archaic haplotype on three chromosomes, and a human haplotype only on one chromosome. Derived alleles were determined using the inferred ancestral base in the EPO six-primate alignments[36]. Genotypes and allele frequencies for the African individuals were obtained from the 1000 Genomes project[8]. We fitted the African derived allele frequencies along each of the archaic genomes using a locally weighted polynomial regression (loess function in *R*), and selected those genomic segments containing at least 10 sites where the fitted curve to the derived African allele frequencies consistently stayed over a frequency of 0.25 across 25 kb. Segments containing incompatible sites, that is, sites that were derived and shared in both archaic individuals, were removed. In the Altai Neanderthal, the average heterozygosity of the putatively introgressed segments is 4.9-fold higher than in random genome regions (Supplementary Information section 9).

Homozygosity segments. Homozygous segments were defined as maximal regions between two heterozygous positions of length between 10 and 100 kb or larger than 100 kb. To compare the hominin samples with great apes, we masked regions for which no data on great apes were available[42] in addition to the filters described in Supplementary Information section 3.

Prediction of functional consequences. We tested the functional consequences of the derived alleles using conservation scores from PhastCons[22]. We calculated the fractions of mutations in deleterious sites for the different human groups (Supplementary Information section 7). We used annotations of transcripts from ENSEMBL[43] to define coding regions, untranslated regions, and 5,000 bases upstream of transcription start sites and downstream of transcription end sites. We used those as well as conserved transcription factor binding sites[44] and conserved elements, and sampled randomly for each category the same number of bases in neutral sites to calculate the ratio of "functional" to "neutral" polymorphism.

30. Rohland, N. & Hofreiter, M. Comparison and optimization of ancient DNA extraction. *Biotechniques* **42,** 343–352 (2007).
31. Meyer, M. & Kircher, M. Illumina sequencing library preparation for highly multiplexed target capture and sequencing. *Cold Spring Harb. Protocols* **2010,** http://dx.doi.org/10.1101/pdb.prot5448 (2010).
32. Kircher, M., Sawyer, S. & Meyer, M. Double indexing overcomes inaccuracies in multiplex sequencing on the Illumina platform. *Nucleic Acids Res.* **40,** e3 (2012).
33. Briggs, A. W. *et al.* Removal of deaminated cytosines and detection of *in vivo* methylation in ancient DNA. *Nucleic Acids Res.* **38,** e87 (2010).
34. Gnirke, A. *et al.* Solution hybrid selection with ultra-long oligonucleotides for massively parallel targeted sequencing. *Nature Biotechnol.* **27,** 182–189 (2009).
35. McKenna, A. *et al.* The Genome Analysis Toolkit: a MapReduce framework for analyzing next-generation DNA sequencing data. *Genome Res.* **20,** 1297–1303 (2010).
36. Paten, B., Herrero, J., Beal, K., Fitzgerald, S. & Birney, E. Enredo and Pecan: genome-wide mammalian consistency-based multiple alignment with paralogs. *Genome Res.* **18,** 1814–1828 (2008).
37. Hudson, R. R. Generating samples under a Wright–Fisher neutral model of genetic variation. *Bioinformatics* **18,** 337–338 (2002).
38. Roach, J. C. *et al.* Analysis of genetic inheritance in a family quartet by whole-genome sequencing. *Science* **328,** 636–639 (2010).
39. Fenner, J. N. Cross-cultural estimation of the human generation interval for use in genetics-based population divergence studies. *Am. J. Phys. Anthropol.* **128,** 415–423 (2005).
40. Freedman, A. H. *et al.* Genome sequencing highlights the dynamic early history of dogs. *PLoS Genet.* **10,** e1004016 (2014).
41. Gravel, S. *et al.* Demographic history and rare allele sharing among human populations. *Proc. Natl Acad. Sci. USA* **108,** 11983–11988 (2011).
42. Prado-Martinez, J. *et al.* Great ape genetic diversity and population history. *Nature* **499,** 471–475 (2013).
43. Durinck, S. *et al.* BioMart and Bioconductor: a powerful link between biological databases and microarray data analysis. *Bioinformatics* **21,** 3439–3440 (2005).
44. Arbiza, L. *et al.* Genome-wide inference of natural selection on human transcription factor binding sites. *Nature Genet.* **45,** 723–729 (2013).

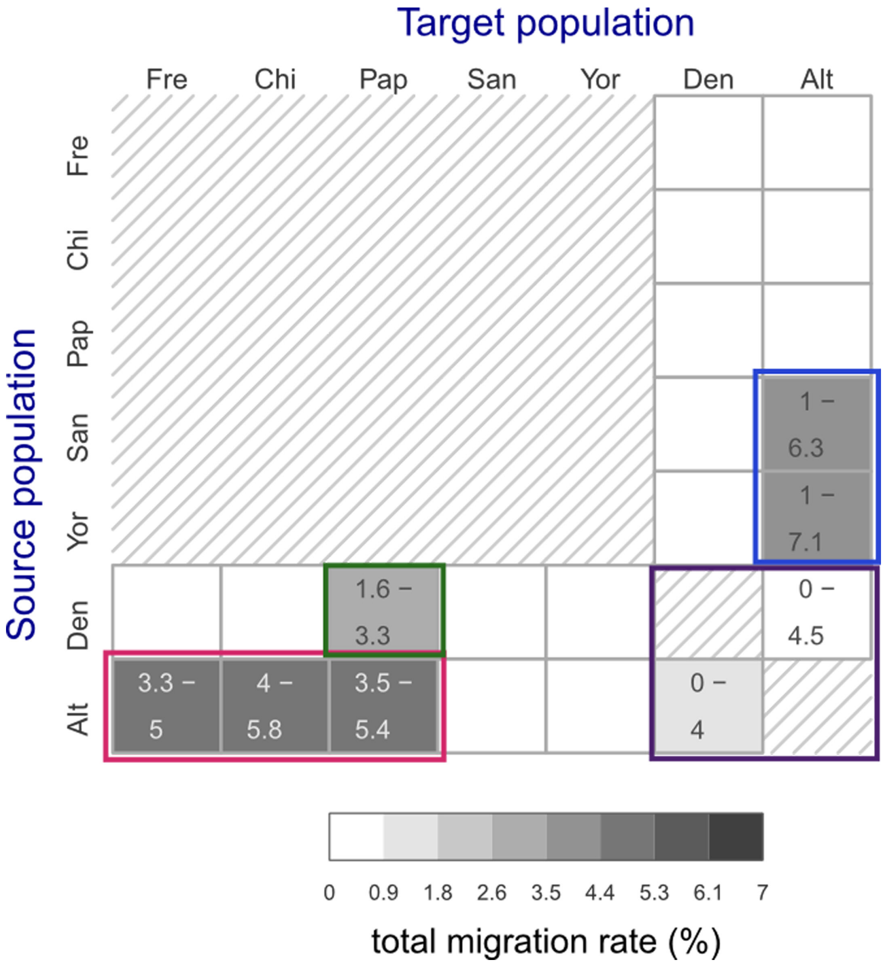

Extended Data Figure 1 | Migration rates in preliminary demographic inference. Total migration rates estimated for 22 directional migration bands in five separate preliminary G-PhoCS runs. Rows correspond to source populations and columns to the target populations. The 20 migration bands between modern and archaic populations were considered in five separate runs, each containing the four bands associated with a different modern human population (Supplementary Fig. 15A). The two migration bands between the Denisovan and the Altai Neanderthal populations were considered in all five runs, and the values shown here correspond to an aggregate of all five runs. The estimates are as shown in Supplementary Fig. 15B. Shade indicates the posterior mean total migration rate (legend), which approximates the probability that a lineage in the target population originated in the source population. The 95% Bayesian credible intervals from 2,000 MCMC replicates are indicated for migration bands whose upper credible interval bound is above 0.3%. We identified four clusters of migration bands, corresponding to what were likely at least four different cases of introgression between populations: (1) Neanderthals into non-African modern humans (red box), (2) Denisovans into Oceanians (green box), (3) between Neanderthals and Denisovans (magenta), and (4) modern humans into Neanderthals (blue box). Alt, Altai Neanderthal; Chi, Chinese; Den, Denisovan; Fre, French; Pap, Papuan; Yor, Yoruba.

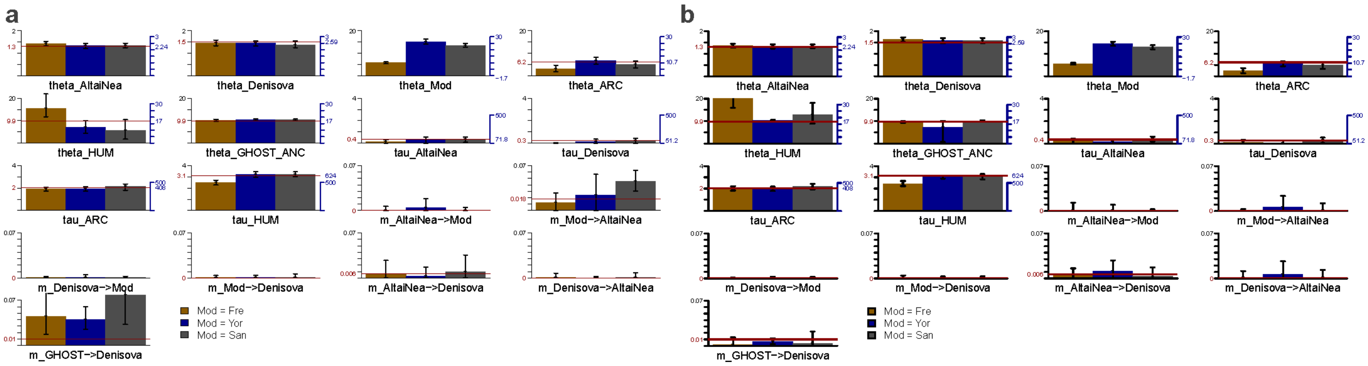

Extended Data Figure 2 | Demographic inference on simulated data. Simulated data were generated under the demographic model as inferred by G-PhoCS (Supplementary Table 13). Each simulated data set consisted of 10,000 loci of 1 kb length. We simulated the Altai Neanderthal, the Denisovan, and three modern human populations corresponding to the San, Yoruba, and French, with modern human demography consistent with recent studies (Supplementary information section 8). Three migration bands were simulated: (1) from the Altai Neanderthal to the Denisovan, (2) from a population that diverged from the ancestors of all present-day humans 300,000 years ago into the Altai Neanderthal, and (3) from a population that diverged from the ancestors of all modern and archaic humans roughly 2.6 million years ago into the Denisovan. **a**, Estimates of effective population sizes (theta, θ), population divergence times (tau, τ) and migration rates (m) from three G-PhoCS runs on data simulated with gene flow from modern humans into the Altai Neanderthal lineage. Each run analyses an individual from a different present-day population, using the exact same setup used in our main analysis (Supplementary Fig. 15A). Parameters are typically estimated accurately, with 95% Bayesian credible intervals containing the values used in simulations (horizontal red lines). Rates of archaic gene flow into Denisovan appear to be somewhat overestimated, and differences between analyses of African and non-African populations are consistent with those observed in the data analysis (Supplementary Fig. 15B). **b**, Similar analysis done on data simulated without gene flow from modern humans into the Altai Neanderthal lineage. Accurate estimates are obtained for all model parameters, and no gene flow is inferred from modern humans into the ancestors of the Altai Neanderthal. Error bars represent the 95% Bayesian credible intervals from 2,000 MCMC replicates.

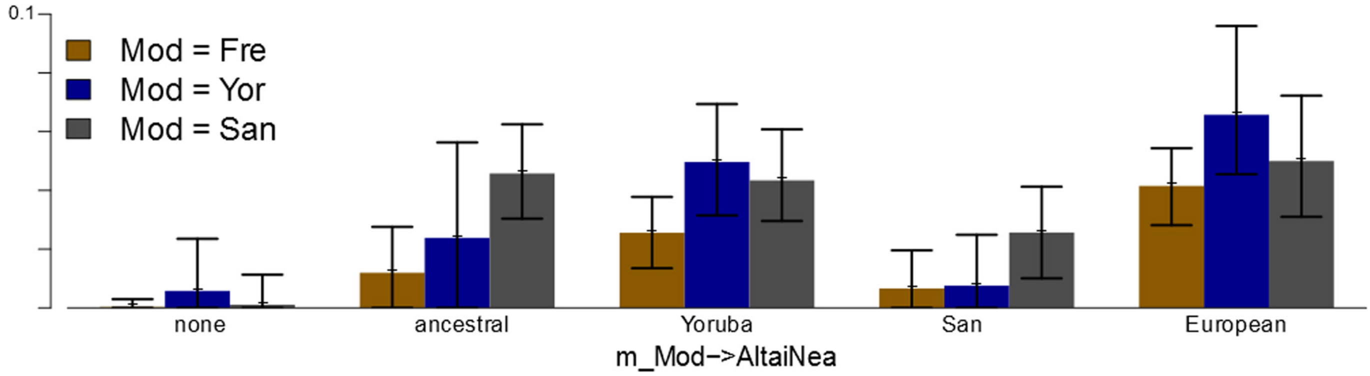

Extended Data Figure 3 | Simulation of different source populations for modern introgression into Neanderthals. Estimated rates of migration from the modern human population to the Altai Neanderthal population obtained from 15 G-PhoCS runs on five simulated data sets. All demographic parameters are set according to the values inferred by G-PhoCS in our data analysis (Supplementary Table 13), and the five data sets differ by the source population for migration: no migration (none), population ancestral to all present-day humans (ancestral), population ancestral to Yoruba and Europeans (Yoruba), San population (San), and European population (European). The first two sets are the ones analysed in Extended Data Fig. 2. Each data set is analysed three times, using different present-day samples: European (French), Yoruba, or San. Significant differences in estimates are observed between the data sets with and without gene flow and the data set with gene flow from a source population related to Europeans. Only minor differences were observed between values inferred for the three data sets with source population diverging from African populations (San, Yoruba, and ancestral). We conclude from this that the source population likely diverged from an African human population before the divergence of present-day Eurasians. The shaded circle in Fig. 3a represents this conclusion. Error bars represent the 95% Bayesian credible intervals from 2,000 MCMC replicates.

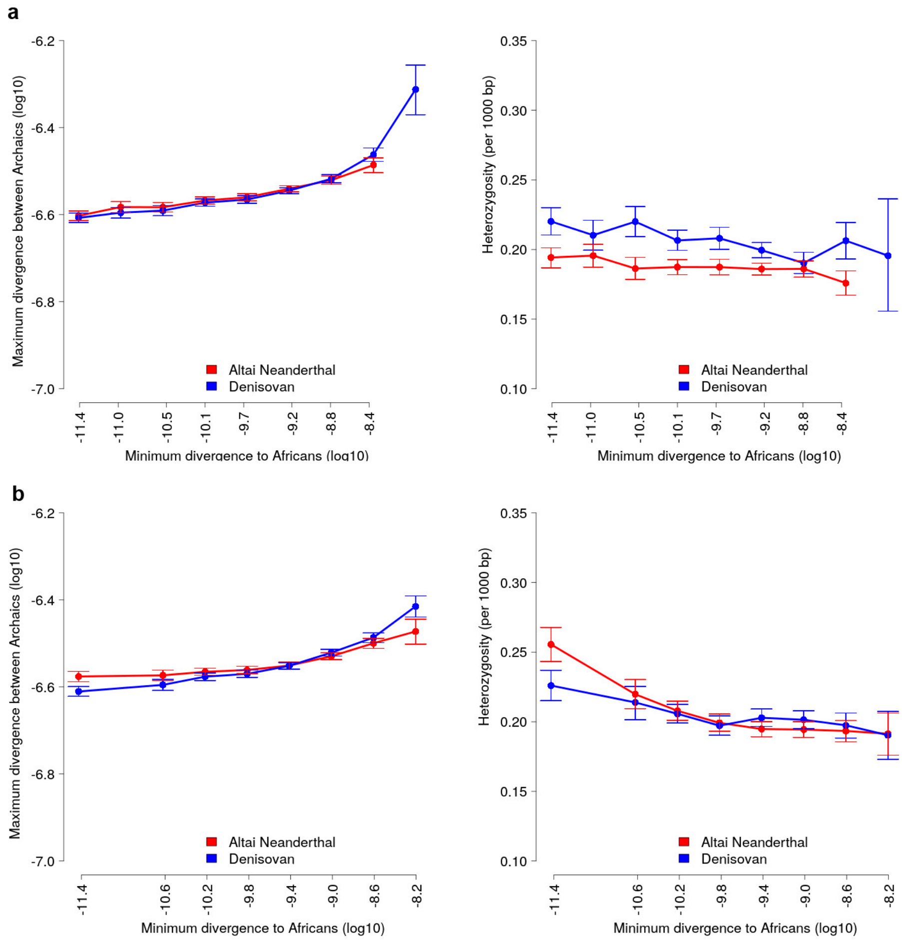

Extended Data Figure 4 | Simulation of present-day human contamination. Simulated windows of 100 kb for the Altai Neanderthal and Denisovan genomes with present-day human contamination of 5% at the genotype level. Windows are binned by their minimum divergence to Africans using derived alleles at >0.9 frequency in the simulated African population. The *x* and *y* axis as in Fig. 1. **a**, Gene flow from a deeply divergent archaic hominin into the Denisovan lineage (1%) and Altai Neanderthal gene flow into the Denisovan lineage (0.65%). **b**, Gene flow from a deeply divergent archaic hominin into the Denisovan lineage, Altai Neanderthal gene flow into the Denisovan lineage and modern human gene flow into the Altai Neanderthal lineage (1.8%). Error bars represent the 95% confidence intervals from 1,000 bootstrap replicates.

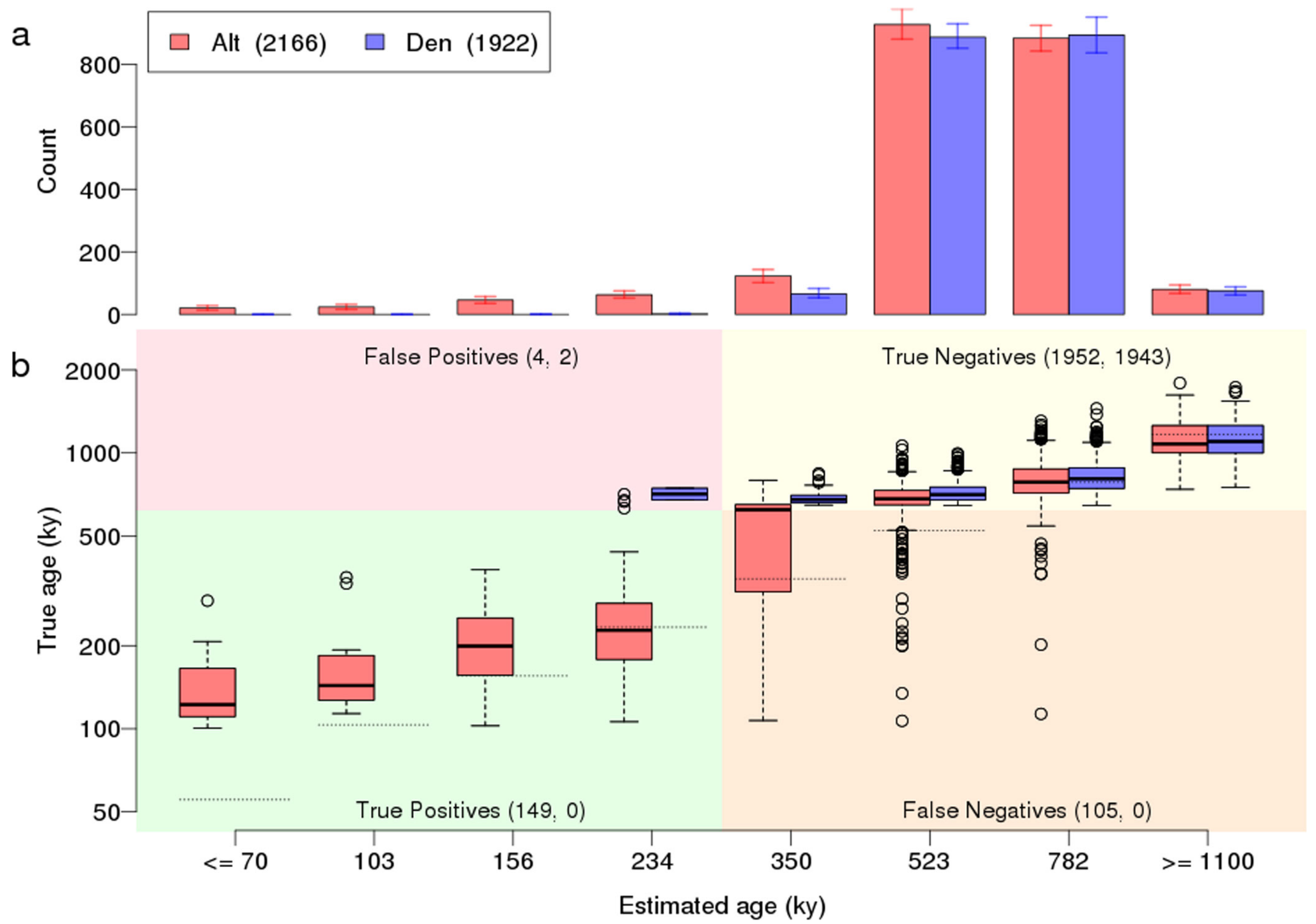

Extended Data Figure 5 | Haplotype ages inferred by ARGweaver on simulated data. a, Distribution of 'African' haplotype ages in sequences simulated with introgression into the Altai Neanderthal lineage from modern humans 100,000 years ago. 'African' haplotypes are identified as in Fig. 2. Error bars represent the 95% Bayesian credible intervals from 302 MCMC replicates. **b**, Distribution of true haplotype ages for each of the estimated ages. The horizontal dotted lines show the estimated age. The plot is divided into four quadrants; the lower half represents 'African' haplotypes having true ages between 100,000 and 620,000 years ago (the divergence time between archaic and present-day humans), which are necessarily due to post-divergence gene flow from modern humans. The left side of the plot represents regions that would be identified as introgressed based on a threshold of ≤ 234,000 years. The counts in each quadrant are for Altai Neanderthal (red) and Denisovan (blue), respectively. The counts for the Denisovan in the lower two quadrants are zero because there was no simulated migration from modern humans into the Denisovan lineage. Note that this is a somewhat nonstandard plot of true age versus estimated age; a more standard, reversed view is given in Supplementary Fig. 33 and demonstrates that the estimated ages are largely unbiased. Error bars as in the standard Tukey box plot (R boxplot function).

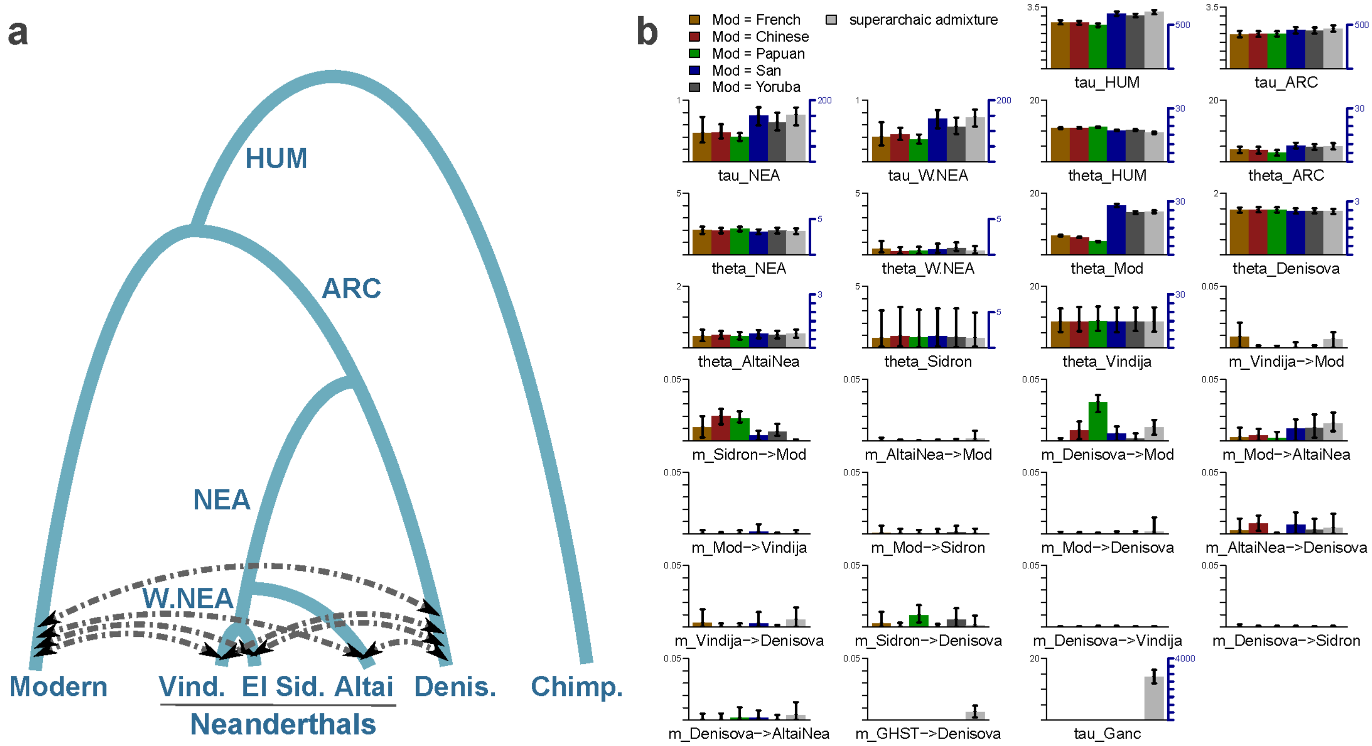

Extended Data Figure 6 | Main G-PhoCS demographic inference. Summary of the main demographic inference using G-PhoCS in a model with four archaic populations and one modern human population. **a**, The population phylogeny assumed in each of the G-PhoCS runs. Labels on internal edges indicate names of the four ancestral populations: population ancestral to the two Western Neanderthals (W.NEA), population ancestral to all three Neanderthals (NEA), population ancestral to all four archaic individuals (ARC), and population ancestral to all human samples (HUM). We augmented the phylogeny with 14 directional migration bands (arrows) between all pairs of sampled populations except for the pairs of Neanderthal populations. In one of the runs we added an unknown 'ghost' population and a migration band from that population into the Denisovan population. **b**, Parameter estimates obtained by G-PhoCS in six separate runs analysing 13,754 neutral and loosely linked loci, substituting samples in the 'Modern' population with pairs of present-day humans from five different modern populations (Supplementary Table 11). The last run has gene flow from the 'ghost' population and uses two Yoruba individuals in the modern human population. Bar heights indicate posterior mean and error bars correspond to 95% Bayesian credible intervals. Estimates of divergence times (τ) and effective population sizes (θ) are given in raw form, scaled by number of mutations per 10 kb (left axis), and calibrated to absolute units, 1,000 years for time, and 1,000 individuals for effective population size, (right axis) assuming an average mutation rate of 0.5×10^{-9} mutations per year per bp and an average generation time of 29 years. For each of the 14 migration bands, we are showing the estimated total migration rates (m). See Supplementary Information section 8 for more information on parameter calibration and setup for G-PhoCS. A graphical summary of these estimates is given in Fig. 3.

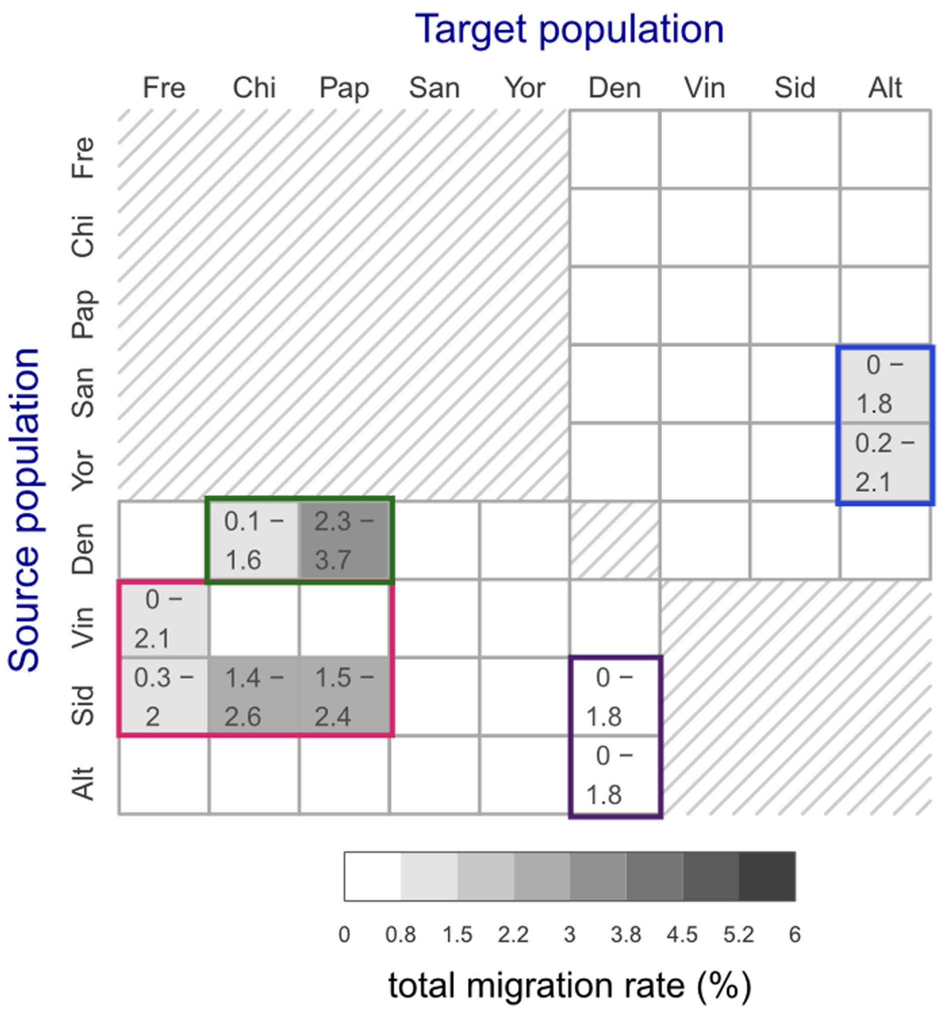

Extended Data Figure 7 | Migration rates in main demographic inference. Total migration rates estimated for 46 directional migration bands in five separate G-PhoCS runs. Rows correspond to source populations and columns to the target populations. The 40 migration bands between modern (present-day) and archaic populations were considered in five separate runs, each containing the eight bands associated with a different modern human population (Extended Data Fig. 6a). The six migration bands between the Denisovan population and the three Neanderthal populations were considered in all six runs, and the values shown here were estimated as an aggregate of all five runs. The estimates are as shown in Extended Data Fig. 6. Shade indicates the posterior mean total migration rate (legend), which approximates the probability that a lineage in the target population originated in the source population. The 95% Bayesian credible intervals from 2,000 MCMC replicates are indicated for migration bands whose upper credible interval bound is above 0.3%. We identified four clusters of migration bands, corresponding to what were likely at least four different cases of introgression between populations: (1) Western (European) Neanderthals into non-African modern humans (red box), (2) Denisovans into East Asian and Oceanians (green box), (3) Neanderthals into Denisovans (magenta), and (4) modern humans into Eastern Neanderthals (blue box). Directed arrows in Fig. 3a depict these introgression events. Sid, El Sidrón Neanderthal; Vin, Vindija Neanderthal.

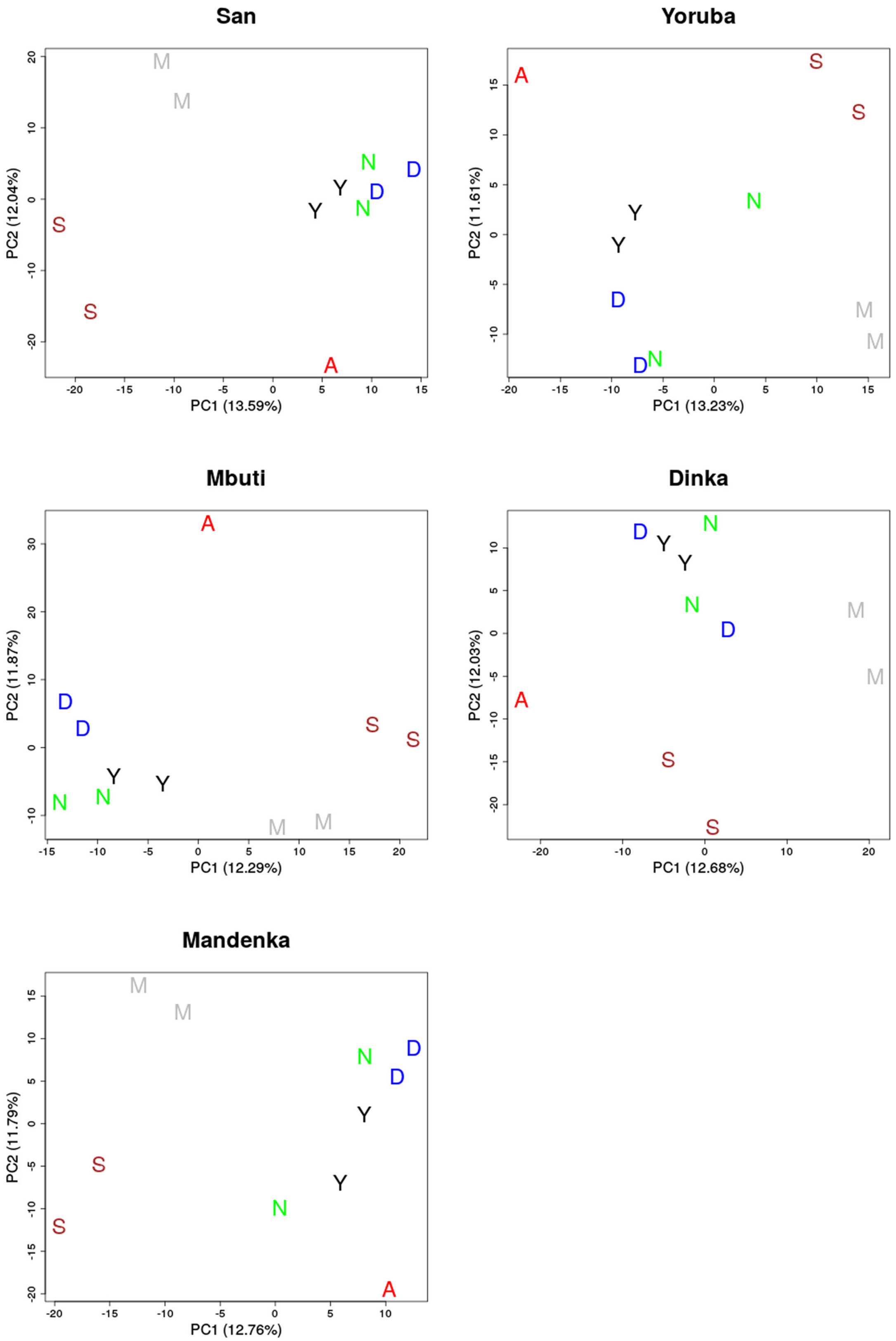

Extended Data Figure 8 | Principal component analysis. The putatively introgressed segments in the Altai Neanderthal genome, defined by derived alleles in two individuals from the San, Yoruba, Mbuti, Dinka or Mandenka populations. The introgressed segments show no clear affinity to one present-day African population. A, Altai Neanderthal; S, San; M, Mbuti; Y, Yoruba; D, Dinka; N, Mandenka.

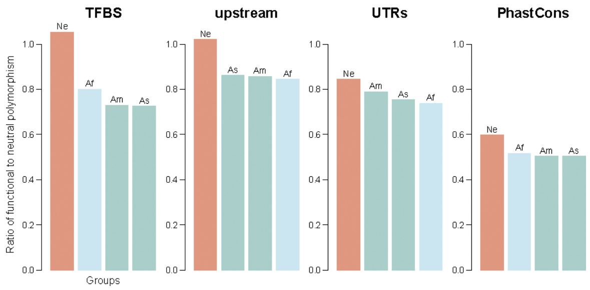

Extended Data Figure 9 | Natural selection in chromosome 21. Ratio of functional (putatively deleterious) to neutral polymorphism in archaic and present-day humans (Supplementary Information section 7). TFBS, transcription factor binding sites; upstream refers to 5 kb before the transcription start site of genes; UTRs, untranslated regions (in the mRNA). PhastCons ≥ 0.9 for a site to be used. Ne, Neanderthals; Af, Africans; As, Asians; Am, Americans.

Extended Data Table 1 | Shared derived alleles

African frequency	0≤f≤0.1	0.1<f ≤ 0.2	0.2<f ≤ 0.3	0.3<f ≤ 0.4	0.4<f ≤ 0.5	0.5<f ≤ 0.6	0.6<f ≤ 0.7	0.7<f ≤ 0.8	0.8<f ≤ 0.9	0.9<f≤ 1	**Fixed**
Altai (%)	66.86	5.01	3.89	3.42	3.11	2.79	2.71	2.55	2.68	**6.99**	**2.98**
Denisovan (%)	72.27	4.35	3.43	2.96	2.60	2.5	2.26	2.12	2.23	**5.30**	**1.90**

Percentage of derived alleles in one archaic genome (Altai Neanderthal or Denisovan) shared with African genomes in sites that are homozygous ancestral in the other archaic genome. The percentages of shared derived alleles are binned by their African allele frequency. Fixed derived alleles in Africans are included in the '$0.9 < f \leq 1$' but also shown separately in the 'fixed' category.

ARTICLE

doi:10.1038/nature16962

Expanding antigen-specific regulatory networks to treat autoimmunity

Xavier Clemente-Casares[1], Jesus Blanco[2,3]*, Poornima Ambalavanan[1]*, Jun Yamanouchi[1]*, Santiswarup Singha[1]*, Cesar Fandos[2], Sue Tsai[1], Jinguo Wang[1], Nahir Garabatos[4], Cristina Izquierdo[4], Smriti Agrawal[5], Michael B. Keough[5], V. Wee Yong[5], Eddie James[6], Anna Moore[7], Yang Yang[1,8], Thomas Stratmann[4], Pau Serra[2] & Pere Santamaria[1,2]

Regulatory T cells hold promise as targets for therapeutic intervention in autoimmunity, but approaches capable of expanding antigen-specific regulatory T cells *in vivo* are currently not available. Here we show that systemic delivery of nanoparticles coated with autoimmune-disease-relevant peptides bound to major histocompatibility complex class II (pMHCII) molecules triggers the generation and expansion of antigen-specific regulatory CD4$^+$ T cell type 1 (T_R1)-like cells in different mouse models, including mice humanized with lymphocytes from patients, leading to resolution of established autoimmune phenomena. Ten pMHCII-based nanomedicines show similar biological effects, regardless of genetic background, prevalence of the cognate T-cell population or MHC restriction. These nanomedicines promote the differentiation of disease-primed autoreactive T cells into T_R1-like cells, which in turn suppress autoantigen-loaded antigen-presenting cells and drive the differentiation of cognate B cells into disease-suppressing regulatory B cells, without compromising systemic immunity. pMHCII-based nanomedicines thus represent a new class of drugs, potentially useful for treating a broad spectrum of autoimmune conditions in a disease-specific manner.

Autoimmune diseases such as type 1 diabetes (T1D), multiple sclerosis and rheumatoid arthritis result from chronic autoimmune responses involving T cells and B cells recognizing numerous antigenic epitopes on incompletely defined lists of autoantigens[1–3]. Eliminating or suppressing all polyclonal autoreactive T-cell specificities (known and unknown) in each individual autoimmune disorder without compromising systemic immunity is not currently possible.

Adoptive transfer of polyclonal FOXP3$^+$CD4$^+$CD25$^+$ regulatory T (T_{reg}) cells expanded *ex vivo* has been proposed as an alternative therapeutic approach[4]. The potential for bystander immunosuppression, the lack of effective strategies for expanding antigen-specific T_{reg} cells *in vitro,* and the lineage instability of FOXP3$^+$ T_{reg} cells, have hindered the clinical translation of this approach[5–7]. T_R1 FOXP3$^-$CD4$^+$CD25$^-$ T cells, which produce the cytokines IL-10 and IL-21, and express the surface markers CD49b and LAG-3 and the transcription factor c-Maf[8], constitute another regulatory T-cell subset recently exploited for the treatment of human inflammatory diseases[9–11]. However, as with FOXP3$^+$ T_{reg} cells, there are no pharmacological approaches that can expand autoantigen- or disease-specific T_R1-like cells *in vivo*.

We recently discovered that systemic delivery of nanoparticles (NPs) coated with T1D-relevant pMHC class I complexes could blunt the progression of T1D by expanding subsets of CD8$^+$ T cells with regulatory potential but conventional memory-like phenotype[12]. As this outcome could be replicated with different pMHC class I complexes, we reasoned that pMHC–NP therapy may utilize a naturally occurring negative feedback regulatory loop, whereby chronic autoantigenic exposure (and exposure to pMHC–NPs) would trigger the differentiation of autoreactive T cells into regulatory T-cell progeny. By this reasoning, we predicted that NPs coated with disease-relevant pMHCII complexes might be able to expand disease-specific regulatory CD4$^+$ T cells *in vivo*.

Expansion of disease-specific T_R1 cells

We treated non-obese diabetic (NOD) and NOD *Foxp3-eGFP* mice (expressing enhanced green fluorescent protein (eGFP) under the control of the mouse *Foxp3* promoter) with uncoated nanoparticles or nanoparticles coated with a pMHC, 2.5mi/IA^{g7} (ref. 13), recognized by the diabetogenic BDC2.5-specific T-cell receptor (TCR), or with 2.5mi/IA^{g7} monomers. Nanoparticles coated in 2.5mi/IA^{g7} induced expansion of cognate CD4$^+$ T cells in blood and spleens of all mice (Fig. 1a, b). These cells had a memory-like (CD44^{hi}CD62L^{low}) FOXP3$^-$ T_R1-like phenotype, expressing ICOS, latent-associated TGF-β and the T_R1 markers CD49b and LAG-3 (Fig. 1c, d). A similar outcome was observed in mice treated with 2.5mi/IA^{g7}–NPs upon depletion of CD4$^+$CD25$^+$ T cells (Extended Data Fig. 1a). Unlike their tetramer$^-$ counterparts, these cells proliferated and secreted IL-10 and to a lesser extent IFNγ, but not IL-2, IL-4 or IL-17, in response to dendritic cells (DCs) pulsed with the 2.5mi peptide (Extended Data Fig. 1b). Real-time reverse-transcription (RT)–PCR analyses confirmed the T_R1-like phenotype of these cells (Supplementary Table 1).

To determine if pMHCII–NPs could directly trigger T_R1 marker and IL-10 expression on cognate CD4$^+$ T cells, we cultured naive and anti-CD3 plus anti-CD28 monoclonal antibody (mAb)-preactivated 2.5mi/IA^{g7}-tetramer$^+$CD4$^+$ T cells from BDC2.5-TCR-transgenic NOD *Foxp3-eGFP* or NOD *Il10^{GFP}* mice (carrying an eGFP insertion in the *Il10* locus)[14] in the presence of 2.5mi/IA^{g7}–NPs, 2.5mi peptide or 2.5mi/IA^{g7} monomer. Naive T cells expressed neither CD49b nor LAG-3, even after incubation with 2.5mi/IA^{g7}–NPs, 2.5mi/IA^{g7} monomer

[1]Julia McFarlane Diabetes Research Centre (JMDRC), and Department of Microbiology, Immunology and Infectious Diseases, Snyder Institute for Chronic Diseases and Hotchkiss Brain Institute, Cumming School of Medicine, University of Calgary, Calgary, Alberta T2N 4N1, Canada. [2]Institut D'Investigacions Biomèdiques August Pi i Sunyer (IDIBAPS), Barcelona, 08036, Spain. [3]Centro de Investigación Biomédica en Red de Diabetes y Enfermedades Metabólicas Asociadas (CIBERDEM), Instituto de Salud Carlos III, Madrid 28029, Spain. [4]Department of Physiology and Immunology, Faculty of Biology, University of Barcelona, Barcelona 08028, Spain. [5]Hotchkiss Brain Institute and Department of Clinical Neurosciences, Faculty of Medicine, University of Calgary, Calgary, Alberta T2N 4N1, Canada. [6]Benaroya Research Institute at Virginia Mason, Seattle, Washington 98101-2795, USA. [7]Molecular Imaging Laboratory, MGH/MIT/HMS Athinoula A. Martinos Center for Biomedical Imaging, Department of Radiology, Massachusetts General Hospital, Charlestown, Massachusetts 02129, USA. [8]Department of Biochemistry and Molecular Biology, Cumming School of Medicine, University of Calgary, Calgary, Alberta T2N 4N1, Canada.
*These authors contributed equally to this work.

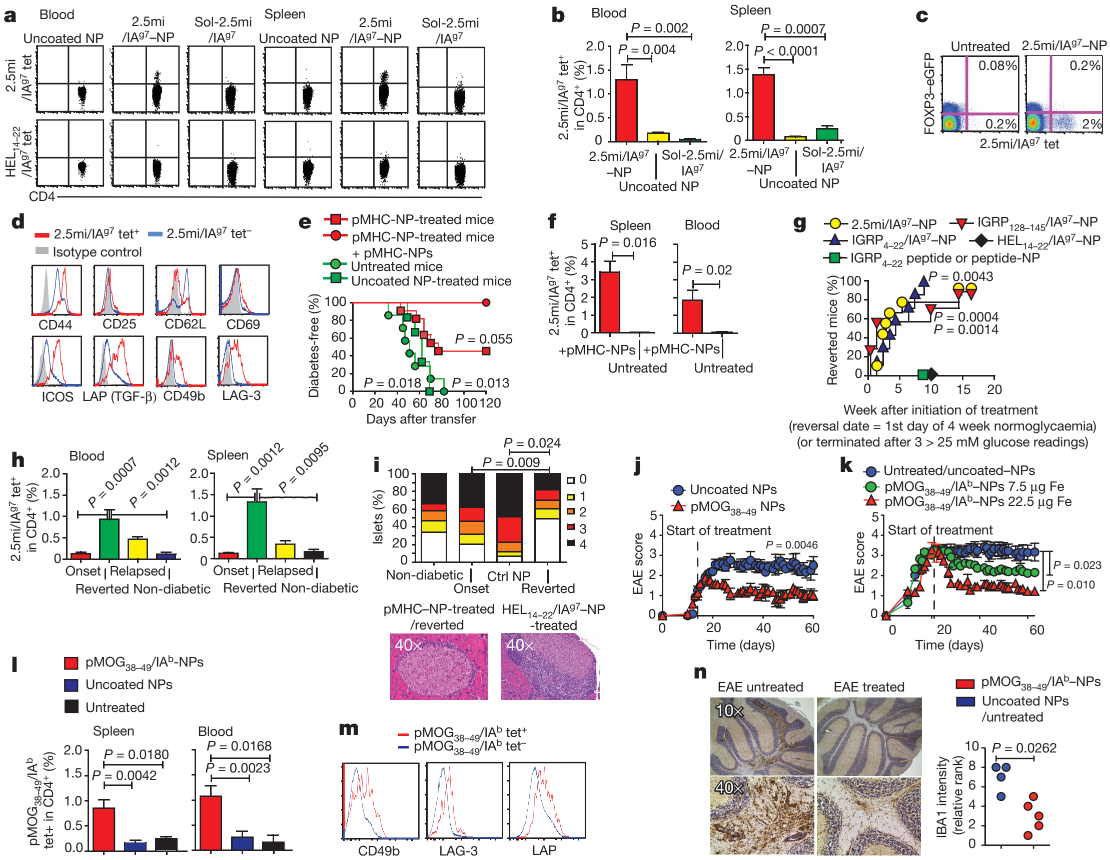

Figure 1 | pMHC–NPs relevant for T1D or EAE expand cognate disease-suppressing T_R1-like CD4$^+$ T cells *in vivo*. a, b, Tetramer-staining profiles (**a**) and percentages of tetramer$^+$CD4$^+$ T cells (**b**). Data correspond to pre-diabetic NOD females treated for 5 weeks (blood: $n=5$, 8 and 6; spleen: $n=5$, 18 and 6, respectively). Tet, tetramer. **c**, Tetramer-staining of splenic CD4$^+$ T cells from treated or untreated NOD *Foxp3-eGFP* mice. **d**, The tetramer$^+$CD4$^+$ T cells of 2.5mi/IA^{g7}–NP-treated mice display a T_R1-like phenotype. **e**, Incidence of diabetes in T-cell-reconstituted NOD *scid* hosts transfused with CD4$^+$ T cells from different donors ± 2.5mi/IA^{g7}–NPs ($n=11$, 5, 7 and 6 from top). **f**, Percentages of tetramer$^+$CD4$^+$ T cells in 2.5mi/IA^{g7}–NP-treated or untreated NOD *scid* hosts ($n=4$–5 per group). **g**, Incidence of disease reversal in diabetic mice treated with pMHC–NPs ($n=9$, 7, 7, 7 from top left to right), or IGRP$_{4-22}$ peptide[16] and IGRP$_{4-22}$ peptide–NP ($n=9$). **h**, Percentage of tetramer$^+$CD4$^+$ T cells in diabetic mice at onset, in response to 2.5mi/IA^{g7}–NP therapy and age-matched non-diabetic controls ($n=8$, 6, 2 and 7 from left). **i**, Insulitis scores ($n=6$, 4, 3 and 6 from left). Bottom, representative images. **j–m**, C57BL/6 mice were immunized with pMOG$_{35-55}$. **j**, EAE scores of mice treated from day 14 ($n=4$ each). **k**, EAE scores of mice treated from day 21 ($n=10$, 7 and 3 from top). **l**, Percentage of tetramer$^+$CD4$^+$ T cells in spleen and blood of mice from **j** and **k** ($n=13$, 14 and 5 from top). **m**, Representative flow profiles of CD4$^+$ T cells from mice in **j** and **k**. **n**, Representative microglial IBA1 stainings and relative rank scores in the cerebellum of mice from **k** ($n=4$–5). *P* values were calculated via Mann–Whitney *U*-test, log-rank (Mantel–Cox) test or two-way ANOVA. Error bars, s.e.m.

or 2.5mi peptide (Extended Data Fig. 1c, d). However, preactivated T cells upregulated both markers as well as eGFP (IL-10) only in response to 2.5mi/IA^{g7}–NPs (Extended Data Fig. 1d, e). In agreement with this, expression of IL-10 in NOD *Il10*^{GFP} mice treated with 2.5mi/IA^{g7}–NPs was largely restricted to the CD49b$^+$LAG-3$^+$CD4$^+$ subset (Extended Data Fig. 1f).

In vitro, the tetramer$^+$CD4$^+$ T cells of pMHC–NP-treated mice suppressed the proliferation of non-cognate (islet-specific glucose-6-phosphatase catalytic subunit-related protein (IGRP)- or LCMV Gp33-specific) CD8$^+$ T cells in response to peptide-pulsed DCs, in an IL-10- and TGF-β-dependent manner (Extended Data Fig. 1g). *In vivo*, splenic CD4$^+$ T cells from donors treated with pMHC–NPs suppressed diabetes development in T-cell-reconstituted NOD *scid* (also known as NOD *Prkdc*^{scid}) hosts (Fig. 1e), an effect that was potentiated by treating hosts with pMHC–NPs (Figs 1e, f).

We next investigated whether 2.5mi/IA^{g7}–NPs or NPs coated with IGRP$_{4-22}$/IA^{g7} or IGRP$_{128-145}$/IA^{g7}, targeted by sub-dominant pools of autoreactive CD4$^+$ T cells[15], could restore normoglycaemia in diabetic NOD mice. Unlike mice treated with nanoparticles coated with hen egg-white lysozyme (HEL)$_{14-22}$/IA^{g7}, 90–100% of the mice that received nanoparticles coated with 2.5mi/IA^{g7}, IGRP$_{4-22}$/IA^{g7} or IGRP$_{128-145}$/IA^{g7} reverted to stable normoglycaemia (Fig. 1g, Extended Data Fig. 1h) and displayed systemic expansion of cognate T_R1-like T cells (Fig. 1h, Extended Data Fig. 2a–g). Treatment with peptide[16] or peptide-coated nanoparticles but without MHC could not reproduce any of these effects (Fig. 1g, Extended Data Figs 1h and 2h). Treatment withdrawal resulted in loss of the normoglycaemic state in 25–60% of mice (Extended Data Fig. 1i), in association with the loss of the tetramer$^+$CD4$^+$ T-cell pools (Fig. 1h, Extended Data Fig. 2a). The animals that maintained normoglycaemia had normal postprandial serum insulin levels, fasting glucose tolerance (Extended Data Fig. 1j–m) and reduced insulitis (Fig. 1i). In addition, their pancreatic lymph nodes (PLNs) could not support the proliferation of carboxyfluorescein succinimidyl ester (CFSE)-labelled IGRP$_{206-214}$/K^d-specific CD8$^+$ T cells *in vivo* (Extended Data Fig. 1n).

We next tested the ability of nanoparticles coated with myelin oligodendrocyte glycoprotein (pMOG)$_{38-49}$/IA^b to blunt the progression of pMOG$_{35-55}$-induced experimental autoimmune encephalomyelitis (EAE, a model of multiple sclerosis) in C57BL/6 mice. pMOG$_{38-49}$/IA^b–NP therapy dampended disease progression when given on day 14 after immunization and restored motor function in paralytic mice when given on day 21 (Fig. 1j, k). These effects were mirrored by weight gain, and were associated with systemic expansion of cognate T_R1-like T cells, reductions in activated macrophage/microglia in the cerebellum,

fewer inflammatory foci and areas of demyelination in the white matter of the cerebellum and decreased demyelination of the spinal cord (Fig. 1l–n, Extended Data Figs 3a–f). Similar therapeutic effects were seen in *HLA-DR4-IE*-transgenic C57BL/6 *IAb*^{null} mice (MHCII knockout mice expressing a transgenic hybrid MHCII molecule composed of the peptide-binding domain of human HLA-DR4 and the membrane-proximal domain of mouse IE (DR4-IE)) immunized with human (h) proteolipid protein (hPLP)$_{175–192}$ or hMOG$_{97–108}$ peptides and treated with hPLP$_{175–192}$/DR4-IE or hMOG$_{97–108}$/DR4-IE–NPs upon developing limb paralysis (Extended Data Figs 4a–d).

Disease and organ specificity

Studies in another autoimmune disease model, collagen-induced arthritis (CIA), showed that nanoparticles displaying mouse collagen (mCII)$_{259–273}$/DR4-IE could reduce joint inflammation in arthritic *HLA-DR4-IE*-transgenic C57BL/10.M mice in association with systemic expansions of cognate T$_R$1-like T cells (Figs 2a–e, Extended Data Fig. 4e). In contrast, nanoparticles coated with hMOG$_{97–108}$/DR4-IE complexes had no effect (Fig. 2a–c)

To investigate further the disease-specificity of pMHC–NP therapy, we induced EAE in C57BL/6 *IAb*^{null} *HLA-DR4-IE*-transgenic mice by immunization with hPLP$_{175–192}$ and treated diseased mice with hPLP$_{175–192}$/DR4-IE–NPs (positive control), uncoated nanoparticles (negative control), EAE-relevant hMOG$_{97–108}$/DR4-IE–NPs (which display a peptide from a CNS autoantigen other than that used to induce disease), or CIA-relevant mCII$_{259–273}$/DR4-IE–NPs. Whereas hMOG$_{97–108}$/DR4-IE–NPs blunted EAE as efficiently as the positive control, mCII$_{259–273}$/DR4-IE–NPs had no therapeutic activity (Fig. 2f, Extended Data Fig. 4f, g). Here, too, therapeutic activity was associated with systemic expansions of cognate T$_R$1-like T cells (Fig. 2g, h). Administration of mCII$_{259–273}$ peptide[16] or of mCII$_{259–273}$-peptide-coated microparticles (MPs)[17] to arthritic C57BL/10.M *HLA-DR4-IE*-transgenic mice (Fig. 2a–d, Extended Data Fig. 4e), or of hMOG$_{97–108}$ peptide, hMOG$_{97–108}$/DR4-IE monomers or hMOG$_{97–108}$-coated

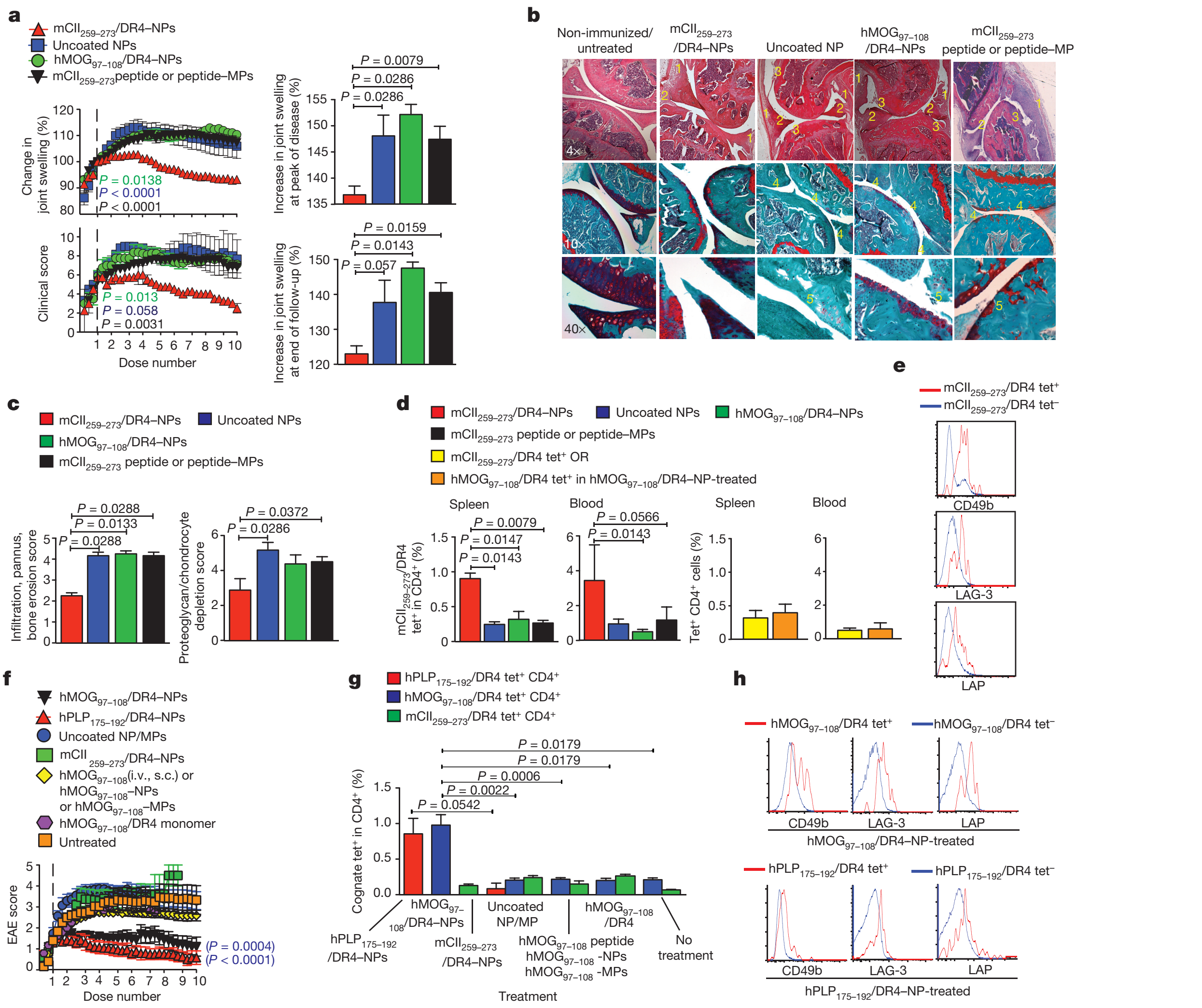

Figure 2 | Therapeutic effects are disease-specific and dependent on both pMHC and nanoparticles. **a**–**f**, C57BL/10.M *HLA-DR4-IE*-transgenic mice immunized with bovine collagen. **a**, Left, changes in joint swelling (top) and clinical scores (bottom) in response to uncoated NPs, pMHC–NPs, peptide s.c.[16] or peptide-coated MPs i.v[17]. Treatment was initiated when joint swelling reached 130% of baseline (data normalized to the initiation of treatment (100% value)) ($n = 4$, 4, 4 and 8 from top). Right, percentage increase in joint swelling relative to pre-immunization baseline (100% value). **b**, Representative haematoxylin and eosin (first row) and O-safranin/fast-green/haematoxylin (second and third rows) knee joint staining images. Third row shows enlarged images of lacunae on the bone and meniscal articular surfaces. 1, panus formation; 2, cellular infiltration of the meniscus; 3, bone erosion; 4, proteoglycan depletion; 5, loss of chondrocyte/lacunnae. **c**, Average pathology scores ($n = 3$–4 per group). **d**, Percentage of tetramer$^+$CD4$^+$ T cells. **e**, Representative flow cytometry profiles for T$_R$1 markers in mCII$_{259–273}$/DR4–NP-treated. **f**–**h**, C57BL/6 *IAb*^{null} *HLA-DR4-IE*-transgenic mice immunized with hPLP. **f**, Changes in EAE scores (($n = 5$, 4, 13 (4–9 per group), 5, 19 (4–5 per group, see also Extended Data Fig. 4h), 4 and 5 from top). **g**, Percentage of tetramer$^+$CD4$^+$ T cells in the spleen of mice from **f** ($n = 4$, 5, 4, 6, 15, 3 and 3 from left). **h**, Representative flow cytometry profiles for T$_R$1 markers. Data were compared using Mann–Whitney *U*-test or two-way ANOVA. Error bars, s.e.m.

nanoparticles or microparticles to C57BL/6 *IAb*^{null} *HLA-DR4-IE*-transgenic mice failed to both expand cognate T_R1-like cells and blunt disease (Fig. 2f, g, Extended Data Fig. 4f–i). Thus, the biological and therapeutic effects of pMHCII–NPs are disease-specific and dissociated from the pathogenic role of epitopes (disease-triggering versus downstream autoantigenic targets), suggesting that these compounds act on pre-activated autoreactive T cells and can generate T_R1-like cell expansions from rare T-cell precursor pools.

Soluble mediators

Blockade of IL-10, TGF-β and IL-21R (but not IFNγ) abrogated the anti-diabetogenic properties of 2.5mi/IA^{g7}–NPs or IGRP$_{4–22}$/IA^{g7}–NPs (Fig. 3a, Extended Data Fig. 5a). With the exception of IL-21R blockade (known to inhibit CD8$^+$ T-cell activation), these interventions also abrogated the suppression of autoantigen crosspresentation by the pMHC–NP-expanded T_R1-like T cells in the PLNs (Extended Data Figs 5b, c, 6). Studies using diabetic NOD *Ifng*$^{-/-}$ and NOD *Il10*$^{-/-}$ mice revealed that development of the T_R1 precursors and/or T_R1-like cells that expand in response to therapy requires IFNγ in addition to IL-10 (Extended Data Figs 5d–f, 6). mAbs against IL-10, TGF-β and IL-21R also abrogated the anti-encephalitogenic activity of hPLP$_{175–192}$/DR4-IE–NPs in C57BL/6 *IAb*^{null} *HLA-DR4-IE*-transgenic mice (Extended Data Fig. 5g–j). pMOG$_{35–55}$-immunized C57BL/6 *Il27r*$^{-/-}$ mice responded to pMOG$_{38–49}$/IA^b–NPs like their wild-type counterparts (Fig. 1j–n, Extended Data Fig. 5k–n). Thus, IFNγ and IL-10, but not IL-27[18], are necessary for pMHC–NP-induced T_R1-like cell development; and autoreactive T_R1-like T cells use IL-10, TGF-β and IL-21 (but not IFNγ) to suppress disease.

Downstream effectors and network formation

The PLNs (but not the mesenteric lymph nodes (MLNs) or spleens) of pMHC–NP-treated NOD mice harboured increased percentages of B cells compared with the PLNs of mice treated with pMHCII–NPs not relevant for T1D (Extended Data Fig. 5o). Studies of mice treated with a range of pMHC–NP doses revealed that the sizes of the PLN (but not splenic) B-cell and T_R1-like cell pools were correlated (Extended Data Fig. 5p). Unlike their splenic or MLN counterparts, the PLN B cells of these mice could not effectively present peptide to cognate CD4$^+$ T cells *ex vivo* (Extended Data Fig. 5q). In addition, these cells produced IL-10 in response to lipopolysaccharide (LPS) (Extended Data Fig. 5r), suggesting that pMHC–NP-induced T_R1-like cells might trigger the formation and expansion of regulatory B (B_{reg}) cells in the PLNs. In fact, 2.5mi-pulsed B cells, but not DCs, underwent expansion in 2.5mi/IA^{g7}–NP-treated hosts within a week of transfer (Extended Data Fig. 5s, t).

To probe this further, we transfused NOD *Il10*^{GFP} splenic B cells that were either pulsed with 2.5mi or a negative control peptide (GPI$_{282–292}$), into 2.5mi/IA^{g7}–NP-treated NOD or NOD *Il10*$^{-/-}$ hosts. Seven days later, the hosts were analysed for the presence of IL-10-producing

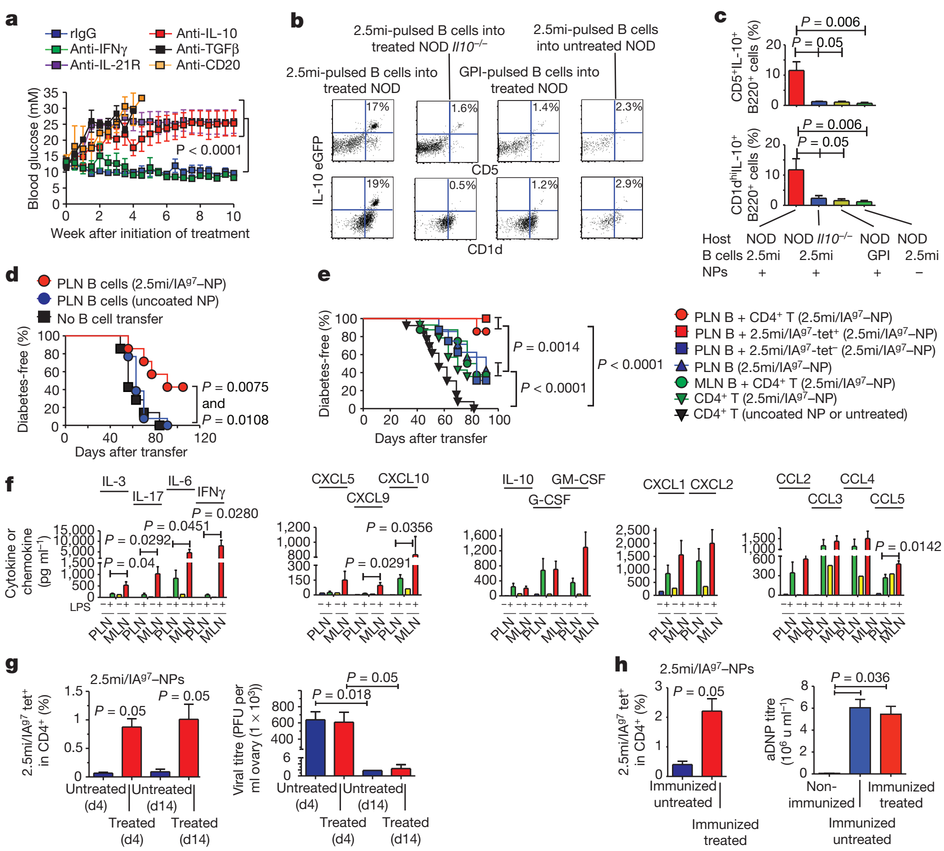

Figure 3 | Disease reversal involves effects of T_R1 cytokines on cognate B cells and local CD11b$^+$ cells, without compromising systemic immunity. a, Blood glucose levels in diabetic NOD mice treated with 2.5mi/IA^{g7}–NPs and blocking antibodies ($n = 8$, 4, 6, 6, 5 and 4 from top to right). **b**, Expression of IL-10 (eGFP) and upregulation of CD5 and CD1d by eGFP$^-$ 2.5mi-pulsed splenic B cells from NOD *Il10*^{GFP} donors in 2.5mi/IA^{g7}–NP-treated NOD hosts. **c**, Averaged results from **b** ($n = 4$, 3, 3 and 7 from left). **d**, Incidence of diabetes in T-cell-reconstituted NOD *scid* hosts left alone or transfused with PLN CD19$^+$ cells ($n = 7$, 13 and 7 from top). **e**, Incidence of diabetes in T-cell-reconstituted NOD *scid* hosts transfused with CD19$^+$ and/or CD4$^+$ cells ($n = 7$, 6, 3, 7, 8, 11 and 13 from top). **f**, Cytokine and chemokine profiles of PLN and MLN CD11b$^+$ cells from 2.5mi/IA^{g7}–NP-treated NOD mice in response to LPS ($n = 3$–4 each). **g**, Percentage of tetramer$^+$CD4$^+$ T cells in the spleens (left), and viral titres in the ovaries (right) of treated compared with untreated NOD mice 4 and 14 days after vaccinia virus infection ($n = 3$ per group). **h**, Percentages of tetramer$^+$CD4$^+$ T cells in the spleens (left) and serum anti-dinitrophenyl (DNP) antibody titres (right) in treated and untreated NOD mice immunized with keyhole limpet haemocyanin (KLH)–DNP ($n = 3$–5 per group). Data were compared using Mann–Whitney *U*-test, log-rank test or two-way ANOVA. Error bars, s.e.m.

(eGFP$^+$) CD5$^+$CD1d^{high} B cells. NOD (but not NOD *Il10*$^{-/-}$) mice treated with 2.5mi/IA^{g7}–NPs efficiently induced formation of B$_{reg}$ cells specifically from 2.5mi-pulsed B cells, and IL-21R but not IL-10 or TGF-β blockade suppressed this effect (Fig. 3b, c, Extended Data Fig. 5u).

In vitro, the PLN B cells of 2.5mi/IA^{g7}–NP-treated mice had a moderate suppressive effect on the proliferative activity of BDC2.5 CD4$^+$ T cells in response to peptide-pulsed DCs (Extended Data Fig. 5v). *In vivo*, these B cells suppressed diabetes development in T-cell-reconstituted NOD *scid* hosts as compared to PLN B cells from control mice (Fig. 3d). Co-transfer of PLN B cells and bulk or 2.5mi/IA^{g7}-tetramer$^+$ splenic CD4$^+$ T cells from 2.5mi/IA^{g7}–NP-treated mice resulted in >95% suppression, as compared to PLN B cells with or without tetramer$^-$CD4$^+$ T cells from 2.5mi/IA^{g7}–NP-treated mice, to CD4$^+$ T cells with or without MLN B cells from 2.5mi/IA^{g7}–NP-treated mice (~40%), or to CD4$^+$ T cells from untreated or control–NP-treated mice (0%) (Fig. 3e), supporting synergistic effects. In agreement with this, treatment of newly diabetic NOD mice with a B-cell-depleting anti-CD20 mAb abrogated the anti-diabetogenic activity of 2.5mi/IA^{g7}–NPs (Fig. 3a, Extended Data Fig. 5x).

Comparison of the cytokine and chemokine profile of CD11b$^+$ cells derived from the PLN or MLN of pMHC–NP-treated NOD mice further revealed that CD11b$^+$ cells from the PLN produced lower levels of the pro-inflammatory mediators IL-3, IL-17, IL-6, IFNγ, CXCL9 and CXCL10 in response to LPS than their MLN counterparts did (Fig. 3f). Importantly, the effects of pMHC–NP therapy on antigen-presenting cells (APC)s from draining lymph nodes were not associated with impaired systemic immunity because pMHC–NP-treated NOD mice cleared an acute viral infection and mounted antibodies against an exogenous antigen as efficiently as untreated mice (Figs 3g, h).

Antigen-experienced T cells as targets

The memory-like phenotype and the upregulation of T-bet mRNA in the expanded T$_R$1-like cells, coupled with the inability of pMHC–NPs to expand cognate T$_R$1-like cells in non-diseased mice or NOD *Ifng*$^{-/-}$ mice suggested that pMHC–NPs expand pre-existing T$_R$1 cells that arise from antigen-experienced precursors; and/or trigger the differentiation of antigen-experienced T$_H$1 cells into T$_R$1-like cells. Indeed, whereas diabetic NOD *G6pc2*$^{-/-}$ mice (which lack IGRP) responded to 2.5mi/IA^{g7}–NPs like wild-type NOD mice, they did not respond to IGRP$_{4-22}$/IA^{g7}–NPs (Figs 4a, b). *In vitro*, 2.5mi/IA^{g7}–NPs triggered the expression of CD49b and LAG-3 and the upregulation of *c-maf*, *Il21*, *Il10* and *Lag3* mRNA exclusively in anti-CD3 plus anti-CD28 mAb-activated, but not naive BDC2.5 CD4$^+$ T cells (Fig. 4c, Extended Data Fig. 1d).

To investigate this further, we transfused naive (CD44^{low}CD62L^{hi}) or memory-like (CD44^{hi}CD62L^{low}) BDC2.5 CD4$^+$ T cells into hosts of the congenic NOD.*Thy1^a* strain and measured changes in their expression of LAG-3 and CD49b protein and *c-maf*, *Il21*, *Il10*, *Ifng*, *Lag3* and *Cd49b* mRNA, both upon 2.5mi/IA^{g7}–NP therapy and in the absence of therapy. Notably, the memory T cells from pMHC–NP-untreated hosts expressed about one hundred-fold higher levels of *c-maf* and *Il21* and, to a lesser extent, *Lag3* and *Cd49b*, but not *Il10* mRNA than their naive counterparts (Fig. 4d). This is in accordance with the observed demethylation of *Il21* and the c-Maf/IL-10- and IL-21-expression competency

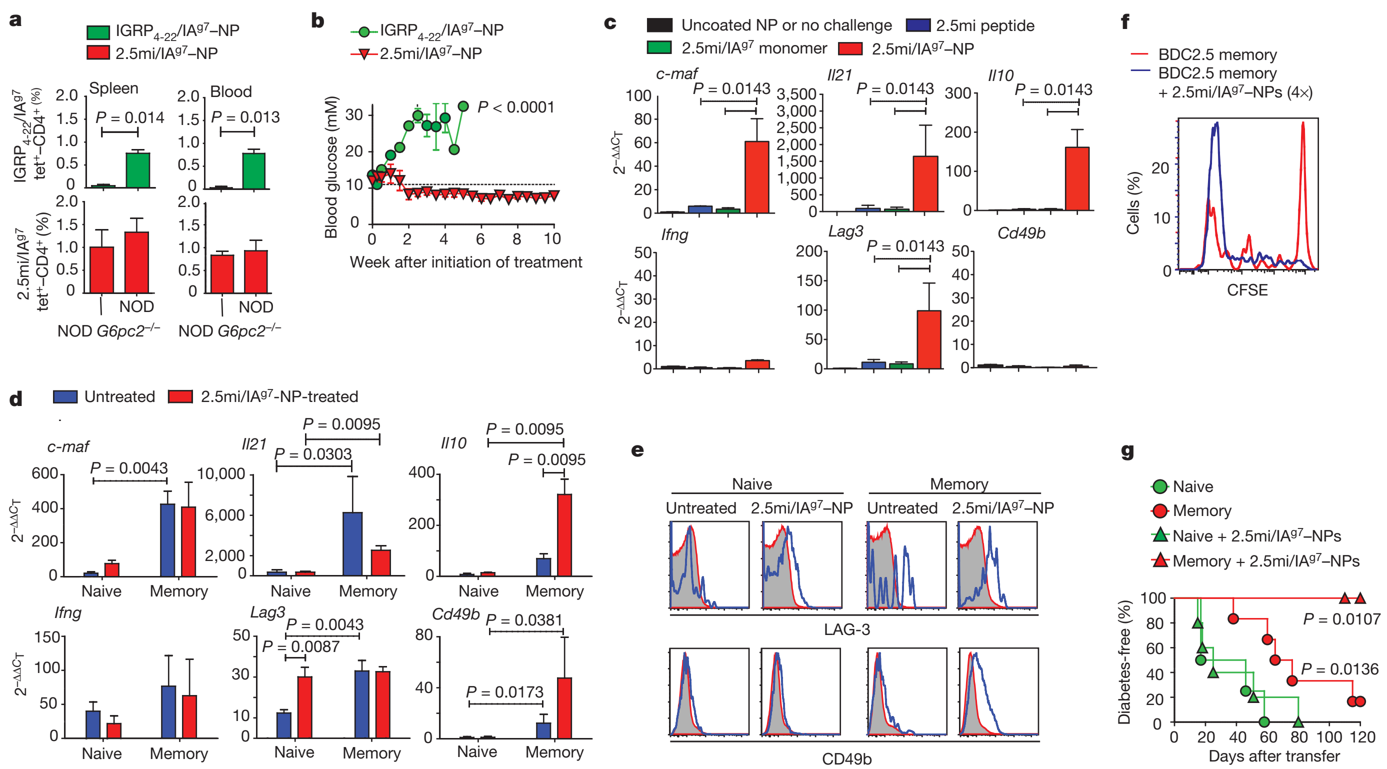

Figure 4 | The T$_R$1-like CD4$^+$ T cells arising in response to pMHCII–NPs are derived from antigen-experienced precursors. a, Percentage of tetramer$^+$CD4$^+$ T cells in hyperglycaemic NOD *G6pc2*$^{-/-}$ compared with NOD mice treated with IGRP$_{4-22}$/IA^{g7}– ($n = 4$ and 7) or 2.5mi/IA^{g7}–NPs ($n = 6$ and 9). **b**, Blood glucose levels in hyperglycaemic NOD *G6pc2*$^{-/-}$ mice in response to pMHC–NP therapy ($n = 4$–6 per group). **c**, Upregulation of T$_R$1 transcripts by anti-CD3/anti-CD28 mAb-activated eGFP$^-$CD4$^+$ T cells from BDC2.5 NOD *Foxp3-eGFP* mice in response to different *in vitro* stimuli ($n = 4$ mice each). **d**, Changes in T$_R$1-relevant transcripts in naive or memory BDC2.5 CD4$^+$ T cells in response to 2.5mi/IA^{g7}-NPs *in vivo* ($n = 6$, 6, 5 and 4 from left). **e**, LAG-3 and CD49b profiles (blue; compared with isotype control in red) of Thy1^{b+} cells from **d**. **f**, Proliferation of CFSE-labelled memory BDC2.5 CD4$^+$ T cells in NOD.*Thy1^a* hosts in response to 2.5mi/IA^{g7}–NPs. **g**, Incidence of diabetes in T-cell-reconstituted NOD *scid* hosts transfused with naive or memory BDC2.5 CD4$^+$ T cells and treated with bi-weekly doses of 2.5mi/IA^{g7}–NPs ($n = 4$ and 3) or left untreated ($n = 4$ and 6). *P* values were calculated via Mann–Whitney *U*-test or log-rank (Mantel–Cox) tests. Error bars, s.e.m.

of effector/memory CD4$^+$ T cells[18–22], and suggests that the memory T-cell pool is enriched for uncommitted T_R1 precursors, expressing a T_R1-poised transcriptional program. Remarkably, whereas pMHC–NP therapy only upregulated *Lag3* mRNA and, to a lesser extent, LAG-3 protein in naive BDC2.5 CD4$^+$ T cells, it promoted the upregulation of *Il10* mRNA and LAG-3 and CD49b protein, and the proliferation of memory BDC2.5 CD4$^+$ T cells (Fig. 4d–f). Similar results were observed using memory eGFP$^-$ (FOXP3$^-$) BDC2.5 CD4$^+$ cells from BDC2.5 NOD *Foxp3-eGFP* mice (Extended Data Fig. 5y).

These effects on antigen-experienced T cells were accompanied by acquisition of anti-diabetogenic properties: whereas pMHC–NP therapy afforded 100% diabetes protection to T-cell-reconstituted NOD *scid* hosts bearing memory BDC2.5 T cells, therapy was inconsequential in hosts receiving naive BDC2.5 T cells (Fig. 4g). Therefore, pMHC–NP therapy promotes the differentiation (and expansion) of c-Maf-expressing antigen-experienced CD4$^+$ T cells into T_R1 progeny.

Translational potential

We determined the ability of human T1D-relevant pMHCII–NPs to expand cognate T_R1-like T cells in NOD *scid Il2rg*$^{-/-}$ (NSG) hosts reconstituted with peripheral blood mononuclear cells (PBMCs) from T1D patients (Supplementary Table 2). Initial assay development focused on NSG hosts reconstituted with PBMCs from five DRB1*0401$^+$ recent-onset T1D patients and treated with nanoparticles coated in either human glutamic acid decarboxylase-65 (GAD65)$_{555–567(F557I)}$/DR4 or preproinsulin (PPI)$_{76–90(K88S)}$/DR4 (Fig. 5a, b, Supplementary Table 2). We then repeated these experiments using NSG hosts reconstituted with PBMCs from 7 DRB1*0301$^+$ T1D patients and a third T1D-relevant pMHC–NP type (hIGRP$_{13–25}$/DR3–NPs) given at a higher dose. We saw expansion of tetramer$^+$CD49b$^+$LAG-3$^+$CD4$^+$ T cells in the spleen and/or PLNs (endogenous mouse (m)IGRP$_{13–25}$ is highly homologous to hIGRP$_{13–25}$) from all seven pMHC–NP-treated mice and none of the untreated controls (Fig. 5c, d, Supplementary Table 2, Extended Data Fig. 7a). The average percentage and numbers of tetramer$^+$CD4$^+$ T cells in IGRP$_{13–25}$/DR3–NP-treated mice were significantly greater than in untreated littermates (Fig. 5d) and expressed *Il10* mRNA (Fig. 5e). These responses could not be induced with peptide or peptide-coated nanoparticles or microparticles (Fig. 5d, Extended Data Fig. 7b and Supplementary Table 2).

The PLNs of the pMHC–NP-treated mice that harboured increased percentages of tetramer$^+$CD4$^+$ T cells had increased cellularity (Fig. 5f). Furthermore, there were correlations between the number of PLN tetramer$^+$CD4$^+$ T cells and the percentage and absolute number of PLN human B cells, and the PLN B cells, unlike their splenic counterparts, produced IL-10 in response to LPS (Fig. 5g–i), suggesting B_{reg} formation and/or recruitment. No such responses were seen in patient hPBMC-reconstituted NSG mice treated with peptide or peptide–NPs/MPs (Fig. 5f).

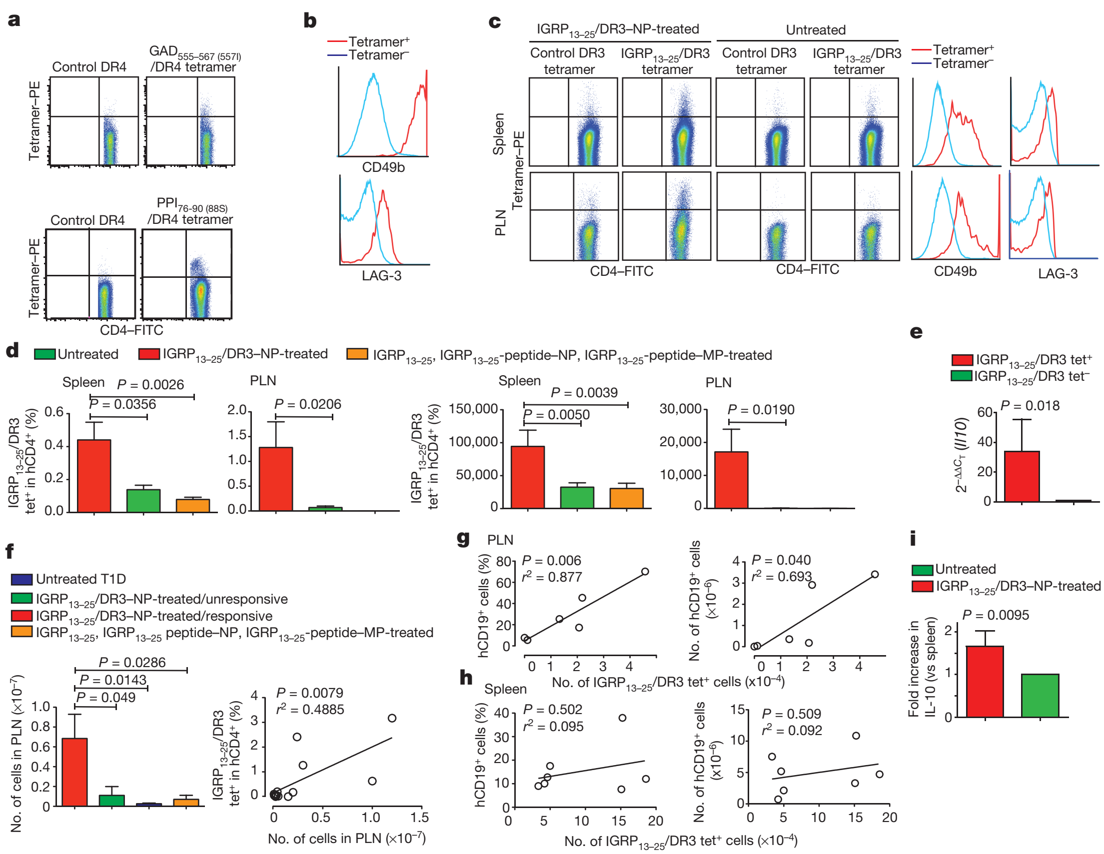

Figure 5 | Human T1D-relevant pMHC–NPs expand cognate T_R1-like CD4$^+$ T cells in human PBMC-engrafted NSG hosts. a, Expansion of cognate CD4$^+$ T cells by GAD$_{555–567(557I)}$/DR4–NPs (top) or PPI$_{76–90(88S)}$/DR4–NPs (bottom) in NSG mice engrafted with PBMCs from DR4$^+$ T1D patients. **b**, CD49b and LAG-3 marker expression on the sample at the bottom of **a**. **c**, Expansion of cognate T_R1-like CD4$^+$ T cells in NSG mice engrafted with PBMCs from DR3$^+$ T1D patients in response to IGRP$_{13–25}$/DR3–NP-therapy. **d**, Percentages (left) and numbers (right) of tetramer$^+$CD4$^+$ T cells in mice engrafted with T1D PBMCs in response to treatment (*n* for spleen and PLN per treatment = 9/6, 7/6 and 14/1 from left legend). **e**, Expression of *Il10* mRNA in IGRP$_{13–25}$/DR3 tetramer$^+$CD4$^+$ T cells from mice treated with IGRP$_{13–25}$/DR3–NPs ($n = 3$ each). **f**, The PLNs of responder mice contained increased numbers of lymphocytes compared to the other groups ($n = 6, 3, 4, 3$ from top legend). **g, h**, Correlation between the absolute numbers of IGRP$_{13–25}$/DR3 tetramer$^+$ cells in the PLNs (**g**) or spleen (**h**) and the percentage or absolute number of PLN or splenic B cells in IGRP$_{13–25}$/DR3–NP-treated mice ($n = 6$ and 7). **i**, Secretion of IL-10 by LPS-stimulated CD19$^+$ cells (*ex vivo*, for 24 h) isolated from the PLNs or spleens of hPBMC-engrafted NSG mice treated with IGRP$_{13–25}$/DR3–NPs ($n = 3$ each). *P* values were calculated by Mann–Whitney *U*-test or Pearson correlation test. Error bars, s.e.m.

Discussion

We have shown that systemic therapy with nanoparticles coated with autoimmune-disease-relevant pMHC class II complexes triggers the expansion of cognate T_R1-like $CD4^+$ T cells, restores normoglycaemia in spontaneously diabetic mice and motor function in paralyzed EAE mice, and resolves joint swelling and destruction in arthritic mice, without compromising systemic immunity. We demonstrate that this outcome is dissociated from genetic background and type of autoimmune disease and can be replicated with ten different human or murine autoimmune-disease-relevant pMHC–NP types. The cell surface phenotype, cytokine secretion pattern, transcriptional profile and function of the T_R1-like cell pools expanded by pMHCII-based nanomedicines are consistent with those described for murine T_R1-like $CD4^+$ T cells and remarkably similar to T_R1 cells derived from healthy individuals and autoimmune disease patients[8]. We demonstrate key roles for prior autoantigenic experience and IFNγ- and IL-10-expression competence in the developmental biology of autoreactive T_R1 cells. We show that pMHCII–NPs promote IL-10 transcription and the upregulation of T_R1 markers in T_R1-poised, antigen-experienced $CD4^+$ T cells in an APC- and IL-27-independent manner, followed by systemic expansion. The need for IFNγ, the expression of the T_H1 transcription factor T-bet, the c-Maf/IL-10- and IL-21-expression competency of effector and memory $CD4^+$ T cells[18–20], and the ability of pMHCII–NPs to turn T cells primed by active immunization into T_R1 suppressors suggest that these T_R1 precursors are effector/memory T_H1 cells. We define the mechanisms of action and uncover a cascade of cellular interactions downstream of the pMHC–NP-expanded T_R1-like cells, including B_{reg} cell formation, that coordinately lead to the resolution of inflammation in an antigen-dependent but antigen-non-specific manner (Extended Data Fig. 8).

Collectively, our data support the contention that any single pMHC involved in a given autoimmune disease could be used to blunt complex autoimmune responses via this approach. Consistent with this prediction, the 20 pMHCI/II-based nanomedicines tested to date have similar efficacy, regardless of antigen prevalence, dominance or role in the disease process. Neither pMHC monomers nor peptides or peptide-coated nanoparticles/microparticles trigger cognate T_R1 cell formation/expansion from the polyclonal T-cell repertoires or reverse T1D, CIA or EAE in the chronic models tested here. pMHC-based nanomedicines thus represent a new class of therapeutics in autoimmunity, capable of resolving cellularly and antigenically complex autoimmune responses in a disease- and organ-specific manner without compromising systemic immunity.

Online Content Methods, along with any additional Extended Data display items and Source Data, are available in the online version of the paper; references unique to these sections appear only in the online paper.

Received 2 September 2014; accepted 24 December 2015.
Published online 17 February 2016.

1. Santamaria, P. The long and winding road to understanding and conquering type 1 diabetes. *Immunity* **32,** 437–445 (2010).
2. Babbe, H. *et al.* Clonal expansions of $CD8^+$ T cells dominate the T cell infiltrate in active multiple sclerosis lesions as shown by micromanipulation and single cell polymerase chain reaction. *J. Exp. Med.* **192,** 393–404 (2000).
3. Firestein, G. S. Evolving concepts of rheumatoid arthritis. *Nature* **423,** 356–361 (2003).
4. Sakaguchi, S. *et al.* $Foxp3^+CD25^+CD4^+$ natural regulatory T cells in dominant self-tolerance and autoimmune disease. *Immunol. Rev.* **212,** 8–27 (2006).
5. Zhou, X. *et al.* Instability of the transcription factor Foxp3 leads to the generation of pathogenic memory T cells *in vivo*. *Nature Immunol.* **10,** 1000–1007 (2009).
6. Komatsu, N. *et al.* Pathogenic conversion of $Foxp3^+$ T cells into T_H17 cells in autoimmune arthritis. *Nature Med.* **20,** 62–68 (2014).
7. Bailey-Bucktrout, S. L. *et al.* Self-antigen-driven activation induces instability of regulatory T cells during an inflammatory autoimmune response. *Immunity* **39,** 949–962 (2013).
8. Gagliani, N. *et al.* Coexpression of CD49b and LAG-3 identifies human and mouse T regulatory type 1 cells. *Nature Med.* **19,** 739–746 (2013).
9. McLarnon, A. IBD: regulatory T-cell therapy is a safe and well-tolerated potential approach for treating refractory Crohn's disease. *Nature Rev. Gastroenterol. Hepatol.* **9,** 559 (2012).
10. Desreumaux, P. *et al.* Safety and Efficacy of Antigen-Specific Regulatory T-Cell Therapy for Patients With Refractory Crohn's Disease. *Gastroenterology* **143,** 1207–1217 (2012).
11. Roncarolo, M. G., Gregori, S., Lucarelli, B., Ciceri, F. & Bacchetta, R. Clinical tolerance in allogeneic hematopoietic stem cell transplantation. *Immunol. Rev.* **241,** 145–163 (2011).
12. Tsai, S. *et al.* Reversal of autoimmunity by boosting memory-like autoregulatory T cells. *Immunity* **32,** 568–580 (2010).
13. Stratmann, T. *et al.* Susceptible MHC alleles, not background genes, select an autoimmune T cell reactivity. *J. Clin. Invest.* **112,** 902–914 (2003).
14. Kamanaka, M. *et al.* Expression of interleukin-10 in intestinal lymphocytes detected by an interleukin-10 reporter knockin tiger mouse. *Immunity* **25,** 941–952 (2006).
15. Mukherjee, R., Wagar, D., Stephens, T., Le-Chan, E. & Singh, B. Identification of $CD4^+$ T cell-specific epitopes of islet-specific glucose-6-phosphatase catalytic subunit-related protein: a novel β cell autoantigen in type 1 diabetes. *J. Immunol.* **174,** 5306–5315 (2005).
16. Burton, B. R. *et al.* Sequential transcriptional changes dictate safe and effective antigen-specific immunotherapy. *Nature Commun.* **5,** 4741–4747 (2014).
17. Getts, D. R. *et al.* Microparticles bearing encephalitogenic peptides induce T-cell tolerance and ameliorate experimental autoimmune encephalomyelitis. *Nature Biotechnol.* **30,** 1217–1224 (2012).
18. Pot, C. *et al.* Cutting edge: IL-27 induces the transcription factor c-Maf, cytokine IL-21, and the costimulatory receptor ICOS that coordinately act together to promote differentiation of IL-10-producing Tr1 cells. *J. Immunol.* **183,** 797–801 (2009).
19. Spensieri, F. *et al.* Human circulating influenza-$CD4^+ICOS1^+IL\text{-}21^+$ T cells expand after vaccination, exert helper function, and predict antibody responses. *Proc. Natl Acad. Sci. USA* **110,** 14330–14335 (2013).
20. Hale, J. S. *et al.* Distinct memory $CD4^+$ T cells with commitment to T follicular helper- and T helper 1-cell lineages are generated after acute viral infection. *Immunity* **38,** 805–817 (2013).
21. Sato, K. *et al.* Marked induction of c-Maf protein during Th17 cell differentiation and its implication in memory Th cell development. *J. Biol. Chem.* **286,** 14963–14971 (2011).
22. Saraiva, M. *et al.* Interleukin-10 production by Th1 cells requires interleukin-12-induced STAT4 transcription factor and ERK MAP kinase activation by high antigen dose. *Immunity* **31,** 209–219 (2009).

Supplementary Information is available in the online version of the paper.

Acknowledgements We thank S. Thiessen, J. DeLongchamp, J. Erickson, J. Luces, R. Barasi and K. Umeshappa for technical contributions; L. Kennedy, L. Robertson and Y. Liu for flow cytometry; F. Jirik for help with histological analyses of arthritic mice; J. Elliott and K. Suzuki for Meso Scale measurements; M. Fritzler for Luminex; and P. Colarusso for assistance with microscopy. This work was funded by the Canadian Institutes of Health Research (CIHR), the Diabetes Research Foundation, the Juvenile Diabetes Research Foundation (JDRF), the Canadian Diabetes Association (CDA), the Multiple Sclerosis Society of Canada (MSSC), the Brawn Family Foundation, National Research Council of Canada–Industrial Research Assistance Program (NRC-IRAP), Instituto de Investigaciones Sanitarias Carlos III (ISCIII) Integrated Projects of Excellence and FEDER, the Ministerio de Economia y Competitividad of Spain (MINECO), the European Association for the study of diabetes (EASD), the Sardà Farriol Research Programme, and the European Community's Seventh Framework Programme. X.C.C. was supported by studentships from the AXA Research Fund and the endMS network. P.A. was supported by the endMS network. J.B. was suported by a Rio Hortega fellowship and by a grant from the Spanish Society for Diabetes. S.T. was supported by a studentship from the Alberta Heritage Foundation of Medical Research (AHFMR). J.W. was funded by a fellowship from the CDA. P.Se. is an investigator of the Ramon y Cajal reintegration program and is supported by a JDRF Career Development Award. P.Sa. is a Scientist of the Alberta Innovates-Health Solutions and a scholar of ISCIII. The JMDRC is supported by the Diabetes Association (Foothills) and the CDA.

Author Contributions X.C.-C. executed most of the experiments in Figs 1, 3a–d, h–j, 4a–f, Supplementary Table 1 and Extended Data Figs 1b–n, 2, 3, 5a–f, n–t, 6, with contributions from J.Y., P.A., S.T. and J.W., and contributed to writing the manuscript with P.Sa. J.Y. executed the experiments in Figs 3e–g, 4g–i and Extended Data Figs 1a, c–f, 2h and 5u, v. P.A. executed all of the experiments described in Figs. 2, 3b, and Extended Data Figs 4 and 5g–m. J.B. recruited T1D patients and healthy controls and performed the experiments leading to Fig. 5, Extended Data Fig. 7 and Supplementary Table 2 under the supervision of P.Se. S.S., Y.Y. and A.M. produced nanoparticles and pMHC–NP conjugates for the study. C.F. produced 2.5mi/IA^{g7} class II monomers for mechanistic experiments. S.A. and M.K. contributed to the execution of the EAE experiments, and analysed histological sections for histopathological features of CNS inflammation and demyelination under the supervision of V.W.Y. E.J. provided human T1D-relevant pMHC class II monomers and tetramers. N.G., C.I. and T.S. produced the pMHC class II monomers used for the studies on the reversal of T1D. P.Sa. designed the study, supervised and coordinated its execution and wrote the manuscript.

Author Information Reprints and permissions information is available at www.nature.com/reprints. The authors declare competing financial interests: details are available in the online version of the paper. Readers are welcome to comment on the online version of the paper. Correspondence and requests for materials should be addressed to P. Santamaria (psantama@ucalgary.ca).

METHODS

Mice. NOD/Ltj, NOD *scid*, BDC2.5-NOD, NOD *Il10*$^{-/-}$, C57BL/6, C57BL/6 *Il27r*$^{-/-}$, C57BL/10.M, NOD *Foxp3-egfp* and NOD *scid Il2rg*$^{-/-}$(NSG) mice were purchased from the Jackson Lab. NOD *Ifng*$^{-/-}$ and LCMV Gp33-specific TCR-transgenic NOD mice were from D. Serreze (Jackson Lab). *HLA-DR4-IE*-transgenic C57BL/6 *IAb*^{null} mice were purchased from Taconic Farms. NOD *Il10*^{GFP} (*tiger*) mice were obtained by backcrossing the *Il10*^{GFP} allele from C57BL/6 *Il10*^{GFP} mice (Jackson Lab) onto the NOD/Ltj background for 10 generations. 8.3-NOD and NOD *G6pc2*$^{-/-}$ mice have been described elsewhere[23,24]. These studies were approved by the corresponding institutional animal care committees. No statistical methods were used to predetermine sample size.

Antibodies, tetramer staining and flow cytometry. FITC, PE, PerCP or biotin-conjugated mAbs against mouse CD4 (RM4-5), CD8α (53-6.7), B220 (RA36B2), CD62L (MEL-1), CD69 (H1.2F3), CD44 (IM7), and CD49b (DX5) and streptavidin–PerCP were purchased from BD Pharmingen. The antibody against murine LAG-3 (C9B7W) was from eBioscience. Anti-latent-associated-TGF-β antibody (TW7-16B4) was from BioLegend. PE-conjugated pMHC class II tetramers were prepared using biotinylated pMHC monomers. Peripheral blood mononuclear cells, splenocytes, lymph node and bone marrow CD4^{+} T cells were incubated with avidin for 15 min at room temperature and stained with tetramer (5 μg ml^{-1}) in FACS buffer (0.05% sodium azide and 1% FBS in PBS) for 30–120 min at 4 °C or 37 °C, depending on the tetramer, washed, and incubated with FITC-conjugated anti-CD4 (5 μg ml^{-1}) and PerCP-conjugated anti-B220 (2 μg ml^{-1}; as a 'dump' channel) for 30 min at 4 °C. Cells were washed, fixed in 1% paraformaldehyde (PFA) in PBS and analysed with FACScan, FACSaria, or BD LSRII flow cytometers. For other phenotypic analyses, single-cell suspensions were stained with pMHC tetramers and antibodies diluted 1:100 in FACS buffer (all used at 4 °C except anti-LAG-3, which was used at 37 °C), washed, fixed in 1% PFA, and analysed by FACS. All phenotypic staining were performed in the presence of an anti-CD16/CD32 mAb (2.4G2; BD Pharmingen) to block Fc receptors. Analysis was done using FlowJo software.

NSG-engrafted human T cells were analysed using the following mAbs: FITC-conjugated anti-CD4 (OKT4, BioLegend), APC-conjugated anti-CD19 (HIB19, BD Pharmingen), PerCP-conjugated polyclonal goat anti-LAG-3 IgG (R&D Systems), biotin-conjugated anti-CD49b (AK7, Pierce Antibodies, Thermo Scientific), and EF450-conjugated streptavidin (eBioscience). Briefly, splenocytes and pancreatic lymph node cells were incubated with avidin (0.25 mg ml^{-1} in FACS buffer) for 30 min at room temperature, washed and stained with tetramer (5 μg ml^{-1}) for 1 h at 37 °C, washed, and incubated with FITC-conjugated anti-CD4 (2/100), APC-conjugated anti-CD19 (5/100; used as a 'dump' channel), PerCP-conjugated anti-LAG-3 (8/100) and biotin-conjugated anti-CD49b (4/100) at 4 °C for 45 min. After washing, the cells were incubated with EF450-conjugated streptavidin for 30 min at 4 °C, washed, fixed in 1% PFA in PBS and cells within the hCD4^{+}/hCD19^{-} gate analysed with a FACSCanto II (BD Bioscience).

Peptides and pMHCs. Unless specified otherwise, recombinant pMHC class II monomers were purified from culture supernatants of induced *Drosophila* SC2 cells transfected with constructs encoding I-Aβ and I-Aα chains carrying c-Jun or c-Fos leucine zippers, respectively, and a BirA and 6×His tags. In these constructs, the peptide-coding sequence was tethered to the amino-terminal end of the I-Aβ chain via a flexible Gly-Ser linker as described[13]. GAD65$_{555(557I)-567}$/DR4, PPI$_{76-90(88S)}$/DR4 and IGRP$_{13-25}$/DR3 monomers were produced by loading the corresponding peptides onto DR4 and DR3 complexes purified from supernatants of induced SC2 cells, as described[25]. Other constructs (those encoding 2.5mi/IA^{g7}, pMOG$_{35-55}$/IA^{b}, hMOG$_{97-108}$/DR4-IE, hPLP$_{175-192}$/DR4-IE and mCII$_{259-273}$/DR4-IE) were purified from supernatants of Chinese Hamster Ovary (CHO) cells transduced with lentiviruses encoding a monocistronic message in which the peptide–MHCβ and MHCα chains of the complex were separated by the ribosome skipping P2A sequence[26]. These monomers were engineered to encode a BirA site, a 6×His tag and a free Cys at the carboxyterminal end of the construct. The self-assembled pMHC class II complexes were purified by nickel chromatography and used for coating onto nanoparticles or processed for biotinylation and tetramer formation as described above. The epitopes encoded in the different monomeric constructs used here include: 2.5mi; AHHPIWARMDA)[13]; IGRP$_{128-145}$ (TAALSYTISRMEESSVTL) and IGRP$_{4-22}$ (LHRSGVLIIHHLQEDYRTY)[15]; HEL$_{14-22}$ (RHGLDNYRG); GAD65$_{555(557I)-567}$ (NFIRMVISNPAAT)[27]; PPI$_{76-90(88S)}$ (SLQPLALEGSLQSRG)[28]; IGRP$_{13-25}$ (QHLQKDYRAYYTF)[25]; pMOG$_{38-49}$ (GWYRSPFSRVVH); hMOG$_{97-108}$ (TCFFRDHSYQEE); hPLP$_{175-192}$ (YIYFNTWTTCQSIAFPSK); and mCII$_{259-273}$ (GIAGFKGDQGPKGET). IGRP$_{4-22}$, IGRP$_{128-145}$ and GPI$_{282-292}$ (LSIALHVGFDH) or 2.5mi, pMOG$_{35-55}$ (MEVGWYRSPFSRVVHLYRNGK), pMOG$_{38-49}$, hMOG$_{97-108}$ and hPLP$_{175-192}$ peptides were purchased from Sigma Genosys, Mimotopes or Genscript.

Nanoparticles, pMHC–NP, peptide–NP and peptide–MP synthesis and purification. We coated pMHCs onto crosslinked dextran-coated or pegylated iron oxide NPs (CLIO– or PFM–NPs, respectively). Briefly, CLIO–NPs were treated with ammonia to produce amino groups (NH_2). Avidin was oxidized with sodium periodate and added to the amino–NPs. Further incubation with sodium cyanoborohydride was used to generate a stable covalent bond. Finally, biotinylated monomers were added to the nanoparticles at a molar ratio of 4 mol biotin/mol avidin[29]. PFM–NPs were produced by thermal decomposition of $Fe(acac)_3$ in the presence of 2 kDa methoxypolyethylene glycol maleimide (S. Singha *et al.*, unpublished data). The NPs were purified using magnetic (MACS) columns (Miltenyi Biotec) or an IMag cell separation system (BD BioSciences). To conjugate pMHC or free peptide to PFM–NPs, we incubated pMHCs or peptide carrying a free carboxyterminal Cys with nanoparticles in 40 mM phosphate buffer, pH 6.0, containing 2 mM EDTA, 150 mM NaCl overnight at room temperature. The pMHC-conjugated nanoparticles were separated from free pMHC or peptide using magnetic columns, sterilized by filtration through 0.2 μm filters and stored in water or PBS at 4 °C. Quality control was performed using transmission electron microscopy, dynamic light scattering, and native and denaturing gel electrophoresis. pMHC or peptide content was measured using different approaches, including Bradford assay (Thermo Scientific), denaturing SDS–PAGE, amino acid analysis (HPLC-based quantification of 17 different amino acids in hydrolyzed pMHC–NP preparations) or dot-ELISA (Singha *et al.*, unpublished data).

Peptide-coated microparticles were made using carboxylated 500 nm diameter polystyrene beads from Polysciences (Warrington, PA) as previously described[17]. The peptides were conjugated to polystyrene beads via carbodiimide chemistry following the manufacturer's instructions. Briefly, we incubated 250 μl PSB (containing ~9×10^{11} beads) with 250 μg peptide in 0.1 M MES buffer, pH 5.0 at room temperature with gentle rolling in the presence of 1 mg EDC for 2 h. The peptide-conjugated polystyrene beads were washed with PBS to remove unconjugated peptides and analysed with native and denaturing PAGE against serial dilutions of unconjugated peptide and microparticle controls.

pMHC–NP and peptide or peptide–NP therapy in NOD mice. Experiments in pre-diabetic NOD mice involved treating (i.v.) cohorts of 10-week-old female mice with 7.5 μg of pMHC–NPs, or equivalent amounts of soluble pMHC monomers or uncoated nanoparticles twice weekly for 5 consecutive weeks. Experiments in diabetic mice involved following cohorts of 10-week-old female NOD/Ltj, NOD *G6pc2*$^{-/-}$, NOD *Il10*$^{-/-}$ or NOD *Ifng*$^{-/-}$mice for diabetes development by measuring blood glucose levels with Accucheck Strips (Roche) twice a week. Mice displaying two consecutive measurements >11 mM were considered diabetic and treated twice weekly with 7.5 μg pMHC–NPs, nanoparticles delivering a molecular equivalent of peptide or free peptide (8 μg per dose)[16], until stably normoglycaemic (defined as 8 consecutive measurements <11 mM) or until hyperglycaemia was considered irreversible (3 measurements >25 mM). In Figs 1g and 4b and Extended Data Figure 1h), mice were randomized into treatment with 2.5mi/IA^{g7}–NPs or HEL$_{14-22}$/IA^{g7}–NPs (Fig. 1g) or with 2.5mi/IA^{g7}–NPs or IGRP$_{4-22}$/IA^{g7}–NPs (Fig. 4b). In Fig. 1g, IGRP$_{4-22}$/IA^{g7} and IGRP$_{128-145}$/IA^{g7} were tested in separate cohorts of mice. Mice treated with peptide or peptide–NPs (Fig. 1g) were randomized into either treatment within the same experiment. *In vivo* cytokine neutralization experiments involved administering mAbs against CD20 (5D2, a gift from A. Chan, Genentech; three doses of 250 μg i.v. on days 0–2 relative to the onset of hyperglycaemia) or 500 μg of HRPN (rIgG1), IFNγ (R4-6A2), IL-10 (JES5-2A5), TGF-β (1D11) or IL-21R (4A9) (BioXcell) i.p. twice a week for 2 weeks, followed by 200 μg per dose for 3 additional weeks. Mice were randomized into cytokine-blocking mAb-treatment (IFNγ, IL-10, TGFβ) or HRPN rat-IgG1 groups. Anti-CD20 and anti-IL21R mAbs were tested in separate cohorts of diabetic mice (Fig. 3a). Animals were assessed daily for glycosuria (corresponding to >16 mM blood glucose) and given human insulin isophane (1 IU per day) s.c. if positive. Upon treatment withdrawal, NOD mice were monitored for recurrence of hyperglycaemia until 50 weeks of age.

Peptide, pMHC, pMHC–NP, peptide–NP or peptide–MP therapy in EAE. Six- to eight-week-old female C57BL/6, C57BL/6 *Il27r*$^{-/-}$ or *HLA-DR4-IE*-transgenic C57BL/6 *IAb*^{null} mice were immunized with 150 μg of pMOG$_{35-55}$ or hMOG$_{97-108}$ or hPLP$_{175-192}$, respectively in CFA s.c. at the base of the tail, under isofluorane anaesthesia. The mice received 300 ng of Pertussis toxin i.v. on days 0 and 3. Mice were weighed and scored daily starting on day 10 after immunization. The score system used was been reported elsewhere[30] and plotted over a 5-point scale. When most of the mice showed signs of advanced disease (day 14) or reached maximum disease scores (day 21), mice were divided into different treatment groups, synchronized for weight and disease score averages, and treated twice a week with pMHC-coated and uncoated nanoparticles, an identical amount of pMHC monomer, peptide-coated nanoparticles (at an equivalent dose of peptide), free peptide (8 μg per dose i.v. or s.c.)[16], peptide-conjugated microparticles (15 μg of peptide per dose)[17] or unconjugated microparticles for 5 weeks. Mice were randomized into treatment with pMHC–NPs (one or two different types, depending on the

experiment, as described in Figs 1j–n and 2f–h and Extended Data Figures 3 and 4), uncoated nanoparticles or no treatment. Peptide, peptide–MPs, peptide–NPs, pMHC monomers and uncoated microparticles were tested together; mice were randomized into each treatment group as mice reached the indicated disease score (Fig. 2f and Extended Data Figures 4f–i). An additional control cohort was treated with a single dose of peptide-conjugated microparticles (Extended Data Fig. 4h). Anti-cytokine and cytokine receptor mAb blocking studies (Extended Data Fig. 5g) involved randomization of mice into each treatment group.

Peptide, pMHC-NP or peptide-MP therapy in CIA. Bovine collagen II (bCII) dissolved in 0.05M acetic acid at 2 mg ml^{-1} was emulsified in CFA (v/v) containing 4 mg ml^{-1} of killed *Mycobacterium tuberculosis* (H37Ra). Eight- to twelve- week-old *HLA-DR4-IE*-transgenic C57BL/10.M mice were immunized intradermally at the base of the tail with 100 μg of bCII in CFA and boosted with 100 μg of bCII in IFA on days 14 and 28. The size of all four paws was measured using a caliper before immunization (day 0) and daily upon disease onset. Disease progression was measured as percentage increase in joint swelling relative to day 0. When this value reached 130%, mice were divided into different treatment groups and treated with pMHC-NPs, Cys-coated (pMHC unconjugated) NPs (25 μg of pMHC for pMHC-NPs, or an equivalent amount of iron for Cys-conjugated NPs), free peptide (8 μg per dose s.c.)[16] or peptide-conjugated MPs (15 μg of peptide per dose)[17] i.v. twice a week for 5 weeks. Mice were randomized into treatment with either pMHC–NP or uncoated nanoparticles, or into peptide or peptide–MP, respectively (Fig. 2a and associated Extended Data Data Figures). Mice were also assessed for clinical signs of disease up to a maximum clinical score of 12 as reported elsewhere[31].

Peptide, pMHC–NP, peptide–NP and peptide–MP therapy in human PBMC-reconstituted NSG hosts. PBMCs from new or recently diagnosed HLA-DRB1*0401^{+} or -DRB1*0301^{+} T1D patients (recruited with informed consent, approved by the Institutional Review Board at Hospital Clinic) were depleted of CD8^{+} T cells using anti-CD8 mAb-coated magnetic beads (Miltenyi Biotech) and injected i.v. (2×10^7) into 8–10-week-old NSG hosts. Mice were treated with pMHC–NPs at the indicated doses, peptide-coated-NPs (at an equivalent dose of peptide), peptide alone (8 μg per dose s.c.)[16] or peptide-conjugated microparticles (15 μg of peptide per dose)[17] starting on day 5 after PBMC transfusion, twice a week for 5 consecutive weeks, or left untreated. Individual patient samples were processed separately and injected into two (for pMHC–NP and peptide–NP experiments) or three separate mice (for peptide and peptide–MP experiments); one or two of the two-to-three hosts used in each of these experiments were treated and the other was left untreated (Supplementary Table 2). Therapy-induced expansion of cognate CD4^{+} T cells was measured in PLNs and/or spleen as described above. The HLA genotype, gender, age, months from diagnosis and type of pMHC–NP tested for each patient are summarized in Supplementary Table 2.

Intraperitoneal glucose tolerance tests. Animals were fasted overnight and challenged with 2 mg kg^{-1} of D-glucose i.p. Blood glucose was monitored from the tail vein with a glucometer at different time points before and after glucose challenge. Serum insulin content was measured using the Mouse Ultrasensitive Insulin ELISA (ALPCO).

Evaluation of systemic cellular and humoral immunity. For the evaluation of cellular responses, pMHC–NP-treated and untreated female mice were injected with 2×10^6 plaque-forming units (pfu) of recombinant Vaccinia Virus (rVV) i.v. Cohorts of mice were killed on day 4 and 14 after infection and processed for pMHC tetramer staining and rVV titre measurements. Briefly, the ovaries were weighed, homogenized using a pestle in 300 ul of RPMI-1640 containing 10% FBS, freezed-thawed 3 times followed by 3 rounds of sonication (20 seconds each). Serial dilutions of the lysates were added to confluent BSC-1 cell cultures in 6-well plates, incubated at 37 °C for 2 h, washed twice with PBS and cultured in DMEM10. On day 2, the supernatants were discarded and the cell layers were stained with crystal violet to reveal plaques.

To evaluate humoral immunity, pMHC–NP-treated and untreated mice were immunized i.p. with 100 μg of DNP–KLH (Alpha Diagnostic International) in CFA. An identical boost was performed 3 weeks later. Mice were killed 10 days later. Anti-DNP antibody titres were measured by diluting serum samples in PBS containing 0.05% Tween 20. Anti-DNP antibodies were semi-quantified using an anti-DNP Ig ELISA Kit (Alphadiagnostic International) following the manufacturer's instructions.

Proliferation and cytokine secretion assays. CD4^{+} T cells from pMHC–NP-treated mice were enriched from peripheral lymphoid organs using a BD Imag enrichment kit, stained with pMHC tetramers as described above and sorted by flow cytometry. For assays using memory and naive BDC2.5 CD4^{+} T cells, cells were enriched using Stem Cell Technologies enrichment kit, stained with antibodies and sorted. FACS-sorted cells ($2–3 \times 10^4$) were co-cultured with bone marrow-derived DCs (2×10^4) pulsed with 2 μg ml^{-1} of peptide. Supernatants were collected 48 h later for measurement of cytokines via Luminex and the cells were pulsed with 1 microcurie (μCi) of (^{3}H)-thymidine and collected after 24 h to measure thymidine incorporation in triplicates.

To ascertain whether pMHC–NP therapy promoted the generation of IL-10-secreting B-cells in the PLNs of PBMC-engrafted NSG hosts, we stained the PLN and splenic cell suspensions of individual mice with anti-hCD4–FITC, anti-hCD19–APC and tetramer–PE as described above, and sorted B-cells by flow cytometry (FACSAria-BD Biosciences). The B cells sorted from each organ were stimulated with LPS (1 μg ml^{-1}, Sigma) for 24 h in RPMI-1640 supplemented with 10% human AB serum. The IL-10 content in the supernatants was measured in duplicates via Meso Scale technology using a V-PLEX Custom Human Cytokine kit for hIL-10 (Meso Scale Discovery). Data were normalized to the splenic B-cell values and reported as fold-change.

Isolation and *in vitro* stimulation of CD11b^{+} cells from the PLNs and MLNs. CD11b^{+} cells from LNs were obtained by digestion in collagenase D (1.25 μg ml^{-1}) and DNase I (0.1 μg ml^{-1}) for 15 min at 37 °C followed by purification with CD11b (BD Imag) mAb-coated magnetic beads. Cells were stimulated for 3 days with LPS (2 μg ml^{-1}) and the supernatants analysed for cytokine content with a Luminex multiplex cytokine assay.

***In vitro* suppression assays.** FACS-sorted 2.5mi/IA^{g7} tetramer positive or negative cells (2×10^4) were co-cultured with bone marrow-derived DCs (2×10^4) pulsed with 2 μg ml^{-1} 'suppressor' (2.5mi or GPI$_{282–292}$) and 'responder' (gp33 or NRP–V7) peptides. Responder cells were CD8^{+} T cells (2×10^4) purified from from 8.3-NOD or LCMV-Gp33-specific TCR-transgenic NOD mice using BD-Imag beads. These cells were labelled with CFSE (5 μM) and added to the DC cultures in duplicates or triplicates. Dilution of CFSE in the responder cells was measured 48 h later by FACS. In other experiments, the wells were supplemented within 24 h of co-culture with HRPN rIgG, anti-IFNγ, anti-IL10 or anti-TGF-β (all 10 μg ml^{-1}) or the IDO inhibitor, 1-methyl tryptophan (1-MT; 400 μM).

***In vivo* suppression of crosspresentation.** For crosspresentation assays in non-transgenic mice, we transfused CFSE-labelled 8.3-CD8^{+} reporter cells ($5–10 \times 10^6$) into untreated or pMHC–NP-treated mice and measured CFSE dilution in the hosts' lymphoid organs within 7 days after transfer.

Adoptive transfer of suppression. Splenic CD4^{+} or CD8^{+} T cells (10^7) from untreated mice or mice treated with 10 doses of 2.5mi/IA^{g7}–NPs or uncoated nanoparticles were transfused into 5–10 week-old NOD *scid* females. The hosts were transfused 24 h later with 2×10^7 CD4^{+} or CD8^{+} T-cell splenocyte mixtures purified from female NOD donors. The hosts were monitored for development of diabetes for at least 90 days after transfer (Fig. 1e). In another experiment, the hosts were treated twice a week with 2.5mi/IA^{g7}–NPs (Fig. 1e). In other experiments (Fig. 3e), CD4^{+} or CD8^{+} T-cell-reconstituted 5–6-week-old NOD *scid* females were transfused with 5×10^5 CD19^{+} cells purified from the PLNs of mice treated with 10 doses of uncoated or 2.5mi/IA^{g7}-coated NPs during the preceding 5 week (Fig. 3d). B-cells were purified using the EasySep Mouse CD19-positive selection Kit II (StemCell Technologies). Other cohorts, studied separately (Fig. 3e), received PLN or MLN CD19^{+} cells (5×10^5) plus total splenic CD4^{+} T cells (10^7) or 2.5mi/IA^{g7} tetramer^{+} (2×10^5) or tetramer^{-} CD4^{+} T cells (10^7) from 2.5mi/IA^{g7}–NP-treated donors. The hosts were randomized into each transfusion group and monitored for development of diabetes together. Figure 3e includes data from the corresponding cohors studied in Figs 1e and 3d. Isolation of 2.5mi/IA^{g7} tetramer^{+} and tetramer^{-} cells from total splenic CD4^{+} T cells of 2.5mi/IA^{g7}–NP-treated mice was performed using anti-PE mAb-coated microbeads and MACS LD columns (Miltenyi Biotec).

B-cell proliferation and B$_{reg}$ induction *in vivo* and B$_{reg}$ suppression *in vitro*. To isolate splenic DCs, spleens were digested in collagenase D and DNase for 15 min at 37 °C and DCs purified using anti-CD11c mAb-coated magnetic beads (MACS). The cells were pulsed with 10 μg ml^{-1} of 2.5mi or GPI$_{282–292}$ peptide for 2 h at 37 °C and labelled with CFSE (0.5 μM) or PKH26 (2 μM), respectively. Labelled cells ($5–10 \times 10^6$; mixed at 1:1 ratio) were administered i.v. into pMHC–NP-treated or untreated NOD mice. Three days later, we compared the ratios of CFSE^{+} versus PKH26^{+} cells in the spleens of the different hosts by FACS. Similar experiments were done using peptide-pulsed splenic B cells isolated from female donor mice using anti-B220 mAb-coated magnetic beads (MACS).

For *in vivo* B$_{reg}$ induction assays, B cells from NOD *Il10^{GFP}* (*tiger*) mice were enriched using a CD19 enrichment kit (Stem Cell Technologies) and pulsed with 2.5mi or GPI$_{282–292}$ peptides (10 μg ml^{-1}) for 2 h at 37 °C. The peptide-pulsed B cells were washed twice with PBS, labelled with PKH26 and transfused (1×10^6) into pMHC–NP-treated or untreated mice. The hosts were killed 7 days later and their spleens labelled with anti-B220-APC and biotinylated anti-CD1d or anti-CD5 mAbs and Streptavidin-PerCP. PKH26^{+} cells were analysed for presence of eGFP^{+}CD1d^{high} or CD5^{+} cells by flow cytometry.

To determine the role of T$_{R}$1-derived cytokines in B$_{reg}$ formation (Extended Data Fig. 5u), we repeated the experiments described above but using 3×10^6

B cells and hosts treated with 250 or 500 μg (given i.p. daily from day −3 to day 6 relative to B-cell transfer) of anti-HRPN (rIgG1), anti-IL-10 (JES5-2A5), anti-TGFβ (1D11) or anti-IL-21R (4A9) mAbs (BioXcell). Hosts were randomized into each antibody-treatment group and studied together.

To measure the ability of the T_R1-induced B_{reg} cells to suppress the antigen-induced activation of T cells *in vitro*, we isolated CD19$^+$ B cells from the PLNs of age-matched untreated NOD mice or NOD mice treated with 10 doses of 2.5mi/IA^{g7}–NPs and cultured these cells with LPS (10 μg ml^{-1}) overnight. We then cultured these cells (2×10^4) with 2.5mi-peptide-pulsed (0.1 μg ml^{-1}) bone marrow-derived DCs (2×10^4) and CFSE-labelled BDC2.5 CD4$^+$ cells (4×10^4). Dilution of CFSE in CD4$^+$ cells was measured 3 days later.

CD25$^+$CD4$^+$ T_{reg} depletion. NOD mice were treated with 500 μg of anti-CD25 (PC61.5.3, BioXcell) i.p. 3 times weekly from 8 weeks of age, followed by 10-injections of pMHC–NPs given twice weekly starting at 10 weeks of age. Average CD4$^+$CD25$^+$ and FOXP3–eGFP$^+$CD4$^+$ T-cell depletion was 90% and 70%, respectively.

Histology. Tissues were fixed in 10% formalin and embedded in paraffin. H&E-stained pancreata were scored for insulitis as reported[23]. Briefly, insulitis was scored as: 0, none; 1, peri-insulitis; 2, infiltration covering <25% of the islet; 3, covering 25–50% of the islet; and 4, covering >50% of the islet.

Spinal cord and brain tissues were fixed in 10% buffered formalin for a minimum of 24 h, embedded in paraffin and sectioned at 6 μm. Slides from paraffin-embedded tissues were deparaffinized and subjected to antigen retrieval by steaming the slides in 10 mM sodium citrate buffer (pH 6.0) for 20 min and cooling at room temperature for 20 min. For immunohistochemistry, slides were fixed with 10% formalin and treated with 3% H_2O_2 in methanol at −20 °C. Sections were permeabilized with 0.25% Triton-X 100 and blocked with a skim milk blocking solution. Rabbit anti-IBA1 (Wako, 1:500) or rat anti-MBP (Abcam) were incubated at 4 °C overnight followed by respective biotinylated secondary antibodies (1:500), avidin-biotin complex, and 3,3′-diaminobenzidine. Sections were counterstained with haematoxylin and eosin, dehydrated with graded ethanol and mounted with Acrytol. For histological myelin staining, slides were fixed with 10% formalin or deparaffinized, dehydrated with graded ethanol, and incubated with 0.2% luxol fast blue in 95% ethanol at 65 °C. Slides were developed in 0.05% lithium carbonate, counterstained with haematoxylin and eosin, and mounted with Acrytol. Images of cerebellum were taken on an Olympus bright-field microscope. Inflammatory foci (dense nuclear clusters or perivascular cuffs with corresponding demyelination) were counted and their size measured using ImageJ software. For quantification of relative IBA1 intensity, blinded observers ranked images from highest to lowest intensity.

Knee joints from bCII-immunized mice were fixed in 4% buffered formalin overnight, and decalcified with 14% EDTA over 3 weeks. Decalcified paws were embedded in paraffin, sectioned at 8 μm and stained with haematoxylin and eosin to score infiltration and pannus formation on a scale of 5, where 5 corresponds to erosive arthritis, with severe infiltration and pannus covering 60% of the joint space. Proteoglycan depletion at the articular surface of the tibia and femur was assessed by the loss of safranin-O stain intensity. For this, sections were deparaffinized, hydrated and stained with haematoxylin before staining with 0.05% aqueous fast green for 5 min. Slides were fixed with 1% acetic acid and stained with 0.1% aqueous safranin-O for 2 min, dehydrated with graded ethanol, cleared with xylene and mounted with DPX. Scoring was done on a scale of 0 to 3 corresponding to: 0, 0% depletion, 1, low (<25%), 2, moderate (25–50%), and 3, severe (>50%). Destruction of articular cartilage included an assessment of the presence of dead chondrocytes (empty lacunae) and was scored on a scale of 3 (0, no empty lacunae; 3, complete loss of chondrocytes on articular cartilage/severe cartilage erosion).

Isolation of CNS-infiltrating lymphocytes. Mice were anesthetized with Ketamine-Xylazine and perfused with PBS through the heart left ventricle. The brain and spinal cord were isolated manually, cut into small fragments and digested with a solution of collagenase D (1.25 μg ml^{-1}) and DNase I (1% w/v) in HBSS for 30 min at 37 °C. The digested CNS was passed through a 70 μm cell strainer. Cells were resuspended in DMEM (supplemented with 2% FBS and 10 mM HEPES) and 100% Percoll (to a final Percoll concentration of 30%). The solution was layered onto 65% Percoll and centrifuged at 380*g* for 30 min at room temperature. The mononuclear cell layer lying at the interphase was washed with RPMI before further analyses.

Quantitative RT–PCR. RNA was extracted from 2.5mi/IA^{g7} tetramer$^+$ or tetramer$^-$ CD4$^+$ T cells sorted from 2.5mi/IA^{g7}–NP-treated NOD mice and stimulated *in vitro* with anti-CD3/anti-CD28 mAb-coated dynabeads.

Each tetramer$^+$ sample corresponded to cells pooled from 2–3 mice. RNA was reverse transcribed and cDNA plated in Mouse Immunology 384 StellArray qPCR plates (Bar Harbour BioTechnology) with 2X SYBR Green Master Mix (Applied Biosystems). The plate was run in a 7900HT Applied Biosystems real-time PCR instrument, and the raw data was analysed using the Global Pattern Recognition (GPR) analysis tool (http://www.gene-quantification.com/qpcr-array.html). mRNA isolated from additional samples was subjected to RT–qPCR using primers specific for IL-21 (Forward: 5′-TCATCATTGACCTCGTGGCCC-3′; Reverse: 5′-ATCGTACTTCTCCACTTGCAATCC-3′), IL-10 (Forward: 5′-CTTGCACTACCAAAGCCACA-3′; Reverse: 5′-GTTATTGTCTTCCCGGCTGT-3′), c-Maf (Forward: 5′-AGCAGTTGGTGACCATGTCG-3′; Reverse: 5′-TGGAGATCTCCTGCTTGAGG-3′), IFN-γ (Forward: 5′-TGAACGCTACACACTGCATCTTGG-3′; Reverse: 5′-CGACTCCTTTTCCGCTTCCTGAG-3′), LAG-3 (Forward: 5′-TCCCAAATCCTTCGGGTTAC-3′; Reverse: 5′-GAGCTAGACTCTGCGGCGTA-3′), CD49b (Forward: 5′-CCGGGTGCTACAAAAGTCAT-3′; Reverse: 5′-GTCGGCCACATTGAAAAAGT-3′), Aryl Hydrocarbon Receptor (Forward: 5′-CGTCCCTGCATCCCACTACTT-3′; Reverse: 5′-GGACATGGCCCCAGCATAG-3′) and ICOS (Forward: 5′-TGACCCACCTCCTTTTCAAG-3′; Reverse: 5′-TTAGGGTCATGCACACTGGA-3′).

pMHC–NP-induced upregulation of T_R1 transcripts in *in vitro*-activated CD4$^+$ T cells was performed by culturing mouse naive eGFP$^-$BDC2.5-CD4$^+$ T cells from BDC2.5 NOD *Foxp3-eGFP* mice (CD62L^{hi}FOXP3$^-$eGFP$^-$; 1.5×10^6 ml^{-1}) with anti-CD3/anti-CD28 mAb-coated microparticles (1 bead per cell) for three days in the absence of APCs, followed by a one day culture of re-purified (microparticle-free) CD4$^+$ T cells in rhIL-2 (30 IU ml^{-1}), and a 6-day culture with 2.5mi peptide (10 μg ml^{-1}), 2.5mi/IA^{g7} monomers (25 μg pMHC per ml), 2.5mi/IA^{g7}–NPs (25 μg pMHC per ml and 50 μg ml^{-1} iron), or unconjugated nanoparticles (50 μg iron per ml). Relative gene expression was calculated using unstimulated cultures as controls.

pMHC–NP-induced upregulation of T_R1 transcripts in naive compared to memory BDC2.5 CD4$^+$ T cells *in vivo* was done by transfusing naive (CD44^{med}CD62L^{hi}) or memory (CD44^{hi}CD62L^{low}) eGFP$^-$CD4$^+$ T cells from BDC2.5-TCR-transgenic NOD or NOD *Foxp3-eGFP* mice (Thy1^{b+}) (1–1.5×10^6 cells per host) into NOD.*Thy1^a* hosts and by treating the hosts with four doses of 2.5mi/IA^{g7}–NPs over two weeks or leaving them untreated. Two and a half weeks later, Thy1^{b+}CD4$^+$ T cells were sorted from the hosts and challenged with anti-CD3 and anti-CD28-coated magnetic Dynabeads for 3 days before mRNA extraction and RT–qPCR using primers specific for c-Maf, IL-21, IL-10, IFNγ, LAG-3 and CD49b.

To compare levels of IL-10 mRNA in the tetramer$^+$ compared with tetramer$^-$ CD4$^+$ T cells of pMHC–NP-treated PBMC-engrafted NSG hosts, we stained splenocytes with anti-hCD4-FITC, anti-hCD19-APC and tetramer–PE as described above, and sorted tetramer$^+$ and tetramer$^-$ cells from individual hosts by FACS (FACSAria-BD Biosciences). Sorted cells were cultured for 72 h in RPMI-1640 containing 10% human AB serum, in the presence of Dynabeads Human T-Activator CD3/CD28 (LifeTechnologies) using a 1:1 cell to bead ratio. Total RNA from cell pellets was reverse-transcribed using a dual reverse transcriptase/lysis solution containing 5 mM DTT, 2 U ml^{-1} RNAase, 500 mM dNTPs, 10 U ml^{-1} of Superscript reverse transcriptase (Invitrogen, LifeTechnologies), 100 mg ml^{-1} bovine serum albumin, 1% Triton X-100, 25 ng ml^{-1} Oligo dT (Invitrogen), 0.5 nM spermidine, and 1X First Strant buffer (Invitrogen) in 20 μl for 60 min at 50 °C and 15 min at 70 °C. We then mixed 1 μl of the cDNA reaction volume with 12.5 μl of Power SyBRGreen PCR master mix solution (Applied Biosystem) and amplified with a real-time PCR machine (7900HT, Applied Biosystems) using the following primers: β-actin (Forward: 5′-CTGGAACGGTGAAGGTGACA-3′; Reverse: 5′-AAGGGACTTCCTGTAACAATGCA-3′), IL-10 (Forward: 5′-AAGACCCAGACATCAAGGCG-3′; Reverse: 5′-AATCGATGACAGCGCCGTAG-3′).

Statistical analyses. The sample size values described in the figure legends correspond to the number of individual mice tested (not replicates) and data shown correspond to pooled data from different experiments. Data were compared by Student's *t*-test, Mann–Whitney *U*-test, chi-square, log-rank (Mantel–Cox), Pearson correlation or two-way ANOVA tests. Statistical significance was assumed at $P < 0.05$.

23. Verdaguer, J. *et al.* Spontaneous autoimmune diabetes in monoclonal T cell nonobese diabetic mice. *J. Exp. Med.* **186,** 1663–1676 (1997).
24. Wang, J. *et al.* *In situ* recognition of autoantigen as an essential gatekeeper in autoimmune CD8$^+$ T cell inflammation. *Proc. Natl Acad. Sci. USA* **107,** 9317–9322 (2010).
25. Yang, J. *et al.* Islet-specific glucose-6-phosphatase catalytic subunit-related protein-reactive CD4$^+$ T cells in human subjects. *J. Immunol.* **176,** 2781–2789 (2006).
26. Holst, J. *et al.* Generation of T-cell receptor retrogenic mice. *Nature Protocols* **1,** 406–417 (2006).
27. Reijonen, H. *et al.* Detection of GAD65-specific T cells by major histocompatibility complex class II tetramers in type 1 diabetic patients and at-risk subjects. *Diabetes* **51,** 1375–1382 (2002).

28. Yang, J. *et al.* $CD4^+$ T cells from type 1 diabetic and healthy subjects exhibit different thresholds of activation to a naturally processed proinsulin epitope. *J. Autoimmun.* **31,** 30–41 (2008).
29. Moore, A., Grimm, J., Han, B. & Santamaria, P. Tracking the recruitment of diabetogenic $CD8^+$ T cells to the pancreas in real time. *Diabetes* **53,** 1459–1466 (2004).
30. Giuliani, F. *et al.* Additive effect of the combination of glatiramer acetate and minocycline in a model of MS. *J. Neuroimmunol.* **158,** 213–221 (2005).
31. Leavenworth, J. W., Tang, X., Kim, H. J., Wang, X. & Cantor, H. Amelioration of arthritis through mobilization of peptide-specific $CD8^+$ regulatory T cells. *J. Clin. Invest.* **123,** 1382–1389 (2013).

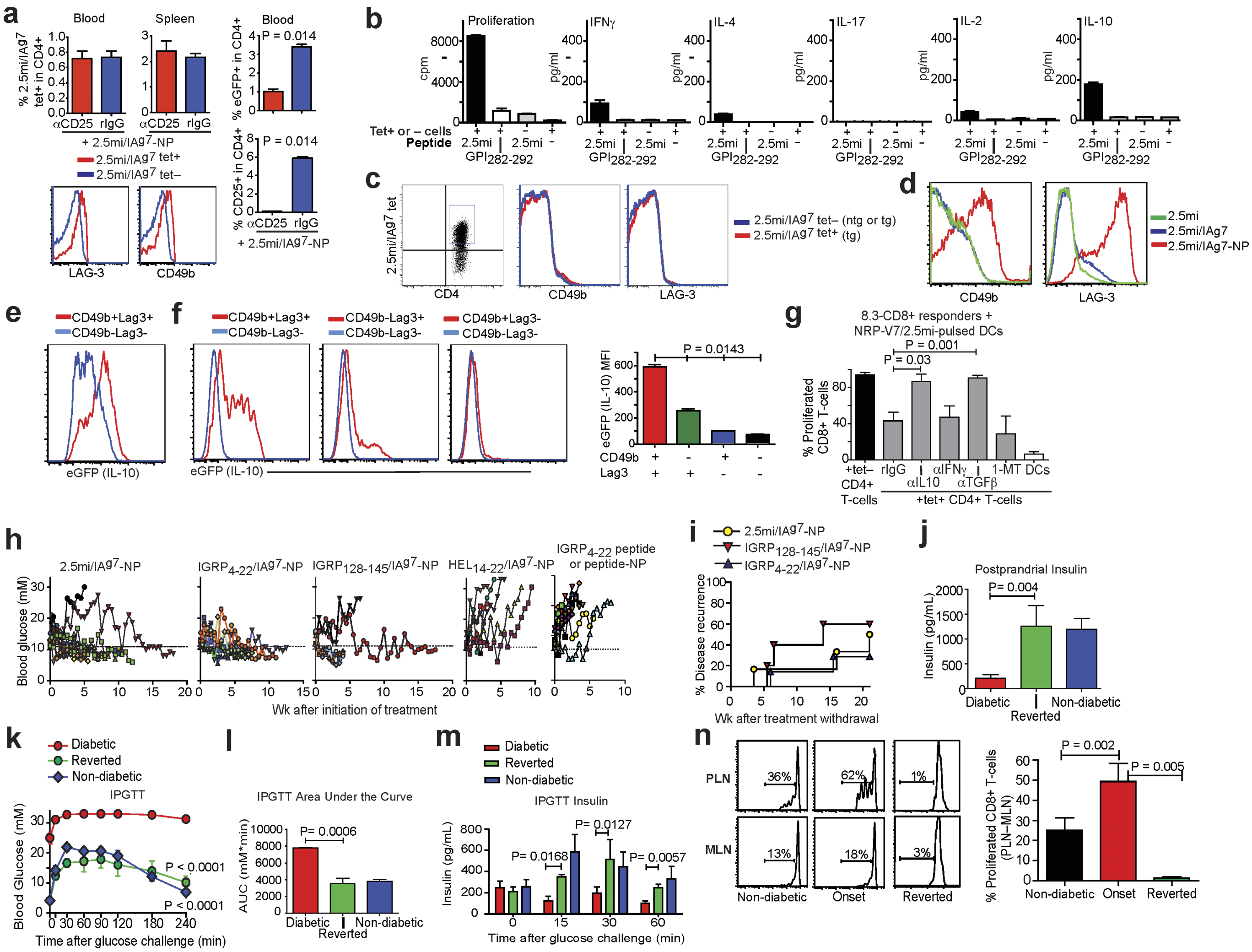

Extended Data Figure 1 | Sustained expansion of cognate T_R1-like $CD4^+$ T cells by pMHCII–NP therapy restores normal glucose homeostasis in diabetic NOD mice by suppressing antigen presentation and the activation of non-cognate autoreactive T cells in the PLNs and the progression of insulitis. **a**, Top left, expansion of cognate $CD4^+$ T cells by 2.5mi/IA^{g7}–NPs in anti-CD25 mAb-treated NOD *Foxp3-eGFP* mice. Data correspond to 8-week-old mice treated three times a week with 500 µg of a depleting anti-CD25 mAb i.p. or control anti-HPRN mAbs, followed by 10 doses of 2.5mi/IA^{g7}–NPs starting at 10 weeks of age (two doses per week; $n = 4$ mice each). Bottom, the tetramer$^+$CD4$^+$ T cells from anti-CD25 mAb-treated mice express T_R1 markers. Right, percentage of circulating FOXP3$^+$eGFP$^+$CD4$^+$ (top) and CD25$^+$CD4$^+$ cells (bottom). **b**, Tetramer$^+$CD4$^+$ T cells sorted from 2.5mi/IA^{g7}–NP-treated mice proliferate and produce IL-10 and, to a lesser extent IFNγ in response to stimulation with 2.5mi peptide-pulsed DCs ($n = 3$ mice). **c**, Representative cell surface CD49b and LAG-3 profiles on tetramer$^+$CD4$^+$ T cells from BDC2.5 NOD *Foxp3-eGFP* mice compared with tetramer$^-$CD4$^+$ T cells from transgenic or wild-type NOD mice ($n = 4$). **d**, Upregulation of CD49b and LAG-3 on anti-CD3/anti-CD28 mAb-activated BDC2.5 $CD4^+$ T cells from BDC2.5 NOD *Foxp3-eGFP* mice in response to 2.5mi/IA^{g7}–NP (25 µg pMHC per ml) versus 2.5mi peptide (10 µg ml^{-1}) or 2.5mi/IA^{g7} monomers (25 µg pMHC per ml). **e**, Upregulation of eGFP (IL-10) in anti-CD3/anti-CD28 mAb-activated BDC2.5 $CD4^+$ T cells from BDC2.5 NOD *Il10*^{GFP} mice in response to 2.5mi/IA^{g7}–NP as a function of CD49b and LAG-3 expression. **f**, Expression of eGFP (IL-10) in the $CD4^+$ T cells of 2.5mi/IA^{g7}–NP-treated NOD *Il10*^{GFP} mice (2 doses per week for 5 weeks) as a function of CD49b and LAG-3 expression (left, representative profiles; right, eGFP MFI values) ($n = 8$). **g**, Proliferation of CFSE-labelled 8.3-TCR-transgenic $CD8^+$ T cells (IGRP$_{206-214}$/NRP–V7-specific) in response to 2.5mi/NRP–V7–peptide-pulsed or unpulsed DCs in the presence of tetramer$^-$ or tetramer$^+$ $CD4^+$ T cells from 2.5mi/IA^{g7}-NP-treated mice and in the presence or absence of cytokine-blocking mAbs, rat IgG (negative control) or 1-methyl-L-tryptophan (1-MT; an IDO inhibitor). Data correspond to average of proliferated cells in 3–7 experiments per condition. **h**, Changes in blood glucose levels of spontaneously hyperglycaemic (>11 mM) female NOD mice treated with 2.5mi/IA^{g7}–NP, IGRP$_{4-22}$/IA^{g7}–NP, IGRP$_{128-145}$/IA^{g7}–NP or HEL$_{14-22}$/IA^{g7}–NP ($n = 6$–9 per group), IGRP$_{4-22}$ peptide or IGRP$_{4-22}$ peptide–NPs ($n = 9$, 4–5 each). Mice received two doses per week until irreversibly hyperglycaemic or normoglycaemic for 4 consecutive weeks, at which point treatment was withdrawn. **i**, Incidence and timing of disease relapse in hyperglycaemic female NOD mice rendered stably normoglycaemic by treatment with 2.5mi/IA^{g7}–NP, IGRP$_{4-22}$/IA^{g7}–NP or IGRP$_{128-145}$/IA^{g7}–NPs upon treatment withdrawal (after 4 consecutive weeks of normoglycaemia). Data correspond to responder mice in Fig. 1g. **j**, Post-prandial serum insulin levels in pMHC–NP-treated mice that reverted to normoglycaemia until 50 weeks of age ($n = 6$) versus newly diabetic ($n = 12$) and non-diabetic age-matched untreated controls ($n = 10$). **k**, Intra-peritoneal glucose tolerance tests (IPGTT) of the mice in **h**. **l**, Areas under the curve (AUC) in the IPGTTs shown in **k**. **m**, IPGTT serum insulin levels corresponding to the mice in **k**. **n**, Proliferation of CFSE-labelled IGRP$_{206-214}$-reactive 8.3-CD8$^+$ T cells in the PLNs compared with MLNs of 2.5mi/IA^{g7}–NP-treated mice that reverted to normoglycaemia until 50 weeks of age, non-diabetic age-matched untreated controls and newly diabetic mice. Left panels show representative FACS profiles. Right panel compares percentages of proliferated cells in the PLNs after subtraction of the background proliferation values in non-draining MLNs ($n = 6$–8 mice per group). *P* values were calculated by Mann–Whitney *U*-test, log-rank (Mantel–Cox) test or two-way ANOVA. Data are averages ± s.e.m.

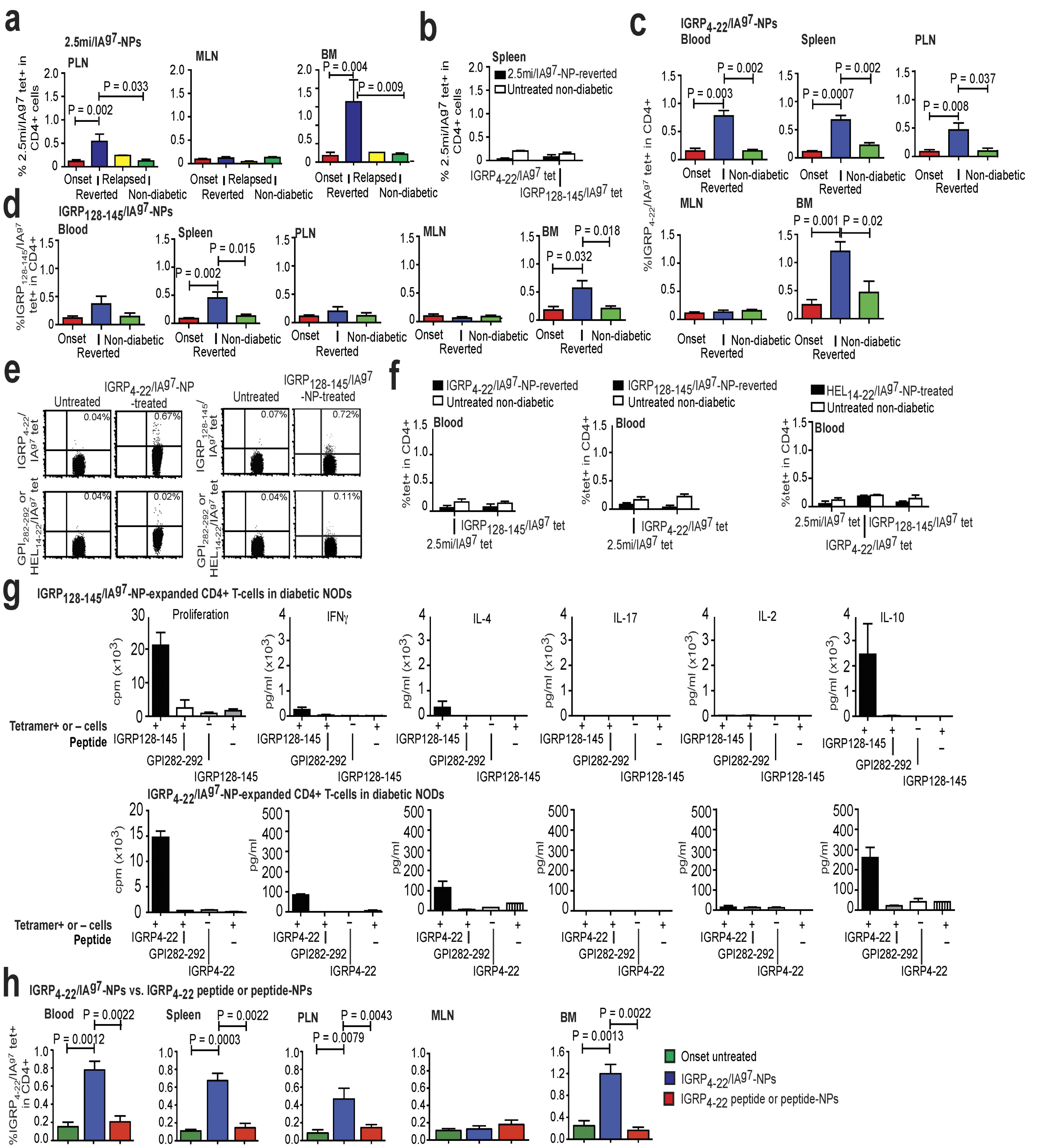

Extended Data Figure 2 | Nanoparticles coated with different T1D-relevant pMHCII complexes expand cognate T_R1-like CD4$^+$ T cells *in vivo* to similar extent, regardless of epitope dominance or role of the target T-cell specificity in the disease process. a, Percentage of tetramer$^+$CD4$^+$ T cells in the PLN, MLN and bone marrow (BM) of 2.5mi/IA^{g7}–NP-treated mice that reverted to normoglycaemia until 50 weeks of age ($n = 5$–6 mice per lymphoid organ) or relapsed ($n = 1$–2) compared with newly diabetic ($n = 5$–6) and non-diabetic age-matched untreated controls ($n = 4$–6). **b**, Percentage of tetramer$^+$CD4$^+$ T cells in the splenic CD4$^+$ T cells of 2.5mi/IA^{g7}–NP-treated mice that reverted to normoglycaemia until 50 weeks of age or of age-matched non-diabetic untreated mice, stained with two T1D-relevant but non-cognate pMHCII tetramers ($n = 3$–4 per group). **c**, Percentage of tetramer$^+$CD4$^+$ T cells in blood, spleen, PLN, MLN and bone marrow of IGRP$_{4-22}$/IA^{g7}–NP-treated mice that reverted to normoglycaemia until 50 weeks of age ($n = 5$–6 mice per lymphoid organ) compared with newly diabetic ($n = 5$–8) and non-diabetic age-matched untreated controls ($n = 4$–6). **d**, Percentage of tetramer$^+$CD4$^+$ T cells in blood, spleen, PLN, MLN and bone marrow of IGRP$_{128-145}$/IA^{g7}–NP-treated mice that reverted to normoglycaemia until 50 weeks of age ($n = 5$–7 mice per lymphoid organ) compared with newly diabetic ($n = 4$–7) and non-diabetic age-matched untreated controls ($n = 5$–7). **e**, Representative IGRP$_{4-22}$/IA^{g7}, IGRP$_{128-145}$/IA^{g7} and GPI$_{282-292}$/IA^{g7} tetramer staining profiles for splenic CD4$^+$ T cells from IGRP$_{4-22}$/IA^{g7}–NP- and IGRP$_{128-145}$/IA^{g7}–NP-treated compared with untreated NOD mice. **f**, Percentages of blood CD4$^+$ T cells of IGRP$_{4-22}$/IA^{g7}–NP- or IGRP$_{128-145}$/IA^{g7}–NP-cured, HEL$_{14-22}$/IA^{g7}–NP-treated and age-matched non-diabetic untreated mice stained with non-cognate pMHCII tetramers ($n = 3$–7 per group). **g**, The tetramer$^+$CD4$^+$ T cells of mice treated with IGRP$_{128-145}$/IA^{g7}–NP (top) and IGRP$_{4-22}$/IA^{g7}–NP (bottom) proliferate and produce IL-10 specifically in response to stimulation with IGRP$_{4-22}$ or IGRP$_{128-145}$-peptide-pulsed DCs, respectively ($n = 3$ mice each). cpm, counts per minute. **h**, Percentages of IGRP$_{4-22}$/IA^{g7} tetramer$^+$CD4$^+$ T cells in blood, spleen, PLN, MLN and bone marrow of NOD mice at the onset of hyperglycaemia or upon treatment with IGRP$_{4-22}$/IA^{g7}–NPs, or IGRP$_{4-22}$ peptide or IGRP$_{4-22}$ peptide-coated nanoparticles ($n = 5$–9 mice per organ). *P* values were calculated by Mann–Whitney *U*-test. Data are averages ± s.e.m.

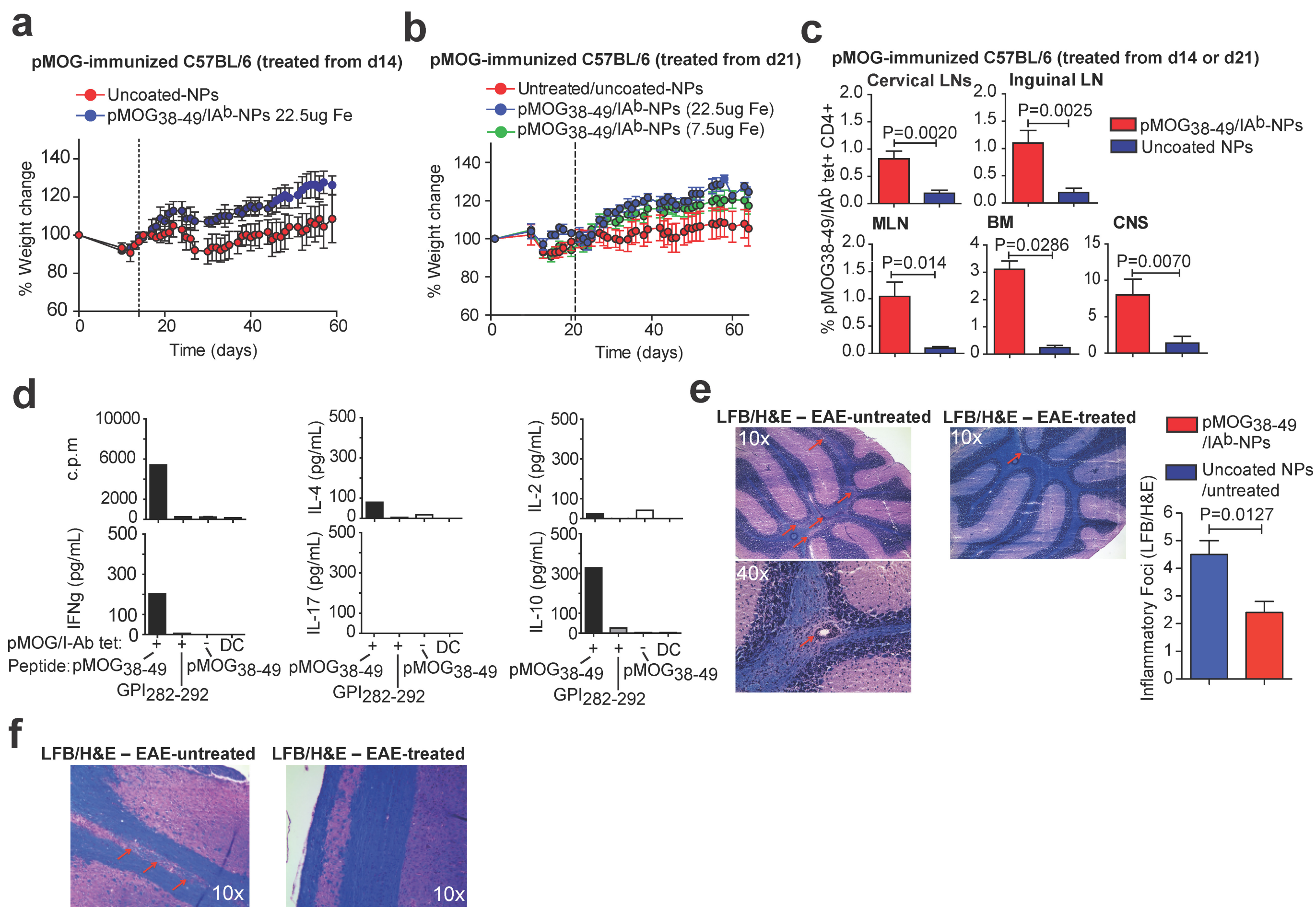

Extended Data Figure 3 | EAE-relevant pMHCII–NPs expand cognate IL-10-secreting T_R1-like CD4$^+$ T cells and ameliorate established clinical and pathological signs of EAE. a, b, Changes in the average weights of C57BL/6 mice immunized with pMOG$_{35-55}$ and treated with pMOG$_{38-49}$/IA^b–NPs or uncoated nanoparticles starting on days 14 (**a**) or 21 (**b**) after immunization. **c**, Percentage of pMOG$_{38-49}$/IA^b tetramer$^+$CD4$^+$ T cells in peripheral lymph nodes, bone marrow and central nervous system (CNS) of mice from **a** and **b**. **d**, The tetramer$^+$CD4$^+$ T cells of pMOG$_{38-49}$/IA^b–NP-treated mice proliferate and produce IL-10 and, to a lesser extent, IFNγ in response to stimulation with pMOG$_{38-49}$ peptide-pulsed DCs. **e**, Left and middle, representative luxol fast blue (LFB)/H&E cerebellum staining images from untreated and treated mice from **b** showing presence of inflammatory foci and areas of demyelination (red arrows). Right, average number of inflammatory foci per section. Data corresponds to 4 untreated and 5 treated mice. **f**, Representative LFB/H&E-stained spinal cord sections from mice in **b**. Data were compared with Mann–Whitney *U*-test. Data are averages ± s.e.m.

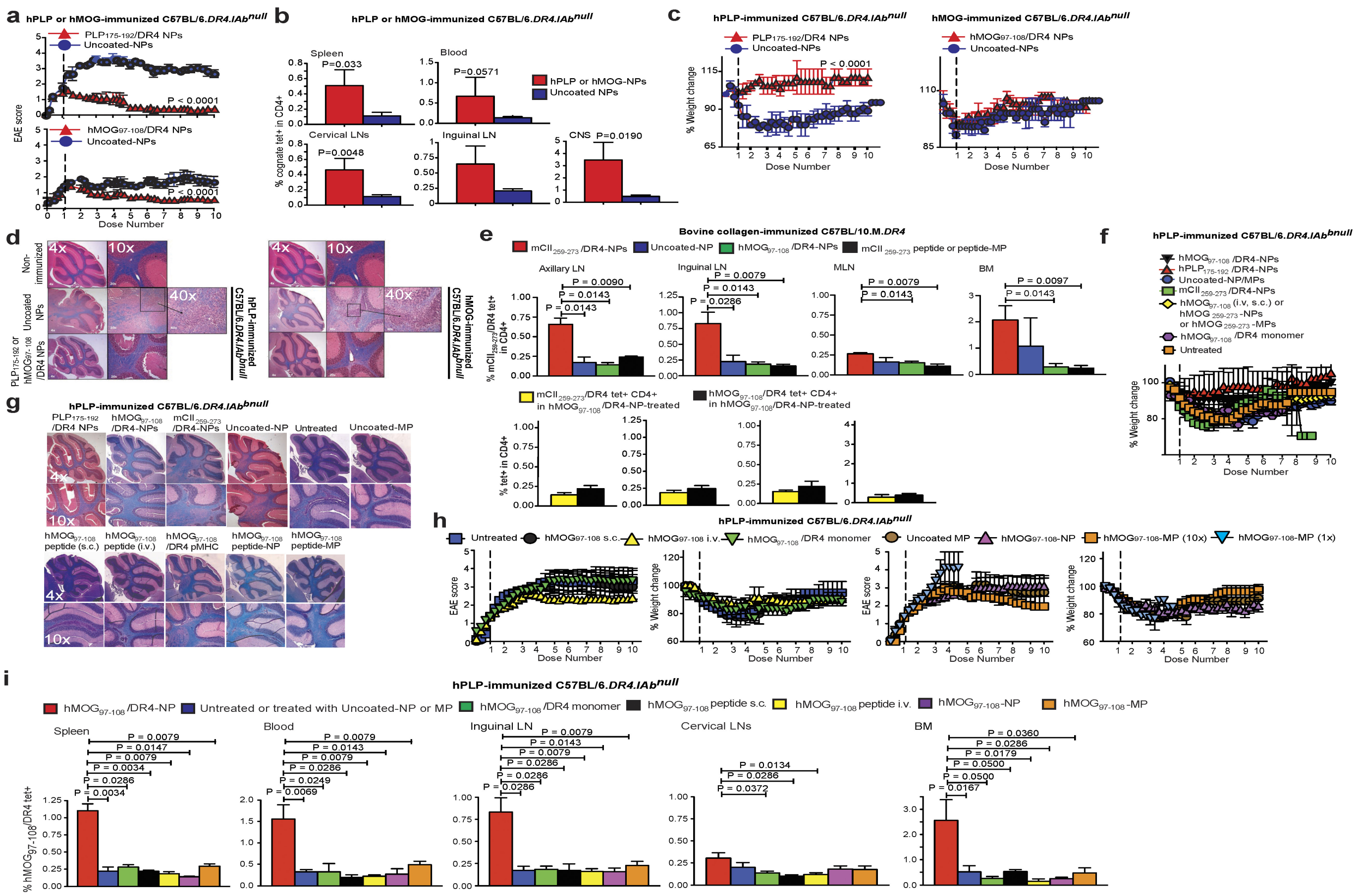

Extended Data Figure 4 | EAE- or CIA-relevant pMHCII–NPs expand cognate T_R1-like CD4$^+$ T cells and ameliorate clinical and pathological signs of EAE or CIA in *HLA-DR4-IE*-transgenic C57BL/6 *IAb*^{null} or C57BL/10.M mice. a, Changes in the average EAE scores of *HLA-DR4-IE*-transgenic C57BL/6 *IAb*^{null} mice immunized with hPLP$_{175-192}$ or hMOG$_{97-108}$ and treated with hPLP$_{175-192}$ /DR4-IE or hMOG$_{97-108}$/DR4-IE–NPs or uncoated nanoparticles starting on the day when mice reached a score of 1.5 (to synchronize the groups for disease activity) ($n = 3$–4 per group). **b**, Percentage of tetramer$^+$CD4$^+$ T cells in spleen, blood, cervical and inguinal LNs and CNS of mice from **a**. Data correspond to 4 pMHC–NP-treated and 6 control-NP-treated mice. **c**, Changes in the average weights of *HLA-DR4–IE*-transgenic C57BL/6 *IAb*^{null} mice from **a**, immunized with hPLP$_{175-192}$ or hMOG$_{97-108}$ and treated with hPLP$_{175-192}$/DR4-IE–NPs, hMOG$_{97-108}$/DR4-IE–NPs or uncoated nanoparticles when the mice reached a score of 1.5. **d**, LFB/H&E staining of the cerebellum of *HLA-DR4-IE*-transgenic C57BL/6 *IAb*^{null} mice from **a** showing reductions in inflammation and demyelination in mice treated with hPLP$_{175-192}$ /DR4-IE or hMOG$_{97-108}$/DR4-IE–NPs compared with controls. **e**, Percentage of tetramer$^+$CD4$^+$ T cells in lymph nodes and bone marrow of the mice in Fig. 2a (C57BL/10.M *HLA-DR4-IE* mice immunized with bovine collagen) at the end of follow-up (10 doses, 5 weeks). **f**, Changes in the average weights of *HLA-DR4-IE*-transgenic C57BL/6 *IAb*^{null} mice immunized with hPLP$_{175-192}$ from Fig. 2f. **g**, Representative LFB/H&E staining of the cerebellum of *HLA-DR4-IE*-transgenic C57BL/6 *IAb*^{null} mice immunized with hPLP$_{175-192}$ and treated with hPLP$_{175-192}$/DR4-IE–NPs, hMOG$_{97-108}$/DR4-IE–NPs, hMOG$_{97-108}$ peptide i.v. or s.c. (8 µg per dose), hMOG$_{97-108}$/DR4-IE monomer (25 µg per dose), hMOG$_{97-108}$ peptide–NPs (using the molar equivalent of peptide delivered via pMHC–NPs; 0.68 µg per dose), or hMOG$_{97-108}$ peptide–MPs (15 µg peptide per dose) compared with mice left untreated or treated with uncoated NPs or MPs (at the same NP/MP number). **h**, Changes in the average EAE scores and body weights of *HLA-DR4-IE*-transgenic C57BL/6 *IAb*^{null} mice immunized with hPLP$_{175-192}$ in response to treatment with hMOG$_{97-108}$ peptide i.v. or s.c. (8 µg per dose[16]), hMOG$_{97-108}$/DR4-IE monomer (25 µg per dose), hMOG$_{97-108}$ peptide–NPs (0.68 µg peptide per dose), hMOG$_{97-108}$ peptide–MPs (15 µg peptide per dose[17]), or a single dose of hMOG$_{97-108}$ peptide–MPs (15 µg peptide[17]) compared with mice left untreated or treated with uncoated NPs or MPs (at the same NP/MP number) ($n = 4$–5 per group). The cohort of mice treated with one dose had to be terminated after 2.5 weeks, owing to rapid progression of disease. **i**, Percentages of tetramer$^+$CD4$^+$ T cells in spleen, blood, cervical and inguinal LNs and bone marrow of mice from **h** ($n = 3$–9 per group). Data were compared with Mann–Whitney *U*-test or two-way ANOVA. Data are averages ± s.e.m.

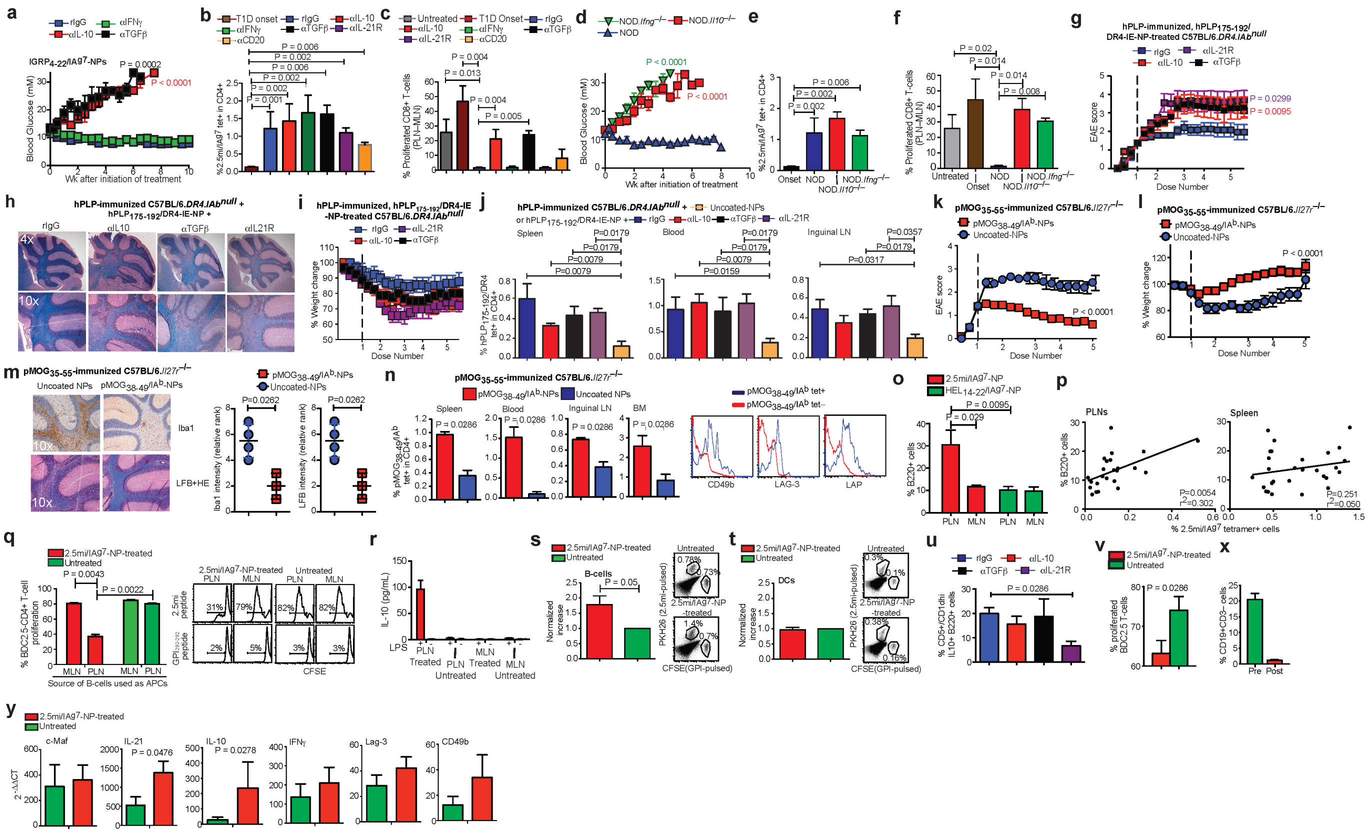

Extended Data Figure 5 | Disease reversal by pMHC–NPs is driven by the T_R1 cytokines IL-21, IL-10 and TGF-β and involves several downstream cellular targets. a, Changes in blood glucose levels in diabetic NOD mice (>11 mM) treated with IGRP$_{4-22}$/IA^{g7}–NPs and blocking anti-IL-10, anti-IFNγ or anti-TGF-β mAbs or anti-HRPN rat-IgG ($n=4$–6 per group). **b, c**, Percentages of tetramer$^+$CD4$^+$ T cells in the spleens (**b**), and proliferation of CFSE-labelled 8.3-CD8$^+$ T cells in the PLNs verus MLN of the mice from Fig. 3a at the end of follow up (**c**). **d**, Changes in blood glucose in hyperglycaemic NOD, NOD *Il10*$^{-/-}$ and NOD *Ifng*$^{-/-}$ mice ($n=3-6$ per group) in response to 2.5mi/IA^{g7}–NPs. **e**, **f**, Percentages of tetramer$^+$CD4$^+$ T cells in the spleens (**e**), and proliferation of CFSE-labelled 8.3-CD8$^+$ T cells in the PLNs versus MLN of the mice from **d** at the end of follow up (**f**). **g**, EAE scores of mice treated with pMHC–NPs and rat-IgG or blocking mAbs ($n=4$ per group). **h**, LFB/H&E staining of the cerebellum of *HLA-DR4-IE*-transgenic C57BL/6 *IAb*^{null} mice from **g**, highlighting differences in inflammation and demyelination in mice treated with hPLP$_{175-192}$/DR4-IE–NPs and rat-IgG versus blocking anti-IL-10, anti-TGF-β or anti-IL-21R mAbs. **i**, Changes in the average body weights of *HLA-DR4-IE*-transgenic C57BL/6 *IAb*^{null} mice from **g**. **j**, Percentage of tetramer$^+$CD4$^+$ T cells in spleen, blood and inguinal LNs of mice from **g** ($n=4$ per group). **k**, **l**, Changes in the average EAE scores (**k**) and body weights (**l**) of C57BL/6 *Il27r*$^{-/-}$ mice immunized with pMOG$_{35-55}$ and treated with pMOG$_{38-49}$/IA^b–NPs or uncoated nanoparticles starting on the day when mice reached a score of 1.5 (to synchronize the groups for disease activity) ($n=7$ and 4, respectively). **m**, Representative IBA1 and LFB/H&E stainings of the cerebellum and the corresponding relative rank scores of mice from **k** ($n=3$ and 4, respectively). **n**, Percentage of tetramer$^+$CD4$^+$ T cells in spleen, blood, inguinal LNs and bone marrow of mice from **k** (left), and representative CD49b and LAG-3 staining profiles of tetramer$^+$ versus tetramer$^-$ cells (right). **o**, Percentage of B220$^+$ cells in the PLNs or MLNs of 2.5mi/IA^{g7}–NP- or HEL$_{14-22}$/IA^{g7}–NP-treated mice ($n=4$ per group). **p**, Correlation between the percentages of PLN and splenic B220$^+$ cells and 2.5mi/IA^{g7} tetramer$^+$CD4$^+$ T cells in additional cohorts of mice treated with 2.5mi/IA^{g7}–NPs, over a range of total pMHC dose (0.75–25 μg of total pMHC) ($n=24$–28). **q**, Left, *in vitro* proliferation of CFSE-labelled BDC2.5 CD4$^+$ T cells against 2.5mi or GPI$_{282-292}$ peptide-pulsed B cells purified from the PLNs or MLNs of untreated NOD mice or mice treated with 2.5mi/IA^{g7}–NPs ($n=5$–6 per group). Right, representative CFSE dilution profiles. Briefly, profiles show the extent of CFSE dilution in CFSE-labelled BDC2.5 CD4$^+$ T cells cultured in the presence of 2.5mi or GPI$_{282-292}$ peptide-pulsed B cells purified from the PLNs or MLNs of untreated or 2.5mi/IA^{g7}–NP-treated NOD mice. **r**, PLN-derived B cells (10^5) from 2.5mi/IA^{g7}–NP-treated mice secrete IL-10 *ex vivo* in response to LPS (1 μg ml^{-1}). Data correspond to 6 pMHC-treated and 5 untreated NOD mice. **s**, **t**, Changes in the percentages of 2.5mi (PKH26-labelled) compared with GPI$_{282-292}$ peptide-pulsed (CFSE-labelled) B cells (**s**) or DCs (**t**) 7 days after transfer (at 1:1 ratio) into untreated or 2.5mi/IA^{g7}–NP-treated NOD mice. Histograms show averaged ratios for each cell type and condition ($n=3$–4 mice per cell type and condition). **u**, Percentages of CD5$^+$CD1d^{hi}eGFP$^+$B220$^+$ cells in mice treated as in Fig. 3b plus blocking Abs ($n=4$ each). **v**, LPS-stimulated PLN B cells from NOD mice treated with 10 doses of 2.5mi/IA^{g7}–NPs suppress the proliferation of CFSE-labelled BDC2.5 CD4$^+$ T cells by 2.5mi peptide-pulsed DCs *in vitro*, as compared to LPS-stimulated PLN B cells from untreated controls. **x**, Percentage of CD19$^+$CD3$^-$ cells in blood before and after 3 doses of 250 μg of anti-CD20 mAb ($n=4$). **y**, 2.5mi/IA^{g7}–NP-induced upregulation of IL-21 and IL-10 mRNA in memory eGFP$^-$ BDC2.5 CD4$^+$ T cells from BDC2.5-TCR-transgenic NOD *Foxp3-eGFP* donors in NOD *Thy1^a* hosts ($n=5$). *P* values were calculated by Pearson correlation, Mann–Whitney *U*-test or two-way ANOVA. Data are averages ± s.e.m.

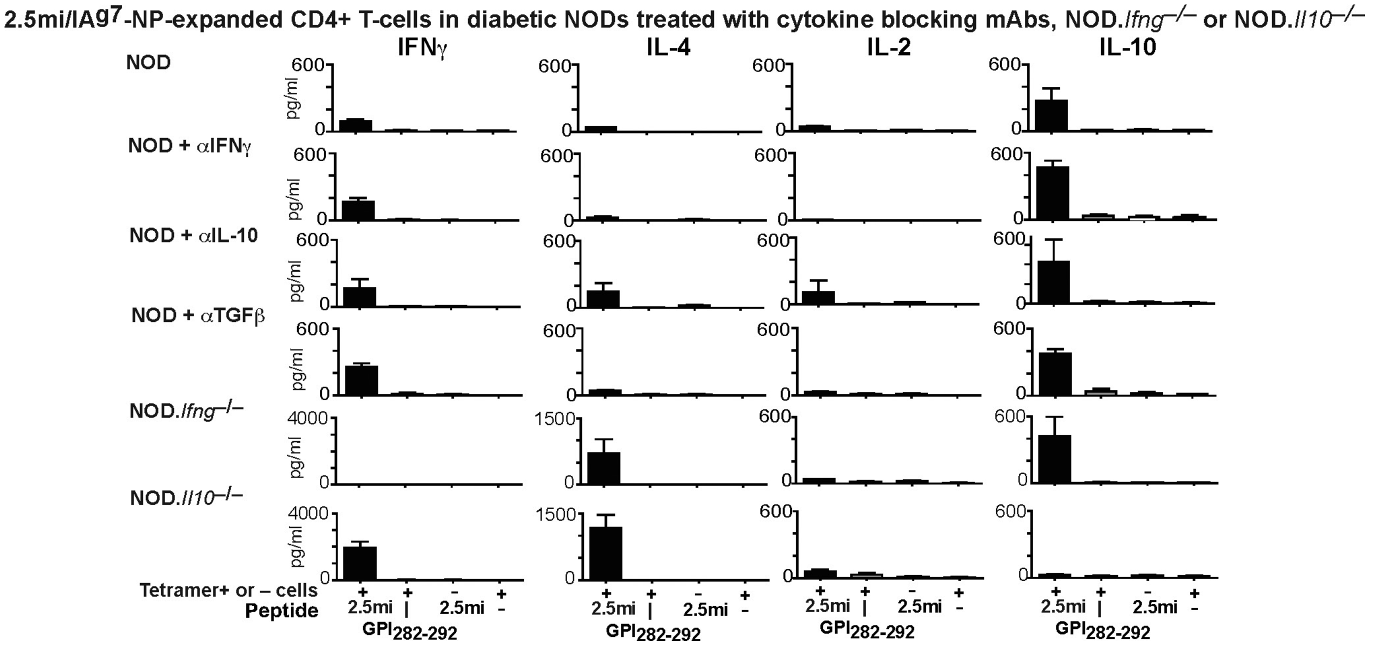

Extended Data Figure 6 | Effects of cytokine blockade or genetic deficiency on the cytokine profile of cognate CD4^{+} T cells expanded by 2.5mi/IA^{g7}–NPs. $n = 3$ mice each. Data are averages ± s.e.m.

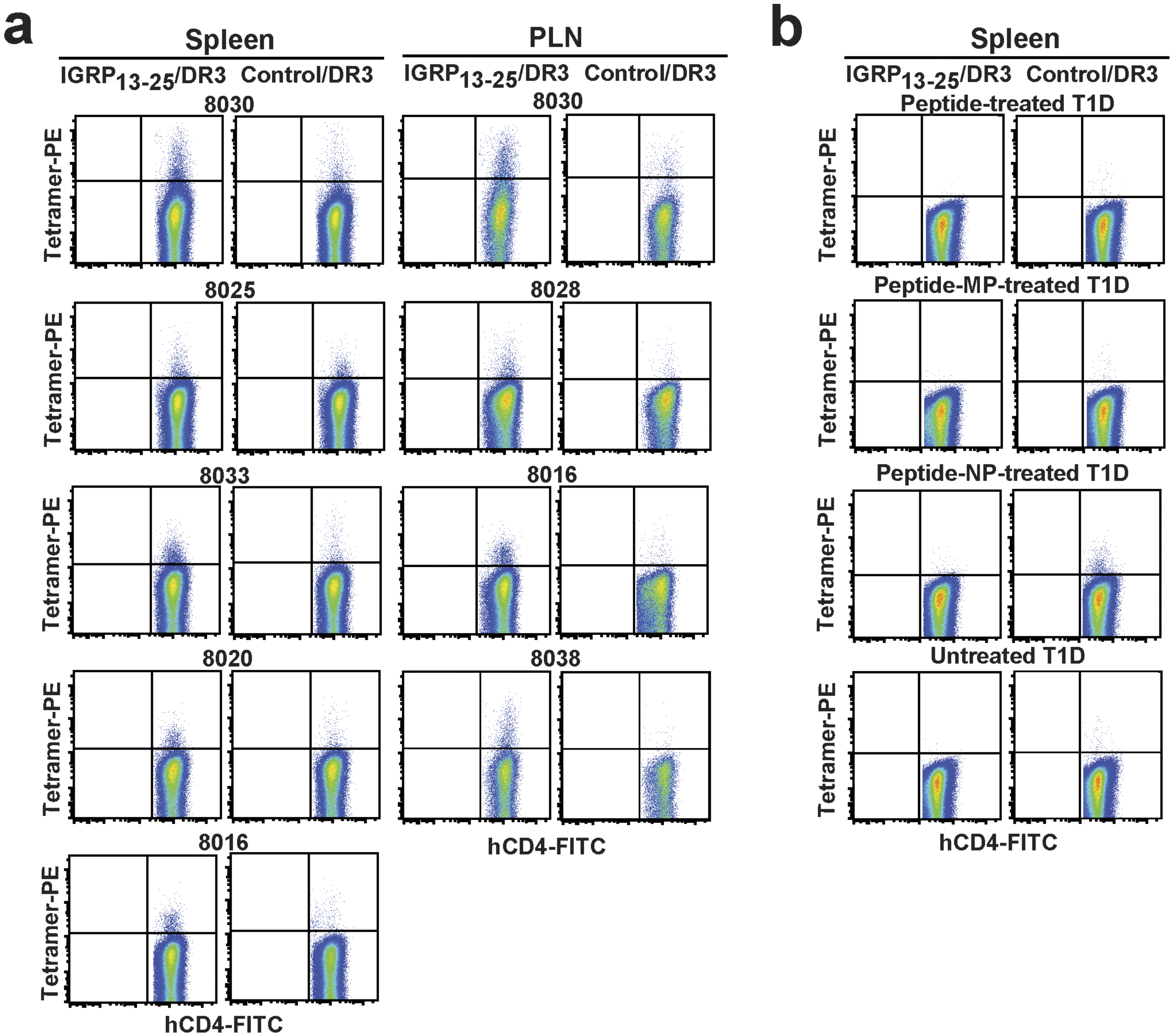

Extended Data Figure 7 | Human T1D-relevant pMHCII–NPs, but not free peptide or peptide-coated nanoparticles or microparticles, expand cognate T_R1-like $CD4^+$ T cells in human PBMC-engrafted NSG hosts. **a**, FACS profiles (cognate versus control tetramer staining in $hCD4^+$ T cells) of samples from mice identified as responders in Supplementary Table 2. Numerical data on $tetramer^+$ T cells are presented on Supplementary Table 2. **b**, Representative FACS profiles (cognate versus control tetramer staining in splenic $hCD4^+$ T cells) of human healthy control PBMC-engrafted NSG hosts treated with $IGRP_{13-25}$/DR3–NPs (left), or human T1D PBMC-engrafted NSG hosts treated with $IGRP_{13-25}$ peptide, $IGRP_{13-25}$ peptide-coated nanoparticles, $IGRP_{13-25}$ peptide-coated microparticles, or left untreated (right). See Fig. 5 legend for details.

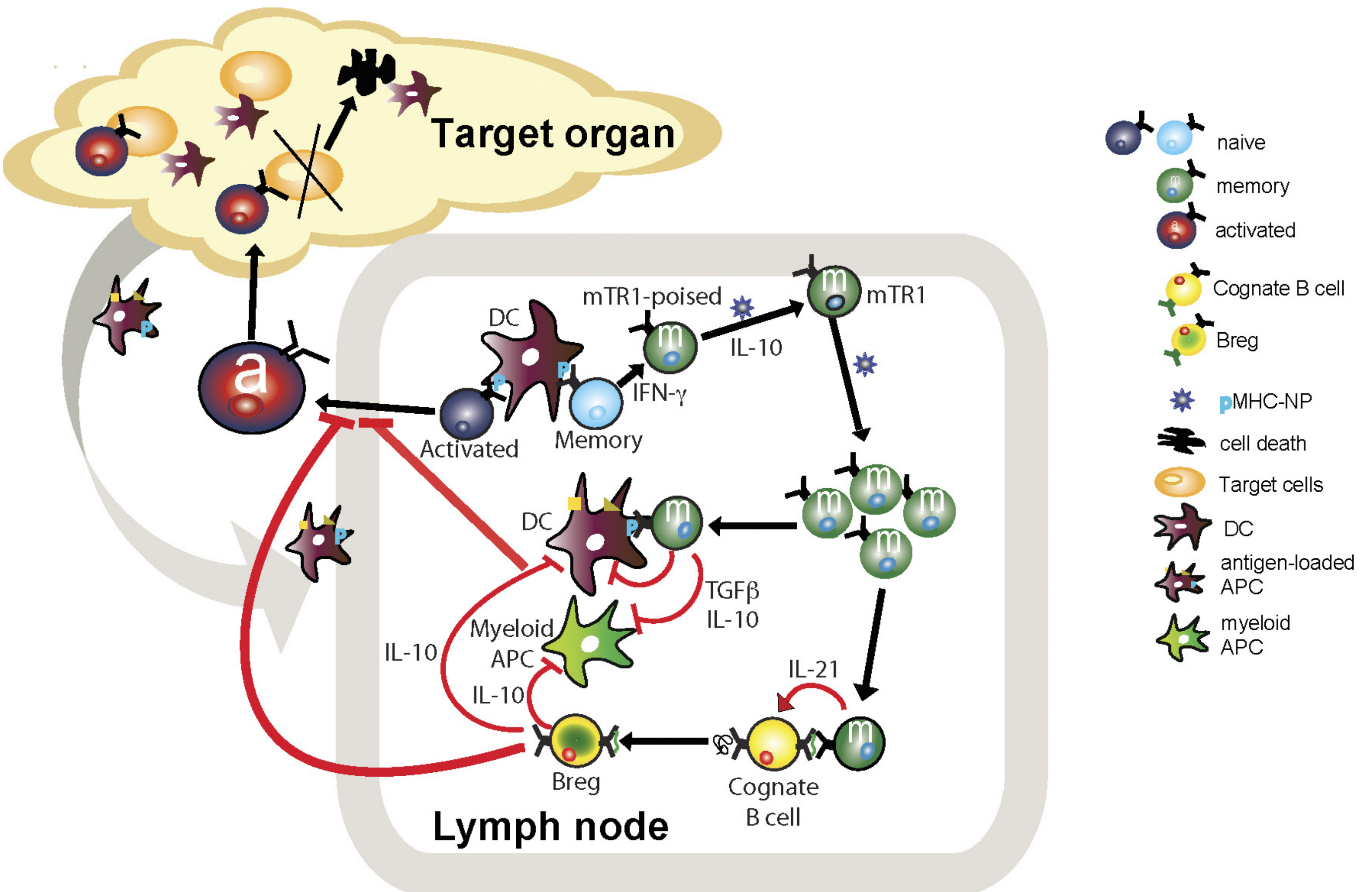

Extended Data Figure 8 | Schematic of the proposed mode of operation of pMHCII-based nanomedicines. pMHCII-coated NPs (pMHC–NP, lacking costimulatory molecules) promote the differentiation of disease-primed (antigen-experienced) IFNγ-producing CD4^{+} T$_{H}$1-cells into memory T$_{R}$1-like CD4^{+} T cells followed by systemic expansion. This differentiation process (but not the subsequent expansion) requires both IFNγ and IL-10, whereas IL-27 is dispensable. The pMHC–NP-expanded (mono-specific) autoreactive T$_{R}$1-like CD4^{+} T cells then suppress other autoreactive T-cell responses by secreting IL-21, IL-10 and TGF-β, which act on local APCs (B cells, CD11c^{+} and CD11b^{+} cells) that have captured the cognate autoantigen and thus present cognate pMHCII complexes to the expanded T$_{R}$1-like cells. This interaction inhibits the proinflammatory function of the targeted APCs and blocks their ability to present other pMHC class I and class II complexes to non-pMHC–NP-cognate autoreactive T-cell specificities (note that the local APCs uptake both cognate and non-cognate autoantigens shed into the milieu simultaneously). Suppression of antigen-presentation requires IL-10 and TGF-β but not IFNγ or IL-21. Furthermore, cognate interactions between the pMHC–NP-expanded T$_{R}$1 CD4^{+} T cells and autoreactive B cells specific for the cognate autoantigen (able to display the cognate pMHCII complex on the surface) promotes their differentiation into B$_{reg}$ cells in an IL-21-dependent manner, which contribute to promote local immunosuppression, likely by secreting IL-10. Suppression of antigen presentation selectively targets APCs displaying the cognate pMHC, but as local APCs that capture the cognate autoantigen also capture other autoantigens simultaneously, the autoregulatory CD4^{+} T cells expanded by pMHC–NPs blunt the presentation of other autoantigenic pMHC complexes to a broad range of autoreactive T cells. This suppression is disease-specific and self-limiting.

doi:10.1038/nature16998

The dynamic N^1-methyladenosine methylome in eukaryotic messenger RNA

Dan Dominissini[1,2*], Sigrid Nachtergaele[1,2*], Sharon Moshitch-Moshkovitz[3*], Eyal Peer[3,4], Nitzan Kol[3], Moshe Shay Ben-Haim[3,4], Qing Dai[1,2], Ayelet Di Segni[3], Mali Salmon-Divon[3], Wesley C. Clark[6], Guanqun Zheng[6], Tao Pan[6], Oz Solomon[3,5], Eran Eyal[3], Vera Hershkovitz[3], Dali Han[1,2], Louis C. Doré[1,2], Ninette Amariglio[3,5], Gideon Rechavi[3,4] & Chuan He[1,2,6]

Gene expression can be regulated post-transcriptionally through dynamic and reversible RNA modifications. A recent noteworthy example is N^6-methyladenosine (m^6A), which affects messenger RNA (mRNA) localization, stability, translation and splicing. Here we report on a new mRNA modification, N^1-methyladenosine (m^1A), that occurs on thousands of different gene transcripts in eukaryotic cells, from yeast to mammals, at an estimated average transcript stoichiometry of 20% in humans. Employing newly developed sequencing approaches, we show that m^1A is enriched around the start codon upstream of the first splice site: it preferentially decorates more structured regions around canonical and alternative translation initiation sites, is dynamic in response to physiological conditions, and correlates positively with protein production. These unique features are highly conserved in mouse and human cells, strongly indicating a functional role for m^1A in promoting translation of methylated mRNA.

Four decades after it was first observed as an abundant constituent of the eukaryotic transcriptome, m^6A has only recently been revealed to broadly affect mRNA metabolism[1,2]. Consequently, a broader notion has emerged that dynamic chemical modifications of mRNA, now also encompassing pseudouridine (Ψ)[3–5] and 5-methylcytosine[6,7], have vital roles in post-transcriptional gene regulation. With the epitranscriptome, as these modifications are now known, RNA joins both DNA and proteins in being subject to dynamic and reversible chemical control[8,9]. Unlike the latter two, however, the functions of RNA chemical adducts are only now being determined. It is likely that the complement of mRNA modifications, at present much smaller than that found on transfer RNA (tRNA) and ribosomal RNA (rRNA)[10], is far from complete.

Transcriptome-wide mapping of m^1A

m^1A was identified in total RNA from several species decades ago[11,12]. It was later characterized in tRNA[13] and rRNA[14] where it has a major influence on structure and function, owing to the presence of both a methyl adduct and a positive charge under physiological conditions[15]. Since m^1A can rearrange to m^6A under alkaline conditions (Dimroth rearrangement)[16], its signature in mRNA might be erased by the purification and measurement process, simultaneously introducing noise in m^6A measurements (Fig. 1a and Extended Data Fig. 1a), as earlier attempts to survey mRNA base modifications acknowledged[17]. To determine whether m^1A is present in mRNA and to quantify it, we performed quantitative mass spectrometry (LC-MS/MS) of pure mRNA preparations under controlled conditions (Supplementary Note 1, Extended Data Fig. 1b–d) and obtained m^1A/A molar ratios in several human and mouse cell lines and tissues, both normal and cancerous. Our results unequivocally show that m^1A is present in pure mammalian mRNA, at m^1A/A ratios ranging from approximately 0.015% to 0.054% in cell lines and up to 0.16% in tissues (Figs 1b, 5d and Extended Data Fig. 1e). Metabolic labelling of cells with deuterated methionine (d_3-Met) results in detection of d_3-m^1A in mRNA, suggesting that *S*-adenosylmethionine (SAM) is the methyl donor (Extended Data Fig. 1f). Although these ratios are smaller than the m^6A/A and Ψ/U ratios in the same samples (Fig. 1b), the absolute and fractional levels of m^1A in mRNA (see stoichiometry below) are sufficiently high to exhibit potential regulatory functions of selectively methylated transcripts.

We adapted an antibody-based approach, methylated RNA immunoprecipitation sequencing (MeRIP-seq), termed here m^1A-seq, for transcriptome-wide localization of m^1A sites and coupled it to an orthogonal chemical method based on Dimroth rearrangement to obtain high-resolution m^1A maps (Supplementary Notes 2, 3; Fig. 1c–e and Extended Data Fig. 1g–m). We applied m^1A-seq to polyA$^+$ RNA from HeLa cells in two replicates and determined the methylated positions (m^1A peaks) using the MACS peak-calling algorithm[18]. We identified 7,154 peaks (fold change (FC) ≥ 2, false discovery rate (FDR) $\leq 5\%$) in 4,151 coding and 63 non-coding adequately expressed (that is, above the 1st quartile of expressed genes) gene transcripts that occurred in both replicates (Fig. 2a, Supplementary Tables 1, 4). On average, each methylated gene carries 1.4 peaks, with most of these genes (over 70%) methylated only once (Fig. 2b). In a conservative estimate, 35% of adequately expressed genes are methylated, attesting to the breadth of the phenomenon. Of note, non-coding genes are significantly underrepresented among methylated genes ($P = 1 \times 10^{-140}$, hypergeometric test). Methylated genes constitute a progressively larger fraction of genes as expression increases (Fig. 2c), and are significantly enriched in several gene ontology terms related to translation and RNA processing (Extended Data Fig. 2a, b).

As most methylated transcripts harbour a single m^1A, methylation stoichiometry can be estimated based on the change in transcript levels following immunodepletion. We used microarrays to determine relative transcript abundance in HepG2 RNA before and after depletion

[1]Department of Chemistry and Institute for Biophysical Dynamics, The University of Chicago, 929 East 57th Street, Chicago, Illinois 60637, USA. [2]Howard Hughes Medical Institute, The University of Chicago, 929 East 57th Street, Chicago, Illinois 60637, USA. [3]Cancer Research Center, Chaim Sheba Medical Center, Tel Hashomer 52621, Israel. [4]Sackler School of Medicine, Tel Aviv University, Tel Aviv 69978, Israel. [5]The Mina and Everard Goodman Faculty of Life Sciences, Bar-Ilan University, Ramat Gan 52900, Israel. [6]Department of Biochemistry and Molecular Biology, The University of Chicago, 929 East 57th Street, Chicago, Illinois 60637, USA.
*These authors contributed equally to this work.

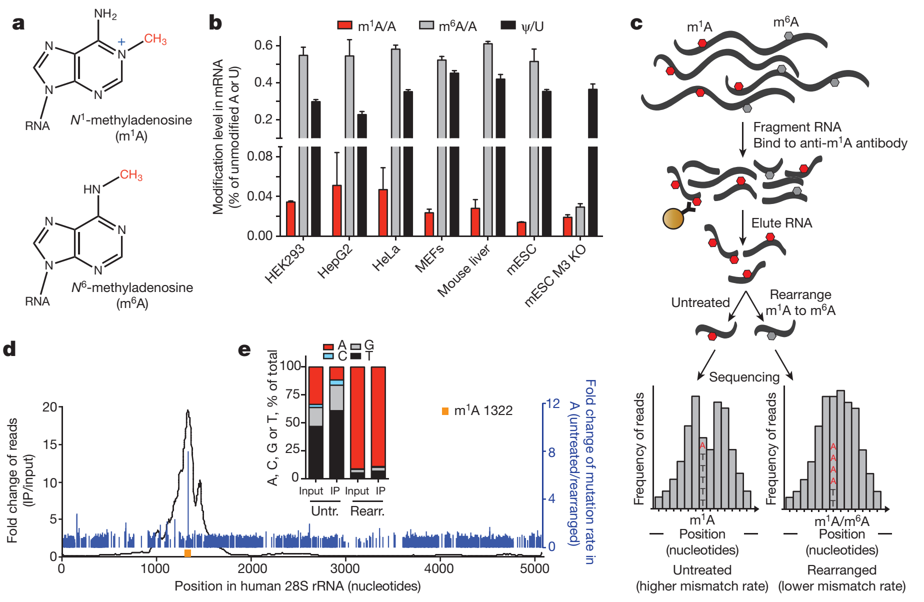

Figure 1 | Development of m^{1}A-seq to map a newly identified constituent of mammalian mRNA. a, Chemical structures of m^{1}A and m^{6}A. Methyl groups (-CH_3) are in red and the positive charge (+) on m^{1}A is in blue. **b**, LC-MS/MS quantitation of m^{1}A, m^{6}A and Ψ in human and mouse mRNA isolated from the indicated cell types. The level of each modified nucleoside is indicated as a percentage of the unmodified one. Mean values ± s.e.m. are shown, $n = 3$. MEFs, mouse embryonic fibroblasts; mESC, mouse embryonic stem cells; M3 KO, *Mettl3* knockout. **c**, Schematic outline of m^{1}A-seq. RNA is fragmented and subjected to immunoprecipitation using anti-m^{1}A antibody. Eluted RNA fragments are converted to cDNA and sequenced, or treated to induce partial m^{1}A-to-m^{6}A rearrangement before cDNA synthesis. m^{1}A causes both reverse transcription stops and read-throughs accompanied by mismatches, to produce typical peaks with a central trough and an adenosine with increased mismatch rate (left). Partial rearrangement of m^{1}A to m^{6}A attenuates the effect (right). m^{1}A is in red, m^{6}A is in grey; mismatch rate is illustrated as the ratio between A (red) and T (black). **d**, Detection of the known m^{1}A 1322 site (yellow) in human 28S rRNA validates m^{1}A-seq (black curve). High fold-change in mismatch rate (before and after m^{1}A-to-m^{6}A rearrangement in immunoprecipitation, blue lines) independently identifies m^{1}A 1322 with single-nucleotide resolution. **e**, Mismatch rates in m^{1}A 1322 increase after immunoprecipitation and decrease upon rearrangement.

with anti-m^{1}A antibody, and found that the average methylation level in single m^{1}A-containing genes is ~20% (Fig. 2e, Extended Data Fig. 2c, Supplementary Table 7). The presence of m^{1}A in a substantial fraction of mRNA transcripts suggests a potentially sizeable effect on mRNA metabolism.

m^{1}A associates with translation initiation sites and the first splice site

We found that m^{1}A peaks appear in all segments of transcripts—5′ untranslated region (UTR), coding sequence (CDS) and 3′ UTR—but are markedly under-represented in the latter (~fivefold depletion

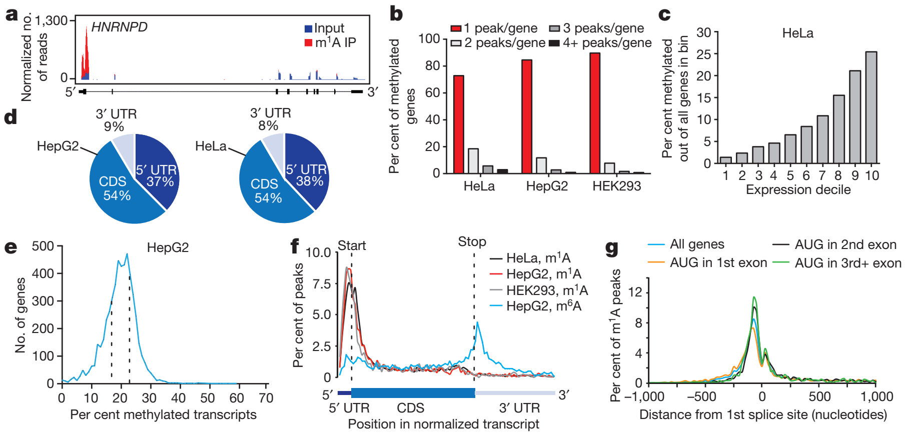

Figure 2 | m^{1}A is associated with translation initiation sites (TISs) in the human transcriptome. a, Representative plot of a methylated transcript. Normalized sequence coverage of immunoprecipitation (m^{1}A IP, red) and input (blue) are indicated above the gene architecture in UCSC format. Thin black boxes represent the 5′ and 3′ untranslated regions (UTRs), thick black boxes represent the coding sequences (CDS) and thin lines represent introns. **b**, The percentage of methylated genes that carry 1, 2, 3 or 4+ peaks per gene in the indicated human cell types. Most methylated genes carry only one m^{1}A peak. **c**, The percentage of methylated genes in HeLa cells increases with expression level. **d**, Pie charts presenting the fraction of m^{1}A peaks in each of three non-overlapping transcript segments (5′ UTR, CDS and 3′ UTR) in the indicated human cell types. **e**, Stoichiometry (fraction) of methylated transcripts in genes that carry one m^{1}A peak in HepG2 mRNA. Plotted is the number of genes sorted by percentage of methylated transcripts. Dashed lines define the stoichiometry interquartile range (17–23%). **f**, Metagene profiles of m^{1}A peak distribution along a normalized transcript composed of three rescaled non-overlapping segments illustrated below, in the indicated human cell types. m^{1}A peaks cluster around the AUG start codon. For comparison, the distribution of m^{6}A peaks in HepG2 is superimposed. **g**, Metagene profiles of m^{1}A peak distribution in a non-normalized window centred on the first splice site. Peaks are sorted by the exon containing the AUG codon in that gene.

relative to chance, $P < 1 \times 10^{-200}$, hypergeometric test, Fig. 2d). m^{1}A-seq of two additional cell lines in replicates, HepG2 and HEK293, produced similar distribution patterns (Fig. 2b, d, Extended Data Fig. 2d–g and Supplementary Tables 1, 4). We noted that while input sequence reads have a typical distribution along transcripts, m^{1}A immunoprecipitation reads pile up towards their 5′ ends (Extended Data Fig. 3a). To investigate this further, metagene profiles were generated in which gene segments were rescaled proportionally so that all segments of one kind appear to have the same length. This revealed that m^{1}A clusters sharply around the start codon to produce a remarkably similar profile in the three human cell lines (Fig. 2f). Over 50% of the peaks reside within a stretch of 300 nucleotides centred on the start codon (Extended Data Fig. 3b–g).

Ribosome profiling[19], and a recently modified version that captures initiating 80S ribosomes[20,21], have uncovered a surprising variety of alternative translation initiation sites (TISs). We examined our data sets from this perspective and found that methylated transcripts have, on average, more alternative TISs than non-methylated ones (1.98 versus 1.59 in HeLa; 2.37 versus 1.69 in HEK293), and that the number of m^{1}A sites per transcript positively correlates with the number of alternative TISs per transcript (Extended Data Fig. 4a–c). Furthermore, transcripts with upstream TISs are more likely to be methylated within the 5′ UTR, whereas transcripts with downstream TISs tend to be methylated within the CDS (Extended Data Fig. 4d, e). The distances of alternative TISs and respective m^{1}A peaks from the annotated start codon are well correlated, particularly those of upstream TISs and 5′ UTR m^{1}A peaks, suggesting that m^{1}A is associated with alternative TISs as well (Extended Data Fig. 4f–h). In summary, m^{1}A in human mRNA seems to be associated with a subset of TISs, both canonical and alternative, in all three cell lines examined.

To gain a deeper understanding of the underlying transcript attribute or processing event that potentially guides m^{1}A deposition to create the observed distribution, we binned methylated transcripts based on the exon that harbours the start codon and plotted the distribution of m^{1}A relative to the start codon. We observed an intriguing dissociation: when the start codon is in the 2nd or 3rd exons, m^{1}A tends to occur closer to the transcription start site (TSS) compared to when the start codon is in the 1st exon (Extended Data Fig. 3h). Whereas 5′ UTRs of transcripts with a start codon in downstream exons are on average longer (323 versus 189 nucleotides), their first splicing event tends to occur closer to the TSS (204 versus 359 nucleotides), mirroring m^{1}A behaviour. Therefore, we plotted the distribution of m^{1}A relative to the TSS in bins based on the length of the 1st exon and observed that m^{1}A moves away from the TSS as the length of the first exon increases (Extended Data Fig. 3i). These observations suggest that neither the TSS nor the start codon 'anchors' m^{1}A, but rather the first splice site does. We substantiated this by plotting m^{1}A relative to the nearest splice site (which is also the first splice site for 85% of m^{1}A peaks) and observed convergence of m^{1}A distribution in all start codon bins mostly upstream of the splice site, engendering the hypothesis that the first splicing reaction somehow guides m^{1}A deposition (Fig. 2g, Extended Data Fig. 3j). Analysis based on the smaller high-resolution m^{1}A trough data set recapitulated all the salient features of the methylome (Extended Data Fig. 3k–q, Supplementary Note 3 and Supplementary Table 6).

Conserved features of methylated transcripts

We next sought to identify sequence patterns that may define or associate with m^{1}A peak locations. GC content, a key determinant of RNA structure, is unusually high in m^{1}A peak areas that appear in all three transcript segments (Extended Data Fig. 5a). Several motif detection algorithms showed enrichment of GC-rich sequences with variable adenosine content, yet did not identify any specific motif *per se* (other than the 'AUG' itself which is expected to appear in peaks centred on the start codon) (Extended Data Fig. 5b). This suggests that a combination of sequence and structure features may specify methylation positions, perhaps similar to the case of m^{1}A deposition in tRNA[22,23]. We were

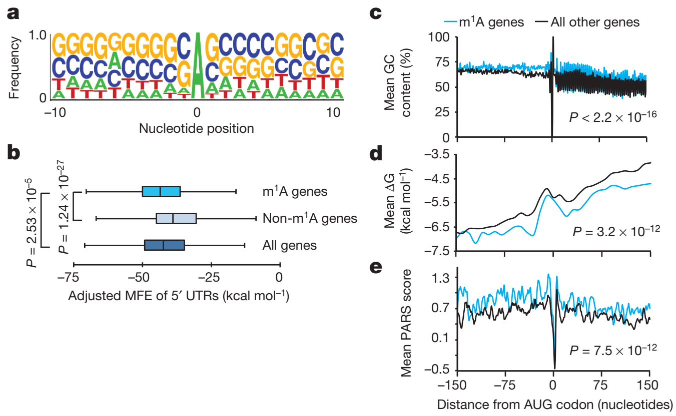

Figure 3 | m^{1}A occurs in GC-rich sequence contexts and in genes with structured 5′ UTRs. a, Sequence frequency logo for a set of 192 adenosines in peak areas that have a higher mismatch rate in immunoprecipitation relative to input (FC $\geq$ 6) in HepG2 demonstrates the GC-rich context of m^{1}A. **b**, Length-adjusted minimum free energy (aMFE) for 5′ UTRs of methylated, unmethylated and all genes. Box limits represent 25th percentile, median and 75th percentile, whiskers represent 2.5 and 97.5 percentiles. *P* values are indicated, *t*-test. Analysis was based on human common peaks (see Methods). **c**–**e**, A sliding window of mean GC content (**c**), ΔG (**d**) and PARS scores (**e**) in a $\pm$150-nucleotide window centred on the AUG start codon of methylated genes compared to all the rest, in HepG2 cells. *P* values are indicated; Kolmogorov–Smirnov test, *t*-test and Kolmogorov–Smirnov test, respectively.

able to identify and score single-nucleotide m^{1}A positions based on the change in mismatch rates between (1) untreated and alkaline-treated (m^{1}A-to-m^{6}A rearranged) immunoprecipitation sequence reads and between (2) input and immunoprecipitation (Supplementary Table 5). A sequence frequency logo of identified positions (Fig. 3a) and representative individual sequences (Extended Data Fig. 5c) demonstrate that m^{1}A sites are embedded in GC-rich environments. Using the m^{1}A trough data set we also identified a GA-rich motif that was present in 10–15% of the cases (Extended Data Fig. 3r).

Attributes of the 5′ UTR such as length, GC content, and associated minimum free energy (MFE), are known to affect the efficiency of translation initiation[24]. 5′ UTRs of methylated transcripts differ significantly from those of non-methylated ones in that their GC content is higher (median of 71% compared to 63.9%) (Extended Data Fig. 5d) and their length-adjusted MFE (aMFE) is lower (median of -43.5 kcal mol^{-1} compared to -38.4 kcal mol^{-1}) (Fig. 3b, Extended Data Fig. 5e). We employed a sliding window approach to further characterize the continuous structural landscape of the AUG window ($\pm$150 nucleotides) in terms of GC content, MFE and experimental parallel analysis of RNA structure (PARS) score (Fig. 3c–e, Extended Data Fig. 5f, g). Both the experimental and calculated parameters agree that m^{1}A decorates highly structured AUG windows.

Evolutionary conservation and dynamics

Evolutionary conservation typically indicates a common fundamental biological function. We show above that m^{1}A is present in murine mRNA at comparable levels to those in human (Fig. 1b). Therefore, m^{1}A-seq was applied to RNA of mouse liver, mouse embryonic fibroblasts (MEFs) and mouse embryonic stem cells (mESC) (Supplementary Tables 2, 4). A previously unreported single m^{1}A position in mouse 28S rRNA was identified in an orthologous location to the known m^{1}A position in human 28S rRNA (Extended Data Fig. 6a–c). The mouse m^{1}A methylome closely resembles that of human: approximately 15% of adequately expressed genes are methylated, the majority of which carry a single m^{1}A (Fig. 4a), and the percentage of methylated genes increases with expression level (Fig. 4b). m^{1}A in mouse mRNA is non-randomly distributed along transcripts with dense clustering around translation initiation sites, mirroring the profile in human

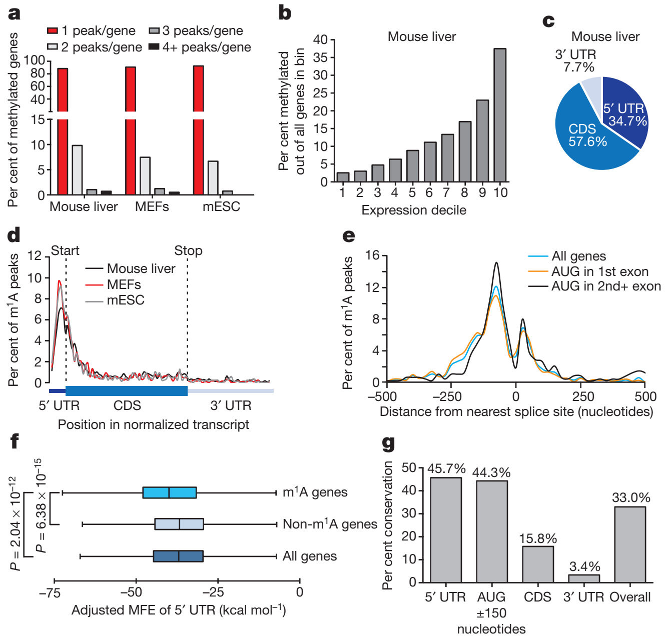

Figure 4 | m^{1}A methylome conservation between human and mouse. **a**, The percentage of methylated genes that carry 1, 2, 3 or 4+ peaks per gene in the indicated mouse cell types. Most genes carry only one m^{1}A peak. **b**, The percentage of methylated genes in mouse liver cells increases with expression level. **c**, Pie chart presenting the fraction of m^{1}A peaks in each of three non-overlapping transcript segments (5′ UTR, CDS and 3′ UTR) in mouse liver. **d**, Metagene profiles of m^{1}A peak distribution along a normalized transcript composed of three rescaled non-overlapping segments illustrated below, in the indicated mouse cell types. m^{1}A peaks cluster around the AUG start codon. **e**, Metagene profiles of mouse m^{1}A peak distribution in a non-normalized window centred on the nearest splice site. Peaks are sorted by the exon containing the AUG codon in that gene. **f**, Length-adjusted minimum free energy (aMFE) for 5′ UTRs of methylated, unmethylated and all genes in mouse liver. Box limits and whiskers are as indicated in Fig. 3b. *P* values are indicated, *t*-test. **g**, Human–mouse m^{1}A conservation expressed as per cent of orthologous positions with shared m^{1}A peaks according to their location in the transcript.

(Fig. 4c–d, Extended Data Fig. 6d–l), including the association with the nearest splice site (Fig. 4e, Extended Data Fig. 6m). Similarly, m^{1}A sites reside within a GC-rich context (Extended Data Fig. 7a, b), and the 5′ UTRs of methylated transcripts have a higher GC content and a lower aMFE than those of all other (unmethylated) transcripts (Fig. 4f and Extended Data Fig. 7c–f).

We systematically assessed the extent of m^{1}A peak conservation between human and mouse and found that it extends to the gene level: out of 1,338 identified mouse liver m^{1}A peaks that could be mapped to adequately expressed, orthologous positions in human HepG2 cells, 441 had an m^{1}A peak at the orthologous position, representing 33% overall conservation ($P < 1.3 \times 10^{-310}$, Mann–Whitney *U* test) (Fig. 4g, Extended Data Fig. 7g). The 5′ UTR and a 300-nucleotide window centred on the AUG codon exhibit the highest degree of conservation with 44–46% conserved peaks, compared to 3–16% in other gene segments (Fig. 4g).

We applied m^{1}A-seq to RNA of *Saccharomyces cerevisiae* and *Schizosaccharomyces pombe* to further examine this mark in simple eukaryotes, and found it to be present in their mRNA transcriptomes, albeit without the characteristic mammalian pattern (Extended Data Fig. 8a–g, Supplementary Tables 3, 4). Importantly, upon transfer to a nitrogen-source deficient medium the *S. pombe* methylome exhibited noticeable changes in the identity of methylated transcripts (some transcripts gained m^{1}A while others lost it), providing an example of how physiological conditions dynamically shape m^{1}A (Extended Data Fig. 8h, i). These results further demonstrate the conservation of m^{1}A as a mark in eukaryotic mRNA, although the distribution pattern and functions in lower eukaryotes could be different from mammals, as also observed for m^{6}A[25,26].

Next, using quantitative LC-MS/MS we surveyed a range of physiological perturbations that could alter the total m^{1}A level in mRNA of mammalian cells. We found that glucose or amino acid starvation reduced m^{1}A level by approximately threefold and twofold, respectively, as early as 4 h; that heat shock increased m^{1}A level by approximately 1.5-fold at 4 h; and that serum starvation resulted in only a modest change within the same time frame (Fig. 5a, Extended Data Fig. 9a, b). Of note, m^{6}A levels measured in parallel do not change, or change slightly in the opposite direction, suggesting that the response is m^{1}A-specific (Fig. 5a). m^{1}A-seq performed after 4 h of glucose starvation or heat shock uncovered a more complex picture: while the overall number of m^{1}A peaks decreased (by 17%) and increased (by 23%), respectively, mirroring the LC-MS/MS measurement, still some individual positions behaved in the opposite direction (Fig. 5b, c; Extended Data Fig. 9c, d).

The m^{1}A levels across various tissues obtained from a single mouse also showed significant variability, with kidney and brain possessing the highest m^{1}A level (about threefold higher than that measured in liver, for example) (Fig. 5d). A comparison between tissues from lean (wt/wt) and obese mice (ob/ob) revealed that brains of the former contain 75% more m^{1}A (Fig. 5d). In sum, m^{1}A in mRNA is a dynamic modification in response to certain stress conditions and potentially physiological signalling, and its level varies between different tissues.

SAM-dependent methyltransferases that install m^{1}A on tRNA and rRNA are known in eukaryotes[23,27]. These or related homologues could mediate mRNA m^{1}A methylation. FTO, the first RNA demethylase to be discovered, belongs to the AlkB family of proteins, and catalyses oxidative demethylation of m^{6}A in mRNA[28]. Other members of the AlkB family are known to perform oxidative demethylation of m^{1}A and m^{3}C lesions in DNA/RNA. In particular, ALKBH3 was shown to have a strong preference for single stranded DNA/RNA, and to demethylate m^{1}A in tRNA and mRNA *in vitro*[29,30]. In line with previous biochemical observations, overexpression of wild-type ALKBH3, but not of an inactive mutant, reduced m^{1}A levels in mRNA (Extended Data Fig. 9e). These results suggest that ALKBH3 and its homologues are likely candidates that could reverse m^{1}A in mRNA and contribute to its dynamic regulation.

m^{1}A correlates with elevated translation

Structure and sequence features of the 5′ UTR and both sides of the start codon affect the scanning process and thereby the efficiency of translation initiation and early elongation[31,32]. We show here that m^{1}A is a widespread and conserved post-transcriptional modification that is associated with TISs in thousands of mammalian transcripts characterized by structured 5′ UTRs. The precise localization of m^{1}A in an area of obvious regulatory importance, coupled with its ability to restructure RNA in other cases (such as tRNA[33]) and to affect RNA–protein interactions, points to possible involvement in translation initiation.

We used published ribosome profiling and proteomic data sets, obtained from the same cell lines and tissues used for m^{1}A profiling, to assess possible effects of m^{1}A on translation (see Methods). The translation efficiency[19] (TE) and ribosome release score[34] (RRS) of genes with a single m^{1}A peak in the start codon window compared to genes devoid of m^{1}A altogether are significantly higher (~1.2–1.4, on average) in both human and mouse cells (Extended Data Fig. 10). Furthermore, correlation of m^{1}A with protein levels normalized to mRNA abundance reveals a similar trend: in all cell types examined, methylated genes tend to have higher protein levels than non-methylated genes (Fig. 6a–f). The average fold-change in protein levels between methylated and non-methylated genes in all cell types—and across all gene expression bins—is ~1.7. Considering that the average fraction of methylated transcripts is ~20%, the isolated true effect of m^{1}A could be even higher. The contribution of m^{1}A remains significant even after accounting for multiple covariates that are known to affect translation (ANCOVA, Supplementary Table 8).

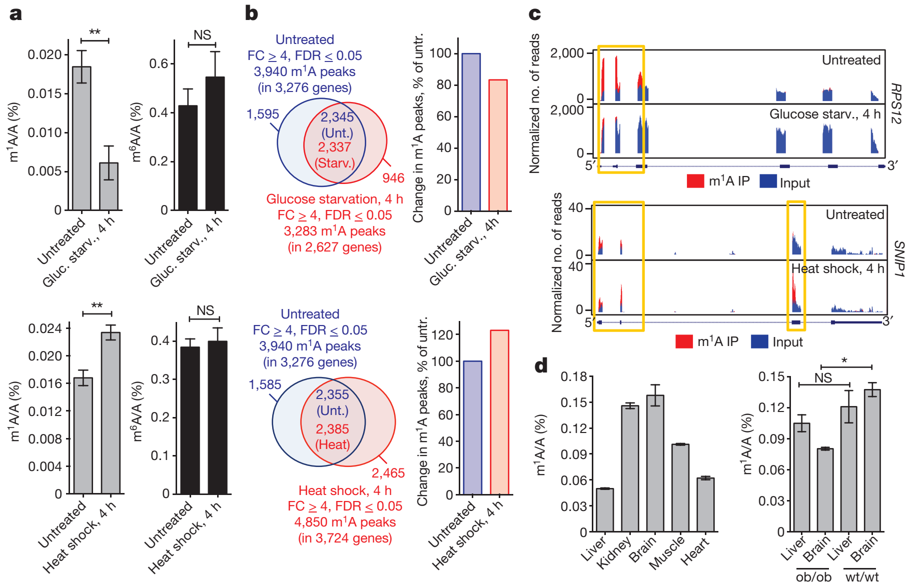

Figure 5 | m¹A in mRNA is a dynamic modification that responds to changing physiological and stress conditions, and varies between tissues. a, LC-MS/MS quantification of m¹A (left, grey) and m⁶A (right, black) in mRNA of untreated and glucose-starved (upper panels) or heat shock-treated (lower panels) HepG2 cells, presented as percentage of unmodified A. Mean values ± s.e.m. are shown, $n = 3$, $^{**}P \leq 0.01$, not significant (NS) $P > 0.05$, unpaired *t*-test. **b**, Venn diagrams of differential and shared m¹A peaks in untreated and glucose-starved (left upper panel) or heat shock-treated (left lower panel) HepG2 cells. The overall change in the number of identified m¹A peaks is presented as per cent of untreated (right upper and lower panels). **c**, Representative plots of differentially methylated transcripts in untreated and glucose starved (upper panel) or heat-shock-treated (lower panel) HepG2 cells. Plot format as in Fig. 2a. Yellow boxes frame differential peaks. **d**, LC-MS/MS quantification of m¹A in the indicated wt/wt and ob/ob mouse tissues, presented as percentage of unmodified A. Mean values ± s.e.m. are shown, $n = 3$, $^{*}P \leq 0.05$, NS, $P > 0.05$, one-way ANOVA.

Discussion

N^1-methylation on RNA adenosine occurs at the Watson–Crick interface and is expected to affect RNA base pairing[35]. In addition to an added methyl group, this modification also endows the modified adenosine with a positive charge under physiological conditions (Fig. 1a), which could markedly alter RNA structure and protein–RNA interactions. The impact of m¹A on the structure and function of tRNA is well documented, where a single m¹A can be essential for correct functional folding of a tRNA molecule[33]. A single charge difference has been shown to induce ~100–1,000-fold affinity difference of protein–DNA interactions[36]. We show here that m¹A is a modification occurring on thousands of mRNA transcripts in several human and mouse cell types, as well as on hundreds of transcripts in two yeast species. Applying m¹A-seq, a method relying on immunoprecipitation of m¹A-containing RNA fragments, we found a striking enrichment of m¹A around the start codon in human and mouse mRNA. Taking advantage of the Dimroth rearrangement, which converts m¹A (mutation prone in reverse transcription) to m⁶A (low mutation rate in reverse transcription[37]) with alkaline treatment, we confirmed the accumulation of m¹A around the start codon at high resolution.

Transcriptome-wide mapping of m¹A revealed unique features of its distribution that strongly indicate functional roles: (1) m¹A resides close to both canonical and alternative TISs found mostly upstream of the first splice site; (2) m¹A is present in highly structured regions around the start codon; (3) m¹A positively correlates with translation efficiency and protein level; (4) the distribution pattern and m¹A peaks are highly conserved in all mouse and human cell types examined; and (5) m¹A is dynamic in response to certain stress, and potentially physiological, signals, and its level varies across mouse tissues. Together, these attributes suggest a positive and dynamic role for m¹A in translation initiation in mammalian cells. The importance of RNA structure in translation initiation is well appreciated[38]. A positively charged m¹A may alter the secondary/tertiary structure of mRNA around TISs by blocking Watson–Crick base pairing or introducing charge–charge interactions. Alternatively, potential binding proteins may specifically recognize m¹A and facilitate translation initiation of methylated transcripts in a way analogous to the role of the m⁶A reader YTHDF1 in translation enhancement[39]. Either way, it is tempting to speculate that m¹A can modulate the strength of a particular translation initiation site, thereby affecting the balance between alternative and canonical initiation sites.

In contrast to m⁶A, which is enriched around the stop codon and in the 3′ UTR[1,2], m¹A preferentially associates with the start codon region in mammalian mRNA. These two marks could complement each other in controlling mRNA metabolism and translation. A single m⁶A modification usually induces ~10-fold change in either duplex stability or protein–RNA affinity, as would be expected by the presence of an extra methyl group[40,41]. The propensity of m⁶A to cluster at 3′ UTRs also enables a wider range of dynamic tuning than a single m⁶A site could

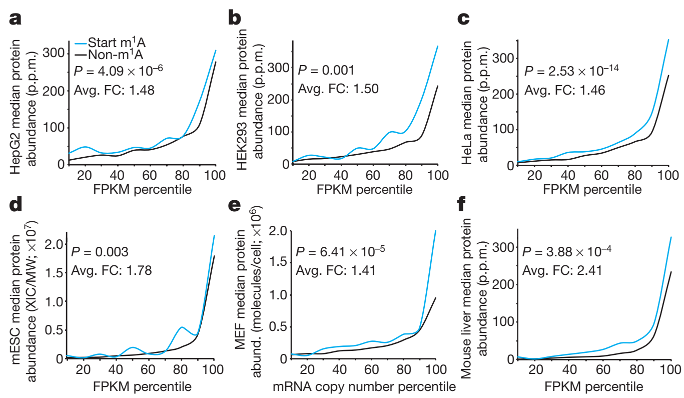

Figure 6 | m¹A around the start codon correlates with higher protein levels. a–f, Genes methylated in a 300-nucleotide window centred on the start codon have higher protein levels than all other genes with similar RNA expression levels in HepG2 (**a**), HEK293 (**b**), HeLa (**c**), mESC (**d**), MEFs (**e**) and mouse liver (**f**). ANOVA m¹A *P* values against $\log_2$ protein levels and the average fold-change (Avg. FC) of median protein levels across all gene expression bins (Start m¹A/Non-m¹A) are indicated. FPKM, fragments per kilobase of transcript per million mapped reads.

offer[1,2]. The unique chemical properties of m[1]A, with both a positive charge and a methyl group, potentially allow each individual modified site to have a stronger effect than m[6]A in terms of RNA structure or protein–RNA interaction.

The discovery of this new mRNA mark that positively correlates with translation adds an exciting new dimension to post-transcriptional gene expression regulation mediated through mRNA modifications. While our paper was in proof, we were alerted to a study by Chengqi Yi and colleagues reporting similar findings on the m[1]A methylome in a human cell line[42].

Online Content Methods, along with any additional Extended Data display items and Source Data, are available in the online version of the paper; references unique to these sections appear only in the online paper.

Received 2 July 2015; accepted 15 January 2016.
Published online 10 February 2016.

1. Dominissini, D. *et al.* Topology of the human and mouse m6A RNA methylomes revealed by m6A-seq. *Nature* **485,** 201–206 (2012).
2. Meyer, K. D. *et al.* Comprehensive analysis of mRNA methylation reveals enrichment in 3′ UTRs and near stop codons. *Cell* **149,** 1635–1646 (2012).
3. Carlile, T. M. *et al.* Pseudouridine profiling reveals regulated mRNA pseudouridylation in yeast and human cells. *Nature* **515,** 143–146 (2014).
4. Schwartz, S. *et al.* Transcriptome-wide mapping reveals widespread dynamic-regulated pseudouridylation of ncRNA and mRNA. *Cell* **159,** 148–162 (2014).
5. Li, X. *et al.* Chemical pulldown reveals dynamic pseudouridylation of the mammalian transcriptome. *Nature Chem. Biol.* **11,** 592–597 (2015).
6. Squires, J. E. *et al.* Widespread occurrence of 5-methylcytosine in human coding and non-coding RNA. *Nucleic Acids Res.* **40,** 5023–5033 (2012).
7. Khoddami, V. & Cairns, B. R. Identification of direct targets and modified bases of RNA cytosine methyltransferases. *Nature Biotechnol.* **31,** 458–464 (2013).
8. Fu, Y., Dominissini, D., Rechavi, G. & He, C. Gene expression regulation mediated through reversible m[6]A RNA methylation. *Nature Rev. Genet.* **15,** 293–306 (2014).
9. Li, S. & Mason, C. E. The pivotal regulatory landscape of RNA modifications. *Annu. Rev. Genomics Hum. Genet.* **15,** 127–150 (2014).
10. Machnicka, M. A. *et al.* MODOMICS: a database of RNA modification pathways—2013 update. *Nucleic Acids Res.* **41,** D262–D267 (2013).
11. Dunn, D. B. The occurrence of 1-methyladenine in ribonucleic acid. *Biochim. Biophys. Acta* **46,** 198–200 (1961).
12. Hall, R. H. Method for isolation of 2′-O-methylribonucleotides and N1-methyladenosine from ribonucleic acid. *Biochim. Biophys. Acta* **68,** 278–283 (1963).
13. El Yacoubi, B., Bailly, M. & de Crécy-Lagard, V. Biosynthesis and function of posttranscriptional modifications of transfer RNAs. *Annu. Rev. Genet.* **46,** 69–95 (2012).
14. Sharma, S., Watzinger, P., Kötter, P. & Entian, K. D. Identification of a novel methyltransferase, Bmt2, responsible for the *N*-1-methyl-adenosine base modification of 25S rRNA in *Saccharomyces cerevisiae*. *Nucleic Acids Res.* **41,** 5428–5443 (2013).
15. Anderson, J. T. & Droogmans, L. in *Fine-Tuning of RNA Functions by Modification and Editing* Vol. 12 (ed. H. Grosjean) 121–139 (2005).
16. Macon, J. B. & Wolfenden, R. 1-Methyladenosine. Dimroth rearrangement and reversible reduction. *Biochemistry* **7,** 3453–3458 (1968).
17. Desrosiers, R., Friderici, K. & Rottman, F. Identification of methylated nucleosides in messenger RNA from Novikoff hepatoma cells. *Proc. Natl Acad. Sci. USA* **71,** 3971–3975 (1974).
18. Zhang, Y. *et al.* Model-based analysis of ChIP-Seq (MACS). *Genome Biol.* **9,** R137 (2008).
19. Ingolia, N. T., Lareau, L. F. & Weissman, J. S. Ribosome profiling of mouse embryonic stem cells reveals the complexity and dynamics of mammalian proteomes. *Cell* **147,** 789–802 (2011).
20. Lee, S. *et al.* Global mapping of translation initiation sites in mammalian cells at single-nucleotide resolution. *Proc. Natl Acad. Sci. USA* **109,** E2424–E2432 (2012).
21. Gao, X. *et al.* Quantitative profiling of initiating ribosomes *in vivo*. *Nature Methods* **12,** 147–153 (2015).
22. Takuma, H. *et al.* Substrate tRNA recognition mechanism of eubacterial tRNA (m1A58) methyltransferase (TrmI). *J. Biol. Chem.* **290,** 5912–5925 (2015).
23. Ozanick, S., Krecic, A., Andersland, J. & Anderson, J. T. The bipartite structure of the tRNA m1A58 methyltransferase from *S. cerevisiae* is conserved in humans. *RNA* **11,** 1281–1290 (2005).
24. Kozak, M. Regulation of translation via mRNA structure in prokaryotes and eukaryotes. *Gene* **361,** 13–37 (2005).
25. Clancy, M. J., Shambaugh, M. E., Timpte, C. S. & Bokar, J. A. Induction of sporulation in *Saccharomyces cerevisiae* leads to the formation of N6-methyladenosine in mRNA: a potential mechanism for the activity of the IME4 gene. *Nucleic Acids Res.* **30,** 4509–4518 (2002).
26. Schwartz, S. *et al.* High-resolution mapping reveals a conserved, widespread, dynamic mRNA methylation program in yeast meiosis. *Cell* **155,** 1409–1421 (2013).
27. Peifer, C. *et al.* Yeast Rrp8p, a novel methyltransferase responsible for m[1]A 645 base modification of 25S rRNA. *Nucleic Acids Res.* **41,** 1151–1163 (2013).
28. Jia, G. *et al.* N6-methyladenosine in nuclear RNA is a major substrate of the obesity-associated FTO. *Nature Chem. Biol.* **7,** 885–887 (2011).
29. Aas, P. A. *et al.* Human and bacterial oxidative demethylases repair alkylation damage in both RNA and DNA. *Nature* **421,** 859–863 (2003).
30. Ougland, R. *et al.* AlkB restores the biological function of mRNA and tRNA inactivated by chemical methylation. *Mol. Cell* **16,** 107–116 (2004).
31. Zur, H. & Tuller, T. New universal rules of eukaryotic translation initiation fidelity. *PLOS Comput. Biol.* **9,** e1003136 (2013).
32. Parsyan, A. *et al.* mRNA helicases: the tacticians of translational control. *Nature Rev. Mol. Cell Biol.* **12,** 235–245 (2011).
33. Helm, M., Giegé, R. & Florentz, C. A Watson-Crick base-pair-disrupting methyl group (m1A9) is sufficient for cloverleaf folding of human mitochondrial tRNALys. *Biochemistry* **38,** 13338–13346 (1999).
34. Guttman, M., Russell, P., Ingolia, N. T., Weissman, J. S. & Lander, E. S. Ribosome profiling provides evidence that large noncoding RNAs do not encode proteins. *Cell* **154,** 240–251 (2013).
35. Lu, L., Yi, C., Jian, X., Zheng, G. & He, C. Structure determination of DNA methylation lesions N[1]-meA and N[3]-meC in duplex DNA using a cross-linked protein-DNA system. *Nucleic Acids Res.* **38,** 4415–4425 (2010).
36. He, C. *et al.* A methylation-dependent electrostatic switch controls DNA repair and transcriptional activation by *E. coli* Ada. *Mol. Cell* **20,** 117–129 (2005).
37. Harcourt, E. M., Ehrenschwender, T., Batista, P. J., Chang, H. Y. & Kool, E. T. Identification of a selective polymerase enables detection of N[6]-methyladenosine in RNA. *J. Am. Chem. Soc.* **135,** 19079–19082 (2013).
38. Sonenberg, N. & Hinnebusch, A. G. Regulation of translation initiation in eukaryotes: mechanisms and biological targets. *Cell* **136,** 731–745 (2009).
39. Wang, X. *et al.* N[6]-methyladenosine modulates messenger RNA translation efficiency. *Cell* **161,** 1388–1399 (2015).
40. Kierzek, E. & Kierzek, R. The thermodynamic stability of RNA duplexes and hairpins containing N[6]-alkyladenosines and 2-methylthio-N[6]-alkyladenosines. *Nucleic Acids Res.* **31,** 4472–4480 (2003).
41. Roost, C. *et al.* Structure and thermodynamics of N[6]-methyladenosine in RNA: a spring-loaded base modification. *J. Am. Chem. Soc.* **137,** 2107–2115 (2015).
42. Li, X. *et al.* Transcriptome-wide mapping reveals reversible and dynamic *N*[1]-methyladenosine methylome. *Nat. Chem. Biol.* http://dx.doi.org/10.1038/nchembio.2040 (2016).

Supplementary Information is available in the online version of the paper.

Acknowledgements The work was supported by the National Institutes of Health HG008688 and GM71440 grants to C.H., GM113194 grant to T.P. and C.H. and grants from the Flight Attendant Medical Research Institute (FAMRI), Israel Science Foundation (ISF grant no. 1667/12), Israeli Centers of Excellence (I-CORE) Program (ISF grants no. 41/11 and no. 1796/12), Ernest and Bonnie Beutler Research Program and Kahn Family Foundation to G.R. A part of this work was funded by the Chicago Biomedical Consortium with support from the Searle Funds at The Chicago Community Trust (to D.D. and C.H.). C.H. is an investigator of the Howard Hughes Medical Institute (HHMI). G.R. is a member of the Sagol Neuroscience Network and holds the Djerassi Chair for Oncology at the Sackler Faculty of Medicine, Tel-Aviv University, Israel. D.D. is supported by a Human Frontier Science Program (HFSP) long-term fellowship. S.N. is an HHMI Fellow of the Damon Runyon Cancer Research Foundation (DRG-2215-15), previously supported by a Yen post-doctoral fellowship in interdisciplinary research. Q.D. is supported by the National Institutes of Health grant HG006699. We wish to thank S. Farage-Barhom, K. Cesarkas and E. Glick-Saar for help with deep sequencing.

Author Contributions D.D. and C.H. conceived the idea. D.D. designed the experiments and analyses, and developed the method. D.D., S.N., and S.M.-M. performed experiments. A.D.S. performed PARS structural mapping. V.H., Q.D., and G.Z. helped with experiments. Q.D. synthesized deuterated standards. D.D., S.M.-M., S.N., M.S.B.-H., E.P., N.K., M.S.-D., O.S., E.E., W.C.C. and D.H. performed analyses and interpreted findings. D.D., S.M.-M., S.N. and C.H. wrote the manuscript with input from M.S.B.-H., E.P., L.C.D., W.C.C., G.Z., T.P., N.A. and G.R.

Author Information Data have been deposited in the NCBI Gene Expression Omnibus (GEO) and are accessible through GEO series accession number GSE70485. Reprints and permissions information is available at www.nature.com/reprints. The authors declare no competing financial interests. Readers are welcome to comment on the online version of the paper. Correspondence and requests for materials should be addressed to D.D. (dandominissini@gmail.com), G.R. (gidi.rechavi@sheba.health.gov.il) or C.H. (chuanhe@uchicago.edu).

METHODS

Cells and tissues. Human HeLa (cervical adenocarcinoma), HepG2 (hepatocellular carcinoma) and HEK293 (embryonic kidney) cell lines (ATCC) and primary mouse embryonic fibroblasts (MEFs) (C57BL/6, ATCC) were maintained in DMEM (Thermo Fisher Scientific) containing 25 mM glucose, 4 mM L-glutamine, supplemented with 100 U ml^{-1} penicillin, 100 $\mu g\ ml^{-1}$ streptomycin and 10% FBS. Mouse embryonic stem cells (mESCs) were maintained in FBS-free N2B27-based media, as previously described[43]. Cells were routinely checked for mycoplasma contamination. Mouse tissues were obtained from wild-type and ob/ob C57BL/6 mice. For metabolic labelling, methionine-devoid DMEM was supplemented with L-methionine-(methyl-d_3) (Sigma-Aldrich).

Cell treatments. HepG2 cells were maintained as described above and subjected to the following growth conditions: (1) heat shock (43 °C for 4 h); (2) glucose starvation (glucose-depleted medium for 4 h); (3) amino acid starvation (amino acid-depleted medium, with or without 200 μM *S*-adenosyl-methionine (SAM) supplementation, for 4 h); and (4) serum starvation (serum-depleted medium for 4 h), following which they were immediately harvested in Cell Lysis Solution (5 Prime).

Yeast strains and growth conditions. Wild-type (BY4741) *S. cerevisiae* cells were grown vegetatively in YPD medium to mid-log phase and harvested. Wild-type heterothallic (Sp1) *S. pombe* cells were grown vegetatively in YES medium to mid-log phase and harvested. For induction of sporulation/arrest, Sp1 cells were washed and transferred to Edinburgh Minimal Medium lacking NH_4Cl (EMM-N) for 4 h and harvested.

RNA purification. Total RNA from cells in culture and mouse tissues was purified using PerfectPure RNA Cultured Cell Kit (5 Prime) and PerfectPure RNA Tissue Kit (5 Prime), respectively, and DNase-treated. Enrichment of polyadenylated RNA (polyA^+ RNA) from total RNA was carried out using one round of GenElute mRNA Miniprep Kit (Sigma-Aldrich). Ribo-Zero Gold rRNA Removal Kit (Illumina) was used to deplete rRNA from polyA^+ RNA before LC-MS/MS.

Dot blot assays. RNA Oligonucleotides were synthesized in-house with either m^1A, m^6A or A at a single internal position (5′-AC(m^1A/m^6A/A)UG-3′), spotted onto a nylon membrane (GE Healthcare) in decreasing amounts (1,000, 200, 40 and 8 pmol) and UV-crosslinked. Membranes were blocked with 5% non-fat dry milk in 1 × PBST (blocking buffer) for 1 h at 25 °C, and incubated overnight with either mouse anti-m^1A antibody (1 $\mu g\ ml^{-1}$, MBL) or rabbit anti-m^6A antibody (1 $\mu g\ ml^{-1}$, Synaptic Systems) in 1 × PBST at 4 °C. Following extensive washing with 1 × PBST, membranes were incubated with either HRP-conjugated goat anti-mouse IgG or anti-rabbit IgG antibody (1:2,500, Thermo Fisher Scientific) in blocking buffer for 1 h at 25 °C. Membranes were washed in 1 × PBST, developed with ECL substrate (Thermo Fisher Scientific) and imaged with FluorChem imager (Protein Simple) or X-ray film. Competitive dot blots were performed on separate membranes spotted with 75 pmol of the m^1A-containing oligonucleotide by co-incubation of anti-m^1A antibody with increasing concentrations of either m^1A or m^6A competitor mononucleoside (0, 1, 2 and 4 μM).

m^1A detection and quantitation. Purified RNA (see 'RNA purification' section above) was subjected to liquid chromatography-tandem mass spectrometry (LC-MS/MS) for detection and accurate quantitation of m^1A, essentially as previously described[44]. 200–400 ng of purified RNA was digested by P1 nuclease (Wako, 2 U) in 40 μl of buffer containing 25 mM NaCl and 2.5 mM $ZnCl_2$ for 2 h at 37 °C. Subsequently, 5 units (1 μl) of Antarctic Phosphatase (New England Biolabs) and 1 × Antarctic Phosphatase reaction buffer were added and the sample was incubated for another 2 h at 37 °C. The sample was then filtered (0.22 μm, Millipore) and injected into a C18 reverse phase column coupled on-line to Agilent 6410 QQQ triple-quadrupole LC mass spectrometer in positive electrospray ionization mode. Quantitation was performed based on nucleoside-to-base ion transitions (268-to-136 for A; 282-to-150 for m^6A and m^1A (retention times of 2.5 and 0.9 min, respectively); 285-to-153 for d_3-m^1A and d_3-m^6A; 245-to-179 for Ψ; 245-to-113 for U) using standard curves of pure nucleosides and stable isotope-labelled internal standards (d_3-m^1A and d_3-m^6A), as previously described[45–47].

Synthesis of stable isotope-labelled internal standards. d_3-m^1A was synthesized following a previously described procedure for the synthesis of m^1A[48], replacing CH_3I with CD_3I. d_3-m^6A was synthesized following a previously described procedure for the synthesis of m^6A[49,50], replacing CH_3NH_2 with CD_3NH_2.

m^1A-seq. Mapping of m^1A in total or mRNA was performed using m^1A-seq, which is based on the previously described m^6A-seq protocol[51] with the following modifications: RNA fragmentation was performed using RNA Fragmentation Reagents (Thermo Fisher Scientific) for 15 min at 70 °C to minimize m^1A-to-m^6A rearrangement followed by column purification (RNA Clean & Concentrator, Zymo). Anti-m^1A antibody (MBL) was pre-coupled to Protein G Dynabeads (Thermo Fisher Scientific) and used to immunoprecipitate methylated RNA fragments for 3 h at 4 °C. Fragment elution was carried out by either digestion with Proteinase K (Sigma-Aldrich; 5 units in 5 mM Tris pH 7.5, 1 mM EDTA and 0.25% SDS for 1.5 h at 37 °C) followed by TRIzol (Thermo Fisher Scientific) extraction of the supernatant and ethanol precipitation, or by competitive elution using m^1A mononucleoside (Santa Cruz Biotechnology), as in m^6A-seq. Induced m^1A-to-m^6A rearrangement was achieved by incubating the input and immunoprecipitation fragments in an alkaline buffer (50 mM Na_2CO_3, 2 mM EDTA, pH 10.4) for 1 h at 50 °C or 60 °C followed by column purification (RNA Clean & Concentrator, Zymo) (Extended Data Fig. 1m). Immunoprecipitated RNA fragments and comparable amounts of input were subjected to first-strand cDNA synthesis using the NEBNext Ultra RNA Library Prep Kit for Illumina (New England Biolabs). Sequencing was carried out on Illumina HiSeq2500 according to the manufacturer's instructions, using 10 pM template per sample for cluster generation, TruSeq SR Cluster kit v3 (Illumina), TruSeq SBS Kit v3-HS (Illumina) and TruSeq Multiplex Sequencing primer kit (Illumina). Summary of read numbers for each replicate can be found in Supplementary Table 4.

Validation of m^1A-seq. Reads were aligned to the 28S ribosomal RNA sequences of human (RefSeq NR_003287.2), mouse (RefSeq NR_003279/NCBI X00525) and *S. cerevisiae* (SGD RDN25-2, ID: S000006485.) using Bowtie2[52] with local alignment option (--local). Enrichment was calculated as the coverage ratio of immunoprecipitation to input. Mismatch rate was assessed using mpileup tool of the SAMtools software package (version 0.1.18)[53] for calling variants over the entire 28S transcript. The frequency of non-adenosine bases at each adenosine position and the coverage of each base in the transcript were reported.

RNA expression level. Reads per kilobase of transcript per million mapped reads (RPKM) expression levels of RefSeq genes were calculated using HTseq-count[54] and R package edgeR[55]. Fragments per kilobase of transcript per million mapped reads (FPKM) values were calculated by the CUFFLINKS tool (version 2.2.1)[56]. Only genes whose expression level was above the first quartile were considered adequately expressed and used for downstream analyses. Adequately expressed genes (RPKM) were divided into 10 expression bins for correlation with methylation and the fraction of methylated genes in each bin was calculated.

Peak calling. Adaptors and low quality bases were trimmed from raw sequencing reads using cutadapt[57]. Reads were aligned to the relevant genome (human-hg19, mouse-mm10, *S. pombe*- ASM294v2.29, and *S. cerevisiae*- S288C with UTR data downloaded from http://genie.weizmann.ac.il/pubs/PARS10/pars10_catalogs.html) using Tophat2 (version 2.0.12)[58]. Peaks enriched in immunoprecipitation over input experiments were identified using MACS2 (version 2.1.0.20140616)[18]. MACS2-identified peaks were intersected with a database of exons of the relevant genome (RefSeq annotation). Peaks were allocated to the feature containing the segment with which they share the largest overlap. Peaks falling in intergenic sequences or having an overlap shorter than 50 nucleotides were excluded from further analyses. For each cell type only peaks identified ($FC \geq 2$ or $FC \geq 4$, as indicated, $FDR \leq 0.05$) in replicates were considered. Common human peaks were defined as peaks independently identified in both HeLa and HepG2 RNA. Negative peaks were identified by switching the immunoprecipitation and input samples.

Coverage analysis. The coverage of unique reads at each nucleotide position at the transcriptomic level, in immunoprecipitation and input reads, was calculated and reported. Only transcripts in which at least one nucleotide exceeded a minimum depth of 10 reads in immunoprecipitation were used in further analysis for reduction of background noise. For whole-transcript coverage plots, each transcript was divided into 100 bins of equal length, and the median coverage for each bin across all transcripts was calculated.

m^1A stoichiometry. HepG2 mRNA was subjected to immunoprecipitation with anti-m^1A antibody in 2 biological replicates. Input and immunodepleted (unbound sup) RNA samples (75 ng each) were hybridized to PrimeView human gene expression microarrays (Affymetrix) and expression levels were determined. Genes expressed below the first quartile (as determined by mRNA-seq, see above) were set as the minimal intensity limit (blank), and only genes with intensities above this threshold were considered. To correct for technical loss of RNA during the different steps of the procedure, the average ratio of sup/input intensity was calculated for never-methylated genes (considering only genes that were unmethylated in all m^1A-seq experiments) and used for ratio correction of methylated genes carrying one m^1A peak. Fractional methylation level per gene was calculated as 1 − (corrected sup/input ratio).

Identification of m^1A-induced mismatches in m^1A peaks. Identification of sequence variants in m^1A peaks due to misincorporation at the m^1A position during reverse transcription was carried out by determining the base composition at each position within peak regions using bam-readcount (https://github.com/genome/bam-readcount). Identified adenosine positions (according to the encoding DNA strand) were then filtered to exclude known genomic polymorphism sites (dbSNP version 141) and identified A-to-I editing sites (Radar database). Variants were considered if the mismatch rate was greater than 0.1 and the overall coverage

was greater than 20 reads. For HepG2 samples the fold enrichment of mismatch rate in untreated over rearranged sequence reads was calculated.

Trough identification. To identify points of lower coverage inside peak areas, we converted the bam files of the immunoprecipitation libraries to BigWig files and subjected them to PeakSplitter[59] with options of –valley 0.65 and –cutoff 30. The trough was identified as the minimal point $\pm$10 nucleotides, between the summits of identified sub-peaks. Only troughs reoccurring in 3 biological repeats were considered.

Bidirectional conversion of genomic and transcriptomic coordinates. Genomic coordinates of all 5′ UTRs, CDS and 3′ UTRs of RefSeq transcripts were downloaded from the University of California, Santa Cruz genome browser (UCSC) table browser in BED format (hg19 and mm10 for human and mouse, respectively). Transcripts with IDs corresponding to more than one genomic location were discarded, as were transcripts of non-coding genes. Custom, in-house, awk and perl scripts were then used to convert transcriptomic coordinates to genomic coordinates and vice versa.

Definition of peak middle point. MACS2-generated genomic m^1A peak coordinates were converted to transcriptomic coordinates. Neighbouring peaks (at a distance of up to 10 nucleotides) on the same transcript were merged using mergeBed from the BEDTools package[60]. This allowed the unification of peaks overlapping more than one exon that were divided by MACS2 due to the presence of introns in genomic coordinates. The middle of the resulting transcriptomic peak was defined as peak middle and referred to as m^1A peak position in further analyses.

Metagene profiling. The relative position of each peak's middle point was located in the corresponding transcript segment (5′ UTR, CDS or 3′ UTR). Each segment was assigned a value corresponding to its average length fraction out of the overall transcript length. The corresponding relative peak position was then deduced within each segment and plotted along a normalized metagene profile with respect to the TSS, AUG start codon and stop codon positions. The distribution of m^1A peaks with respect to the canonical AUG start codon, TSS, first and nearest splice sites, and stop codon was also drawn in actual nucleotide distances.

Sliding window analysis of AUG start codon window. Structural features of a 300-nucleotide window centred on the AUG start codon were compared between methylated and non-methylated RefSeq genes. GC content was calculated as the average percent in a sliding window of 3 nucleotides. Local free energy (ΔG) was calculated in a 30-nucleotide consecutive jumping window (in steps of 10 nucleotides) using the RNAfold tool in the ViennaRNA package[61] with default parameter settings.

Minimum free energy (MFE) calculation. The 5′ UTR sequence of the predominant isoform of each gene (the highest expressed isoform in the input sample) was used to calculate GC content, MFE, length-adjusted MFE (aMFE) and MFE density (MFEden) using the ViennaRNA package[61] and as previously described[62].

PARS-seq and PARS scores calculations. Parallel analysis of RNA structure (PARS) was performed as previously described[63] on HepG2 polyA$^+$ RNA. Reads were mapped to the human transcriptome (UCSC known canonical genes) using Bowtie2[52] with local alignment option (--local). Only uniquely aligned reads were used for analysis. Read start positions were counted for each base in the transcriptome, as the read start is +1 to the nuclease cleavage site and therefore informative regarding local RNA 2D structure[64]. Only reads with more than 5 consecutive bases matching the transcript at the start of the read were counted. Read counts were normalized to the respective library size. PARS-scores were then calculated based on the following equation:

$$\text{PARS-score}(i,j) = \log_2(V1'_{ij} \,/\, S1'_{ij})$$

$V1'_{ij}$ and $S1'_{ij}$ are the normalized read-start counts at base (i) in transcript (j) for V1 or S1, respectively.

PARS scores at the region around the start-codon ($\pm$150 nucleotides from the AUG) were averaged and used for a metagene analysis.

Motif search. To search for a motif, 101-nucleotide sequences in the AUG start codon window, centred on m^1A peaks in HeLa and mouse liver, were used. Compatible background sequences were used to prevent skewing of the results due to over-representation of known motifs in the region of the start codon, such as Kozak sequences and the AUG. The findMotifs program from the HOMER package[65] was then run using the settings -rna -len 6,7,8,9,10 –noweight. The same peak areas were used with MEME[66] for *de novo* motif enrichment analysis, with the settings -dna -minw 6 -maxw 10 -evt 0.01 -maxsize 1,000,000. A similar analysis was performed on m^1A peaks falling in the CDS with background sequences randomly generated from non-methylated exons. 199 sequences of 20 nucleotides, surrounding the mutations identified above, were used to create a frequency plot of the nucleotides surrounding the mutation sites using WebLogo[67].

Comparison of m^6A and m^1A profiles. m^1A and m^6A peaks[1,42,68] were intersected using BEDTools[60]. Similarity between sets was also evaluated by comparing the metagene profiles of the two modifications.

TIS correlation. TISs data was downloaded from http://www.ncbi.nlm.nih.gov/sra?term=SRA160745 (ref. 21) and genomic locations were converted to transcriptomic locations (as described above). For each alternative TIS, the closest m^1A peak was identified and the distance of both from the canonical AUG start codon was calculated. Correlation of alternative TISs with the number of m^1A peaks per gene was carried out by dividing the genes containing alterative TISs to bins according to the number of peaks per gene.

Gene ontology (GO) enrichment. Methylated gene RefSeq IDs were uploaded to DAVID Bioinformatics Resources (http://david.abcc.ncifcrf.gov) and functional enrichment analysis was performed using all adequately expressed genes as background. Resulting enriched GO terms were restricted to fold enrichment $\geq$ 1.5, Bonferroni corrected $P \leq 0.005$.

Human–mouse conservation. m^1A mouse liver peaks were converted to the homologous coordinates in the human hg19 genome, using the LiftOver tool of the UCSC genome browser[69]. To assess the significance of these results we chose at random an equal number of 200 bp sized areas from within mouse genes that have a human orthologue. The areas were chosen from all gene segments in the same proportion as observed in the original data set. Randomly chosen areas were similarly converted and intersected with HepG2 m^1A peaks. To calculate the statistical significance the randomization was repeated 1,000 times and Mann–Whitney U test was used.

ALKBH3 overexpression. Plasmids encoding wild-type and mutant (D193A) FLAG-tagged human ALKBH3 were transfected into 293 Freestyle cells using polyethylenimine (PEI; Polysciences, Inc.) at a ratio of 3 μl PEI per 1 μg plasmid DNA. After 24 h, cells were pelleted and washed once with cold PBS before being lysed in Cell Lysis Solution (5 Prime). mRNA was purified and digested for LC-MS/MS analysis as described in the 'RNA purification' and 'm^1A detection and quantitation' sections above.

Translation efficiency (TE) and ribosome release score (RRS). Sequencing data was downloaded: for HEK293, mouse liver and MEFs - SRA160745[21], http://www.ncbi.nlm.nih.gov/sra?term=SRA160745; for mESCs - GSE30839[19], http://www.ncbi.nlm.nih.gov/geo/query/acc.cgi?acc=GSE30839. Reads were aligned and FPKM values were calculated (see above). For TE calculation, the Ribo-Seq FPKM of the most highly expressed transcript of each gene was divided by the mRNA-Seq FPKM of the same transcript. Only transcripts with FPKM and Ribo-Seq FPKM above first quartile were considered. TE data for mESCs was downloaded as-is from the original paper[19]. TE and RRS for HeLa were calculated using our published data[44]. RRS values were calculated using mRNA-Seq and Ribo-Seq reads as described previously[34,42].

Protein abundance. All protein abundance data analysed in this study was downloaded from the MOPED database (Multi-Omics Profiling Expression Data, https://www.proteinspire.org): HeLa, HepG2, HEK293 (Experiment ID: Geiger_MCP_2012)[70], and mouse liver (Experiment ID: Baylor_mouse_liver_profiling), or from Supplementary Data (mESCs[71] and MEFs[72], corrected as described[73]). For all cell types, excluding mESCs, we used the normalized abundances as provided. For mESCs, raw intensities were divided by each leading protein molecular weight. Protein abundance data was then $\log_2$ transformed and subjected to an analysis of variance (ANOVA) with mRNA expression (FPKM) percentile bins for start m^1A and non-m^1A genes. For MEFs, the published mRNA expression data was used along with the corresponding protein abundance. Genes with mRNA expression below the lowest expressed gene containing m^1A or with FPKM < 0.2 were discarded.

Analysis of covariance (ANCOVA). ANCOVA was calculated for genes methylated at the AUG start codon window (start m^1A) versus unmethylated genes (non-m^1A) as a fixed factor against $\log_2$ protein abundances, while cleaning the contribution of the following covariates: $\log_2$ mRNA expression, TIS Kozak score[74], MFE calculated by RNAfold and divided by 5′ UTR length, G-quadruplex motif in 5′ UTR[75,76], 5′ TOP motif in 5′ UTR from UTRdb (http://utrdb.ba.itb.cnr.it/), number of conserved miR sites (PCT score < 0) from TargetScan[77], and number of u/dTISs and u/dAUGs in human and mouse form QTI-seq[21]. The remaining factors, % GC Content in 5′ UTR, length of 5′ and 3′ UTRs, and number of exons in 5′ and 3′ UTRs were downloaded and calculated from the UCSC genome browser (hg19 and mm10). We considered the most expressed RefSeq genes in our data for unique transcript-associated parameters and gene symbols for general features. Variables were examined for linearity with protein output and for normal distribution. Log transformations were employed where appropriate. Tolerance was kept above 0.2 for all variables.

43. Geula, S. *et al.* m^6A mRNA methylation facilitates resolution of naïve pluripotency toward differentiation. *Science* **347,** 1002–1006 (2015).
44. Wang, X. *et al.* N^6-methyladenosine-dependent regulation of messenger RNA stability. *Nature* **505,** 117–120 (2014).

45. Hienzsch, A., Deiml, C., Reiter, V. & Carell, T. Total synthesis of the hypermodified RNA bases wybutosine and hydroxywybutosine and their quantification together with other modified RNA bases in plant materials. *Chemistry* **19,** 4244–4248 (2013).
46. Pearson, D. *et al.* LC-MS based quantification of 2′-ribosylated nucleosides Ar(p) and Gr(p) in tRNA. *Chem. Commun. (Camb.)* **47,** 5196–5198 (2011).
47. Hauenschild, R. *et al.* The reverse transcription signature of N-1-methyladenosine in RNA-Seq is sequence dependent. *Nucleic Acids Res.* **43,** 9950–9964 10.1093/nar/gkv895 (2015).
48. Jones, J. W. & Robins, R. K. Purine Nucleosides. III. Methylation studies of certain naturally occurring purine nucleosides. *J. Am. Chem. Soc.* **85,** 193–201 (1963).
49. Dai, Q. *et al.* Identification of recognition residues for ligation-based detection and quantitation of pseudouridine and N^6-methyladenosine. *Nucleic Acids Res.* **35,** 6322–6329 (2007).
50. Hobartner, C. *et al.* The synthesis of 2′-*O*-[(triisopropylsilyl)oxy] methyl (*TOM*) phosphoramidites of methylated ribonucleosides (m^1G, m^2G, $m^2{}_2G$, m^1I, m^3U, m^4C, m^6A, $m^2{}_6A$) for use in automated RNA solid-phase synthesis. *Monatsh. Chem.* **134,** 851–873 (2003).
51. Dominissini, D., Moshitch-Moshkovitz, S., Salmon-Divon, M., Amariglio, N. & Rechavi, G. Transcriptome-wide mapping of N^6-methyladenosine by m^6A-seq based on immunocapturing and massively parallel sequencing. *Nature Protocols* **8,** 176–189 (2013).
52. Langmead, B. & Salzberg, S. L. Fast gapped-read alignment with Bowtie 2. *Nature Methods* **9,** 357–359 (2012).
53. Li, H. *et al.* The Sequence Alignment/Map format and SAMtools. *Bioinformatics* **25,** 2078–2079 (2009).
54. Anders, S., Pyl, P. T. & Huber, W. HTSeq—a Python framework to work with high-throughput sequencing data. *Bioinformatics* **31,** 166–169 (2015).
55. Robinson, M. D., McCarthy, D. J. & Smyth, G. K. edgeR: a Bioconductor package for differential expression analysis of digital gene expression data. *Bioinformatics* **26,** 139–140 (2010).
56. Trapnell, C. *et al.* Transcript assembly and quantification by RNA-Seq reveals unannotated transcripts and isoform switching during cell differentiation. *Nature Biotechnol.* **28,** 511–515 (2010).
57. Martin, M. Cutadapt removes adapter sequences from high-throughput sequencing reads. *EMBnet.journal* **17,** 10–12 (2011).
58. Kim, D. *et al.* TopHat2: accurate alignment of transcriptomes in the presence of insertions, deletions and gene fusions. *Genome Biol.* **14,** R36 (2013).
59. Salmon-Divon, M., Dvinge, H., Tammoja, K. & Bertone, P. PeakAnalyzer: genome-wide annotation of chromatin binding and modification loci. *BMC Bioinformatics* **11,** 415 (2010).
60. Quinlan, A. R. & Hall, I. M. BEDTools: a flexible suite of utilities for comparing genomic features. *Bioinformatics* **26,** 841–842 (2010).
61. Lorenz, R. *et al.* ViennaRNA Package 2.0. *Algorithms Mol. Biol.* **6,** 26 (2011).
62. Trotta, E. On the normalization of the minimum free energy of RNAs by sequence length. *PLoS One* **9,** e113380 (2014).
63. Wan, Y., Qu, K., Ouyang, Z. & Chang, H. Y. Genome-wide mapping of RNA structure using nuclease digestion and high-throughput sequencing. *Nature Protocols* **8,** 849–869 (2013).
64. Kertesz, M. *et al.* Genome-wide measurement of RNA secondary structure in yeast. *Nature* **467,** 103–107 (2010).
65. Heinz, S. *et al.* Simple combinations of lineage-determining transcription factors prime cis-regulatory elements required for macrophage and B cell identities. *Mol. Cell* **38,** 576–589 (2010).
66. Bailey, T. L. & Elkan, C. Fitting a mixture model by expectation maximization to discover motifs in biopolymers. *Proc. Int. Conf. Intell. Syst. Mol. Biol.* **2,** 28–36 (1994).
67. Crooks, G. E., Hon, G., Chandonia, J. M. & Brenner, S. E. WebLogo: a sequence logo generator. *Genome Res.* **14,** 1188–1190 (2004).
68. Linder, B. *et al.* Single-nucleotide-resolution mapping of m^6A and m^6Am throughout the transcriptome. *Nature Methods* **12,** 767–772 (2015).
69. Hinrichs, A. S. *et al.* The UCSC Genome Browser Database: update 2006. *Nucleic Acids Res.* **34,** D590–D598 (2006).
70. Geiger, T., Wehner, A., Schaab, C., Cox, J. & Mann, M. Comparative proteomic analysis of eleven common cell lines reveals ubiquitous but varying expression of most proteins. *Mol. Cell Proteomics* http://dx.doi.org/10.1074/mcp.M111.014050 (2012).
71. Graumann, J. *et al.* Stable isotope labeling by amino acids in cell culture (SILAC) and proteome quantitation of mouse embryonic stem cells to a depth of 5,111 proteins. *Mol. Cell. Proteomics* **7,** 672–683 (2008).
72. Schwanhäusser, B. *et al.* Global quantification of mammalian gene expression control. *Nature* **473,** 337–342 (2011).
73. Li, J. J., Bickel, P. J. & Biggin, M. D. System wide analyses have underestimated protein abundances and the importance of transcription in mammals. *PeerJ* **2,** e270 (2014).
74. Noderer, W. L. *et al.* Quantitative analysis of mammalian translation initiation sites by FACS-seq. *Mol. Syst. Biol.* **10,** 748 (2014).
75. Huppert, J. L., Bugaut, A., Kumari, S. & Balasubramanian, S. G-quadruplexes: the beginning and end of UTRs. *Nucleic Acids Res.* **36,** 6260–6268 (2008).
76. Beaudoin, J. D. & Perreault, J. P. 5′-UTR G-quadruplex structures acting as translational repressors. *Nucleic Acids Res.* **38,** 7022–7036 (2010).
77. Lewis, B. P., Burge, C. B. & Bartel, D. P. Conserved seed pairing, often flanked by adenosines, indicates that thousands of human genes are microRNA targets. *Cell* **120,** 15–20 (2005).

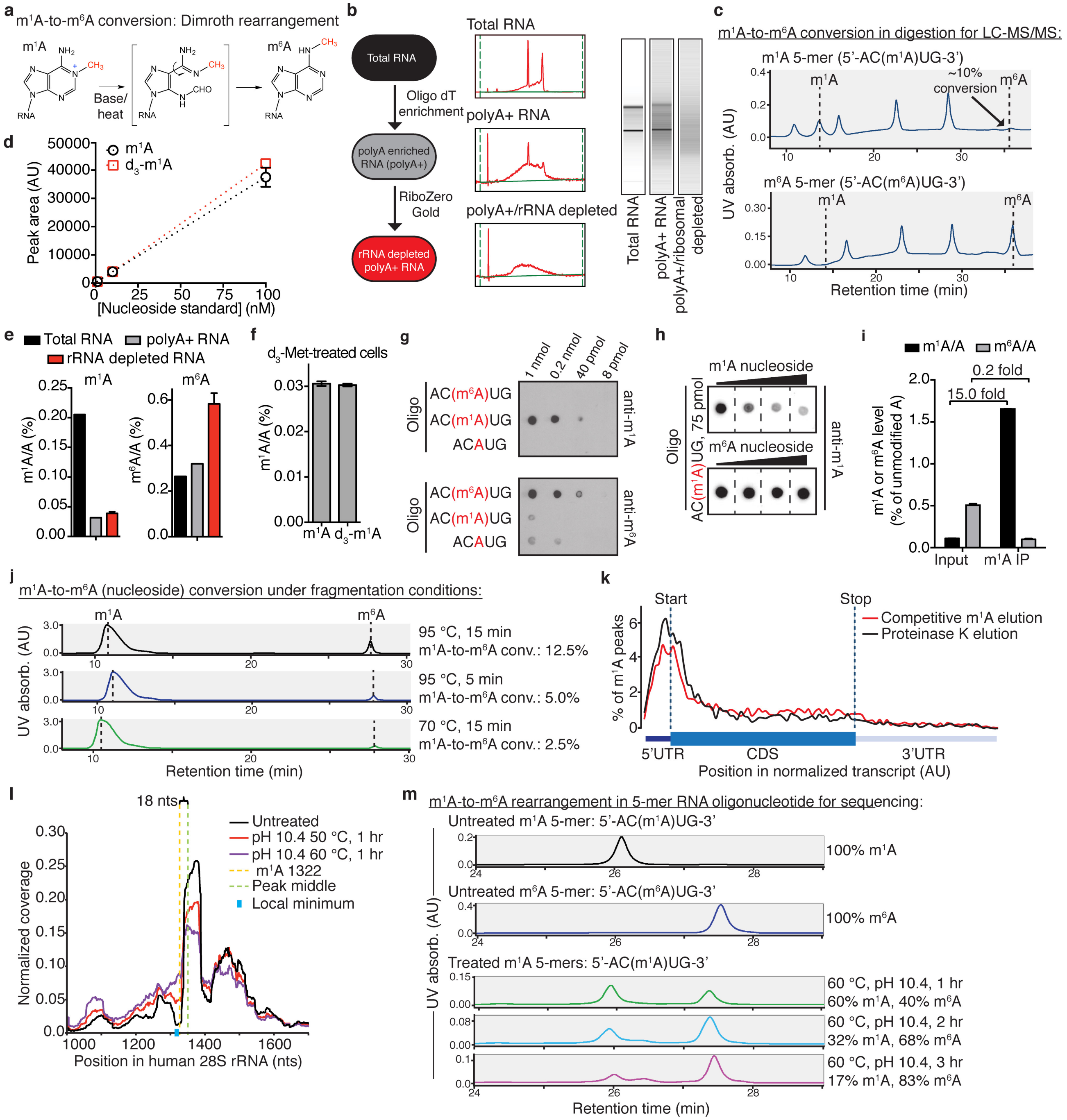

Extended Data Figure 1 | See next page for figure caption.

Extended Data Figure 1 | Experimental conditions for detection, quantitation and sequencing of m^{1}A in mRNA. a, Schematic illustration of m^{1}A-to-m^{6}A rearrangement (Dimroth rearrangement) under alkaline conditions at elevated temperatures. **b**, mRNA purification scheme before LC-MS/MS m^{1}A quantitation (left). Corresponding RNA electrophoresis profiles obtained by Agilent 2100 Bioanalyzer (middle and right). **c**, Monitoring m^{1}A-to-m^{6}A rearrangement levels during sample preparation for LC-MS/MS. Synthetic 5-nucleotide long RNA oligonucleotides containing m^{1}A (upper panel) or m^{6}A (lower panel) were digested to mononucleotides, dephosphorylated (see methods) and analysed by HPLC-UV. Only minimal (<10%) m^{1}A-to-m^{6}A rearrangement was observed (arrow). **d**, Standard curves for m^{1}A and deuterium-labelled m^{1}A (d$_3$-m^{1}A) demonstrate very similar detection sensitivity in LC-MS/MS. Mean values ± s.e.m. are shown, $n = 3$. **e**, The change in m^{1}A/A and m^{6}A/A molar ratios (%) during the purification scheme outlined in **b**. Mean values ± s.e.m. are shown, $n = 3$. **f**, LC-MS/MS of mRNA isolated from HepG2 cells labelled with deuterated methionine (d$_3$-Met) for 24 h detects d$_3$-m^{1}A, suggesting *S*-adenosyl-methionine (SAM) is the methyl donor. Mean values ± s.e.m. are shown, $n = 3$. **g**, Dot blots demonstrating high anti-m^{1}A antibody specificity. Increasing amounts (indicated above the top blot) of synthetic RNA oligonucleotides containing m^{1}A, m^{6}A or unmodified A residues were spotted onto a membrane and probed with either anti-m^{1}A or anti-m^{6}A antibodies. Anti-m^{1}A antibody detects m^{1}A and does not exhibit cross-reactivity with m^{6}A or A (upper blot); anti-m^{6}A antibody demonstrates low, yet detectable, cross-reactivity with both m^{1}A and A (lower blot). For blot source data, see Supplementary Fig. 1. **h**, Competitive dot blots were performed on separate membranes spotted with 75 pmol of synthetic m^{1}A-containing RNA oligonucleotide. Whereas increasing concentrations of free m^{1}A mononucleoside progressively attenuate anti-m^{1}A binding, increasing concentrations of free m^{6}A mononucleoside do not. For blot source data, see Supplementary Fig. 1. **i**, Quantitative LC-MS/MS demonstrates m^{1}A enrichment—and m^{6}A depletion—following immunoprecipitation (IP) with anti-m^{1}A antibody compared to total RNA input. Mean values ± s.e.m. are shown, $n = 3$. **j**, Monitoring m^{1}A-to-m^{6}A rearrangement levels under different RNA fragmentation conditions for use in m^{1}A-seq. Pure m^{1}A mononucleoside in 1× fragmentation buffer (see Methods) was subjected to the conditions specified to the right of the chromatograms and directly analysed by injection to HPLC-UV for rearrangement to m^{6}A. **k**, Comparison of competitive m^{1}A elution and Proteinase K elution of immunoprecipitated m^{1}A-containing RNA fragments from anti-m^{1}A-coupled magnetic beads shows that the two elution modes are equivalent. **l**, Identification of the known m^{1}A site in position 1322 of human 28S rRNA validates the accuracy of m^{1}A-seq and the use of peak middle points as a close approximation for m^{1}A sites. Partial m^{1}A-to-m^{6}A rearrangement increases the coverage around this site. **m**, Conditions for induced m^{1}A-to-m^{6}A rearrangement of RNA oligonucleotides that maintain RNA integrity for use in m^{1}A-seq. A synthetic 5-nucleotide long RNA oligonucleotide of the sequence 5′-AC(m^{1}A)UG-3′ was subjected to various base/heating conditions (indicated to the right of the chromatograms) and directly analysed by injection to HPLC-UV for rearrangement to 5′-AC(m^{6}A)UG-3′. Incubation at pH 10.4, 60 °C for 1 h results in rearrangement to m^{6}A in 40% of oligonucleotides; longer incubation times result in increased rates of rearrangement. Chromatograms of untreated RNA oligonucleotides appear above and mark the expected retention times.

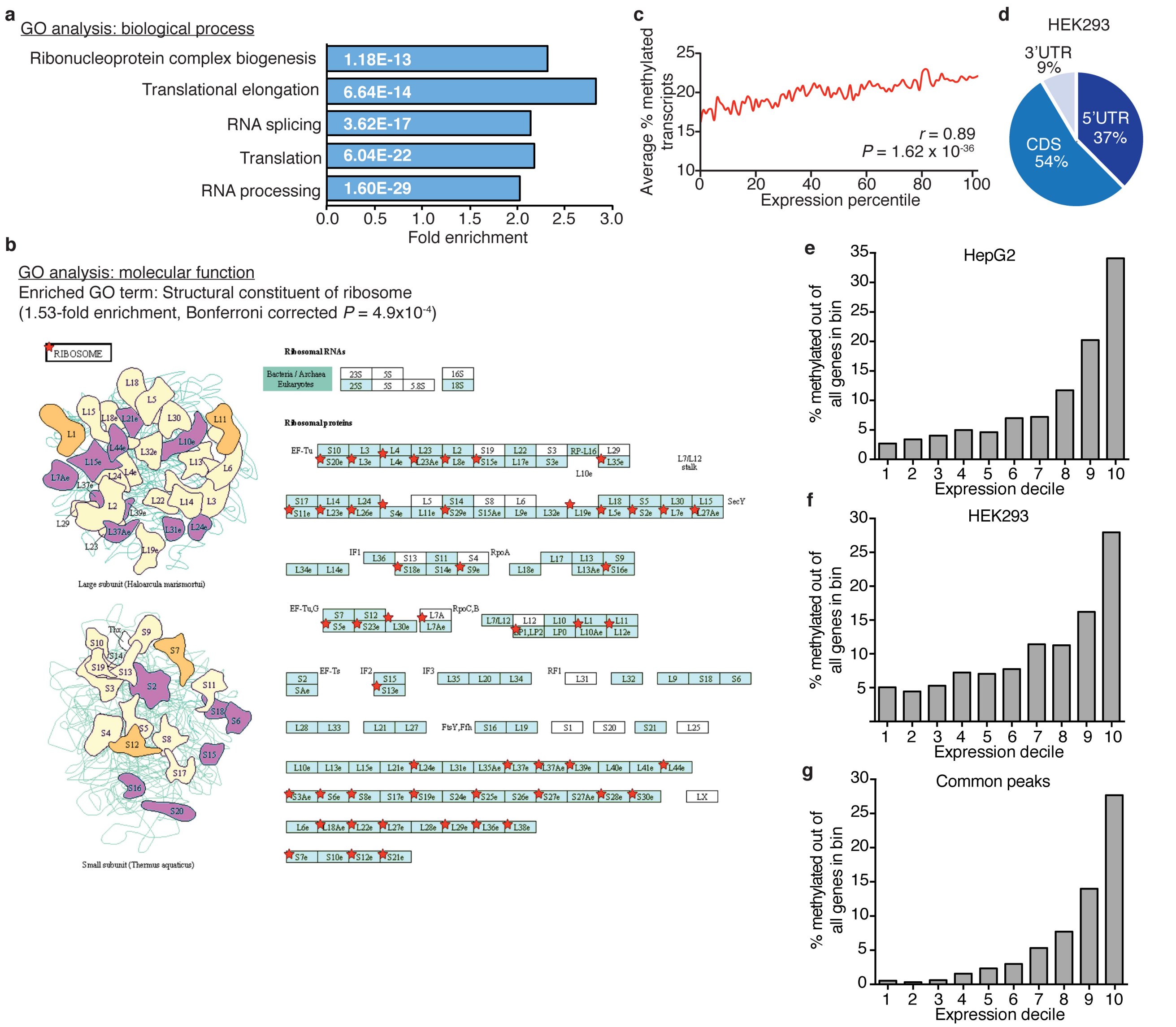

Extended Data Figure 2 | Characterization of human m¹A-methylated genes. **a**, Gene ontology (GO) analysis of methylated HeLa genes relative to all adequately expressed genes (above the 1st quartile) reveals enrichment of biological processes related to translation and RNA metabolism. Fold-enrichment and *P* values are indicated for each category. **b**, GO analysis of molecular functions reveals enrichment of structural constituents of the ribosome. Scheme based on an illustration obtained from DAVID bioinformatics website of the KEGG human ribosome pathway. Red stars indicate methylated genes in the pathway. Colouring of the boxes and ribosome constituents is according to KEGG pathway maps showing interacting proteins and hyperlinks to gene entries that can be reached through http://www.genome.jp/kegg-bin/show_pathway? hsa03010. **c**, The average fraction of methylated transcripts (stoichiometry) increases with gene expression level. *r* and *P* values are indicated, Pearson correlation. **d**, Pie chart presenting the fraction of m¹A peaks in each of three non-overlapping transcript segments (5′ UTR, CDS and 3′ UTR) in HEK293 cells. **e**–**g**, The fraction of methylated genes increases with gene expression levels in HepG2 (**e**), HEK293 (**f**) and common human peaks (see Methods) (**g**).

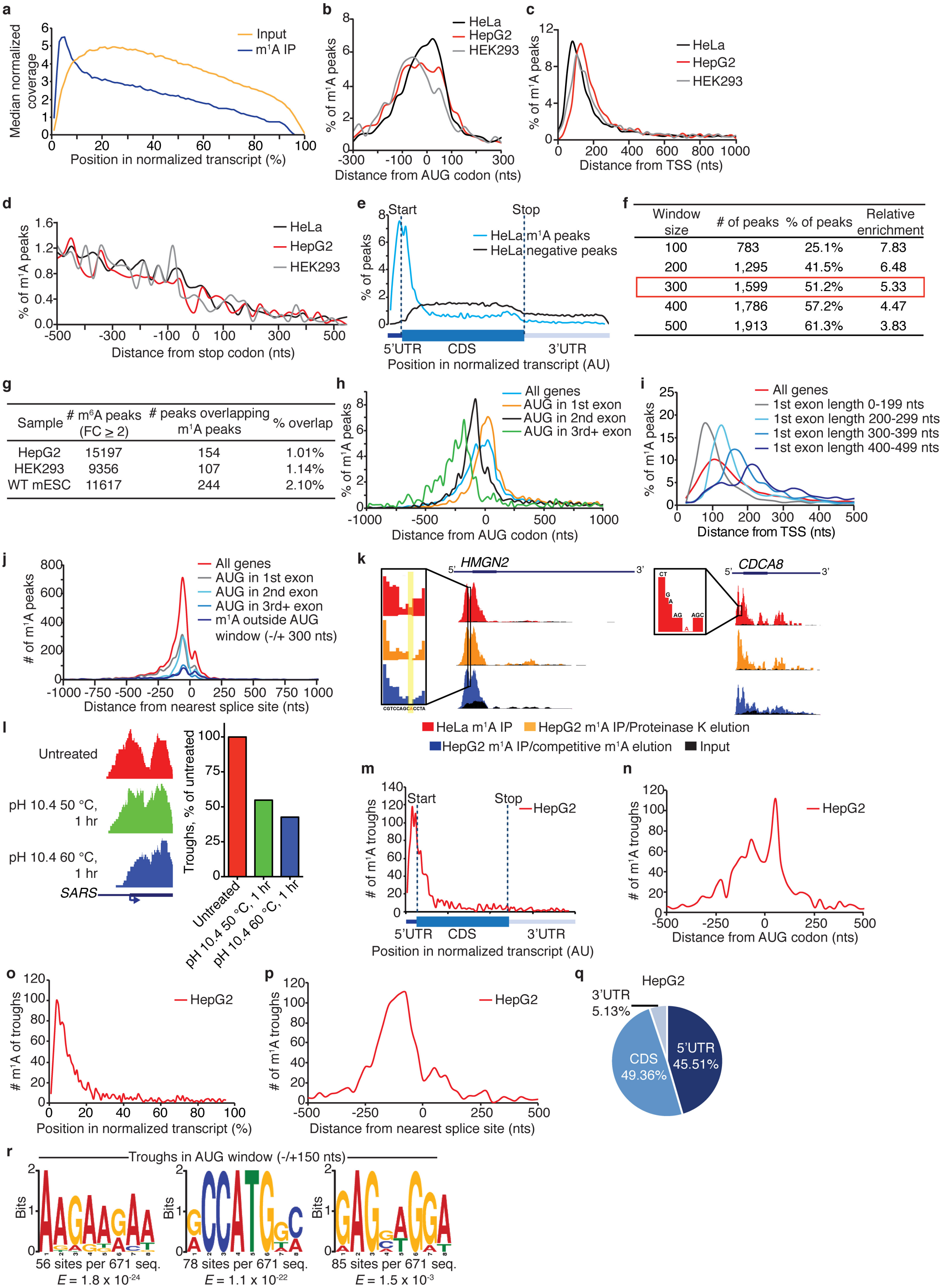

Extended Data Figure 3 | See next page for figure caption.

Extended Data Figure 3 | Metagene analyses of human m^{1}A peaks. **a**, Metagene profiles demonstrating sequence coverage along a normalized gene transcript. Sequence reads of m^{1}A immunoprecipitation and input in HeLa cells are indicated in blue and orange, respectively. **b**–**d**, Metagene profiles of m^{1}A peak distribution in a non-normalized window centred on the AUG start codon (**b**), extending downstream from the transcription start site (TSS) (**c**) and centred on the stop codon (**d**), in the indicated human cell types. **e**, Metagene profiles comparing the distribution of m^{1}A peaks (blue) to that of negative peaks (black) along a normalized transcript composed of three rescaled non-overlapping segments illustrated below, in HeLa cells. **f**, Table demonstrating m^{1}A peak enrichment in growing windows centred on the AUG start codon in HeLa cells. Enrichment is calculated as number of peaks in the window divided by window size (nucleotides). **g**, Table summarizing the overlap between m^{6}A and m^{1}A peaks in HepG2, HEK293 and WT mESCs. m^{6}A peaks are sourced from Dominissini *et al.*[1], Linder *et al.*[67] and Geula *et al.*[42], respectively. m^{1}A peaks are from the current study. **h**, **i**, Metagene profiles of m^{1}A peak distribution in a non-normalized window centred on the AUG codon (**h**) and extending downstream from the TSS (**i**). Peaks are sorted by the exon containing the AUG codon and the length of the first exon, respectively. **j**, Metagene profiles of m^{1}A peak distribution in a non-normalized window centered on the nearest splice site. Peaks are sorted by the exon containing the AUG codon in that gene. **k**, m^{1}A-induced reverse transcription (RT) arrests produce typical m^{1}A peaks characterized by a central region of reduced coverage with a local minimum (m^{1}A trough) Examples are shown. **l**, m^{1}A-to-m^{6}A rearrangement results in a reduced number of identified m^{1}A troughs. Higher rates of rearrangement further reduce the number of identified m^{1}A troughs (right panel). Example is shown (left panel). **m**, Metagene profile of m^{1}A trough distribution along a normalized transcript composed of three rescaled non-overlapping segments illustrated below, in HepG2 cells. **n**, Metagene profile of m^{1}A trough distribution in a non-normalized window centred on the AUG start codon in HepG2 cells. **o**, Metagene profile of m^{1}A trough distribution along a normalized transcript in HepG2 cells. **p**, Metagene profile of m^{1}A trough distribution in a non-normalized window centred on the nearest splice site in HepG2 cells. **q**, Pie chart presenting the fraction of m^{1}A troughs in each of three non-overlapping transcript segments (5′ UTR, CDS and 3'UTR) in HepG2 cells. **r**, MEME motifs identified in 100-nucleotide windows centred on m^{1}A troughs that lie within the AUG start codon window (±150 nucleotides) in HepG2 cells.

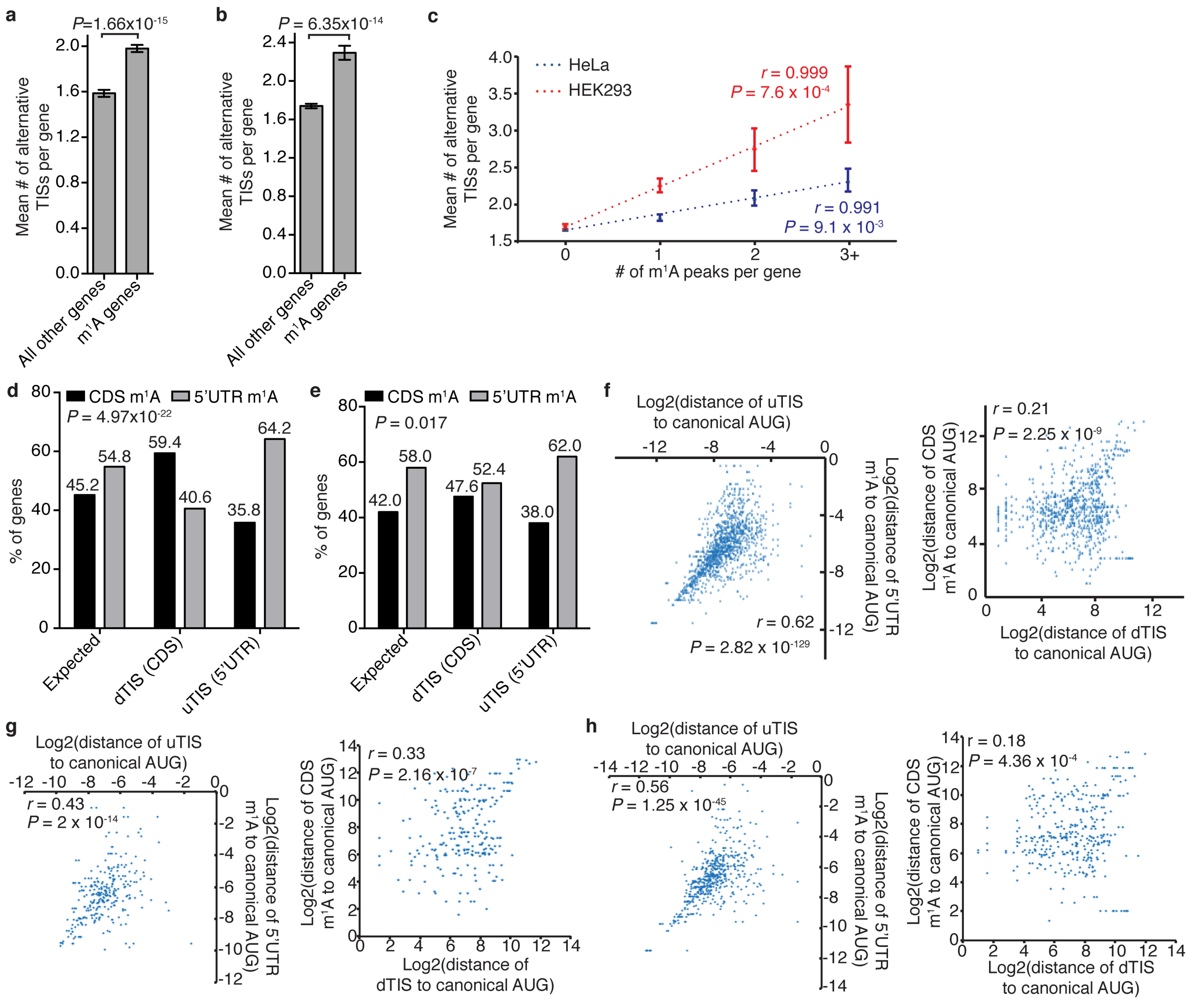

Extended Data Figure 4 | Correlation between m^{1}A sites and TISs in human. a, **b**, The mean number of alternative TISs in methylated (m^{1}A) versus all other (unmethylated) genes in HeLa (**a**) and HEK293 (**b**) cells. Mean values ± s.e.m. are shown. *P* values are indicated, Mann–Whitney *U* test. **c**, The mean number of alternative TISs per gene as a function of the number of m^{1}A peaks per gene in HeLa and HEK293 cells. Mean values ± s.e.m. are shown; *r* and *P* values are indicated, Pearson correlation; regression line is drawn. **d**, **e**, The percentage of genes with upstream (=5′ UTR) or downstream (=CDS) m^{1}A sites out of all genes that have either downstream or upstream TISs, compared to the expected percentage in HeLa (**d**) and HEK293 (**e**) cells. *P* values are indicated, χ^2 test. **f**–**h**, Scatter plots showing the correlation between the locations ($\log_2$) of alternative TISs and m^{1}A peaks with respect to the canonical AUG start codon (0) in HeLa (**f**), HEK293 (**g**) and HepG2 (**h**) cells: left, upstream TISs (uTIS) and 5′ UTRs m^{1}A peaks; right, downstream TISs (dTIS) and CDS m^{1}A peaks. *r* and *P* values are indicated, *t*-test.

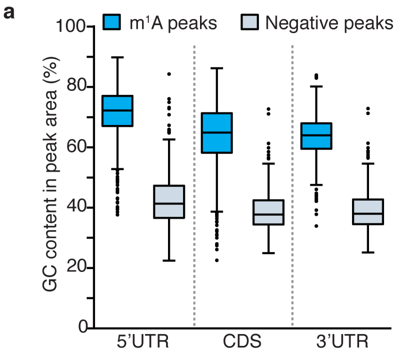

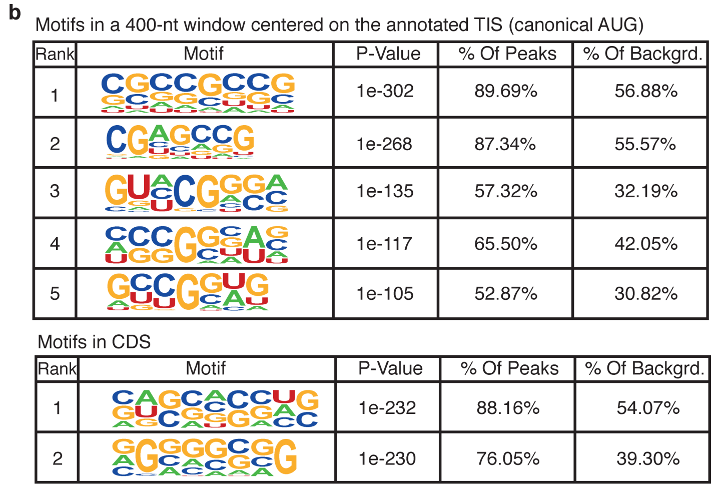

c

Chr	Position	Gene symbol	Surrounding sequence	Fold enrichment
chr2	232577666	*PTMA*	TGAGTAGAG**A**GGCCCGCCC	7.0
chr19	39220095	*ACTN4*	TGACCCAAC**A**CCCCCGACG	5.3
chr16	2802751	*SRRM2*	GGACCGGCG**A**GGCGAGGCG	4.7
chr19	13264215	*IER2*	CTCGCCTGC**A**CCCGCCCCG	3.6
chr20	57466549	*GNAS*	CTCGGCTCG**A**GGGGCGGGG	3.0
chr5	44809179	*MRPS30*	CTCGCGGCG**A**CCCCCGTCG	2.9
chr9	131940433	*IER5L*	GGCAGGGGT**A**ACGGAGTCC	2.8
chr18	12308292	*TUBB6*	GCGCCCGCC**A**TGAGGGAGA	2.4
chr1	54871941	*SSBP3*	GGCGGCGGC**A**CCCCCAGGC	2.4
chr2	232319939	*NCL*	CGGAGGATG**A**CCAGCAAGC	2.3

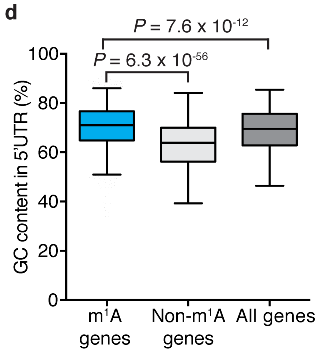

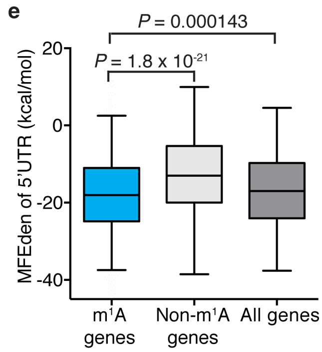

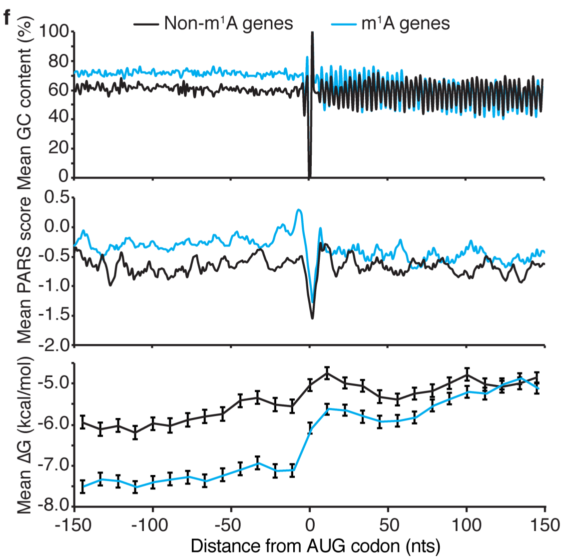

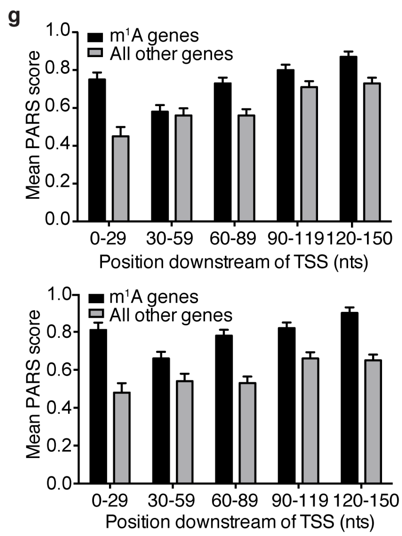

Extended Data Figure 5 | Structure and sequence features of m^{1}A sites in human mRNA. a, m^{1}A peaks have a significantly higher GC content compared to negative peaks in all three transcript segments: 5′ UTR, CDS and 3′ UTR. Box limits represent 25th percentile, median and 75th percentile, whiskers represent 2.5 and 97.5 percentiles, and dots indicate outliers. $P = 1.5 \times 10^{-278}$, $P = 8.2 \times 10^{-259}$ and $P = 3.3 \times 10^{-271}$, respectively, *t*-test. **b**, Motifs identified in 400-nucleotide windows centred on the canonical AUG start codon in genes with m^{1}A peaks in this window (upper table), or around m^{1}A peaks located in the CDS, outside the AUG start codon window (lower table). **c**, Examples of adenosines around m^{1}A peak middles with increased mismatch rates. Fold-enrichment values are the ratios of mismatch rates in untreated relative to rearranged samples. The top ten highest fold enrichment samples are shown.
d, **e**, GC content (**d**) and minimum free energy density (MFEden) (**e**) of 5′ UTRs of methylated (m^{1}A), unmethylated (Non-m^{1}A) and all genes. Box limits represent 25th percentile, median and 75th percentile, whiskers represent 2.5 and 97.5 percentiles. *P* values are indicted, *t*-test. **f**, Mean GC content (upper panel), PARS score (middle panel) and free energy (ΔG, lower panel) in a 300-nucleotide window centred on the start codon of commonly methylated genes relative to non-methylated genes (see Methods). Error bars represent s.e.m. **g**, The PARS scores of methylated compared to all other genes in HepG2 cells in a 150-nucleotide window extending downstream from the TSS, calculated in 30-nucleotide sliding windows. Each plot represents data from an independent PARS experiment. Error bars represent s.d.

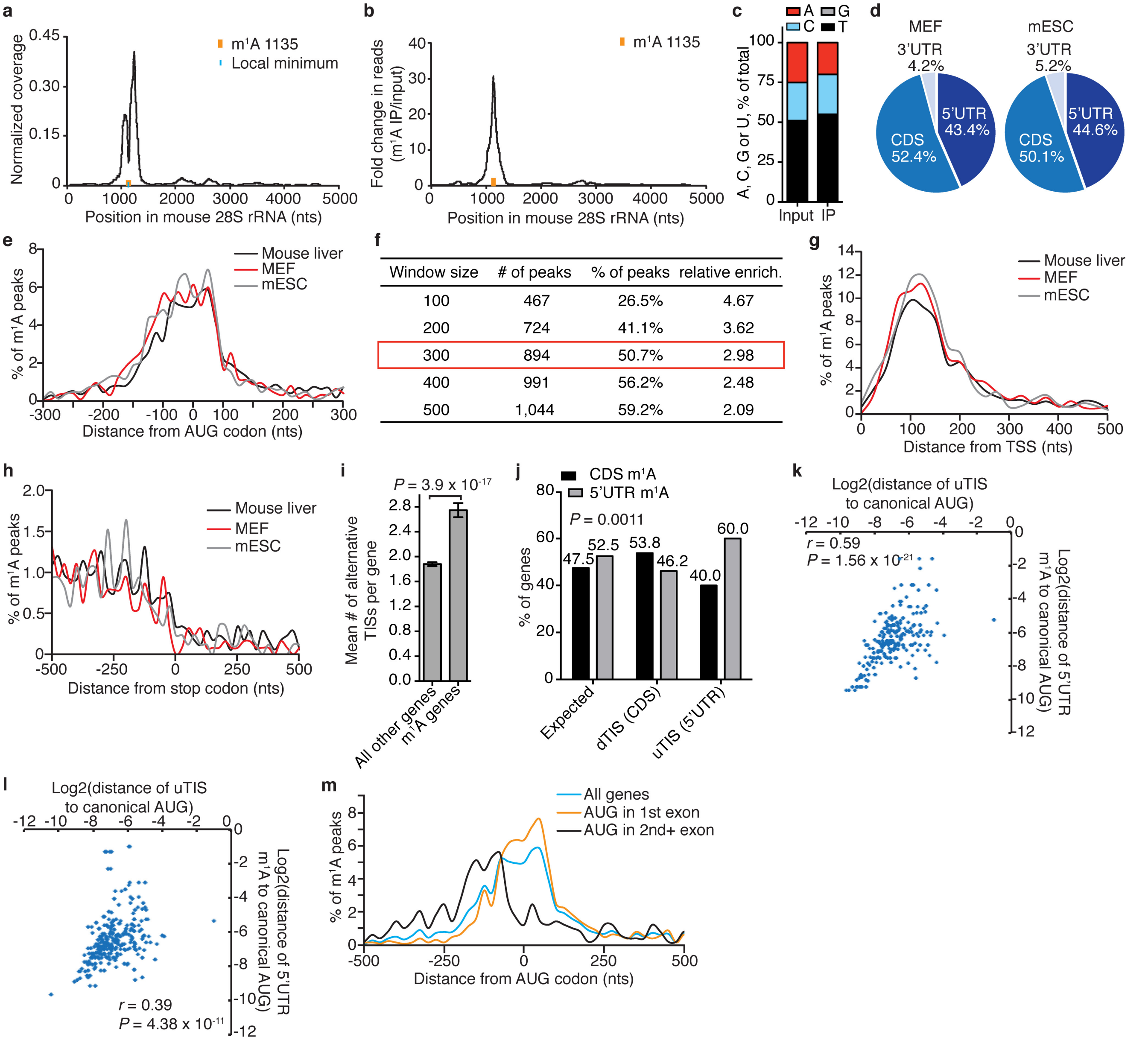

Window size	# of peaks	% of peaks	relative enrich.
100	467	26.5%	4.67
200	724	41.1%	3.62
300	894	50.7%	2.98
400	991	56.2%	2.48
500	1,044	59.2%	2.09

Extended Data Figure 6 | Features of the mouse m^{1}A methylome (part 1). a, Detection of an m^{1}A site at position 1135 of mouse 28S rRNA, in mouse liver m^{1}A immunoprecipitation. A drop in sequence read coverage can be seen at the methylated position. **b**, Fold-enrichment (immunoprecipitation over input reads) identifies an m^{1}A peak. **c**, High mismatch rate at the identified m^{1}A 1135 in mouse 28S rRNA. **d**, Pie charts presenting the fraction of m^{1}A peaks in each of three non-overlapping transcript segments (5′ UTR, CDS and 3′ UTR) in the indicated mouse cell types. **e**, Metagene profiles of m^{1}A peak distribution in a non-normalized window centred on the AUG start codon in the indicated mouse cell types. **f**, Table showing m^{1}A peak enrichment in growing windows centred on the AUG start codon in mouse liver. Enrichment is calculated as the number of peaks in the window divided by window size (nucleotides). **g**, **h**, Metagene profiles of m^{1}A peak distribution in a non-normalized window extending downstream from the TSS (**g**) and centred on the stop codon (**h**) in the indicated mouse cell types. **i**, The mean number of alternative TISs in methylated (m^{1}A) versus all other (unmethylated) genes in MEF cells. Mean values ± s.e.m. are shown; *P* value is indicated, Mann–Whitney *U* test. **j**, The percentage of genes with upstream (=5′ UTR) and downstream (=CDS) m^{1}A sites out of all genes that have either downstream or upstream alternative TISs, compared to the expected percentage in MEF cells. *P* value is indicated, χ^2 test. **k**, **l**, Scatter plots showing the correlation between the locations ($\log_2$) of upstream TISs (uTIS) and 5′ UTR m^{1}A peaks relative to the canonical AUG start codon (0) in mouse liver (**k**) and MEF (**l**) cells. *r* and *P* values are indicated, *t*-test. **m**, Metagene profiles of mouse m^{1}A peak distribution in a non-normalized window centred on the AUG codon. Peaks are sorted by the exon containing the AUG codon in that gene.

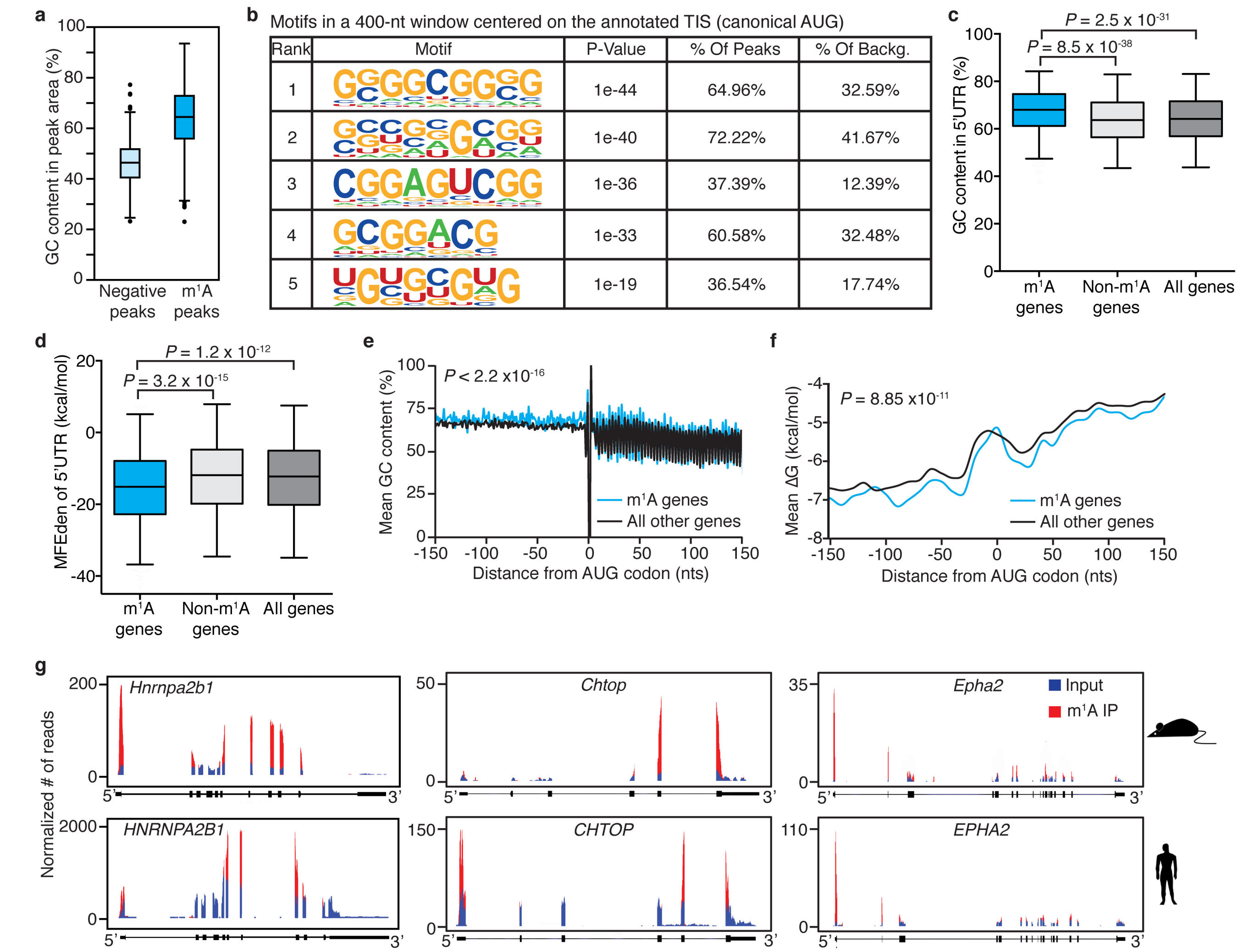

Extended Data Figure 7 | Features of the mouse m^{1}A methylome (part 2). **a**, Mouse m^{1}A peaks have a significantly higher GC content compared to negative peaks. Box limits represent 25th percentile, median and 75th percentile, whiskers represent 2.5 and 97.5 percentiles, and dots indicate outliers. $P = 4.4 \times 10^{-175}$, *t*-test. **b**, Motifs identified in 400-nucleotide windows centred on the canonical AUG start codon in genes with m^{1}A peaks in this window in mouse liver. **c**, **d**, GC content (**c**) and MFEden (**d**) of 5′ UTRs of methylated (m^{1}A), unmethylated (Non-m^{1}A) and all genes. Box limits represent 25th percentile, median and 75th percentile, whiskers represent 2.5 and 97.5 percentiles. *P* values are indicted, *t*-test. **e**, **f**, A sliding window profile of mean GC content (**e**) and mean ΔG (**f**) in a 300-nucleotide window centred on the canonical AUG start codon in methylated (m^{1}A) genes compared to all other genes in mouse liver. *P* values are indicated, Kolmogorov–Smirnov test and *t*-test. **g**, Representative plots of human-mouse orthologous genes with conserved m^{1}A peaks. Plot format as in Fig. 2a.

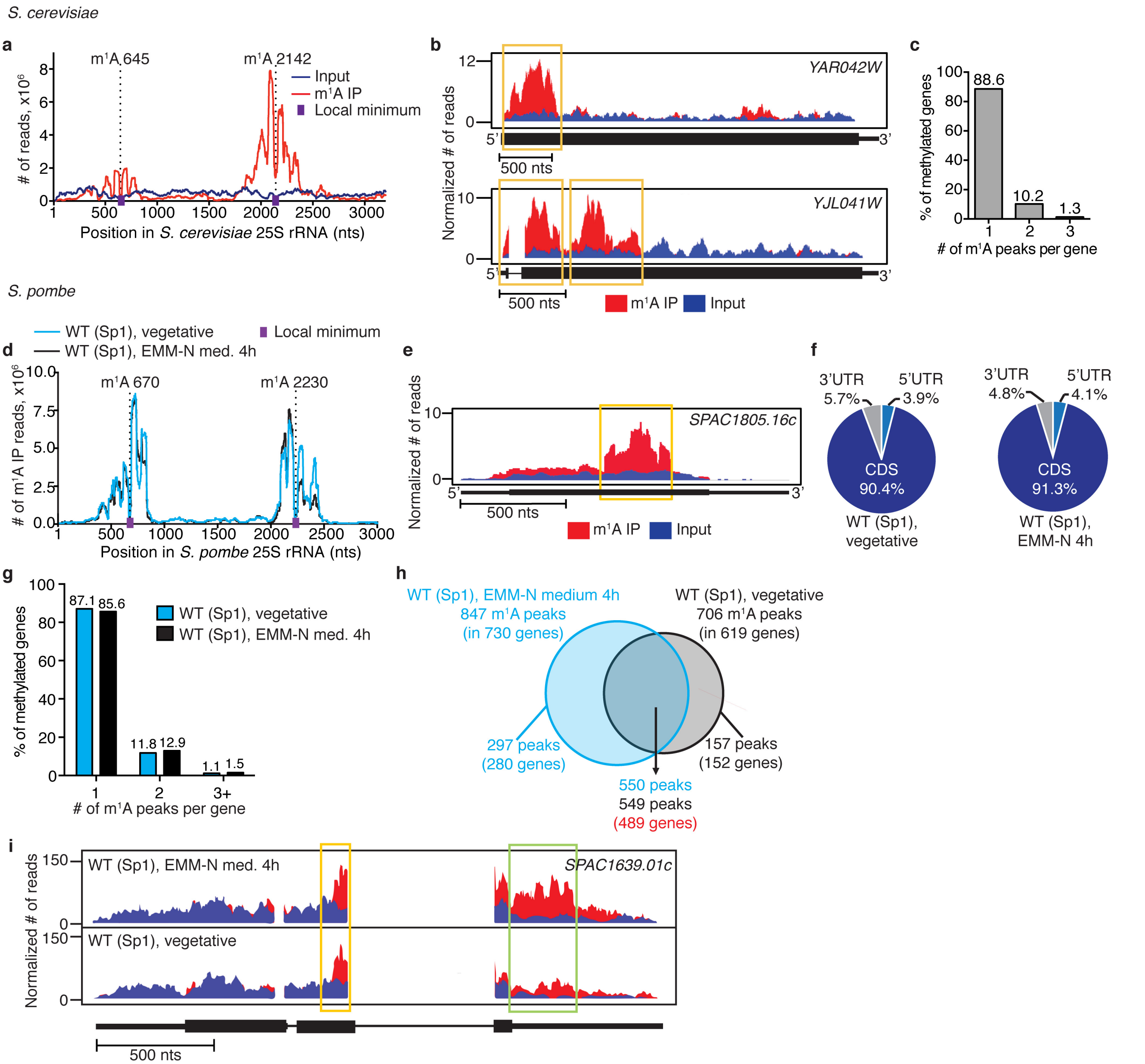

Extended Data Figure 8 | The yeast m^{1}A methylome. a, m^{1}A-seq identifies the known m^{1}A sites (645 and 2142) in *S. cerevisiae* 25S rRNA. A drop in sequence read coverage (indicated by purple dots) occurs around the methylated positions (indicated by dashed lines). **b**, Representative plots of methylated transcripts in *S. cerevisiae*. Plot format as in Fig. 2a. **c**, The percentage of methylated genes that carry 1, 2 or 3 m^{1}A peaks per gene in *S. cerevisiae*. Out of 843 m^{1}A peaks (FC $\geq$ 4, FDR $\leq$ 5%) in 778 genes, most (88.6%) are methylated only once. Unlike in mammals, m^{1}A is distributed across the coding transcriptome without an apparent preferred location. **d**, m^{1}A-seq identified the known m^{1}A sites (670 and 2230) in *S. pombe* 25S rRNA. A drop in sequence read coverage (indicated by purple dots) occurs around the methylated positions (indicated by dashed lines). **e**, Representative plot of a methylated transcript in *S. pombe*. Plot format as in Fig. 2a. **f**, Pie charts presenting the fraction of m^{1}A peaks in each of three non-overlapping transcript segments (5′ UTR, CDS and 3′ UTR) in *S. pombe* Sp1 strain under the indicated conditions. Under vegetative growth, we identified 706 m^{1}A peaks (FC $\geq$ 4, FDR $\leq$ 5%) in 619 gene transcripts, most of which (90.4%) distributed along the CDS. Four hours after transfer to a nitrogen-source deficient 'sporulation' medium, 157 out of the vegetative state m^{1}A peaks were no longer detected, and 297 new peaks appeared. Importantly, transcripts that harbour differential peaks were adequately expressed (above the 1st quartile) in both conditions. **g**, The percentage of methylated genes that carry 1, 2, or 3 + m^{1}A peaks per gene in *S. pombe* Sp1 strain under the indicated conditions. **h**, Venn diagram representing differential and shared m^{1}A peaks in *S. pombe* Sp1 strain under the indicated conditions. **i**, Representative plots of a differentially methylated transcript in *S. pombe* Sp1 strain under the indicated conditions. Yellow box, conserved peak; green box, differential peak.

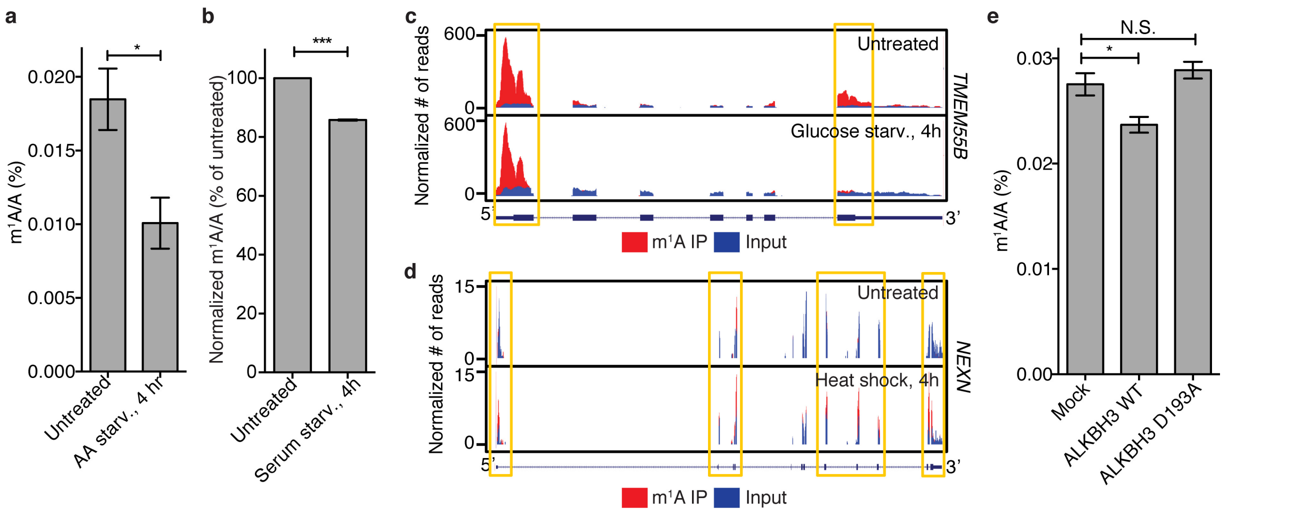

Extended Data Figure 9 | m^{1}A in mRNA is a dynamic modification. **a**, **b**, LC-MS/MS quantification of m^{1}A in mRNA of untreated and amino acid (AA)-starved (**a**) or serum-starved (**b**) HepG2. Mean values ± s.e.m. are shown, $n = 3$, $*P \leq 0.05$, $***P \leq 0.001$, unpaired t-test. **c**, **d**, Representative plots of differentially methylated transcripts in untreated and glucose-starved (**c**) or heat shock-treated (**d**) HepG2 cells. Plot formats as in Fig. 2a. **e**, LC-MS/MS quantification of m^{1}A in mRNA of 293F cells overexpressing WT FLAG-ALKBH3 or an inactive mutant (D193A), presented as percentage of unmodified A. Mean values ± s.e.m. are shown, $n = 3$, $*P \leq 0.05$, NS, $P > 0.05$, one-way ANOVA with Dunnet's multiple comparison test.

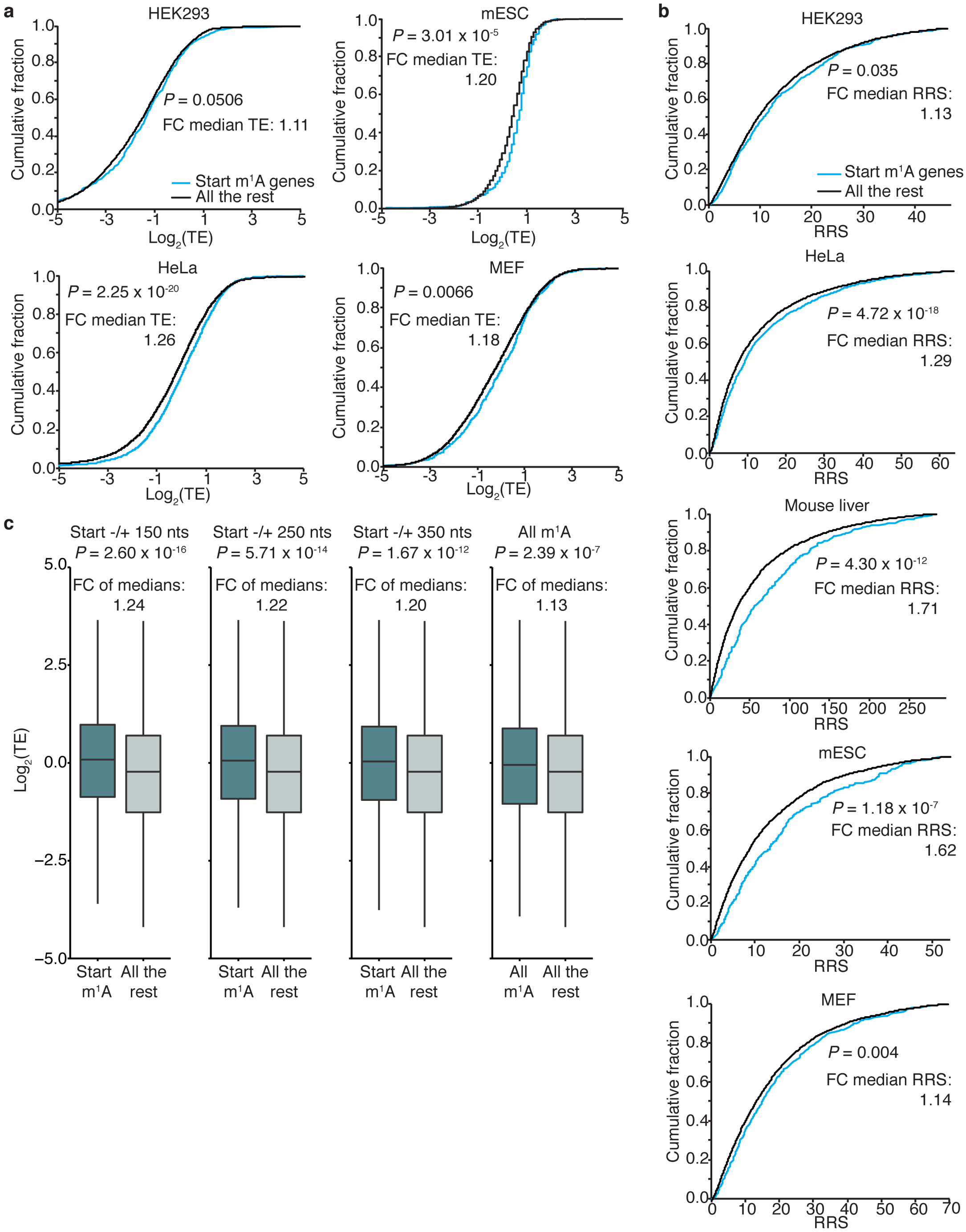

Extended Data Figure 10 | m^{1}A around the start codon correlates with higher translation efficiency (TE). a, Cumulative distribution of log$_2$(TE) in genes methylated in a 300-nucleotide window centred on the start codon compared to all other genes, in the indicated human and mouse cell types. *P* values (*t*-test) and fold-changes (FC) of median TE values (Start m^{1}A genes/All the rest) are indicated. **b**, Genes methylated in a 300-nucleotide window centred on the AUG start codon have a higher ribosome release score (RRS = TE[CDS]/TE[3′ UTR]) compared to all other genes in the indicated cell types. RRSs, which are 'normalized' to ribosomal drop-off in the 3′ UTR, are in line with TE scores. *P* values (Mann–Whitney *U* test) and fold-changes (FC) of median RRS values (Start m^{1}A genes/All the rest) are indicated. **c**, Genes methylated in different start codon window sizes have higher TE compared to all other genes, in HeLa cells. When considering all m^{1}A genes, including those methylated outside the start codon window, the effect is reduced. *P* values (*t*-test) and fold-changes (FC) of median TE values (Start m^{1}A genes/All the rest) are indicated. Box limits represent 25th percentile, median and 75th percentile; whiskers extend from the limit to the highest and lowest value within 1.5 IQR (interquartile range).

doi:10.1038/nature16952

Structural basis for activity regulation of MLL family methyltransferases

Yanjing Li[1,2], Jianming Han[1,2], Yuebin Zhang[3], Fang Cao[4], Zhijun Liu[1,2], Shuai Li[5], Jian Wu[1,2], Chunyi Hu[1,2], Yan Wang[1,2], Jin Shuai[1,2], Juan Chen[1,2], Liaoran Cao[3], Dangsheng Li[6], Pan Shi[7], Changlin Tian[7,8], Jian Zhang[5], Yali Dou[4], Guohui Li[3], Yong Chen[1,2] & Ming Lei[1,2]

The mixed lineage leukaemia (MLL) family of proteins (including MLL1–MLL4, SET1A and SET1B) specifically methylate histone 3 Lys4, and have pivotal roles in the transcriptional regulation of genes involved in haematopoiesis and development. The methyltransferase activity of MLL1, by itself severely compromised, is stimulated by the three conserved factors WDR5, RBBP5 and ASH2L, which are shared by all MLL family complexes. However, the molecular mechanism of how these factors regulate the activity of MLL proteins still remains poorly understood. Here we show that a minimized human RBBP5–ASH2L heterodimer is the structural unit that interacts with and activates all MLL family histone methyltransferases. Our structural, biochemical and computational analyses reveal a two-step activation mechanism of MLL family proteins. These findings provide unprecedented insights into the common theme and functional plasticity in complex assembly and activity regulation of MLL family methyltransferases, and also suggest a universal regulation mechanism for most histone methyltransferases.

Methylation of histone H3 Lys4 (H3K4), which is predominantly associated with actively transcribed genes[1–3], is mainly mediated by MLL family histone lysine methyltransferases (HKMTs). Mammalian MLL family HKMTs contain six members (MLL1–MLL4, SET1A and SET1B)[2–4], each of which has crucial yet non-redundant roles in cells[4–6]. MLL1 has been the most intensively studied because of its involvement by chromosomal translocations in a variety of acute lymphoid and myeloid leukaemias[6,7]. Recently, inactivating mutations in *MLL3* (also known as *KMT2C*) and *MLL4* (*KMT2D*) have been identified in several types of human tumours and in Kabuki syndrome[8–12].

In contrast to most SET [SU(VAR)3-9, E(Z) and TRX]-domain-containing methyltransferases, MLL1 protein alone exhibits poor HKMT activity[13,14]. The crystal structure of the MLL1 SET domain ($MLL1_{SET}$) reveals an open conformation that is not efficient for the methyl transfer from the cofactor *S*-adenosyl-L-methionine (AdoMet) to the target lysine[15]. The optimal HKMT activity of MLL1 requires additional factors, WDR5, RBBP5 and ASH2L, which are shared core components of all MLL complexes and also evolutionarily conserved from yeast to humans[13,16]. Depletion of any of these components results in the global loss of H3K4 methylation to varying degrees[16–18]. Despite the importance of WDR5, RBBP5 and ASH2L, it is still unclear how these factors stimulate the HKMT activity of MLL proteins. In this work, our biochemical and structural analyses reveal how RBBP5–ASH2L binds and activates MLL family methyltransferases through a conserved mechanism.

RBBP5–ASH2L binds and activates MLLs

We first examined the effects of individual components (WDR5, RBBP5 and ASH2L) and their combinations on the HKMT activities of MLL family methyltransferases. We selected the carboxy-terminal conserved regions of MLL proteins containing both the WIN (WDR5-interaction) motif and the SET domain in activity assays[14] (Fig. 1a). For simplicity, hereafter we use 'MLL' to represent the MLL WIN-SET fragment, and 'MLL_{SET}' to represent the MLL SET domain unless stated otherwise. Consistent with previous observations[14,15,19], activity assays showed that the RBBP5–ASH2L heterodimer substantially upregulated the HKMT activity of MLL1, and this activity was further stimulated by the addition of WDR5 (Fig. 1b and Extended Data Fig. 1a–c). By contrast, MLL2–MLL4, SET1A and SET1B can be fully activated by just RBBP5–ASH2L, and WDR5 was dispensable for activity regulation (Fig. 1b and Extended Data Fig. 1a–c). The stimulatory effect of RBBP5–ASH2L on MLL HKMT activities indicated a possible direct interaction between RBBP5–ASH2L and MLL proteins[20–22]. Indeed, a glutathione *S*-transferase (GST) pull-down assay clearly showed that all MLL proteins directly interact with RBBP5–ASH2L (Fig. 1c and Extended Data Fig. 2a). Among them, MLL2–MLL4 could be efficiently pulled down by GST–ASH2L–RBBP5, whereas SET1A and SET1B maintained a medium level of interaction with RBBP5–ASH2L (Fig. 1c and Extended Data Fig. 2a). By contrast, MLL1 only exhibited a very weak interaction with RBBP5–ASH2L under low-salt buffer conditions (Fig. 1c and Extended Data Fig. 2a). Fluorescence polarization analysis also revealed that MLL proteins interact with RBBP5–ASH2L with very different binding affinities ranging from $\sim$100 nM (for MLL3) to more than 100 μM (for MLL1) (Extended Data Fig. 2b). Formation of the RBBP5–ASH2L heterodimer is a prerequisite for MLL binding, as neither RBBP5 nor ASH2L alone can stably associate with MLL proteins (Extended Data Fig. 2c, d). Notably, MLL proteins can also stabilize the RBBP5–ASH2L interaction when high-salt buffer was used in the pull-down assay (Extended Data Fig. 2a), consistent with the observation that the RBBP5–ASH2L interaction is highly sensitive to ionic strength (Extended Data Fig. 2e).

[1]National Center for Protein Science Shanghai, State Key Laboratory of Molecular Biology, Institute of Biochemistry and Cell Biology, Shanghai Institutes for Biological Sciences, Chinese Academy of Sciences, 333 Haike Road, Shanghai 201210, China. [2]Shanghai Science Research Center, Chinese Academy of Sciences, Shanghai 201204, China. [3]Laboratory of Molecular Modeling and Design, State Key Laboratory of Molecular Reaction Dynamics, Dalian Institute of Chemical Physics, The Chinese Academy of Sciences, Dalian, Liaoning 116023, China. [4]Department of Pathology, University of Michigan Medical School, 1301 Catherine, Ann Arbor, Michigan 48109, USA. [5]Department of Pathophysiology, Key Laboratory of Cell Differentiation and Apoptosis of the Chinese Ministry of Education, Shanghai JiaoTong University School of Medicine, Shanghai 200025, China. [6]Shanghai Information Center for Life Sciences, Shanghai Institutes for Biological Sciences, Chinese Academy of Sciences, Shanghai 200031, China. [7]High Magnetic Field Laboratory, Chinese Academy of Sciences, Hefei 230031, China. [8]National Laboratory for Physical Science at the Microscale and School of Life Sciences, University of Science and Technology of China, Hefei 230026, China.

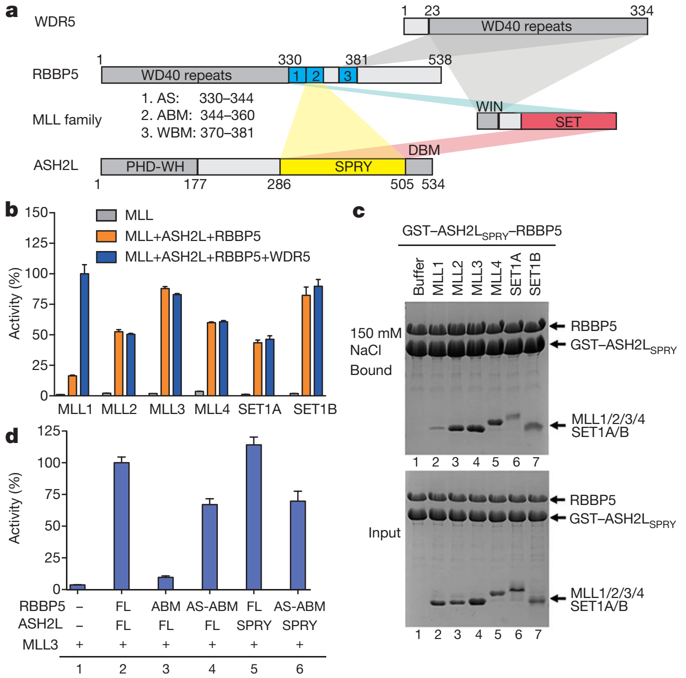

Figure 1 | RBBP5–ASH2L interacts and activates MLL proteins. **a**, Domain organization of human ASH2L, RBBP5, WDR5 and MLL proteins. Only the C-terminal domain of MLL is shown. DBM, DPY30 binding motif; PHD-WH, plant homeodomain-winged helix. Shaded areas denote the interacting domains among these proteins. **b**, The normalized HKMT activities determined by a ^{3}H-methyl-incorporation assay. Mean ± s.d. ($n = 3$) are shown. **c**, GST pull-down assay shows MLL proteins directly interact with the RBBP5–ASH2L$_{SPRY}$ heterodimer. **d**, The normalized HKMT assays revealed that an activation segment of RBBP5 (residues 330–344) is crucial for the stimulation of MLL3 activity. FL, full-length. Mean ± s.d. ($n = 3$) are shown.

Because MLL1 only maintained a weak direct interaction with RBBP5–ASH2L, we proposed that full activation of MLL1 by RBBP5–ASH2L requires the bridging molecule WDR5 that can interact with both MLL1 and RBBP5–ASH2L simultaneously. Consistent with this idea, the stimulatory effect of WDR5 on MLL1 HKMT activity is minimized when the protein concentration was increased in the assay (Extended Data Fig. 2f). Furthermore, the fusion of RBBP5 and MLL1 together achieved a robust HKMT activity that cannot be further stimulated by the addition of WDR5 (Extended Data Fig. 2g), suggesting that WDR5 per se is not directly involved in the MLL HKMT enzymatic reaction. Collectively, we conclude that RBBP5–ASH2L is the major functional unit that binds and activates MLL proteins. Conversely, WDR5 may have an indirect role in promoting HKMT activity by acting as a bridging molecule to facilitate the formation of MLL complexes under certain assay conditions, and this may explain the apparent discrepancy in reports about the role of WDR5 in the activity regulation of MLL complexes[19–22].

Complex structure of MLL3–RBBP5–ASH2L

To determine the structural basis of how RBBP5–ASH2L activates MLL proteins, we first dissected the interactions among RBBP5, ASH2L and the SET domains of MLL proteins. Consistent with previous studies[23,24], the ASH2L C-terminal SPRY (splA and ryanodine receptor) domain is sufficient to form a heterodimer with RBBP5 to stimulate the HKMT activity of MLL proteins (Fig. 1d, compare lanes 1 and 5). Three adjacent short motifs of RBBP5 were identified for the stimulation of MLL HKMT activity (residues 330–344, activation segment, AS), the interaction with ASH2L (residues 344–363, ASH2L-binding motif, ABM), and the association with WDR5 (residues 369–381, WDR5-binding motif, WBM)[24,25] (Fig. 1a). A preformed RBBP5$_{AS\text{-}ABM}$–ASH2L$_{SPRY}$ complex can stimulate MLL3$_{SET}$ HKMT activity to levels of ~70% of full-length RBBP5–ASH2L (Fig. 1d, compare lanes 2, 4 and 6), indicating that this minimized RBBP5$_{AS\text{-}ABM}$–ASH2L$_{SPRY}$ heterodimer is essential for the stimulation of MLL3$_{SET}$ activity, and that other regions of RBBP5 might have a minor role in this process. We determined the crystal structure of this minimized ternary complex composed of MLL3$_{SET}$, RBBP5$_{AS\text{-}ABM}$ and ASH2L$_{SPRY}$ (hereafter referred to as M3RA) in the presence of *S*-adenosyl-L-homocystein (AdoHcy) and a substrate peptide (H3 residues 1–9) (Fig. 2a, Extended Data Table 1 and Extended Data Fig. 3a). Notably, we crystallized the M3RA complex both with and without the H3 peptide in one asymmetric unit (Extended Data Fig. 3b).

In the M3RA complex, RBBP5$_{AS\text{-}ABM}$ adopts an extended conformation that consists sequentially of two β-strands (activation segment) and a rigid coil (ABM), which respectively mediate the interactions with MLL3$_{SET}$ and ASH2L$_{SPRY}$ (Fig. 2a). The overall fold of MLL3$_{SET}$ is similar to other SET-domain proteins, and shares the conserved features of N- and C-terminal regions (SET-N and SET-C), an insertion region (SET-I) and post-SET motifs[15,26,27] (Fig. 2b). The active site residues of MLL3$_{SET}$, the conformation of the target lysine and an invariant water molecule, are almost identical to those of the active site of DIM-5 (ref. 28), suggesting a catalytically active configuration of MLL3$_{SET}$ (Fig. 2c). The 'U'-shaped cofactor product AdoHcy binds into a well-defined surface pocket on MLL3$_{SET}$ through an extensive network of highly conserved interactions as observed in other SET-domain structures (Fig. 2d and Extended Data Fig. 3c, d). The H3 substrate peptide sits in an opposite groove on the surface of MLL3$_{SET}$, and an intricate network of hydrogen bonds stabilizes the binding (Fig. 2e and Extended Data Fig. 3e). The unique geometry of the H3-binding groove specifically recognizes Thr3^{H3} and Arg2^{H3}, defining the substrate specificity of MLL3$_{SET}$ (Extended Data Fig. 3f, g). Since all the H3-peptide-binding residues in MLL3$_{SET}$ are highly conserved in other MLL proteins (Extended Data Fig. 4), we conclude that all MLL proteins achieve the substrate specificity towards H3K4 through the same recognition mechanism as observed in the M3RA complex.

Interfaces in the M3RA complex

The structure of the M3RA complex reveals extensive interactions among ASH2L$_{SPRY}$, RBBP5$_{AS\text{-}ABM}$ and MLL3$_{SET}$. ASH2L$_{SPRY}$ recognizes RBBP5$_{ABM}$ through extensive salt-bridge and hydrogen-bonding interactions; the C-terminal portion of RBBP5$_{ABM}$ adopts a coiled conformation sitting on two arginine residues (Arg343 and Arg367) at the centre of the basic pocket of ASH2L$_{SPRY}$ (Fig. 3a). Mutations of ASH2L Arg343 and its interacting residues in RBBP5$_{ABM}$ (Glu349 and Asp353) completely abrogated the RBBP5$_{ABM}$–ASH2L$_{SPRY}$ interaction (Extended Data Fig. 5a) and impaired the HKMT activity of the MLL3 complex (Extended Data Fig. 5b). The primary feature of the RBBP5$_{AS}$–MLL3$_{SET}$ interaction is the intermolecular β-sheet interactions involving two strands of the L-shaped RBBP5$_{AS}$ paring with β4 and an induced strand β7 immediately before helix αC of MLL3$_{SET}$ (Fig. 3b). Mutations of residues on this L-shaped motif partially decreased the HKMT activity of the MLL3 complex (Extended Data Fig. 5c). In addition to these binary contacts, the side chain of the conserved Arg4806 of MLL3$_{SET}$ sticks outside towards an acidic pocket formed by both RBBP5$_{ABM}$ and ASH2L$_{SPRY}$, forming five salt-bridge and hydrogen-bonding interactions with Glu347^{RBBP5}, Tyr313^{ASH2L} and Gln354^{ASH2L} (Fig. 3c). This extensive electrostatic network functions as an anchor point to fix the relative position of MLL3$_{SET}$ to ASH2L$_{SPRY}$, and is crucial for assembly of the MLL3–RBBP5–ASH2L complex.

Because the RBBP5$_{AS\text{-}ABM}$–ASH2L$_{SPRY}$-interacting residues are highly conserved in MLL-family proteins (Extended Data Fig. 4), we proposed that all MLL$_{SET}$ domains including MLL1$_{SET}$ should interact with RBBP5–ASH2L through the same molecular surface as observed in the M3RA complex. In support of this idea, alanine

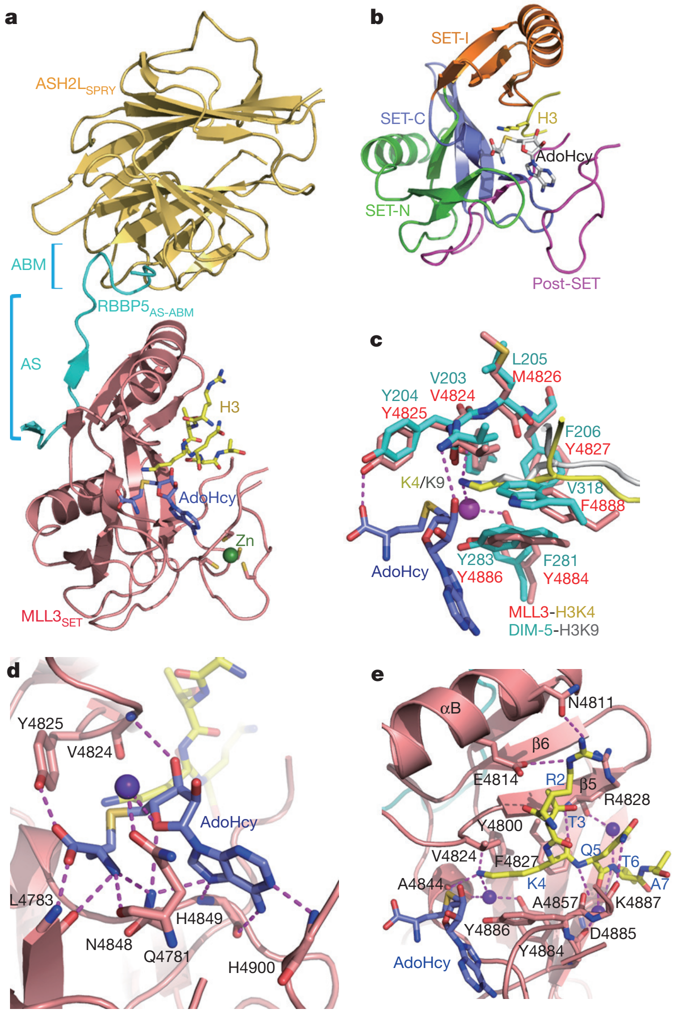

Figure 2 | Crystal structure of the M3RA complex. a, The crystal structure of MLL3$_{SET}$–RBBP5$_{AS\text{-}ABM}$–ASH2L$_{SPRY}$ in complex with cofactor product AdoHcy and the H3 peptide. **b**, MLL3$_{SET}$ shares the conserved features of SET-N, SET-I, SET-C and post-SET motifs. **c**, Comparison of the active centre of MLL3 and DIM-5 (PDB accession 1PEG) complex structures. **d**, The AdoHcy binding pocket in MLL3$_{SET}$. **e**, The substrate H3 binding channel. Hydrogen bonds are indicated by dashed magenta lines; purple sphere denotes a water molecule.

substitutions of the conserved arginine residues in all MLL proteins, which do not affect the overall fold of MLL proteins (Extended Data Fig. 5d), abolished the interaction between MLL$_{SET}$ and RBBP5–ASH2L (Fig. 3d), and substantially decreased the HKMT activities of all MLL complexes (Fig. 3e). Accordingly, mutations of the arginine-interacting residues on RBBP5 and ASH2L (RBBP5 Glu347 and ASH2L Gln354) also weakened the association of MLL$_{SET}$ with RBBP5–ASH2L, and reduced the HKMT activities of MLL complexes (Extended Data Fig. 5e, f). Together, our data confirmed that the electrostatic network observed at the MLL3$_{SET}$–RBBP5–ASH2L interface is essential for the interaction between RBBP5–ASH2L and all MLL proteins. Interestingly, an inactivating mutation of the same key arginine residue in MLL4 (Arg5432Trp) that was identified in patients with non-Hodgkin lymphoma[9] also disrupted the interaction between MLL4 and RBBP5–ASH2L and abolished the HKMT activity (Fig. 3d, e), indicating that loss of a stable MLL4–RBBP5–ASH2L association leads to lymphomagenesis.

Difference between MLL1 and other MLL proteins

The structure of the M3RA complex revealed that subtle sequence differences in the RBBP5–ASH2L-binding region (residues 4804–4814 in MLL3) are probably responsible for the ability of RBBP5–ASH2L to distinguish MLL1 from other MLL proteins (Fig. 4a). Most notably, the side chain of Val4809 in the SET-I motif of MLL3$_{SET}$ fits snugly in a shallow pocket formed by both RBBP5 and MLL3$_{SET}$ (Fig. 4b), which can also accommodate the corresponding residues of MLL2, MLL4, SET1A and SET1B at the equivalent positions, but not for the bulky residue Gln3867 of MLL1 (Fig. 4a, b). In addition, the side-chain methyl group of MLL3$_{SET}$ Thr4803 is surrounded by three hydrophobic resides of RBBP5$_{AS}$ (Leu339, Val343 and Tyr345) (Fig. 4c). By contrast, a large hydrophilic residue Asn3861 at this position in MLL1 is incompatible with RBBP5 binding (Fig. 4c). Thus, we proposed that two residues (Asn3861 and Gln3867) in MLL1 weaken the otherwise stable interaction between RBBP5–ASH2L and MLL1. Indeed, both MLL1-to-MLL2 (Asn3861Ile/Gln3867Leu) and MLL1-to-MLL3 (Asn3861Thr/Gln3867Val) double mutants of MLL1 re-gained stable interactions with RBBP5–ASH2L (Fig. 4d), and WDR5 had no further stimulatory effect on the HKMT activities of these mutants (Fig. 4e). Therefore, mutations of these two residues restore the strong RBBP5–ASH2L binding ability of MLL1 and thus bypass the requirement of WDR5 as the bridging molecule for the optimal HKMT activity of the MLL1 complex. This idea is further supported by the crystal structure of the MLL1$_{SET}^{N3861I/Q3867L}$–RBBP5$_{AS\text{-}ABM}$–ASH2L$_{SPRY}$ complex (hereafter referred to as M1^{M}RA, in which 'M' denotes mutant) (Fig. 4f and Extended Data Table 2). The structure of M1^{M}RA highly resembles that of M3RA, with an identical interface as the one between MLL3$_{SET}$ and RBBP5–ASH2L (Fig. 4g), strongly indicating that the RBBP5–ASH2L heterodimer interacts with and activates all MLL proteins through a conserved mechanism. Notably, the equivalent residues of MLL1 Asn3861 in SET1A (Gln1600) and SET1B (Gln1816) also have large hydrophilic side chains and therefore are not optimal for RBBP5–ASH2L binding (Fig. 4a). This is consistent with the medium levels of interaction of SET1A and SET1B with RBBP5–ASH2L observed in the pull-down and fluorescence polarization assays (Extended Data Fig. 2a, b).

Activation mechanism of MLL complexes

Next we asked why MLL proteins by themselves are catalytically inactive, and how RBBP5–ASH2L stimulates their HKMT activities. One prevailing model suggests that the SET domain of MLL adopts an open conformation, and the interaction with regulatory factors induces MLL SET domain into a closed conformation[15]. To test this model, we crystallized apo MLL3$_{SET}$ and determined its structure in complex with AdoHcy (Extended Data Fig. 6a). Surprisingly, the apo structure of MLL3$_{SET}$ was almost indistinguishable from the active conformation of MLL3$_{SET}$ in the M3RA complex (Fig. 5a). In addition, we also determined the crystal structure of MLL1$_{SET}^{M}$ (MLL1$_{SET}^{N3861I/Q3867L}$), the SET-I motif of which exhibits an even more closed conformation than that in the M1^{M}RA complex (Fig. 5b and Extended Data Fig. 6b). Nevertheless, our data clearly showed that both MLL3 and MLL1^{M} by themselves are catalytically inactive (Fig. 4e and Extended Data Fig. 1). This apparent discrepancy between the low enzymatic activity and the closed conformation of MLL1$_{SET}^{M}$ or MLL3$_{SET}$ led us to propose that, in the absence of RBBP5–ASH2L, MLL$_{SET}$ might be highly dynamic, and the configuration of MLL SET-I motif captured in the crystal structure is a snapshot of a spectrum of conformations of a mobile motif. In support of this idea, normal mode analysis revealed a highly dynamic motion of the SET-I motif in apo MLL1$_{SET}^{M}$ and MLL3$_{SET}$, which is substantially suppressed upon the association with RBBP5–ASH2L (Supplementary Videos 1–5). To test this model experimentally, we use ^{19}F-NMR (fluorine-19 nuclear magnetic resonance) to probe the structural dynamics of MLL3$_{SET}$ in solution. The ^{19}F-NMR spectrum of Phe4827, a key residue at the substrate-binding site in the SET-I motif, displayed two peaks at different chemical shifts, defining at least two different conformations or states with dynamic exchanges (Fig. 5c). With titration of RBBP5–ASH2L, the ^{19}F-NMR spectrum showed prominent changes with conformational equilibrium towards a single

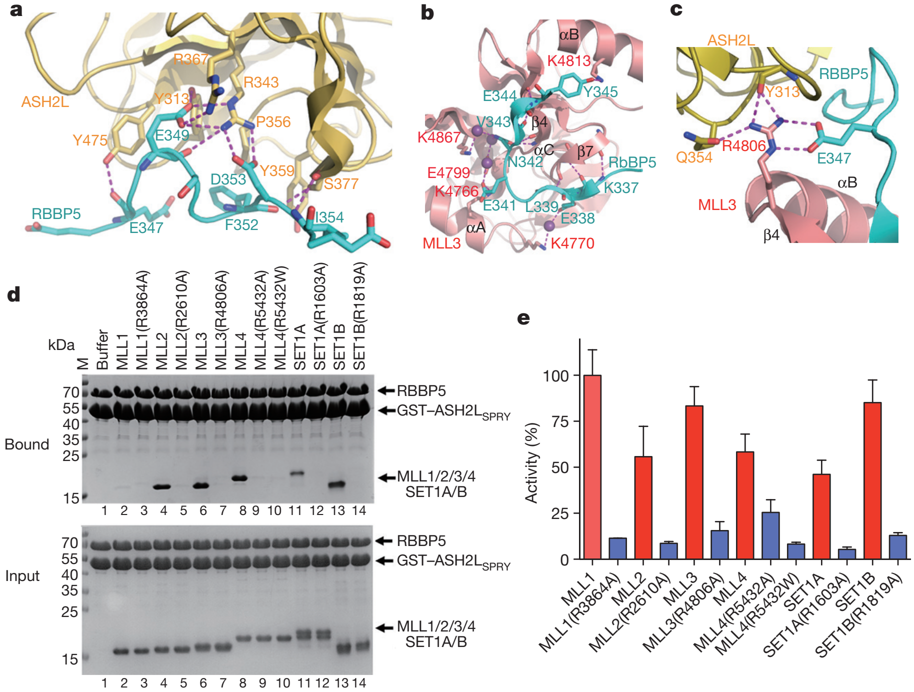

Figure 3 | Interfaces among MLL3$_{SET}$, RBBP5$_{AS-ABM}$ and ASH2L$_{SPRY}$. **a**, Detailed view of the ASH2L$_{SPRY}$–RBBP5$_{ABM}$ interface. **b**, The interface between MLL3$_{SET}$ and RBBP5$_{AS}$. **c**, MLL3 Arg4806 forms an extensive salt-bridge and hydrogen-bonding network with ASH2L and RBBP5. **d**, Mutations of the conserved arginine in MLL proteins disrupt interactions with RBBP5–ASH2L, as shown by the GST pull-down assay in 300 mM NaCl buffer. **e**, Arginine mutations impair the HKMT activities of MLL family proteins. Activities of all complexes are normalized to the activity of wild-type MLL1–WDR5–RBBP5–ASH2L, and shown as mean ± s.d. ($n = 3$).

active state, indicating that RBBP5–ASH2L reduced the flexibility of SET-I to lock it in an active state (Fig. 5c). By contrast, Tyr4762 that is located in the SET-N motif exhibited no peak shift upon the addition of RBBP5–ASH2L (Fig. 5c).

To provide further insight into this dynamic process, we carried out molecular dynamics simulation to investigate how RBBP5–ASH2L affects the structures of MLL3$_{SET}$ and MLL1$^{M}_{SET}$. Results showed that RBBP5–ASH2L reduces the root mean square fluctuation of helix αB and strand β7 of MLL3$_{SET}$ substantially (Fig. 5d). This coincides with our observation that the most variable element in apo MLL$_{SET}$ is the αB helix, illustrated by the superimposition of four apo MLL$_{SET}$ structures (Extended Data Fig. 6c). Furthermore, a flexible loop in apo MLL3$_{SET}$ (L$_{6C}$) is induced to form strand β7 by pairing with strand β1 of RBBP5$_{AS}$ (Fig. 5e). Other than the structural variation of individual residues, molecular dynamics simulation also clearly showed that the cross-correlation within the SET-I motif was greatly enhanced upon RBBP5–ASH2L association (Fig. 5f and Extended Data Fig. 6d–f). The reduced flexibility of the SET-I motif may help cofactor binding and

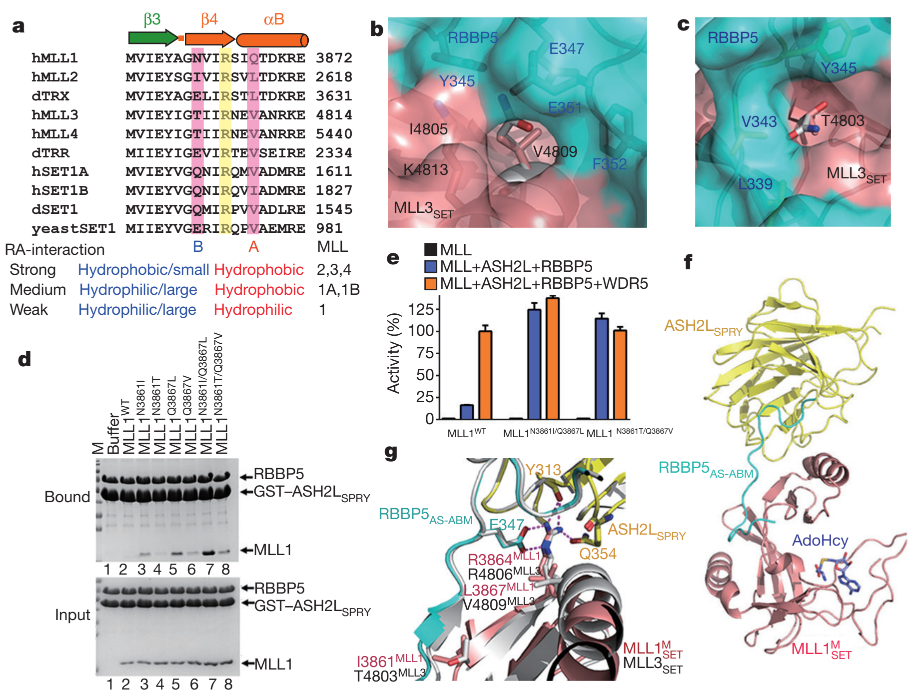

Figure 4 | Difference between MLL1 and other MLL proteins. **a**, Sequence alignment of the RBBP5–ASH2L binding fragments from MLL family proteins. Two key residues that explain the RBBP5–ASH2L binding affinity difference between MLL1 and other MLL proteins are indicated by A and B sites. d, *Drosophila*; h, human. RA denotes RBBP5–ASH2L. **b**, The MLL3–RBBP5 interface around MLL3 Val4809. MLL1 Gln3867 (grey) cannot fit into this pocket. **c**, The MLL3–RBBP5 interface around MLL3 Thr4803, which is not compatible with MLL1 Asn3861 (grey). **d**, GST pull-down assay for the interactions of RBBP5–ASH2L with MLL1$_{SET}$ and its mutants. **e**, The normalized HKMT activities of MLL1^{WT} and MLL1$^{N3861I/Q3867L}$ in the presence of full-length RBBP5–ASH2L and WDR5–RBBP5–ASH2L. Mean ± s.d. ($n = 3$) are shown. **f**, The overall structure of the M1^{M}RA complex. **g**, Superposition of the structures of M1^{M}RA and M3RA shows conserved interfaces between MLL$_{SET}$ and RBBP5–ASH2L.

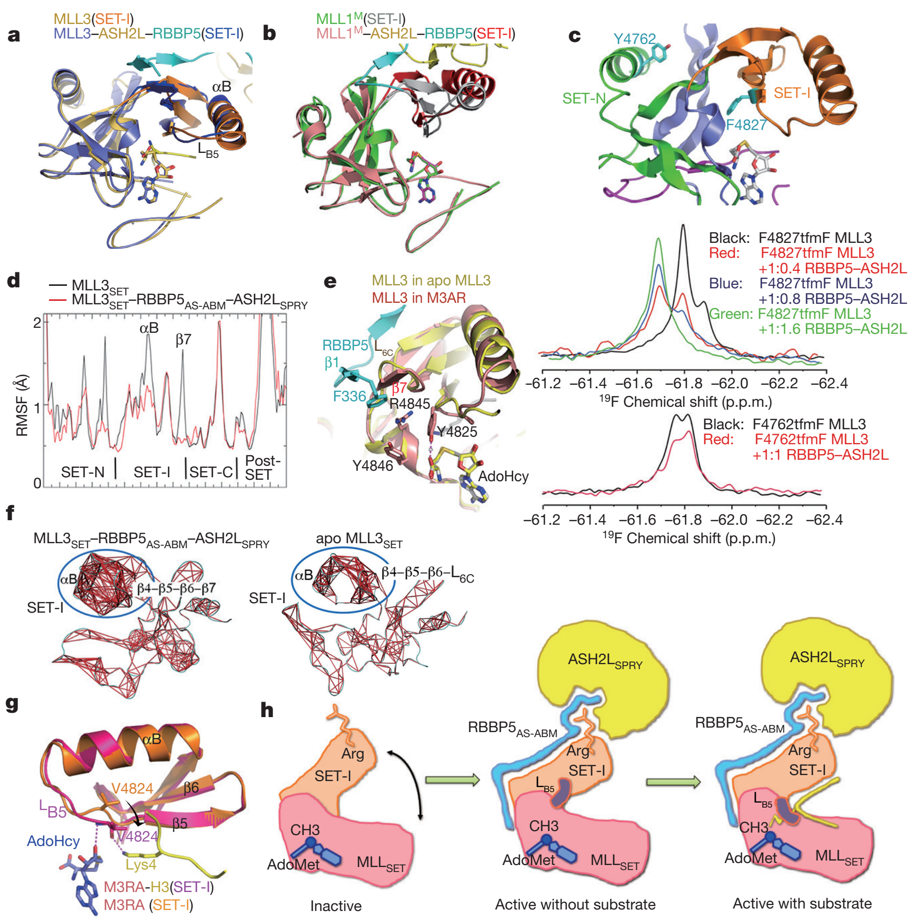

Figure 5 | Activation mechanism of MLL proteins by RBBP5–ASH2L. **a**, Structural comparison of the apo $MLL3_{SET}$ and $MLL3_{SET}$ in the M3RA complex. The structures are superimposed according to AdoHcy. **b**, Structural comparison of the apo $MLL1^{M}_{SET}$ and $MLL1^{M}_{SET}$ in the $M1^{M}RA$ complex. **c**, One-dimensional ^{19}F-NMR measurements of $MLL3_{SET}$ with substitution of F4827tfmF (top) or Y4762tfmF (bottom) in the absence or presence of RBBP5–ASH2L. The locations of these two residues on MLL_{SET} are shown. tfmF, L-4-trifluoromethylphenylalanine. **d**, Root mean square fluctuation (RMSF) of the SET domains in apo $MLL3_{SET}$ (black line) and in the M3RA complex (red line). **e**, RBBP5 Phe336 together with MLL3 Arg4845, Tyr4846 and Tyr4825 maintain a configuration that favours cofactor binding. **f**, The most highly correlated residues (correlation coefficients greater than 0.55) of SET-I in molecular dynamics simulation are indicated by red lines. **g**, Structural superimposition of the M3RA and M3RA–H3 complexes by the SET-I motifs highlights the local rearrangement of loop L_{B5}. **h**, A working model for the activation of MLL family methyltransferases.

substrate recognition. Indeed, isothermal titration calorimetry (ITC) analysis showed that the binding affinities of cofactor to $MLL3_{SET}$ and $MLL1^{M}_{SET}$ are markedly increased in the presence of RBBP5–ASH2L (Extended Data Fig. 7a, b). Furthermore, the association with RBBP5–ASH2L also facilitates MLL3 binding with the H3 substrate peptide (Extended Data Fig. 7c). Notably, Phe336 at the beginning of β1 in $RBBP5_{AS}$ stacks together with the side chains of $MLL3_{SET}/MLL1^{M}_{SET}$ Arg4845/Arg3903, Tyr4846/Phe3904 and Tyr4825/Tyr3883, and the latter makes a direct hydrogen-bonding interaction with AdoHcy (Fig. 5e). Molecular dynamics simulation revealed an obvious stabilizing effect of RBBP5–ASH2L on this network of interactions, which could explain the enhanced cofactor-binding ability for the M3RA complex (Extended Data Fig. 7d). Quantum mechanics/molecular mechanics (QM/MM) investigations further indicated that the presence of RBBP5–ASH2L facilitated the methyl transfer process from the cofactor AdoMet to the target lysine by lowering the energy barrier (Extended Data Fig. 7e). Taken together, we conclude that the RBBP5–ASH2L-induced conformational constraints on the SET-I motif help to stabilize MLL_{SET} in a conformation competent for cofactor binding and substrate recognition.

Structural comparison of the M3RA complex structures with and without the H3 peptide revealed a role of the substrate peptide in further stabilizing the active conformation of $MLL3_{SET}$, which has been observed in other SET-domain methyltranferases[28]. After H3 binding, a marked local structural rearrangement occurs to loop L_{B5} between helix αB and strand β5 in the SET-I motif, leading to the completion of a narrow hydrophobic channel that orients the H3 Lys4 side chain for catalysis (Fig. 5g). Remarkably, the side chain of MLL3 Val4824 shifts ~4.1 Å and rotates ~50° relative to its position in the H3-peptide-free structure, enclosing the target lysine access channel (Extended Data Fig. 7f). Collectively, our studies suggest a novel two-step mechanism for MLL_{SET} activation: interaction with the RBBP5–ASH2L heterodimer reduces the inherent flexibility of MLL_{SET} and favours formation of a catalytically competent conformation; and then H3 substrate binding induces a local conformational change in the SET-I motif of MLL_{SET} to achieve the fully active configuration that facilitates the methyl transfer process (Fig. 5h).

Implications for other methyltransferases

Structural comparison of the $M1^{M}RA$ and M3RA complexes with a large group of SET domain proteins reveals a striking similarity with other intrinsic active methyltransferases. In all SUV39- and SET2-family proteins, a short fragment amino-terminal to the pre-SET region (referred to as the activation segment) interacts with the SET-I motif in the same manner as $RBBP5_{AS}$ binding to $MLL3_{SET}$ (Extended Data Fig. 8a, b). Deletion of this activation segment from DIM-5 did not affect the overall fold of the protein but completely abrogated the HKMT activity of DIM-5, underscoring the importance of this segment in DIM-5 activity regulation (Extended Data Fig. 8c, d). Such an activation segment is also found in the EZH2 complex structure[29], further supporting a conserved activation mechanism for a subset of SET-domain-containing methyltransferases.

In summary, the present structural, biochemical and computational analyses provide new insights into the assembly and regulation mechanism of MLL family complexes. Our results suggest that a minimized RBBP5–ASH2L heterodimer is the structural unit to interact with and activate all MLL family histone methyltransferases. By contrast, WDR5 is not directly involved in the enzymatic stimulation of MLL complexes. WDR5 may serve as a recruitment module or crosstalk mediator to regulate H3K4 methylation *in vivo*[30–34].

Online Content Methods, along with any additional Extended Data display items and Source Data, are available in the online version of the paper; references unique to these sections appear only in the online paper.

Received 27 January; accepted 21 December 2015.
Published online 17 February 2016.

1. Barski, A. *et al.* High-resolution profiling of histone methylations in the human genome. *Cell* **129,** 823–837 (2007).
2. Shilatifard, A. Molecular implementation and physiological roles for histone H3 lysine 4 (H3K4) methylation. *Curr. Opin. Cell Biol.* **20,** 341–348 (2008).
3. Ruthenburg, A. J., Allis, C. D. & Wysocka, J. Methylation of lysine 4 on histone H3: intricacy of writing and reading a single epigenetic mark. *Mol. Cell* **25,** 15–30 (2007).
4. Ansari, K. I. & Mandal, S. S. Mixed lineage leukemia: roles in gene expression, hormone signaling and mRNA processing. *FEBS J.* **277,** 1790–1804 (2010).
5. Wang, P. *et al.* Global analysis of H3K4 methylation defines MLL family member targets and points to a role for MLL1-mediated H3K4 methylation in the regulation of transcriptional initiation by RNA polymerase II. *Mol. Cell. Biol.* **29,** 6074–6085 (2009).
6. Krivtsov, A. V. & Armstrong, S. A. MLL translocations, histone modifications and leukaemia stem-cell development. *Nature Rev. Cancer* **7,** 823–833 (2007).
7. Ansari, K. I., Mishra, B. P. & Mandal, S. S. MLL histone methylases in gene expression, hormone signaling and cell cycle. *Front. Biosci.* **14,** 3483–3495 (2009).
8. Parsons, D. W. *et al.* The genetic landscape of the childhood cancer medulloblastoma. *Science* **331,** 435–439 (2011).
9. Morin, R. D. *et al.* Frequent mutation of histone-modifying genes in non-Hodgkin lymphoma. *Nature* **476,** 298–303 (2011).
10. Li, Y. *et al.* A mutation screen in patients with Kabuki syndrome. *Hum. Genet.* **130,** 715–724 (2011).
11. Pleasance, E. D. *et al.* A small-cell lung cancer genome with complex signatures of tobacco exposure. *Nature* **463,** 184–190 (2010).
12. Dalgliesh, G. L. *et al.* Systematic sequencing of renal carcinoma reveals inactivation of histone modifying genes. *Nature* **463,** 360–363 (2010).
13. Dou, Y. *et al.* Regulation of MLL1 H3K4 methyltransferase activity by its core components. *Nature Struct. Mol. Biol*. **13,** 713–719 (2006).
14. Patel, A., Dharmarajan, V., Vought, V. E. & Cosgrove, M. S. On the mechanism of multiple lysine methylation by the human mixed lineage leukemia protein-1 (MLL1) core complex. *J. Biol. Chem.* **284,** 24242–24256 (2009).
15. Southall, S. M., Wong, P. S., Odho, Z., Roe, S. M. & Wilson, J. R. Structural basis for the requirement of additional factors for MLL1 SET domain activity and recognition of epigenetic marks. *Mol. Cell* **33,** 181–191 (2009).
16. Steward, M. M. *et al.* Molecular regulation of H3K4 trimethylation by ASH2L, a shared subunit of MLL complexes. *Nature Struct. Mol. Biol*. **13,** 852–854 (2006).
17. Dou, Y. & Hess, J. L. Mechanisms of transcriptional regulation by MLL and its disruption in acute leukemia. *Int. J. Hematol.* **87,** 10–18 (2008).
18. Wysocka, J. *et al.* WDR5 associates with histone H3 methylated at K4 and is essential for H3 K4 methylation and vertebrate development. *Cell* **121,** 859–872 (2005).
19. Cao, F. *et al.* An Ash2L/RbBP5 heterodimer stimulates the MLL1 methyltransferase activity through coordinated substrate interactions with the MLL1 SET domain. *PLoS ONE* **5,** e14102 (2010).
20. Shinsky, S. A., Monteith, K. E., Viggiano, S. & Cosgrove, M. S. Biochemical reconstitution and phylogenetic comparison of human SET1 family core complexes involved in histone methylation. *J. Biol. Chem.* **290,** 6361–6375 (2015).
21. Shinsky, S. A. & Cosgrove, M. S. Unique role of the WD-40 repeat protein 5 (WDR5) subunit within the mixed lineage leukemia 3 (MLL3) histone methyltransferase complex. *J. Biol. Chem.* **290,** 25819–25833 (2015).
22. Zhang, P., Lee, H., Brunzelle, J. S. & Couture, J. F. The plasticity of WDR5 peptide-binding cleft enables the binding of the SET1 family of histone methyltransferases. *Nucleic Acids Res.* **40,** 4237–4246 (2012).
23. Zhang, P. *et al.* A phosphorylation switch on RBBP5 regulates histone H3 Lys4 methylation. *Genes Dev.* **29,** 123–128 (2015).
24. Chen, Y., Cao, F., Wan, B., Dou, Y. & Lei, M. Structure of the SPRY domain of human Ash2L and its interactions with RbBP5 and DPY30. *Cell Res.* **22,** 598–602 (2012).
25. Odho, Z., Southall, S. M. & Wilson, J. R. Characterization of a novel WDR5-binding site that recruits RbBP5 through a conserved motif to enhance methylation of histone H3 lysine 4 by mixed lineage leukemia protein-1. *J. Biol. Chem.* **285,** 32967–32976 (2010).
26. Zhang, Y. *et al.* evolving catalytic properties of the MLL family set domain. *Structure* **23,** 1921–1933 (2015).
27. Cheng, X., Collins, R. E. & Zhang, X. Structural and sequence motifs of protein (histone) methylation enzymes. *Annu. Rev. Biophys. Biomol. Struct.* **34,** 267–294 (2005).
28. Zhang, X. *et al.* Structural basis for the product specificity of histone lysine methyltransferases. *Mol. Cell* **12,** 177–185 (2003).
29. Sirinupong, N., Brunzelle, J., Doko, E. & Yang, Z. Structural insights into the autoinhibition and posttranslational activation of histone methyltransferase SmyD3. *J. Mol. Biol.* **406,** 149–159 (2011).
30. Wang, K. C. *et al.* A long noncoding RNA maintains active chromatin to coordinate homeotic gene expression. *Nature* **472,** 120–124 (2011).
31. Ang, Y. S. *et al.* Wdr5 mediates self-renewal and reprogramming via the embryonic stem cell core transcriptional network. *Cell* **145,** 183–197 (2011).
32. Gan, Q. *et al.* WD repeat-containing protein 5, a ubiquitously expressed histone methyltransferase adaptor protein, regulates smooth muscle cell-selective gene activation through interaction with pituitary homeobox 2. *J. Biol. Chem.* **286,** 21853–21864 (2011).
33. Dou, Y. *et al.* Physical association and coordinate function of the H3 K4 methyltransferase MLL1 and the H4 K16 acetyltransferase MOF. *Cell* **121,** 873–885 (2005).
34. Thompson, B. A., Tremblay, V., Lin, G. & Bochar, D. A. CHD8 is an ATP-dependent chromatin remodeling factor that regulates β-catenin target genes. *Mol. Cell. Biol.* **28,** 3894–3904 (2008).

Supplementary Information is available in the online version of the paper.

Acknowledgements We thank staffs of beamlines BL18U, BL19U1 and 17U at the National Center for Protein Sciences Shanghai and Shanghai Synchrotron Radiation Facility for their assistance in data collection. We are grateful to protein expression, protein purification and mass spectrometry facilities at the National Center for Protein Sciences Shanghai for their instrument support and technical assistance. This work was supported by grants from the Strategic Priority Research Program of the Chinese Academy of Sciences (XDB08010201 to M.L. and Y.C., XDB08030302 to C.T.), the Ministry of Science and Technology of China (2013CB910402 to M.L., 2013CB910401 to Y.C., 2012AA01A305 and 2012CB721002 to G.L., 2011CB910400 to C.T.), the National Science and Technology Major Project 'Key New Drug Creation and Manufacturing Program' of China (2014ZX09507002-005 to M.L.), the National Natural Science Foundation of China (31330040 to M.L., 31470737 to Y.C. ,and 91430110 to G.L.), the Basic Research Project of Shanghai Science and Technology Commission (14JC1407200 to Y.C.), the National Institutes of Health (R01 GM082856 to Y.D.), and Fundamental Research for the Central University (WK2340000064 to C.T.). Y.C. is a recipient of the Thousand Young Talents Program of the Chinese government.

Author Contributions M.L. and Y.C. conceived and supervised the project. M.L. and Y.D. initiated the project. Y.L., J.H., C.H. and Y.C. purified the proteins, performed crystallization and determined the crystal structure. Y.L., J.H., F.C., C.H., J.W., Y.W. and Y.C. performed the biochemical assays. Z.L., P.S. and C.T. performed ^{19}F-NMR experiments. S.L. and J.Z. performed normal mode analysis. Y.Z., L.C. and G.L. performed molecular dynamics and QM/MM simulation. D.L. and Y.D. contributed to manuscript preparation. G.L., Y.C. and M.L. analysed the data and wrote the manuscript.

Author Information The atomic coordinates have been deposited in the Protein Data Bank (PDB) under the following accessions: 5F59 (MLL3$_{SET}$), 5F6K (MLL3$_{SET}$–RBBP5$_{AS\text{-}ABM}$–ASH2L$_{SPRY}$), 5F5E (MLL1$_{SET}^{N3861I/Q3867L}$) and 5F6L (MLL1$_{SET}^{N3861I/Q3867L}$–RBBP5$_{AS\text{-}ABM}$–ASH2L$_{SPRY}$). Reprints and permissions information is available at www.nature.com/reprints. The authors declare no competing financial interests. Readers are welcome to comment on the online version of the paper. Correspondence and requests for materials should be addressed to M.L. (leim@sibcb.ac.cn), Y.C. (yongchen@sibcb.ac.cn) or G.L. (ghli@dicp.ac.cn).

METHODS

No statistical methods were used to predetermine sample size.

Protein expression and purification. The SET domains of MLL family proteins (with or without the WIN motif), RBBP5, ASH2L, WDR5 and their truncations or mutants were purified as described before[19]. *Escherichia coli* Rosetta cells bearing expression plasmids were induced for 16 h with 0.1 mM IPTG at 18 °C, and the cells were collected by centrifugation. For MLL expression, 10 μM $ZnSO_4$ was included in the media. The cell pellets were resuspended in lysis buffer (50 mM Tris-HCl, pH 8.0, 400 mM NaCl, 10% glycerol, 2 mM 2-mercaptoethanol, and home-made protease inhibitor cocktail). The cells were broken by sonication and cleared by ultracentrifugation at 100,000*g* for 30 min. The proteins were purified using Ni-NTA agarose beads (Qiagen) for His-tagged proteins or Glutathione Sepharose 4B beads (GE) for GST-tagged proteins, followed by enzyme digestion to remove the tags and gel-filtration chromatography. MLL_{SET}, $ASH2L_{SPRY}$, WDR5 and RBBP5 fragments were separated on Hiload Superdex 75, while full-length proteins of ASH2L and RBBP5 were separated on Hiload Superdex 200. The buffer for gel-filtration chromatography contains 25 mM Tris-HCl, pH 8.0, 150 mM NaCl except for MLL_{SET} (which is in buffer 50 mM Tris-HCl, 300 mM NaCl and 10% glycerol, pH 8.0). The purified proteins were concentrated to 10–20 mg ml^{-1} and store at −80 °C. RBBP5 peptides were separated on Hiload Superdex 75 after tag digestion in buffer (100 mM NH_4HCO_3) and the peptide-containing fractions were lyophilized. The MLL_{SET}–$RBBP5_{AS\text{-}ABM}$–$ASH2L_{SPRY}$ complex was obtained by step-wise gel-filtration chromatography; binary complex of $RBBP5_{AS\text{-}ABM}$–$ASH2L_{SPRY}$ was first purified, and then mixed with $MLL1^{M}_{SET}$ or $MLL3_{SET}$, followed by separation on Hiload Superdex 75. Mutations were introduced by PCR-based site-directed mutagenesis, and mutated proteins were purified using the same protocol as described above.

Crystallization, data collection and structural determination. For structural studies, more than 50 different combinations of numerous RBBP5 fragments, $ASH2L_{SPRY}$ constructs, and SET domains from different MLL proteins were tested for crystallization. $MLL3_{SET}$ was crystallized in 100 mM Tris-HCl, pH 8.5, 3 M NaCl at 4 °C in the presence of 1 mM AdoHcy. Zinc single-wavelength anomalous dispersion (SAD) and native data sets of $MLL3_{SET}$ were collected at SSRF (Shanghai Synchrotron Radiation Facility in China) beamline BL17U at wavelengths of 1.2818 Å and 0.9793 Å, respectively. Data were indexed, integrated, and scaled using program HKL2000 (ref. 35). Crystals belong to space group $P4_132$ and contain one $MLL3_{SET}$ per asymmetric unit. Zinc SAD phase determination, density modification and automatic model building were carried out using SHARP[36]. The initial model was further refined using the native data set diffracted at 2.8 Å. After several rounds of refinement in PHENIX package[37] with manual rebuilding in COOT[38], the final model has good stereochemistry with an R value of 18.0% and an R_{free} of 22.9%.

The $MLL3_{SET}$–$ASH2L_{SPRY}$–$RBBP5_{AS\text{-}ABM}$ complex was crystallized in 100 mM sodium cacodylate, pH 6.5, 10% PEG-3350, 0.1 M $MgCl_2$ at 4 °C in the presence of 1 mM AdoHcy. The co-crystal with H3 peptide (ARTKQTARK) was obtained by soaking crystals in reservoir solution with 1 mM H3 peptide for 2 h before collection. A data set of 2.4 Å resolution was collected at Advanced Photon Source beamline 21ID-D at wavelength of 1.1272 Å. The crystal belongs to space group $P2_12_12$ with cell dimension $a = 80.342$ Å, $b = 236.076$ Å, $c = 44.416$ Å. The complex structure was solved by molecular replacement using PHASER[39] with $ASH2L_{SPRY}$ structure (PDB accession 3TOJ) and the MLL3 structure SET-N, SET-I, and SET-C motifs as search models. There are two $MLL3_{SET}$–$ASH2L_{SPRY}$–$RBBP5_{AS\text{-}ABM}$ complexes in one asymmetrical unit, and we can only observed H3 peptide in the density map of one complex. The model was further refined using PHENIX with manually rebuilding in COOT.

$MLL1^{N3861I/Q3867L}_{SET}$ crystals were grown by sitting drop vapour diffusion method at 4 °C in a solution containing 35% (v/v) tacsimate, pH 7.0, in the presence of 2 mM AdoHcy, and the crystals were cryo-protected in the same reservoir solution supplemented with 20% glycerol. Data sets were screened and collected at SSRF BL18U and BL19U. The structures were solved by molecular replacement (starting model PDB accession 2W5Y). The $MLL1^{N3861I/Q3867L}_{SET}$–$ASH2L_{SPRY}$–$RBBP5_{AS\text{-}ABM}$ complex was crystallized at 200 mM NaCl, 20% PEG3350 in the presence of 2 mM AdoHcy. A data set of 1.9 Å resolution was collected at SSRF BL17U at wavelength of 0.9792 Å. The structures were solved by molecular replacement and further refined with PHENIX. All structure figures were generated using PyMOL (The PyMOL Molecular Graphics System, version 1.4.1 Schrödinger, LLC.).

Histone methyltransferase assay. *In vitro* methyltransferase assays were performed using an H3 peptide as the substrate. Two assay systems were used. The first one is the ^{3}H-methyl-incorporation assay that measured the incorporation of ^{3}H from [^{3}H]AdoMet (*S*-adenosyl-L-[methyl-^{3}H]-methionine) into the H3 peptide (9 mer: ARTKQTARK). Reactions were carried out at 22 °C for 1 h in the buffer containing 20 mM HEPES, pH 7.8, 5% glycerol, 5 mM dithiothreitol (DTT), 0.5 mM EDTA, 1 μCi [^{3}H]AdoMet as previously described[19]. Unmodified H3 K4 peptides (0.25 mM) and 1 μM of WDR5, RBBP5, ASH2L and MLL proteins were used, except for SET1A (5 μM). For all activity assays, full-length WDR5, RBBP5 and ASH2L were used unless stated otherwise. MLL constructs containing both the WIN motif and SET domain were used. Each assay was performed in triplicate, and the mean ± s.d. was reported. The second assay system is to monitor the methylation kinetics of the H3 peptide substrate using MALDI–TOF (matrix-assisted laser desorption ionization–time-of-flight) mass spectrometry.

Mass spectrometry analysis of the methylation process. Methylation reactions were carried out in 20 mM HEPES, pH 7.8, 10 mM NaCl, 5 mM DTT, 250 μM AdoMet, 10 μM histone peptide (ARTKQTARKS) and 1 μM MLL complexes at 22 °C. The reaction was quenched at different time points by addition of trifluoroacetate (TFA) to 0.5%. Reaction mixture was diluted in 10 mg ml^{-1} CHCA (α-cyano-4-hydroxycinnamic acid) matrix and was spotted onto sample plate and air-dried. The molecular mass was measure by MALDI–TOF (AB SCIEX TOF/TOF 5800) operated in reflectron mode. Final spectra were the average of 200 shots per position at 200 different positions chosen randomly on each spot. To estimate the pseudo-first-order rate constants, we fit the decrease in the relative intensity of the unmodified peptide over time using a model for a single irreversible reaction $[\mathrm{Lys4}]_t = [\mathrm{Lys4}]_0 e^{-kt}$, in which $[\mathrm{Lys4}]_0$ is the initial concentration of the unmodified peptide, $[\mathrm{Lys4}]_t$ represents the concentrations of the unmodified peptide at time t and k is the pseudo-first-rate constant.

GST pull-down assays. GST-fusion proteins and interacting partners were incubated with glutathione Sepharose 4B beads for 2 h at 4 °C in 100 μl buffer (50 mM Tris-HCl, 300 mM NaCl and 2 mM DTT, pH 8.0). After extensive wash with the same buffer, the bound proteins were eluted in elution buffer (50 mM Tris-HCl, pH 8.0, 300 mM NaCl and 15 mM reduced glutathione). The input samples and eluted samples were visualized on 12% SDS–PAGE by Coomassie blue staining. Initially, different pull-down buffers were tested and it was found that the interaction between ASH2L and RBBP5 could be disrupted by high ionic strength used in the pull-down assay, whereas the formation of the MLL–RBBP5–ASH2L trimeric complex is relatively insensitive to salt concentration. Thus, in most pull-down assays, buffer with 300 mM NaCl was chosen to assure undisrupted RBBP5–ASH2L interaction and also keep protein stable through pull-down experiments unless stated otherwise.

Isothermal titration calorimetry. The equilibrium dissociation constants of cofactor binding to MLL_{SET} or MLL_{SET}–$RBBP5_{AS\text{-}ABM}$–$ASH2L_{SPRY}$ were determined by an ITC200 calorimeter (GE healthcare). The binding of proteins (20–200 μM) and cofactor AdoMet (0.5–2mM) were measure in the 25 mM Tris-HCl, pH 8.0, 300 mM NaCl at 20 °C. ITC data were analysed and fit using Origin 7 (OriginLab) using one-site model. Owing to instability of apo MLL protein during ITC experiments, curve fitting errors for apo MLL titration are relatively large, so the binding parameters of apo MLL proteins are rough estimations.

Fluorescence polarization assay. Different MLL proteins were diluted in 20 mM HEPES, pH 7.8, 150 mM NaCl, 10% glycerol, 0.5 mg ml^{-1} BSA to a serial of concentrations from 25 nM to 50 μM. The FAM-labelled RBBP5 peptide (residues 330–363) was mixed with $ASH2L_{SPRY}$ and used at a final concentration of 100 nM. The final volume was brought up to 100 μl with dilution buffer (20 mM HEPES, pH 7.8, 150 mM NaCl, 10% glycerol and 0.5 mg ml^{-1} BSA) and incubated in dark for 30 min. The fluorescence polarization values were measured using Synergy Neo Multi-Mode Reader (Bio-Tek) at 27 °C. Excitation wavelength was 485 nm and emission was detected at 528 nm. Fluorescence was quantitated with GEN 5 software and date was analysed with Prism 6. For MLL1, SET1A and SET1B, the binding is not saturated even at the highest protein concentration, so the calculated K_d should be an estimated lower limit of K_d value.

^{19}F-NMR spectra measurements. Expression of ^{19}F-labelled proteins was achieved by an established protocol by incorporation of non-natural amino acid tfmF (L-4-trifluoromethylphenylalanine) into specific sites using genetic code TAG[40]. The ^{19}F-labelled $MLL3_{SET}$ proteins were purified using the same protocol as for wild-type $MLL3_{SET}$ protein. The ^{19}F-NMR spectra were obtained on a Bruker DMX Avance-500 MHz spectrometer equipped with a 5 mM PABBO room temperature probe. The spectra of 0.3 mM MLL3 F4827tfmF or 0.35 mM $MLL3_{SET}$ Y4762tfmF with or without RBBP5–ASH2L were collected at 293 K. The observation channel was tuned to ^{19}F (470.54 MHz), with 512 free induction decay accumulations in every 3-s recycling delay. Each one-dimensional ^{19}F-spectrum was acquired with a standard pulse program with a 90° pulse width of 16.75 μs and power at 35.9 W. ^{19}F-chemical shifts were referenced to an external standard TFA. The free induction decay accumulations, which consisted of 20,480 complex points, was linear predicted to 40,560 points, backward linear predicated three points, and apodized with 20 Hz Lorentzian filter. All spectral processing was performed with Topspin 3.2 software.

Normal mode analysis. Normal modes were calculated using the NOMAD-Ref method[41]. For all $MLL3_{SET}$, $MLL1^{M}_{SET}$, M3RA and $M1^{M}RA$ structures, default

parameters in the method were used, including the analysis of 'all atoms', 'default distance weight parameters for elastic constant' of 5.0 Å, 'ENM cutoff values' of 1 Å, 'average RMSD in output trajectories' of 1.0 Å and 'output' of the lowest 16 modes. The first six trivial normal modes are discarded because they represent only translation and rotation. The motion patterns under certain mode and angle monitoring were achieved by using PyMOL.

Molecular dynamics simulation. To delineate how RBBP5–ASH2L modulates the dynamic behaviour of MLL_{SET} domain, we performed molecular dynamic simulations (100 ns) of $MLL3_{SET}$ and $MLL1_{SET}$ in the presence or absence of RBBP5–ASH2L, respectively. The complex structure of MLL_{SET} with RBBP5–ASH2L were centred into a $115 \times 115 \times 115$ Å^3 cubic box and dissolved with TIP3P waters. 0.1 M NaCl ions were used to neutralize the net charge of the system. While for the systems of MLL_{SET} alone, we just removed the RBBP5–ASH2L from the complex to make sure the identical conformations of MLL_{SET} before performing molecular dynamics simulations. The same procedures were used in setting up the MLL_{SET} domains without RBBP5–ASH2L except for a smaller cubic box ($83 \times 83 \times 83$ Å^3). All molecular dynamics simulations were performed using Gromacs 5.0.4 with Charmm36 force field. After the energy minimization of the whole system using the steepest descent algorithm, we first gradually heated the system to 300 K under NVT condition. Then we equilibrated the solvent and ions around the protein using NPT ensemble. In the equilibrations, the backbone of the protein was constrained with a harmonic potential of 1,000 kJ mol^{-1}. The leap-frog integrator was used with an integration time-step of 2 fs. The Berendsen barostat was used to control the pressure at 1 bar with a coupling constant of 2 ps and the modified Berendsen (V-rescale) thermostat was employed to control the temperature of the systems at 300 K with a time constant of 0.1 ps. The Particle Mesh Ewald method was used to compute the electrostatic interactions with a real-space cut-off distance of 1 nm. The same cutoff value was chosen for treating the van der Waals interactions. After a 5 ns equilibration, we conducted the production molecular dynamics by changing the pressure and the thermostat coupling to Parrinello–Rahman and Nose–Hoover with coupling constants of 5 ps and 1 ps, respectively.

The dynamical network analysis of $MLL3_{SET}$ and MLL^{M}_{SET} were performed using networkSetup in VMD. Cα atoms of MLL_{SET} were defined as the node domains and the dynamical contact was drawn if two nodes were within a cutoff distance of 4.5 Å for at least 75% of the molecular dynamics trajectory. The cross correlation data were also calculated to weight edges in the dynamical network. The edge distances d_{ij}, which define the probability of information transfer across a given edge: $d_{ij} = -\log(|C_{ij}|)$, were derived from pairwise correlations (C_{ij}) using program Carma.

To investigate how RBBP5–ASH2L affects methyl transfer process from the cofactor AdoMet to the target lysine of the H3 substrate, we performed QM/MM simulations to calculate the potentials of mean force for the methyl transfer reaction along the reaction coordinate (RC) of $r(C_M - S_\delta) - r(C_M - N_{\eta 1})$. Initial structures of the QM/MM simulations were derived from the snapshots of molecular dynamics trajectories in the presence of AdoMet and H3 substrates, simultaneously. Then each structure was solvated in an equilibrated 25 Å spherical water box represented by the TIP3P water model. The water box was centred at the centre of mass of the target lysine residue accepting the methyl group. In total, 20 atoms were selected as the QM zone, including the sulfur atom and the to-be-transferred methyl group on the peptide as well as the lysine residue. The simulation was performed in NVT ensemble at 300 K. The hybrid QM/MM method was used in the simulation. QM interactions are calculated using semi-empirical AM1 method and three GHO atoms (C4′ and CB, which connect the sulfur atom to the other two methyl group, and CD of the lysine residue) were selected as the boundary between QM and MM regions. The solvent boundary potential was treated by the generalized solvent boundary potential method and all atoms out of the water box were fixed. The umbrella sampling method was used to model the reaction process, with the reaction coordinate set as the difference between the sulfur atom on the peptide and the nitrogen atom on the QM lysine. The whole reaction process was distributed into 46 windows and the corresponding reaction coordinate ranged from −1.5 to 2.0 Å with an interval of 0.1 Å. Systems were restrained to each window with a force constant of 500 kcal mol^{-1} Å^{-2}.

35. Otwinowski, Z. & Minor, W. Processing of X-ray diffraction data collected in oscillation mode. *Methods Enzymol.* **276,** 307–326 (1997).
36. Vonrhein, C., Blanc, E., Roversi, P. & Bricogne, G. Automated structure solution with autoSHARP. *Methods Mol. Biol.* **364,** 215–230 (2007).
37. Adams, P. D. *et al.* PHENIX: building new software for automated crystallographic structure determination. *Acta Crystallogr. D* **58,** 1948–1954 (2002).
38. Emsley, P. & Cowtan, K. Coot: model-building tools for molecular graphics. *Acta Crystallogr. D* **60,** 2126–2132 (2004).
39. Storoni, L. C., McCoy, A. J. & Read, R. J. Likelihood-enhanced fast rotation functions. *Acta Crystallogr. D* **60,** 432–438 (2004).
40. Shi, P. *et al.* Site-specific ^{19}F NMR chemical shift and side chain relaxation analysis of a membrane protein labeled with an unnatural amino acid. *Protein Sci.* **20,** 224–228 (2011).
41. Lindahl, E., Azuara, C., Koehl, P. & Delarue, M. NOMAD-Ref: visualization, deformation and refinement of macromolecular structures based on all-atom normal mode analysis. *Nucleic Acids Res.* **34,** W52–W56 (2006).

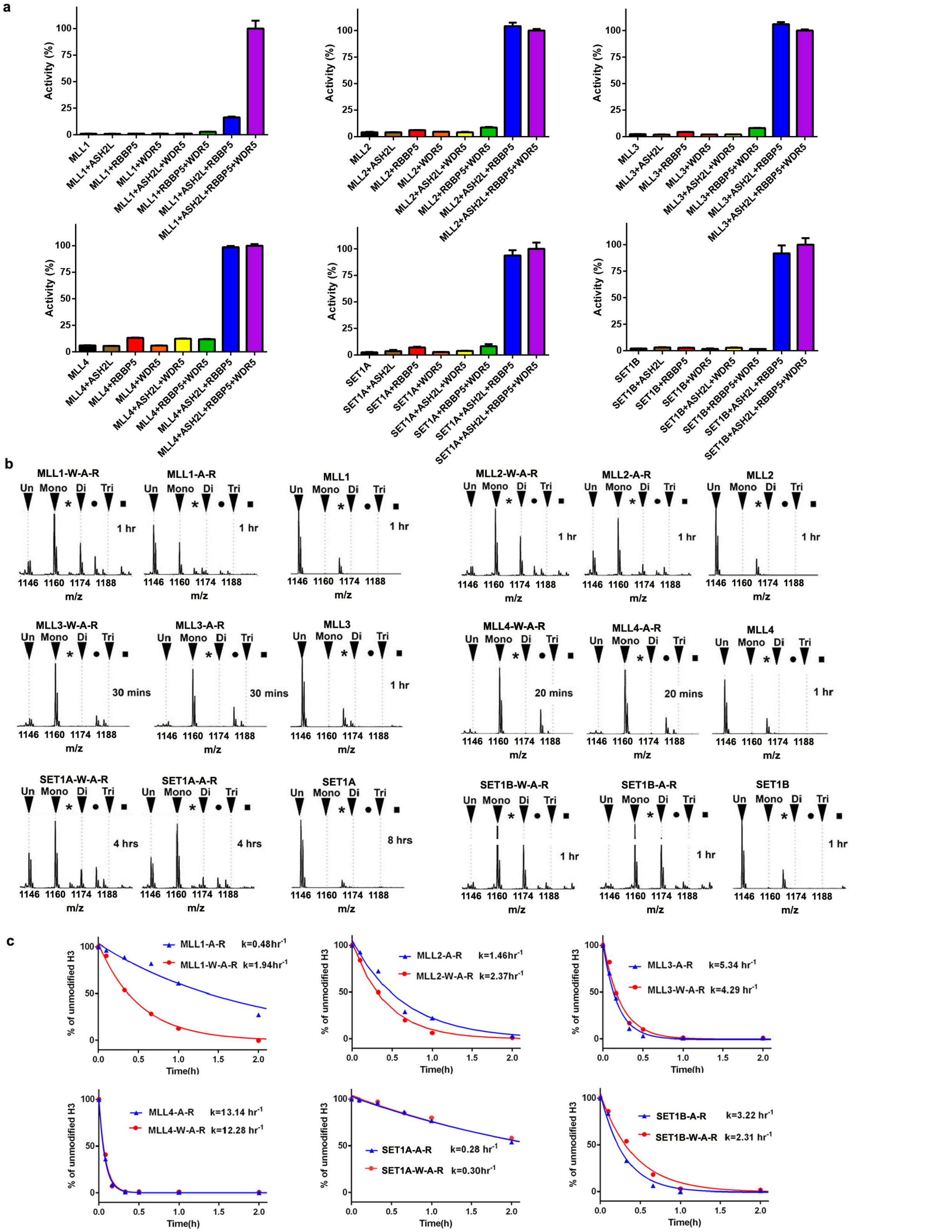

Extended Data Figure 1 | Methyltransferase activity of MLL1–MLL4, SET1A and SET1B with the different combinations of WDR5, RBBP5 and ASH2L. a, HKMT activities determined by the ^{3}H-methyl-incorporation assay. MLL constructs were chosen to contain both the WIN motif and the SET domain. Full-length WDR5, RBBP5 and ASH2L were used. The HKMT activities are normalized to the activity of the MLL–WDR5–RBBP5–ASH2L complexes setting at 100%. Mean ± s.d. ($n=3$) are shown. **b**, Representative MALDI–TOF spectra at different time points for MLL complexes and apo MLL proteins clearly revealed that MLL complexes have much higher HKMT activities than apo MLL proteins. The peaks for unmodified (un) and mono-, di- and tri-methylated products are labelled. The minor peaks are sodium adducts of major peaks (+22 Da). Asterisks denote the adduct of un-peaks; filled circles denote the adduct of mono-peaks; and filled squares denote the adduct of di-peaks. **c**, Comparison of the overall rates of the methylation reactions catalysed by different MLL proteins in the presence of WDR5–ASH2L–RBBP5 or ASH2L–RBBP5. The overall rates were derived by fitting the decrease in the relative intensity of the unmodified H3 peptide peaks in MALDI–TOF mass spectra using one-phase exponential decay model $[\mathrm{Lys4}]_t = [\mathrm{Lys4}]_0 e^{-kt}$.

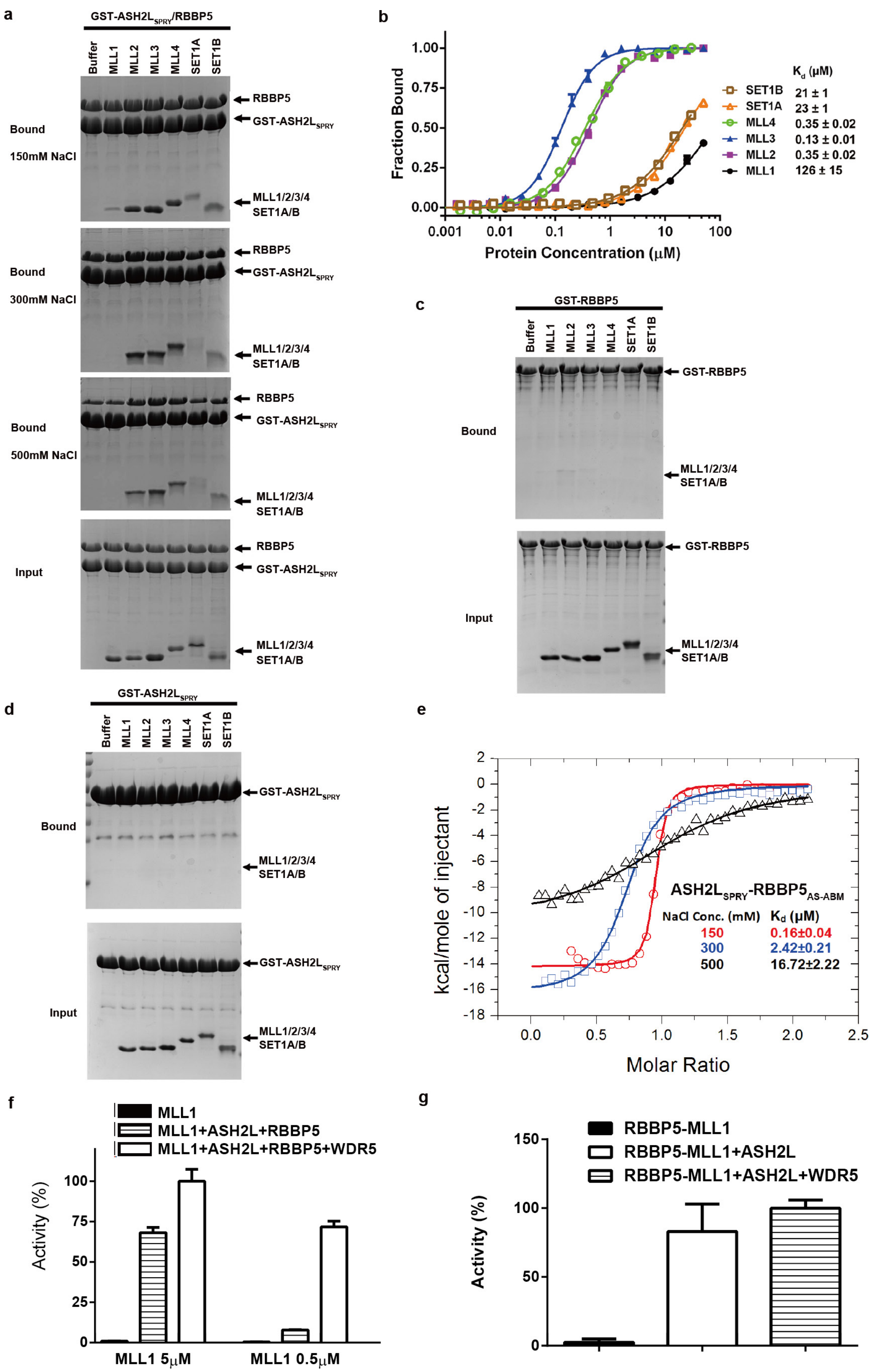

Extended Data Figure 2 | See next page for figure caption.

Extended Data Figure 2 | Interactions between MLL proteins and RBBP5–ASH2L. a, GST pull-down assays showed direct interactions between MLL proteins and RBBP5–ASH2L. ASH2L C-terminal SPRY domain has been previously shown to interact with RBBP5. GST-fused $ASH2L_{SPRY}$ was incubated with full-length RBBP5 and different MLL_{SET} proteins in the GST pull-down assay. Bound proteins were eluted and separated by SDS–PAGE. Three different salt concentration buffers were tested. **b**, Fluorescence polarization assay shows that MLL proteins can interact with $RBBP5_{AS\text{-}ABM}$–$ASH2L_{SPRY}$ with different affinities. For MLL1, SET1A and SET1B, lower limits of the K_d values are reported because saturation of the binding could not be achieved in fluorescence polarization assays. **c**, GST–RBBP5 alone cannot pull down MLL proteins in the buffer with 300 mM NaCl. **d**, GST–$ASH2L_{SPRY}$ alone cannot pull down MLL proteins in the buffer with 300 mM NaCl. **e**, The RBBP5–ASH2L interaction is highly dependent on the salt concentration used in the assay. ITC measurements were carried out using $ASH2L_{SPRY}$ and $RBBP5_{AS\text{-}ABM}$ under buffer conditions with different salt concentrations. **f**, The requirement of WDR5 in methyltransferase activity of the MLL1 complex is sensitive to protein concentration. MLL1 (5 μM) could be markedly stimulated by equal amounts of ASH2L–RBBP5, and WDR5 had a minor stimulation effect. **g**, HKMT activities of RBBP5–MLL1 fusion proteins in the presence of ASH2L or ASH2L and WDR5. Full-length RBBP5 was fused to MLL1 (residues 3754–3969) with a GGSGGS linker. The addition of ASH2L substantially stimulated the HKMT activity of the RBBP5–MLL1 fusion protein, while further addition of WDR5 only had a marginal effect.

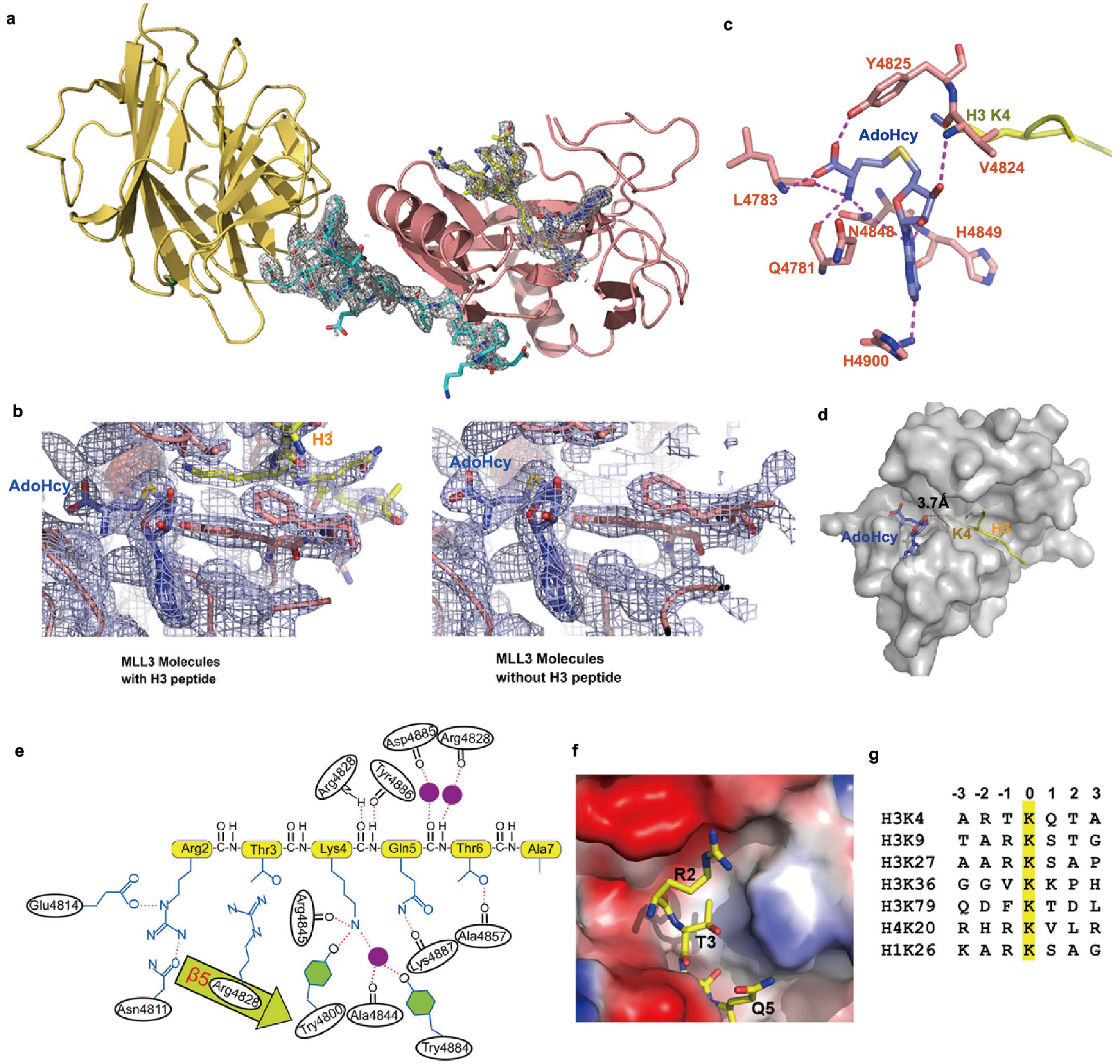

Extended Data Figure 3 | The overall structure of the MLL3$_{SET}$–RBBP5$_{AS\text{-}ABM}$–ASH2L$_{SPRY}$–H3 complex. **a**, The overall structure of the MLL3$_{SET}$–RBBP5$_{AS\text{-}ABM}$–ASH2L$_{SPRY}$–H3 complex in cartoon diagram. ASH2L is in yellow-orange, RBBP5 in cyan, MLL3$_{SET}$ in salmon, the H3 peptide in yellow, and cofactor product (AdoHcy) in blue. The electron density ($2F_o - F_c$) map, contoured at 1σ, is shown for the RBBP5 fragment, the H3 peptide and AdoHcy. **b**, The electron density ($2F_o - F_c$) map, contoured at 1σ, is shown around the substrate-binding channel. There are two complexes in one asymmetric unit. One complex has clear electron density for H3 residues 2–7 (left), while the other exhibits no extra density in the substrate channel (right). **c**, Cofactor interaction network. Residues important for the AdoHcy–MLL3$_{SET}$ interaction are shown in stick models. Hydrogen bonds are indicated by dashed magenta lines. **d**, The space-filling model of MLL3$_{SET}$ shows that AdoHcy and H3 bind to the opposite surfaces on MLL3$_{SET}$. The distance between the sulfur atom and ε-amine of Lys4 is shown. **e**, The binding interface between MLL3$_{SET}$ and H3. **f**, MLL3$_{SET}$ is in surface representation and coloured according to its electrostatic potential. Thr3 of H3 sits snugly on a shallow hydrophobic depression, which cannot accommodate residues with a large side chain. Arg2 is involved in electrostatic interactions with MLL3$_{SET}$. **g**, Sequence alignment of histone methylation sites. Residues are numbered relative to the target lysine. Because only the Lys4 site of H3 contains a large basic residue and a small residue occupying the −2 and −1 positions respectively, Arg(−2) and Thr(−1) define the substrate specificity of MLL complexes.

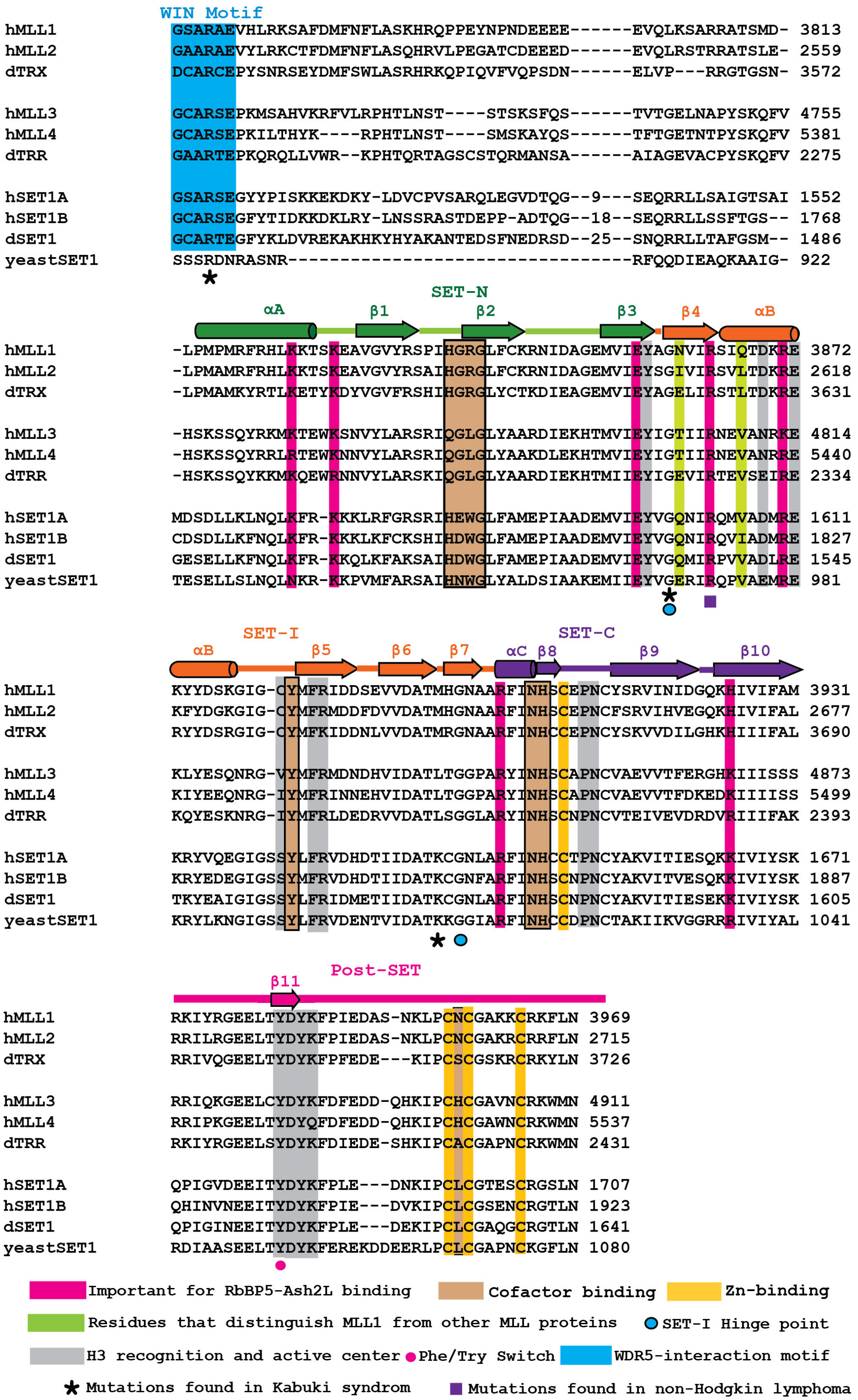

Extended Data Figure 4 | Sequence alignment of MLL homologues from human, *Drosophila* and *Saccharomyces cerevisiae*. The WDR5-interacting motif (WIN) and SET domain are aligned. Secondary structure assignments based on the MLL3 structure are shown as cylinders (α-helices) and arrows (β-strands) above the sequences. The WIN motif is coloured in blue, SET-N in green, SET-I in orange, SET-C in purple and post-SET in magenta. Conserved residues important for RBBP5–ASH2L interactions are highlighted in magenta. Four Zn-binding cysteine residues are highlighted in pale yellow. Residues important for cofactor binding are in brown; residues important for substrate H3 binding and maintenance of the active centre are in grey. Two glycine residues, which serve as the hinge for SET-I motif rotation, are indicated by blue dots. The residues with the corresponding MLL4 mutations found in Kabuki syndrome and non-Hodgkin lymphoma are indicated by stars.

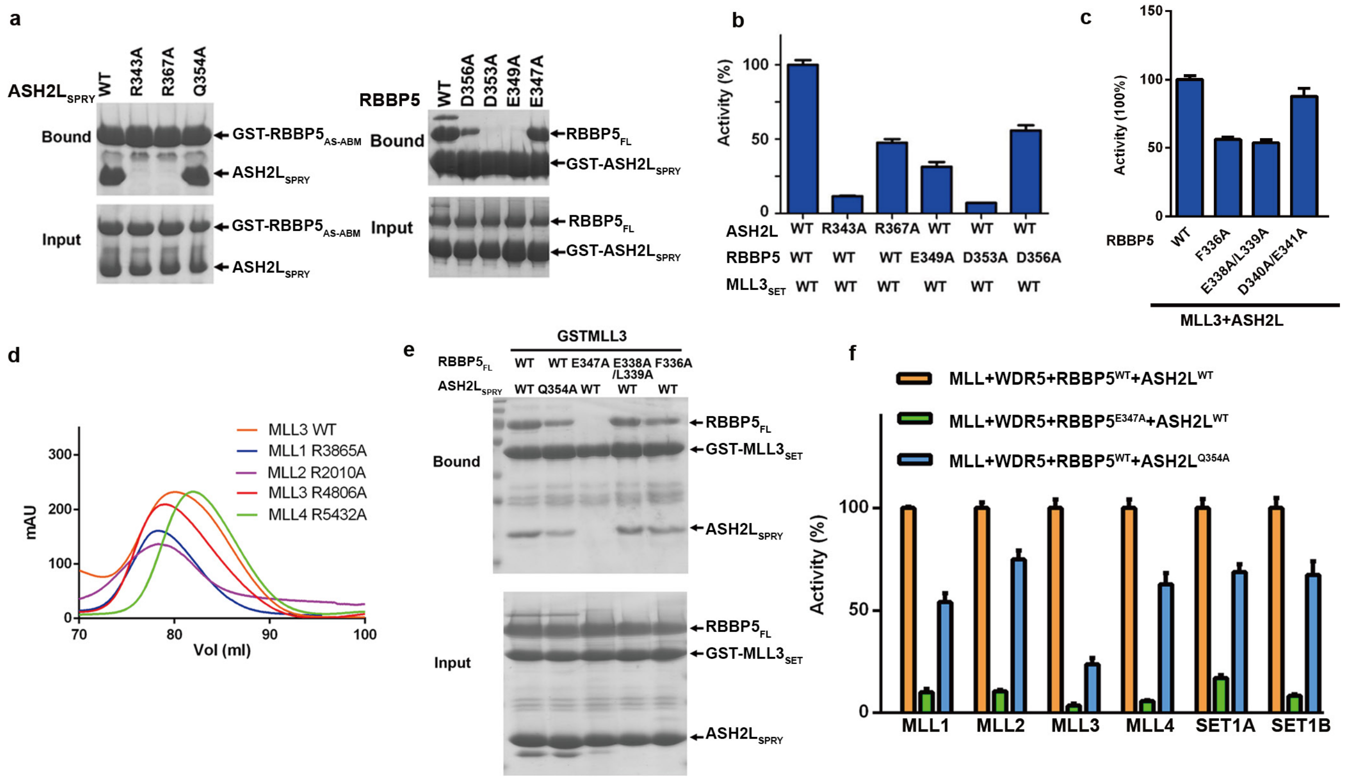

Extended Data Figure 5 | The ternary interaction interface among MLL, RBBP5 and ASH2L. **a**, Mutations of RBBP5 and ASH2L disrupted the interaction between ASH2L$_{SPRY}$ and RBBP5. Left, GST–RBBP5$_{330–381}$ was used to pull down ASH2L$_{SPRY}$ and its mutants. Right, GST–ASH2L$_{SPRY}$ was used to pull down full-length RBBP5 and its mutants. Several control mutations (such as ASH2L(Q354A) and RBBP5(E347A)), which are not on the RBBP5–ASH2L interface, did not affect the interaction between ASH2L and RBBP5. **b**, ASH2L and RBBP5 mutants that disrupted the RBBP5–ASH2L interaction decreased the HKMT activities of the MLL3 complex. The activities of the mutant proteins are normalized to the wild-type MLL3–RBBP5–ASH2L complex. Mean ± s.d. ($n = 3$) are shown. **c**, Mutations of RBBP5$_{AS}$ residues decreased the HKMT activity of the MLL3 complex. **d**, Representative gel-filtration profiles for MLL and MLL mutant proteins indicate MLL mutant proteins have a similar fold to wild-type protein. **e**, GST–MLL3$_{SET}$ was used to pull down full-length RBBP5, ASH2L$_{SPRY}$ and their mutants. Mutations of RBBP5 Glu347 and ASH2L Gln354 in the ternary interface impaired the interaction with MLL3$_{SET}$. Mutations of RBBP5$_{AS}$ residues (Phe336Ala, Glu338Ala/Leu339Ala) also decreased the interaction with MLL3$_{SET}$ to different degrees. **f**, RBBP5(Glu347Ala) and ASH2L(Gln354Ala) compromised the HKMT activities of all MLL complexes, indicating that RBBP5–ASH2L regulates MLL family proteins through the same mechanism. Activities of mutant complexes are normalized to the activity of wild-type MLL$_{SET}$–RBBP5–ASH2L, setting at 100%. Mean ± s.d. ($n = 3$) are shown.

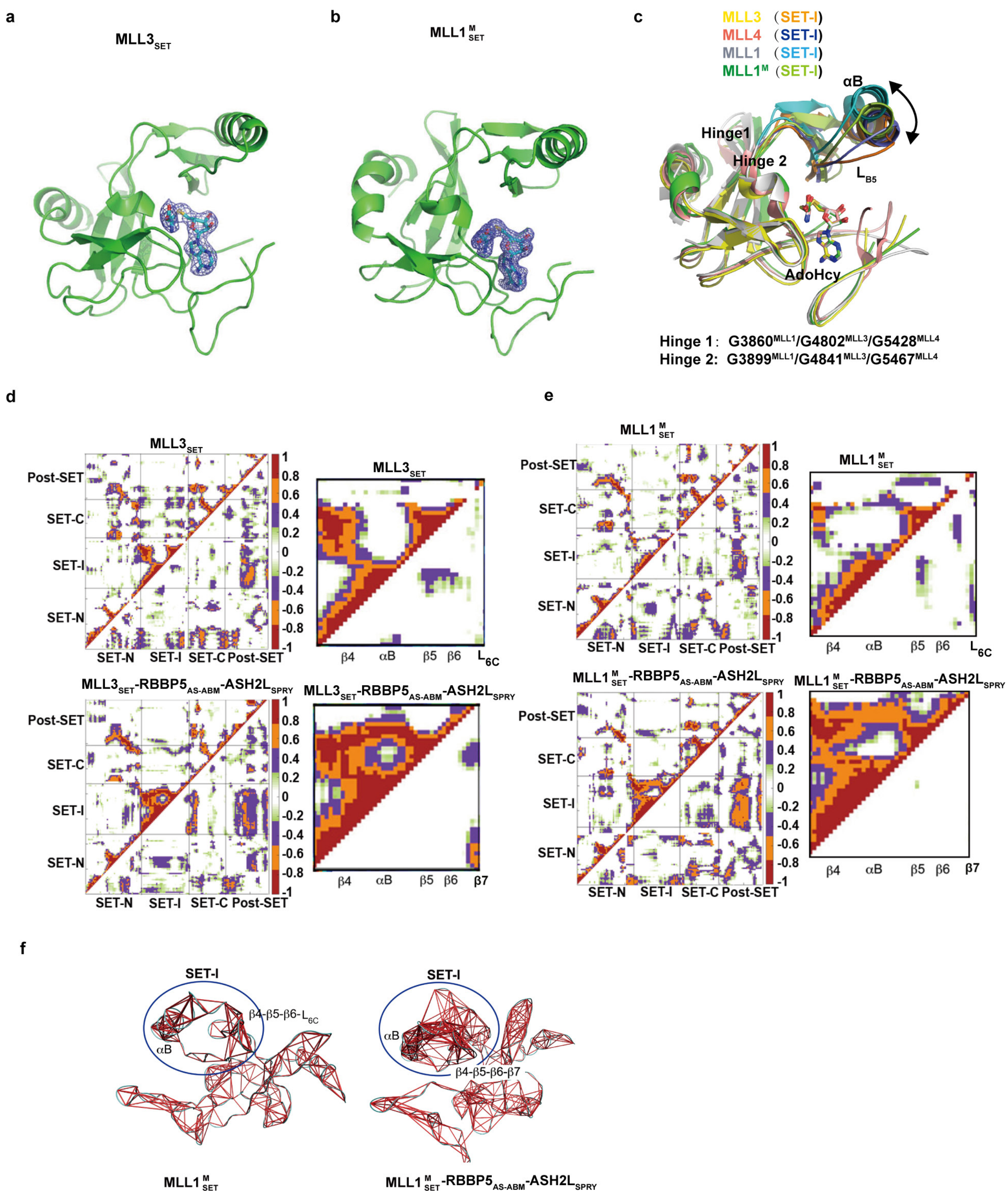

Extended Data Figure 6 | Activation mechanism of MLL proteins. a, The structure of MLL3$_{\mathrm{SET}}$ is shown in cartoon diagram. The electron density ($2F_o - F_c$) maps (contoured at 1σ) of AdoHcy are shown. **b**, The structure of MLL1$^{\mathrm{M}}_{\mathrm{SET}}$ is shown in cartoon diagram. The electron density ($2F_o - F_c$) maps (contoured at 1σ) of AdoHcy are shown. **c**, Structural comparison of MLL1$_{\mathrm{SET}}$ (PDB 2W5Y), MLL1$^{\mathrm{M}}_{\mathrm{SET}}$, MLL3$_{\mathrm{SET}}$ and MLL4$_{\mathrm{SET}}$ (PDB 4Z4P) suggests that the SET-I motif is intrinsically flexible, and can be captured in different configurations by crystallization. There are two highly conserved glycine residues serving as hinge points that connect the SET-I motif to the rest of MLL$_{\mathrm{SET}}$. The rotation of helix αB in the SET-I motif refers to an axis defined by the two hinge points of SET-I as indicated. **d**, Dynamic cross-correlation matrix for motions of all Cα atoms in apo MLL3$_{\mathrm{SET}}$ and MLL3$_{\mathrm{SET}}$ in the M3RA complex over the course of the simulation. The right panel shows enlarged cross-correlation maps of the SET-I motif. **e**, Dynamic cross-correlation matrix for motions of all Cα atoms in apo MLL1$^{\mathrm{M}}_{\mathrm{SET}}$ and MLL1$^{\mathrm{M}}_{\mathrm{SET}}$ in the M1$^{\mathrm{M}}$RA complex over the course of the simulation. The right panel shows enlarged cross-correlation maps of the SET-I motif. **f**, The most highly correlated residues of the SET-I motif by molecular dynamics simulation are indicated by red lines. Left panel is for apo MLL1$^{\mathrm{M}}_{\mathrm{SET}}$ and right panel is for MLL1$^{\mathrm{M}}_{\mathrm{SET}}$ in the MLL1$^{\mathrm{M}}$RA complex. Red lines are connected Cα atoms for pairs of residues with calculated correlation coefficients greater than 0.55.

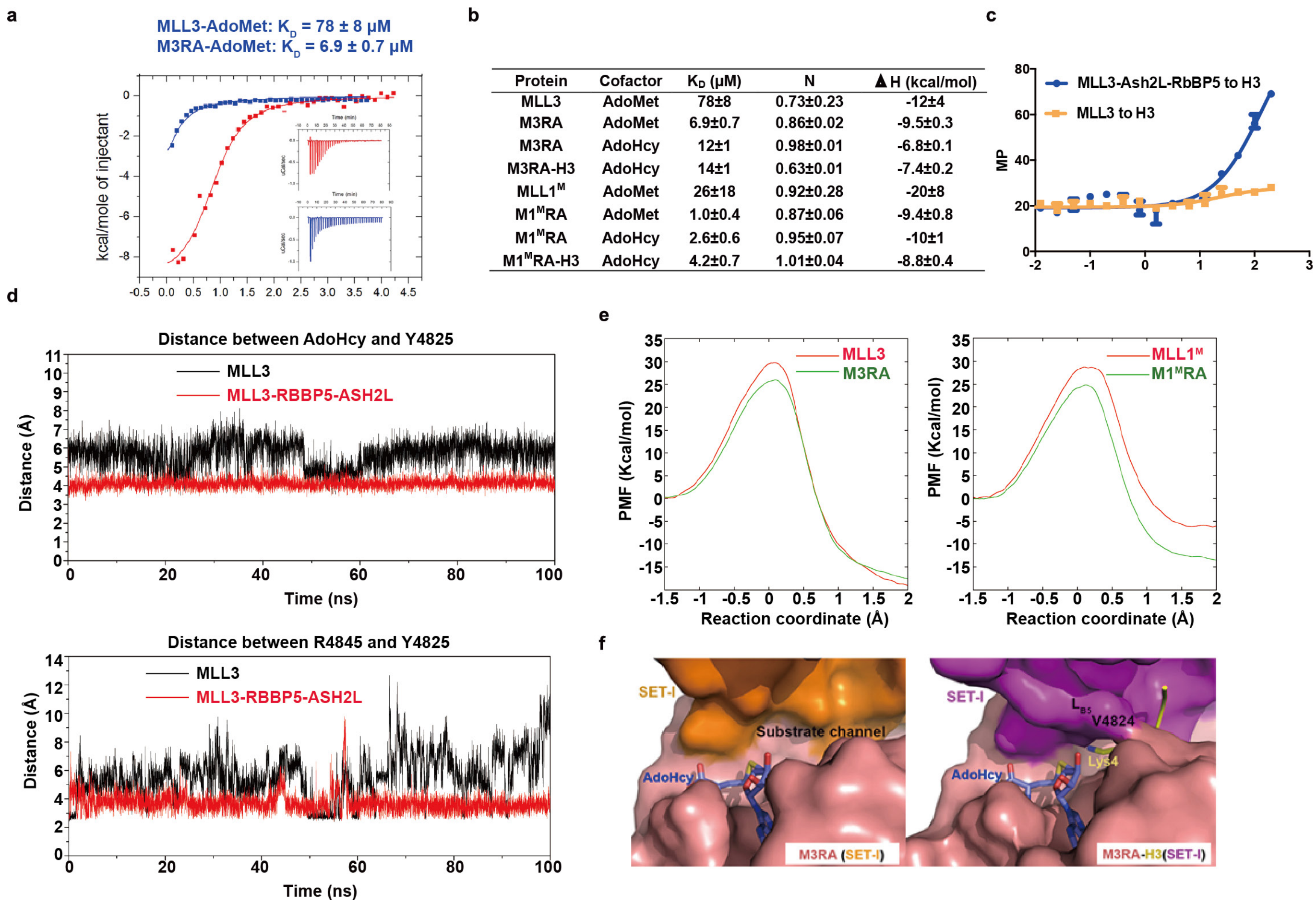

Protein	Cofactor	K_D (μM)	N	ΔH (kcal/mol)
MLL3	AdoMet	78±8	0.73±0.23	-12±4
M3RA	AdoMet	6.9±0.7	0.86±0.02	-9.5±0.3
M3RA	AdoHcy	12±1	0.98±0.01	-6.8±0.1
M3RA-H3	AdoHcy	14±1	0.63±0.01	-7.4±0.2
MLL1^M	AdoMet	26±18	0.92±0.28	-20±8
M1^{M}RA	AdoMet	1.0±0.4	0.87±0.06	-9.4±0.8
M1^{M}RA	AdoHcy	2.6±0.6	0.95±0.07	-10±1
M1^{M}RA-H3	AdoHcy	4.2±0.7	1.01±0.04	-8.8±0.4

Extended Data Figure 7 | Association of RBBP5–ASH2L increases the binding affinities of MLL to cofactor and substrate peptide. **a**, ITC measurement of interactions of AdoMet with $MLL3_{SET}$ alone (blue) and the M3RA complex (red). The insets show the ITC titration data. **b**, Equilibrium dissociation constants between cofactor and MLL proteins obtained from ITC measurements. **c**, Fluorescence polarization assay shows that RBBP5–ASH2L increases the binding affinity between MLL3 and the H3 peptide substrate. **d**, Molecular dynamics simulation show dynamics of the cofactor binding pocket. Top, the distance between AdoHcy and Tyr4825; bottom, the distance between Arg4845 and Tyr4825. These distances are almost fixed in the M3RA complex, while the distances in apo MLL3 have large variations, explaining why the MLL3 complex has a higher binding affinity to cofactor than apo MLL3 does. **e**, The potentials of mean force for the methyl transfer reaction along the reaction coordinate range from −1.5 to 2.0 Å with an interval of 0.1 Å. It clearly shows that the MLL_{SET}–RBBP5–ASH2L complex is more energetic favourable for the methyl transfer reaction than MLL_{SET} alone. **f**, The space-filling surface model shows that the $Ly4^{H3}$ binding channel exhibits open and closed conformations in the M3RA and M3RA–H3 structures.

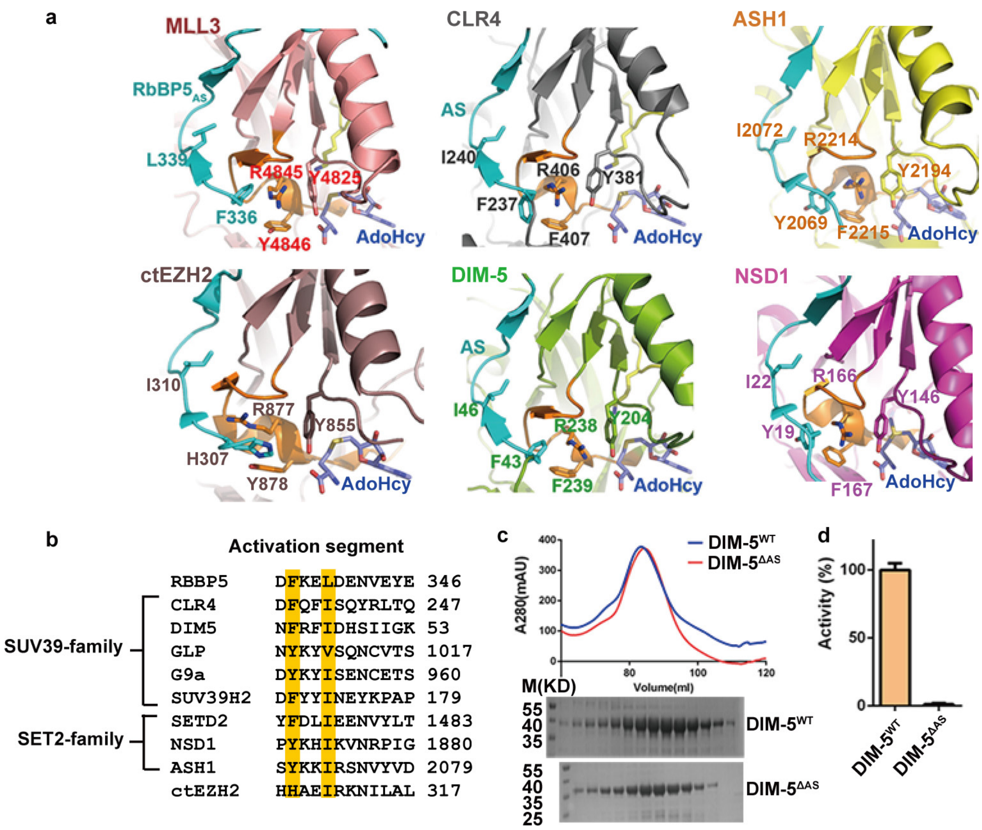

Extended Data Figure 8 | A conserved activation mechanism for SET-domain-containing HKMTs. a, Structural comparison of $MLL3_{SET}$ in the M3RA–H3–AdoHcy complex, and the SET domains of CLR4 (PDB 1MVH), DIM-5 (PDB 1PEG), EZH2 (PDB 5CH1), ASH1 (PDB 3OPE) and NSD1 (PDB 3OOI). Histone H3 peptide and AdoHcy in the CLR4 structure were modelled based on the M3RA–H3–AdoHcy complex structure. $RBBP5_{AS}$ and the corresponding activation segments in these proteins are almost identical in overall conformation (coloured in cyan). The recently reported EZH2 complex structure also revealed such an activation segment. Most notably, an aromatic residue (shown as stick model), equivalent to Phe336 in RBBP5, stacks with another two aromatic residues to form an aromatic cage to sandwich a conserved arginine. Another conserved hydrophobic residue (shown as stick model) is also important for the stable association between the activation segment and the SET-I motif. **b**, Sequence alignment of the activation segments of RBBP5 and several representative HKMTs, including members from the SUV39 and SET2 families. **c**, Gel-filtration profiles and SDS–PAGE for DIM-5 and DIM-5ΔAS show that activation segment does not affect protein folding. DIM-5ΔAS denotes DIM-5 (residues 51–319) that does not contain the activation segment. **d**, HKMT activities of DIM-5 and its mutants. Activities of mutant proteins are normalized to the activity of the wild-type protein setting at 100%. Mean ± s.d. ($n = 3$) are shown.

Extended Data Table 1 | Data collection and refinement statistics for MLL3$_{SET}$ and the MLL3$_{SET}$–RBBP5$_{AS\text{-}ABM}$–ASH2L$_{SPRY}$ complex

	MLL3$_{SET}$ Native †	MLL3$_{SET}$ Peak (Zn-SAD) †	MLL3$_{SET}$-RBBP5$_{AS\text{-}ABM}$-ASH2L$_{SPRY}$ †
Data collection			
Space group	$P4_132$	$P4_132$	$P2_12_12$
Cell dimensions			
a, b, c (Å)	129.056	129.323	80.342,236.076,44.416
α, β, γ (°)	90	90	90, 90, 90
Wavelength (Å)	0.9793	1.2818	1.1272
Resolution (Å)	50-2.8	50-3.4	100-2.4
R_{merge}	0.135(0.530) *	0.204(0.563)	0.110 (0.654)
$I/\sigma I$	31.6(7.0)	31.0(12.3)	32.6 (5.1)
Completeness (%)	99.9(100)	99.9(100)	99.9(100)
Redundancy	10.1(10.6)	13.3(13.9)	7.1 (7.3)
Refinement			
Resolution (Å)	38.9-2.8		44.4-2.4
No. reflections	9521		33458
R_{work}/R_{free} (%)	18.0/22.9		18.0/22.8
No. atoms			
Protein	1198		5570
Ligand	27		54
Water	52		220
B-factors (Å^2)			
Protein	36.22		46.65
Ligand	33.13		52.53
Water	32.30		41.28
R.m.s deviations			
Bond lengths (Å)	0.011		0.003
Bond angles (°)	1.039		0.654

*Values in parentheses are for the highest-resolution shell.
†The data are collected from one crystal.

Extended Data Table 2 | Data collection and refinement statistics for $MLL1_{SET}^{N3861I/Q3867L}$ and $MLL1_{SET}^{N3861I/Q3867L}$–$RBBP5_{AS\text{-}ABM}$–$ASH2L_{SPRY}$ complex

	$MLL1_{SET}^{N3861I/Q3867L}$ †	$MLL1_{SET}^{N3861I/Q3867L}$-$RBBP5_{AS\text{-}ABM}$-$ASH2L_{SPRY}$ †
Data collection		
Space group	$P3_221$	C2
Cell dimensions		
a, b, c (Å)	54.547,54.574,104.656	74.966, 44,410, 117.792
α, β, γ (°)	90,90,122	90,106.157,90
Wavelength (Å)	0.9785	0.9792
Resolution (Å)	50-1.8	50-1.9
R_{merge}	0.090(0.421) *	0.158 (0.548)
I /σI	36.5(4.1)	11.3(2.4)
Completeness (%)	100(100)	99.7(99.8)
Redundancy	9.6(9.9)	3.6 (3.3)
Refinement		
Resolution (Å)	28.1-1.8	37.5-1.9
No. reflections	17284	29678
R_{work}/R_{free} (%)	20.2/23.6	16.6/21.3
No. atoms		
Protein	1156	2804
Ligand	27	27
Water	142	361
B-factors (Å^2)		
Protein	45.34	20.31
Ligand	33.19	27.14
Water	45.77	29.99
R.m.s deviations		
Bond lengths (Å)	0.011	0.008
Bond angles (°)	1.105	1.044

†The data are collected from one crystal.
*Values in parentheses are for highest-resolution shell.

LETTER

doi:10.1038/nature17140

The host galaxy of a fast radio burst

E. F. Keane[1,2,3], S. Johnston[4], S. Bhandari[2,3], E. Barr[2], N. D. R. Bhat[3,5], M. Burgay[6], M. Caleb[2,3,7], C. Flynn[2,3], A. Jameson[2,3], M. Kramer[8,9], E. Petroff[2,3,4], A. Possenti[6], W. van Straten[2], M. Bailes[2,3], S. Burke-Spolaor[10], R. P. Eatough[8], B. W. Stappers[9], T. Totani[11], M. Honma[12,13], H. Furusawa[12], T. Hattori[14], T. Morokuma[15,16], Y. Niino[12], H. Sugai[16], T. Terai[14], N. Tominaga[16,17], S. Yamasaki[11], N. Yasuda[16], R. Allen[2], J. Cooke[2,3], J. Jencson[18], M. M. Kasliwal[18], D. L. Kaplan[19], S. J. Tingay[3,5], A. Williams[5], R. Wayth[3,5], P. Chandra[20], D. Perrodin[6], M. Berezina[8], M. Mickaliger[9] & C. Bassa[21]

In recent years, millisecond-duration radio signals originating in distant galaxies appear to have been discovered in the so-called fast radio bursts[1–9]. These signals are dispersed according to a precise physical law and this dispersion is a key observable quantity, which, in tandem with a redshift measurement, can be used for fundamental physical investigations[10,11]. Every fast radio burst has a dispersion measurement, but none before now have had a redshift measurement, because of the difficulty in pinpointing their celestial coordinates. Here we report the discovery of a fast radio burst and the identification of a fading radio transient lasting ∼6 days after the event, which we use to identify the host galaxy; we measure the galaxy's redshift to be $z = 0.492 \pm 0.008$. The dispersion measure and redshift, in combination, provide a direct measurement of the cosmic density of ionized baryons in the intergalactic medium of $\Omega_{\rm IGM} = 4.9 \pm 1.3$ per cent, in agreement with the expectation from the Wilkinson Microwave Anisotropy Probe[12], and including all of the so-called 'missing baryons'. The ∼6-day radio transient is largely consistent with the radio afterglow of a short γ-ray burst[13], and its existence and timescale do not support progenitor models such as giant pulses from pulsars, and supernovae. This contrasts with the interpretation[8] of another recently discovered fast radio burst, suggesting that there are at least two classes of bursts.

As part of the SUrvey for Pulsars and Extragalactic Radio Bursts (SUPERB) project at the Parkes radio telescope, we perform real-time searches of the sky at high time resolution (see Methods). On 2015 April 18 UTC we detected a fast radio burst (FRB) which we refer to as FRB 150418. Its dispersion measure (DM) is 776.2(5) $\rm cm^{-3}$ pc, which is 4.1 times the maximum Galactic contribution expected from this line of sight through the Milky Way[14]. (Throughout, the figure in parentheses indicates the uncertainty in the last digit.) The UTC at which the FRB was detected is 04:29:07.056 at 1,382 MHz, or 04:29:05.370 at infinite frequency with the dispersion delay removed (Fig. 1). The observed pulse width is 0.8 ± 0.3 ms, consistent with dispersion smearing due to the finite frequency resolution of the spectrometer, indicating that the intrinsic width is unresolved. No scattering is evident, consistent with the expected contribution from the Galaxy, which is ≪1 ms at this latitude[15]. The linear polarization is not large at 8.5 ± 1.5% and the circular polarization is consistent with zero. Given the low level of linear polarization the rotation measure is not known precisely and is 36 ± 52 rad $\rm m^{-2}$. In 13 h of follow-up observations no repeat burst was detected (see Methods).

Upon detection of FRB 150418 at Parkes, a network of telescopes was triggered across a wide range of wavelengths (see Methods). Beginning two hours after the FRB, observations with the Australia Telescope Compact Array (ATCA) were carried out at 5.5 GHz and 7.5 GHz, identifying two variable compact sources. One of the variable sources is consistent with a GHz-peaked-spectrum source, with a positive spectral index, as previously identified in observations at these frequencies[16]. The other variable source (right ascension, RA 07 h 16 min 34.6 s; declination, dec. −19° 00′ 40″), offset by 1.944 arcmin from the centre of the Parkes beam, was seen at 5.5 GHz at a brightness of 0.27(5) mJy per beam just 2 h after the FRB. The source was then seen to fade over subsequent epochs, settling at a brightness of ∼0.09(2) mJy per beam (Fig. 2). The source is also seen at 7.5 GHz at 0.18(3) mJy per beam in the first epoch but subsequently not detected. These observations indicate a ∼6-day transient with a negative spectral index; we obtain $\alpha = -1.37$ in the first epoch, for a power-law spectrum of the form $F_\nu \propto \nu^\alpha$. The subsequent quiescent level is consistent with the level expected[17] from an early-type galaxy at $z \approx 0.5$. To estimate the likelihood that this transient could occur by chance we consider the results of radio imaging surveys (see Methods). By comparing to a recent survey with the Very Large Array[18] in the 2–4 GHz band, we expect a 95% (99%) confidence upper limit of <0.001 (<0.002) such transients to occur in the ATCA observations of the FRB field, or equivalently an upper limit chance coincidence probability of <0.1% (<0.2%). We find that the detection of a fading transient source is therefore sufficiently rare that we conclude that it is the afterglow from the FRB event.

We obtained optical observations of the field using Suprime-Cam on the 8.2-m Subaru Telescope on 2015 April 19 and April 20. From these images, we identify a source within the ∼1-arcsec positional uncertainty derived from the ATCA image (Fig. 3). The source is seen to be a galaxy with a half-light radius of 1.4 ± 0.2 arcsec with a surface brightness profile well fitted by de Vaucouleurs' law (see Methods), thus consistent with being an elliptical galaxy. In addition to the Subaru r' and i' band photometry, we obtained J, H and $K_{\rm s}$ band photometry with the Wide-field Infrared Camera on the Palomar 200″ telescope. The source is also detected in the WISE W1 and W2 filters, enabling a seven-band spectral energy distribution fit (see Extended Data Fig. 1) and the determination of a photometric redshift of $0.48 < z < 0.56$ (68% confidence). To confirm this redshift, we performed a 3-h spectroscopic observation in good seeing conditions (full-width at half-maximum,

[1]Square Kilometre Array Organisation, Jodrell Bank Observatory, SK11 9DL, UK. [2]Centre for Astrophysics and Supercomputing, Swinburne University of Technology, Mail H29, PO Box 218, Victoria 3122, Australia. [3]Australian Research Council Centre of Excellence for All-sky Astrophysics (CAASTRO), Australia. [4]Commonwealth Science and Industrial Research Organisation (CSIRO), Astronomy and Space Science, Australia Telescope National Facility, PO Box 76, Epping, New South Wales 1710, Australia. [5]International Centre for Radio Astronomy Research, Curtin University, Bentley, Western Australia 6102, Australia. [6]Instituto Nazionale di Astrofisica (INAF)—Osservatorio Astronomico di Cagliari, Via della Scienza 5, I-09047 Selargius (CA), Italy. [7]Research School of Astronomy and Astrophysics, Australian National University, Canberra, Australian Capital Territory 2611, Australia. [8]Max-Planck-Institut für Radioastronomie (MPIfR), Auf dem Hügel 69, D-53121 Bonn, Germany. [9]Jodrell Bank Centre for Astrophysics, School of Physics and Astronomy, University of Manchester, Manchester M13 9PL, UK. [10]National Radio Astronomy Observatory, Socorro, New Mexico, USA. [11]Department of Astronomy, the University of Tokyo, Hongo, Tokyo 113-0033, Japan. [12]National Astronomical Observatory of Japan, 2 Chome-21-1 Osawa, Mitaka, Tokyo 181-8588, Japan. [13]Department of Astronomical Science, SOKENDAI (Graduate University for the Advanced Study), Osawa, Mitaka 181-8588, Japan. [14]Subaru Telescope, National Astronomical Observatory of Japan, 650 North A'ohoku Place, Hilo, Hawaii 96720, USA. [15]Institute of Astronomy, Graduate School of Science, University of Tokyo, 2-21-1 Osawa, Mitaka, Tokyo 181-0015, Japan. [16]Kavli Institute for the Physics and Mathematics of the Universe (WPI), Institutes for Advanced Study, University of Tokyo, Kashiwa, Chiba 277-8583, Japan. [17]Department of Physics, Faculty of Science and Engineering, Konan University, 8-9-1 Okamoto, Kobe, Hyogo 658-8501, Japan. [18]Cahill Center for Astrophysics, California Institute of Technology, 1200 East California Boulevard, Pasadena, California 91125, USA. [19]Department of Physics, University of Wisconsin-Milwaukee, Milwaukee, Wisconsin 53201, USA. [20]National Centre for Radio Astrophysics, Tata Institute of Fundamental Research, Pune University Campus, Ganeshkhind, Pune 411 007, India. [21]ASTRON, the Netherlands Institute for Radio Astronomy, Postbus 2, NL-7990 AA Dwingeloo, The Netherlands.

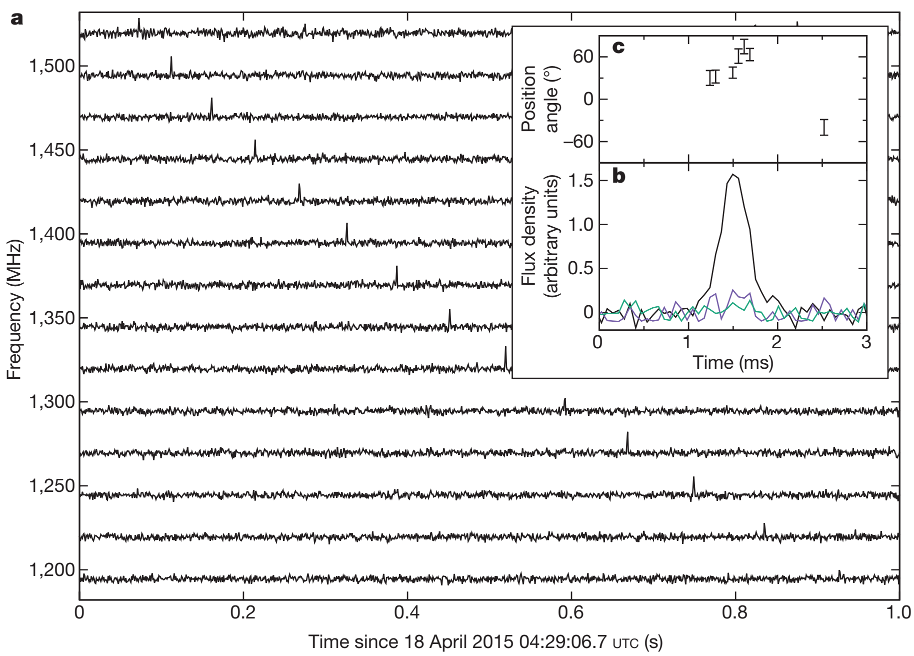

Figure 1 | The FRB 150418 radio signal. **a**, A waterfall plot of the FRB signal with 15 frequency sub-bands across the Parkes observing bandwidth, showing the characteristic quadratic time–frequency sweep. To increase the signal-to-noise ratio, the time resolution is reduced by a factor of 14 from the raw 64-μs value. **b**, The pulse profile of the FRB signal with the total intensity, linear and circular polarization flux densities shown as black, purple and green lines respectively. **c**, The polarization position angle is shown with 1σ error bars, for each 64-μs time sample where the linear polarization was greater than twice the uncertainty in the linear polarization.

FWHM ≈ 0.8 arcsec) using the Faint Object Camera and Spectrograph (FOCAS) on Subaru on 2015 November 03. This yielded a spectrum consistent with a reddened elliptical galaxy at $z = 0.492 \pm 0.008$ (Fig. 3). An earlier 1-h observation, on a night which was not spectrophotometric, using the Deep Imaging Multi-Object Spectrograph (DEIMOS) on the Keck telescope, was also taken and found to be consistent with the Subaru result.

Dispersion in the intergalactic medium is related to the cosmic density of ionized baryons $\Omega_{\rm IGM}$ and the redshift[19,20] according to the following expression:

$$\mathrm{DM_{IGM}} = \frac{3cH_0\Omega_{\rm IGM}}{8\pi G m_{\rm p}} \int_0^z \frac{(1+z')f_{\rm e}(z')\mathrm{d}z'}{[(1+z')^3\Omega_{\rm m}+\Omega_\Lambda]^{0.5}} \qquad (1)$$

Here, we take $\mathrm{DM_{IGM}} = \mathrm{DM_{FRB}} - \mathrm{DM_{MW}} - \mathrm{DM_{halo}} - \mathrm{DM_{host}}(1+z)^{-1}$ (see Methods). It is appropriate to account for a Milky Way halo contribution[21] of $\mathrm{DM_{halo}} = 30\,\mathrm{cm^{-3}\,pc}$ and we derive $189\,\mathrm{cm^{-3}\,pc}$ for $\mathrm{DM_{MW}}$ (the DM for the rest of the Milky Way, excluding its halo, that is, the non-dark-matter component of the Milky Way) from the NE2001 Galactic electron density model[14]. An elliptical galaxy can be modelled[22] with a modified version of NE2001 with an average rest-frame value of $\sim 37\,\mathrm{cm^{-3}\,pc}$. The NE2001 components are uncertain at the 20% level[14], and there is an additional uncertainty of $\sim 100\,\mathrm{cm^{-3}\,pc}$ owing to line-of-sight inhomogeneities in the intergalactic medium[10]. We therefore obtain:

$$\Omega_{\rm IGM} = \left(\frac{0.88}{f_{\rm e}}\right) 0.049 \pm 0.013 \qquad (2)$$

The ionization factor is $f_{\rm e} = 1$ for fully ionized hydrogen, whereas allowing for a helium abundance of 25%, $f_{\rm e} = 0.88$ is appropriate[20].

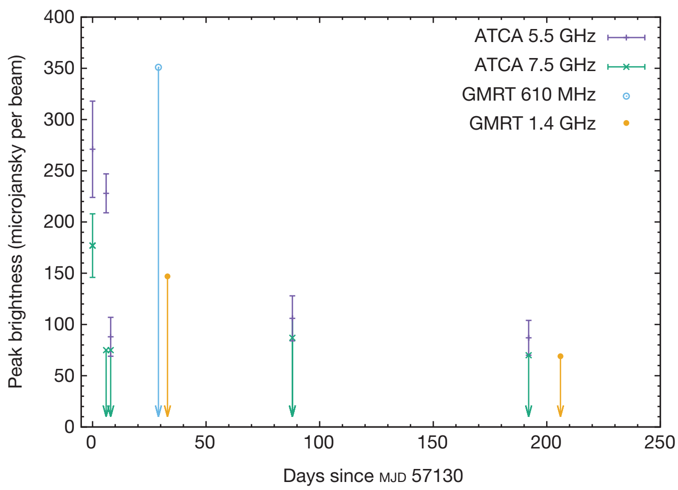

Figure 2 | The FRB host galaxy radio light curve. Detections have 1σ error bars, and 3σ upper limits are indicated with arrows. The afterglow event appears to last ~6 days, after which time the brightness settles at the quiescent level for the galaxy. Here MJD denotes modified Julian day.

Table 1 | Summary of FRB 150418 observed and derived properties

Event time at 1,382 MHz	2015 April 18 04:29:07.056 UTC
Event time at infinite frequency	2015 April 18 04:29:05.370 UTC
Parkes beam number	4, inner ring
Beam FWHM diameter	14.1′
Beam centre (RA, dec.)	07 h 16 min 30.9 s, −19° 02′ 24.4″
Beam centre (l, b)	232.684°, −3.261°
Galaxy position (RA, dec.) ATCA epoch 1	07 h 16 min 35(3) s, −19° 00′ 40(1)″
Galaxy position (l, b) ATCA epoch 1	232.6654(1)°, −3.2348(3)°
Signal-to-noise ratio	39
Observed width, $W_{\rm obs}$	0.8 ± 0.3 ms
FRB dispersion measure	776.2(5) cm^{-3} pc
Dispersion index, β	−2.00(1)
Milky Way dispersion measure	188.5 cm^{-3} pc
Redshift, z	0.492(8)
Peak flux density, $S_{1382\,\rm MHz}$	$>2.2^{+0.6}_{-0.3}$ Jy (beam centre) $>2.4^{+0.5}_{-0.4}$ Jy (galaxy position)
Fluence, $\mathcal{F}_{1382\,\rm MHz}$ (Jy ms)	$1.9^{+1.1}_{-0.8}$ Jy ms (beam centre) $2.0^{+1.2}_{-0.8}$ Jy ms (galaxy position)
Linear polarization, L/I	8.5 ± 1.5%
Circular polarization, $\lvert V\rvert/I$	<4.5% (3σ)
Rotation measure	36 ± 52 rad m^{-2}
Spectral index, α	$\alpha > -3.0$ (3σ, Parkes-MWA) $\alpha = +1.3 \pm 0.5$ (Parkes)
Comoving distance	1.88 gigaparsecs
Luminosity distance	2.81 gigaparsecs
Energy	$8^{+1}_{-5} \times 10^{38}$ ergs (galaxy position)
Luminosity	$>1.3 \times 10^{42}$ ergs s^{-1} (galaxy position)

The peak flux density is a band average and a lower limit due to the intrinsic width not being resolved; similarly luminosity is a lower limit. The energy quoted is the product of the band-averaged fluence, the blueshifted effective bandwidth of the observations and the square of the luminosity distance. MWA denotes the Murchison Widefield Array.

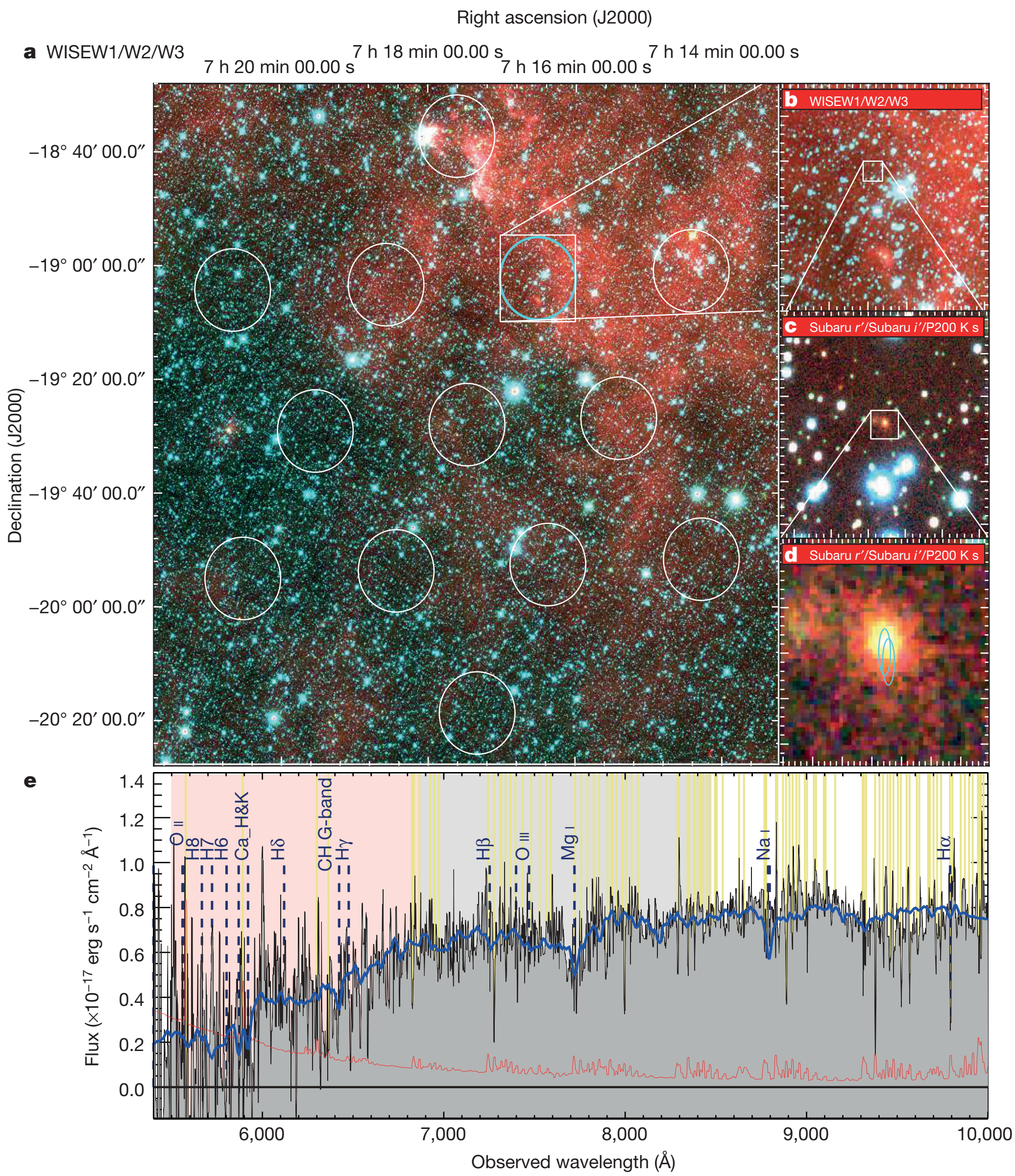

Figure 3 | Optical analysis of the FRB host galaxy. a, A wide-field composite false-colour RGB (red–green–blue) image, overplotted with the half-power beam pattern of the Parkes multi-beam receiver. Panels **b** and **c** show successive zooms on the beam 4 region, and on the fading ATCA transient location respectively. P200 K s denotes the Palomar telescope 200-inch K_s band. Panel **d** is further zoomed in with the error ellipses for the ATCA transient, as derived from both the first and second epoch, overplotted. **e**, The Subaru FOCAS spectrum de-reddened with $E(B-V)=1.2$, smoothed by five pixels and fitted to an elliptical galaxy template at $z=0.492$, denoted by the blue line. Common atomic transitions observed in galaxies are denoted by vertical dashed lines and yellow lines denote bright night sky lines. The Subaru r' and i' filter bandpasses are denoted by light red and grey background shading. The red line is the 1σ per pixel uncertainty (not smoothed).

From fitting ΛCDM cosmological models to Wilkinson Microwave Anisotropy Probe (WMAP) observations one derives[12] the cosmic density of all baryons $\Omega_{\rm baryons}=0.046\pm0.002$. Of these, about 10% are not ionized or are in stellar interiors[23] so that we expect to measure a cosmic density of ionized baryons in the intergalactic medium of $\Omega_{\rm IGM}\approx0.9\times\Omega_{\rm baryons}\approx0.041\pm0.002$. Thus, our measurement independently verifies the ΛCDM model and the WMAP observations, and constitutes a direct measurement of the ionized material associated with all of the baryonic matter in the direction of the FRB, including the so-called "missing baryons"[24]. Alternatively, if we take $\Omega_{\rm IGM}\equiv0.041$, our measurements show that $\mathrm{DM}_{\rm host}$ is negligible.

FRB localization allows us to correct a number of observable quantities that are corrupted by the unknown gain correction factor owing to a lack of knowledge of the true position within the telescope beam. Accounting for the frequency-dependent beam response[25] we can derive a true spectral index for the FRB. We obtain $\alpha=+1.3\pm0.5$ for a fit centred at 1.382 GHz. Similarly, we derive a corrected flux density and fluence, and these, in combination with the redshift measurement, enable us to derive the distances, the energy released, the luminosity and other parameters (Table 1).

In considering the nature of the progenitor we first consider the host galaxy. An upper limit to the star-formation rate can be determined from the upper limit Hα luminosity indicated by the Subaru spectrum (see Methods) to be $\lesssim0.2M_\odot\,\mathrm{yr}^{-1}$, where $M_\odot$ is the solar mass. Such a low star-formation rate implies, in the simplest interpretation, that FRB models directly related to recent star formation such as magnetar flares or blitzars are disfavoured. This problem might be avoided if either some residual star formation occurred in an otherwise 'dead' galaxy, or if the FRB originated in one of the many satellite galaxies that are expected to surround an elliptical galaxy at this redshift, but that cannot be resolved in our observations. Failing these, the lack of star formation favours models such as compact merger events. This may be supported by the existence of the ~6-day radio transient, which we interpret as

the afterglow from the FRB. The presence of this short-duration radio afterglow would not be expected from models involving giant pulses from pulsars (which last only a few nanoseconds), whereas supernovae and tidal disruption events would be expected to have a longer-lasting afterglow[26]. The afterglow is consistent with the four short γ-ray bursts for which radio afterglows have been detected[27]. The stellar mass of the galaxy, derived from the optical photometry and spectroscopy (see Methods), is $\sim 10^{11} M_{\odot}$, which is in accord with the masses of elliptical host galaxies of short γ-ray bursts[28]. For a duration of 6 days for the afterglow we infer a brightness temperature of $\sim 10^{14}$ K, above the Compton cooling limit of 10^{12} K, implying a modest Doppler boosting factor. It is possible that the initial variability in brightness and spectral index is caused by scintillation, similar to that seen in the light curves of γ-ray bursts[29]. If so, this indicates a very compact initial source size.

Our conclusion that FRB 150418 is likely to be from a one-off event in an older stellar population may be at odds with the recent discovery[8] of FRB 110523. It is possible that there are two or more classes of FRB progenitor. These FRBs differ in their observed pulse widths and we speculate that this parameter might act as a discriminator between differing progenitors. FRB 150418 is not resolved (in time), but FRB 110523 appears to be (see Methods). This trend is seen in the published FRB population: some are clearly resolved, some are clearly not, although extra care needs to be taken in re-analysing this, as very slight errors in DM, as well as the effect of multi-path scattering, can make an FRB appear to have a longer intrinsic timescale.

Unresolved events like FRB 150418 might thus be ascribed to cataclysmic events (such as short γ-ray bursts), while events like FRB 110523, where the intrinsic timescale is ~ 1 ms, could be associated to magnetar flares[30]. If so, events like FRB 150418 are unique events, whereas events like FRB 110523 could repeat, although the timescale for this is unclear. To answer these questions, and others such as whether or not some or all FRBs are standard candles, this study will need to be repeated for a large number of FRBs, and requires continued monitoring of the known FRB fields.

Online Content Methods, along with any additional Extended Data display items and Source Data, are available in the online version of the paper; references unique to these sections appear only in the online paper.

Received 27 November 2015; accepted 13 January 2016.

1. Lorimer, D. R., Bailes, M., McLaughlin, M. A., Narkevic, D. J. & Crawford, F. A bright millisecond radio burst of extragalactic origin. *Science* **318,** 777–780 (2007).
2. Keane, E. F., Stappers, B. W., Kramer, M. & Lyne, A. G. On the origin of a highly dispersed coherent radio burst. *Mon. Not. R. Astron. Soc.* **425,** L71–L75 (2012).
3. Thornton, D. *et al.* A population of fast radio bursts at cosmological distances. *Science* **341,** 53–56 (2013).
4. Spitler, L. G. *et al.* Fast radio burst discovered in the Arecibo pulsar ALFA survey. *Astrophys. J.* **790,** 101–110 (2014).
5. Burke-Spolaor, S. & Bannister, K. W. The galactic position dependence of fast radio bursts and the discovery of FRB 011025. *Astrophys. J.* **792,** 19–26 (2014).
6. Ravi, V., Shannon, R. M. & Jameson, A. A fast radio burst in the direction of the Carina dwarf spheroidal galaxy. *Astrophys. J.* **799,** L5–L10 (2015).
7. Petroff, E. *et al.* A real-time fast radio burst: polarization detection and multiwavelength follow-up. *Mon. Not. R. Astron. Soc.* **447,** 246–255 (2015).
8. Masui, K. *et al.* Dense magnetized plasma associated with a fast radio burst. *Nature* **528,** 523–525 (2015).
9. Champion, D. *et al.* Five new fast radio bursts from the HTRU high latitude survey: RST evidence for two-component bursts. *Mon. Not. R. Astron. Soc.* (submitted); preprint at http://arxiv.org/abs/1511.07746 (2015).
10. McQuinn, M. Locating the "missing" baryons with extragalactic dispersion measure estimates. *Astrophys. J.* **780,** L33 (2014).
11. Zhou, B., Li, X., Wang, T., Fan, Y.-Z. & Wei, D.-M. Fast radio bursts as a cosmic probe? *Phys. Rev. D* **89,** 107303 (2014).
12. Hinshaw, G. *et al.* Nine-year Wilkinson Microwave Anisotropy Probe (WMAP) observations: cosmological parameter results. *Astrophys. J.* **208** (Suppl.), 19 (2013).
13. Chandra, P. & Frail, D. A. A. Radio-selected sample of gamma-ray burst afterglows. *Astrophys. J.* **746,** 156 (2012).
14. Cordes, J. M. & Lazio, T. J. W. NE2001.I. A new model for the Galactic distribution of free electrons and its fluctuations. Preprint at http://arxiv.org/abs/astro-ph/0207156 (2002).
15. Bhat, N. D. R., Cordes, J. M., Camilo, F., Nice, D. J. & Lorimer, D. R. Multifrequency observations of radio pulse broadening and constraints on interstellar electron density microstructure. *Astrophys. J.* **605,** 759–783 (2004).
16. Bell, M. E. *et al.* A search for variable and transient radio sources in the extended Chandra Deep Field South at 5.5 GHz. *Mon. Not. R. Astron. Soc.* **450,** 4221–4232 (2015).
17. Brown, M. J. I., Jannuzi, B. T., Floyd, D. J. E. & Mould, J. R. The ubiquitous radio continuum emission from the most massive early-type galaxies. *Astrophys. J.* **731,** L41 (2011).
18. Mooley, K. P. *et al.* The Caltech-NRAO Stripe 82 Survey (CNSS) paper I: the pilot radio transient survey in 50 deg^2. *Astrophys. J.* (in the press); http://arxiv.org/abs/1601.01693 (2016).
19. Ioka, K. The cosmic dispersion measure from gamma-ray burst afterglows: probing the reionization history and the burst environment. *Astrophys. J.* **598,** L79–L82 (2003).
20. Inoue, S. Probing the cosmic reionization history and local environment of gamma-ray bursts through radio dispersion. *Mon. Not. R. Astron. Soc.* **348,** 999–1008 (2004).
21. Dolag, K., Gaensler, B. M., Beck, A. M. & Beck, M. C. Constraints on the distribution and energetics of fast radio bursts using cosmological hydrodynamic simulations. *Mon. Not. R. Astron. Soc.* **451,** 4277–4289 (2015).
22. Xu, J. & Han, J. L. Extragalactic dispersion measures of fast radio bursts. *Res. Astron. Astrophys.* **15,** 1629 (2015).
23. Fukugita, M. & Peebles, P. J. E. The cosmic energy inventory. *Astrophys. J.* **616,** 643–668 (2004).
24. Bregman, J. N. The search for the missing baryons at low redshift. *Annu. Rev. Astron. Astrophys.* **45,** 221–259 (2007).
25. Staveley-Smith, L. *et al.* The Parkes 21 cm multibeam receiver. *Publ. Astron. Soc. Aust.* **13,** 243–248 (1996).
26. Pietka, M., Fender, R. P. & Keane, E. F. The variability time-scales and brightness temperatures of radio flares from stars to supermassive black holes. *Mon. Not. R. Astron. Soc.* **446,** 3687–3696 (2015).
27. Fong, W., Berger, E., Margutti, R. & Ashley, B. A. A decade of short-duration gamma-ray burst broad-band afterglows: energetics, circumburst densities, and jet opening angles. *Astrophys. J.* **815,** 102 (2015).
28. Berger, E. Short-duration gamma-ray bursts. *Annu. Rev. Astron. Astrophys.* **52,** 43–105 (2014).
29. Frail, D. A., Kulkarni, S. R., Nicastro, L., Feroci, M. & Taylor, G. B. The radio afterglow from the γ-ray burst of 8 May 1997. *Nature* **389,** 261–263 (1997).
30. Kulkarni, S. R., Ofek, E. O. & Neill, J. D. The Arecibo fast radio burst: dense circum-burst medium. Preprint at http://arxiv.org/abs/1511.09137 (2015).

Acknowledgements The Parkes radio telescope and the Australia Telescope Compact Array are part of the Australia Telescope National Facility, which is funded by the Commonwealth of Australia for operation as a National Facility managed by CSIRO. Parts of this research were conducted by the Australian Research Council Centre of Excellence for All-sky Astrophysics (CAASTRO) and used the gSTAR national facility at Swinburne University of Technology. Parts of this work are based on data collected at the Subaru Telescope, which is operated by the National Astronomical Observatory of Japan, the Murchison Radio-astronomy Observatory operated by CSIRO, the Giant Metrewave Radio Telescope (GMRT), which is run by the National Centre for Radio Astrophysics of the Tata Institute of Fundamental Research, the Sardinia Radio Telescope as part of scientific commissioning of the telescope, and the 100-m telescope of the MPIfR at Effelsberg. We acknowledge the Wajarri Yamatji people as the traditional owners of the MWA Observatory site.

Author Contributions E.F.K. is the principal investigator of the SUPERB project, created SUPERB survey infrastructure at Parkes and Swinburne, led survey planning, formulated and wrote (with input from co-authors) the contents of this manuscript, performed the $\Omega_{\rm IGM}$ calculation, calculated the FRB spectral index, produced the FRB waterfall plot and the light curve plot. S.J. and S.B. performed ATCA observations and data analysis. S.J. and B.W.S. worked on radio light curve interpretation. S.B., N.D.R.B. and P.C. performed GMRT observations and data analysis. E.B. created survey infrastructure at Parkes and Swinburne and created the MWA shadowing infrastructure. Additionally, E.F.K., S.J., S.B., E.B., N.D.R.B., M. Burgay, M.C., C.F., M.K., E.P., A.P., W.v.S., M. Bailes., S.B.-S. and R.P.E. all performed observations for the SUPERB survey at Parkes. A.J. created and maintained the Parkes and Swinburne hardware and software infrastructure and performed data management for the SUPERB project. M. Bailes additionally provided Parkes and Swinburne hardware. C.F. and M.K. also worked on the calculation of the cosmic density of ionized baryons in the intergalactic medium. M.K. additionally performed FRB radio profile fitting. Polarization analysis of the FRB signal was performed by M.C., E.P. and W.v.S. W.v.S. also produced the polarization profile plot. E.P. additionally performed the Swift analysis. Non-imaging radio follow-up was performed by M. Burgay, A.P. and D.P. with the Sardinia Radio Telescope, by R.P.E. and M. Berezina with the Effelsberg Radio Telescope, and by B.W.S., M.M. and C.B. at the Lovell Telescope at Jodrell Bank. T. Totani, M.H., H.F., T.H., T.M., Y.N., H.S., T. Terai, N.T, S.Y. and N.Y. performed the Subaru observations. T. Totani, T.H., N.T. and S.Y. additionally performed Subaru data analysis, determined the spectral redshift and created the optical profile plot. C.F., T. Totani, S.Y. and R.A. performed the optical profile fitting. J.C. performed data analysis on the Keck and Subaru data, also obtained the spectral redshift and produced the optical spectrum plot. J.J. performed the Palomar observations. M.M.K. performed the Keck observation. MWA observations were performed by N.D.R.B., D.L.K., S.J.T., A.W. and R.W. with data analysis by D.L.K. and S.J.T. D.L.K. additionally measured the photometric redshift and produced the RGB (red–green–blue) image and photo-z plots (Extended Data Fig. 1).

Author Information Reprints and permissions information is available at www.nature.com/reprints. The authors declare no competing financial interests. Readers are welcome to comment on the online version of the paper. Correspondence and requests for materials should be addressed to E.F.K. (e.keane@skatelescope.org).

METHODS

DM contributions. When radio signals propagate through a plasma, the travel time is longer than the light travel time in a vacuum. The additional delay depends on the radio wave frequency, f, in units of GHz, and obeys a precise physical law of the form: $t_{\rm DM} = 4.149\,{\rm ms} \times ({\rm DM} \times f^{-2})$, where the DM is the integrated electron density along the line of sight in units of $\rm cm^{-3}\,pc$. If travelling across cosmological distances there are several contributions to the observed DM—from the host, the intergalactic medium and the Milky Way. The quantity of interest is the intergalactic medium component because this can be used, in conjunction with redshift measurements, to perform a number of fundamental studies, for example, detecting the missing baryons[10], determining the dark energy equation of state[11] and, if the signal is linearly polarized, measuring magnetic field strengths in the intergalactic medium[31]. For these applications the DM contributions other than those from the intergalactic medium are essentially foregrounds which must be understood so that they can be removed. Here we examine each contribution in turn and note the uncertainties in each case; it is important to note that the precision in the observed DM value is high (see Table 1) and does not therefore contribute to the uncertainty in determining the DM for the intergalactic medium.

The Milky Way component consists of two parts, the first of which is that due to the interstellar medium. This is in principle known[14], because the NE2001 model of the Galaxy's electron density can determine this to an accuracy of approximately 20%. The second Milky Way component is the contribution from the dark matter halo, which is thought to exist, yet which is not included in the NE2001 model. We follow previous work[21], which has calculated this term to be $30\,\rm cm^{-3}\,pc$. It is unclear how to assign an uncertainty to this component so (considering that the other components are dominant regardless) we take it to be zero. The host component is suppressed by a factor of $(1+z)^1$. Its magnitude depends on both the nature of the progenitor and of the host galaxy.

The observed FRB signal can be used to constrain the progenitor's local DM contribution—a non-negligible contribution could imply a high density of electrons to be located close to the source. Such a high density configuration[32] could produce higher-order dispersion terms (that is, the pulse's frequency dispersion would deviate from the quadratic form), could result in plasma frequencies comparable to the emitted frequency (that is, radiation would not escape), and could produce scattering in the pulse profile. None of these effects are observed for FRB 150418, implying that any local-progenitor DM component is negligible.

The host galaxy contribution has been examined recently[22] for spiral, dwarf and elliptical galaxies. This work considered modified versions of NE2001, with various sub-components of the model included or excluded as appropriate and suitable scalings to the Hα luminosity applied. For an elliptical galaxy, which is relevant in the case of FRB 150418, the average DM contribution over all inclination angles is 37 $\rm cm^{-3}$ pc (this is the value before being suppressed by the $(1+z)^1$ factor) and we use this as our estimate of the host contribution. As this is based upon NE2001 we assume that a 20% uncertainty applies. In addition to the uncertainties mentioned already the intergalactic medium component itself is uncertain at the level of $\sim$100 $\rm cm^{-3}$ pc, owing to inhomogeneities between different lines of sight through the intergalactic medium[10].

SUPERB. SUPERB is a project ongoing at the 64-m Parkes radio telescope since April 2014 with goals of discovering FRBs and pulsars. The central frequency of the survey is 1.382 GHz, with a bandwidth of 400 MHz, of which about 340 MHz is typically usable. It uses optimized graphics processing unit codes for performing real-time radio frequency interference mitigation and searches for short-duration radio bursts and pulsars in relativistic binary systems. In the real-time search we use the following criteria to define candidate FRB events: (1) the DM of the burst must be at least 1.5 times the expected maximum Milky Way contribution; (2) the signal-to-noise ratio must be at least 10; (3) the signal cannot be detected in more than four beams of the 13-beam receiver used for the SUPERB project at Parkes—an event detected in more beams cannot originate from a boresight signal and therefore cannot be of a celestial origin; (4) the width must be less than or equal to 8.192 ms, that is, 128 times our native time sampling of 64 μs; and (5) the number of independent events detected in a 4-s window centred on the event in question must be no greater than 5. The lag between the FRB signal hitting the dish and our software informing us of the detection[7] is only $\sim$10 s. We further search the data, offline, with more stringent interference rejection and covering corners of parameter space ignored for expediency during the real-time search. We note that since instigating this search system at Parkes no FRB has been missed by the real-time search pipeline, including FRB 150418.

FRB 150418 was detected in beam 4 of the 21-cm multi-beam receiver. The FRB profile was fitted simultaneously for time of arrival, DM, width, amplitude and dispersion index using 4 and 8 different sub-bands. The results were consistent with an unresolved pulse, where the width is purely given by the dispersion smearing across the 390.625-kHz filterbank channels. Uncertainties were determined using CERN's MINUIT packages (http://seal.web.cern.ch/seal/snapshot/work-packages/mathlibs/minuit/). The burst was found to have a DM of 776.2(5) $\rm cm^{-3}$ pc, and a dispersion index of $\beta = -2.00(1)$, where the dispersion delay is proportional to ν^{β}, and so is consistent with propagation through a cold plasma.

The gain of beam 4 is well fitted by a Gaussian[25] with FWHM of 14.1 arcmin, so to derive corrected values for the flux density, fluence, and so on we boost the measured values by a factor of $\exp(\ln 2(2\theta/{\rm FWHM})^2)$, where θ is the offset of the signal from the beam centre. The offset between the ATCA position determined from the first epoch (RA 07 h 16 min 34.557 s, dec. $-19°\,00'\,39.954''$) and the centre of the Parkes beam (RA 07 h 16 min 30.9 s, dec. $-19°\,02'\,24.4''$) is $\theta = 1.944$ arcmin, yielding a boost factor of 1.054. The observed peak flux density, if the FRB were at the centre of the beam, is 2.2 Jy with a corresponding fluence of 1.9 Jy ms; correcting these to the location of the host galaxy, we estimate values of 2.4 Jy and 2.0 Jy ms.

A calibration observation was taken 17 min post-burst and the polarization calibration was performed using the PSRCHIVE software package[33]. On the basis of observations of PSR J1644–4459, a bright polarized pulsar which we use to calibrate the off-axis response, taken three days before the FRB, we determine that the difference in the Jones matrix coefficients is not statistically different off-boresight. Therefore the boresight calibration was used to determine the polarization fraction of the pulse. This FRB is not seen to have a large linear polarization L, the rotation-measure-corrected linear polarization is $L/I = 8.5 \pm 1.5\%$ (where I is total intensity) and the circular polarization is consistent with zero. An additional systematic uncertainty exists in the leakage of total intensity to polarization. Our analysis of PSR J1644–4459 provides an upper limit on the magnitude (but not orientation) of the leakage vector that is <6% of the total intensity, meaning that the true L/I value may be either smaller or larger than quoted by up to this amount. Owing to the low linear polarization the rotation measure estimate is not very precise at 36 ± 52 rad $\rm m^{-2}$. As the rotation measure is consistent with zero, examination of the intergalactic medium magnetic field strength is not possible with this FRB, although for completeness we note that the 3σ upper limit on the electron weighted intergalactic medium magnetic field strength is $\sim$0.4 μG for this line of sight. There is no evidence for a large host contribution to the rotation measure for this FRB, although we note that an extremely large rotation measure exceeding 10^5 rad $\rm m^{-2}$ would result in depolarization within a single frequency channel, meaning we are insensitive to such large values.

The Murchison Widefield Array (MWA)[34] was shadowing our Parkes observations but did not detect a counterpart. The resulting 3σ fluence upper limit of 1,050 Jy ms at 185 MHz gives us the first simultaneous multi-frequency observation of an FRB, and hence the first broadband limit on the spectral index. The spectral index limit from the Parkes and MWA data combined is $\alpha > -3.0$. Properties of the FRB are summarized in Table 1.

Follow-up observations. After the discovery of the FRB we triggered observations at numerous telescopes and performed a calibration observation at Parkes. We continued to observe with the Parkes telescope, obtaining 4.5 h of observation over the course of the next 7.5 h, in order to search for any repeat bursts. The MWA was shadowing during the discovery observation and continued to track the FRB position for another $\sim$7.5 h. The ATCA was on source 2 h after the burst and also observed until $T + 7.5$ h (where T is the time of the FRB) when the source set at both Parkes and ATCA. Swift was on source 8 h after the burst, and 10 h after the burst the Lovell telescope continued the monitoring for 2.5 h. On April 19 and 20 we obtained optical observations with Subaru, and on April 20 and 21 continued to search for repeated radio bursts with the Effelsberg, Sardinia and Parkes radio telescopes. The longer term follow-up campaign consisted of radio imaging (four further ATCA epochs, three GMRT epochs), high time resolution radio (with the Lovell telescope), X-ray (one further Swift epoch), optical photometry (with the Palomar telescope) and optical spectroscopy (with the Keck and Subaru telescopes). We did not detect any subsequent bursts in our high time resolution radio follow-up (limiting flux densities in Extended Data Table 1); however, regular emission at a much weaker level cannot be ruled out. The follow-up observations are summarized in Extended Data Table 1. We additionally note that no γ-ray burst was detected in temporal coincidence, or in the months before, by telescopes on either of the Fermi or Swift satellites. Furthermore, at a comoving distance of 1.8 gigaparsecs or a luminosity distance of 2.8 gigaparsecs, this galaxy is beyond the LIGO[35] horizon for gravitational wave signatures from short γ-ray bursts.

Imaging transients. The radio transient sky is not very well studied at frequencies of 5.5 GHz and 7.5 GHz to the flux density levels relevant to this study. Additionally there are no archival data of the FRB field with which to compare our follow-up observations. To estimate the likelihood of the 6-day fading transient being detected by chance in our ATCA follow-up of the Parkes FRB field we first considered a previous ATCA study[16]. This is the only such work performed on the same timescales and at the same observing frequency using the ATCA. In that work, which also covered a wider area of sky than our FRB follow-ups and to a

deeper level, no transient sources were discovered. A 95% (99%) confidence upper limit event rate of $<7.5\ \mathrm{deg}^{-2}$ ($<11.1\ \mathrm{deg}^{-2}$) with a flux density of $>69\ \mu$Jy/beam was obtained. Scaling this to obtain the expectation of a transient with flux density in excess of 200 μJy yields an upper limit event rate of $<1.5\ \mathrm{deg}^{-2}$ ($<2.2\ \mathrm{deg}^{-2}$). Considering the 0.04-deg^2 field-of-view of a Parkes beam, which corresponds to the uncertainty in the FRB's position, the upper limit on the expected number of events in our follow-up observations is thus <0.06 (<0.09). We can rephrase this by interpreting the upper limit number of expected events as the upper limit on λ, the Poisson rate parameter; then the probability of a chance temporal coincidence is $P(1; \lambda) = \lambda\exp(-\lambda)$. This yields an upper-limit probability of $<6\%$ ($<8\%$).

One can also obtain estimates of the false-positive rate from considering studies[36–40] at other telescopes. As other studies are not ideally matched in terms of observing frequency and sensitivity, one must scale the findings appropriately. For example, for studies performed at different observing frequencies we must scale the flux densities by a spectral index; we adopt the spectral index of our 6-day transient as measured in the first epoch of our follow-up. Additionally, sensitivity levels must be scaled to the 200-μJy level; for this operation we adopt the standard $N \propto S^{-3/2}$ scaling. With this approach we consider a recent deep Very Large Array study[18] which operated at 2–4 GHz. Applying the appropriate scaling, this study yields an expected number of events in our follow-up observations of <0.001 (<0.002) at 95% (99%) confidence. The equivalent upper limit chance temporal coincidence probability is $<0.1\%$ ($<0.2\%$). This result is more constraining than the ATCA-derived numbers by a factor of at least 60. From this assessment we deem it statistically unlikely that we would have detected, by chance, this fading negative spectral index radio source at this location and time, resulting in our interpretation that this source is likely to be associated with the FRB.

Ideally, we might expand upon this calculation by estimating probabilities of chance coincidence in each independent wave-band (radio, optical and X-ray) in our follow-up campaign, and then compute a joint probability of a transient occurring in any of the bands. It is unclear what the appropriate statistics are for the X-ray and optical bands, but if we take the observed γ-ray burst and supernova rates as indicative, we find that the upper limit expectation in these wave bands is much smaller than in the radio bands. Deeper all-sky radio transient surveys are therefore the key to tightening constraints on transient associations like that reported here.

Optical analysis. The i' optical profile of the Galaxy was fitted with a Sersic function of the form $I(r) \propto \exp(-kR^{1/n})$. The best-fit parameters (see Extended Data Fig. 2) are a Sersic index of $n = 3.6 \pm 0.5$, consistent with the $n = 4$ value seen in elliptical galaxies. The half-light radius is $R_e = 6.9 \pm 1.2$ pixels, or $R_e = 1.4 \pm 0.2$ arcsec. At $z = 0.492$ the angular diameter distance is 1.62 gigaparsecs so that this implies $R_e = 10.9 \pm 1.8$ kpc as the physical half-light radius of the galaxy. The profile fitting also yields an estimate of the major to minor axes ratio for the galaxy of $b/a = 0.68 \pm 0.03$. We note that there are additional systematic uncertainties involved in the fit of the Sersic index, depending on the exact method of sky subtraction employed; our analysis suggests that the systematic errors are probably of equal magnitude to the statistical errors quoted above.

We obtained the following photometry of the FRB host galaxy: with Subaru Suprime-Cam[41] we determined AB magnitudes of 23.45(16) and 22.07(31), for the r' and i' bands respectively. Between the two Subaru epochs no variability is seen—a subtraction of the epochs yields an upper limit on any variation of 25.2 and 24.7 magnitudes (5σ). The galaxy is also detected in two WISE filters with Vega magnitudes of 15.204(0.044) and 15.050(082), for the W_1 and W_2 bands respectively. With the Palomar 200″ (P200) telescope we obtained further information, obtaining Vega magnitudes of 18.92(10), 17.55(25) and 16.51(05) for the J, H and K_s bands respectively. We corrected the observed photometry for the Milky Way extinction using $A_V = 3.7$ mag and standard extinction coefficients[42], and converted those magnitudes into flux densities using the established zero-points[43,44]. We fitted for the photometric redshift using the 2015 November version of EAZY[45], finding 68% confidence limits for $0.48 < z < 0.56$. This was robust to different choices of galaxy template, with good overall fits (χ^2 of 5–8). We then fitted the spectral energy distribution of the host galaxy using MAGPHYS[46]. We were able to achieve an acceptable fit (see Extended Data Fig. 1) to all of the photometry with a model for a passive ($\leq 0.2 M_\odot\ \mathrm{yr}^{-1}$), massive (stellar mass $\sim 10^{11} M_\odot$) galaxy with a modest amount of dust (in-host extinction A_V in the range 0–4 mag). The exact fit was rather degenerate because of our limited wavelength coverage, with only the stellar mass well determined. Future observations at shorter wavelengths should be able to determine more robust properties.

The spectrum that confirmed the redshift was obtained on 2015 November 2 in a 3-h observation using FOCAS on the Subaru telescope. An earlier attempt to obtain a spectroscopic redshift on 2015 October 21 using DEIMOS on the Keck telescope in poorer sky conditions had proved difficult to calibrate and resulted in an imprecise redshift estimate, no better than the photometric estimate. In that case difficulties in calibration are compounded by the spectrum's lack of any relevant emission lines. The well calibrated Subaru spectrum is found to be consistent with a reddened $z = 0.492(8)$ early-type galaxy with $E(B-V) = 1.2 \pm 0.1$ (Fig. 3), noting that r' and i' are approximations to restframe B and V filters. This implies absolute magnitudes of $M_B \approx -21.6$ and $M_V \approx -22.1$. As the galaxy is elliptical we can apply the Faber–Jackson relation[47] to estimate the velocity dispersion of $\sim 230\ \mathrm{km\ s^{-1}}$. From the virial theorem and the observed half-light radius we can thus estimate the stellar (and total) mass[48] to be $\sim 10^{11} M_\odot$ (and $\sim 2 \times 10^{12} M_\odot$). An upper limit to the Hα luminosity of $2.6 \times 10^{40}\ \mathrm{erg\ s^{-1}}$ (3σ) can be derived from the optical spectrum, and from this we can, in the standard way[49], derive a star-formation rate of $\leq 0.2 M_\odot\ \mathrm{yr}^{-1}$.

The very faint companion galaxy ($r' = 24.22(16)$ mag, $i' = 23.22(31)$ mag) visible to the northeast is not inconsistent with a galaxy at the same redshift. If confirmed the two galaxies may be in the process of merging. The absolute K-band magnitude of the galaxy is -25.7 mag (Vega). The radio continuum level can be estimated from this[17] and is consistent with the quiescent level of the galaxy after the ~6-day fading event. This shows that the background level seen is not surprising for an early-type galaxy, and implies that the FRB afterglow had already faded below this level by the third ATCA epoch.

FRB 110523. After the initial submission of this manuscript a study was published[8] announcing the discovery of FRB 110523, which we have compared and contrasted with FRB 150418 in the main text. There are now strong indications that there are two or more FRB progenitors, and we speculate that the observed pulse width may act as a useful discriminator between these. To this end we consider the time sampling and frequency resolution of the study that discovered FRB 110523, as well as its DM, in an effort to see whether the pulse was resolved in the Green Bank observations[8]. We would expect an unresolved FRB to have an observed width of no more than 1.08 ms, 1.14 ms and 1.26 ms in the highest, central and lowest frequency channels, respectively, in the Green Bank study[8]. This is inconsistent with the reported observed width (after the effects of scattering had been removed) at the 3σ to 4σ level, indicating that FRB 110523 appears to be resolved and therefore to have an intrinsic timescale of ~1 ms.

31. Zheng, Z., Ofek, E. O., Kulkarni, S. R., Neill, J. D. & Juric, M. Probing the intergalactic medium with fast radio bursts. *Astrophys. J.* **797,** 71 (2014).
32. Dennison, B. Fast radio bursts: constraints on the dispersing medium. *Mon. Not. R. Astron. Soc.* **443,** L11–L14 (2014).
33. Hotan, A. W., van Straten, W. & Manchester, R. N. PSRCHIVE and PSRFITS: an open approach to radio pulsar data storage and analysis. *Publ. Astron. Soc. Aust.* **21,** 302–309 (2004).
34. Tingay, S. J. *et al.* The Murchison Widefield Array: The Square Kilometre Array precursor at low radio frequencies. *Publ. Astron. Soc. Aust.* **30,** e007 (2013).
35. Abbott, B. P. *et al.* LIGO: the Laser Interferometer Gravitational-Wave Observatory. *Rep. Prog. Phys.* **72,** 076901 (2009).
36. Becker, R. H., Helfand, D. J., White, R. L. & Proctor, D. D. Variable radio sources in the Galactic Plane. *Astron. J.* **140,** 157–166 (2010).
37. Ofek, E. O. *et al.* A very large array search for 5 GHz radio transients and variables at low galactic latitudes. *Astrophys. J.* **740,** 65 (2011).
38. Frail, D. A., Kulkarni, S. R., Ofek, E. O., Bower, G. C. & Nakar, E. A revised view of the transient radio sky. *Astrophys. J.* **747,** 70 (2012).
39. Croft, S., Bower, G. C. & Whysong, D. The Allen Telescope Array Pi GHz Sky Survey. III. The ELAIS-N1, Coma, and Lockman hole fields. *Astrophys. J.* **762,** 93 (2013).
40. Gal-Yam, A. *et al.* Radio and optical follow-up observations of a uniform radio transient search: implications for gamma-ray bursts and supernovae. *Astrophys. J.* **639,** 331–339 (2006).
41. Miyazaki, S. *et al.* Subaru Prime Focus Camera—Suprime-Cam. *Publ. Astron. Soc. Jpn* **54,** 833–853 (2002).
42. Davenport, J. R. A. *et al.* The SDSS-2MASS-WISE 10-dimensional stellar colour locus. *Mon. Not. R. Astron. Soc.* **440,** 3430–3438 (2014).
43. Cohen, M., Wheaton, W. A. & Megeath, S. T. Spectral irradiance calibration in the infrared. XIV. The absolute calibration of 2MASS. *Astron. J.* **126,** 1090–1096 (2003).
44. Jarrett, T. H. *et al.* The Spitzer-WISE survey of the ecliptic poles. *Astrophys. J.* **735,** 112 (2011).
45. Brammer, G. B., van Dokkum, P. G. & Coppi, P. EAZY: a fast, public photometric redshift code. *Astrophys. J.* **686,** 1503–1513 (2008).
46. da Cunha, E., Charlot, S. & Elbaz, D. A simple model to interpret the ultraviolet, optical and infrared emission from galaxies. *Mon. Not. R. Astron. Soc.* **388,** 1595–1617 (2008).
47. Faber, S. M. & Jackson, R. E. Velocity dispersions and mass-to-light ratios for elliptical galaxies. *Astrophys. J.* **204,** 668–683 (1976).
48. Bullock, J. S. *et al.* Profiles of dark haloes: evolution, scatter and environment. *Mon. Not. R. Astron. Soc.* **321,** 559–575 (2001).
49. Kennicutt, R. C. Jr. The global Schmidt law in star-forming galaxies. *Astrophys. J.* **498,** 541–552 (1998).

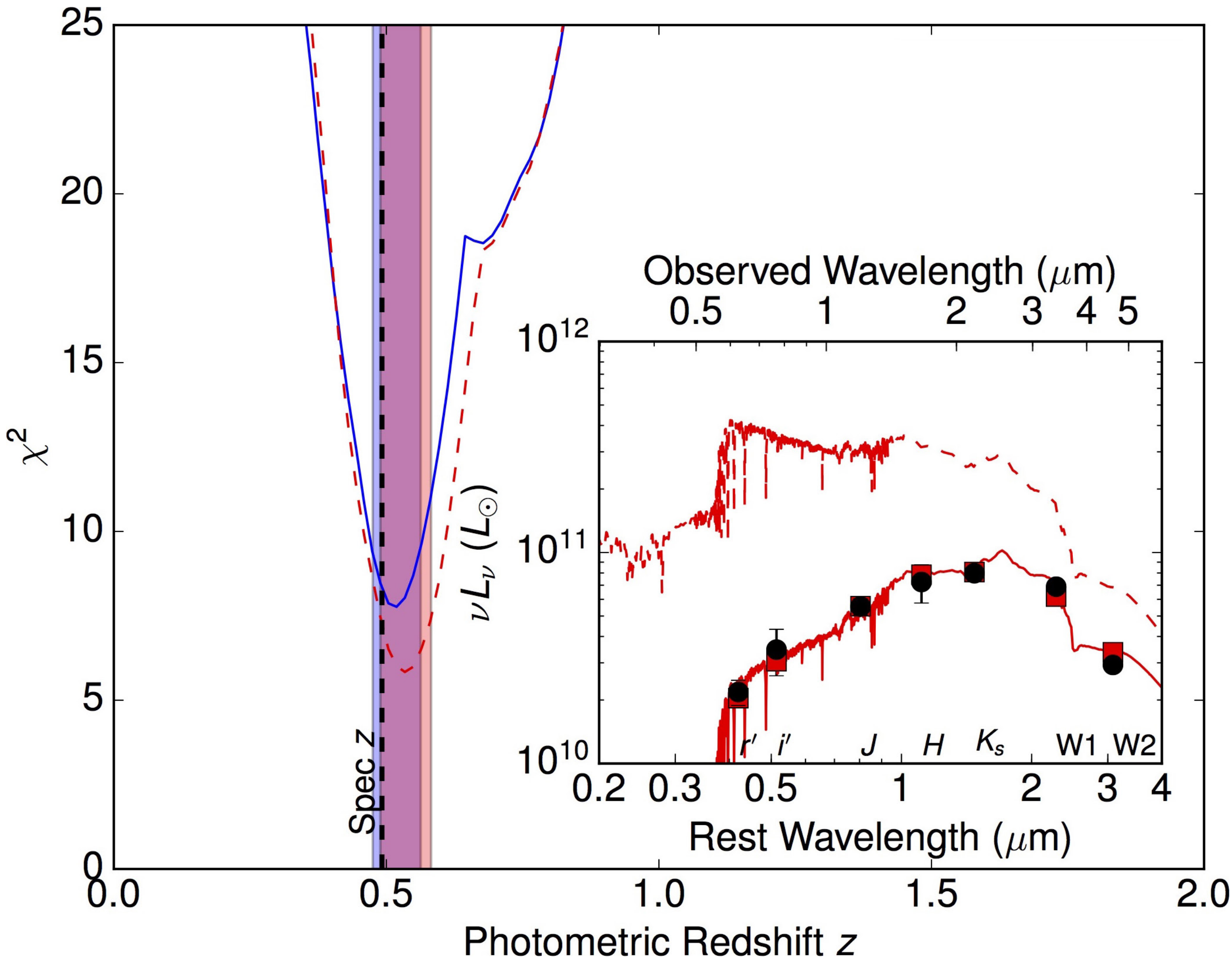

Extended Data Figure 1 | The photometric redshift of the FRB host galaxy. A χ^2 fit of the redshift of the galaxy based on the spectral energy (L_ν) distribution is shown. The photometric redshift determined from this is $0.48 < z < 0.56$ (68% confidence, denoted by the shaded regions). Two spectral fits are shown, and these are denoted by the red and blue shading respectively. The spectral redshift is denoted by the dashed vertical line. The inset shows the spectral energy distribution fit, with the seven photometric estimates overplotted with 1σ error bars.

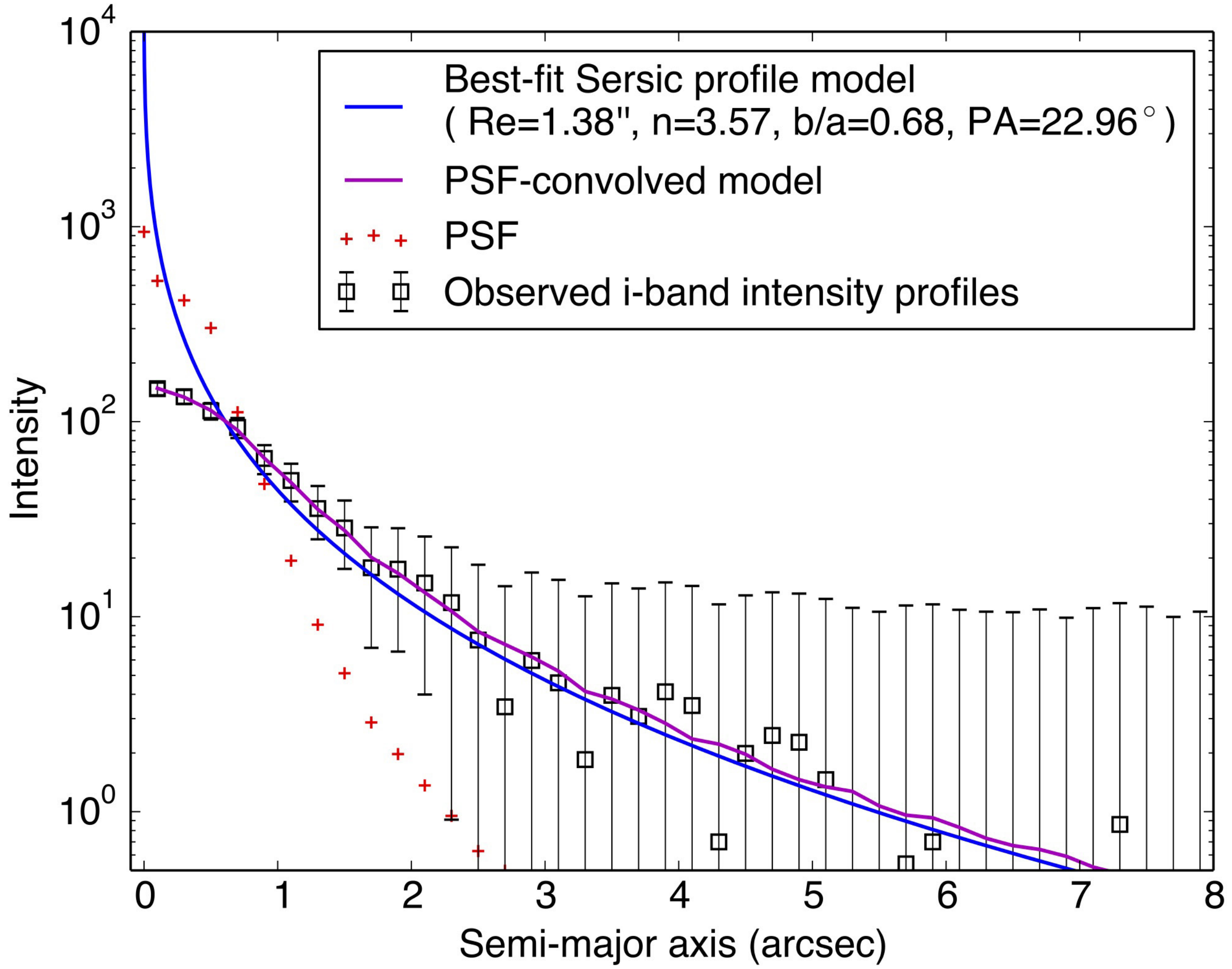

Extended Data Figure 2 | The optical surface brightness profile of the FRB host galaxy. The surface brightness profile of the galaxy in the Subaru i' band image was fitted to an ellipsoidal Sersic function. Best-fit values for the half-light radius (R_e), Sersic index (n), axis ratio (b/a) and position angle (PA) are given in the inset. The model profiles and data are shown as the flux along an ellipse as a function of semi-major axis. The image point spread function (PSF) profile is also shown as a function of radius. Error bars give the root-mean-square scatter of the pixel counts along the axis.

Extended Data Table 1 | Summary of follow-up observations of FRB 150418

Time (UTC)	Telescope	Band	Tobs (s)	Mode	Level/limit
2015-04-18-04:21:15	Parkes	1.4 GHz	561	TD*	2.2 Jy
Shadowing	MWA	185 MHz	27000	TD	< 1050 Jy ms
2015-04-18-04:31:08	Parkes	1.4 GHz	465	TD	$< 0.17(W/0.9\ \mathrm{ms})^{-0.5}$ Jy
2015-04-18-05:04:35	Parkes	1.4 GHz	1181	TD	$< 0.17(W/0.9\ \mathrm{ms})^{-0.5}$ Jy
2015-04-18-06:30:15	ATCA	5.5,7.5 GHz	19800	RI*	$0.27(5)$ mJy/beam, $0.18(3)$ mJy/beam
2015-04-18-07:46:27	Parkes	1.4 GHz	3618	TD	$< 0.17(W/0.9\ \mathrm{ms})^{-0.5}$ Jy
2015-04-18-08:47:28	Parkes	1.4 GHz	3618	TD	$< 0.17(W/0.9\ \mathrm{ms})^{-0.5}$ Jy
2015-04-18-09:48:09	Parkes	1.4 GHz	3617	TD	$< 0.17(W/0.9\ \mathrm{ms})^{-0.5}$ Jy
2015-04-18-10:48:59	Parkes	1.4 GHz	3617	TD	$< 0.17(W/0.9\ \mathrm{ms})^{-0.5}$ Jy
2015-04-18-11:49:37	Parkes	1.4 GHz	758	TD	$< 0.17(W/0.9\ \mathrm{ms})^{-0.5}$ Jy
2015-04-18-12:20:57	*Swift*	X-ray	3976	PC	$< 7.1 \times 10^{-14}$ erg/cm^2/s
2015-04-18-14:22:52	Lovell	1.4 GHz	7200	TD	$< 0.11(W/0.9\ \mathrm{ms})^{-0.5}$ Jy
2015-04-19-06:06:19	Subaru	i'	600	Ph*	22.06(31) mag (AB)
2015-04-19-06:37:12	Subaru	r'	900	Ph*	23.33(16) mag (AB)
2015-04-20-05:50:27	Subaru	i'	1200	Ph*	22.08(31) mag (AB)
2015-04-20-06:30:53	Subaru	r'	1200	Ph*	23.59(16) mag (AB)
2015-04-20-15:49:09	Effelsberg	1.4 GHz	8300	TD	$< 0.11(W/0.9\ \mathrm{ms})^{-0.5}$ Jy
2015-04-21-06:40:42	Parkes	1.4 GHz	3600	TD	$< 0.17(W/0.9\ \mathrm{ms})^{-0.5}$ Jy
2015-04-21-17:21:40	SRT	1.4 GHz	3600	TD	$< 0.61(W/0.9\ \mathrm{ms})^{-0.5}$ Jy
2015-04-24-02:44:15	ATCA	5.5,7.5 GHz	72900	RI*	$0.23(2)$ mJy/beam, < 0.08 mJy/beam
2015-04-26-01:45:05	ATCA	5.5,7.5 GHz	74700	RI*	$0.09(2)$ mJy/beam, < 0.08 mJy/beam
2015-05-07-03:18:42	*Swift*	X-ray	2908	PC	$< 9.3 \times 10^{-14}$ erg/cm^2/s
2015-05-18-12:30:00	GMRT	0.61 GHz	7200	RI	< 0.35 mJy/beam
2015-05-22-12:42:00	GMRT	1.4 GHz	7140	RI	< 0.15 mJy/beam
2015-06-04-21:12:15	ATCA	5.5,7.5 GHz	26700	RI*	$0.11(2)$ mJy/beam, < 0.09 mJy/beam
2015-10-15-05:32:23	Lovell	1.4 GHz	7200	TD	$< 0.14(W/0.9\ \mathrm{ms})^{1/2}$ Jy ms
2015-10-21-00:14:15	Keck	OIR	3600	Sp*	see Subaru observation
2015-10-27-14:09:35	ATCA	5.5,7.5 GHz	30600	RI*	$0.09(2)$ mJy/beam, < 0.07 mJy/beam
2015-10-31-11:15:54	P200	J	1080	Ph*	18.92(10) mag (Vega)
2015-10-31-11:38:31	P200	H	450	Ph*	17.55(25) mag (Vega)
2015-10-31-11:51:15	P200	K_s	810	Ph*	16.51(5) mag (Vega)
2015-11-03-11:57:41	Subaru	OIR	10800	Sp*	see Figure 3
2015-11-11-18:40:00	GMRT	1.4 GHz	22020	RI	< 0.07 mJy/beam

The start times, telescope name, observing band and observing duration are listed. In the fifth column time domain, radio imaging, photon counting, photometric and spectroscopic observations are denoted TD, RI, PC, Ph and Sp respectively, and detections (of either the FRB, fading transient or host galaxy) are denoted with an asterisk. The final column gives the detection level, or 3σ upper limits in the case of non-detections. 'Shadowing' refers to when the MWA was observing simultaneously with the Parkes telescope.

doi:10.1038/nature16513

Non-destructive state detection for quantum logic spectroscopy of molecular ions

Fabian Wolf[1], Yong Wan[1]†, Jan C. Heip[1], Florian Gebert[1], Chunyan Shi[1] & Piet O. Schmidt[1,2]

Precision laser spectroscopy[1] of cold and trapped molecular ions is a powerful tool in fundamental physics—used, for example, in determining fundamental constants[2], testing for their possible variation in the laboratory[3,4], and searching for a possible electric dipole moment of the electron[5]. However, the absence of cycling transitions in molecules poses a challenge for direct laser cooling of the ions[6], and for controlling[7–11] and detecting their quantum states. Previously used state-detection techniques based on photodissociation[12] or chemical reactions[13] are destructive and therefore inefficient, restricting the achievable resolution in laser spectroscopy. Here, we experimentally demonstrate non-destructive detection of the quantum state of a single trapped molecular ion through its strong Coulomb coupling to a well controlled, co-trapped atomic ion. An algorithm based on a state-dependent optical dipole force[14] changes the internal state of the atom according to the internal state of the molecule. We show that individual quantum states in the molecular ion can be distinguished by the strength of their coupling to the optical dipole force. We also observe quantum jumps (induced by black-body radiation) between rotational states of a single molecular ion. Using the detuning dependence of the state-detection signal, we implement a variant of quantum logic spectroscopy[15,16] of a molecular resonance. Our state-detection technique is relevant to a wide range of molecular ions, and could be applied to state-controlled quantum chemistry[17] and to spectroscopic investigations of molecules that serve as probes for interstellar clouds[18,19].

One of the salient features of trapped-ion systems is that the universal Coulomb interaction allows strong coupling of diverse quantum objects—such as different species of atomic ions, or of atomic and molecular ions. Being able to perform quantum logic operations (for example, in the form of gates[14,20,21]) between such quantum objects has proven useful for quantum information processing and quantum simulations. The use of quantum logic operations in trapped-ion systems also allows the advantages of different atomic species to be combined. Quantum logic spectroscopy is one application, in which the high degree of control achieved over selected atomic ions is extended to species over which such control is lacking[15,16]. Here, we demonstrate quantum logic operations between a single molecular ion and a co-trapped atomic ion. Our findings make a wide range of molecular ions accessible to quantum logic operations. Our technique also allows single molecules to be investigated in a well isolated system without being disturbed by the environment (the limiting factor in other implementations of single-molecule spectroscopy, such as surface-enhanced Raman spectroscopy[22]).

Quantum logic operations between atoms are based on quantum-state-dependent forces, often induced by laser fields. The same approach is applicable to molecular ions. Unlike with atomic ions, however, the laser coupling to the molecular ion is distributed over many rotational–vibrational transitions, which weakens the interaction strength for individual transitions (see Methods). The strength of the optical dipole force (ODF) on the molecular ion is inversely proportional to the detuning of the dipole laser from an optical transition in the ion. This transition frequency depends on the rotational state of the molecule. By measuring the strength of the dipole force, we can thus infer the rotational state. If the strength of this force is oscillating with a frequency close to one of the secular motional frequencies of a two-ion crystal (consisting of a molecular and an atomic ion), it is resonantly enhanced, generating coherent states of motion, which can be detected on the atomic ion[23–25].

Here, we extend this simple detection scheme. We detect the small ODF that arises from a laser field tuned near the $X^1\Sigma^+(J=1) \rightarrow A^1\Sigma^+(J=0)$ resonance (detuning Δ_{MgH}) in a $^{24}\mathrm{MgH}^+$ molecular ion, in the presence of a background force (which is nearly independent of detuning) from a co-trapped $^{25}\mathrm{Mg}^+$ atomic ion (Fig. 1c; $X^1\Sigma^+$ and $A^1\Sigma^+$ label the molecular energy levels, and the superscript '1' refers to the multiplicity of the electron spin). Black-body radiation induces transitions between rotational states (J), resulting in a thermal rotational-state population with a maximum at $J=4$ for temperatures near 300 K. We chose to probe the $J=1$ state (which makes up around 8% of the population of rotational states), because of its long average dwell time of around 3 seconds (see Extended Data Fig. 1). The vibrational population with vibrational quantum number $v>0$ in $^{24}\mathrm{MgH}^+$ is negligible at room temperature, owing to the large vibrational spacing[26]. Applying the ODF resonant with either the in-phase or the out-of-phase mode implements a displacement operator that results in coherent states of motion[25], which are impractical for state discrimination because of their non-orthogonality. Instead, we map the molecule's internal state information to an engineered motional two-level quantum system (motional qubit) that is coupled by the ODF. This approach allows us to suppress the background force from $^{25}\mathrm{Mg}^+$ and enables advanced coherent-population-transfer schemes, such as composite pulses[21].

The state-detection algorithm starts with both axial motional modes of the two-ion crystal (which consists of a $^{25}\mathrm{Mg}^+$ and a $^{24}\mathrm{MgH}^+$ ion) initialized in the motional ground state $|0\rangle_{\mathrm{m}} \equiv |0\rangle_{\mathrm{IP}}|0\rangle_{\mathrm{OP}}$ via the atomic ion[27]. ('IP' denotes 'in-phase'; 'OP' denotes 'out-of-phase'.) Two long-lived hyperfine states in $^{25}\mathrm{Mg}^+$ serve as the atomic qubit denoted by $|\downarrow\rangle_{\mathrm{Mg}}$, $|\uparrow\rangle_{\mathrm{Mg}}$ (Fig. 1a), initialized to $|\downarrow\rangle_{\mathrm{Mg}}$. The motional qubit is prepared in the state $|\downarrow\rangle_{\mathrm{m}} \equiv |1\rangle_{\mathrm{IP}}|0\rangle_{\mathrm{OP}}$ by driving a π-pulse on the blue sideband transition (BSB) of the in-phase mode on the atomic ion while changing its internal state from $|\downarrow\rangle_{\mathrm{Mg}}$ to $|\uparrow\rangle_{\mathrm{Mg}}$. The ODF is implemented by applying two counter-propagating laser beams along the axial direction of the ion trap, forming an oscillating one-dimensional optical lattice. By adjusting the relative detuning, δ, between the two beams to the difference between the motional frequencies of the axial in-phase and out-of-phase modes, $\delta = \omega_{\mathrm{OP}} - \omega_{\mathrm{IP}} = \omega_{\mathrm{IP}}(\sqrt{3}-1)$, a Raman coupling involving only the motional states $|\downarrow\rangle_{\mathrm{m}} \leftrightarrow |\uparrow\rangle_{\mathrm{m}} \equiv |0\rangle_{\mathrm{IP}}|1\rangle_{\mathrm{OP}}$ is implemented. This then results in Rabi flopping between the two composite states (Fig. 2 and Extended Data Fig. 2).

[1]Physikalisch-Technische Bundesanstalt, 38116 Braunschweig, Germany. [2]Institut für Quantenoptik, Leibniz Universität Hannover, 30167 Hannover, Germany. †Present address: National Institute of Standards and Technology, 325 Broadway, Boulder, Colorado 80305, USA.

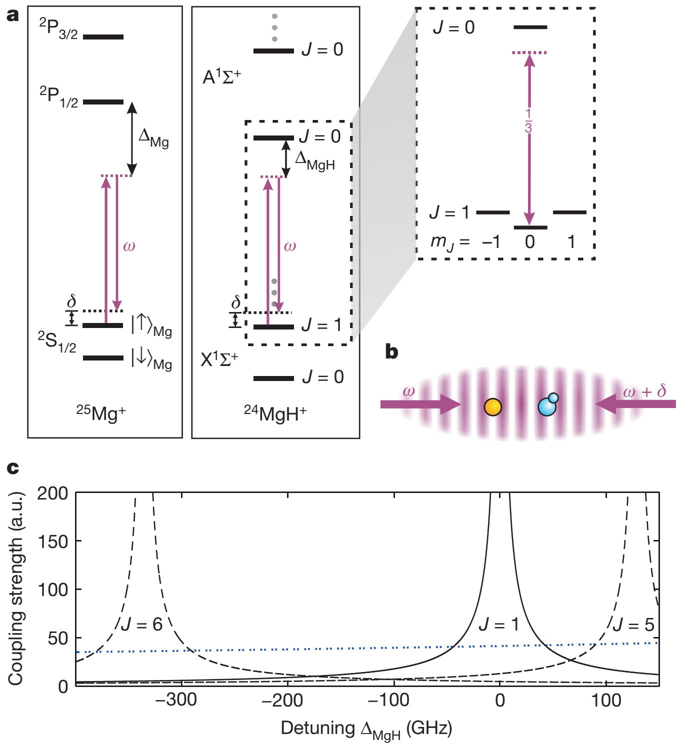

Figure 1 | Coupling strength of an optical dipole force to the atomic and molecular ions. a, Partial level scheme of the relevant atomic (left) and molecular states (right) and their laser coupling to the lattice laser. J refers to the rotational state; ω is the laser frequency; $^2P_{3/2}$, $^2P_{1/2}$, $^2S_{1/2}$, $A^1\Sigma^+$ and $X^1\Sigma^+$ are atomic/molecular energy levels, with the superscripts denoting the multiplicity of the electron spin; Δ_{Mg} and Δ_{MgH} represent the amount of detuning from atomic/molecular resonance; δ represents the relative detuning of the two laser beams forming the optical lattice. The inset shows the molecular substructure for the states involved in our state-detection sequence. The number on the transition in the inset is the experimentally implemented geometric coupling coefficient. **b**, The two lattice beams form a moving interference pattern, leading to a temporally and spatially varying light force on both ions (yellow, $^{25}Mg^+$; blue, $^{24}MgH^+$). **c**, Rotational state (J, $m_J = 0$) and detuning-dependent coupling strength of the optical dipole force, interacting with a $^{24}MgH^+$ molecular ion on the P-branch ($J \rightarrow J-1$, solid line) and R-branch ($J \rightarrow J+1$, dashed line) of the $X^1\Sigma^+ \rightarrow A^1\Sigma^+$ electronic transition. The blue dotted line denotes the coupling strength to the $^{25}Mg^+$ ion.

The interaction between the lattice laser field and the motional qubit is described by the Hamiltonian (see Methods):

$$H = \hbar\Omega_{\mathrm{eff}}\eta_{\mathrm{IP}}\eta_{\mathrm{OP}}(a_{\mathrm{IP}}a_{\mathrm{OP}}^{\dagger} + a_{\mathrm{IP}}^{\dagger}a_{\mathrm{OP}}) \quad (1)$$

where $a_{\mathrm{IP(OP)}}^{\dagger}/a_{\mathrm{IP(OP)}}$ is the creation/annihilation operator for the in-phase (or out-of-phase) mode, $\eta_{\mathrm{IP(OP)}}$ is the Lamb–Dicke parameter for the in-phase (or out-of-phase) mode[27], $\hbar$ is Planck's constant divided by 2π; and Ω_{eff} is the effective Rabi frequency. It is given by:

$$\Omega_{\mathrm{eff}} = \Omega_{\mathrm{Mg}}\sqrt{1 - 2R(\Delta_{\mathrm{MgH}})\cos(\delta\varphi) + R(\Delta_{\mathrm{MgH}})^2} \quad (2)$$

where $R(\Delta_{\mathrm{MgH}}) = \Omega_{\mathrm{MgH}}(\Delta_{\mathrm{MgH}})/\Omega_{\mathrm{Mg}}$ is the ratio between the Rabi frequencies of the Raman couplings in the molecular and atomic ions, depending on the detuning Δ_{MgH}. The distance between the ions determines the relative phase, $\delta\varphi$, between the forces on the ions[14]. In a Bloch-sphere picture, the effect of the ODF on the atom and the molecule can be illustrated as the vector sum of two torques, $\boldsymbol{F}_{\mathrm{ODF}} = \boldsymbol{F}_{\mathrm{Mg}} + \boldsymbol{F}_{\mathrm{MgH}}$, acting on the motional qubit (Fig. 2b, c). In the experiment, the time, t_{latt}, in which the lattice laser interacts with the ions is adjusted such that for $\Omega_{\mathrm{MgH}} = 0$ (that is, the molecular ion is not in $J = 1$) a π-pulse is performed on the motional qubit (Fig. 2b). If the molecule is in the probed state ($\Omega_{\mathrm{MgH}} \neq 0$), the additional force changes the population transfer (Fig. 2c). This step transfers the internal information of the molecular state to the motional qubit. The second BSB π-pulse maps the motional-state population (containing the molecule's internal state information) to the atomic qubit. The population in state $|\downarrow\rangle_{\mathrm{Mg}}$ follows:

$$P_{|\downarrow\rangle_{\mathrm{Mg}}} = \frac{1}{2}\left[1 + \cos\left(\pi\sqrt{1 - 2R(\Delta_{\mathrm{MgH}})\cos(\delta\varphi) + R(\Delta_{\mathrm{MgH}})^2}\right)\right] \quad (3)$$

and is detected using state-dependent fluorescence on the $^{25}Mg^+$ ion, where $|\downarrow\rangle_{\mathrm{Mg}}$ fluoresces and $|\uparrow\rangle_{\mathrm{Mg}}$ does not. The full sequence is shown in Extended Data Fig. 3.

The calculated signal $P_{|\downarrow\rangle_{\mathrm{Mg}}}$ is shown in Fig. 3a for different phases ($\delta\varphi$) and different detuning Δ_{MgH} values. The maxima correspond to rotations of $2\pi n$ on the Bloch sphere of the motional qubit, with $n \in \mathbb{N}$. In particular, at the outermost peaks (Fig. 3b), the forces from the atomic and molecular ions cancel or add up to 2π exactly, depending on the sign of Δ_{MgH}. There is a trade-off in the choice of lattice-laser detuning from the molecular resonance. That is, if the detuning is too large, the ODF will not be detectably different for a molecule in the rotational state of interest compared with a molecule in any other state. For a detuning too small, spontaneous Raman scattering will change the rotational state before it can be detected. Under ideal experimental conditions, it is possible to choose a combination of the phase $\delta\varphi$ and the detuning Δ_{MgH} to perform state detection in a single experimental repetition (cycle), because it is free from quantum projection noise ($P_{|\downarrow\rangle_{\mathrm{Mg}}} = 1$ if the molecule is in $J = 1$, and $P_{|\downarrow\rangle_{\mathrm{Mg}}} = 0$ if it is not). In this case, the experimental sequence can be understood in terms of a CNOT gate acting on the motional qubit with the molecular rotational qudit $|J\rangle_{\mathrm{MgH}}$ as a control (Fig. 2a):

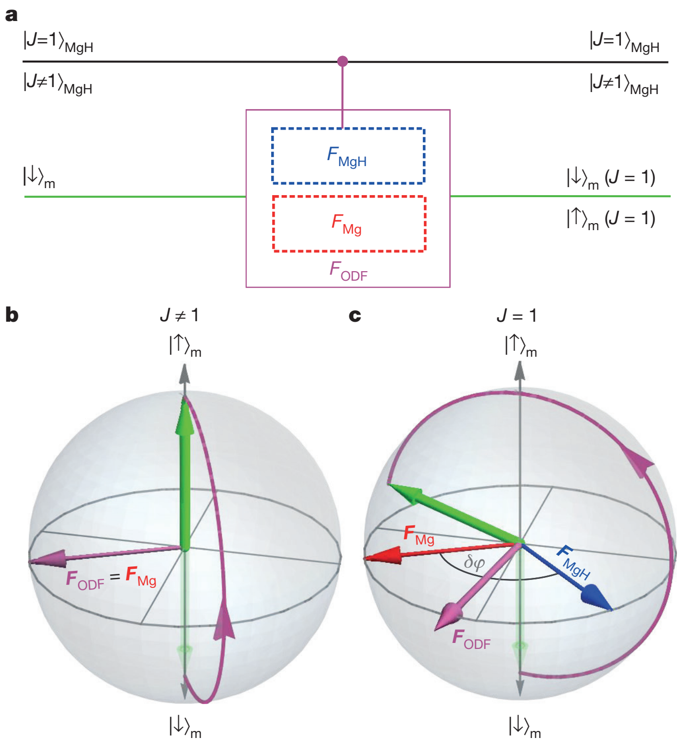

Figure 2 | Mapping of the molecular state to the motional qubit. a, Circuit description of the mapping process. For ideally chosen parameters Δ_{MgH} and $\delta\varphi$, the circuit is equivalent to a CNOT. The action of the optical dipole force (ODF) on the motional qubit is represented by the torque $\boldsymbol{F}_{\mathrm{ODF}} = \boldsymbol{F}_{\mathrm{Mg}} + \boldsymbol{F}_{\mathrm{MgH}}$. **b**, For $J \neq 1$, only the atomic ion interacts with the lattice. The ODF creates a torque, $\boldsymbol{F}_{\mathrm{Mg}}$, on the Bloch sphere (purple arrows). **c**, If $J = 1$, the additional force on the molecule (torque $\boldsymbol{F}_{\mathrm{MgH}}$, depicted in blue) is added to the force on the atom, leading to a modified population transfer.

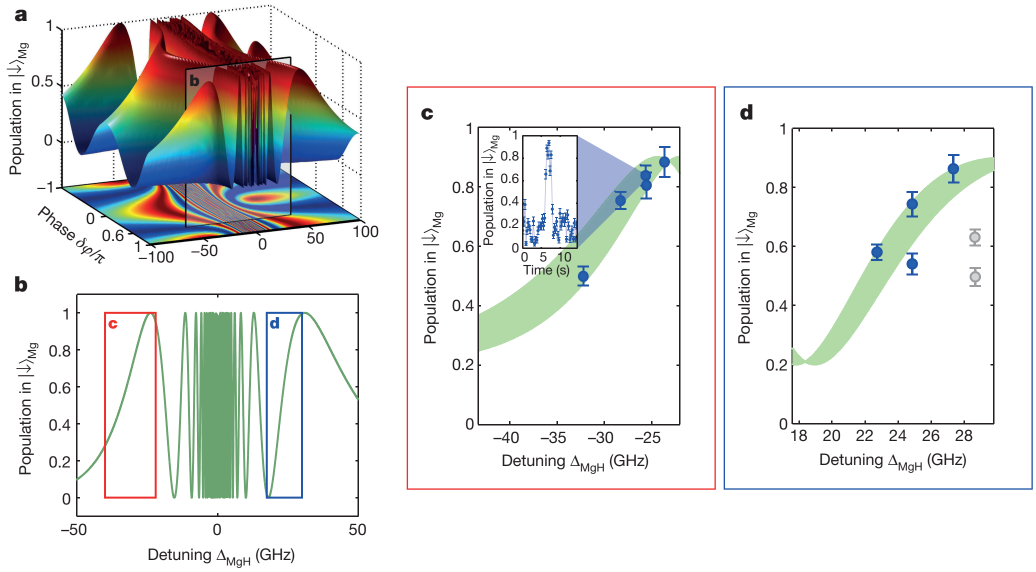

Figure 3 | Non-destructive state detection. a, The theoretically calculated signal $P_{|\downarrow\rangle_{Mg}}$ on the atomic ion (that is, the proportion of the population that is in the $|\downarrow\rangle_{Mg}$ state), for $^{24}MgH^+$ in the $|J=1, m_J=0\rangle_{MgH}$ state, and its dependence on the relative phase, $\delta\varphi$, of the optical force between the atomic and molecular ion, and on the detuning, Δ_{MgH}, from molecular resonance. **b,** Cross-section of panel **a**, for the phase $\delta\varphi \approx 0.6\pi$, corresponding to a trap frequency of $\omega_{IP} \approx 2.17$ MHz. **c, d,** The height of the observed signals as a function of detuning for the regions indicated in **b**. The inset in **c** shows a typical measurement result for a quantum jump (driven by black-body radiation) into and out of the $J=1$ rotational state. The error bars (68% confidence interval) are dominated by quantum projection noise. The thickness of the theory bands (green areas in **c**, **d**) accounts for small changes in trap frequency (and thus in $\delta\varphi$) for the different data points. The grey data points are excluded from the analysis in Fig. 4, because they could not be assigned to a specific slope of the theoretical prediction, thus preventing unambiguous inversion of equation (3).

$$|J\neq 1\rangle_{MgH}|\downarrow\rangle_m \rightarrow |J\neq 1\rangle_{MgH}|\uparrow\rangle_m$$

$$|J\neq 1\rangle_{MgH}|\uparrow\rangle_m \rightarrow |J\neq 1\rangle_{MgH}|\downarrow\rangle_m$$

$$|J=1\rangle_{MgH}|\downarrow\rangle_m \rightarrow |J=1\rangle_{MgH}|\downarrow\rangle_m$$

$$|J=1\rangle_{MgH}|\uparrow\rangle_m \rightarrow |J=1\rangle_{MgH}|\uparrow\rangle_m$$

A typical measurement with a positive detection event can be seen in the inset of Fig. 3c. If the molecular ion is not in the probed rotational state, the π-pulse on the motional qubit is successful and we observe low fluorescence, ($P_{|\downarrow\rangle_{Mg}} \approx 0$). After entering the $J=1$ state, the additional force on the molecule will change the π-time on the motional qubit and we observe fluorescence on the $^{25}Mg^+$ ion ($P_{|\downarrow\rangle_{Mg}} > 0$), until the rotational state changes again. The signal corresponds to a quantum jump of the rotational state in the molecular ion, induced by black-body radiation. The signal background of $P_{|\downarrow\rangle_{Mg}} \approx 0.2$ and reduced contrast arises from experimental imperfections in implementing the logic gates (see Methods). Because the algorithm implements a quantum non-demolition measurement of the molecular state, we reduce quantum projection noise by averaging each data point over 30 experimental cycles with a duration of about 9.3 milliseconds per cycle. We identified an experimental event as a positive detection event if at least three consecutive data points were significantly (1.5σ) above background (see Methods). In a total measuring time of approximately 23 hours, we observed 18 positive detection signals of up to several seconds' duration. The estimated average number of scattered photons from the optical lattice beams that interact with the molecular ion during a single detection cycle at $\Delta_{MgH} = 25$ GHz is around 0.04 (see Methods). If we assume that a single scattered photon removes the molecule from its rotational state, this results in an average single-cycle detection efficiency of 96%, neglecting imperfections in any of the qubit and gate operations; this therefore represents an upper bound. Estimates of the expected number of events—calculated using this detection efficiency, the mean population and the required averaging time of about 1 second for a positive signal event—agree well with the experimental results (see Methods).

The lattice light introduces an AC Stark shift in the molecule's spectral lines of the order of several hundred kilohertz, which is much larger than all magnetic couplings in the molecular ion. Therefore, the substates are labelled by m_J with the quantization axis along the electric-field direction of the lattice light. In this coordinate system, only π-polarized light is present, coupling only to states with $m_J = 0$ (Fig. 1a inset). The resulting signal as a function of the detuning and the molecular quantum state is shown in Fig. 3c, d for $\delta\varphi \approx 0.6\pi$, corresponding to a normal mode frequency of $\omega_{IP} \approx 2.17$ MHz. Experimental data for $\delta\varphi \approx 0$ are shown in Extended Data Fig. 4.

The dependence of $R(\Delta_{MgH})$ on the detuning Δ_{MgH} from a molecular resonance allows us to perform spectroscopy, because forces arising from coupling to other rotational states are negligible over a large range of detunings (Fig. 1b). For this, we have combined data taken for different detuning Δ_{MgH} values and different phases ($\delta\varphi$) by inverting equation (3) numerically and accounting for the reduced contrast (Extended Data Fig. 2). The measured Rabi frequency ratios, $R(\Delta_{MgH})$, for the $X^1\Sigma^+(J=1) \rightarrow A^1\Sigma^+(J=0)$ transition are summarized in Fig. 4. Also shown in Fig. 4 is a fit to the wings of a simplified model, $R_{fit}(f) = A/|f-f_0|$, with the free parameters A and f_0, where we assumed a detuning-independent background coupling to the far-detuned transition in the $^{25}Mg^+$ ion (Fig. 1c). We determine the transition frequency to be $f_0 = 1067.74789(40)$ THz (68% confidence interval), which is in agreement with a previous measurement of $f_0 = 1067.7473(15)$ THz (ref. 26). The fitted characteristic detuning for the Rabi frequency ratio is $A = 45.98(73)$ GHz (68% confidence interval).

We estimate that non-destructive detection of the internal state of a molecular ion with near 100% efficiency could take less than 10 milliseconds, given a larger detuning Δ_{MgH} of roughly 100 GHz and improvements in preparing and manipulating the co-trapped atomic ion (see Methods). This represents a major advance over previous, destructive detection techniques, which require frequent reloading. Our technique will realise its potential in high-precision spectroscopic investigations of narrow transitions between states in molecules using an independent spectroscopy laser. However, whereas in our present

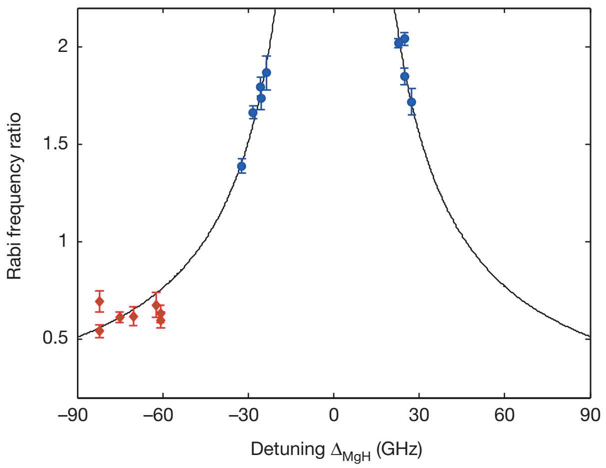

Figure 4 | Quantum logic spectroscopy. The Rabi frequency ratio, $R = \Omega_{MgH}(\Delta_{MgH})/\Omega_{Mg}$, as a function of detuning Δ_{MgH} from a molecular resonance, for all data for which equation (3) could be inverted unambiguously (see Fig. 3c, d). Measurement data recorded at $\omega_{IP} \approx 2.17$ MHz ($\delta\varphi \approx 0.6\pi$; nine points; see Fig. 3) and $\omega_{IP} \approx 2.21$ MHz ($\delta\varphi \approx 0$; seven points; see Extended Data Fig. 4) are indicated by blue circles and red diamonds, respectively. The solid line is a fit to the combined data set, resulting in $f_0 = 1067.74789(40)$ THz. The error bars correspond to the errors shown in Fig. 3 and Extended Data Fig. 4 (68% confidence intervals).

work black-body radiation probabilistically populates the detected state, precision spectroscopy will require more-efficient state-preparation schemes[28,29] or rotational–vibrational cooling techniques[7–11]. A combination of these tools will enable the realization of optical clocks based on molecular ions approaching fractional frequency uncertainties at the 10^{-18} level[30]—where the underlying clock transitions, or combinations of transitions, can be sensitive to variations in fundamental constants[3], to an electron electric dipole moment[5], or to parity violation in chiral molecules.

Online Content Methods, along with any additional Extended Data display items and Source Data, are available in the online version of the paper; references unique to these sections appear only in the online paper.

Received 30 June; accepted 27 November 2015.
Published online 8 February 2016.

1. Germann, M., Tong, X. & Willitsch, S. Observation of electric-dipole-forbidden infrared transitions in cold molecular ions. *Nature Phys*. **10,** 820–824 (2014).
2. Koelemeij, J., Roth, B., Wicht, A., Ernsting, I. & Schiller, S. Vibrational spectroscopy of HD^+ with 2-ppb accuracy. *Phys. Rev. Lett.* **98,** 173002 (2007).
3. Schiller, S. & Korobov, V. Tests of time independence of the electron and nuclear masses with ultracold molecules. *Phys. Rev. A* **71,** 032505 (2005).
4. Flambaum, V. & Kozlov, M. Enhanced sensitivity to the time variation of the fine-structure constant and m_p/m_e in diatomic molecules. *Phys. Rev. Lett.* **99,** 150801 (2007).
5. Loh, H. *et al.* Precision spectroscopy of polarized molecules in an ion trap. *Science* **342,** 1220–1222 (2013).
6. Shuman, E. S., Barry, J. F. & DeMille, D. Laser cooling of a diatomic molecule. *Nature* **467,** 820–823 (2010).
7. Rellergert, W. G. *et al.* Evidence for sympathetic vibrational cooling of translationally cold molecules. *Nature* **495,** 490–494 (2013).
8. Schneider, T., Roth, B., Duncker, H., Ernsting, I. & Schiller, S. All-optical preparation of molecular ions in the rovibrational ground state. *Nature Phys.* **6,** 275–278 (2010).
9. Staanum, P. F., Højbjerre, K., Skyt, P. S., Hansen, A. K. & Drewsen, M. Rotational laser cooling of vibrationally and translationally cold molecular ions. *Nature Phys*. **6,** 271–274 (2010).
10. Lien, C.-Y. *et al.* Broadband optical cooling of molecular rotors from room temperature to the ground state. *Nature Commun*. **5,** 4783 (2014).
11. Hansen, A. K. *et al.* Efficient rotational cooling of Coulomb-crystallized molecular ions by a helium buffer gas. *Nature* **508,** 76–79 (2014).
12. Højbjerre, K., Hansen, A. K., Skyt, P. S., Staanum, P. F. & Drewsen, M. Rotational state resolved photodissociation spectroscopy of translationally and vibrationally cold MgH^+ ions: toward rotational cooling of molecular ions. *New J. Phys.* **11,** 055026 (2009).
13. Tong, X., Winney, A. & Willitsch, S. Sympathetic cooling of molecular ions in selected rotational and vibrational states produced by threshold photoionization. *Phys. Rev. Lett.* **105,** 143001 (2010).
14. Leibfried, D. *et al.* Experimental demonstration of a robust, high-fidelity geometric two ion-qubit phase gate. *Nature* **422,** 412–415 (2003).
15. Schmidt, P. O. *et al.* Spectroscopy using quantum logic. *Science* **309,** 749–752 (2005).
16. Wan, Y. *et al.* Precision spectroscopy by photon-recoil signal amplification. *Nature Commun*. **5,** 4096 (2014).
17. Ratschbacher, L., Zipkes, C., Sias, C. & Köhl, M. Controlling chemical reactions of a single particle. *Nature Phys*. **8,** 649–652 (2012).
18. Brünken, S. *et al.* H_2D^+ observations give an age of at least one million years for a cloud core forming Sun-like stars. *Nature* **516,** 219–221 (2014).
19. Campbell, E. K., Holz, M., Gerlich, D. & Maier, J. P. Laboratory confirmation of C_{60}^+ as the carrier of two diffuse interstellar bands. *Nature* **523,** 322–323 (2015).
20. Cirac, J. I. & Zoller, P. Quantum computations with cold trapped ions. *Phys. Rev. Lett.* **74,** 4091 (1995).
21. Schmidt-Kaler, F. *et al.* Realization of the Cirac-Zoller controlled-NOT quantum gate. *Nature* **422,** 408–411 (2003).
22. Nie, S. & Emory, S. R. Probing single molecules and single nanoparticles by surface-enhanced Raman scattering. *Science* **275,** 1102–1106 (1997).
23. Schmidt, P. O. et al. in *Proceedings of Non-Neutral Plasma Physics VI, Workshop on Non-Neutral Plasmas,* Vol. 862 (eds Drewsen, M., Uggerhøj, U. & Knudsen, H.) 305–312 (Aarhus, 2006).
24. Vogelius, I. S., Madsen, L. B. & Drewsen, M. Probabilistic state preparation of a single molecular ion by projection measurement. *J. Phys. At. Mol. Opt. Phys*. **39,** S1259–S1265 (2006).
25. Hume, D. B. *et al.* Trapped-ion state detection through coherent motion. *Phys. Rev. Lett.* **107,** 243902 (2011).
26. Balfour, W. J. Rotational analysis of the $A^1\Sigma^+ \to X^1\Sigma^+$ and $B^1\Pi \to X^1\Sigma^+$ systems of $^{24}MgH^+$, $^{25}MgH^+$, and $^{26}MgH^+$. *Can. J. Phys.* **50,** 1082–1091 (1972).
27. Wan, Y., Gebert, F., Wolf, F. & Schmidt, P. O. Efficient sympathetic motional-ground-state cooling of a molecular ion. *Phys. Rev. A* **91,** 043425 (2015).
28. Leibfried, D. Quantum state preparation and control of single molecular ions. *New J. Phys.* **14,** 023029 (2012).
29. Ding, S. & Matsukevich, D. N. Quantum logic for the control and manipulation of molecular ions using a frequency comb. *New J. Phys.* **14,** 023028 (2012).
30. Schiller, S., Bakalov, D. & Korobov, V. I. Simplest molecules as candidates for precise optical clocks. *Phys. Rev. Lett.* **113,** 023004 (2014).

Acknowledgements We acknowledge the support of the Deutsche Forschungsgemeinschaft through QUEST and grant SCHM2678/3-1. This work was financially supported by the State of Lower-Saxony, Hannover, Germany. Y.W. acknowledges support from the Braunschweig International Graduate School of Metrology. We thank E. Tiemann, H. Knöckel, O. Dulieu and I.D. Leroux for discussions; M. Drewsen and O. Dulieu for the transition-matrix elements for $^{24}MgH^+$; and E. Tiemann, B. Hemmerling, and I.D. Leroux for reading the manuscript.

Author Contributions P.O.S. conceived and supervised the experiment. F.W. developed the read-out algorithm. F.W., J.C.H. and C.S. carried out the measurements. Y.W. performed the simulations and calculated the lattice coupling strength. F.W. and P.O.S. wrote the main part of the manuscript. Y.W. and F.G. built essential parts of the experiment. All authors discussed the results and contributed to the manuscript.

Author Information Reprints and permissions information is available at www.nature.com/reprints. The authors declare no competing financial interests. Readers are welcome to comment on the online version of the paper. Correspondence and requests for materials should be addressed to P.O.S. (piet.schmidt@quantummetrology.de).

METHODS

Experimental set-up. The experiments are carried out in a linear Paul trap, with a typical axial trap frequency of 2.21 MHz for $^{25}Mg^+$. We use a hyperfine qubit consisting of the states $|\downarrow\rangle_{Mg} = |F=3, m_F=3\rangle$ and $|\uparrow\rangle_{Mg} = |F=2, m_F=2\rangle$ of the $^2S_{1/2}$ electronic ground state (m_F is the projection of the total spin, F, on the quantization axis). The Raman laser system for coherent manipulation of the $^{25}Mg^+$ qubit via the $^2P_{3/2}$ level is based on a frequency-quadrupled fibre laser[31]. The detuning from the atomic resonance is fixed at 9.2 GHz, limiting ground-state cooling efficiency[27] and qubit operations owing to spontaneous Raman scattering[32]. The same laser is also used for internal state discrimination by applying an optical sideband tuned near resonance of the $|\downarrow\rangle_{Mg} \rightarrow |^2P_{3/2}, F=4, m_F=4\rangle$ component of the D2 transition. A similar laser system addressing the $^2S_{1/2} \rightarrow {}^2P_{1/2}$ (D1) transition is used for optical repumping and quenching during sideband cooling[27].

The light fields creating the optical lattice for molecular-state detection and spectroscopy are provided by a frequency-doubled dye laser whose frequency is tuned close to the $X^1\Sigma^+(J=1) \rightarrow A^1\Sigma^+(J=0)$ transition of $^{24}MgH^+$, with a variable detuning Δ_{MgH} typically smaller than $\sim$100 GHz from the molecular transition, and detuned by $\Delta_{MgH} \approx 1.5$ THz from the atomic D1 transition of $^{25}Mg^+$. Two counter-propagating laser beams derived from this laser are linearly polarized in the horizontal plane with a relative detuning δ. They are aligned along the trap axis to form an angle of $\pi/4$, with the atomic quantization axis being given by a static applied magnetic field of $\sim$0.58 mT. The detuning between the two laser fields results in a moving optical lattice, providing a temporally and spatially varying force on the two ions with a relative phase $\delta\varphi$, which depends on the distance between the two ions. Two optical fibres suitable for ultraviolet single-mode transmission[33] are used to reduce the effect of beam-pointing fluctuations on the coupling strength, and aid in the initial alignment of the beams onto the molecular ion. The frequency of the spectroscopy light is monitored by a commercial wavemeter (High Finesse WS/7). We assign an uncertainty of less than 100 MHz to the measured value.

To reduce quantum projection noise resulting from imperfect single-qubit operations, we average over 30 measurement cycles to get a single measurement point. This procedure takes 280 ms. If at least three consecutive points are significantly above the threshold (1.5σ), we assign them to a positive detection signal from the molecule. To determine the signal height, we take the first and last measurement points into account only if they are at least 2σ above the background. This procedure improves the signal quality, because we remove data points that contain only a fraction of positive detection events during the 30 repetitions.

Hamiltonian for lattice coupling. The Hamiltonian (H) for N ions coupled by a one-dimensional moving optical lattice in the interaction picture can be written as:

$$H = \sum_j^N \hbar\Omega_j e^{-i(\delta t - \varphi_j)} \exp\left[\sum_k^N i\eta_{jk}(a_k e^{-i\omega_k t} + a_k^\dagger e^{i\omega_k t})\right] + \text{h.c.}$$

where j labels the ions; k labels the axial motional modes with frequency ω_k; η_{jk} is the Lamb–Dicke parameter; $a_k^\dagger$ is the creation operator; h.c. is the hermitean conjugate; φ_j is a phase. $\Omega_j = \Omega_{1j}\Omega_{2j}/(2\Delta)$ is the two-photon Rabi frequency for the two lattice beams coupling to an electronically excited state with detuning Δ. Considering the case of two ions $j \in \{1, 2\}$, we have to take two axial motional modes into account, namely $k \in \{\text{IP, OP}\}$, denoting the in-phase and out-of-phase motion of the two ions, respectively. In the following, the relative detuning of the two lattice beams, δ, is chosen to be $\delta = \omega_{OP} - \omega_{IP}$. After the rotating wave approximation, only the second-order mixed term in the Lamb–Dicke approximation survives, resulting in the following interaction Hamiltonian, mediating the coupling between the two modes:

$$H = -\sum_{j=1,2} \hbar\Omega_j e^{i\varphi_j}\eta_{j,\text{IP}}\eta_{j,\text{OP}} a_{\text{IP}} a_{\text{OP}}^\dagger + \text{h.c.}$$

In adding up the forces on the two ions, we have to consider the different effect on both modes, and take into account the signs in the matrix for transformation between normal modes and laboratory frame[34]. We find for two ions with equal mass the Lamb–Dicke factors:

$$\eta_{1,\text{IP}} = \eta_{2,\text{IP}} \equiv \eta_{\text{IP}}$$

$$\eta_{1,\text{OP}} = -\eta_{2,\text{OP}} \equiv \eta_{\text{OP}}$$

and the Hamiltonian reads:

$$H = -\hbar\eta_{\text{IP}}\eta_{\text{OP}} a_{\text{IP}} a_{\text{OP}}^\dagger [\Omega_1 e^{i\varphi_1} - \Omega_2 e^{i\varphi_2}] + \text{h.c.}$$

It is convenient to define:

$$\delta\varphi \equiv \varphi_1 - \varphi_2$$

$$\Phi \equiv \varphi_1 + \varphi_2$$

The Hamiltonian can then be written as:

$$H = -e^{i\Phi/2}\hbar\eta_{\text{IP}}\eta_{\text{OP}} a_{\text{IP}} a_{\text{OP}}^\dagger [\Omega_1 e^{i\delta\varphi/2} - \Omega_2 e^{-i\delta\varphi/2}] + \text{h.c.}$$

We introduce the modified Rabi frequency:

$$\Omega = \Omega_{\text{eff}} e^{i\Phi_{\text{eff}}} \equiv -e^{i\Phi/2}[\Omega_1 e^{i\delta\varphi/2} - \Omega_2 e^{-i\delta\varphi/2}]$$

with amplitude:

$$\Omega_{\text{eff}} = \Omega_2\sqrt{1 - 2R\cos(\delta\varphi) + R^2}$$

where $R = \Omega_1/\Omega_2$ is the ratio between the Rabi frequencies and Φ_{eff} is an effective phase. Identifying $\Omega_1 = \Omega_{MgH}$ and $\Omega_2 = \Omega_{Mg}$ with the Raman Rabi frequencies for the molecular and atomic ions, respectively, we arrive at equation (2) of the main text. For very large detunings from either the atomic or the molecular ion, the effective Rabi frequency reduces to Ω_{MgH} and Ω_{Mg}, respectively. The final interaction Hamiltonian is then given by:

$$H = \hbar\Omega_{\text{eff}}\eta_{\text{IP}}\eta_{\text{OP}}(e^{i\Phi_{\text{eff}}} a_{\text{IP}} a_{\text{OP}}^\dagger + e^{-i\Phi_{\text{eff}}} a_{\text{IP}}^\dagger a_{\text{OP}}) \quad (4)$$

which is a Hamiltonian that describes a system consisting of $n+1$ coupled levels, where n is the number of initial excitations. In the case $n=1$, we get a two-level system consisting of the states $|\downarrow\rangle_m \equiv |1\rangle_{\text{IP}}|0\rangle_{\text{OP}}$, $|\uparrow\rangle_m \equiv |0\rangle_{\text{IP}}|1\rangle_{\text{OP}}$, which are coupled with the Rabi frequency Φ_{eff}. The action of this Hamiltonian can be described as Rabi flopping between motional states. Results from an experimental implementation are shown in Extended Data Fig. 2 for a two-ion crystal consisting of a $^{25}Mg^+$ ion and a molecular ion in a rotational state not addressed by the lattice. The reduced initial contrast and its decay are attributed to imperfect ground-state cooling, off-resonant scattering of the Raman beams that are interacting with the atom, and dephasing of the lattice beams. Starting from both axial modes near the ground state, a quantum of motion is added using a BSB π-pulse. The lattice coupling is then switched on for a variable time and the motional information is mapped back onto the electronic qubit by a second BSB π-pulse (see Extended Data Fig. 3). In such a sequence, we are not sensitive to the phase factors, $e^{\pm i\Phi_{\text{eff}}}$, which can therefore be neglected in the Hamiltonian, resulting in equation (1) of the main text. Note that an additional phase of π is introduced if the sign of the detuning differs for the atomic and molecular resonances, so the relative phase is given by:

$$\delta\varphi = \begin{cases} 2\pi d\Delta k \\ 2\pi\left(d\Delta k + \dfrac{1}{2}\right) \end{cases}$$

where d is the distance between ions and $\Delta k = k_1 - k_2 \approx 2k_1$ is the difference between the wavenumbers of the two lattice beams (the top part of the equation relates to the same sign, and the bottom part to the opposite sign).

Coupling of the optical lattice to the molecular ion. The coupling strength of the lattice laser to the molecular ion can be described by the transition matrix element between two states, $|\xi''\Lambda''\nu''J''m_J''\rangle$ and $|\xi'\Lambda'\nu'J'm_J'\rangle$, with Λ being the projection of the angular momentum on the molecular axis, which is $\Lambda' = \Lambda'' = 0$ for both involved states, since we have a $\Sigma \rightarrow \Sigma$ transition without electron angular momentum. The electronic part of the wavefunctions is given by $\xi' = \text{A}$ and $\xi'' = \text{X}$ in spectroscopic notation. The vibrational and rotational quantum numbers are given by ν and J, respectively, and m_J is the projection of J onto the quantization axis. Note that the quantization axis for the molecule is given by the electric field of the lattice light, since the AC Stark shift causes dominant-level splitting. The transition-dipole matrix element is usually approximated by:

$$\langle\xi'\nu'J'm_J'\Lambda'|d_q|\xi''\nu''J''m_J''\Lambda''\rangle =$$

$$\mu_{XA}\sqrt{S^{FC}(\nu',\nu'')S^{HL}(J',\Lambda';J'',\Lambda'')S^{geom}(J',m_J';J'',m_J'')}$$

where μ_{XA} is the electronic transition dipole moment. The Franck–Condon factor describing the overlap of the wave functions of the two vibrational ground states can be calculated from the data given in ref. 36:

$$S^{FC}(\nu'=0,\nu''=0) = \left[\int \psi_{\nu'=0}^*\psi_{\nu''=0}\,dr\right]^2 \approx 0.0919$$

The Hönl–London factor describing the dependence of the transition strength on the rotational quantum numbers is given in ref. 37:

$$S^{\mathrm{HL}}(J', \Lambda'=0;\ J'', \Lambda''=0) = \max(J', J'')$$

The geometric factor describing the addition of total angular momentum of the molecule and the angular momentum of the photon is given by:

$$S^{\mathrm{geom}}_{m_J' q}(J'm_J'; J''m_J'') = \left| \varepsilon^q \begin{pmatrix} J' & 1 & J'' \\ -m_J' & q & m_J'' \end{pmatrix}_{3j} \right|^2$$

with the Wigner 3j-symbol and the polarization components ε^q. Because the quantization axis is given by the lattice, it is convenient to calculate the coupling in a basis parallel to the lattice electric field, where the polarization components are $\varepsilon^{-1} = \varepsilon^1 = 0$ and $\varepsilon^0 = 1$.

The Rabi frequency from the interaction of the optical lattice with the molecular ion (equation (4)) starting from a specific rotational state $|\xi''\nu''J''m_J''\rangle$ is given by[38]:

$$\Omega_{\mathrm{MgH}} = \frac{E_1E_2}{2\hbar^2}\sum_{m_J'}\sum_{q}\frac{|\varepsilon^q\langle\xi'\nu'J'm_J'|d_q|\xi''\nu''J''m_J''\rangle|^2}{\Delta_{\mathrm{MgH}}}$$

$$= \frac{E_1E_2}{2\hbar^2}\frac{\mu_{\mathrm{XA}}^2}{\Delta_{\mathrm{MgH}}}S^{\mathrm{FC}}S^{\mathrm{HL}}\sum_{m_J'}\sum_{q}S^{\mathrm{geom}}_{m_J' q}$$

$$= \frac{E_1E_2}{2\hbar^2}\frac{\mu_{\mathrm{XA}}^2}{\Delta_{\mathrm{MgH}}}S^{\mathrm{FC}}S^{\mathrm{HL}}S^{\mathrm{geom}}$$

where E_1 and E_2 are the electric-field amplitudes of the two counter-propagating laser beams forming the optical lattice, and Δ_{MgH} is the detuning from the molecular resonance. Using a similar approach for the atomic ion, we get a Rabi frequency ratio that is independent of the applied electric field. From the well-known transition strengths in $^{25}\mathrm{Mg}^+$ and the fitted value for A of 45.98(73) GHz (68% confidence interval), we extract a dipole matrix element for the molecular transition of $\mu_{\mathrm{XA}}^{\mathrm{exp}} = 1.2510(99)ea_0$, which is smaller than the matrix element $\mu_{\mathrm{XA}}^{\mathrm{th}} = 1.779ea_0$ extracted from the theoretical data presented in ref. 36. We use the experimental dipole matrix element for the curves in Fig. 3 and Extended Data Fig. 4.

Scattering rate and single-cycle detection efficiency. We assume that scattering of a single photon on the optical transition of the molecular ion will change its rotational–vibrational state, owing to the non-vanishing Franck–Condon factors between different vibrational states. Therefore, a small scattering rate is desired. In the following we use a simplified model in which the molecular ion is treated as a two-level system to estimate the order of magnitude for the spontaneous emission rate of the molecular ion that is subject to the ODF. The number of scattered photons from a two-level system, with excited-state linewidth Γ_0, interacting for a time t_π with an optical lattice formed by two laser beams of equal Rabi frequency Ω and detuned by Δ_{Mg} from resonance is given by:

$$\Gamma_{\mathrm{sc}}t_\pi = \frac{\Gamma_0\Omega^2}{2\Delta_{\mathrm{MgH}}^2}t_\pi$$

For the implemented quantum algorithm, the time t_π is chosen such that the coupling to the atomic ion drives a π-pulse between the two motional states, $t_\pi = \pi/(\Omega_{\mathrm{Mg}}\eta_{\mathrm{IP}}\eta_{\mathrm{OP}})$. Using $R = \Omega_{\mathrm{MgH}}/\Omega_{\mathrm{Mg}}$ and $\Omega_{\mathrm{MgH}} = \Omega^2/(2\Delta_{\mathrm{MgH}})$, we obtain:

$$\Gamma_{\mathrm{sc}}t_\pi = \frac{\Gamma_0\pi R}{\Delta_{\mathrm{MgH}}\eta_{\mathrm{IP}}\eta_{\mathrm{OP}}}$$

where Γ_0 for the molecular ion is given by:

$$\Gamma_0 = \frac{\omega_0^3}{3\pi\epsilon_0\hbar, c^3}\mu_{\mathrm{XA}}^2$$

with the scaled transition dipole moment μ_{XA} given above. For Poissonian photon distribution, the probability to scatter no photon follows:

$$P_{\mathrm{scatt}}(0) = \mathrm{e}^{-\Gamma_{\mathrm{sc}}t_\pi}$$

For a detuning of roughly 25 GHz, we expect to scatter on average 0.04 photons, which corresponds to a fundamentally limited single-cycle detection efficiency of $E_{\mathrm{ss}} = P_{\mathrm{scatt}}(0) \approx 96\%$. For an increased detuning of −100 GHz, the number of scattered photons on average would be reduced to 0.0026 for a π-pulse with the optical lattice. However, to get a large enough signal contrast for single-cycle detection, it would be necessary to perform a 2π-pulse with the lattice, which leads to a single-cycle detection efficiency of 99.5%.

The number of positive detection events, N_{ev}, for a total number N_{total} of trials can be estimated from:

$$N_{\mathrm{ev}} = (E_{\mathrm{SS}})^{3N_{\mathrm{cycle}}}P_{\mathrm{therm}}P_{t\geq 3}N_{\mathrm{total}}$$

where P_{therm} is the probability of the molecule being in the probed state for a thermal distribution at 300 K, and $P_{t\geq 3}$ is the probability of the molecular ion staying at least for the time of three measurement points in the probed state, which is a prerequisite for positive detection in the experiment. In our case, we have $N_{\mathrm{total}} \approx 2\times 10^5$, $P_{\mathrm{therm}} = 0.08$, $P_{t\geq 3} = 0.8$ (see Monte Carlo simulation in Extended Data Fig. 1) and $N_{\mathrm{cycle}} = 30$. For a single-shot-detection efficiency of the order of $E_{\mathrm{ss}} \approx 95\%$, this results in an expected number of points belonging to a detection signal of N_{ev} of about 130, which is in agreement with the observed number of points $N_{\mathrm{ev}}^{\mathrm{exp}} \approx 100$ assigned to the 18 positive detection events.

Uncertainties of the fitted parameters. We extracted the centre frequency and the line strength from a weighted nonlinear least-squares fit. The assigned uncertainties correspond to the 68% confidence bounds, C, that have been calculated assuming a normal distribution of errors and according to $C = b \pm t\sqrt{S}$, where b is the fitted coefficient, t is the inverse of the Student's cumulative distribution function for the required confidence, and $S = (X^{\mathrm{T}}X)^{-1}s^2$, with the mean squared error s^2 and the Jacobian X of the fitted values with respect to the coefficients.

31. Hemmerling, B. *et al.* A single laser system for ground state cooling of $^{25}\mathrm{Mg}^+$. *Appl. Phys. B* **104,** 583590 (2011)
32. Ozeri, R. *et al.* Hyperfine coherence in the presence of spontaneous photon scattering. *Phys. Rev. Lett.* **95,** 030403 (2005).
33. Gebert, F. *et al.* Damage-free single-mode transmission of deep-UV light in hollow-core PCF. *Opt. Express* **22,** 15388–15396 (2014).
34. James, D. F. V. Quantum dynamics of cold trapped ions with application to quantum computation. *Appl. Phys. B* **66,** 181–190 (1998).
35. Hemmerling, B., Gebert, F., Wan, Y. & Schmidt, P. O. A novel, robust quantum detection scheme. *New J. Phys.* **14,** 023043 (2012).
36. Aymar, M., Guérout, R., Sahlaoui, M. & Dulieu, O. Electronic structure of the magnesium hydride molecular ion. *J. Phys. At. Mol. Opt. Phys.* **42,** 154025 (2009).
37. Hansson, A. & Watson, J. K. A comment on Hönl-London factors. *J. Mol. Spectrosc.* **233,** 169–173 (2005).
38. Bergmann, K. & Shore, B. W. *Coherent Population Transfer,* Ch. 9 (eds Dai, H.-L. & Field, R. W.) 367 (World Scientific, 1995).

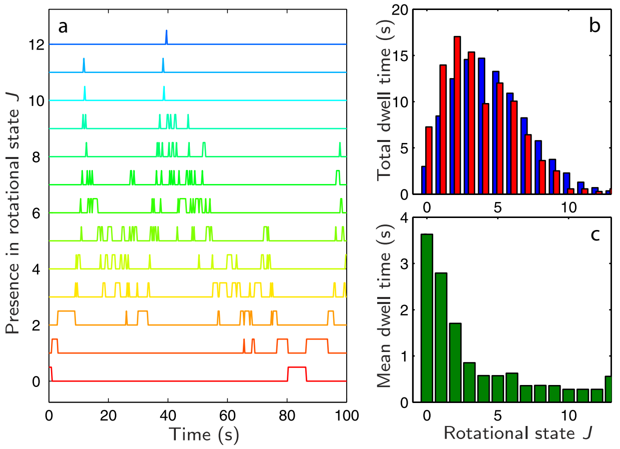

Extended Data Figure 1 | Single trajectory from a Monte Carlo simulation of molecular dynamics. a, The ion initially prepared in the rotational ground state is transferred to higher rotational states because of coupling to black-body radiation at 300 K. **b**, The probability of finding the ion in a certain rotational state in the simulation (red bars) follows a thermal distribution. The blue bars are calculated values from a master equation approach. The deviation between the red and blue bars results from the finite time interval of the Monte Carlo wavefunction simulation. **c**, The dwell time decreases for higher rotational states.

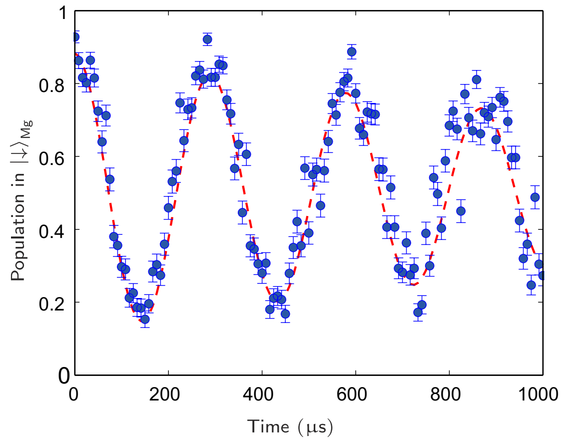

Extended Data Figure 2 | Rabi flopping between motional states. Implementation of the sequence shown in Fig. 2 for $\Omega_{MgH} = 0$. The duration of the applied optical lattice is varied to induce Rabi flopping between the motional qubit states $|\downarrow\rangle_m$ and $|\uparrow\rangle_m$. The error bars show the 95% confidence interval of the photon-distribution fit[35]. The red dashed line shows a fit to a damped oscillation.

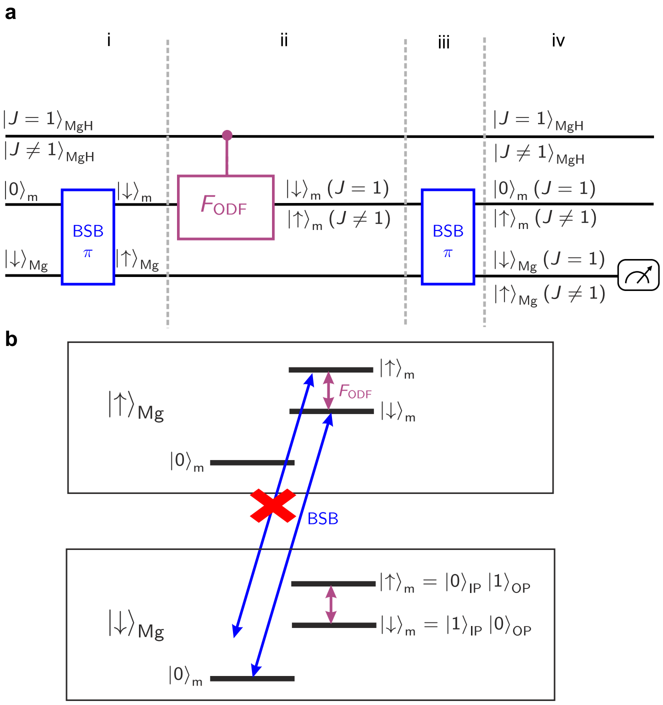

Extended Data Figure 3 | Full experimental sequence. a, Circuit description of the sequence. i, A BSB π-pulse initializes the atom in the state $|\uparrow\rangle_{\mathrm{Mg}}$ and the motional state in the qubit state $|\downarrow\rangle_{\mathrm{m}}$. ii, The ODF rotates the motional qubit controlled by the internal state of the molecule (see Fig. 2). iii, A second BSB π-pulse maps the motional state (which contains the information about the molecule's internal state) to the atomic qubit. iv, The atomic qubit's state is read out by state-dependent fluorescence. **b**, Pictorial representation of the laser couplings in a simplified level scheme.

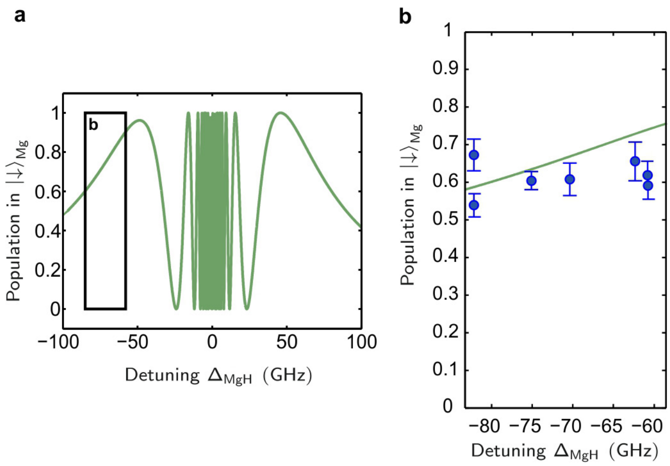

Extended Data Figure 4 | Raw data for $\delta\varphi \approx 0$. a, Theoretically predicted signal for $\delta\varphi \approx 0$, corresponding to $\omega_{IP} \approx 2.21$ MHz. **b**, Expansion of the region shown in **a** with the seven measured data points that are shown as red diamonds in Fig. 4. The error bars indicate the 68% confidence interval of the photon-distribution fit[35].

doi:10.1038/nature16522

Possible light-induced superconductivity in K_3C_{60} at high temperature

M. Mitrano[1], A. Cantaluppi[1,2], D. Nicoletti[1,2], S. Kaiser[1], A. Perucchi[3], S. Lupi[4], P. Di Pietro[3], D. Pontiroli[5], M. Riccò[5], S. R. Clark[1,6,7], D. Jaksch[7,8] & A. Cavalleri[1,2,7]

The non-equilibrium control of emergent phenomena in solids is an important research frontier, encompassing effects such as the optical enhancement of superconductivity[1]. Nonlinear excitation[2,3] of certain phonons in bilayer copper oxides was recently shown to induce superconducting-like optical properties at temperatures far greater than the superconducting transition temperature, T_c (refs 4–6). This effect was accompanied by the disruption of competing charge-density-wave correlations[7,8], which explained some but not all of the experimental results. Here we report a similar phenomenon in a very different compound, K_3C_{60}. By exciting metallic K_3C_{60} with mid-infrared optical pulses, we induce a large increase in carrier mobility, accompanied by the opening of a gap in the optical conductivity. These same signatures are observed at equilibrium when cooling metallic K_3C_{60} below T_c (20 kelvin). Although optical techniques alone cannot unequivocally identify non-equilibrium high-temperature superconductivity, we propose this as a possible explanation of our results.

Molecular solids of chemical formula A_3C_{60} often crystallize in face-centred cubic structures (Fig. 1a) in which each C_{60}^{3-} ion contributes three half-filled molecular orbitals to form narrow bands[9]. These electronic states give rise to superconductivity at equilibrium[10,11], mediated by a combination of electronic correlations[12,13] and local molecular vibrations[14–16].

In the experiments reported here, femtosecond mid-infrared optical pulses were used to excite K_3C_{60} powders (see Methods and Extended Data Fig. 1 for sample characterization). The excitation ('pump') pulses were tuned to wavelengths between 6 μm and 15 μm (200–80 meV photon energy), a spectral region in which both the metallic plasma and local molecular vibrations could be excited. The resulting changes in terahertz (THz)-frequency reflectivity and optical conductivity were measured with a second pulse (the 'probe'), a quasi-single-cycle THz-field transient, which was detected after reflection from the photo-excited material (see Methods and Extended Data Figs 2, 3). These transient changes were determined at different pump–probe time delays and normalized to the absolute equilibrium optical properties measured on the same sample (Extended Data Fig. 4).

Figure 1c displays two representative frequency-dependent equilibrium reflectivity spectra $R(\omega)$ measured above and below T_c (20 K). The corresponding real and imaginary part of the optical conductivity, $\sigma_1(\omega)$ and $\sigma_2(\omega)$, as extracted by Kramers–Kronig transformations, are shown respectively in Fig. 1d and e. Similar to what has been reported for K_3C_{60} single crystals[17–19], in the metallic state ($T = 25$ K) the optical conductivity displayed a narrow Drude peak and a polaronic band[20] centred at 55 meV. When cooling below T_c, a saturated reflectivity ($R = 1$), an optical gap in $\sigma_1(\omega)$ and a divergent $\sigma_2(\omega)$ emerged from the metal.

This equilibrium superconducting response is to be compared with that measured in metallic high-temperature K_3C_{60} after excitation at 7 μm wavelength (180 meV photon energy), which is tuned to the $T_{1u}(4)$ vibration (see Fig. 2 for measurements at 1 ps time delay). For all temperatures between $T_c = 20$ K and $T = 100$ K, photo-excitation drove transient changes in the optical properties, which were very similar to those observed when cooling at equilibrium (see also Extended Data Fig. 5). At a 1 ps pump–probe time delay, we observed a saturated reflectivity ($R = 1$; Fig. 2a and d), gapped $\sigma_1(\omega)$ (Fig. 2b and e), and divergent $\sigma_2(\omega)$ (Fig. 2c and f).

Furthermore, all transient optical spectra could be fitted with the same function used for the low-temperature superconductor at equilibrium. An extension of the Mattis–Bardeen model was used, applicable to superconductors of arbitrary purity and taking into account both an optical gap (a superconducting component) and a fluid of normal quasi-particles (a Drude component)[21]. The non-equilibrium fits evidenced an 11 meV gap in the non-equilibrium $\sigma_1(\omega)$, nearly twice as large as the 6 meV superconducting gap at equilibrium.

Figure 3 reports similar measurements taken at higher temperatures, for which the effect progressively disappeared as temperature increased.

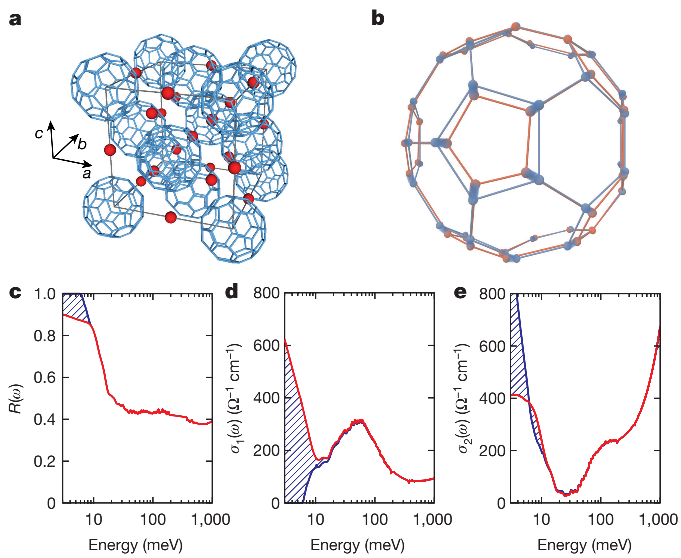

Figure 1 | Structure and equilibrium optical properties of K_3C_{60}. **a**, Face-centred cubic (f.c.c.) unit cell of K_3C_{60} (ref. 26). Blue bonds link the C atoms in each C_{60} molecule. K atoms are represented as red spheres. **b**, C_{60} molecular distortion (red) along the $T_{1u}(4)$ vibrational mode coordinates. The equilibrium structure is displayed in blue. **c–e**, Equilibrium reflectivity at the sample–diamond interface $R(\omega)$ (**c**) and complex optical conductivity (**d**, real, $\sigma_1(\omega)$; **e**, imaginary, $\sigma_2(\omega)$) of K_3C_{60} measured at $T = 25$ K (red) and $T = 10$ K (blue). Hatched regions highlight changes across the superconducting transition.

[1]Max Planck Institute for the Structure and Dynamics of Matter, Luruper Chaussee 149, 22761 Hamburg, Germany. [2]The Hamburg Centre for Ultrafast Imaging, Luruper Chaussee 149, 22761 Hamburg, Germany. [3]INSTM UdR Trieste-ST and Elettra–Sincrotrone Trieste S.C.p.A., Area Science Park, 34012 Basovizza, Trieste, Italy. [4]CNR-IOM and Dipartimento di Fisica, Università di Roma "Sapienza", Piazzale A. Moro 2, 00185 Roma, Italy. [5]Dipartimento di Fisica e Scienze della Terra, Università degli Studi di Parma, Parco Area delle Scienze, 7/a, 43124 Parma, Italy. [6]Department of Physics, University of Bath, Claverton Down, Bath BA2 7AY, UK. [7]Department of Physics, Oxford University, Clarendon Laboratory, Parks Road, Oxford OX1 3PU, UK. [8]Centre for Quantum Technologies, National University of Singapore, 3 Science Drive 2, Singapore 117543, Singapore.

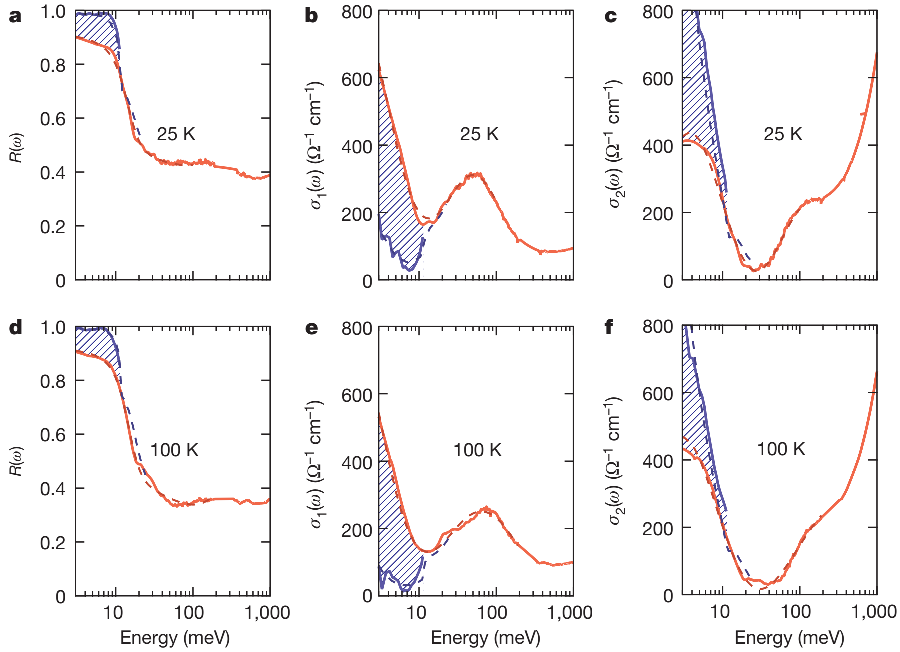

Figure 2 | Transient optical response of photo-excited K_3C_{60} at $T=25$ K and $T=100$ K. Columns as Fig. 1; data taken at equilibrium (red) and 1 ps after photo-excitation (blue) at a pump fluence of 1.1 mJ cm^{-2}, measured at temperatures $T=25$ K (**a**–**c**) and $T=100$ K (**d**–**f**). Fits to the data are displayed as dashed lines. Hatched regions highlight pump-induced changes.

Only a partial reduction in $\sigma_1(\omega)$ and a less pronounced divergence in $\sigma_2(\omega)$ were observed. For these higher temperatures the Drude component alone was sufficient to fit the transient spectra, which did not exhibit a clear gap. However, we note that the $\sigma_1(\omega)$ Drude peak in the light-induced phase (blue curves in Fig. 3b and e) was always narrower than for the equilibrium metal (red curves in Fig. 3b and e), underscoring an optical enhancement in carrier mobility for all temperatures.

In Fig. 4, we plot the transient integrated loss in spectral weight (0.75–2.5 THz, that is, 3.1–10.3 meV) as a function of base temperature (Fig. 4a), pump–probe time delay (Fig. 4b), excitation fluence (Fig. 4c) and wavelength (Fig. 4d). The regions in which the optical properties required the full Mattis–Bardeen fit are shaded in blue, whereas those regions in which the fit yielded a gapless, Drude conductivity are shaded in white.

Figure 4a displays a crossover between a light-induced state with a Mattis–Bardeen gap (blue), observed up to $T=100$ K, and a high-mobility metal (white) observed at higher temperatures. Similarly, in the time-delay dependence (Fig. 4b) a spectral-weight reduction was observed immediately after the excitation pulse (red curve), followed by a gap opening only at later time delays (blue shading). The gapped state disappeared after approximately 2 ps, and the rest of the decay involved relaxation of a high-mobility metal (white shading) with an exponential time constant of ~10 ps (see Extended Data Fig. 6 for representative spectra as a function of pump–probe delay).

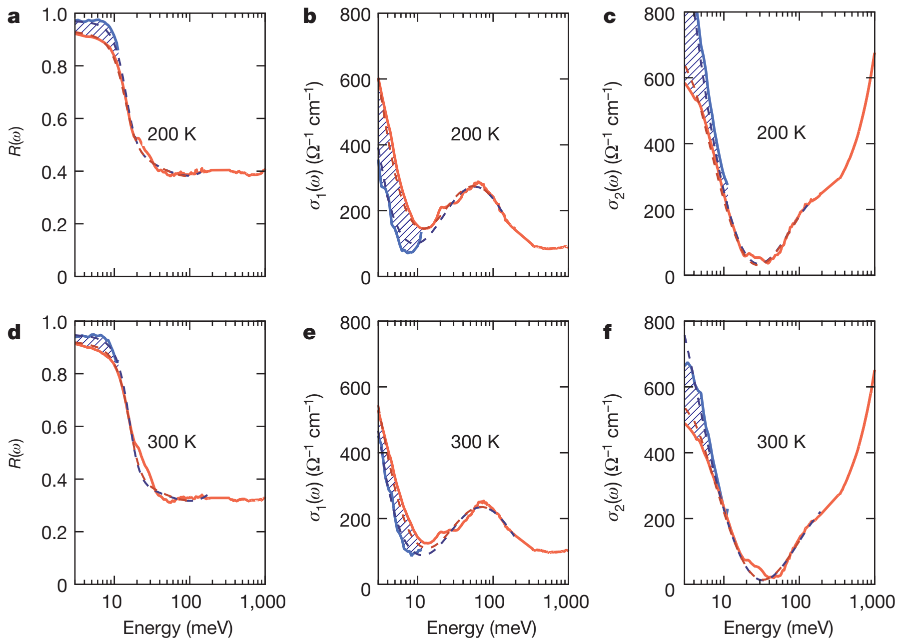

Figure 3 | Transient optical response of photo-excited K_3C_{60} at $T=200$ K and $T=300$ K. Columns as Fig. 1; data taken at equilibrium (red) and 1 ps after photo-excitation (blue) with a pump fluence of 1.1 mJ cm^{-2}, measured at temperatures $T=200$ K (**a**–**c**) and $T=300$ K (**d**–**f**). Fits to the data are displayed as dashed lines. Hatched regions highlight pump-induced changes.

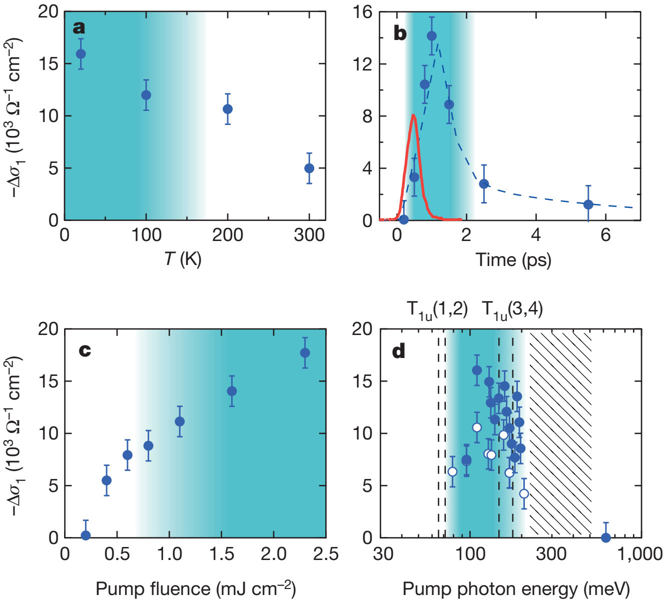

Figure 4 | Scaling of the $\sigma_1(\omega)$ gap with experimental parameters. In all panels, the photo-induced reduction in $\sigma_1(\omega)$ spectral weight, $-\Delta\sigma_1$, integrated between 0.75 THz and 2.5 THz, is plotted on the y axis (represented by filled circles). **a–d**, The lost spectral weight is plotted as a function of temperature (**a**), pump–probe time delay (**b**), pump fluence (**c**) and pump wavelength (**d**). Error bars represent maximum uncertainties determined from different sets of measurements. The regions shaded in blue indicate the parameter ranges for which the transient response was fitted with a model for a superconductor. The red curve in **b** is the pump pulse profile (cross-correlation signal), while the dashed line is a double exponential fit ($\tau_1 \approx 1$ ps, $\tau_2 \approx 10$ ps). Dashed vertical lines in **d** are the frequencies of the four T_{1u} vibrational modes. The experiments were not possible for pump wavelengths between 6 μm and 3 μm (hatched region in **d**) owing to absorption in the diamond window that contained the K_3C_{60} powders. White and blue filled circles are data taken at fluence values of 0.4 mJ cm^{-2} and 1.1 mJ cm^{-2}, respectively. Data in **b–d** were measured at $T = 25$ K.

The pump fluence dependence of Fig. 4c reveals a similar crossover. Metallic conductivities (white) were observed for low excitation levels ($F \lesssim 0.8$ mJ cm^{-2}), whereas fully gapped states (blue) emerged only at higher fluences ($F \gtrsim 0.8$ mJ cm^{-2}).

Finally, when tuning the pump to short wavelengths (2 μm, 620 meV photon energy) no response was found (Fig. 4d). On the contrary, a strong response was measured when the pump was made resonant with the $T_{1u}(4)$ and $T_{1u}(3)$ modes, which correspond both to stretching and compressing of the hexagons and pentagons of the fullerene molecule (see Fig. 1b). A weaker response was still observed for wavelengths extending towards the $T_{1u}(2)$ and $T_{1u}(1)$ resonances.

One possible interpretation for the data above posits that excitation of molecular vibrations can coherently stimulate a transition from the high-temperature metallic state into a non-equilibrium superconducting phase.

To first order, T_{1u} vibrations do not couple to the t_{1u} electronic states that cross the Fermi level, because $T_{1u} \neq t_{1u} \times t_{1u}$. However, for the strong optical fields used here (~1.5 MV cm^{-1}), and from the polarizability of the T_{1u} molecular vibrations, we estimate large oscillatory distortions of the C–C bonds amounting to several per cent of their equilibrium bond lengths. Hence, the large amplitude excitation is expected to extend beyond a linear response, and to deform the structure of the solid along other, anharmonically coupled coordinates. To lowest order, these couplings are described by $q_{T1u}{}^2Q$ terms in the nonlinear lattice Hamiltonian[2,22,23], where q_{T1u} is the directly driven mode coordinate, and Q is the coordinate of any distortion contained in the irreducible representation of $T_{1u} \times T_{1u}$.

As discussed in the Methods section, excitation of the T_{1u} molecular mode is expected to drive a sizeable distortion along normal mode coordinates of H_g symmetry. Because H_g modes are thought to assist pairing at equilibrium[9], it is possible that a quasi-static H_g molecular deformation might favour stronger superconductivity, for example by causing an increase in the electron–phonon coupling (see Extended Data Fig. 7).

Excitation of T_{1u} vibrations is also expected to modulate local electronic correlations. For a molecular mode of coordinate q_{IR} with classical vibrational coordinate $q_{IR}(\tau) = C\sin(\Omega_{IR}\tau)$, where C is a proportionality constant, Ω_{IR} is the driving frequency and τ the time delay, we expect the charge density on each molecule to 'slosh' backwards and forwards[24]. Deformation of the molecular orbital causes a modification of the Coulomb repulsion U_a for the t_{1u} orbital ($a = \{x, y, z,\}$), which can be written as $U_a(\tau) = U_a + \Delta U_a(1 - \cos(2\Omega_{IR}\tau))$. This highlights two effects: a modulation of the onsite Coulomb integral at twice the frequency of the driven molecular mode, and an average change in correlation energy, ΔU_a, which have both been observed in a different organic compound[25].

Although a complete quantitative analysis requires a dynamical quantum chemistry calculation, an order-of-magnitude estimate for these changes in local electronic correlations can be extracted from frozen atomic motions for the $T_{1u}(4)$ mode. This estimate predicts a change in electronic repulsion ΔU_a as high as ~10% of the equilibrium correlation energy for the orbitals orthogonal to the vibrational polarization (see Methods and Extended Data Fig. 8). Such a large asymmetric increase in U_a for only one orbital unbalances the occupancy of the three t_{1u} orbitals. This effect may interact with the dynamical Jahn–Teller coupling known to contribute to superconductivity near equilibrium[9].

However, the interpretation of the data proposed above is not unique. First, some other transient non-superconducting states would also be consistent with the optical properties revealed by our experiments. A large reduction in carrier scattering rate without condensation may be sufficient to explain these results. The measured gap in the transient conductivity would then simply emerge from the equilibrium polaronic band at 55 meV as the broad Drude absorption narrows. However, this scenario is difficult to reconcile with the estimated increase, rather than decrease, of the carrier effective mass (see Methods). Alternatively, one may also consider a sliding, non-commensurate charge density wave, which would be promoted by the enhanced electron–phonon coupling.

Second, the mid-infrared pulses used to excite the sample couple not only to the vibrations but also to the metallic plasma. The measured photo-conductivity signal exhibits a peak in the region of the molecular vibrations (Fig. 4d), but this peak appears broadened compared to the mode linewidths. This might be an indication that a modulation of the local charge density also plays a role in driving the photo-induced state.

Other observations, not mentioned above, appear important but are not well understood. The light-induced high-mobility phase is only induced for temperatures above, but not below, $T_c = 20$ K. Unlike in the case of light-enhanced superconductivity in the cuprates, in which excitation of a phonon below T_c caused a stiffening of the Josephson plasma resonance[4], in the present case we did not observe any widening of the equilibrium superconducting gap at temperatures below T_c. Rather, we measured very little perturbation at the same pump–probe delay (1 ps) for which the response above T_c was maximum (Extended Data Fig. 9), followed by a filling in of the gap by hot quasi-particles at later time delays (Extended Data Fig. 10). This suggests that the equilibrium superconductor and the high-mobility transient state compete with one another. One may rationalize this observation by hypothesizing that equilibrium superconductivity depletes states near the Fermi level, which then cannot participate in the formation of the non-equilibrium state when stimulated by the light.

On balance, although a definitive assignment should rest on further experimentation and theoretical analysis, we favour an interpretation based on stimulated superconductivity. However, the data above are

indicative of striking emergent physics away from equilibrium regardless of the specific mechanism, and provide many new opportunities and challenges for both theory and experiments.

Online Content Methods, along with any additional Extended Data display items and Source Data, are available in the online version of the paper; references unique to these sections appear only in the online paper.

Received 9 August; accepted 4 December 2015.
Published online 8 February 2016.

1. Fausti, D. *et al.* Light-induced superconductivity in a stripe-ordered cuprate. *Science* **331,** 189–191 (2011).
2. Mankowsky, R. *et al.* Nonlinear lattice dynamics as a basis for enhanced superconductivity in $YBa_2Cu_3O_{6.5}$. *Nature* **516,** 71–73 (2014).
3. Mankowsky, R. *et al.* Coherent modulation of the $YBa_2Cu_3O_{6+x}$ atomic structure by displacive stimulated ionic Raman scattering. *Phys. Rev. B* **91,** 094308 (2015).
4. Kaiser, S. *et al.* Optically-induced coherent transport far above T_c in underdoped $YBa_2Cu_3O_{6+\delta}$. *Phys. Rev. B* **89,** 184516 (2014).
5. Hu, W. *et al.* Optically enhanced coherent transport in $YBa_2Cu_3O_{6.5}$ by ultrafast redistribution of interlayer coupling. *Nature Mater.* **13,** 705–711 (2014).
6. Hunt, C. R. *et al.* Two distinct kinetic regimes in the relaxation of light induced superconductivity in $La_{1.675}Eu_{0.2}Sr_{0.125}CuO_4$. *Phys. Rev. B* **91,** 020505 (2015).
7. Först, M. *et al.* Melting of charge stripes in vibrationally driven $La_{1.875}Ba_{0.125}CuO_4$: assessing the respective roles of electronic and lattice order in frustrated superconductors. *Phys. Rev. Lett.* **112,** 157002 (2014).
8. Först, M. *et al.* Femtosecond X-rays link melting of charge density wave correlations and light enhanced coherent transport in $YBa_2Cu_3O_{6.6}$. *Phys. Rev. B* **90,** 184514 (2014).
9. Gunnarsson, O. *Alkali-doped Fullerides: Narrow-band Solids with Unusual Properties* (World Scientific, 2004).
10. Hebard, A. F. *et al.* Superconductivity at 18 K in potassium-doped C_{60}. *Nature* **350,** 600–601 (1991).
11. Xiang, X.-D. *et al.* Synthesis and electronic transport of single crystal K_3C_{60}. *Science* **256,** 1190–1191 (1992).
12. Chakravarty, S., Gelfand, M. P. & Kivelson, S. Electronic correlation effects and superconductivity in doped fullerenes. *Science* **254,** 970–974 (1991).
13. Capone, M. *et al.* Strongly correlated superconductivity. *Science* **296,** 2364–2366 (2002).
14. Varma, C. M., Zaanen, J. & Raghavachari, K. Superconductivity in the fullerenes. *Science* **254,** 989–992 (1991).
15. Schluter, M. *et al.* Electron-phonon coupling and superconductivity in alkali-intercalated C_{60} solid. *Phys. Rev. Lett.* **68,** 526–529 (1992).
16. Han, J. E., Gunnarson, O. & Crespi, V. H. Strong superconductivity with local Jahn Teller phonons in C_{60} solids. *Phys. Rev. Lett.* **90,** 167006 (2003).
17. Degiorgi, L. *et al.* Optical properties of the alkali-metal-doped superconducting fullerenes: K_3C_{60} and Rb_3C_{60}. *Phys. Rev. B* **49,** 7012–7025 (1994).
18. Degiorgi, L. *et al.* Optical measurements of the superconducting gap in single-crystal K_3C_{60} and Rb_3C_{60}. *Nature* **369,** 541–543 (1994).
19. Degiorgi, L. The complete excitation spectrum of the alkali-metal-doped superconducting fullerenes. *Mod. Phys. Lett. B* **9,** 445–468 (1995).
20. Rice, M. G. & Choi, H.-Y. Charged-phonon absorption in doped C_{60}. *Phys. Rev. B* **45,** 10173–10176 (1992).
21. Zimmermann, W. *et al.* Optical conductivity of BCS superconductors with arbitrary purity. *Physica C* **183,** 99–104 (1991).
22. Först, M. *et al.* Nonlinear phononics as a new ultrafast route to lattice control. *Nature Phys.* **7,** 854–856 (2011).
23. Subedi, A., Cavalleri, A. & Georges A. Theory of nonlinear phononics for coherent light control of solids. *Phys. Rev. B* **89,** 220301(R) (2014).
24. Kaiser, S. *et al.* Optical properties of a vibrationally modulated solid state Mott insulator. *Sci. Rep.* **4,** 3823 (2014).
25. Singla, R. *et al.* THz-frequency modulation of the Hubbard *U* in an organic Mott insulator. *Phys. Rev. Lett.* **115,** 187401 (2015).
26. Stephens, P. W. *et al.* Structure of single-phase superconducting K_3C_{60}. *Nature* **351,** 632–634 (1991).

Acknowledgements We acknowledge S. Kivelson and A. Georges for discussion. We are also grateful to A. Subedi for sharing microscopic calculations of anharmonic mode coupling. We thank L. Degiorgi for sharing optical data measured on single crystals. Technical support during sample handling was provided by H.-P. Liermann and M. Wendt. We additionally acknowledge support from M. Gaboardi (for SQUID magnetometry) and from J. Harms (for graphics). The research leading to these results received funding from the European Research Council under the European Union's Seventh Framework Programme (FP7/2007-2013)/ERC Grant Agreement no. 319286 (QMAC). We acknowledge support from the Deutsche Forschungsgemeinschaft via the excellence cluster 'The Hamburg Centre for Ultrafast Imaging — Structure, Dynamics and Control of Matter at the Atomic Scale' and the priority program SFB925. This work was also supported by the Swiss National Supercomputing Center (CSCS) under the project ID s497.

Author Contributions A. Cavalleri conceived the project and the experiments together with M.M. and S.K. The time-resolved THz set-up was built by M.M. and A. Cantaluppi, who performed the pump–probe measurements and analysed the data with support from D.N. and S.K. Equilibrium optical properties were measured and analysed by M.M. and A. Cantaluppi, with support from A.P., S.L. and P.D.P. Samples were grown and characterized by D.P. and M.R. S.R.C. and D.J. provided calculations of time-dependent on-site correlation energies. The manuscript was written by A. Cavalleri, D.N. and M.M., with input from all authors.

Author Information Reprints and permissions information is available at www.nature.com/reprints. The authors declare no competing financial interests. Readers are welcome to comment on the online version of the paper. Correspondence and requests for materials should be addressed to A. Cavalleri (andrea.cavalleri@mpsd.mpg.de).

METHODS

Sample growth and characterization. Stoichiometric amounts of finely ground C_{60} powder and potassium metal were sealed in a cylindrical vessel and closed in a Pyrex vial under vacuum ($\sim 10^{-6}$ torr). The potassium was kept separated from the fullerene powder during the thermal treatment, therefore only potassium vapour came in contact with C_{60}. The two reagents were heated at 523 K for 72 h and then at 623 K for 28 h. The vessel was then opened and the recovered black powder was reground and pelletized. Afterwards, the pellets were further annealed at 623 K for 5 days. All described operations were performed in inert atmosphere (vacuum or Ar glove box with <0.1 p.p.m. O_2 and H_2O). The final product, K_3C_{60}, was characterized by laboratory powder X-ray diffraction and SQUID magnetometry (Extended Data Fig. 1).

Equilibrium optical properties and fitting models. The K_3C_{60} equilibrium optical response was measured on compacted powder pellets (100–400 nm average grain size) sealed in a custom sample holder and pressed against a diamond window, ensuring an optically flat interface.

Broadband infrared reflectivity measurements were carried out at the SISSI beamline (Elettra Synchrotron Facility, Trieste)[27]. The sample was mounted on a cryostat coupled to a Bruker Vertex70 interferometer through a Hyperion microscope. The sample temperature was varied between 300 K and 25 K. The spectra were referenced against the reflectivity of a gold mirror placed into the holder at the sample position.

Data below 3 meV have been extrapolated with the Hagen–Rubens formula, while at high frequency the recalculated sample–diamond reflectivity from single crystal data was used[18]. The complex optical conductivity was determined through a Kramers–Kronig algorithm for samples in contact with a transparent window[28].

All spectra at $T > T_c$ are reported in Extended Data Fig. 4a. The low energy ($\lesssim$ 200 meV) part of the complex conductivity was fitted at all $T > T_c$ with a Drude term and a Lorentz oscillator, which reproduced the polaronic absorption centred at $\sim$55 meV (ref. 17; a representative fit to the 25 K data is also displayed).

The sample reflectivity in the superconducting state was determined as follows. We first measured the reflected electric field at different $T < T_c$ using THz time domain spectroscopy. Each spectrum was then referenced against the reflected field at 25 K, for which the broadband reflectivity was known from the synchrotron measurements.

In Extended Data Fig. 4b the reflectivity measured at different $T < T_c$ is shown. The data were extrapolated below 3 meV using the Zimmermann model[21], a generalization of the Mattis–Bardeen optical conductivity for BCS superconductors with arbitrary purity. The optical conductivity was determined through the same Kramers–Kronig procedure described above. The real and imaginary conductivities are also reported in Extended Data Fig. 4b.

The gap opening in $\sigma_1(\omega)$ and the $1/\omega$ divergence in $\sigma_2(\omega)$ observed upon cooling below T_c are indicative of the superconducting transition. Through fits to the data performed with the Zimmermann model[21], the optical gap 2Δ could be determined as a function of temperature. Both its zero temperature value $2\Delta(T=0) \approx 6$ meV and temperature dependence $2\Delta(T)$—closely following the mean field prediction—were found to be in full agreement with previously published data on K_3C_{60} single crystals[18], as shown in Extended Data Fig. 4b inset.

In Extended Data Fig. 4c, d we show a direct comparison of the equilibrium optical properties (below and above T_c) measured on our K_3C_{60} powders with those reported for single crystals[18]. First, we observe that the polaronic absorption at $\sim$55 meV maintains the very same shape and central frequency. Second, the effect that the superconducting transition has on the low-frequency optical properties in our K_3C_{60} powder is identical to that measured in the single crystals, which exhibit the same $T_c \approx 20$ K and the same optical gap $2\Delta(T=0) \approx 6$ meV.

The only difference between the single crystal data and the present measurements is in the carrier density and scattering rate. As is well known for this class of materials[19], in powdered samples both these quantities can be different from those of a single crystal. From Drude–Lorentz fits to the data, we could estimate a reduction of a factor of $\sim$4 in carrier density n (the Drude plasma frequency $\omega_p \propto \sqrt{n}$ reduces from $\omega_p^{\text{crystal}} \approx 410$ meV to $\omega_p^{\text{powder}} \approx 175$ meV) and of a factor of $\sim$4 in the scattering rate (from $\Gamma^{\text{crystal}} \approx 18$ meV to $\Gamma^{\text{powder}} \approx 4$ meV).

Also the spectral weight Ω_{pol}^2 of the 55 meV polaronic band is a factor of $\sim$4 higher in the single crystal ($\Omega_{\text{pol}}^{\text{crystal}} \approx 1{,}100$ meV against $\Omega_{\text{pol}}^{\text{powder}} \approx 540$ meV). This implies that the quantity $\omega_p^2 / \Omega_{\text{pol}}^2$ extracted for our sample is very close to that reported in ref. 17, thus indicating that the relative ratio between mobile and localized carriers is the same in powders and single crystals.

Determination of the transient optical properties. THz-frequency probe pulses, generated by optical rectification of 800 nm pulses in a ZnTe crystal, were used to measure the transient response of the sample after excitation. These probe pulses were detected after reflection from the sample–diamond interface in a second ZnTe crystal, yielding pump-induced reflectivity changes for frequencies between 0.75 THz and 2.5 THz (3.1–10.3 meV) and with a pump–probe time-delay resolution of approximately 300 fs.

The pump-induced change in the THz electric field $\Delta E_R(t,\tau) = E_R^{\text{pumped}}(t,\tau) - E_R(t)$ was acquired at each time delay τ by filtering the electro-optic sampling signal with a lock-in amplifier, triggered by modulation of the mid-infrared pump with a mechanical chopper. This measurement yielded 'pump on' minus 'pump off' reflected electric field.

The differential electric field $\Delta E_R(t,\tau)$ and the stationary reflected electric field $E_R(t)$ were independently Fourier transformed to obtain the complex-valued, frequency dependent $\Delta\tilde{E}_R(\omega,\tau)$ and $\tilde{E}_R(\omega)$.

Importantly, because the pump-induced changes were large ($\sim$2%), the same measurement was repeated by directly recording $\tilde{E}_R^{\text{pumped}}(\omega,\tau)$ and $\tilde{E}_R(\omega)$ without chopping the pump, and then calculating $\Delta\tilde{E}_R(\omega,\tau) = \tilde{E}_R^{\text{pumped}}(\omega,\tau) - \tilde{E}_R(\omega)$. This method does not require calibration of the absolute phase of the lock-in amplifier, and avoids phase errors in estimating the optical properties. The two methods yielded identical results.

In Extended Data Fig. 2, $E_R(t)$ and $\Delta E_R(t, \tau > 0)$ are displayed both below and above T_c with the corresponding normalized reflectivity changes. For all measured $T > T_c$ and for any $\tau > 0$, all $\Delta E_R(t,\tau)$ and $E_R(t)$ have the same phase, indicating that above T_c one always finds an increase in reflectivity. On the other hand, all measurements below T_c exhibit an opposite phase, that is, reflectivity is reduced upon excitation.

The complex reflection coefficient of the photo-excited material, $\tilde{r}(\omega,\tau)$, was determined using the relation

$$\frac{\Delta\tilde{E}_R(\omega,\tau)}{\tilde{E}_R(\omega)} = \frac{\tilde{r}(\omega,\tau) - \tilde{r}_0(\omega)}{\tilde{r}_0(\omega)}$$

To calculate these ratios, the stationary reflection coefficient $\tilde{r}_0(\omega)$ was extracted at all temperatures from the equilibrium optical properties, determined independently (at the same temperature and in the same sample holder) with synchrotron-based infrared spectroscopy.

These 'raw' light-induced changes, which indicate increase and decrease of the reflectivity above and below T_c, respectively, were reprocessed to take into account the penetration depth mismatch between THz probe ($L \approx 700$–800 nm) and mid-infrared pump ($d \approx 200$ nm) (Extended Data Fig. 3a). Importantly, this renormalization only affects the size of the response, whereas the qualitative change in optical properties is independent of it and of the specific model chosen.

As in, for example, ref. 1, this mismatch can be taken into account most simply by modelling the response of the system as that of a homogeneously photo-excited layer with the unperturbed bulk beneath it (Extended Data Fig. 3b). However, this model applies well only in case of large pump–probe penetration depth mismatches ($d/L \approx 10^2$–10^3).

A more precise method consists of treating the excited surface as a stack of thin layers with a homogeneous refractive index, and describing the excitation profile by an exponential decay[4] (see Extended Data Fig. 3c). By calculating the coupled Fresnel equations of such a multi-layer system, the refractive index at the surface, $\tilde{n}(\omega,\tau)$, can be retrieved, and from this the complex conductivity for a volume that is homogeneously transformed:

$$\tilde{\sigma}(\omega,\tau) = \frac{\omega}{4\pi i}[\tilde{n}(\omega,\tau)^2 - \varepsilon_\infty]$$

In Extended Data Fig. 3d–f we compare the transient optical properties obtained with the exponential decay model (same curves as in Fig. 2a–c) with those obtained with the single-layer description (having used the same pump penetration depth $d = 220$ nm). Both treatments yield very similar results, although we consider the exponential model more accurate.

Note that the extracted optical properties from pump–probe data can sometimes be affected at the earliest time delays by perturbed free induction decay[29]. This issue was raised recently in discussing transient THz probing of superconductors[30]. However, this effect occurs only when coherence is transiently induced on a timescale far shorter than the momentum relaxation time and the response time of the detector[31]. Here the excitation of the transient high-mobility state is achieved with 300 fs mid-infrared pulses, the rise time of the signal is 1 ps, and the relaxation occurs within 2–10 ps. Therefore these effects are negligible[32].

Comparing transient conductivities below and above T_c. Transient optical properties above and below T_c measured at the same time delay after photo-excitation are shown in Extended Data Fig. 9 ($\tau = 1$ ps, same above-T_c data as in Fig. 2a–c).

Importantly, although the equilibrium properties of the unperturbed solid are very different (normal and superconducting state, red and blue curves in Extended

Data Fig. 9a–c and d–f, respectively), the two light-induced states are quite similar to one another (light blue curves). In both cases, the state at $\tau = 1$ ps after excitation is gapped.

As shown in Extended Data Fig. 2, these transient properties derive in one case ($T > T_c$) from a light-induced increase in reflectivity (which saturates to $R \approx 1$ at $\omega < 2\Delta$), while in the other case ($T < T_c$), from a decrease in reflectivity (partial gap filling).

The relaxation dynamics of these two states towards equilibrium are shown in Extended Data Figs 6, 10. Above T_c, the gapped state measured at $\tau = 1$ ps rapidly relaxes into a state with a gapless optical conductivity. The metallic ground state is then recovered within ~5 ps. Below T_c, after the early time response shown in Extended Data Fig. 9, at $\tau = 3$ ps the conductivity gap becomes filled. The superconducting ground state is then recovered over relatively long timescales (>20 ps).

Uncertainties in determining the transient optical properties. We examine here different sources of uncertainty and their propagation. The uncertainty in the absolute value of the measured equilibrium reflectivity is of the order of ±1%. Extended Data Fig. 5a shows as coloured bands the propagated error bars in the equilibrium and transient optical properties for a ±1% and a larger ±2.5% uncertainty in $R(\omega)$. In both cases the response remains gapped.

We next examine uncertainty in the Fresnel phase coefficient β, used in the Kramers–Kronig transformations. This has been set to $\beta = 217$ meV to precisely match the central frequency of the polaronic band (55 meV) with that reported in previous optical studies[17,18] on the same compound. In Extended Data Fig. 5b we show how a ±10% uncertainty in β would affect the equilibrium and transient optical response.

Another possible source of error resides in the pump penetration depth value used to retrieve the transient reflectivities and optical conductivities. This value was set to $d = 220$ nm for all analysed data. In Extended Data Fig. 5c we show how a ±25% change in d would affect the transient optical properties.

Finally, in Extended Data Fig. 5d we show the effect of a different choice of functional form for the decay of $\tilde{n}(\omega, z)$ in the multi-layer model. The exponential decay used for all data analysed in the paper is compared with a single layer (already introduced above) and with a Gaussian-like decay, all having the same d value.

In all these cases the impact of the different sources of error on the calculated reflectivities and optical conductivities is moderate and the qualitative behaviour of the spectra is not affected.

Estimate of the carbon atom displacement. The peak electric field of the mid-infrared pulses can be estimated from

$$E = \sqrt{\frac{F}{2\varepsilon_0 c \Delta t}}$$

where c is the speed of light, ε_0 is the vacuum permittivity and Δt is the pulse duration. The fluence F typically used in these experiments is 1 mJ cm^{-2}, which, for a pulse duration of approximately 300 fs, corresponds to a peak electric field $E = 800$ kV cm^{-1}.

From previous optical measurements[33], it is known that the real part of the optical conductivity on the pumped $T_{1u}(4)$ phonon is $\sigma_1[T_{1u}(4)] = 120\ \Omega^{-1}\ \mathrm{cm}^{-1}$, while its central frequency is $\omega_0 = 168.62$ meV. The pump-induced polarization P (in units of C cm^{-2}) is then given by

$$P = \frac{\sigma_1(\omega_0)}{\omega_0} E = 2.35 \times 10^{-6}$$

The polarization arises owing to a light-induced dipole moment $P = n\delta Z_{\mathrm{eff}} e$, where n is the number of dipoles per unit volume, $Z_{\mathrm{eff}}\, e$ is the effective charge defined as in ref. 34 and δ is the atomic displacement. The Z_{eff} determined for this vibration is 0.147. Under the assumption that all the incident photons are contributing to the excitation, one can estimate from the polarizability a displacement $\delta = 0.24$ Å, that is, approximately 17% of the C–C bond length.

Mode coupling and electronic structure calculations. Electronic structure, lattice dynamics, and nonlinear phonon couplings after excitation of the $T_{1u}(4)$ phonon were obtained using density functional theory (DFT) calculations with a plane-wave basis set and projector augmented wave pseudopotentials (VASP software package)[35]. These calculations were performed within the local density approximation (LDA) with a 900 eV cut-off for the plane-wave basis set. A $6 \times 6 \times 6$ k-point grid and a 0.1 eV Gaussian smearing were used for the Brillouin-zone integration during the self-consistency cycles. Lattice parameters and atomic positions were obtained by energy minimization, ignoring the C_{60} orientational disorder. The calculated lattice constant is 13.888 Å, in good agreement with the experimental value of 14.240 Å.

Phonon frequencies and eigenvectors were determined using the frozen-phonon approach (as implemented in the PHONOPY software package)[36]. After the normal modes were identified, total energy curves as a function of the Raman mode amplitude Q were calculated while simultaneously keeping the amplitude of the pumped $T_{1u}(4)$ mode finite. A shift of the Raman mode energy minimum for finite amplitude of the $T_{1u}(4)$ vibration allowed to identify a cubic $q_{T1u}{}^2 Q$ coupling between the pumped infrared mode and the Raman vibration (see Extended Data Fig. 7a).

Electron–phonon calculations were performed using DFT-LDA (as implemented in the Quantum ESPRESSO software package)[37] with 42 Ry and 420 Ry cut-offs for the plane-wave basis set and the charge-density expansions, respectively. A $6 \times 6 \times 6$ k-point grid and a 0.020 Ry Gaussian smearing were used for Brillouin-zone integration during the self-consistency cycles.

The majority of Raman modes couple to the $T_{1u}(4)$ mode. In Extended Data Fig. 7a we show the shift in the $H_g(1)$ mode minimum when the amplitude of the $T_{1u}(4)$ mode is 2.0 Å $\sqrt{\mathrm{amu}}$. Such a shift implies that the structure is displaced along the $H_g(1)$ coordinate while the $T_{1u}(4)$ mode is pumped. We also report the band structure, electronic density of states (Extended Data Fig. 7b), and electron–phonon coupling (Extended Data Fig. 7c) for a structure displaced along the $H_g(1)$ coordinate with an amplitude of 1.5 Å $\sqrt{\mathrm{amu}}$. We find that such displacement slightly lifts the degeneracy of the t_{1u} states. However, these bands remain part of a single manifold, crossing each other at various points along the high-symmetry path of the Brillouin zone.

We also find a modest change in the density of states, which is caused by the shift of a van Hove singularity near Γ as the bands are moved by the $H_g(1)$ mode displacement. Furthermore, the bandwidth of the t_{1u} manifold steadily increases as a function of $H_g(1)$ mode amplitude. This is reasonable, since the $H_g(1)$ displacements elongate the C_{60} molecule and reduce the intermolecular distances, thus increasing the intermolecular hopping.

The $H_g(1)$ displaced structure develops strong coupling between electrons and intermolecular phonon modes (Extended Data Fig. 7c). At equilibrium the three intermolecular modes with 5 meV energy do not couple to the t_{1u} electrons, while under displacement along the $H_g(1)$ coordinate two of these modes exhibit very large electron–phonon coupling.

The electron–phonon coupling, obtained by integrating the Eliashberg function $\alpha^2F(\omega)$, is 0.52 at equilibrium and 1.44 for the $H_g(1)$ displaced structure. Energy-resolved changes in the electron–phonon coupling function, evaluated as $\Delta\alpha^2F(\omega) = \alpha^2F(\omega)_{\mathrm{Hg(1)}} - \alpha^2F(\omega)_{\mathrm{equilibrium}}$, are reported in Extended Data Fig. 7d. The increased coupling at low energy and a strong reshaping at high frequency (>130 meV) are apparent.

Time-dependent onsite correlation energies. We estimated the magnitude of changes to the inter- and intra-orbital Coulomb repulsion of the t_{1u} orbitals on a single C_{60} molecule when the $T_{1u}(4)$ vibrational mode is driven. The relevant C_{60} molecular orbitals are described by pπ orbitals projecting radially outwards at each C atom. A tight-binding Hückel model captures the hybridization of these orbitals in the C_{60} cage. Hopping amplitudes are assumed to vary with the distance d between C atoms as

$$V(d) = \frac{\Lambda}{d^2} \tag{1}$$

where $\Lambda = 5.63$ eV Å^2. We take the C–C and C=C bond lengths as $d_S = 1.45$ Å and $d_D = 1.37$ Å, corresponding to $V_S = 2.69$ eV and $V_D = 3.00$ eV hopping integrals for the pentagonal-hexagonal and hexagonal-hexagonal edges of the C_{60} cage. The x, y and z t_{1u} orbitals are the degenerate 31st to 33rd single electron eigenstates of the Hückel model and the lowest unoccupied molecular orbitals of free C_{60} (ref. 38). In Extended Data Fig. 8a, the wavefunction (chosen to be real) for each t_{1u} orbital is plotted over the buckyball with the size of the spheres denoting the magnitude and the colour denoting the sign.

C atom motions corresponding to the $T_{1u}(4)$ vibrational mode were taken from a complete nearest-neighbour force field model calculation for C_{60}, optimized to fit the optically accessible frequencies of the molecule[39]. We applied a 'frozen-phonon' approach, which assumes the Born–Oppenheimer approximation to be strictly obeyed and that the molecular orbitals adiabatically follow the atomic distortions. Although this model is not appropriate for high-frequency vibrations and low-energy electronic properties, we posit that this approach can provide the order of magnitude of the response. The t_{1u} orbitals were then computed for $T_{1u}(4)$ distorted configurations of C_{60} using the Hückel model with hopping integrals varied according to equation (1). Snapshots of the driven $t_{1u}(z)$ orbital are shown in Extended Data Fig. 8b.

The Hubbard Us on each C_{60} site are estimated from

$$U = F^0 = \int d^3 r_1 \int d^3 r_2 \frac{\rho(\boldsymbol{r}_1)\rho(\boldsymbol{r}_2)}{4\pi\epsilon_{\mathrm{eff}}\epsilon_0 |\boldsymbol{r}_1 - \boldsymbol{r}_2|} \tag{2}$$

where $\rho(\boldsymbol{r})$ is the charge density corresponding to a t_{1u} orbital.

This bare U will be reduced due to screening from valence electrons, intramolecular correlations and metallic background in a solid. However, since we

are concerned with relative changes in U this renormalization is not crucial. We estimated F^0 by assuming point charges on each C atom and calculating their mutual interactions as

$$F^0 = \sum_{i\neq j} \frac{p_i p_j e^2}{4\pi\epsilon_{\text{eff}}\epsilon_0|\mathbf{r}_1 - \mathbf{r}_2|} + \sum_i p_i^2 F_{\text{C}}^0 \quad (3)$$

where p_i is the probability given by a t_{1u} orbital of an electron being on the ith C atom, and $F_{\text{C}}^0 \approx 12\,\text{eV}$ is the atomic on-site repulsion[40]. The variation of U with the vibrational driving was then obtained using the p_i values of the driven t_{1u} orbitals and is shown, together with the single-particle energies of the orbitals over a vibration period, in Extended Data Fig. 8c, d. The amplitude of the vibrational driving A denotes the maximum displacement of any C atom. For $A = 5$ pm, both quantities in the y, z t_{1u} orbitals vary by nearly 10% at twice the frequency of the vibration.

Since the vibration is polarized along the x axis, the y, z orbitals remain degenerate and possess identical U values. The modulation in y, z is significantly larger than that in x because these orbitals have the equatorial distribution running across the vibrational axis, causing their charge distribution to compress at the poles of the x axis (Extended Data Fig. 8b).

The modulation magnitudes as a function of vibrational driving amplitude are shown in Extended Data Fig. 8e, f. An amplitude $A = 5$ pm is consistent with the strong vibrational driving considered in this work.

Sample size. No statistical methods were used to predetermine sample size.

27. Lupi, S. *et al.* Performance of SISSI, the infrared beamline of the ELETTRA storage ring. *J. Opt. Soc. Am. B* **24,** 959–964 (2007).
28. Plaskett, J. S. & Schatz, P. N. On the Robinson and Price (Kramers-Kronig) method of interpreting reflection data taken through a transparent window. *J. Chem. Phys.* **38,** 612–617 (1963).
29. Brito Cruz, C. H. *et al.* Dynamics of spectral hole burning. *IEEE J. Quantum Electron.* **24,** 261–269 (1988).
30. Orenstein, J. & Dodge, J. S. Terahertz time-domain spectroscopy of transient metallic and superconducting states. *Phys. Rev. B* **92,** 134507 (2015).
31. Beard, M. C., Turner, G. M. & Schmuttenmaer, C. A. Subpicosecond carrier dynamics in low-temperature grown GaAs as measured by time-resolved terahertz spectroscopy. *J. Appl. Phys.* **90,** 5915–5923 (2001).
32. Nicoletti, D., Mitrano, M., Cantaluppi, A. & Cavalleri, A. Comment on "Terahertz time-domain spectroscopy of transient metallic and superconducting states" (arXiv:1506.06758). Preprint at http://arXiv.org/abs/1506.07846 (2015).
33. Iwasa, Y. & Kaneyasu, T. Optical study of electronic structures and phonons in alkali-metal-doped C_{60}. *Phys. Rev. B* **51,** 3678–3685 (1995).
34. Kuzmenko, A. *et al.* Gate tunable infrared phonon anomalies in bilayer graphene. *Phys. Rev. Lett.* **103,** 116804 (2009).
35. Kresse, G. & Furthmüller, J. Efficient iterative schemes for *ab initio* total energy calculations using a plane-wave basis set. *Phys. Rev. B* **54,** 11169–11186 (1996).
36. Togo, A., Oba, F. & Tanaka, I. First-principles calculations of the ferroelastic transition between rutile-type and $CaCl_2$-type SiO_2 at high pressures. *Phys. Rev. B* **78,** 134106 (2008).
37. Giannozzi, P. *et al.* QUANTUM ESPRESSO: a modular and open-source software project for quantum simulations of materials. *J. Phys. Condens. Matter* **21,** 395502 (2009).
38. Laouini, N., Andersen, O. K. & Gunnarsson, O. Analytical molecular orbitals and band structures of solid C_{60}. *Phys. Rev. B* **51,** 17446–17478 (1995).
39. Hands, I. D., Dunn, J. L. & Bates, C. A. A complete nearest-neighbor force field model for C_{60}. *J. Chem. Phys.* **120,** 6912–6921 (2004).
40. Antropov, V. P., Gunnarsson, O. & Jespen, O. Coulomb integrals and model Hamiltonians for C_{60}. *Phys. Rev. B* **46,** 13647–13650 (1992).

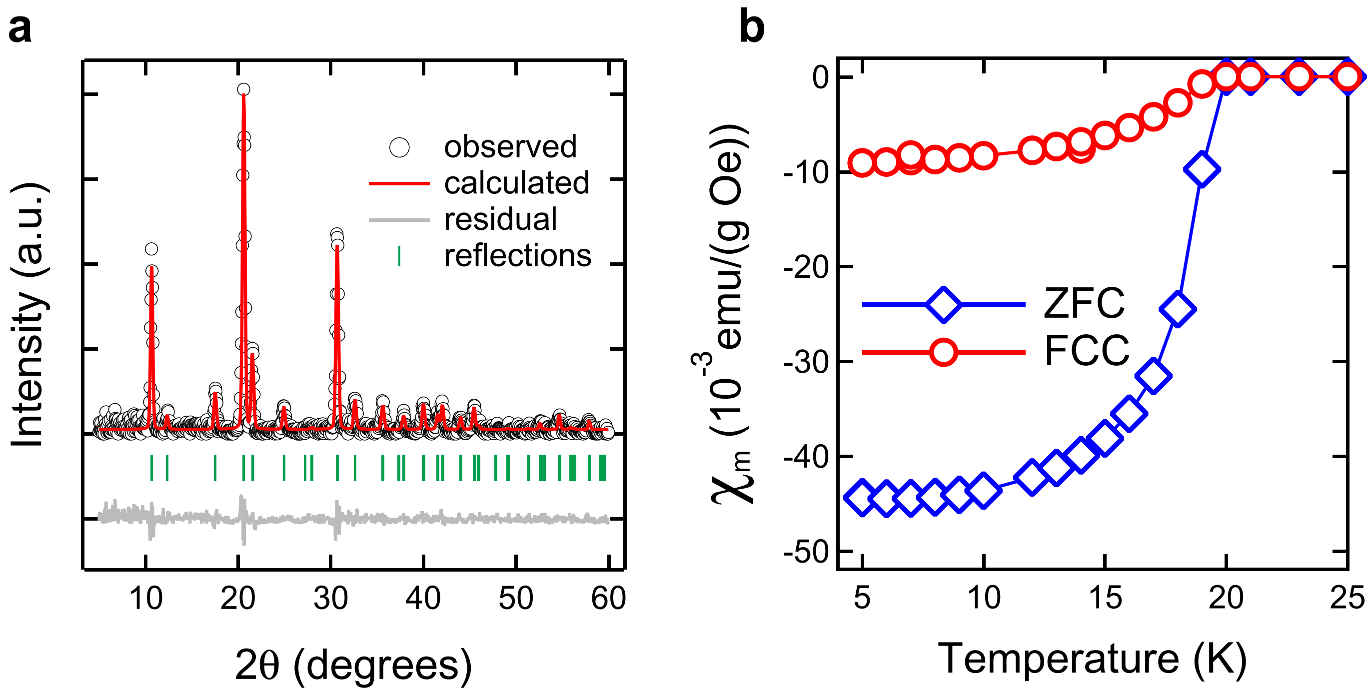

Extended Data Figure 1 | K_3C_{60} sample characterization. a, Powder X-ray diffraction of K_3C_{60} (black circles) fitted with a single f.c.c. phase Rietveld refinement (red). Positions of reflections are shown in green, fit residuals are in grey. **b**, Temperature dependent magnetic susceptibility, χ_m (FCC, field-cooled cooling; ZFC, zero-field cooling). The extracted superconducting transition temperature is $T_c = 19.8$ K.

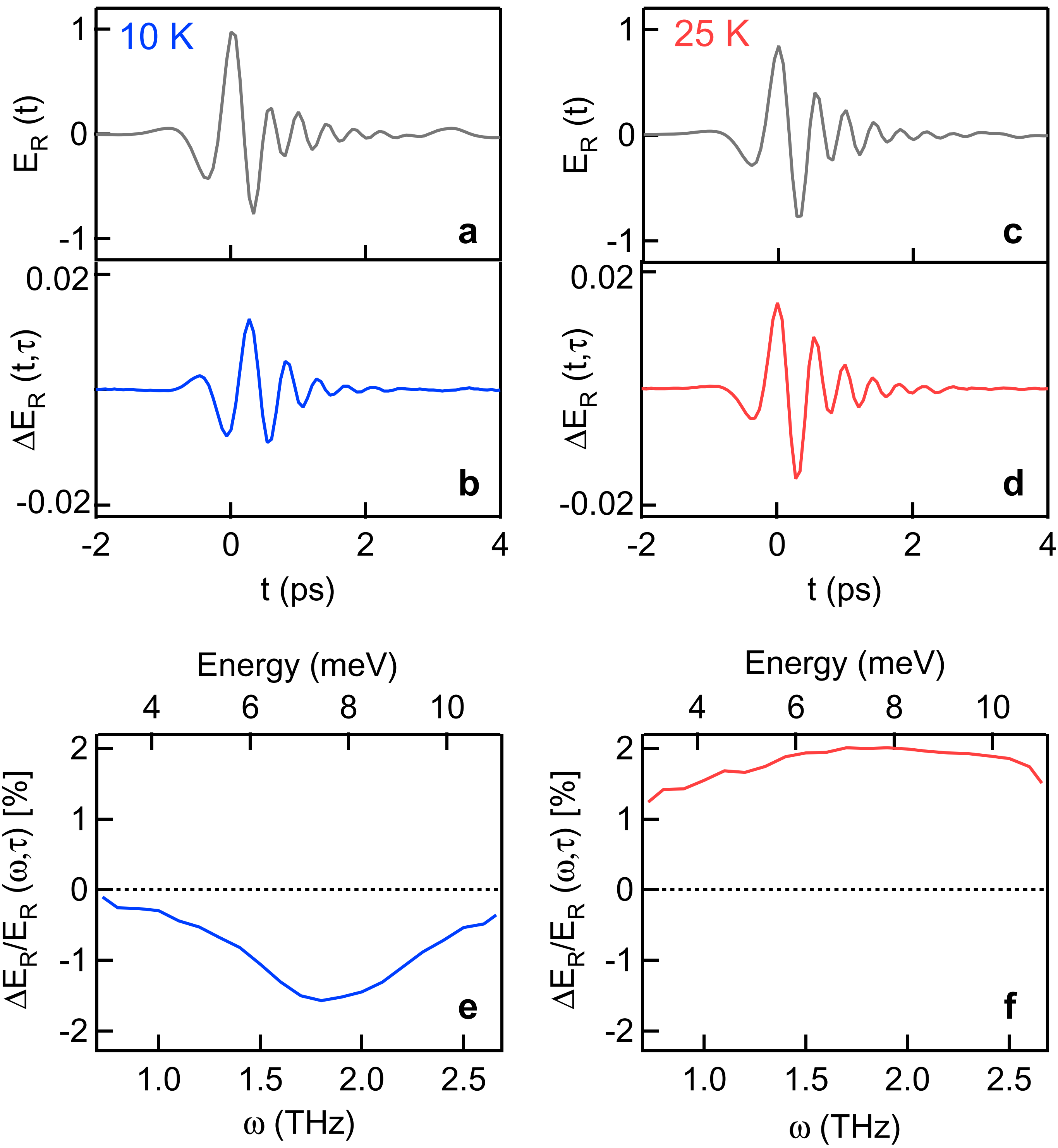

Extended Data Figure 2 | 'Raw' electric field transients below and above T_c. a–d, Stationary electric field (**a**, **c**; grey) reflected at the sample–diamond interface, $E_R(t)$, and pump-induced changes in the same quantity, $\Delta E_R(t, \tau)$, measured at $\tau = 3$ ps (**b**) and at $\tau = 1$ ps (**d**). Data are shown both below (blue) and above T_c (red). **e**, **f**, Corresponding frequency-dependent differential changes in reflectivity, $\Delta E_R/E_R(\omega, \tau)$, calculated as Fourier transform magnitude ratios of the quantities in **a**–**d**.

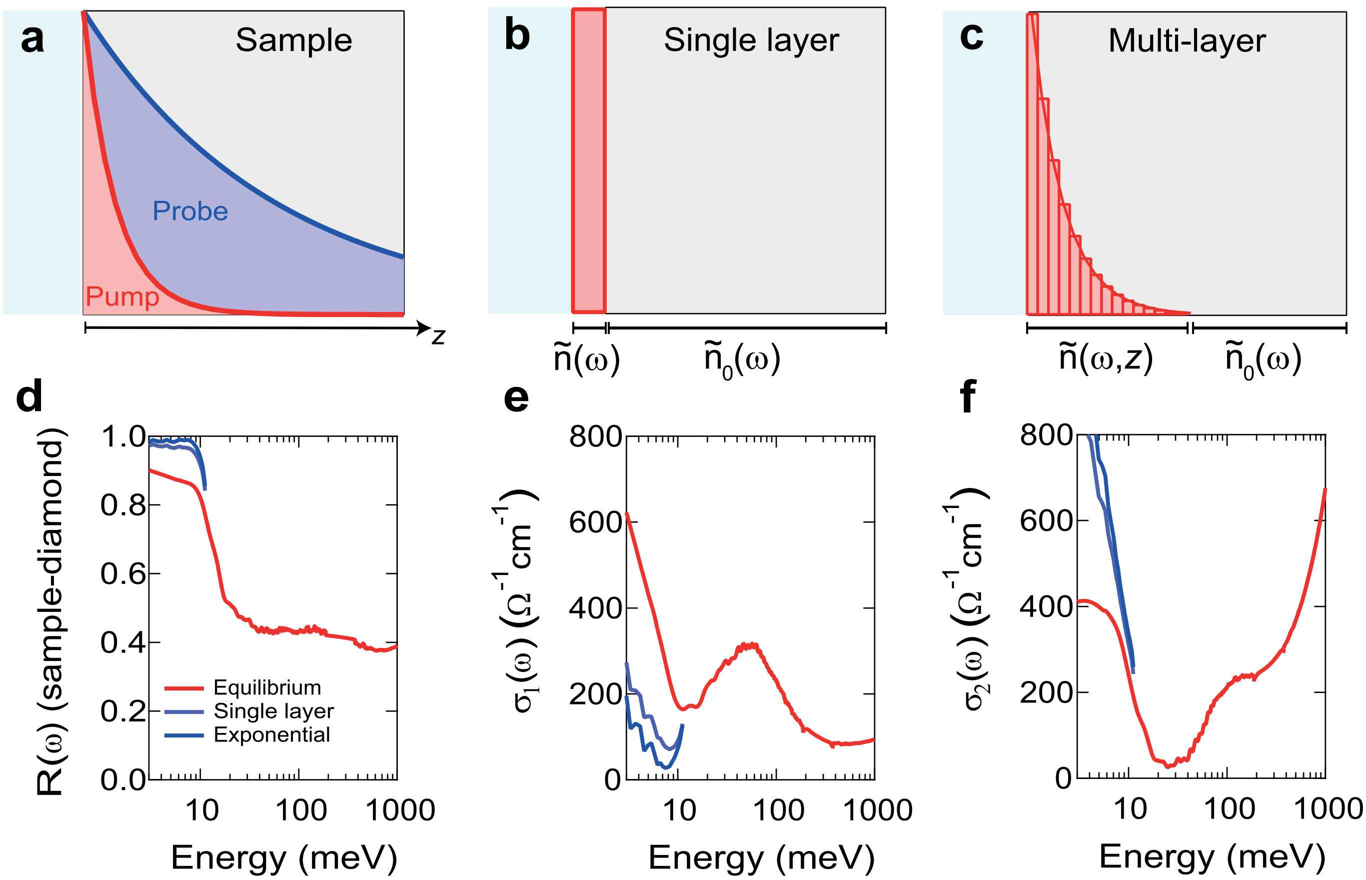

Extended Data Figure 3 | Models for penetration depth mismatch. **a**, Schematics of pump–probe penetration depth mismatch. **b**, **c**, Also shown are the single-layer model (**b**) and the multi-layer model with exponential decay (**c**) (see Methods) used to calculate the pump-induced changes in the complex refractive index, $\tilde{n}(\omega)$. **d**–**f**, Reflectivity, $R(\omega)$, and complex optical conductivity, $\sigma(\omega)$, of K_3C_{60} at $\tau = 1$ ps pump–probe delay and $T = 25$ K, extracted using the single-layer model (light blue) and the multi-layer model with exponential decay (dark blue).

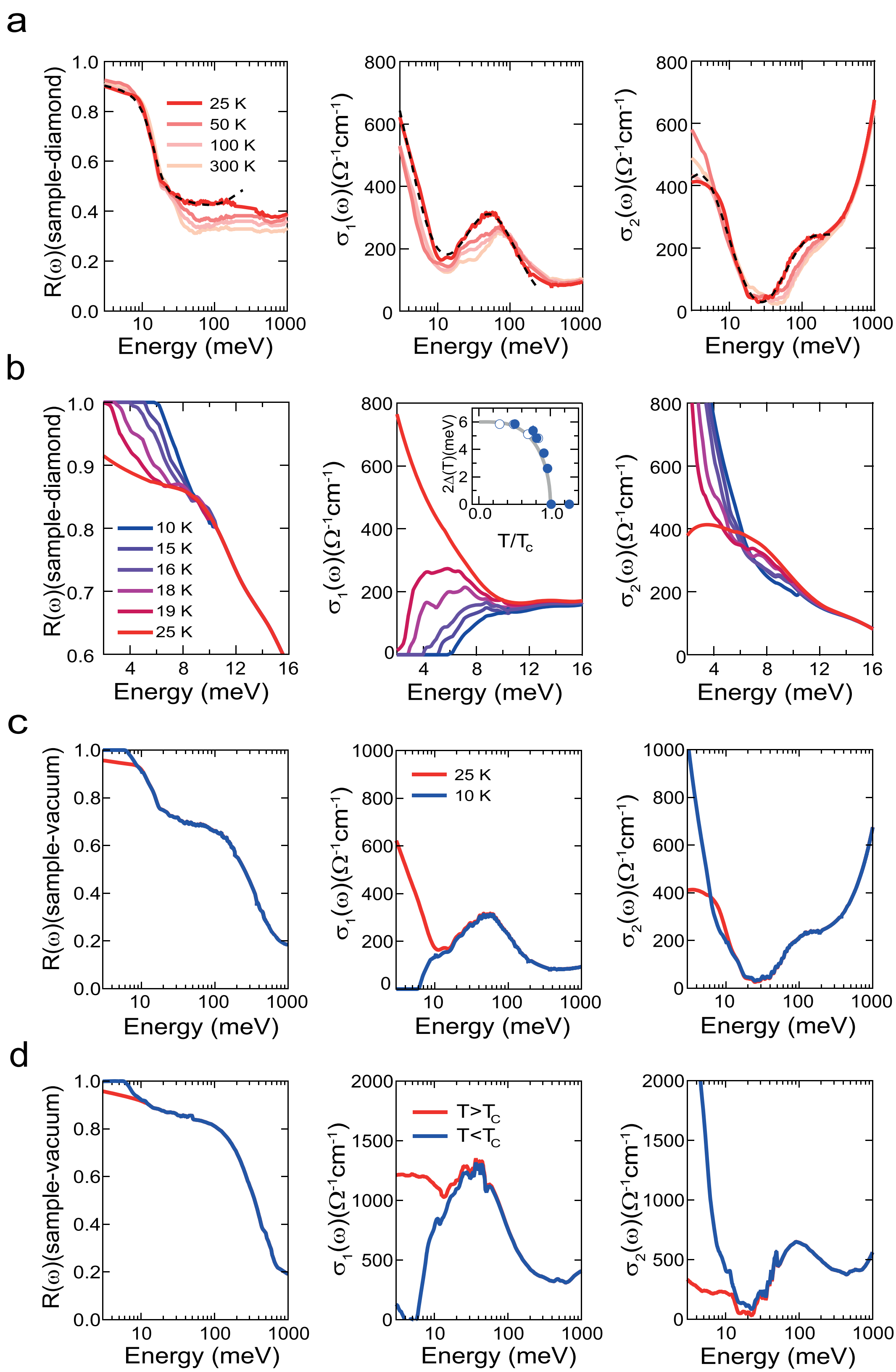

Extended Data Figure 4 | Equilibrium optical properties. a, Reflectivity (left column), and real and imaginary parts (respectively middle and right columns) of the optical conductivity of K_3C_{60} displayed at different temperatures above T_c. Dashed lines are fits to the 25 K data performed with a Drude–Lorentz model. **b**, Same quantities displayed at different $T < T_c$. In the inset, the temperature dependent optical gap (filled circles) is compared with previously published data on K_3C_{60} single crystals (open circles[18]). **c**, Optical properties of compressed powders of K_3C_{60} from **a** and **b** shown at representative temperatures below and above T_c. The $R(\omega)$ has been recalculated at the sample–vacuum interface. **d**, Same quantities as in **c**, measured on single crystals[18].

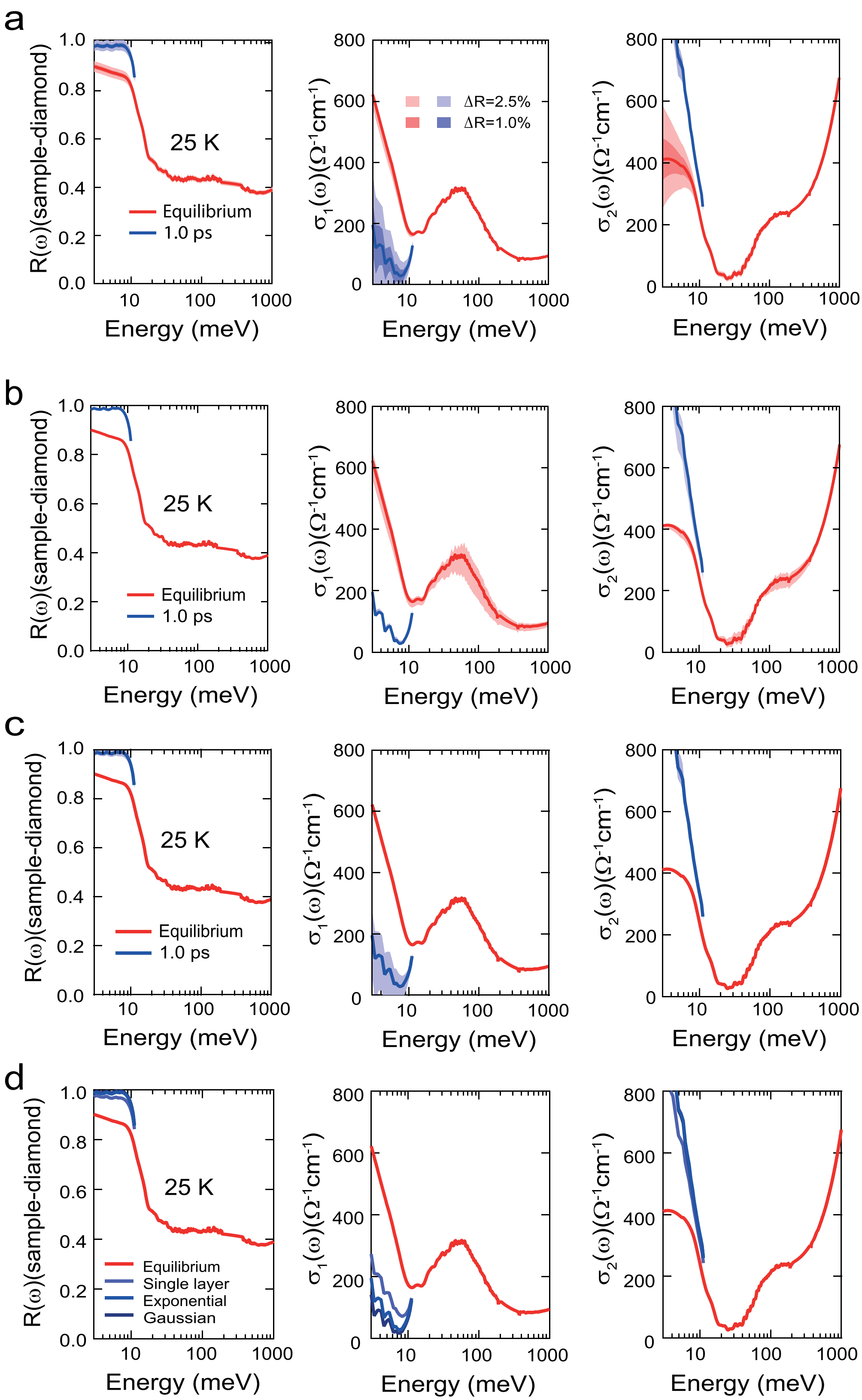

Extended Data Figure 5 | Uncertainties in determining the transient optical properties. Columns as Extended Data Fig. 4; shown are values for K_3C_{60} at equilibrium (red) and 1 ps after photo-excitation (blue) at $T = 25$ K. Error bars, displayed as coloured bands, have been propagated as follows: **a**, ±1% and ±2.5% uncertainty in the equilibrium $R(\omega)$; **b**, ±10% uncertainty in the equilibrium Fresnel phase coefficient β (see Methods); **c**, ±25% change in the pump penetration depth $d = 220$ nm. In **d** we analyse the effect of different functional forms for modelling the pump–probe penetration depth mismatch (see Methods): a single-layer model, or a multi-layer model with exponential decay or with Gaussian-like decay, all with the same pump penetration depth $d = 220$ nm.

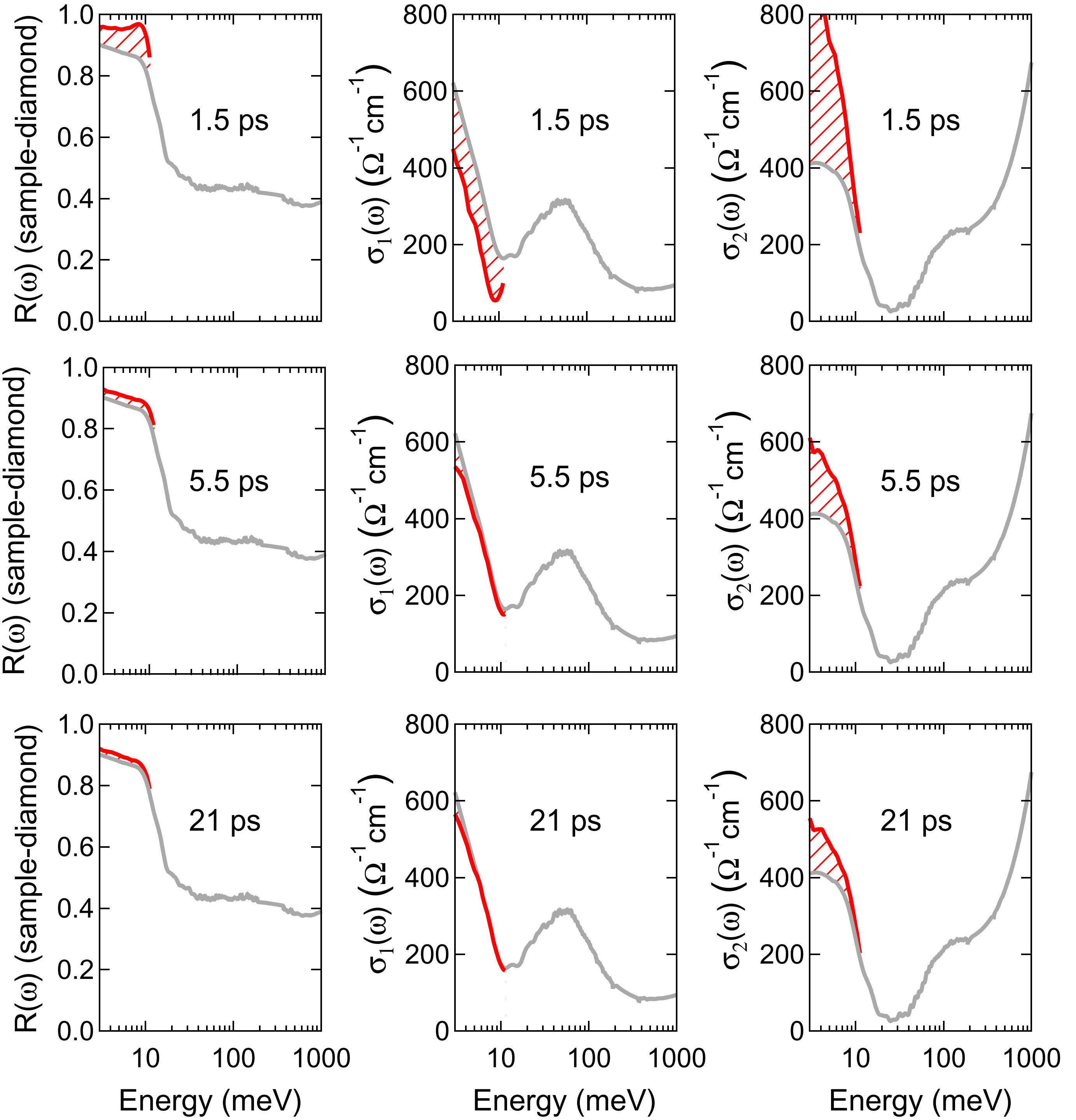

Extended Data Figure 6 | Relaxation dynamics at $T > T_c$. Reflectivity (left column) and complex optical conductivity (middle and right columns) of K_3C_{60} at equilibrium (grey) and after photo-excitation (red) at $T = 25$ K. Data have been measured with a pump fluence of ~1 mJ cm^{-2} and are shown at selected pump–probe time delays: 1.5 ps, 5.5 ps and 21 ps (top, middle and bottom rows, respectively). Hatched areas highlight pump-induced changes.

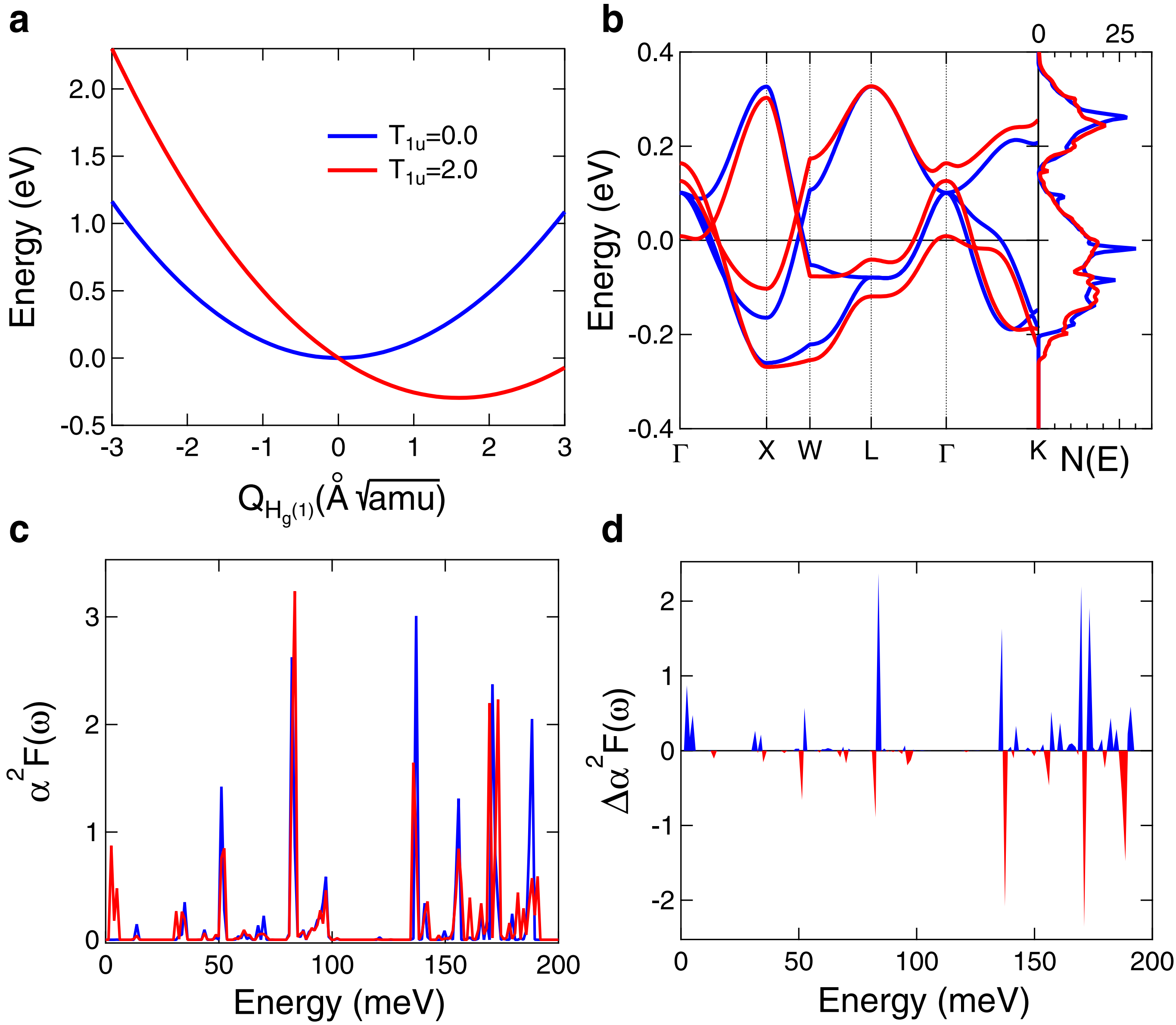

Extended Data Figure 7 | Mode coupling and electronic structure calculations. a, Calculated total energy curves as a function of $H_g(1)$ mode amplitude ($Q_{H_g(1)}$) when the amplitude of the $T_{1u}(4)$ mode is 0.0 (blue) and 2.0 Å √amu (red). **b**, Calculated band structure and electronic density of states $N(E)$ of K_3C_{60}. **c**, Calculated electron–phonon coupling function, $\alpha^2F(\omega)$. In **b** and **c**, blue lines are for the equilibrium structure and red lines are for the structure displaced along the $H_g(1)$ coordinate with an amplitude of 1.5 Å √amu. **d**, Differential changes in the electron–phonon coupling function, evaluated from the curves in **c**.

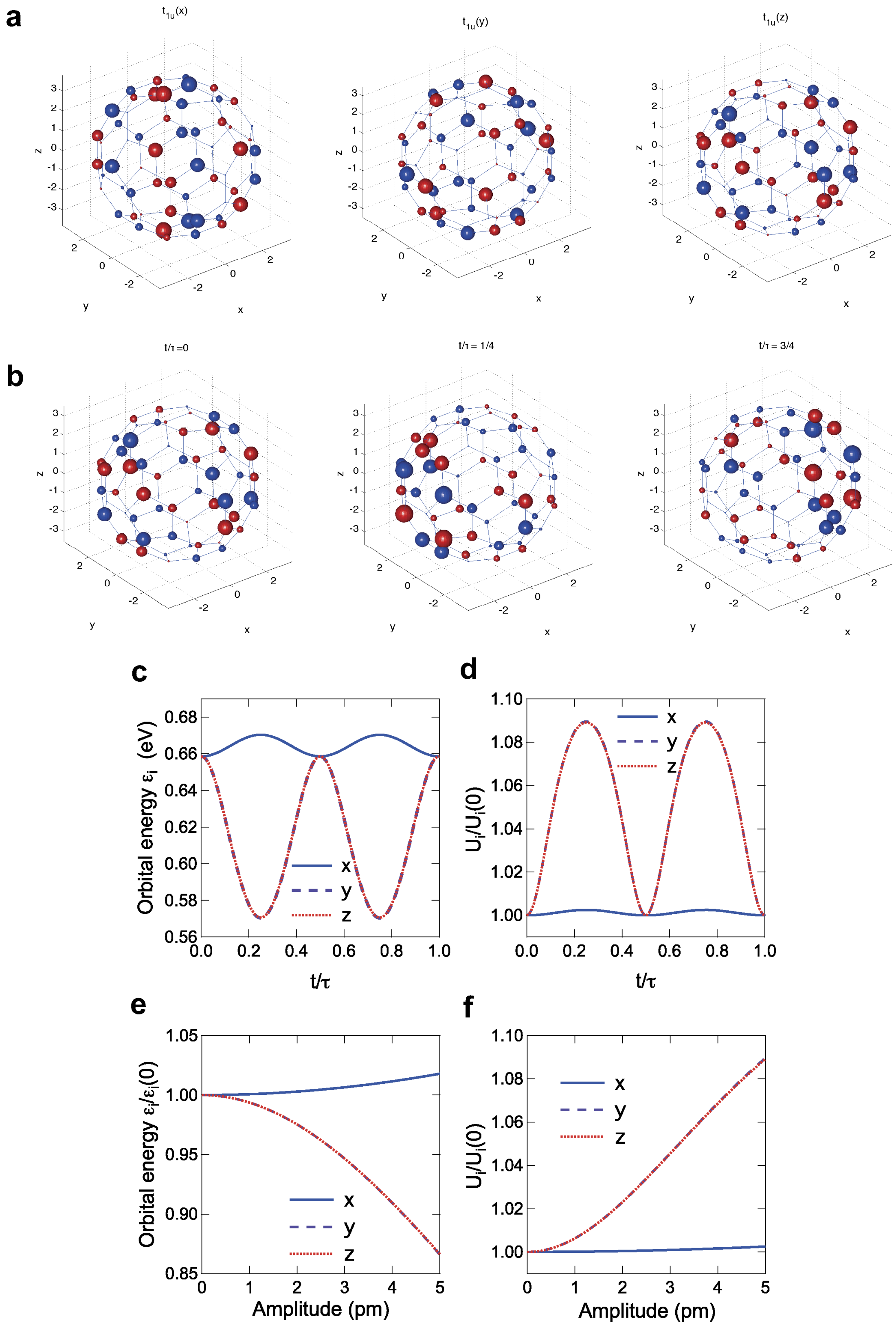

Extended Data Figure 8 | Changes in time of single particle energy and Coulomb repulsion. a, Depiction of the *x*, *y*, *z* t_{1u} orbital wavefunctions of C_{60} according to the Hückel model (left, middle and right column respectively, see Methods). Sphere sizes denote the magnitude of the wavefunction and colours indicate the sign. **b**, Snapshots of the calculated $t_{1u}(z)$ orbital at various points in the $T_{1u}(4)$ vibration polarized along the *x* axis. Colours and sizes follow those of **a**. **c**, Changes in the single-particle energies, ε_i, of the t_{1u} orbitals over one period of the $T_{1u}(4)$ vibration with an amplitude $A = 5$ pm. **d**, Relative changes in the intra-orbital Coulomb repulsions, $U_i/U_i(0)$. **e**, Maximum relative changes in the single-particle energies of the t_{1u} orbitals, $\varepsilon_i/\varepsilon_i(0)$, as a function the driving amplitude, *A*. **f**, Relative changes in the intra-orbital Coulomb repulsions, $U_i/U_i(0)$, under the same driving conditions.

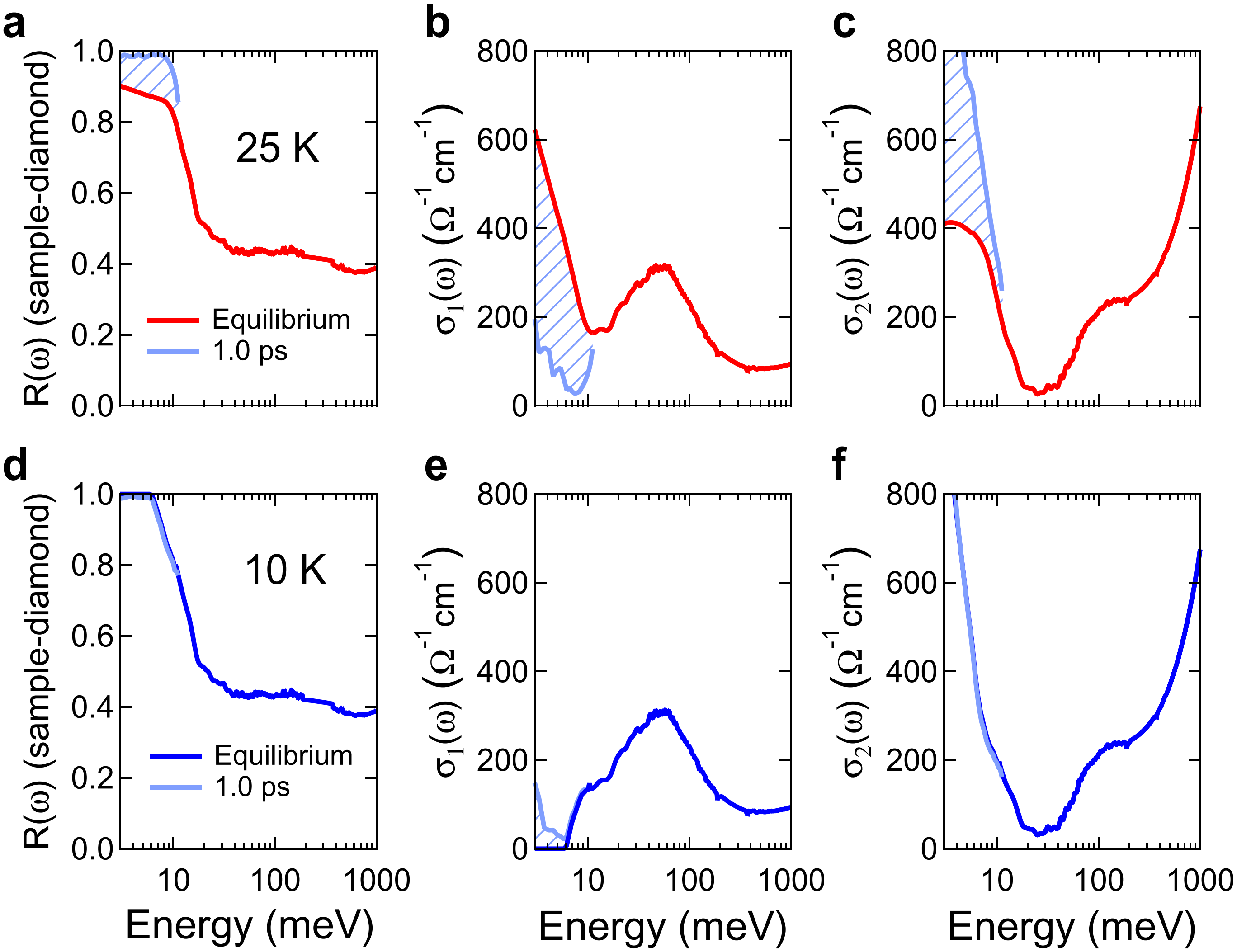

Extended Data Figure 9 | Response at early time delays below and above T_c. Reflectivity, $R(\omega)$, and complex optical conductivity, $\sigma(\omega)$, of K_3C_{60} at equilibrium (red, dark blue) and 1 ps after photo-excitation (light blue), measured at $T > T_c$ (**a–c**) and $T < T_c$ (**d–f**). Data were taken using pump fluences of ~1 mJ cm^{-2} in **a–c** and ~0.5 mJ cm^{-2} in **d–f**. Hatched areas highlight pump-induced changes.

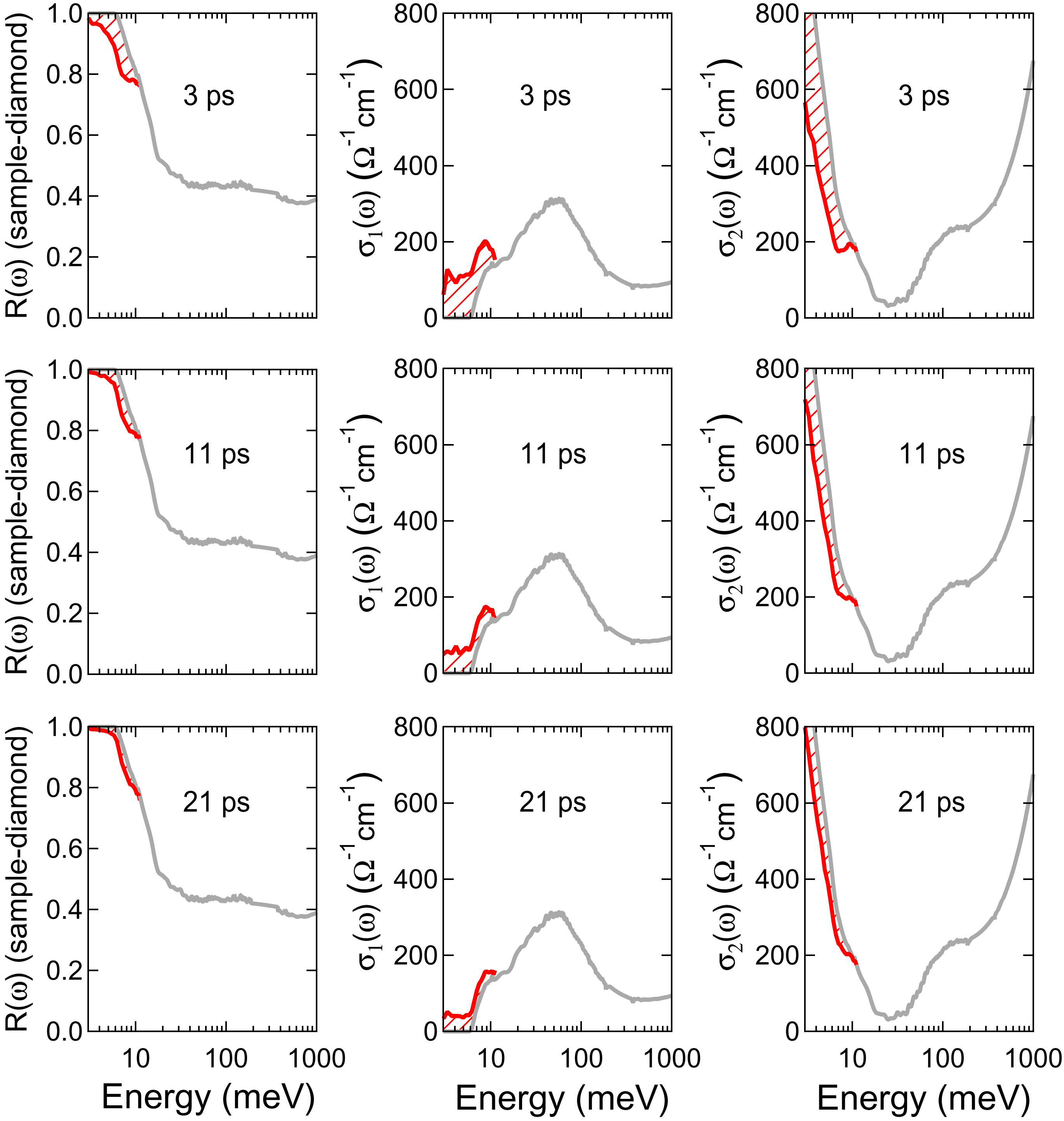

Extended Data Figure 10 | Relaxation dynamics at $T < T_c$. Columns as Extended Data Fig. 9; data were measured at equilibrium (grey) and after photo-excitation (red) at $T = 10$ K, with a pump fluence of ~0.5 mJ cm^{-2}. Data are shown at selected pump–probe time delays: 3 ps (top row), 11 ps (middle row) and 21 ps (bottom row). Hatched areas highlight pump-induced changes.

doi:10.1038/nature16529

A pentanuclear iron catalyst designed for water oxidation

Masaya Okamura[1,2], Mio Kondo[1,2,3,4], Reiko Kuga[1], Yuki Kurashige[2,5,6], Takeshi Yanai[2,5], Shinya Hayami[7], Vijayendran K. K. Praneeth[1], Masaki Yoshida[1], Ko Yoneda[8], Satoshi Kawata[9] & Shigeyuki Masaoka[1,2,3]

Although the oxidation of water is efficiently catalysed by the oxygen-evolving complex in photosystem II (refs 1 and 2), it remains one of the main bottlenecks when aiming for synthetic chemical fuel production powered by sunlight or electricity. Consequently, the development of active and stable water oxidation catalysts is crucial, with heterogeneous systems[3,4] considered more suitable for practical use and their homogeneous counterparts more suitable for targeted, molecular-level design guided by mechanistic understanding[5–19]. Research into the mechanism of water oxidation has resulted in a range of synthetic molecular catalysts, yet there remains much interest in systems that use abundant, inexpensive and environmentally benign metals such as iron (the most abundant transition metal in the Earth's crust and found in natural[20,21] and synthetic[22] oxidation catalysts). Water oxidation catalysts based on mononuclear iron complexes have been explored[9,12,16,18], but they often deactivate rapidly and exhibit relatively low activities. Here we report a pentanuclear iron complex that efficiently and robustly catalyses water oxidation with a turnover frequency of 1,900 per second, which is about three orders of magnitude larger than that of other iron-based catalysts. Electrochemical analysis confirms the redox flexibility of the system, characterized by six different oxidation states between Fe^{II}_5 and Fe^{III}_5; the Fe^{III}_5 state is active for oxidizing water. Quantum chemistry calculations indicate that the presence of adjacent active sites facilitates O–O bond formation with a reaction barrier of less than ten kilocalories per mole. Although the need for a high overpotential and the inability to operate in water-rich solutions limit the practicality of the present system, our findings clearly indicate that efficient water oxidation catalysts based on iron complexes can be created by ensuring that the system has redox flexibility and contains adjacent water-activation sites.

We assumed that for iron-based molecular complexes to effectively catalyse water oxidation ($2H_2O \rightarrow O_2 + 4H^+ + 4e^-$), they should have multinuclear structures and contain two water-activation sites separated by a distance appropriate for promoting intramolecular O–O bond formation. A multinuclear core typically gives rise to redox flexibility that is expected to be advantageous when reactions involve multi-electron transfer (Fig. 1a), as illustrated by multinuclear clusters acting as active centres in enzymes catalysing such reactions (for example, the Mn_4Ca cluster in photosystem II for the four-electron oxidation of water[1,2], and the Fe_7Mo cluster in nitrogenase for the six-electron reduction of nitrogen[23]). The benefit of the catalyst containing two suitably placed activation sites (Fig. 1b) is due to kinetics, in that intermolecular O–O bond formation through association of two molecules is often so slow that it can be the rate-determining step[11,14,15,17] in the water oxidation reaction—and a catalyst design that ensures intramolecular O–O bond formation avoids such a slow association step. Note that dinuclear iron cores are known to serve as active sites for O–O bond formation and/or scission[24,25].

Implementing this strategy, we employed a pentanuclear iron complex with open coordination sites, $[Fe^{II}_4Fe^{III}(\mu_3\text{-O})(\mu\text{-}\mathbf{L})_6]^{3+}$ (**1**; **L**H = 3,5-bis(2-pyridyl)pyrazole; Fig. 1c). **1** has quasi-D_3 symmetry and consists of a $[Fe_3(\mu_3\text{-O})]$ core wrapped by two $[Fe(\mu\text{-}\mathbf{L})_3]$ units. The two iron ions at the apical positions are hexa-coordinated by three $\mathbf{L}^-$ to form $[Fe(\mu\text{-}\mathbf{L})_3]$ units with distorted octahedral geometries, whereas the three iron ions in the triangular $[Fe_3(\mu_3\text{-O})]$ core are penta-coordinated by two $\mathbf{L}^-$ and an O^{2-} anion with distorted trigonal bipyramidal geometries. These penta-coordinated, or coordinatively unsaturated, iron ions in the triangular core are expected to serve as the active sites for O–O bond formation.

We synthesized complex **1** by mixing stoichiometric amounts of $Fe(SO_4)_2{\cdot}7H_2O$ and **L**H in the presence of base in MeOH at room temperature under aerobic conditions[26]. Single crystal X-ray structural analysis, elemental analysis, electrospray-ionization time-of-flight mass spectrometry and ^{57}Fe Mössbauer spectroscopy revealed that one iron ion in the triangular core of **1** is oxidized to Fe^{III}, leading to the isolation of the $Fe^{II}_4Fe^{III}$ oxidation state (for experimental details, see Supplementary Information sections 1, 3 and 4).

The cyclic voltammogram (CV) of **1** (0.2 mM) in an acetonitrile solution containing Et_4NClO_4 (0.1 M) at a scan rate of 10 mV s^{-1} (Fig. 2a) revealed one reversible reduction wave at $E_{1/2} = -0.55$ V versus ferrocene/ferrocenium (Fc/Fc$^+$) and four reversible oxidation waves at $E_{1/2} = 0.13$, 0.30, 0.68 and 1.08 V, assigned to five sequentially occurring one-electron redox reactions involving in turn each of the iron ion Fe^{III}/Fe^{II} couples. Thus, **1** possesses high redox flexibility, with six different redox states that are accessible under electrochemical conditions. The open-circuit potential of **1** was determined to be −0.26 V, indicating a $Fe^{II}_4Fe^{III}$ state in solution and the solid state (see above). Addition of water dramatically changed the profile of the CV of **1** (Fig. 2b): large irreversible anodic currents appeared at the potential corresponding to the $Fe^{III}_5/Fe^{II}Fe^{III}_4$ redox couple, suggesting electrocatalytic O_2 evolution from water.

To quantify the evolution of O_2 from water, controlled potential electrolysis was conducted in a two-compartment cell separated by an anion-exchange membrane (Supplementary Fig. 3). A solution of **1** (0.2 mM) in an acetonitrile/water (10:1) mixed solution containing Et_4NClO_4 (0.1 M) was electrolysed at an indium tin oxide (ITO) electrode with a cell operating potential of 1.42 V versus Fc/Fc$^+$, and the evolved O_2 was quantified by gas chromatography. With a total amount of passed charge of 41.0 C over a period of 120 min (Fig. 2c)

[1]Department of Life and Coordination-Complex Molecular Science, Institute for Molecular Science, Higashiyama 5-1, Myodaiji, Okazaki, Aichi 444-8787, Japan. [2]SOKENDAI (The Graduate University for Advanced Studies), Shonan Village, Hayama, Kanagawa 240-0193, Japan. [3]Research Center of Integrative Molecular Systems, Institute for Molecular Science, Nishigo-naka 38, Myodaiji, Okazaki, Aichi 444-8585, Japan. [4]Advanced Catalytic Transformation Program for Carbon Utilization (ACT-C), Japan Science and Technology Agency, Honcho 4-1-8, Kawaguchi, Saitama 332-0012, Japan. [5]Department of Theoretical and Computational Molecular Science, Institute for Molecular Science, Nishigo-naka 38, Myodaiji, Okazaki, Aichi 444-8585, Japan. [6]Precursory Research for Embryonic Science and Technology (PRESTO), Japan Science and Technology Agency, Honcho 4-1-8, Kawaguchi, Saitama 332-0012, Japan. [7]Department of Chemistry, Graduate School of Science and Technology, Kumamoto University, Kurokami 2-39-1, Kumamoto 860-8555, Japan. [8]Department of Chemistry and Applied Chemistry, Graduate School of Science and Engineering, Saga University, Honjo-machi 1, Saga, 840-8502, Japan. [9]Department of Chemistry, Faculty of Science, Fukuoka University, Nanakuma, Jonan-ku 8-19-1, Fukuoka 814-0180, Japan.

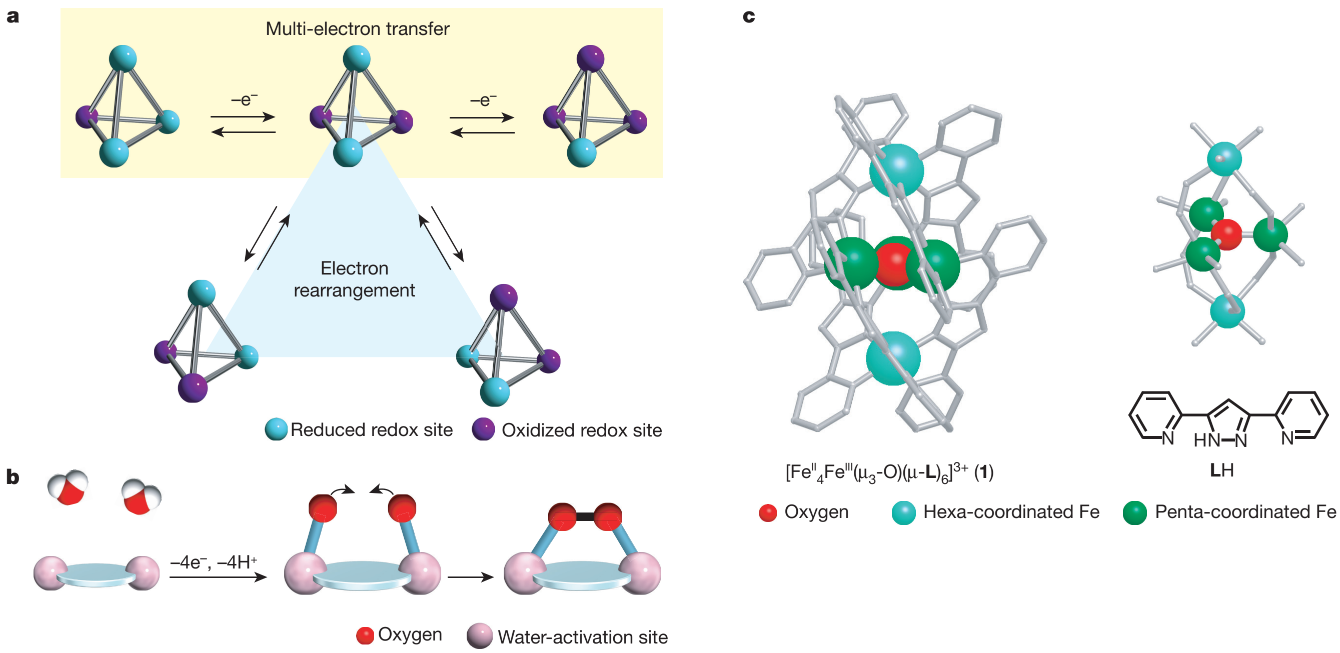

Figure 1 | Design of molecular catalysts for water oxidation. a, Redox flexibility arising from a multinuclear core. Multi-electron transfer to afford several oxidation states and electron rearrangement among valence tautomers enable the accumulation of positive charges required for water oxidation. **b**, Adjacent water-activation sites to promote intramolecular O–O bond formation. **c**, Ball-and-stick representations of the molecular structure (left) and the Fe_5O core structure (right) of $[Fe^{II}_4Fe^{III}(\mu_3\text{-}O)(\mu\text{-}\mathbf{L})_6]^{3+}$ (**1**); the chemical structure of **L**H is also shown (bottom right). Three penta-coordinated iron centres are bridged by an oxygen atom in μ_3-fashion to form a triangle structure, and two hexa-coordinated iron centres are connected to the triangle structure by six **L**s.

leading to 2.5 ml of evolved O_2, the Faradaic efficiency is 96% based on a $4e^-$ process. We also note the nearly linear nature of the water oxidation curve, indicating that the steady-state intermediate of the catalyst remained stable in solution throughout the catalytic cycles. Electrochemical testing of the stability of **1** during catalysis revealed that both the wave shape of each Fe^{III}/Fe^{II} process and the catalytic current for water oxidation were maintained over 100 scans of the CVs for 9 h (see Supplementary Fig. 4) and after controlled potential electrolysis for 1 h (see Supplementary Fig. 5). There was no evidence for formation of insoluble material on the electrode after the controlled potential electrolysis (Supplementary Figs 6–8). In the absence of **1**, catalysis was not observed (black line in Fig. 2c). Taken together, these observations strongly indicate that **1** works as a robust homogeneous water oxidation catalyst.

Figure 3 illustrates a possible catalytic cycle for the generation of O_2 mediated by **1**, informed by electrochemical measurements revealing a four-step, one-electron oxidation that converts the initial $Fe^{II}_4Fe^{III}$ state ($\mathbf{S_0}$ in Fig. 3) to the Fe^{III}_5 state ($\mathbf{S_4}$). Note that water attack on the $Fe^{II}_4Fe^{III}$ ($\mathbf{S_0}$), $Fe^{II}_3Fe^{III}_2$ ($\mathbf{S_1}$), $Fe^{II}_2Fe^{III}_3$ ($\mathbf{S_2}$) and $Fe^{II}Fe^{III}_4$ states ($\mathbf{S_3}$) can be excluded because their oxidation potentials were unchanged upon water addition (Fig. 2b). No change in the onset potential of water oxidation was seen in CVs performed over a range of solution pH (Supplementary Fig. 9), indicating that water attack on the $\mathbf{S_4}$ state does not involve proton-coupled electron transfer. Therefore, subsequent insertion of a water molecule into the $\mathbf{S_4}$ state results in the formation of the $Fe^{III}_5(OH_2)$ species with a hexa-coordinated Fe^{III} ion in the triangular core (**A** in Fig. 3). Quantum chemical calculations of the system using density functional theory (for details, see Supplementary Information sections 9.1 and 9.2) gave an estimated activation barrier for the water attack of about 15 kcal mol^{-1} relative to the $\mathbf{S_4}$ state (see Supplementary Videos 1–4 for illustrations of insertion pathways). Coordination of another water molecule, together with sequential or simultaneous deprotonation, results in the formation of the bis-oxo species that calculations suggest to be at

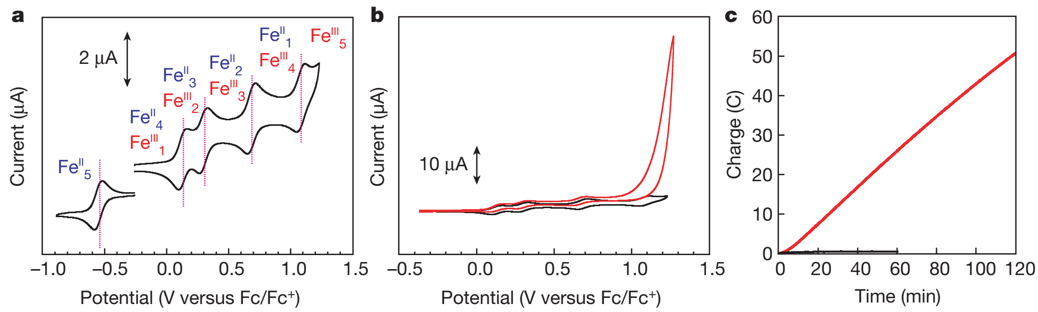

Figure 2 | Evaluation of electrochemical properties and catalytic activity of 1. a, CVs of **1** (0.2 mM) in an acetonitrile solution with Et_4NClO_4 (0.1 M) swept to negative (left) and positive (right) potentials from the open circuit potential at a scan rate of 10 mV s^{-1}. Red vertical dotted lines represent the redox potentials of five reversible redox waves. The oxidation states of iron ions are indicated by the red and blue coloured labels. **b**, CVs of **1** (0.2 mM) in acetonitrile solutions with Et_4NClO_4 (0.1 M) at a scan rate of 10 mV s^{-1} with 5 M of H_2O (red line) and without water (black line, the same data as in Fig. 2a). **c**, Electrolysis data in acetonitrile/water (10:1) mixed solutions with Et_4NClO_4 (0.1 M) at a potential of 1.42 V versus Fc/Fc^+ with 0.2 mM of **1** (red line) and without the catalyst (black line).

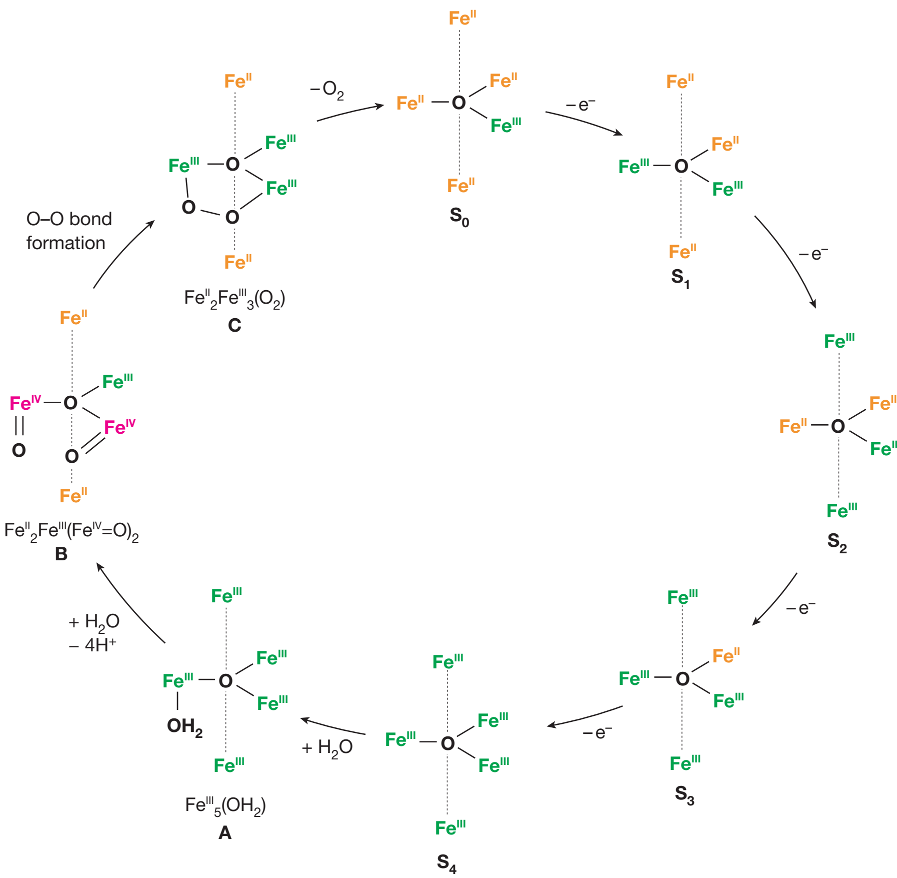

Figure 3 | Mechanism of O_2 evolution from water catalysed by 1. Bottom, one water molecule reacts with the $\mathbf{S_4}$ state formed by the four-electron oxidation of the $\mathbf{S_0}$ state (via $\mathbf{S_1}$, $\mathbf{S_2}$, $\mathbf{S_3}$). Further reaction with an additional water molecule ($\mathbf{S_4} \rightarrow \mathbf{A}$) and the deprotonation of the coordinated water molecules afford the adjacent two metal-oxo moieties in one molecule (**B**), which promotes rapid intramolecular O–O bond formation (**B** → **C**) to evolve O_2 (**C** → $\mathbf{S_0}$). Fe^{II}, orange; Fe^{III}, green; and Fe^{IV}, red.

an energy minimum in the mixed-valence $Fe^{II}_2Fe^{III}(Fe^{IV}{=}O)_2$ state (**B** in Fig. 3). Note that intramolecular electron transfer from the hexa-coordinated Fe^{III} ions in the triangular core to iron ions at the apical position results in the formation of $Fe^{IV}{=}O$ units at the triangular core. The O–O bond formation can proceed between the co-facial oxo groups in **B** to afford the peroxo species (**C** in Fig. 3) without spin rearrangement and with an estimated reaction barrier of less than 10 kcal mol^{-1} (for details, see Supplementary Information sections 9.1–9.3). Liberation of O_2 from **C** forms the $\mathbf{S_0}$ state to close the catalytic cycle.

To evaluate catalytic activity of **1** in terms of turnover frequency (TOF) under electrochemical conditions, we used equation (1) below. We note that when the electron transfer rate of the catalyst and the concentration of the substrate are sufficiently high and when the catalytic current is limited only by the chemical reaction in solution, that is, under purely kinetic conditions[14,27–29], the equation can be used to

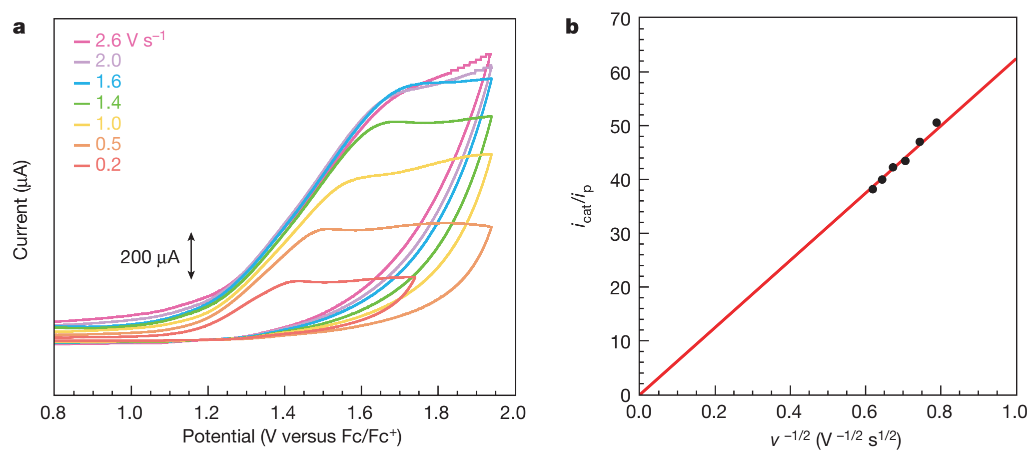

Figure 4 | Determination of the TOF value for electrocatalytic O_2 evolution. a, CV of **1** (0.2 mM) in an acetonitrile/water (10:1) mixed solution with Et_4NClO_4 (0.1 M) at scan rates of 0.2–2.6 V s^{-1}. **b**, A plot of the ratio of i_{cat} to i_p as a function of the inverse of the square root of the scan rate v, showing the linear relationship. Data obtained from the measurements with scan rates (in V s^{-1}) of 1.60, 1.80, 2.00, 2.20, 2.40 and 2.60 were used for the calculation of the TOF. The TOF value was estimated from the slope of the plot as 1,900 s^{-1}. The red line is forced to go through the origin. Each data point represents a single measurement. For the numerical data and further details, see also Supplementary Table 13.

calculate the pseudo-first-order rate constant k_{cat}, which corresponds to the TOF value for O_2 evolution (for details, see Supplementary Information section 10.1).

$$\frac{i_{cat}}{i_p} = 2.242 n_{cat} \left(\frac{k_{cat} RT}{F} \right)^{\frac{1}{2}} v^{-\frac{1}{2}} \quad (1)$$

In this equation, i_{cat} is the catalytic current, i_p is the peak current measured in the absence of the substrate, n_{cat} is the number of electrons involved in the catalytic reaction, F is Faraday's constant, k_{cat} is the pseudo-first-order rate constant, R is the universal gas constant, T is the temperature in kelvin, and v is the scan rate. As shown in Fig. 4a and Supplementary Fig. 28, constant limiting currents were observed when the scan rates were in the range 1.6–2.6 V s^{-1}. A plot of the ratio of i_{cat} to i_p as a function of the inverse of the square root of the scan rate shows a linear relationship (Fig. 4b), and gives a TOF estimate of 1,900 s^{-1} (for details of the calculation of the TOF value, see Supplementary Information sections 10.2–10.5). An independent though rough estimate can also be derived from the amount of O_2 evolved in the controlled potential electrolysis (Fig. 2c). With the assumption that the thickness of the reaction-diffusion layer adjacent to the electrode surface (μ) is of the order of $\mu \approx \sqrt{D/k_{cat}}$ (ref. 30), we obtain a TOF value of about 140–1,400 s^{-1} and a TON (turnover number) of about 10^6–10^7 for 120 min. These TOF and TON values indicate that **1** is an efficient and robust molecular catalyst for water oxidation.

Taken together, our experimental and computational results indicate the effectiveness of our catalyst design strategy, where redox flexibility of the pentanuclear iron complex enables the accumulation of positive charges ($\mathbf{S_0} \rightarrow \mathbf{S_4}$ in Fig. 3) and intramolecular electron rearrangement ($\mathbf{A} \rightarrow \mathbf{B}$) to form a reactive high-valent oxo species, and where adjacent active sites ensure formation of cofacial oxo units that can be converted to peroxo species via intramolecular O–O bond formation with a low activation barrier and without spin-rearrangement ($\mathbf{B} \rightarrow \mathbf{C}$). Given the high TOF value achieved with **1**, which is about 1,000 times greater than that of other reported iron-based catalysts[9], we expect that our strategy will prove more generally effective for creating from abundant metals efficient and robust molecular catalysts for water oxidation. Regarding the present system, it should be mentioned that the high reaction rate was achieved in an acetonitrile/water mixture and using a large overpotential of more than 0.5 V (see Supplementary Fig. 9), each of which prevents practical use. One of the next goals is therefore the design of a water oxidation catalyst operating similarly efficiently and robustly but with a low overpotential and in water.

Received 10 August; accepted 3 December 2015.
Published online 10 February 2016.

1. Umena, Y., Kawakami, K., Shen, J.-R. & Kamiya, N. Crystal structure of oxygen-evolving photosystem II at a resolution of 1.9 Å. *Nature* **473,** 55–60 (2011).
2. Dismukes, G. C. *et al.* Development of bioinspired Mn_4O_4 – cubane water oxidation catalysts: lessons from photosynthesis. *Acc. Chem. Res.* **42,** 1935–1943 (2009).
3. Kanan, M. W. & Nocera, D. G. In situ formation of an oxygen-evolving catalyst in neutral water containing phosphate and Co^{2+}. *Science* **321,** 1072–1075 (2008).
4. Hocking, R. K. *et al.* Water-oxidation catalysis by manganese in a geochemical-like cycle. *Nature Chem.* **3,** 461–466 (2011).
5. Gersten, S. W., Samuels, G. J. & Meyer, T. J. Catalytic oxidation of water by an oxo-bridged ruthenium dimer. *J. Am. Chem. Soc.* **104,** 4029–4030 (1982).
6. Wada, T., Tsuge, K. & Tanaka, K. Electrochemical oxidation of water to dioxygen catalyzed by the oxidized form of the bis(ruthenium-hydroxo)complex in H_2O. *Angew. Chem. Int. Edn* **39,** 1479–1482 (2000).
7. Zong, R. & Thummel, R. P. A new family of Ru complexes for water oxidation. *J. Am. Chem. Soc.* **127,** 12802–12803 (2005).
8. Concepcion, J. J., Jurss, J. W., Templeton, J. L. & Meyer, T. J. One site is enough. Catalytic water oxidation by $[Ru(tpy)(bpm)(OH_2)]^{2+}$ and $[Ru(tpy)(bpz)(OH_2)]^{2+}$. *J. Am. Chem. Soc.* **130,** 16462–16463 (2008).
9. Ellis, W. C., McDaniel, N. D., Bernhard, S. & Collins, T. J. Fast water oxidation using iron. *J. Am. Chem. Soc.* **132,** 10990–10991 (2010).
10. Yin, Q. *et al.* A fast soluble carbon-free molecular water oxidation catalyst based on abundant metals. *Science* **328,** 342–345 (2010).
11. Yoshida, M., Masaoka, S., Abe, J. & Sakai, K. Catalysis of mononuclear aquaruthenium complexes in oxygen evolution from water: a new radical coupling path using hydroxocerium(IV) species. *Chem. Asian J.* **5,** 2369–2378 (2010).
12. Fillol, J. L. *et al.* Efficient water oxidation catalysts based on readily available iron coordination complexes. *Nature Chem.* **3,** 807–813 (2011).
13. Duan, L. *et al.* A molecular ruthenium catalyst with water-oxidation activity comparable to that of photosystem II. *Nature Chem.* **4,** 418–423 (2012).
14. Barnett, S. M., Goldberg, K. I. & Mayer, J. M. A soluble copper-bipyridine water-oxidation electrocatalyst. *Nature Chem.* **4,** 498–502 (2012).
15. Vigara, L. *et al.* Experimental and quantum chemical characterization of the water oxidation cycle catalysed by $[Ru^{II}(damp)(bpy)(H_2O)]^{2+}$. *Chem. Sci.* **3,** 2576–2586 (2012).
16. Hong, D. *et al.* Water oxidation catalysis with nonheme iron complexes under acidic and basic conditions: homogeneous or heterogeneous? *Inorg. Chem.* **52,** 9522–9531 (2013).
17. Wang, D. & Groves, J. T. Efficient water oxidation catalyzed by homogeneous cationic cobalt porphyrins with critical roles for the buffer base. *Proc. Natl Acad. Sci. USA* **110,** 15579–15584 (2013).
18. Coggins, M. K., Zhang, M.-T., Vannucci, A. K., Dares, C. J. & Meyer, T. J. Electrocatalytic water oxidation by a monomeric amidate-ligated Fe(III)–aqua complex. *J. Am. Chem. Soc.* **136,** 5531–5534 (2014).
19. Matheu, R. *et al.* Intramolecular proton transfer boosts water oxidation catalyzed by a Ru complex. *J. Am. Chem. Soc.* **137,** 10786–10795 (2015).
20. Meunier, B., de Visser, S. P. & Shaik, S. Mechanism of oxidation reactions catalyzed by cytochrome P450 enzymes. *Chem. Rev.* **104,** 3947–3980 (2004).
21. Tinberg, C. E. & Lippard, S. J. Dioxygen activation in soluble methane monooxygenase. *Acc. Chem. Res.* **44,** 280–288 (2011).
22. Costas, M., Chen, K. & Que, L. Jr Biomimetic nonheme iron catalysts for alkane hydroxylation. *Coord. Chem. Rev.* **200–202,** 517–544 (2000).
23. Einsle, O. *et al.* Nitrogenase MoFe-protein at 1.16 Å resolution: a central ligand in the FeMo-cofactor. *Science* **297,** 1696–1700 (2002).
24. Kodera, M. *et al.* Reversible O-O bond scission of peroxodiiron(III) to high-spin oxodiiron(IV) in dioxygen activation of a diiron center with a bis-tpa dinucleating ligand as a soluble methane monooxygenase model. *J. Am. Chem. Soc.* **134,** 13236–13239 (2012).
25. Kundu, S. *et al.* O-O bond formation mediated by a hexanuclear iron complex supported on a stannoxane core. *Chem. Eur. J.* **18,** 2787–2791 (2012).
26. Yoneda, K. *et al.* An $[Fe^{II}_3O]^{4+}$ core wrapped by two $[Fe^{II}L_3]^-$ units. *Angew. Chem. Int. Edn* **45,** 5459–5461 (2006).
27. Helm, M. L., Stewart, M. P., Bullock, R. M., DuBois, M. R. & DuBois, D. L. A synthetic nickel electrocatalyst with a turnover frequency above 100,000 s^{-1} for H_2 production. *Science* **333,** 863–866 (2011).
28. McCrory, C. C. L., Uyeda, C. & Peters, J. C. Electrocatalytic hydrogen evolution in acidic water with molecular cobalt tetraazamacrocycles. *J. Am. Chem. Soc.* **134,** 3164–3170 (2012).
29. Marinescu, S. C., Winkler, J. R. & Gray, H. B. Molecular mechanisms of cobalt-catalyzed hydrogen evolution. *Proc. Natl Acad. Sci. USA* **109,** 15127–15131 (2012).
30. Costentin, C., Drouet, S., Robert, M. & Savéant, J.-M. A local proton source enhances CO_2 electroreduction to CO by a molecular Fe catalyst. *Science* **338,** 90–94 (2012).

Supplementary Information is available in the online version of the paper.

Acknowledgements This study was supported by MEXT/JSPS Grants-in-Aid as follows: for Young Scientists A (no. 25708011 (S.M.) and no. 15H05480 (M.K.)), for Challenging Exploratory Research (no. 26620160 (S.M.)), for Scientific Research on Innovative Areas ("AnApple" (no. 15H00889 (S.M.) and no. 25107526 (S.M.)), for Photosynergetics (no. 15H01097 (T.Y.)), for Soft Molecular Systems (no. 26104538 (Y.K.)), for a JSPS Fellowship (no. 254037 (M.O.)), for Scientific Research B (no. 25288013 (T.Y.)), and for Scientific Research C (no. 25410030 (Y.K.)). This work was also supported by JST ACT-C (M.K.), JST PRESTO (Y.K. and S.M.), the NINS Program for Cross-Disciplinary Study (S.M.) and the Morino Foundation for Molecular Science (Y.K.). The computations were performed using the Research Center for Computational Science, Okazaki, Japan. We also thank S. Furukawa for discussions.

Author Contributions M.O., M.K. and S.M. conceived the project. M.O., M.K., M.Y., K.Y., S.K. and S.M. designed the experiments. M.O. and R.K. performed all synthesis and characterisation experiments. Y.K. and T.Y. performed the DFT calculations. S.H. measured the Mössbauer spectra. V.K.K.P. performed the isolation of reaction intermediates. M.O., M.K. and S.M. analysed the data and co-wrote the manuscript. All authors discussed the results and commented on the manuscript.

Author Information The X-ray crystal structure of $\mathbf{1}(BF_4)_3$ is deposited in the Cambridge Crystallographic Data Centre (CCDC 996195). Reprints and permissions information is available at www.nature.com/reprints. The authors declare no competing financial interests. Readers are welcome to comment on the online version of the paper. Correspondence and requests for materials should be addressed to S.M. (masaoka@ims.ac.jp).

doi:10.1038/nature16958

Timescales for detection of trends in the ocean carbon sink

Galen A. McKinley[1,2,3], Darren J. Pilcher[1,4], Amanda R. Fay[3], Keith Lindsay[5], Matthew C. Long[5] & Nicole S. Lovenduski[6]

The ocean has absorbed 41 per cent of all anthropogenic carbon emitted as a result of fossil fuel burning and cement manufacture[1,2]. The magnitude and the large-scale distribution of the ocean carbon sink is well quantified for recent decades[3,4]. In contrast, temporal changes in the oceanic carbon sink remain poorly understood[5–7]. It has proved difficult to distinguish between air-to-sea carbon flux trends that are due to anthropogenic climate change and those due to internal climate variability[5,6,8–13]. Here we use a modelling approach that allows for this separation[14], revealing how the ocean carbon sink may be expected to change throughout this century in different oceanic regions. Our findings suggest that, owing to large internal climate variability, it is unlikely that changes in the rate of anthropogenic carbon uptake can be directly observed in most oceanic regions at present, but that this may become possible between 2020 and 2050 in some regions.

Recent observationally based syntheses have quantified mean ocean carbon uptake and its spatial distribution[1,3,4,15] (Extended Data Fig. 1). In addition, interior ocean observations analysed under the assumption of constant ocean circulation suggest a steady increase in the integrated sink over the last century[1,15]. Yet surface observations clearly indicate that carbon uptake is strongly affected by variability in surface climate and ocean circulation[5,8–13]. This variability impedes our ability to develop a detailed, regional picture of how the ocean carbon sink is changing in response to increasing atmospheric partial pressure of carbon dioxide (p_{CO_2}) and the associated climate change. Although climate models suggest that the ocean should be a net sink for anthropogenic carbon for at least the next several centuries, they also suggest that climate warming and circulation changes will act to reduce the sink's magnitude[7,16]. Monitoring current and future effects from the combined impact of increasing atmospheric p_{CO_2} and climate change—that is, the forced trend—on ocean carbon uptake presents a major observational challenge due to the strong influence of the variability inherent to the climate system[14,17,18].

Previous modelling studies have attempted to separate internal variability from forced trends in ocean carbon uptake using several approaches. Variability in air-to-sea carbon fluxes has been linked to modes of climate variability in realistic hindcast models[19–21]. However, anthropogenic change can project onto these modes, leading to an incomplete separation. The ocean's response to increasing atmospheric CO_2 in the absence of variability and change has been studied[13], but this approach ignores both mean impacts on ocean circulation from variable climate and indirect impacts on the carbon sink due to circulation change. Collections of Earth System Models have been used to assess relationships between natural variability and carbon cycle trends[22,23], but diverse model structures—for example, the spatial resolution of the atmosphere and ocean components, parameterization of the lower food web, or numerical schemes—can influence resulting trends[24]. Structural uncertainty precludes clear identification of the influence of internal variability[24].

We make use here of a large ensemble of a single Earth system model, the Community Earth System Model–Large Ensemble (CESM-LE, ref. 25) to assess variability and change in the ocean carbon cycle in recent decades and through 2100. CESM is a comprehensive coupled climate model consisting of atmosphere, ocean, land surface, and sea ice components. The CESM-LE experiment includes 32 members with ocean biogeochemistry output. The experiment included a control integration of >2,000 years. A transient integration (ensemble member 1) started at year 402 of the control and was integrated for 251 years under historical forcing (1850–2005) and then the Intergovernmental Panel on Climate Change Representative Concentration Pathway (IPCC RCP) 8.5 scenario for 2006–2100. Additional ensemble members were initialized from ensemble member 1 at 1 January 1920, with round-off level perturbations applied to the air temperature field. See Methods for more details.

Here, the use of a single model eliminates structural differences inherent to multi-model ensembles[24], allowing the spread across the ensemble to be wholly attributed to the internal variability of the modelled climate system[14,17,18,26]. For each ensemble member, temporal trends in any variable can be separated into two parts: (1) the forced trend that is common across all ensembles, and (2) the unforced, or internal trend, that occurs only in that ensemble member. The spread of trends across the ensemble indicates how much internal variability causes individual ensemble members to deviate from the forced trend[14,17,18,26]. The forced trend, as its name suggests, is due to the model forcing, here including anthropogenic greenhouse gases and aerosols, as well as natural forcings (for example, solar variability and volcanoes) during the historical period[14,25]. In the case of the ocean carbon sink, there are two components to the forced trend. The first is the direct influence of increasing atmospheric p_{CO_2} driving continued ocean carbon uptake. The second is the indirect effect of changing climate that influences the physical state of the ocean and modulates air-to-sea carbon fluxes.

Comparisons to observations illustrate that CESM captures the dominant modes and magnitudes of ocean carbon cycle variability and trends at regional to global scales (ref. 21, Methods, Extended Data Tables 1 and 2). To further validate the simulated mean CO_2 flux, we compare to fluxes estimated from observations[5], and to a multi-model ensemble of 12 Coupled Model Intercomparison Project 5 (CMIP5) Earth system models (Fig. 1, Extended Data Fig. 1, Extended Data Table 3). For the 30-year mean CO_2 flux, CESM-LE is consistent with the observed estimates in most regions and for the global average, with small differences across the individual ensemble members (Fig. 1). In contrast, there is a substantial spread in CO_2 flux estimates from CMIP5[23]. It is to be expected that structural differences between models would dominate differences in the multi-decadal mean CO_2 flux, since the long averaging period integrates over the timescales of the dominant modes of variability. This is exactly what we find; a much greater spread in mean CO_2 flux for CMIP5 than for CESM-LE for all biomes

[1]Department of Atmospheric and Oceanic Sciences, University of Wisconsin—Madison, Madison, Wisconsin, USA. [2]Center for Climatic Research, University of Wisconsin—Madison, Madison, Wisconsin, USA. [3]Space Science and Engineering Center, University of Wisconsin—Madison, Madison, Wisconsin, USA. [4]NOAA Pacific Marine Environmental Laboratory, Seattle, Washington, USA. [5]National Center for Atmospheric Research, Boulder, Colorado, USA. [6]Department of Atmospheric and Oceanic Sciences and Institute of Arctic and Alpine Research, University of Colorado Boulder, Boulder, Colorado, USA.

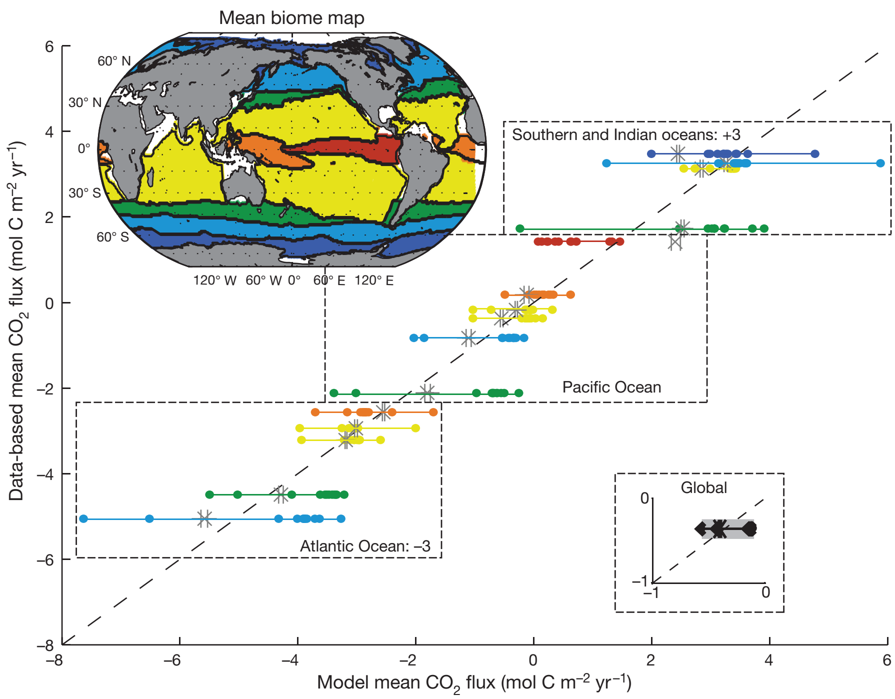

Figure 1 | Modelled and observed mean 1982–2011 CO_2 flux in 15 ocean biomes. The CESM-LE mean is shown as a grey cross, with max/min in grey ($N=32$), aligned with horizontal lines for each biome. Coloured dots represent CMIP5 models ($N=12$), corresponding to the biome colours on the inset mean biome map (ICE, dark blue; SPSS, light blue; STSS, green; STPS, yellow; EQ, orange and red; full names are given in Extended Data Table 4). There is insufficient data to plot the Northern Hemisphere ICE biomes[28]. The Atlantic Ocean is offset by $-3\,\mathrm{mol\,C\,m^{-2}\,yr^{-1}}$, and the Southern and Indian oceans by $+3\,\mathrm{mol\,C\,m^{-2}\,yr^{-1}}$. The global mean is shown in the bottom right inset (scale is twice that of the main panel); the uncertainty on the observed value (grey band) is $0.12\,\mathrm{mol\,C\,m^{-2}\,yr^{-1}}$ (ref. 28; P. Landschützer, personal communication).

(Fig. 1). These structural differences across CMIP5 also affect CO_2 flux trends (Methods, Extended Data Fig. 2), indicating that a clean separation of forced trends from trends driven by internal variability is not possible with the CMIP5 multi-model ensemble, as it is with CESM-LE.

Our model analysis considers forced trends and the spread of internal trends in the ocean carbon sink across timeframes from decadal to centennial, all starting in 1990. Forced trends are shown only if they can be distinguished from trends due to internal variability with 95% confidence[14] (Methods).

For the decade starting in 1990, internal variability is large enough to preclude identification of forced trends in the carbon sink across most of the ocean (Fig. 2a). Internally driven variability in trends (Fig. 2d) is largest in the equatorial Pacific due to El Niño/Southern Oscillation effects, and in regions of strong seasonal and interannual climate variability, such as the high latitudes of the North Pacific and Atlantic and north of seasonal sea ice in the Southern Ocean[5,8,10,11,13,22,27,28]. Only in the subpolar North Atlantic, equatorial Atlantic and in some locations in the Southern Ocean are forced trends large enough to emerge from the variability over this period, and in these locations CO_2 uptake increases (Fig. 2a).

As a result of anthropogenic CO_2 emissions from 1990–2019, the ocean carbon sink increases in most locations outside the subtropics

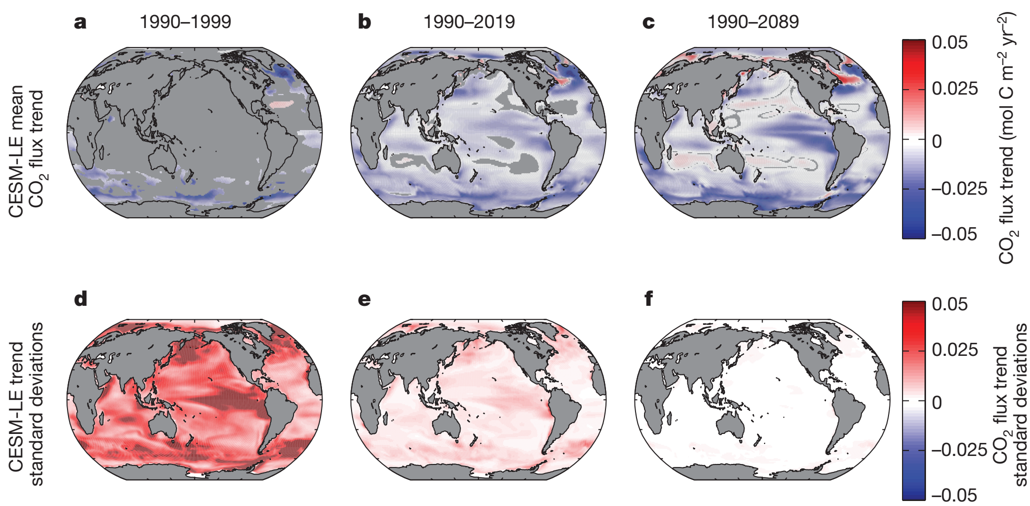

Figure 2 | Forced trends and internal variability of CESM-LE trends in sea-to-air CO_2 flux. Forced trends for **a**, 1990–1999, **b**, 1990–2019 and **c**, 1990–2089. Light-grey ocean areas show where the forced trend cannot be identified with 95% confidence (Methods). CO_2 flux trend standard deviations, indicating the impact of internal variability on CO_2 flux trends, for **d**, 1990–1999, **e**, 1990–2019 and **f**, 1990–2089. Negative values indicate increasing ocean carbon uptake.

(Fig. 2b). In isolated regions within the subtropics, the forced trend in carbon uptake for 1990–2019 is not large enough to be identifiable at the 95% level, despite the fact that internally driven variability is substantially reduced relative to the decadal timeframe (Fig. 2d, e). Over 100 years (1990–2089), anthropogenic forcing leads to strong increases in uptake in the high latitudes, and to reduced outgassing in the equatorial Pacific and the eastern upwelling zones off South America and Africa. In the Pacific and Indian subtropics, the forced trend illustrates weakened carbon uptake by 2100 (Fig. 2c). Internal variability has minimal impact on 100-year CO_2 flux trends (Fig. 2f).

The ocean's capacity to absorb increasing amounts of anthropogenic CO_2 is not uniformly distributed. Across multi-decadal to centennial timescales, CO_2 flux does not change or decreases in the subtropical gyres (Fig. 2b, c). This is consistent with a convergent large-scale circulation and strong stratification that isolates the surface from the deep ocean's large capacity to hold carbon. Long-term warming also reduces CO_2 solubility[10,13,16]. In contrast, the regions where ocean carbon uptake strongly increases are those with strong exchange between the surface and the deep ocean. In the equatorial Pacific, in eastern boundary zones, and in the Southern Ocean, upwelling deep waters have been out of contact with the atmosphere for hundreds of years and thus hold little, if any, anthropogenic carbon. As time progresses, upwelling waters encounter an ever-higher atmospheric p_{CO_2}, which diminishes outgassing of natural carbon[4,22,28] (Extended Data Fig. 1). In the North Atlantic, the direction of the exchange with the deep is reversed, with surface waters being transformed into deep waters by rapid buoyancy loss and deep convection. During this transformation, these waters increasingly absorb more carbon as atmospheric p_{CO_2} rises. There is a large-scale correspondence of the regions of mean carbon uptake at present[3] with the regions where carbon uptake is predicted to grow most rapidly in the twenty-first century.

The ability to separate forced from internal trends in CESM-LE (Fig. 2) allows for an assessment of timescales over which observations would be required in order to detect anthropogenically driven change in ocean carbon uptake from observations (Fig. 3). Consistent with previous studies[26,29], detectability is assessed using 'time of emergence', which is the year in which the signal of the forced trend would emerge from the noise of the internal variability. This analysis assumes observations began in 1990 (Methods).

The forced trend emerges early (by 2010) in some of the Southern Ocean and the Atlantic, where there is a large short-term change in the sink. Given the strong internal variability and the smaller forced trend in the equatorial Pacific, time of emergence is generally intermediate here (by 2030–2050). The latest emergence occurs in the Pacific and Indian subtropical regions (2050+). Where the net effect of the forcing is to drive long-term steady carbon uptake, no change should be detected before 2100 (white areas in Fig. 3). If internal variability were to be substantially underestimated or overestimated at a location, estimates of time of emergence would be too short or too long, respectively. However, comparison with data indicates that CESM-LE captures carbon cycle variability reasonably well (Extended Data Tables 1 and 2).

Using our current observational system for surface ocean carbon, should we be able to detect these predicted changes? At seven ocean time series stations, direct measurements of the ocean carbon cycle have been made at quarterly to monthly intervals for one to several decades[9] (Fig. 3). In the Atlantic, these locations are situated such that if observations had occurred since 1990 at a frequency sufficient to constrain the annual mean flux, they should be able to reveal change in the ocean carbon sink as distinct from internal variability at present (Irminger Sea, by 2015) or in the near future (BATS, ESTOC, CARIACO, by 2020; Iceland Sea, by 2040) (Fig. 3). However, for the Pacific sites, detection of change in carbon uptake should not be expected until at least 2050 (HOT, by 2050; Munida, beyond 2100). Unfortunately, at the time series site where CESM-LE suggests the forced trend may be first detectable (Irminger Sea), the p_{CO_2} data set is short (1983–2005) and highly variable[9], making it impossible to determine if a trend towards increasing carbon flux is, in fact, occurring.

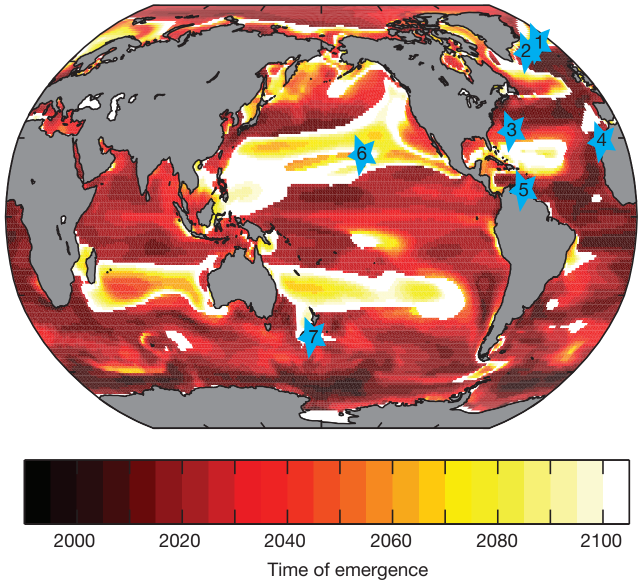

Figure 3 | Time of emergence for sea-to-air CO_2 flux. Time of emergence is when the forced trend becomes detectable given the internal variability (Methods). Blue stars indicate seven ocean timeseries stations[9], from North to South in the Atlantic: (1) Iceland Sea, (2) Irminger Sea, (3) Bermuda Atlantic Time-series Study (BATS), (4) European Station for Time series in the Ocean at the Canary Islands (ESTOC), (5) Carbon Retention In A Colored Ocean (CARIACO) and from North to South in the Pacific, (6) Hawaii Ocean Time-series (HOT) and (7) Munida. Mean times of emergence for each biome are presented in Extended Data Table 4.

Surface ocean carbon data from volunteer commercial and scientific ships are presently too sparse for direct estimation of multi-decadal carbon cycle trends in most regions[5,8,10,12]. However, in the subtropics of the North Atlantic and Pacific, there are sufficient data to indicate a steady ocean carbon sink, and in the equatorial Atlantic to indicate an increasing sink for 1981–2009[10]. These changes are consistent with the 30-year forced signals expected from CESM-LE (Fig. 2b). More data, from all sources, will be required to determine whether these signals are, in fact, illustrating the forced trend in ocean carbon uptake[10].

Going forward, ocean carbon monitoring efforts can benefit from this new ability to separate internal variability from forced trends. Long-term records can be interpreted in the context of the expected forced change in the ocean carbon sink; monitoring can be targeted to regions where the largest forced changes are expected; and regional aggregation approaches that optimally seek the forced signal can be developed. Concurrently, expansion of these analyses to large ensembles of other Earth system models[18,26] will further elucidate the mechanisms, magnitudes, and timescales of forced trends in the ocean carbon sink.

Online Content Methods, along with any additional Extended Data display items and Source Data, are available in the online version of the paper; references unique to these sections appear only in the online paper.

Received 10 April; accepted 21 December 2015.

1. Khatiwala, S., Primeau, F. & Hall, T. Reconstruction of the history of anthropogenic CO_2 concentrations in the ocean. *Nature* **462,** 346–349 (2009).
2. Ciais, P. & Sabine, C. in *Climate Change. The Physical Science Basis. Contribution of Working Group I to the Fifth Assessment Report of the Intergovernmental Panel on Climate Change* (eds Stocker, T. F. *et al.*) Ch. 6, 1535 (Cambridge Univ. Press, 2013).
3. Gruber, N. *et al.* Oceanic sources, sinks, and transport of atmospheric CO_2. *Glob. Biogeochem. Cycles* **23,** GB1005 (2009).
4. Takahashi, T. *et al.* Climatological mean and decadal change in surface ocean pCO_2, and net sea–air CO_2 flux over the global oceans. *Deep Sea Res. Part II* **56,** 554–577 (2009).

5. Landschützer, P. *et al.* The reinvigoration of the Southern Ocean carbon sink. *Science* **349,** 1221–1224 (2015).
6. Schuster, U. *et al.* An assessment of the Atlantic and Arctic sea–air CO_2 fluxes, 1990–2009. *Biogeosciences* **10,** 607–627 (2013).
7. Randerson, J. T. *et al.* Multicentury changes in ocean and land contributions to the climate-carbon feedback. *Glob. Biogeochem. Cycles* **29,** 744–759 (2015).
8. Munro, D. R. *et al.* Recent evidence for a strengthening CO_2 sink in the Southern Ocean from carbonate system measurements in the Drake Passage (2002–2015). *Geophys. Res. Lett.* **42,** 7623–7630 (2015).
9. Bates, N. *et al.* A time-series view of changing ocean chemistry due to ocean uptake of anthropogenic CO_2 and ocean acidification. *Oceanography* **27,** 126–141 (2014).
10. Fay, A. R. & McKinley, G. A. Global trends in surface ocean pCO_2 from in situ data. *Glob. Biogeochem. Cycles* **27,** 541–557 (2013).
11. McKinley, G. A., Fay, A. R., Takahashi, T. & Metzl, N. Convergence of atmospheric and North Atlantic carbon dioxide trends on multidecadal timescales. *Nature Geosci*. **4,** 606–610 (2011).
12. Le Quéré, C., Raupach, M. R., Canadell, J. G. & Al, G. M. E. Trends in the sources and sinks of carbon dioxide. *Nature Geosci*. **2,** 831–836 (2009).
13. Le Quéré, C., Takahashi, T., Buitenhuis, E. T., Rödenbeck, C. & Sutherland, S. C. Impact of climate change and variability on the global oceanic sink of CO_2. *Glob. Biogeochem*. *Cycles* **24,** GB4007 (2010).
14. Deser, C., Phillips, A., Bourdette, V. & Teng, H. Uncertainty in climate change projections: the role of internal variability. *Clim. Dyn.* **38,** 527–546 (2012).
15. DeVries, T. The oceanic anthropogenic CO_2 sink: storage, air-sea fluxes, and transports over the industrial era. *Glob. Biogeochem. Cycles* **28,** 631–647 (2014).
16. Sarmiento, J. L. & LeQuéré, C. Oceanic carbon dioxide uptake in a model of century-scale global warming. *Science* **274,** 1346–1350 (1996).
17. Deser, C., Knutti, R., Solomon, S. & Phillips, A. S. Communication of the role of natural variability in future North American climate. *Nature Clim. Change* **2,** 775–779 (2012).
18. Frölicher, T. L., Joos, F., Plattner, G.-K., Steinacher, M. & Doney, S. C. Natural variability and anthropogenic trends in oceanic oxygen in a coupled carbon cycle-climate model ensemble. *Glob. Biogeochem. Cycles* **23,** GB1003 (2009).
19. Ullman, D. J., McKinley, G. A., Bennington, V. & Dutkiewicz, S. Trends in the North Atlantic carbon sink: 1992–2006. *Glob. Biogeochem. Cycles* **23,** GB4011 (2009).
20. Lovenduski, N. & Gruber, N. Toward a mechanistic understanding of the decadal trends in the Southern Ocean carbon sink. *Glob. Biogeochem. Cycles* **22,** GB3016 (2008).
21. Long, M. C., Lindsay, K., Peacock, S., Moore, J. K. & Doney, S. C. Twentieth-century oceanic carbon uptake and storage in CESM1 (BGC). *J. Clim.* **26,** 6775–6800 (2013).
22. Resplandy, L., Séférian, R. & Bopp, L. Natural variability of CO_2 and O_2 fluxes: what can we learn from centuries-long climate models simulations? *J. Geophys. Res.* **120,** 384–404 (2015).
23. Frölicher, T. L. *et al.* Dominance of the Southern Ocean in anthropogenic carbon and heat uptake in CMIP5 models. *J. Clim.* **28,** 862–886 (2015).
24. Hawkins, E. & Sutton, R. The potential to narrow uncertainty in regional climate predictions. *Bull. Am. Meteorol. Soc.* **90,** 1095–1107 (2009).
25. Kay, J. E. *et al.* The Community Earth System Model (CESM) Large Ensemble Project: a community resource for studying climate change in the presence of internal climate variability. *Bull. Am. Meteorol. Soc.* **96,** 1333–1349 (2014).
26. Rodgers, K. B., Lin, J. & Frolicher, T. L. Emergence of multiple ocean ecosystem drivers in a large ensemble suite with an Earth system model. *Biogeosciences* **12,** 3301–3320 (2015).
27. Lovenduski, N. S., Fay, A. R. & McKinley, G. A. Observing multi-decadal trends in Southern Ocean CO_2 uptake: what can we learn from an ocean model? *Glob. Biogeochem. Cycles* **29,** 416–426 (2015).
28. Landschützer, P., Gruber, N., Bakker, D. C. E. & Schuster, U. Recent variability of the global ocean carbon sink. *Glob. Biogeochem. Cycles* **28,** 927–949 (2014).
29. Hawkins, E. & Sutton, R. Time of emergence of climate signals. *Geophys. Res. Lett.* **39,** L01702 (2012).

Acknowledgements The National Science Foundation sponsors National Center for Atmospheric Research, where the Community Earth System Model is developed. Computing resources were provided by the Climate Simulation Laboratory at NCAR's Computational and Information Systems Laboratory, sponsored by the NSF and other agencies. NCAR's Advanced Study Program sponsored D.J.P., K.L., M.C.L. and G.A.M. to initiate this analysis. We also thank NASA for funding (grants NNX11AF53G and NNX13AC53G to G.A.M., D.J.P., A.R.F. and N.S.L.). N.S.L. also thanks the NSF (grant OCE-1155240) and NOAA (grant NA12OAR4310058).

Author Contributions G.A.M. conceived the analysis, which was further refined by all authors. K.L. coordinated inclusion of ocean biogeochemistry in CESM-LE. D.J.P. and A.R.F. did the analysis. All authors discussed results and contributed to writing the manuscript.

Author Information Reprints and permissions information is available at www.nature.com/reprints. The authors declare no competing financial interests. Readers are welcome to comment on the online version of the paper. Correspondence and requests for materials should be addressed to G.A.M. (gamckinley@wisc.edu).

METHODS

The Large Ensemble of the Community Earth System Model. The Community Earth System Model (CESM) is a comprehensive coupled climate model consisting of atmosphere, ocean, land surface, and sea ice component models[30]. The ocean physical model is the ocean component of the Community Climate System Model version 4[31]. The model has nominal 1° horizontal resolution and 60 vertical levels. Mesoscale eddy transport, diapycnal mixing, and mixed layer restratification by submesoscale eddies are parameterized with state-of-the-art approaches. The biogeochemical-ecosystem ocean model includes multi-nutrient co-limitation on phytoplankton growth and specific phytoplankton functional groups as well as full-depth ocean carbonate system thermodynamics, sea-to-air CO_2 fluxes, and a dynamic iron cycle[30]. The biogeochemical-ecosystem model compares favourably to observations, though there are some important biases, including weak Southern Ocean CO_2 uptake[21].

The CESM-LE began with a multi-century 1850 control simulation with constant pre-industrial forcing; the ocean physical state was initialized from observations, ocean biogeochemical tracers were initialized from a separate 600-year spin-up, and other component models were initialized from previous CESM1 simulations. Once the control simulation climate achieved quasi-equilibrium with the 1850 forcing, the first ensemble member was initialized from a randomly selected year in the 1850 control run: 1 January, model year 402. Ensemble member 1 was integrated forward from 1850 to 2100. The remaining ensemble members were integrated from 1920 to 2100 using slightly different initial conditions: Ensemble member 2 used one-day lagged ocean initial conditions, while spread in the remaining ensemble members was generated by round-off level perturbations to their initial air temperature fields[25]. After initial condition memory was lost, each ensemble member evolved independently. A total of 38 ensemble members were generated in this fashion, but 6 of these had corrupted ocean biogeochemical output due to a setup error and affected fields were discarded. All ensemble members have the same specified external forcing: historical forcing from 1920 to 2005, and RCP8.5 forcing from 2006 to 2100. Differences from observed atmospheric p_{CO_2} for RCP8.5 for the 2006–2014 period are minimal[32]. Since atmospheric CO_2 concentrations are prescribed, CESM-LE ocean carbon fluxes do not feed back on the modelled climate.

Analysis methods. We consider the linear trend at each model gridcell of annual mean CO_2 flux, in units of moles of carbon per square metre per year squared. The trend for CO_2 flux is calculated for each ensemble member. The forced trend is the average trend across the 32 ensembles. Each ensemble member's unforced (internal) trend, due to internal variability, is the difference between that ensemble's trend and the forced trend. The 95% confidence level for identification of the forced trend is calculated, for each grid cell and time frame, based on the number of ensembles required to resolve the ensemble mean response: $N_{\min} = 8/(X/\sigma)^2$, where X is the forced trend and σ is the standard deviation of trends[14]. If $N_{\min}$ exceeds the number of ensembles in CESM-LE ($N_{\text{ensembles}} = 32$), the forced trend cannot be identified with 95% confidence. Time of emergence is the first year in which the signal-to-noise ratio exceeds a threshold value of 2, where the signal is the forced trend and the noise is the ensemble standard deviation[29]. For efficiency of computation and presentation, signal-to-noise ratios are calculated at 5-year intervals (that is, 1990–1995, 1990–2000, 1990–2005, and so on). The signal-to-noise ratio must remain greater than 2 for all subsequent years.

Model comparisons to observations. To assess the representation of internal variability in CESM-LE, Extended Data Table 1 compares CESM-LE modelled to observed variability in annual mean p_{CO_2} and CO_2 flux for 1982–2011, and Extended Data Table 2 compares trends over the same period. p_{CO_2} data are from the Surface Ocean CO_2 Atlas (SOCATv2)[33] averaged to monthly means at $1° \times 1°$ resolution. CESM-LE members are each sampled in p_{CO_2} to reflect the data density available in SOCATv2. A background mean climatology[4] is removed at $1° \times 1°$ resolution in order to address the potential of spatial aliasing when averaging to biome-scale[10,34,35]. An area-weighted average is then used to arrive at biome-scale annual means, and the 30-year trend is removed before calculating the standard deviation. For the CO_2 flux, we utilize monthly $1° \times 1°$ resolution flux estimates that have full spatial and temporal coverage over the period 1982–2011[28]. These estimates are based on the same p_{CO_2} data set (SOCATv2). With the full global coverage of the CO_2 flux product, there is no need to sample or to remove a background climatology from CESM-LE before biome averaging. Otherwise, the same processing is employed as for p_{CO_2}. The uncertainty reported in Extended Data Table 1 is one standard deviation of the variability represented by the 32 CESM-LE members for each variable. There is insufficient data to make an independent uncertainty estimate with respect to variability from the observations. In Extended Data Table 2, linear trends in observed annual mean p_{CO_2} and CESM-LE p_{CO_2}, sampled in the same way as these observations, are compared. Sampling in the same way as the observations allows for a direct model-to-observation comparison in spite of the fact that the sparse data coverage may lead to inaccurate observed estimates of annual mean p_{CO_2} for some biomes in some years. Since the CO_2 flux product offers full coverage in space and time, there is no need for sampling prior to the calculation of trends.

Within the uncertainty, modelled p_{CO_2} variance is correct in seven of the biomes, underestimated in five biomes and overestimated in three biomes (Extended Data Table 1). However, in two of the three biomes where p_{CO_2} variability is overestimated by the model (SO STSS, SO SPSS), comparison to the CO_2 flux product suggests that the model underestimates variability. In the third (NP STPS), the flux product comparison indicates that the model appropriately simulates variability. Conversely, in the biomes where p_{CO_2} variability is underestimated, the CO_2 flux product comparison indicates either variability consistent with observations (NA STSS, EQ Atl), too high (NP STSS), or too low (NA SPSS, SA STPS). Similarly, in the biomes where p_{CO_2} variability is consistent with the observations, the CO_2 flux comparison indicates overestimation by the model (East EQ Pac, West EQ Pac, IND STPS), underestimation (NP SPSS, SO ICE), or consistency (SP STPS).

Modelled trends in p_{CO_2} and CO_2 flux (Extended Data Table 2) are largely consistent with observed trends, given the uncertainty. In one biome (West EQ Pac), the trend in p_{CO_2} in the model is overestimated, though in this biome the CO_2 flux trend is consistent with the observed estimates. In three biomes (NP STPS, East EQ Pac, IND STPS), the flux trend is too large, and in one (SO SPSS), it is too small. However, in all four of these biomes, the p_{CO_2} trends are consistent with the observed estimates. There is no clear relationship between over- and underestimation of trends and over- and underestimation of variability (Extended Data Table 1).

In the CESM-LE, p_{CO_2} variability and trends dominantly control CO_2 flux variability and trends[21]. Thus, the fact that these comparisons for p_{CO_2} and CO_2 flux variability and trends differ substantially suggests that there is additional, unquantified uncertainty driven by the sparse sampling for p_{CO_2} and assumptions made in the development of the flux product[28]. That CESM-LE falls clearly within the range of observed p_{CO_2} and estimated CO_2 flux variability and trends indicates that the model's representation of the carbon cycle is, on the whole, consistent with our current observational understanding. More observations are needed to better constrain internal variability and trends in the surface ocean carbon cycle.

Forced trends in the CMIP5 ensemble. Twelve CMIP5 Earth system models are included in the analysis in addition to the CESM-LE for the historical period. The CMIP5 models included are those models that report CO_2 flux at monthly timescales for a historical simulation through 2005 and with the RCP8.5 scenario for 2006–2100; see Extended Data Table 3 for included models. The CESM1-Biogeochemistry (CESM1-BGC) model included in the CMIP5 model suite is a predecessor to the CESM-LE.

Owing to the combined effect of a smaller number of ensemble members for CMIP5 and the larger variability across these ensembles (Extended Data Fig. 2d–f), due in part to structural differences[29], the forced trend in CO_2 flux cannot be identified from CMIP5 across most of the global oceans, even for the time frame 1990-2089 (Extended Data Fig. 2a–c). Where the forced trend from CMIP5 is discernible, primarily in the equatorial Pacific and Southern Ocean, it is of the same sign as CESM-LE (increasing uptake) but of weaker magnitude.

Data sources. Surface Ocean CO_2 Atlas (SOCAT v2)[33] p_{CO_2} data were taken from www.socat.info/access.html. CO_2 flux estimates[28] were obtained from http://cdiac.esd.ornl.gov/oceans/SPCO2_1982_2011_ETH_SOM_FFN.html.

Model output sources. CESM-LE[25] is available from https://www.earthsystemgrid.org/dataset/ucar.cgd.ccsm4.CESM_CAM5_BGC_LE.html. CMIP5[36] is available from http://www.ipcc-data.org/sim/gcm_monthly/AR5/WG1-Archive.html.

Code availability. Code for analysis and production of figures is available upon request. Please contact G.A.M. (gamckinley@wisc.edu).

30. Hurrell, J. W. *et al.* The community earth system model: a framework for collaborative research. *Bull. Am. Meteorol. Soc.* **94,** 1339–1360 (2013).
31. Moore, J. K. *et al.* Marine ecosystem dynamics and biogeochemical cycling in the Community Earth System Model [CESM1 (BGC)]: comparison of the 1990s with the 2090s under the RCP4.5 and RCP8.5 scenarios. *J. Clim.* **26,** 9291–9312 (2013).
32. Danabasoglu, G. S. C. *et al*. The CCSM4 Ocean Component. *J. Clim.* **25,** 1361–1389 (2012).
33. Bakker, D. C. E. *et al.* An update to the surface ocean CO_2 atlas (SOCAT version 2). *Earth Syst. Sci. Data* **6,** 69–90 (2014).
34. Fay, A. R. & McKinley, G. A. Global open-ocean biomes: mean and temporal variability. *Earth Syst. Sci. Data* **6,** 273–284 (2014).
35. Fay, A. R., McKinley, G. A. & Lovenduski, N. S. Southern Ocean carbon trends: sensitivity to methods. *Geophys. Res. Lett.* **41,** 6833–6840 (2014).
36. Taylor, K. E., Stouffer, R. J. & Meehl, G. A. An overview of CMIP5 and the experiment design. *Bull. Am. Meteorol. Soc.* **93,** 485–498 (2012).

37. Chylek, P., Li, J., Dubey, M. K., Wang, M. & Lesins, G. Observed and model simulated 20th century Arctic temperature variability: Canadian Earth System Model CanESM2. *Atmos. Chem. Phys. Discuss*. **11,** 22893–22907 (2011).
38. Collins, W. J. *et al.* Development and evaluation of an Earth-system model—HadGEM2. *Geosci. Model Dev.* **4,** 1051–1075 (2011).
39. Dufresne, J.-L. *et al.* Climate change projections using the IPSL-CM5 Earth System Model: from CMIP3 to CMIP5. *Clim. Dyn.* **40,** 2123–2165 (2013).
40. Dunne, J. P. *et al.* GFDL's ESM2 global coupled climate-carbon Earth System Models. Part I: physical formulation and baseline simulation characteristics. *J. Clim.* **25,** 6646–6665 (2012).
41. Fogli, P. G. *et al.* INGV-CMCC carbon (ICC): a carbon cycle earth system model. *CMCC Res. Pap.* 61, http://ssrn.com/abstract=1517282 (Social Science Research Network, 2009).
42. Giorgetta, M. *et al.* CMIP5 simulations of the Max Planck Institute for Meteorology (MPI-M) based on the MPI-ESM-LR model: the historical experiment. http://dx.doi.org/10.1594/WDCC/CMIP5.MXELhi (World Data Centre for Climate, Earth System Grid Federation, 2012).
43. Giorgetta, M. *et al.* CMIP5 simulations of the Max Planck Institute for Meteorology (MPI-M) based on the MPI-ESM-LR model: the RCP85 experiment. http://dx.doi.org/10.1594/WDCC/CMIP5.MXELr8 (World Data Centre for Climate, Earth System Grid Federation, 2012).
44. Ji, D. *et al.* Description and basic evaluation of Beijing Normal University Earth System Model (BNU-ESM) version 1. *Geosci. Model Dev*. **7,** 2039–2064 (2014).
45. Lindsay, K. *et al.* Preindustrial-control and twentieth-century carbon cycle experiments with the Earth System Model CESM1 (BGC). *J. Clim.* **27,** 8981–9005 (2014).
46. Tjiputra, J. F. *et al.* Evaluation of the carbon cycle components in the Norwegian Earth System Model (NorESM). *Geosci. Model Dev*. **6,** 301–325 (2013).
47. Volodin, E. M., Dianskii, N. A. & Gusev, A. V. Simulating present-day climate with the INMCM4.0 coupled model of the atmospheric and oceanic general circulations. *Izv. Atmos. Ocean. Phys.* **46,** 414–431 (2010).
48. Watanabe, S. *et al.* MIROC-ESM 2010: model description and basic results of CMIP5-20c3m experiments. *Geosci. Model Dev.* **4,** 845–872 (2011).
49. Wu, T. *et al.* Global carbon budgets simulated by the Beijing Climate Center Climate System Model for the last century. *J. Geophys. Res.* **118,** 4326–4347 (2013).

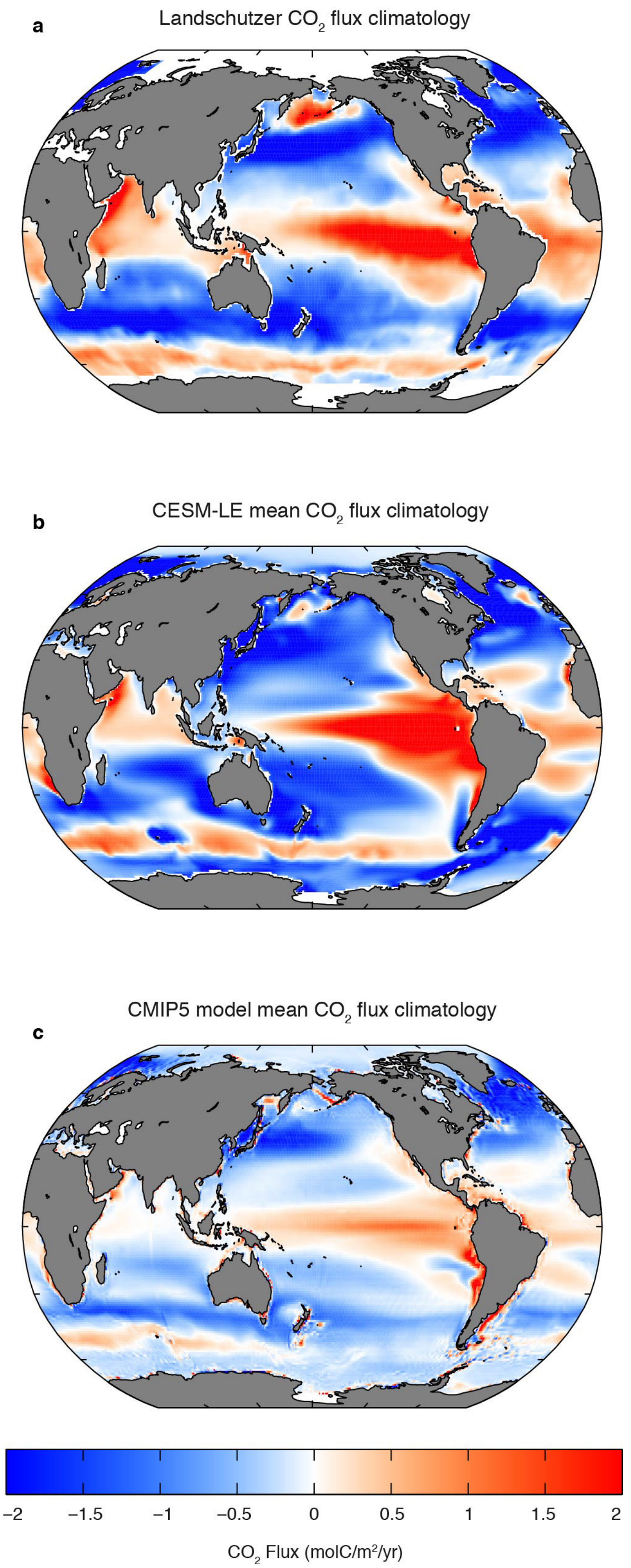

Extended Data Figure 1 | Comparison of 1982–2011 mean CO_2 flux. **a**, Data-based climatology (ref. 28). **b**, CESM large ensemble 32-member mean. **c**, Mean of 12 CMIP5 models.

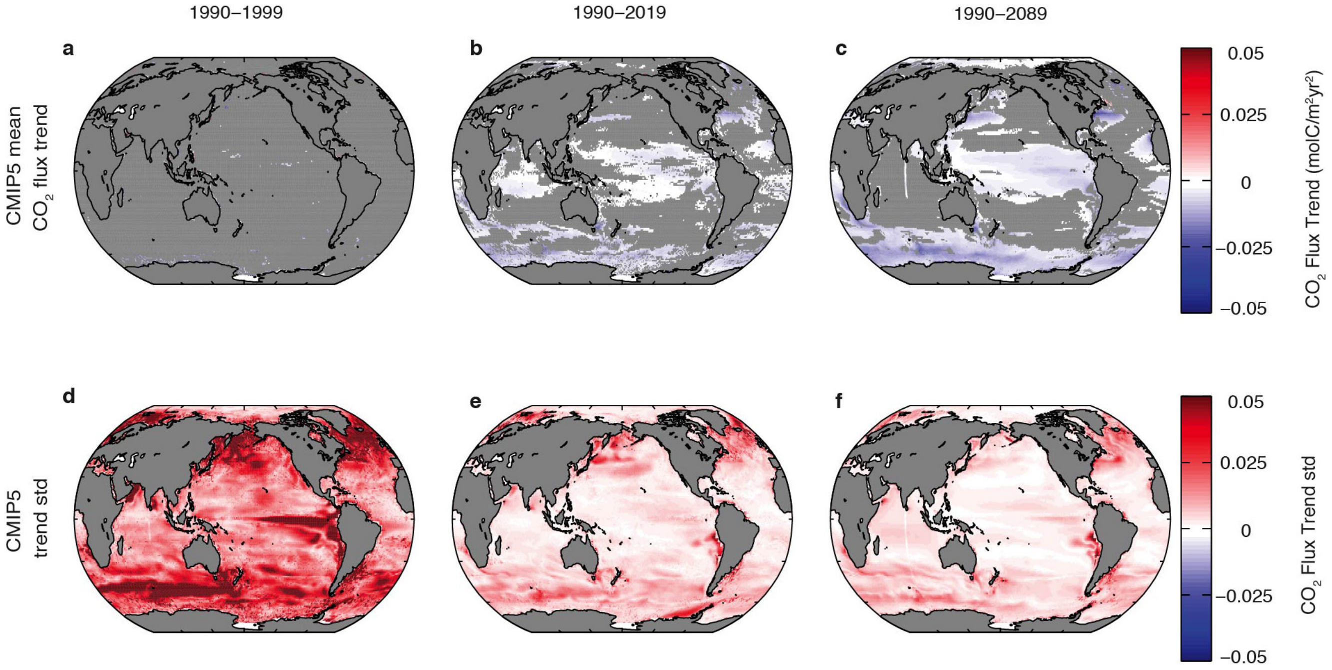

Extended Data Figure 2 | Forced trends and variability of CMIP5 trends in sea-to-air CO_2 flux. Forced trends for **a**, 1990–1999, **b**, 1990–2019 and **c**, 1990–2089. Grey areas are where the forced trend cannot be distinguished from the variability with 95% confidence (Methods). CO_2 flux trend standard deviations, indicating the impact of variability on CO_2 flux trends, for **d**, 1990–1999, **e**, 1990–2019 and **f**, 1990–2089. Negative values indicate increasing ocean carbon uptake.

Extended Data Table 1 | Comparison of observed and modelled p_{CO_2} and CO_2 flux variability for 1982–2011

Biome	pCO₂ Data variability (µatm)	pCO₂ CESM-LE mean variabiilty (µatm)	pCO₂ Uncertainty (µatm)	CO₂ flux Data-based variability (molC/m²/yr)	CO₂ flux CESM-LE mean variability (molC/m²/yr)	CO₂ flux Uncertainty (molC/m²/yr)
NP SPSS	7.9	10.2	2.0	<u>0.42</u>	<u>0.13</u>	<u>0.02</u>
NP STSS	<u>7.3</u>	<u>5.9</u>	<u>0.4</u>	*0.09*	*0.13*	*0.01*
NP STPS	*4.2*	*5.4*	*0.5*	0.05	0.07	0.01
East EQ Pac	6.3	5.9	0.7	*0.07*	*0.15*	*0.02*
West EQ Pac	13.0	12.6	2.0	*0.23*	*0.36*	*0.05*
SP STPS	8.3	6.4	1.0	0.07	0.08	0.01
NA SPSS	<u>22.4</u>	<u>19.7</u>	<u>1.0</u>	<u>0.25</u>	<u>0.12</u>	<u>0.01</u>
NA STSS	<u>7.4</u>	<u>5.2</u>	<u>0.6</u>	0.10	0.10	0.02
NA STPS	5.2	5.6	0.4	<u>0.09</u>	<u>0.06</u>	<u>0.01</u>
EQ Atl	<u>8.8</u>	<u>6.5</u>	<u>0.6</u>	0.07	0.06	0.01
SA STPS	<u>9.7</u>	<u>8.5</u>	<u>0.5</u>	<u>0.10</u>	<u>0.06</u>	<u>0.007</u>
IND STPS	11.1	10.6	1.0	*0.04*	*0.10*	*0.01*
SO STSS	*5.9*	*12.4*	*2.0*	<u>0.14</u>	<u>0.08</u>	<u>0.01</u>
SO SPSS	*4.8*	*12.8*	*2.0*	<u>0.22</u>	<u>0.11</u>	<u>0.01</u>
SO ICE	15.4	17.0	2.0	<u>0.22</u>	<u>0.05</u>	<u>0.005</u>

Variability is the standard deviation of the annual means from 1982 to 2011. Uncertainty of the variability is the standard deviation of the variability estimates for each of the 32 CESM-LE ensemble members. Underlining indicates that the modelled variability is lower than the observed variability, and italics indicates that the modelled variability is higher than the observed variability, in both cases taking into account the model-estimated uncertainty. p_{CO_2} data are from ref. 33; CO_2 flux data are from ref. 28.

Extended Data Table 2 | Comparison of observed and modelled p_{CO_2} and CO_2 flux trends for 1982–2011

	pCO_2		CO_2 flux	
Biome	Data trend (µatm/yr)	CESM-LE forced trend (µatm/yr)	Data-based trend ($molC/m^2/yr^2$)	CESM-LE forced trend ($molC/m^2/yr^2$)
NP SPSS	1.18 ± 0.42	1.59 ± 0.41	-0.012 ± 0.017	-0.004 ± 0.002
NP STSS	1.99 ± 0.32	2.16 ± 0.24	-0.011 ± 0.004	-0.008 ± 0.002
NP STPS	1.76 ± 0.19	2.01 ± 0.24	-0.008 ± 0.002	-0.004 ± 0.001
West EQ Pac	*1.21 ± 0.28*	*1.67 ± 0.15*	-0.001 ± 0.003	-0.005 ± 0.002
East EQ Pac	1.43 ± 0.60	1.74 ± 0.37	-0.023 ± 0.010	-0.005 ± 0.004
SP STPS	1.17 ± 0.41	1.54 ± 0.26	-0.006 ± 0.003	-0.003 ± 0.001
NA SPSS	1.06 ± 1.33	1.44 ± 1.11	-0.014 ± 0.11	-0.016 ± 0.002
NA STSS	1.73 ± 0.51	1.77 ± 0.32	-0.014 ± 0.004	-0.014 ± 0.001
NA STPS	1.57 ± 0.27	1.88 ± 0.28	-0.006 ± 0.004	-0.003 ± 0.001
EQ Atl	1.48 ± 0.45	1.50 ± 0.30	-0.001 ± 0.003	-0.005 ± 0.001
SA STPS	0.92 ± 0.53	1.49 ± 0.44	-0.004 ± 0.005	-0.005 ± 0.001
IND STPS	2.35 ± 0.73	2.55 ± 0.65	-0.008 ± 0.002	-0.003 ± 0.001
SO STSS	2.00 ± 0.29	1.57 ± 0.59	-0.005 ± 0.006	-0.007 ± 0.001
SO SPSS	1.58 ± 0.24	0.97 ± 0.55	*0.004 ± 0.010*	*-0.010 ± 0.001*
SO ICE	1.42 ± 0.84	0.51 ± 0.85	-0.010 ± 0.010	-0.016 ± 0.001

Underlining indicates that the modelled trend is lower than the observed trend, and italics indicate that the modelled trend is higher than the observed trend, given the uncertainty (95% trend confidence intervals). Trends are based on annual means. p_{CO_2} data are from ref. 33; CO_2 flux data are from ref. 28.

Extended Data Table 3 | CMIP5 models used in this work

Modeling Group	Model Name	Citation
Beijing Climate Center (BCC), China Meteorological Administration, China	BCC-CSM1.1m	49
Beijing Normal University (BNU), China College of Global Change and Earth System Science, China	BNU-ESM	44
Canadian Centre for Climate Modeling and Analysis, Victoria BC, Canada	CanESM2	37
National Center for Atmospheric Research, USA	CESM1-BGC	45
Centro Euro-Mediterraneo sui Cambiamenti Climatici, Lecce, Italy	CMCC-ESM	41
NOAA Geophysical Fluid Dynamics Laboratory, USA	GFDL-ESM2M	40
Met Office Hadley Centre, UK	HadGEM2	38
Institut Pierre-Simon Laplace, IPSL Climate Modelling Centre, France	IPSL-CM5-MR	39
Institute for Numerical Mathematics, Russia	INM-CM4	47
Japan Agency for Marine-Earth Science and Technology, Atmosphere and Ocean Research Institute, The University of Tokyo, Japan	MIROC-ESM	48
Max-Planck-Institute for Meteorology, Germany	MPI-ESM-LR	42, 43
Norwegian Climate Centre, Norway	NorESM1-ME	46

See refs 37–49.

Extended Data Table 4 | Biome long names and mean time of emergence

Biome acronym	Biome long name	Mean Time of Emergence
NP SPSS	North Pacific subpolar seasonally stratified	2063
NP STSS	North Pacific subtropical seasonally stratified	2038
NP STPS	North Pacific subtropical permanently stratified biome	2069
West EQ Pac	West Pacific equatorial	2048
East EQ Pac	East Pacific equatorial	2031
SP STPS	South Pacific subtropical permanently stratified biome	2054
NA SPSS	North Atlantic subpolar seasonally stratified	2054
NA STSS	North Atlantic subtropical seasonally stratified	2030
NA STPS	North Atlantic subtropical permanently stratified biome	2051
EQ Atl	Atlantic equatorial	2018
SA STPS	South Atlantic subtropical permanently stratified biome	2027
IND STPS	Indian subtropical permanently stratified biome	2048
SO STSS	Southern Ocean subtropical seasonally stratified	2032
SO SPSS	Southern Ocean subpolar seasonally stratified	2029
SO ICE	Southern Ocean marginal sea ice	2018

Names are taken from ref. 34.

doi:10.1038/nature16981

Third-party punishment as a costly signal of trustworthiness

Jillian J. Jordan[1], Moshe Hoffman[2], Paul Bloom[1] & David G. Rand[1,3,4]

Third-party punishment (TPP)[1–7], in which unaffected observers punish selfishness, promotes cooperation by deterring defection. But why should individuals choose to bear the costs of punishing? We present a game theoretic model of TPP as a costly signal[8–10] of trustworthiness. Our model is based on individual differences in the costs and/or benefits of being trustworthy. We argue that individuals for whom trustworthiness is payoff-maximizing will find TPP to be less net costly (for example, because mechanisms[11] that incentivize some individuals to be trustworthy also create benefits for deterring selfishness via TPP). We show that because of this relationship, it can be advantageous for individuals to punish selfishness in order to signal that they are not selfish themselves. We then empirically validate our model using economic game experiments. We show that TPP is indeed a signal of trustworthiness: third-party punishers are trusted more, and actually behave in a more trustworthy way, than non-punishers. Furthermore, as predicted by our model, introducing a more informative signal—the opportunity to help directly—attenuates these signalling effects. When potential punishers have the chance to help, they are less likely to punish, and punishment is perceived as, and actually is, a weaker signal of trustworthiness. Costly helping, in contrast, is a strong and highly used signal even when TPP is also possible. Together, our model and experiments provide a formal reputational account of TPP, and demonstrate how the costs of punishing may be recouped by the long-run benefits of signalling one's trustworthiness.

Costly third-party punishment (TPP) is widely observed in laboratory[1–4,7] and field[5,6] experiments (although see ref. 12), and appears to be universal across cultures[13]. While collectively beneficial, TPP poses a puzzle: why should individuals incur the costs of punishment?

We propose an answer based on reputation[4,14–18]. Specifically, we introduce a game theoretic model of TPP as a costly signal of trustworthiness: if you see me punish selfishness, it can signal that I will not be selfish to you. Our model involves a partner-choice[19] game with two roles. In each interaction, the 'Signaller' decides whether to send one or more costly signals; then the 'Chooser' decides whether to partner with the Signaller.

As with all costly signalling models[8–10], our model is based on individual differences: two 'types' of Signallers differ in their quality as interaction partners. For trustworthy types, it is payoff-maximizing to cooperate when trusted; for exploitative types, it is payoff-maximizing to defect. Choosers thus benefit from partnering with trustworthy Signallers, but are harmed by partnering with exploitative Signallers.

Signallers' types are fixed, but not directly observable. Therefore, Choosers must base their partner choice on the aforementioned costly signals. In each interaction, the Signaller's cost of signalling is either small (less than the benefit of being chosen as a partner) or large (greater than the benefit of being chosen). It is thus beneficial to signal (in order to be chosen) when the cost is small, but not large. The key premise of costly signalling is that high-quality types are more likely to experience small signalling costs than low-quality types (and are thus more likely to signal). Therefore, signals convey information about Signallers' types, and Choosers benefit from preferring partners who signal.

How does this relate to TPP and trustworthiness? We argue that TPP will typically be less net costly for trustworthy types (that is, individuals who find it payoff-maximizing to cooperate when trusted). Because TPP deters future harm against others, punishing may benefit the punisher (for example, via direct reciprocity from the victim of the punished transgression, or rewards from institutions or leaders seeking to promote cooperation); and these benefits should be larger for trustworthy types, because the same mechanisms[11] that make trustworthy behaviour advantageous also increase the benefits of preventing harm against others. (This argument implies that the costly signalling mechanism we propose may interact positively with other mechanisms for TPP that are based on deterrence benefits.) Furthermore, because trustworthy types are more desirable to interact with than exploitative types, they typically attract more partners—which may reduce TPP costs by offering protection against retaliation and facilitating coordinated punishment[20]. See Supplementary Information sections 1.2.3 and 1.3 and Extended Data Fig. 1 for formal models of these two microfoundations for our central argument.

When TPP is less net costly for trustworthy types, it can serve as a costly signal of trustworthiness. Agents should thus sometimes punish for the express purpose of signalling their trustworthiness to Choosers (like a peacock's tail signals genetic quality)—specifically, when the deterrence benefits of TPP are too small to outweigh the costs on their own (otherwise, TPP would occur without signalling), but the reputational benefit of appearing trustworthy makes TPP worthwhile.

Although TPP can convey information about type, there are often several possible ways to signal trustworthiness, and TPP is not always the most informative. Therefore, a crucial prediction of this signalling account is that when a more informative signal is available, the signalling value of TPP should be attenuated and less TPP should occur. To illustrate this fact, our model also includes the possibility of signalling via costly helping of third parties: because being trustworthy and helping both involve paying costs to benefit others, helping should typically be a very informative signal of trustworthiness (see Supplementary Information section 1.2.3).

Agents in our model make decisions across three different scenarios in which Signallers have the opportunity to engage in (1) TPP, (2) third-party helping, or (3) both. In each scenario, Choosers know which signals were available to Signallers. An agent's strategy specifies her actions as both the Signaller and Chooser in each scenario.

Our equilibrium analysis identifies Nash equilibria that are robust against indirect invasion (RAII)[21] (and thus likely to be favoured by natural selection; see Supplementary Information section 2.1). We also directly test which strategies are favoured by selection using stochastic evolutionary dynamics where agents interact at random to earn payoffs, strategies with higher payoffs become more common, and mutation

[1]Department of Psychology, Yale University, New Haven, Connecticut 06511, USA. [2]Program for Evolutionary Dynamics, Harvard University, Cambridge, Massachusetts 02138, USA. [3]Department of Economics, Yale University, New Haven, Connecticut 06511, USA. [4]School of Management, Yale University, New Haven, Connecticut 06511, USA.

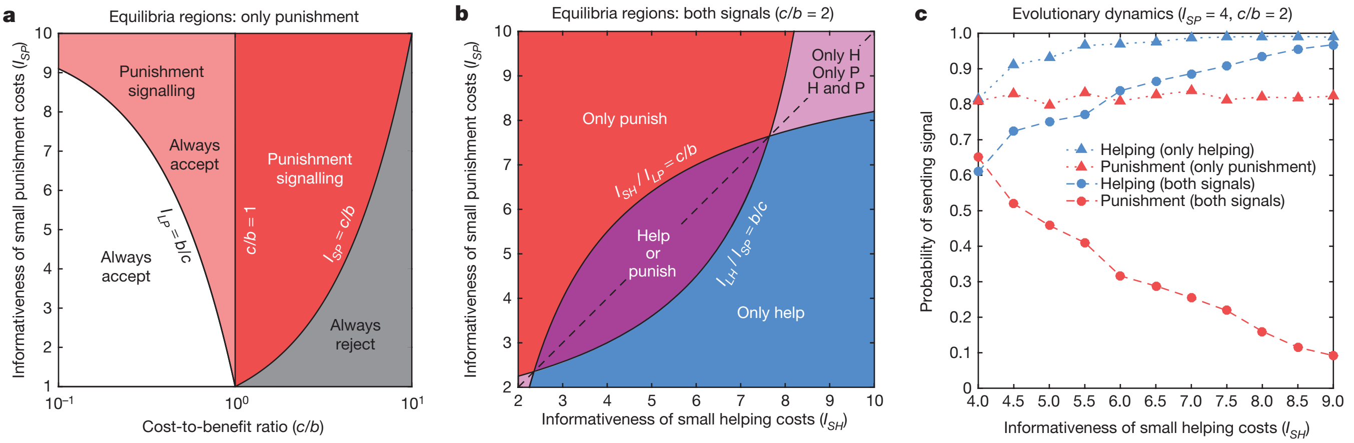

Figure 1 | A model of TPP as a costly signal of trustworthiness. Shown are the results of equilibrium calculations (in which we identify Nash equilibria that are RAII) and evolutionary dynamics, where I_{SP} (I_{SH}) is the informativeness of small punishing (helping) costs (that is, the ratio between the probabilities that trustworthy versus exploitative Signallers experience small punishment (helping) costs), I_{LP} (I_{LH}) is the informativeness of large punishing (helping) costs (the inverse ratio, using large costs instead of small), b is the expected benefit of partner choice (product of the probability a Signaller is trustworthy and the gain to Choosers of accepting trustworthy Signallers), and c is the expected cost of partner choice (the same product, but for exploitative Signallers). **a**, Equilibria when only punishment is possible. 'Punishment-signalling', in which Signallers punish when their punishing costs are small and Choosers only accept punishers, is an equilibrium in red and pink, when (i) large punishment costs are informative enough that the expected payoff of accepting a Signaller with a large cost is negative ($I_{LP} > b/c$); and (ii) small punishment costs are informative enough that the expected payoff of accepting a Signaller with a small cost is positive ($I_{SP} > c/b$). It is the unique equilibrium in red when also (iii) the expected payoff of accepting a random Signaller is negative ($c/b > 1$). We also see pooling equilibria in which Signallers never punish and Choosers always accept (in white and pink) or reject (in grey). For visualization, we fix the probability that an exploitative Signaller has a small punishment cost at 0.1, and vary the probability that a trustworthy Signaller has a small punishment cost (showing the resulting I_{SP}). **b**, Equilibria when both signals are possible. We consider parameters where punishment-signalling and helping-signalling are the unique equilibria in scenarios 1 and 2, respectively (fixing $c/b = 2$, and showing I_{SP} and I_{SH} values >2). In scenario 3, an only-helping strategy profile, in which Signallers help when their helping costs are small but never punish, and Choosers demand helping but ignore punishment, is an equilibrium in blue and light purple, when (i) large helping costs are sufficiently more informative than small punishment costs that the expected payoff of accepting any Signaller with a large helping cost is negative, even if she also has a small punishing cost ($I_{LH} / I_{SP} > b/c$). It is the unique equilibrium in blue, when also (ii) small helping costs are sufficiently more informative than large punishment costs that the expected payoff of accepting a Signaller with a small helping cost remains positive even if she also has a large punishing cost ($I_{SH} / I_{LP} > c/b$). When helping and punishment are similarly informative (around the diagonal), we also see equilibria in which Choosers treat them equally, demanding helping or punishment (dark purple), or helping and punishment (light purple). For visualization, we vary the informativeness of both punishment and helping as in **a**, showing the resulting I_{SP} and I_{SH} values. **c**, Evolutionary dynamics when punishment is moderately informative and helping is increasingly more informative. Here we use agent-based simulations and fix $I_{SP} = 4$, $I_{LP} = 1.5$ and $c/b = 2$, such that when punishment is the only signal (red triangles), it is favoured by evolution (regardless of how informative helping is, because helping is not possible in that scenario). We then vary the informativeness of helping as in **b**. We see that when both signals are available, evolution increasingly disfavours punishment as helping becomes increasingly informative (red circles). In contrast, Signallers help at high rates regardless of whether helping is the only signal (blue triangles) or both signals are available (blue circles). We plot Signallers' probabilities of sending each signal when the cost is low; for scenario 3, we plot the average of the probabilities of punishing (helping) when (i) only the punishing (helping) cost is low, and (ii) both costs are low. See Extended Data Fig. 2 for Chooser strategies and disaggregated Signaller strategies.

maintains variation (see Supplementary Information section 3.1). This process can describe genetic evolution, as well as social learning whereby people imitate successful others.

We first consider scenario 1, where Signallers have the opportunity to punish but not help. Here a punishment-signalling strategy profile (in which Signallers punish when experiencing small signalling costs, and Choosers only accept Signallers who punish) can be an equilibrium when punishment is sufficiently informative: that is, when trustworthy types are sufficiently more likely to receive small punishment costs, and less likely to receive large punishment costs, than exploitative types (see Fig. 1a for precise conditions). Thus, we confirm that TPP can signal trustworthiness when it is the only available signal. By symmetry, the same is true for helping when it is the only available signal (scenario 2). See Supplementary Information section 2.2 for details.

What, then, happens in scenario 3 when TPP and helping are both possible? If helping is more informative, TPP may be ignored. To see why, consider a Signaller who punishes but does not help. If she did not have the opportunity to help, her choice to punish conveys positive information, and a Chooser might accept her. However, if helping was possible, her choice not to help conveys negative information—and when not helping is informative enough to outweigh the positive effect of punishing, the same Chooser might reject her.

To formalize this argument, we vary the informativeness of TPP and helping in scenario 3. We focus on the parameter region where both TPP and helping are informative enough to serve as signals on their own (that is, punishment-signalling and helping-signalling are the unique equilibria in scenarios 1 and 2, respectively; everywhere in Fig. 1b). We find that when the informativeness of the two signals is sufficiently similar, there are equilibria in which Signallers are equally likely to engage in TPP and helping, and Choosers equally demand TPP and helping. However, as the informativeness of helping increases, and/or the informativeness of TPP decreases, the unique equilibrium becomes an only-helping strategy profile in which helping is signalled and demanded, and TPP is ignored. Specifically, only-helping becomes the unique equilibrium when Choosers receive (i) a positive expected payoff from accepting any Signaller with a small helping cost (even if she has a large punishing cost), and (ii) a negative expected payoff from accepting any Signaller with a large helping cost (even if she has a small punishing cost). See Fig. 1b for precise conditions.

Critically, then, there are parameter regions in which it is an equilibrium to punish (and condition partner choice on punishment) in scenario 1 but not in scenario 3. Evolutionary dynamics show that as a result, TPP can evolve as a costly signal that is preferentially used when helping is not possible (Fig. 1c and Extended Data Fig. 2).

Our model thus makes clear predictions. First, when TPP is the only possible signal, it should be perceived as, and should actually be, an honest signal of trustworthiness. Second, when a more informative signal (for example, helping) is also available, third parties should be less likely to punish, and the perceived and actual signalling value of TPP should be attenuated. Third, the same should not be true of helping, which should continue to serve as a strong signal even when TPP is possible.

We next test these predictions in a two-stage economic game conducted using Amazon Mechanical Turk in which TPP and helping signals can be sent, and then partner choice occurs (Extended Data Fig. 3 illustrates the experimental setup, and Supplementary Information section 4 discusses the link between our theoretical and experimental setups). As in our model, there are two roles in this game: Signaller and Chooser.

In the first stage, the Signaller participants in a TPP game[1] (TPPG), interacting with people other than the Chooser. In the TPPG, a Helper decides whether to share money with a Recipient, and an unaffected Punisher decides whether to pay to punish the Helper if the Helper is selfish. To investigate the three scenarios from the model in which helping, punishment or both are available as signals, we manipulate whether the Signaller participates in the TPPG as the Helper, Punisher or both (playing twice with two different sets of other people).

The second stage captures the psychology of partner choice using a trust game (TG). Here, both the Signaller and Chooser participate. The Chooser first decides how much of an endowment to send to the Signaller; any money sent is tripled. The Signaller then decides how much to return to the Chooser. The Chooser can condition her sending on the Signaller's behaviour in the TPPG—and the Signaller knows this when deciding how to behave in the TPPG.

Overall, therefore, our experiment is designed to include opportunities to signal via TPP and/or helping, and to make helping more informative than TPP (see Supplementary Information section 5.1 for further discussion).

The results confirm our theoretical predictions. First, in the punishment-only condition (where punishment is the only available signal, $n = 397$ Signaller–Chooser pairs), punishment is perceived by Choosers as a signal of trustworthiness: Choosers trust Signallers who punish in the TPPG more than those who do not (sending 16 percentage points more to punishers than non-punishers, $P < 0.001$, Fig. 2a). Furthermore, punishment actually is an honest signal of trustworthiness: Signallers who punish return significantly more in the TG than non-punishers (returning 8 percentage points more, $P = 0.001$, Fig. 2b). P values generated using linear regression with robust standard errors; see Supplementary Information section 5.2.

Second, in the punishment-plus-helping condition (where helping is also possible, $n = 393$ Signaller–Chooser pairs), Signallers use punishment less than in the punishment-only condition: only 30% of Signallers punish in punishment-plus-helping, compared to 41% in punishment-only ($P = 0.002$, Fig. 2c). Furthermore, providing the option to help attenuates the perceived and actual signalling value of punishment: in the punishment-plus-helping condition, controlling for helping, Choosers only trust punishers slightly more than non-punishers (4 percentage points more sent to punishers than non-punishers, $P = 0.004$, Fig. 2a), and Signallers who punish in the TPPG do not return significantly more in the TG than non-punishers (0.3 percentage points less returned by punishers than non-punishers, $P = 0.900$, Fig. 2b). Thus the effects of punishment on trust and trustworthiness are significantly smaller in punishment-plus-helping than punishment-only (interactions: $P < 0.001$ and $P = 0.016$, respectively). See Supplementary Information section 5.2 for details.

Third, in the helping-only condition ($n = 409$ Signaller–Chooser pairs), just as many Signallers help (81%) as in the punishment-plus-helping condition (82%) ($P = 0.650$, Fig. 2c). Furthermore, in both conditions, Choosers preferentially trust Signallers who help (39 percentage points more sent to helpers in helping-only, $P < 0.001$; 37 percentage points more sent in punishment-plus-helping (controlling for TPP), $P < 0.001$, Fig. 2a), and Signallers who help are more trustworthy (25 percentage points more returned by helpers in helping-only, $P < 0.001$; 22 percentage points more returned in punishment-plus-helping (controlling for TPP), $P < 0.001$, Fig. 2b). These differences between conditions are not significant (interactions: $P = 0.539$ and $P = 0.623$, respectively). Thus, while helping attenuates the signalling value of TPP, TPP does not attenuate the signalling value of helping.

These results offer clear support for our model of TPP as a costly signal of trustworthiness. We therefore provide evidence that people may punish to provide information about their character to observers, rather than just to harm defectors or deter selfishness. This theory helps to reconcile conflicting previous experimental results about whether TPP

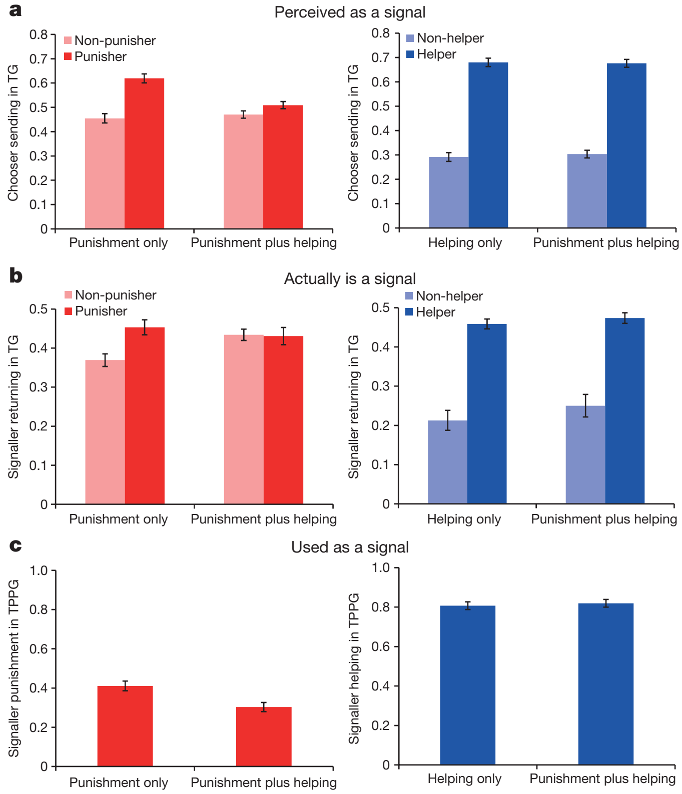

Figure 2 | Behavioural experiments confirm key predictions of our model. a, TPP is perceived as a signal of trustworthiness. In the TG, Choosers trust Signallers who punished in the TPPG more than non-punishers. This effect is much larger, however, when punishment is the only available signal (punishment-only) than when both punishment and helping are possible (punishment-plus-helping) (left column). In contrast, Choosers trust Signallers who helped in the TPPG much more than non-helpers, regardless of whether punishment is possible (right column). **b**, TPP actually is a signal of trustworthiness. Signallers who punished in the TPPG return more in the TG than non-punishers, but this effect is much larger when Signallers did not have the chance to help (punishment-only) than when they did (punishment-plus-helping) (left column). In contrast, Signallers who helped in the TPPG return more than non-helpers, regardless of whether they had the opportunity to punish (right column). **c**, TPP is used as a signal of trustworthiness. Signallers are more likely to punish when they do not have the opportunity to help (punishment-only) than when they do (punishment-plus-helping) (left column). In contrast, they are just as likely to help when they do not have the opportunity to punish (helping-only) as when they do (punishment-plus-helping) (right column). **a** and **b** show predicted mean trust and trustworthiness, respectively (in punishment-plus-helping, regression models include terms for both punishment and helping, but not their interaction, as there were no significant punishment-by-helping interactions); **c** shows predicted probability of sending the relevant signal from logistic regressions including condition. Error bars are ± 1 s.e.m.

confers reputational benefits. Our conclusion that the signalling value of TPP is mitigated when more informative signals of trustworthiness are also available explains why a large positive effect of punishment on trust was found in one experiment in which helping information was absent[22], while little effect was found in another experiment in which helping was observable[16]. This conclusion also provides an explanation for why TPP and trustworthiness were found to be uncorrelated in an experiment in which both punishment and helping were possible[23]. Finally, our theory also explains why participants preferred punishers as partners to a greater extent in situations in which participants could benefit from choosing a prosocial partner[24].

Our results cannot be explained by the alternative theory that TPP is perceived as a signal of willingness to retaliate when harmed directly (although TPP may signal retaliation in other contexts), because retaliation is not possible in the TG. Even if Choosers sent more to punishing Signallers out of an 'irrational' fear of retaliation, helping information should not attenuate this effect (as helping is unlikely to be a more informative signal of retaliation than TPP). Furthermore, an additional experiment (Extended Data Fig. 4 and Supplementary Information section 6) finds that TPP elicits larger reputational benefits when stage 2 is a TG than an ultimatum game (where signalling retaliatoriness is advantageous).

Importantly, punishers need not be consciously seeking to signal their trustworthiness; at a proximate level, TPP may be motivated by emotions like moral outrage[1,3]. Thus, TPP may be based on social heuristics[25] rather than explicit reasoning, and is unlikely to be perfectly sensitive to context—signalling motives may 'spill over'[26] to settings where TPP cannot function as a signal (for example, anonymous interactions, or settings in which engaging with trustworthy Signallers is not actually advantageous to Choosers, such as the Dictator Game[27]).

Relatedly, while our model assumes that different types of individuals have different costs of TPP and helping, and different optimal responses to being trusted, our experiments do not vary subjects' payoffs of punishing, helping and being trustworthy. Instead, the experiments tap into participants' pre-existing inclinations to punish, help and reciprocate the trust of others, reflecting the incentives experienced in daily life[25]. Thus, because we do not exactly recreate the model in the laboratory, our results are consistent with the idea that the model operates outside of the laboratory (rather than merely showing that participants can reason strategically about a novel game).

In sum, we help answer a fundamental question regarding human nature: why do humans care about selfish behaviours that do not affect them personally? Although TPP may often appear 'altruistic', we show how punishing can be self-interested in the long-run because of reputational benefits. Sometimes punishing wrongdoers is the best way to show that you care.

Online Content Methods, along with any additional Extended Data display items and Source Data, are available in the online version of the paper; references unique to these sections appear only in the online paper.

Received 9 November 2015; accepted 8 January 2016.

1. Fehr, E. & Fischbacher, U. Third-party punishment and social norms. *Evol. Hum. Behav.* **25,** 63–87 (2004).
2. Goette, L., Huffman, D. & Meier, S. The impact of group membership on cooperation and norm enforcement: evidence using random assignment to real social groups. *Am. Econ. Rev.* **96,** 212–216 (2006).
3. Jordan, J. J., McAuliffe, K. & Rand, D. G. The effects of endowment size and strategy method on third party punishment. *Exp. Econ.* http://dx.doi.org/10.1007/s10683-015-9466-8 (2015).
4. Kurzban, R., DeScioli, P. & O'Brien, E. Audience effects on moralistic punishment. *Evol. Hum. Behav.* **28,** 75–84 (2007).
5. Balafoutas, L. & Nikiforakis, N. Norm enforcement in the city: a natural field experiment. *Eur. Econ. Rev.* **56,** 1773–1785 (2012).
6. Mathew, S. & Boyd, R. Punishment sustains large-scale cooperation in prestate warfare. *Proc. Natl Acad. Sci. USA* **108,** 11375–11380 (2011).
7. FeldmanHall, O., Sokol-Hessner, P., Van Bavel, J. J. & Phelps, E. A. Fairness violations elicit greater punishment on behalf of another than for oneself. *Nature Commun.* **5,** 5306 (2014).
8. Zahavi, A. Mate selection—a selection for a handicap. *J. Theor. Biol.* **53,** 205–214 (1975).
9. Gintis, H., Smith, E. A. & Bowles, S. Costly signaling and cooperation. *J. Theor. Biol.* **213,** 103–119 (2001).
10. Roberts, G. Competitive altruism: from reciprocity to the handicap principle. *Proc. Biol. Sci.* **265,** 427–431 (1998).
11. Rand, D. G. & Nowak, M. Human cooperation. *Trends Cogn. Sci.* **17,** 413–425 (2013).
12. Guala, F. Reciprocity: weak or strong? What punishment experiments do (and do not) demonstrate. *Behav. Brain Sci.* **35,** 1–15 (2012).
13. Henrich, J. *et al.* Costly punishment across human societies. *Science* **312,** 1767–1770 (2006).
14. Nowak, M. A. & Sigmund, K. Evolution of indirect reciprocity. *Nature* **437,** 1291–1298 (2005).
15. Raihani, N. J. & Bshary, R. The reputation of punishers. *Trends Ecol. Evol.* **30,** 98–103 (2015).
16. Barclay, P. Reputational benefits for altruistic punishment. *Evol. Hum. Behav.* **27,** 325–344 (2006).
17. Fessler, D. M. & Haley, K. J. in *The Genetic and Cultural Evolution of Cooperation* (ed. Hammerstein, P.) (MIT Press, 2003).
18. Panchanathan, K. & Boyd, R. Indirect reciprocity can stabilize cooperation without the second-order free rider problem. *Nature* **108,** 432–502 (2014).
19. Baumard, N., André, J.-B. & Sperber, D. A mutualistic approach to morality: the evolution of fairness by partner choice. *Behav. Brain Sci.* **36,** 59–78 (2013).
20. Boyd, R., Gintis, H. & Bowles, S. Coordinated punishment of defectors sustains cooperation and can proliferate when rare. *Science* **328,** 617–620 (2010).
21. van Veelen, M. Robustness against indirect invasions. *Games Econ. Behav.* **74,** 382–393 (2012).
22. Nelissen, R. M. A. The price you pay: cost-dependent reputation effects of altruistic punishment. *Evol. Hum. Behav.* **29,** 242–248 (2008).
23. Peysakhovich, A., Nowak, M. A. & Rand, D. Humans display a 'cooperative phenotype' that is domain general and temporally stable. *Nature Commun.* **5,** 4939 (2014).
24. Horita, Y. Punishers may be chosen as providers but not as recipients. *Lett. Evol. Behav. Sci.* **1,** 6–9 (2010).
25. Bear, A. & Rand, D. G. Intuition, deliberation, and the evolution of cooperation. *Proc. Natl Acad. Sci. USA* **113,** 936–941 (2016).
26. Peysakhovich, P. & Rand, D. G. Habits of virtue: creating norms of cooperation and defection in the laboratory. *Management Science* http://dx.doi.org/10.1287/mnsc.2015.2168 (2015).
27. Raihani, N. J. & Bshary, R. Third-party punishers are rewarded, but third-party helpers even more so. *Evolution* **69,** 993–1003 (2015).

Supplementary Information is available in the online version of the paper.

Acknowledgements We gratefully acknowledge the John Templeton Foundation for financial support; A. Bear, R. Boyd, M. Crockett, J. Cone, F. Cushman, E. Fehr, M. Krasnow, R. Kurzban, J. Martin, M. Nowak, N. Raihani, L. Santos, and A. Shaw for helpful feedback; and A. Arechar, Z. Epstein, and G. Kraft-Todd for technical assistance.

Author Contributions J.J.J., M.H. and D.G.R. designed and analysed the model. J.J.J., P.B. and D.G.R. designed the experiments. J.J.J. conducted the experiments and analysed the results. J.J.J., M.H., P.B. and D.G.R. wrote the paper.

Author Information Reprints and permissions information is available at www.nature.com/reprints. The authors declare no competing financial interests. Readers are welcome to comment on the online version of the paper. Correspondence and requests for materials should be addressed to J.J.J. (jillian.jordan@yale.edu) or D.G.R. (david.rand@yale.edu).

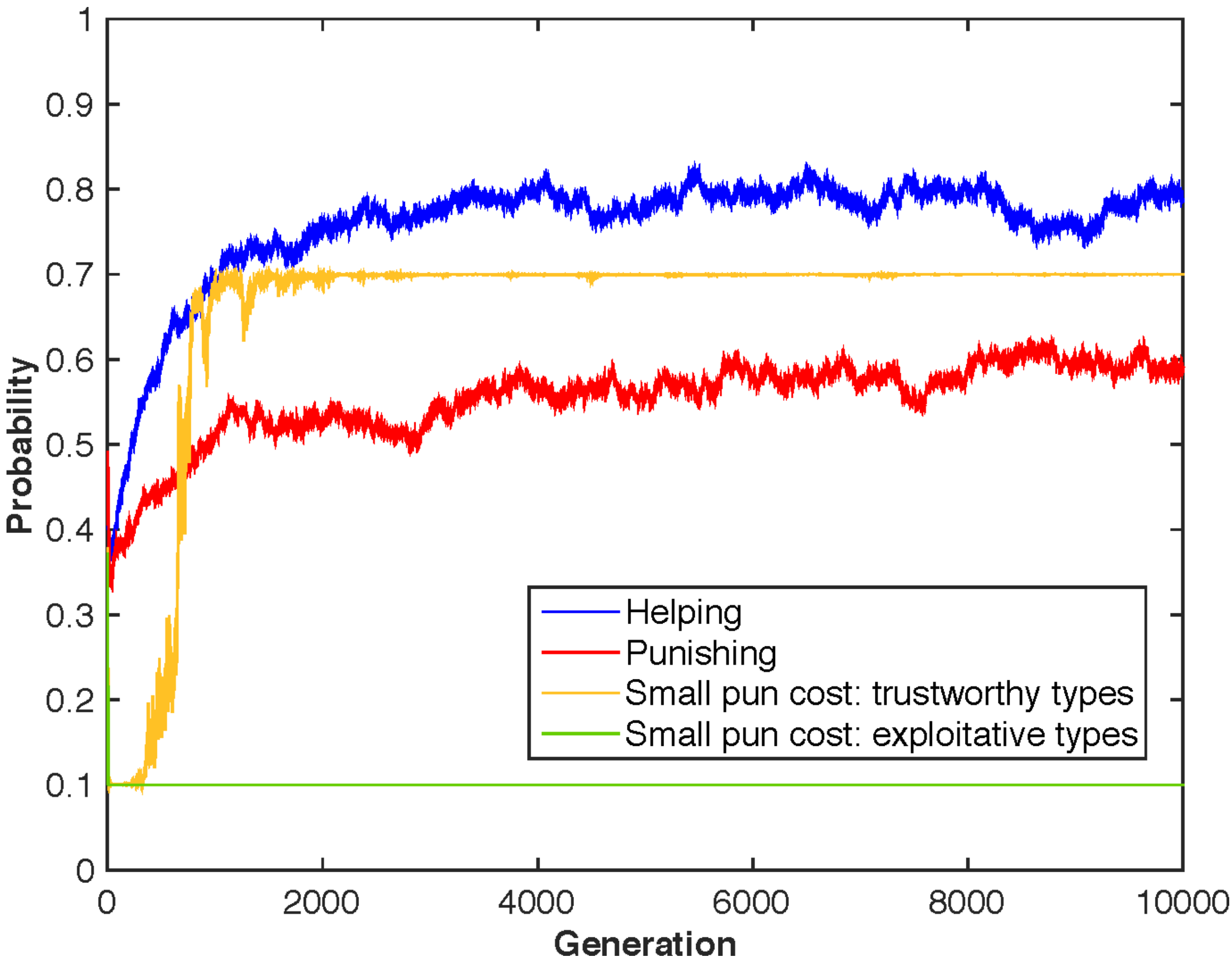

Extended Data Figure 1 | Agent-based simulations from our second microfoundation model in which gaining interaction partners reduces TPP costs. TPP evolves over time in this modified model, in which a Signaller's punishment costs are endogenous (decreasing in the number of times she has been accepted as a partner), rather than exogenously fixed as lower for trustworthy types. We use parameters similar to the main text agent-based simulations, where punishment is moderately informative and helping is more informative. Shown is the average over 500 simulations of Signallers' average probability of helping and punishing (when experiencing the small signalling cost) in each generation, as well as the expected probability of experiencing the small punishing cost for trustworthy and exploitative types (based on the average number of times trustworthy and exploitative types were chosen as partners) at the end of each generation. See Supplementary Information section 1.3.2 for a detailed description of our second microfoundation model.

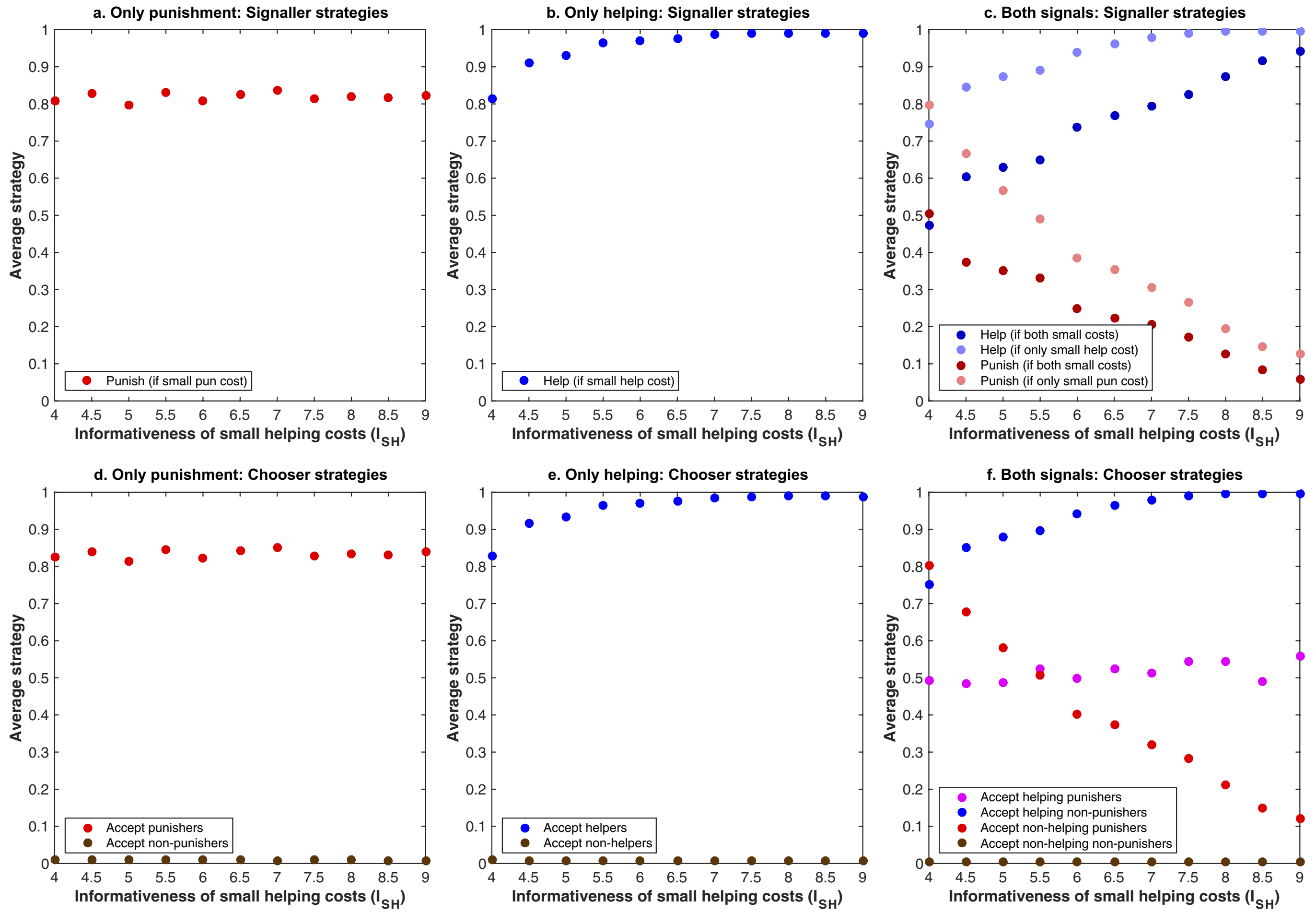

Extended Data Figure 2 | Full agent-based simulation results from the main text model. Here, we present the Signaller and Chooser strategies for each scenario from our main model agent-based simulations, a summary of which is shown in Fig. 1c. In scenario 1, when only punishment is possible, punishment-signalling evolves, regardless of the informativeness of small helping costs I_{SH}. **a**, Signallers are likely to punish when the punishment cost is small and **b**, Choosers are likely to accept Signallers who punish, while they almost always reject those who do not. In scenario 2, when only helping is possible, helping-signalling evolves, and becomes stronger as I_{SH} increases. **c**, Signallers are increasingly likely to help when the helping cost is small and **d**, Choosers are increasingly likely to accept Signallers who help, while they almost always reject those who do not. In scenario 3, when both signals are available, agents evolve to use both signals with equal frequency when they are equally informative, but to favour helping as I_{SH} increases. **e**, As I_{SH} increases, Signallers are increasingly likely to help, both when they have only a small helping cost (light blue dots), and when they have both small costs (dark blue dots); and are decreasingly likely to pay to punish, both when they only have a small punishing cost (light red dots), and when they have both small costs (dark red dots). **f**, As I_{SH} increases, Choosers are increasingly likely to accept Signallers who help but do not punish (blue dots), and increasingly likely to reject Signallers who punish but do not help (red dots). Furthermore, regardless of I_{SH}, Choosers almost always reject Signallers who neither help nor punish (brown dots). However, Chooser behaviour in response to Signallers who both punish and help (purple dots) stays at chance levels across all values of I_{SH} (because Signallers never send both signals, and thus Choosers do not face selection pressure to respond optimally to such Signallers).

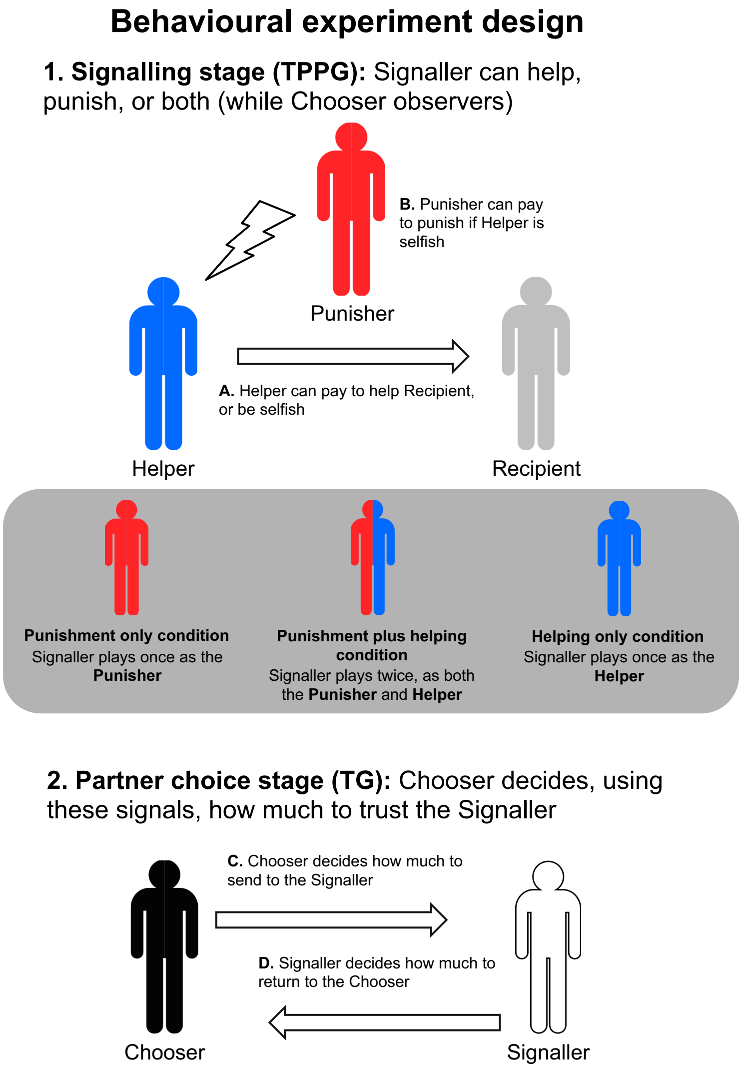

Extended Data Figure 3 | Our two-stage experimental design involving Signallers and Choosers. First, in the signalling stage, the Signaller participates in a third-party punishment game (TPPG). Here a Helper decides whether to share with a Recipient, and then a third-party Punisher decides whether to pay to punish the Helper if the Helper was selfish (chose not to share). In our three experimental conditions, we manipulate the role(s) the Signaller plays in the TPPG. In the punishment-only condition, the Signaller plays once as the Punisher; in the punishment-plus-helping condition, the Signaller plays twice (with two different sets of other people) as the Punisher and the Helper; in the helping-only condition, the Signaller plays once as the Helper. Thus we vary which signal(s) are available. Second, in the partner choice stage, the Chooser plays a trust game with the Signaller. The Chooser decides how much to send the Signaller and any amount sent is tripled by the experimenter. The Signaller then decides how much of the tripled amount to return. Choosers use the strategy method to condition their sending on Signallers' TPPG decisions.

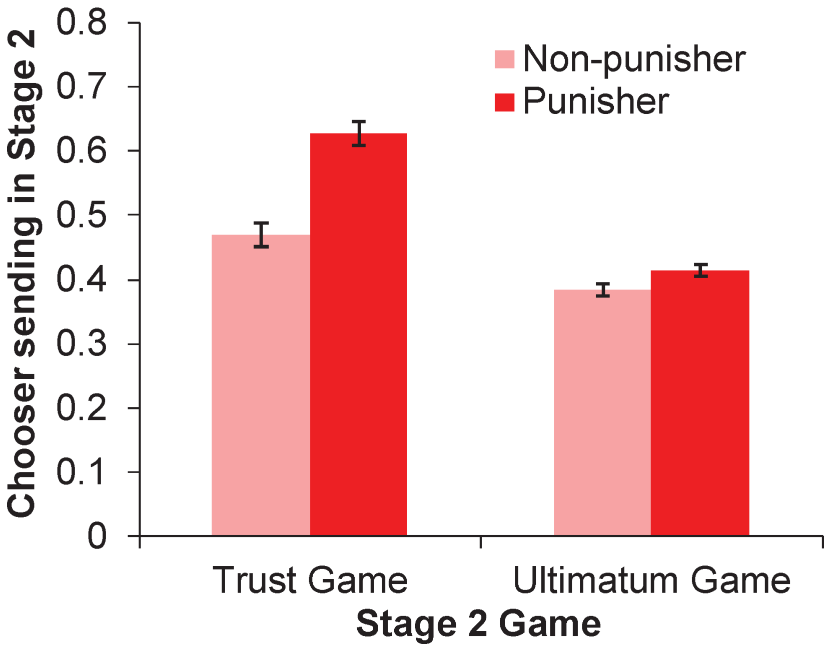

Extended Data Figure 4 | Third-party punishment is perceived as a stronger signal of trustworthiness than retaliation in our additional experiment (study 2). In our additional experiment, we manipulate whether the second stage of our game is a trust game (TG) or an ultimatum game (UG). In the TG, Choosers maximize their payoffs by sending more money to trustworthy Signallers (who will return a large amount); thus, preferential sending to punishers reflects expectations of punisher trustworthiness. In this game (left bars), punishment has large reputational benefits: replicating study 1, Choosers ($n = 405$) send 16 percentage points more to punishers than non-punishers, $P < 0.001$. In the UG, Choosers ($n = 421$) maximize their payoffs by sending more money to retaliatory Signallers (who are willing to pay the cost required to reject low offers); thus, preferential sending to punishers reflects expectations of punisher retaliation. In this game (right bars), punishment has smaller reputational benefits: Choosers send 3 percentage points more to punishers than non-punishers, $P = 0.001$. This difference between conditions is significant ($P < 0.001$) and robust to accounting for the fact that there is less overall variance in UG offers than TG transfers (see Supplementary Information section 6). Thus TPP is perceived as a stronger signal of trustworthiness (in the TG) than willingness to retaliate (in UG). These findings provide further evidence that our TG experiment results (study 1) are not driven by a perception that TPP signals retaliation (although TPP may also signal retaliation in other contexts). Shown is mean sending in each game. Error bars are ± 1 s.e.m.

doi:10.1038/nature16972

A simple rule governs the evolution and development of hominin tooth size

Alistair R. Evans[1,2], E. Susanne Daly[3,4], Kierstin K. Catlett[3,4], Kathleen S. Paul[4,5], Stephen J. King[6], Matthew M. Skinner[7,8], Hans P. Nesse[4], Jean-Jacques Hublin[8], Grant C. Townsend[9], Gary T. Schwartz[3,4] & Jukka Jernvall[10]

The variation in molar tooth size in humans and our closest relatives (hominins) has strongly influenced our view of human evolution. The reduction in overall size and disproportionate decrease in third molar size have been noted for over a century, and have been attributed to reduced selection for large dentitions owing to changes in diet or the acquisition of cooking[1,2]. The systematic pattern of size variation along the tooth row has been described as a 'morphogenetic gradient' in mammal, and more specifically hominin, teeth since Butler[3] and Dahlberg[4]. However, the underlying controls of tooth size have not been well understood, with hypotheses ranging from morphogenetic fields[3] to the clone theory[5]. In this study we address the following question: are there rules that govern how hominin tooth size evolves? Here we propose that the inhibitory cascade, an activator–inhibitor mechanism that affects relative tooth size in mammals[6], produces the default pattern of tooth sizes for all lower primary postcanine teeth (deciduous premolars and permanent molars) in hominins. This configuration is also equivalent to a morphogenetic gradient, finally pointing to a mechanism that can generate this gradient. The pattern of tooth size remains constant with absolute size in australopiths (including *Ardipithecus*, *Australopithecus* and *Paranthropus*). However, in species of *Homo*, including modern humans, there is a tight link between tooth proportions and absolute size such that a single developmental parameter can explain both the relative and absolute sizes of primary postcanine teeth. On the basis of the relationship of inhibitory cascade patterning with size, we can use the size at one tooth position to predict the sizes of the remaining four primary postcanine teeth in the row for hominins. Our study provides a development-based expectation to examine the evolution of the unique proportions of human teeth.

Nearly 80 years ago, Butler[3,7] described the morphogenetic gradient in mammalian postcanine teeth. From anterior to posterior, the deciduous premolars and molars increase in size, and in some species the posterior molars then decrease, with only one local maximum of tooth size along the row. Butler[3] interpreted this pattern to be generated by a morphogenetic field, where the concentration of a diffusible morphogen determined size. The pattern appeared to apply both to deciduous premolars and to molars, which together are considered primary teeth[8]. Unlike molars, deciduous premolars are replaced with a secondary dentition, called the permanent premolars. While several authors have investigated the morphogenetic gradient in hominins[4,9], they have generally investigated permanent premolars rather than their deciduous predecessors.

In 2007, a developmental mechanism controlling relative molar size in mice either by separating adjacent molars or by applying growth factors in the culture was experimentally discovered[6]. In the resulting 'inhibitory cascade' model, molar activator/inhibitor ratio determines the size of subsequently developing molars. Whereas activation is principally considered to be mesenchymal, previously initiated molars are the source of inhibition, thereby causing a patterning cascade from anterior to posterior molars. The model appears to explain a high proportion of the variation in relative molar size in murines, primates and fossil mammaliaforms[6,10–15]. Mice, however, lack all premolars, but the inhibitory cascade implies that a previously initiated tooth should always inhibit the subsequently developing tooth (for example, the fourth deciduous premolar, dp4, should inhibit the first molar, m1).

Here, we test whether the inhibitory cascade explains the morphogenetic gradient in the primary postcanine tooth size of hominins and great apes. We partition the lower dentition into triplets: (1) the third and fourth deciduous premolars, dp3 and dp4, and the first molar, m1 (dp3–dp4–m1); (2) dp4–m1–m2; and (3) the three molars (m1–m2–m3). If a triplet follows the inhibitory cascade pattern, then the central tooth is the average size of the two outer teeth. This is mathematically equivalent to the central tooth being one-third of the total triplet size, a manifestation of the inhibitory cascade[6] (Supplementary Information). As a result, the three teeth show a linear change in size with tooth position; hence, linearity of size change is a proxy for the inhibitory cascade.

Our analysis of 58–66 modern human populations for lower molars and 8 populations for lower deciduous premolars shows a linear increase of the average sizes of the first triplet (dp3–dp4–m1; ordinary least squares (OLS) regression $R^2 = 0.9998$; Fig. 1). The third triplet (molars) also follows the inhibitory cascade pattern, but here size decreases linearly from m1 to m3 ($R^2 = 0.974$). On average, m1 is the largest tooth in the row, with size first increasing and then decreasing about this central tooth position. The second triplet dp4–m1–m2 does not follow the linear pattern predicted by the inhibitory cascade because the middle tooth is the largest. We call this change in direction a reversal of the inhibitory cascade patterning.

Fourteen species of fossil hominins (eight with data on both deciduous premolars) also follow the inhibitory cascade in the first triplet (Fig. 1 and Extended Data Fig. 1). The close fit of the dp3–dp4–m1 triplet for hominins allows us to predict that the mean size of the undiscovered dp4 of *Ardipithecus ramidus* will be the average of the dp3 and m1 sizes, that is, 73 mm^2 in area (star in Fig. 1a). In all extinct hominins the second or third molar is the largest tooth on average. In most australopiths (for example, *Paranthropus boisei*; Fig. 1) the second triplet (dp4–m1–m2) also follows the inhibitory cascade, as the m1 is the average of the two adjacent teeth, pushing the reversal position to m2 or m3. This contrasts with a reversal position at m1 in *Homo sapiens*.

Here we used a simple measure of tooth size, length by width rectangular area, because it is the most commonly used and, therefore, extensive data sets are available. To assess alternative measures of size we calculated three additional metrics from micro-computed tomography

[1]School of Biological Sciences, Monash University, Victoria 3800, Australia. [2]Geosciences, Museum Victoria, Victoria 3001, Australia. [3]Institute of Human Origins, Arizona State University, Tempe, Arizona 85287, USA. [4]School of Human Evolution and Social Change, Arizona State University, Tempe, Arizona 85287, USA. [5]Center for Bioarchaeological Research, Arizona State University, Tempe, Arizona 85287, USA. [6]Department of Anthropology, University of Massachusetts Amherst, Amherst, Massachusetts 01003, USA. [7]School of Anthropology and Conservation, University of Kent, Canterbury CT2 7NR, UK. [8]Department of Human Evolution, Max Planck Institute for Evolutionary Anthropology, Leipzig 04103, Germany. [9]School of Dentistry, The University of Adelaide, South Australia 5005, Australia. [10]Institute of Biotechnology, University of Helsinki 00014, Finland.

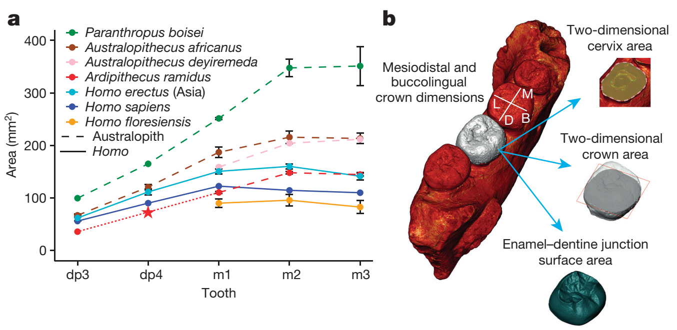

Figure 1 | All hominins show the inhibitory cascade pattern for dp3–dp4–m1 triplet, but species of *Homo* show greater reduction in size of posterior molars. a, Area (mediodistal length × buccolingual width) of each lower postcanine primary tooth for 7 of the 15 hominin species in this study. The inhibitory cascade predicts a linear relationship of the sizes of three adjacent teeth, as seen for dp3–dp4–m1 triplet and dp4–m1–m2 triplet for *P. boisei*. Red dotted line shows expected linear relationship for dp3–dp4–m1 triplet for *Ar. ramidus*; red star shows predicted size of undiscovered dp4 (73 mm^2). Mean ± s.e.m. of populations for *H. sapiens* (dark blue), and of individuals for fossil hominin species. **b**, Measurements of tooth area used in this study illustrated on *H. erectus* Sangiran 1B: mesiodistal length × buccolingual width (the principal measure used in the analyses), 3D enamel–dentine junction area, 2D crown area and 2D cervix area.

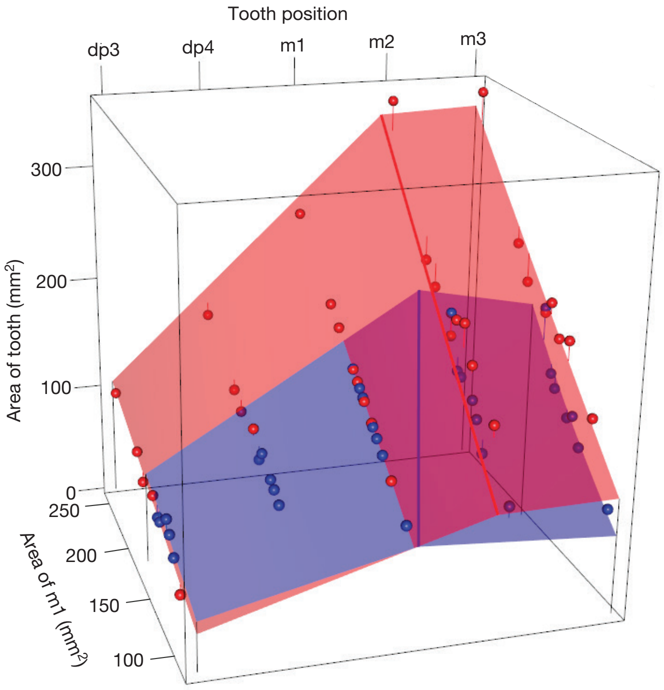

Figure 2 | Prediction surfaces for hominin tooth sizes based on inhibitory cascade and scaling of inhibitory cascade reversal with m1 size. Tooth area (vertical axis) for each tooth position (dp3–m3) and area of m1. Species mean tooth areas (spheres) and prediction surface for *Homo* species are plotted in blue, and australopiths in red. Vertical lines connecting spheres to surface show deviation of the species means from predicted size. Areas are in square millimetres. See Supplementary Video 5 for 3D rotating graph animation.

scans using a subset of fossil hominin specimens: tooth occlusal outline area, enamel–dentine junction 3D surface area, and cervical cross-sectional area (Fig. 1b). All show the same general pattern of size relationships (Extended Data Fig. 2). The first two of these were very highly correlated with rectangular area ($R^2 > 0.94$), cervical area only slightly less so ($R^2 = 0.86$; Extended Data Fig. 3).

Expressing the relative size of each tooth in a row as a proportion of the largest tooth in the row reveals a close relationship between absolute m1 size and relative tooth size for *Homo* species (Extended Data Fig. 4). This contrasts with the remaining hominin taxa (that is, the australopiths), where the proportions are essentially constant with m1 size. Great ape tooth proportions are intermediate to *Homo* species and australopiths.

In a 3D plot combining tooth position, the relative size of each tooth and the absolute size of m1, all data points generally fall on two distinct planes in 3D space (meaning that relative size has linear relationships both with m1 size and with tooth position; Extended Data Fig. 5 and Supplementary Videos 1 and 2). The tight fit of the teeth to both the anterior plane A and the posterior plane B reveals two important findings: (1) these species follow the expected inhibitory cascade pattern of linear change for the first three (or four) teeth in the primary tooth row; (2) there is a strong relationship between tooth position and proportional sizes in all hominins. In *Homo* the reversal position (intersection between planes A and B) changes with absolute m1 size, while in the australopiths the reversal position is constant with absolute m1 size. Using these planar relationships, we can convert proportional size to absolute size based on a given m1 size (Extended Data Fig. 6; Supplementary Information). Standardizing m1 size to a straight line in 3D space produces 3D surfaces that can represent primary postcanine tooth sizes for australopiths or *Homo* species (Fig. 2). This diagram essentially shows how absolute tooth sizes and proportions vary with changes in m1 size. Deviations of the species means from these surfaces are relatively minor (average and maximum deviation for *Homo* species are 7.1% and 18.0% respectively; for australopiths, 7.6% and 24.5%; Extended Data Fig. 7).

For a given tooth position and size, Supplementary Spreadsheet 1 predicts the sizes of the remaining positions in the primary postcanine row. These predictions are based on species means and interspecific scaling relationships, and so represent sizes and proportions typical of species for that m1 size. Figure 3 illustrates the 3D prediction surfaces as contour plots for *Homo* species and australopiths, showing the sizes at each tooth position for a given m1 size in that row (see also Extended Data Fig. 8).

Given the close fit of almost all australopiths to their prediction surface (Fig. 2) and a very similar pattern in the great apes, we postulate that a tight association between tooth proportions and m1 size existed at the base of the hominin clade (Extended Data Figs 1, 4 and 5). Near the origin of the genus *Homo*, a change in the scaling relationship between m1 size and inhibitory cascade patterning occurs, such that the reversal position changes with absolute m1 size and shifts mesially (Fig. 4). Interestingly, *Homo habilis* shows proportions more similar to australopiths than its congeners, which suggests this shift occurred after the origin of *H. habilis*, and agreeing with *H. habilis* perhaps belonging to the genus *Australopithecus*[16]. The Dmanisi specimens demonstrate the heterogeneity present in the early *Homo* pattern: one specimen (D2600) resembles the australopith pattern whereas the others are closer to the *Homo* pattern (Supplementary Information).

The smallest-bodied hominin, *Homo floresiensis*, is most similar to the smallest-bodied great ape, *Pan paniscus*, in tooth sizes and proportions and is smaller than tooth rows of human populations with the largest tooth at m2 (Extended Data Fig. 1). Among fossil hominins, *H. floresiensis* exhibits proportions similar to *Homo heidelbergensis* and *Homo erectus*, but ~40% smaller in absolute area. The recently described *Australopithecus deyiremeda*[17] and *Australopithecus sediba* both follow the australopith pattern.

H. sapiens is similar to its congeners but at smaller m1 sizes, producing disproportionately reduced third molars. For most modern humans m1 is the largest tooth, but a small proportion of humans have m2 as the largest tooth (11–19% of individuals in some populations[18], and 8.6% of the population means in our sample).

We note that specimen-level predictions can deviate from the species-level scaling patterns. When the size of each tooth is used to

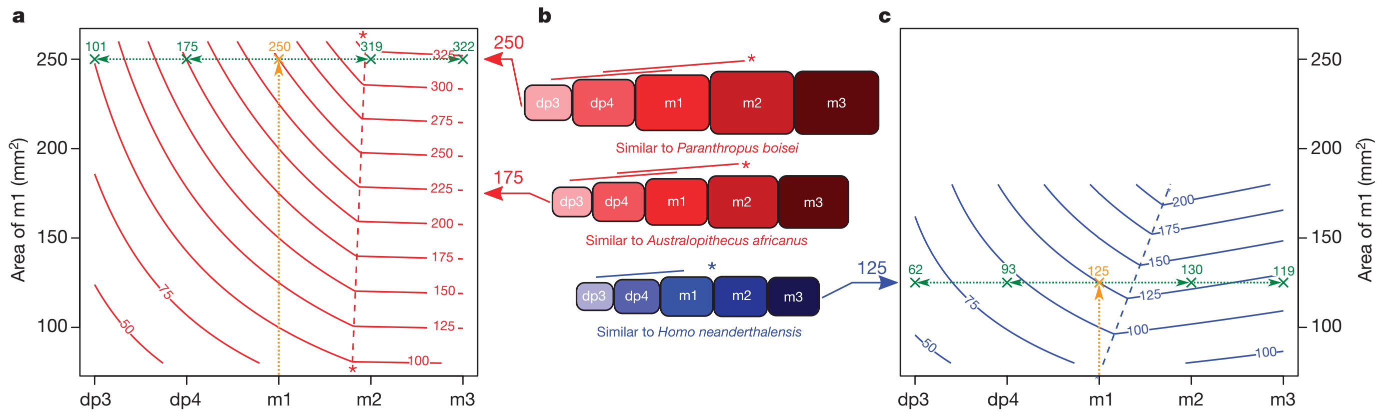

Figure 3 | Hominin prediction plot for primary postcanine rows. **a**, **c**, Contour plot of prediction surfaces in Fig. 2. Contours show tooth areas in square millimetres. Red contours are for australopiths (**a**), blue for *Homo* species (**c**). To predict the mean sizes of remaining four teeth in a row from the mean size of one tooth position (for example, an australopith m1 of 250 mm^2), start at the known tooth's position (*x* axis), move vertically (orange arrow) to the red contour of the measured size, then move horizontally (green arrows) to the other tooth positions (green crosses) and read off sizes from the red contours. Asterisks and dashed lines indicate position of inhibitory cascade reversal. **b**, Predicted tooth row sizes for mean m1 areas of 175 and 250 mm^2 for australopiths and 125 mm^2 for *Homo*, which are similar in size to the species listed below each tooth row. Lines above tooth rows indicate triplets that follow the inhibitory cascade (deviation from inhibitory cascade less than 5%).

predict the other teeth in the same specimen, the average error is 10.3% and 7.9% for *Homo* and australopiths, respectively (Supplementary Information). The largest prediction errors (above 30%) are found in *H. erectus* (D211, Thomas I), *H. heidelbergensis* (Arago 1) and *H. neanderthalensis* (KMH1, Krapina 1,7,79 and Krapina 64). Some of the discrepancies are probably related to errors in size estimation owing to developmental age, preservation and wear, and potential identification inaccuracies in making composite specimens. Increased intraspecific variation in *Homo* species could also result from relaxed selection, implicated by the increased fluctuating asymmetry found in most *Homo* dentitions compared with australopiths and great apes[19,20], or multiple selection pressures. Another possibility is developmental instability when molars in a tooth row approach equal size: for example, extra molar presence in mouse experiments seems linked to the molars being of equal size[6].

Developmentally, in the activator–inhibitor model, higher or lower relative inhibition yields smaller or larger posterior molars, respectively. Absolute tooth size was independent of the inhibitory cascade in the mouse-derived model (ref. 6 and Extended Data Fig. 9), whereas size and proportions are linked in hominins (Extended Data Fig. 4). The simplest way to incorporate size into the inhibitory cascade is through the activation, because the first tooth in a developmental series is unimpeded by the inhibition by other teeth. Therefore, we hypothesize a decrease in mesenchymal activation drives the change in tooth proportions in *Homo*. The mechanism controlling reversal position, however, remains to be determined. While the inhibitory cascade has been invoked to account for patterns in vertebrate limbs, digits and somites[21], a link between absolute size and patterning in multiple vertebrate systems remains to be established.

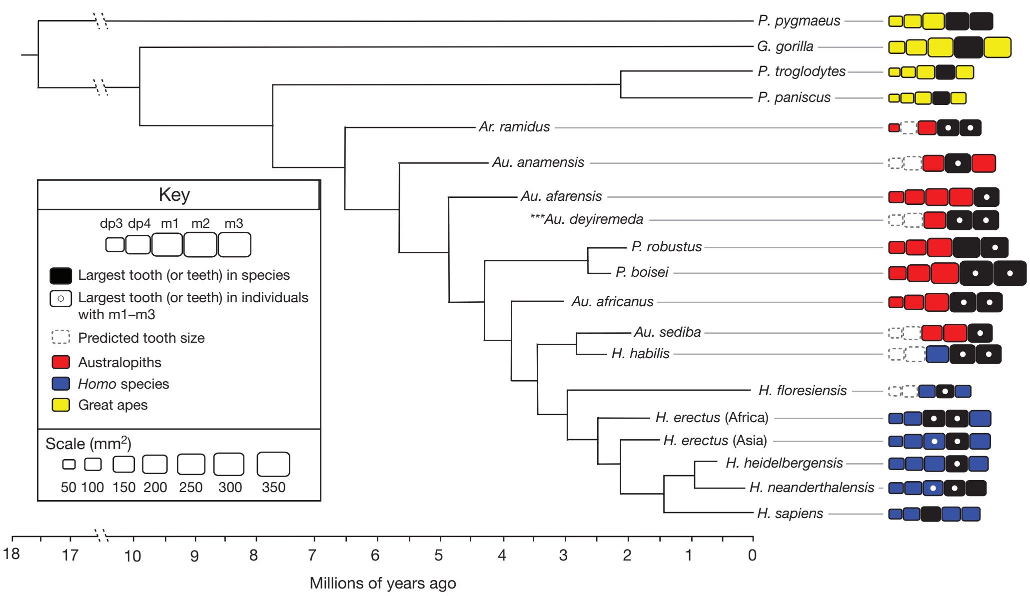

Figure 4 | Phylogenetic distribution of tooth sizes and proportions in hominins shows an origin of the *Homo* pattern shortly after the origin of the genus. Tooth sizes plotted to scale for all species in the current study. Supplementary Spreadsheet 1 was used to predict measurements for unavailable tooth positions. The largest tooth for the species mean is filled black, as is any other tooth that is within 5% of the size of the largest tooth. The largest tooth/teeth for fossil individuals with all three molars preserved are indicated with a white circle. The phylogeny is modified from ref. 28 to include only taxa represented in this study, with the addition of *P. paniscus*, *Pongo pygmaeus* and *Au. deyiremeda* (***) (Supplementary Information).

In conclusion, previous work comparing relative molar sizes using step indices[22] and ratios[23] identified significant changes in these proportions throughout hominin evolution; here we explain such changes based on the developmental inhibitory cascade mechanism. Whereas selective pressures emphasizing function, such as changing bite force, have been used to explain the variation in tooth proportions[24–27], only by including development can one explain the details of the changes. By providing a development-based expectation for the evolution of the hominin dentition, the inhibitory cascade framework moves this research towards a predictive science, further testable with additional fossils.

Online Content Methods, along with any additional Extended Data display items and Source Data, are available in the online version of the paper; references unique to these sections appear only in the online paper.

Received 5 July 2015; accepted 7 January 2016.

1. Brace, C. L. Environment, tooth form, and size in the Pleistocene. *J. Dent. Res.* **46,** 809–816 (1967).
2. Bermúdez de Castro, J. M. & Nicolas, M. E. Posterior dental size reduction in hominids: the Atapuerca evidence. *Am. J. Phys. Anthropol.* **96,** 335–356 (1995).
3. Butler, P. M. Studies of the mammalian dentition. Differentiation of the post-canine dentition. *Proc. R. Soc. Lond. B* **109,** 1–36 (1939).
4. Dahlberg, A. A. The changing dentition of man. *J. Am. Dent. Assoc.* **32,** 676–690 (1945).
5. Osborn, J. W. in *Development, Function and Evolution of Teeth* (eds P.M. Butler & K.A. Joysey) 171–201 (Academic, 1978).
6. Kavanagh, K. D., Evans, A. R. & Jernvall, J. Predicting evolutionary patterns of mammalian teeth from development. *Nature* **449,** 427–432 (2007).
7. Butler, P. M. Studies of the mammalian dentition: I. The teeth of *Centetes ecaudatus* and its allies. *Proc. R. Soc. Lond. B* **107,** 103–132 (1937).
8. Owen, R. *Odontography* (Hippolyte Bailliere, 1840–1845).
9. Townsend, G. C. & Brown, T. Morphogenetic fields within the dentition. *Aust. Orthod. J.* **7,** 3–12 (1981).
10. Polly, P. D. Evolutionary biology: development with a bite. *Nature* **449,** 413–415 (2007).
11. Renvoisé, E. *et al.* Evolution of mammal tooth patterns: new insights from a developmental prediction model. *Evolution* **63,** 1327–1340 (2009).
12. Wilson, L. A. B., Madden, R. H., Kay, R. F. & Sanchez-Villagra, M. R. Testing a developmental model in the fossil record: molar proportions in South American ungulates. *Paleobiology* **38,** 308–321 (2012).
13. Bernal, V., Gonzalez, P. N. & Ivan Perez, S. Developmental processes, evolvability, and dental diversification of New World monkeys. *Evol. Biol.* **40,** 532–541 (2013).
14. Halliday, T. J. D. & Goswami, A. Testing the inhibitory cascade model in Mesozoic and Cenozoic mammaliaforms. *BMC Evol. Biol.* **13,** 79 (2013).
15. Schroer, K. & Wood, B. Modeling the dental development of fossil hominins through the inhibitory cascade. *J. Anat.* **226,** 150–162 (2015).
16. Wood, B. & Collard, M. The human genus. *Science* **284,** 65–71 (1999).
17. Haile-Selassie, Y. *et al.* New species from Ethiopia further expands Middle Pliocene hominin diversity. *Nature* **521,** 483–488 (2015).
18. Garn, S. M., Lewis, A. B. & Kerewsky, R. S. Molar size sequences and fossil taxonomy. *Science* **142,** 1060 (1963).
19. Kieser, J. A. & Groeneveld, H. T. The assessment of fluctuating odontometric asymmetry from incomplete hominid fossil data. *Anthropol. Anz.* **44,** 175–182 (1986).
20. Kegley, A. D. T. & Hemingway, J. in *Voyages in Science: Essays by South African Anatomists in Honour of Phillip V. Tobias' 80th birthday* (eds G. Strkalj, N. Pather, & B. Kramer) 35–49 (Content Solutions, 2005).
21. Young, N. M., Winslow, B., Takkellapati, S. & Kavanagh, K. Shared rules of development predict patterns of evolution in vertebrate segmentation. *Nature Commun.* **6,** 6690 (2015).
22. Selmer-Olsen, R. An odontometrical study on the Norwegian Lapps. *Skrift Norske Vidensk-Akademi* **3,** 1–167 (1949).
23. Wolpoff, M. H. *Metric Trends in Hominid Dental Evolution*. Case Western Reserve University Studies in Anthropology 2 (Case Western Reserve Univ. Press, 1971).
24. Lucas, P. W. *Dental Functional Morphology* (Cambridge Univ. Press, 2004).
25. Greaves, W. S. The jaw lever system in ungulates: a new model. *J. Zool.* **184,** 271–285 (1978).
26. Spencer, M. A. Force production in the primate masticatory system: electromyographic tests of biomechanical hypotheses. *J. Hum. Evol.* **34,** 25–54 (1998).
27. Lucas, L. *Variation in Dental Morphology and Bite Force along the Tooth Row in Anthropoids*. PhD thesis, Arizona State Univ. (2012).
28. Dembo, M., Matzke, N. J., Mooers, A. O. & Collard, M. Bayesian analysis of a morphological supermatrix sheds light on controversial fossil hominin relationships. *Proc. R. Soc. B* **282,** http://dx.doi.org/10.1098/rspb.2015.0943 (2015).

Supplementary Information is available in the online version of the paper.

Acknowledgements This contribution is dedicated to the late Professor Percy Butler, the inspiration for much of this work and discoverer of the morphogenetic gradient in teeth, who unfortunately did not see this work completed. We thank M. Fortelius, G. Evans, A.-L. Khoo, F. Grine, P. Trusler, J. Adams, J. Clutterbuck, L. Chieu, D. Hocking, M. McCurry, Q. Nasrullah, T. Park and the Evans EvoMorph Laboratory for discussions and criticism of the manuscript. Thanks to M. Collard for supplementary information on the hominin phylogeny. We thank the Powell-Cotton Museum (M. Harman), American Museum of Natural History, Cleveland Museum of Natural History (L. Jellema), Museum of Comparative Zoology (J. Chupasko), Royal Belgian Institute of Natural Sciences (G. Lenglet), Royal Museum for Central Africa (E. Gilissen and W. Wendelen), National Museum of Natural History (USA), The Bavarian State Collection of Zoology (M. Hiermeier and C. Lang) and Anthropological Institute and Museum (Switzerland) (M. Ponce de León and C. Zollikofer) for access to great ape material. For access to computed tomography scans of fossil hominin material we thank the following individuals and institutions: National Museums of Kenya (E. Mbua), Ditsong National Museum of Natural History (S. Potze), University of Witwatersrand (C. Menter and B. Zipfel), Senckenberg Natural History Museum (F. Schrenk and O. Kullmer) and the Royal Belgian Institute of Natural Sciences (M. Toussaint). This study was made possible by use of material from the Burlington Growth Centre, Faculty of Dentistry, University of Toronto, which was supported by funds provided by grant (1) (number 605-7-299) National Health Grant (Canada), (data collection); (2) Province of Ontario Grant PR 33 (duplicating); and (3) the Varsity Fund (for housing and collection). All research protocols were reviewed and granted exemption by Arizona State University's (ASU) Institutional Review Board and the Burlington Growth Centre, and informed consent was obtained for all human subjects. This research was financially supported by grants from the Australian Research Council Future Fellowship (A.R.E., FT130100968), Academy of Finland (J.J.), National Science Foundation (GRFP number 2011121784; K.S.P.), Max Planck Society (M.M.S.), Wenner-Gren Foundation (K.K.C.), Graduate and Professional Student Association at ASU (E.S.D., K.K.C.), and ASU Sigma XI chapter (E.S.D., K.K.C.). This research was also facilitated in part by a grant (48952) from the John Templeton Foundation (G.T.S.). The opinions expressed in this publication do not necessarily reflect the views of the John Templeton Foundation.

Author Contributions J.J. and A.R.E. conceived the project. A.R.E., E.S.D., K.K.C., K.S.P., S.J.K., M.M.S., G.C.T., G.T.S. and J.J. collected data. E.S.D. and K.K.C. independently validated application of the inhibitory cascade model to deciduous premolars. G.T.S. performed hominin taxonomic classification. M.M.S. conducted the computed tomography scanning and measurements. J.-J.H. and G.C.T. provided materials. A.R.E. performed the analyses. H.P.N. implemented individual-level prediction accuracy and confidence interval calculations. A.R.E. and J.J. took the lead in writing the paper with contributions from all co-authors.

Author Information Reprints and permissions information is available at www.nature.com/reprints. The authors declare no competing financial interests. Readers are welcome to comment on the online version of the paper. Correspondence and requests for materials should be addressed to A.R.E. (alistair.evans@monash.edu).

METHODS

Tooth size data. Human lower primary postcanine tooth sizes, defined as rectangular areas of mesiodistal length × maximum buccolingual width, were collated from the literature, and measured from dental casts at the Burlington Growth Centre, Toronto, Canada. All research protocols were reviewed and granted exemption by Arizona State University's Institutional Review Board and the Burlington Growth Centre, and informed consent was obtained for all human subjects. Population-level means of molar sizes were collated from studies where all three molars were measured and wear was not excessive, largely from compilations[23,29] (see Supplementary Information). No statistical methods were used to predetermine sample size. Fossil hominin tooth size measurements were compiled at the specimen level and assigned to taxonomic groups (see Supplementary Information), using measurements adjusted for wear when available. *H. erectus* specimens from Asia and Africa were grouped separately. Ape tooth size measurements were obtained from the literature[30] or measured from museum specimens (see Supplementary Information). For all individual-level data, measurements taken from both sides of the same individual were averaged. Individuals of the same sex were averaged, then sexes were averaged to obtain a population or species mean size for each tooth.

Analyses. For each primary tooth row (mean of sex, population or species), all teeth were scaled so that the largest tooth in the row equalled 1, called Prop Max in Row. For hominins and great apes separately, we used R version 3.1.3 (ref. 31) to perform multiple linear regression for Prop Max in Row ~ Tooth Position + Area of m1, and linear regression for Max Area in Row ~ Area of m1. For hominins, Prop Max in Row was converted to Area by multiplying it by Max Area in Row for the given m1 size. This function was then divided by the ratio of the expected Area of m1 to that calculated for m1 to give m1 size a 1:1 relationship with Area in the predictive surface (see Supplementary Information and Extended Data Fig. 10 for calculations and plots). Individual-level fossil data were used for the prediction error calculation using the relevant *Homo* or australopith prediction surface. Prediction error was calculated as $100 \times |(\text{observed} - \text{predicted})|/\text{observed}$.

Three-dimensional tooth size data. X-ray microtomographic scans of six hominin specimens with three sufficiently unworn lower molars were performed at the Max Planck Institute for Evolutionary Anthropology, Leipzig, Germany. Three-dimensional tooth models were measured for rectangular area, tooth occlusal outline area, enamel–dentine junction 3D surface area, and cervical cross-sectional area (Fig. 1b).

29. Kieser, J. A. *Human Adult Odontometrics* (Cambridge Univ. Press, 1990).
30. Johanson, D. C. Some metric aspects of the permanent and deciduous dentition of the pygmy chimpanzee (*Pan paniscus*). *Am. J. Phys. Anthropol.* **41,** 39–48 (1974).
31. R Development Core Team. R: a language and environment for statistical computing (R Foundation for Statistical Computing, 2015).

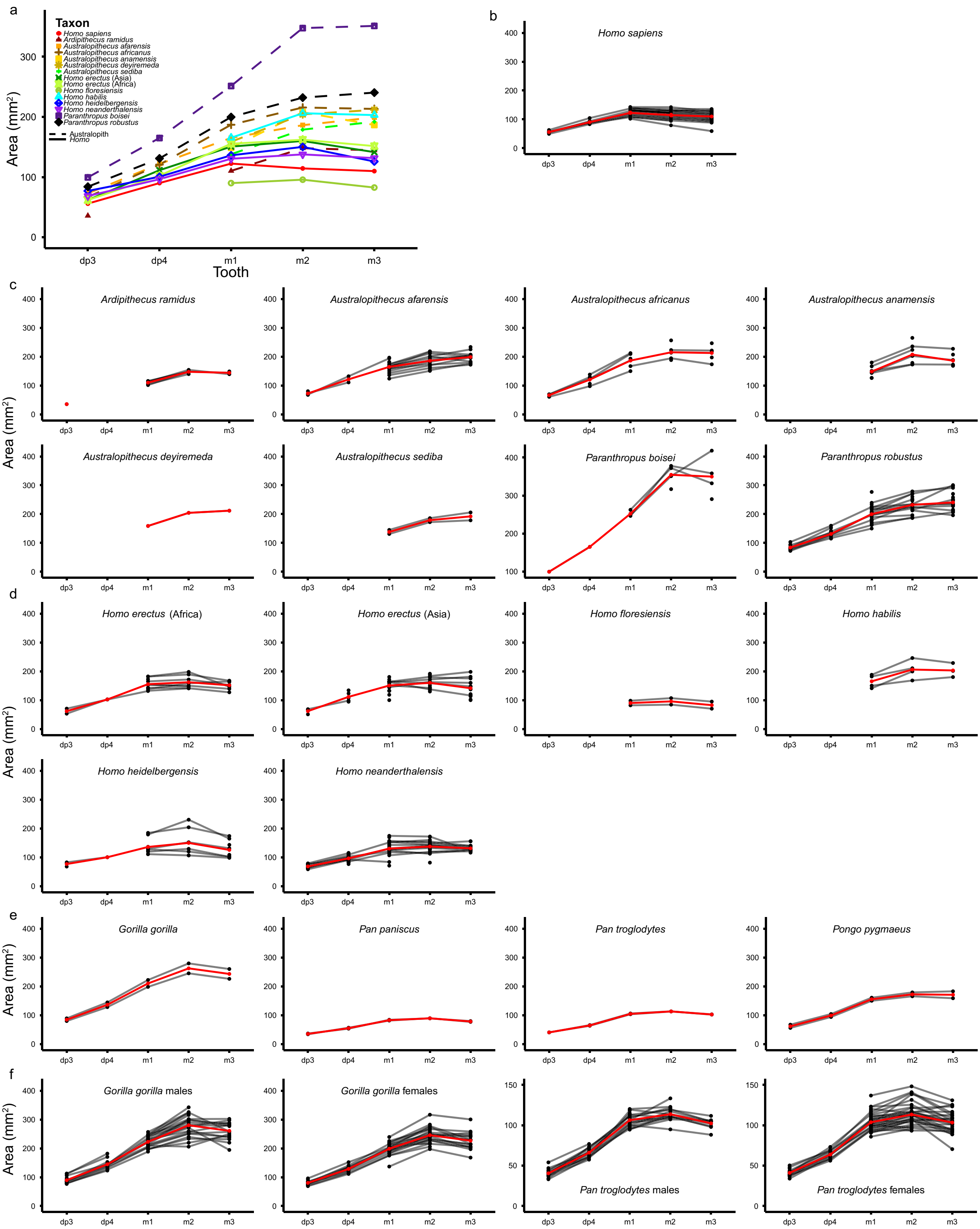

Extended Data Figure 1 | *Homo* species and australopiths differ in their pattern of tooth sizes, but all hominins and great apes follow the inhibitory cascade for dp3–dp4–m1 triplet. The inhibitory cascade predicts that there is a linear relationship among three adjacent teeth. Area (in square millimetres) of each lower postcanine primary tooth. **a**, Mean area of each tooth for 15 hominin species. **b**–**e**, Red points and lines are species means. **b**, *H. sapiens*; black points and lines represent means of populations. **c**, Eight australopith species and (**d**) six fossil *Homo* species; black points and lines represent individual tooth rows (left and right rows of each specimen plotted separately). **e**, Four great ape species; black points and lines represent means of each sex. **f**, Two great ape species; black points and lines represent individuals, red points and lines are means for each sex. Sex and species means show clearer inhibitory cascade patterns than most individuals.

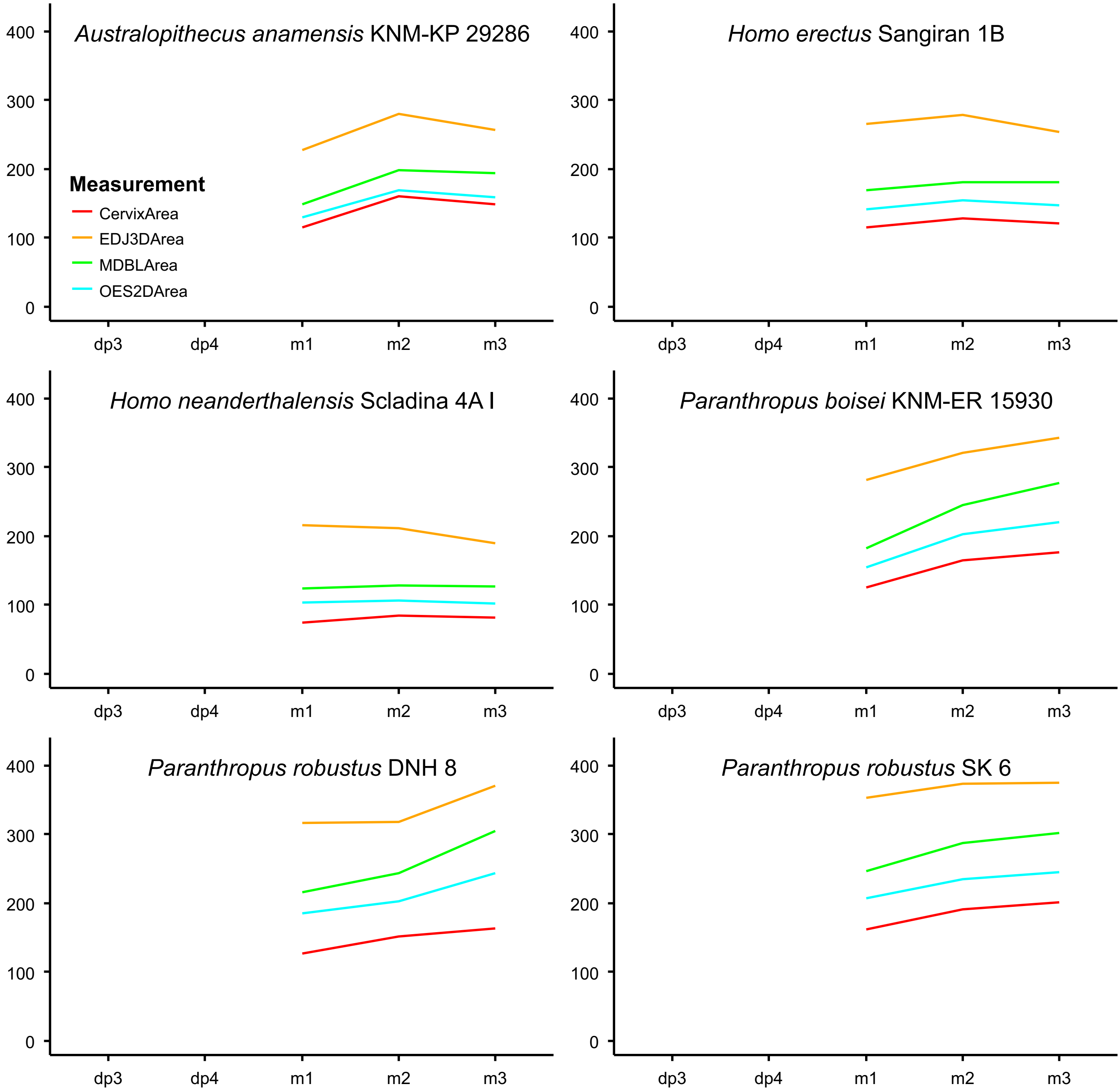

Extended Data Figure 2 | Two- and three-dimensional measures of tooth size for six fossil hominin specimens. Rectangular area (mesiodistal length × buccolingual width, MDBLArea), 3D area of the enamel–dentine junction (EDJ3DArea), cross-sectional area of the tooth at the cervix (CervixArea) and outline area of the outer enamel surface (OES2DArea) for each tooth position.

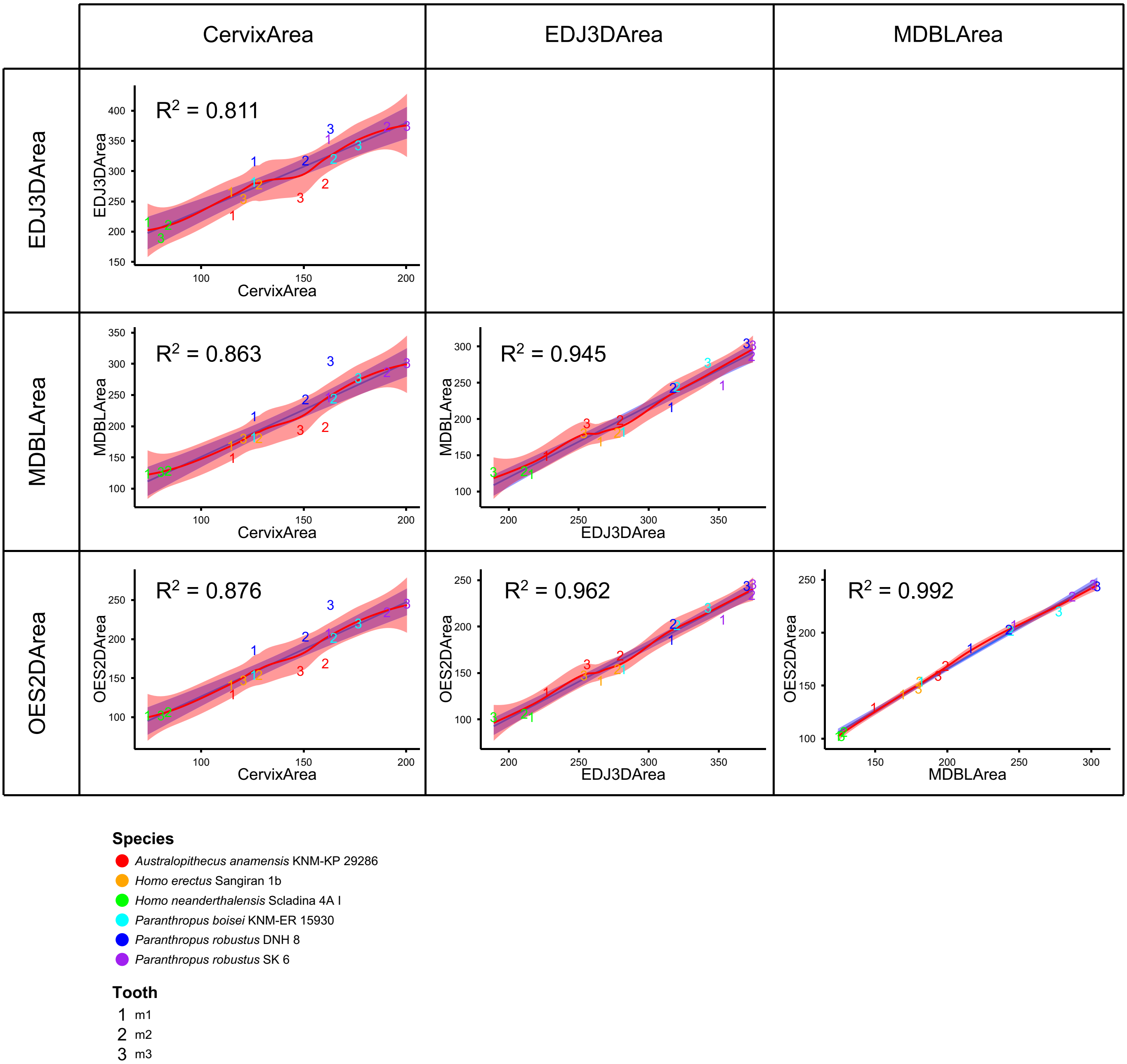

Extended Data Figure 3 | Two- and three-dimensional measures of tooth size are highly correlated. Bivariate plots for planar area (mesiodistal length × buccolingual width, MDBLArea), 3D area of the enamel–dentine junction (EDJ3DArea), cross-sectional area of the tooth at the cervix (CervixArea) and outline area of the outer enamel surface (OES2DArea). R^2 shown for each plot. Blue line and shaded area, OLS regression and 95% confidence interval; red line and shaded area, loess smoothing and 95% confidence interval.

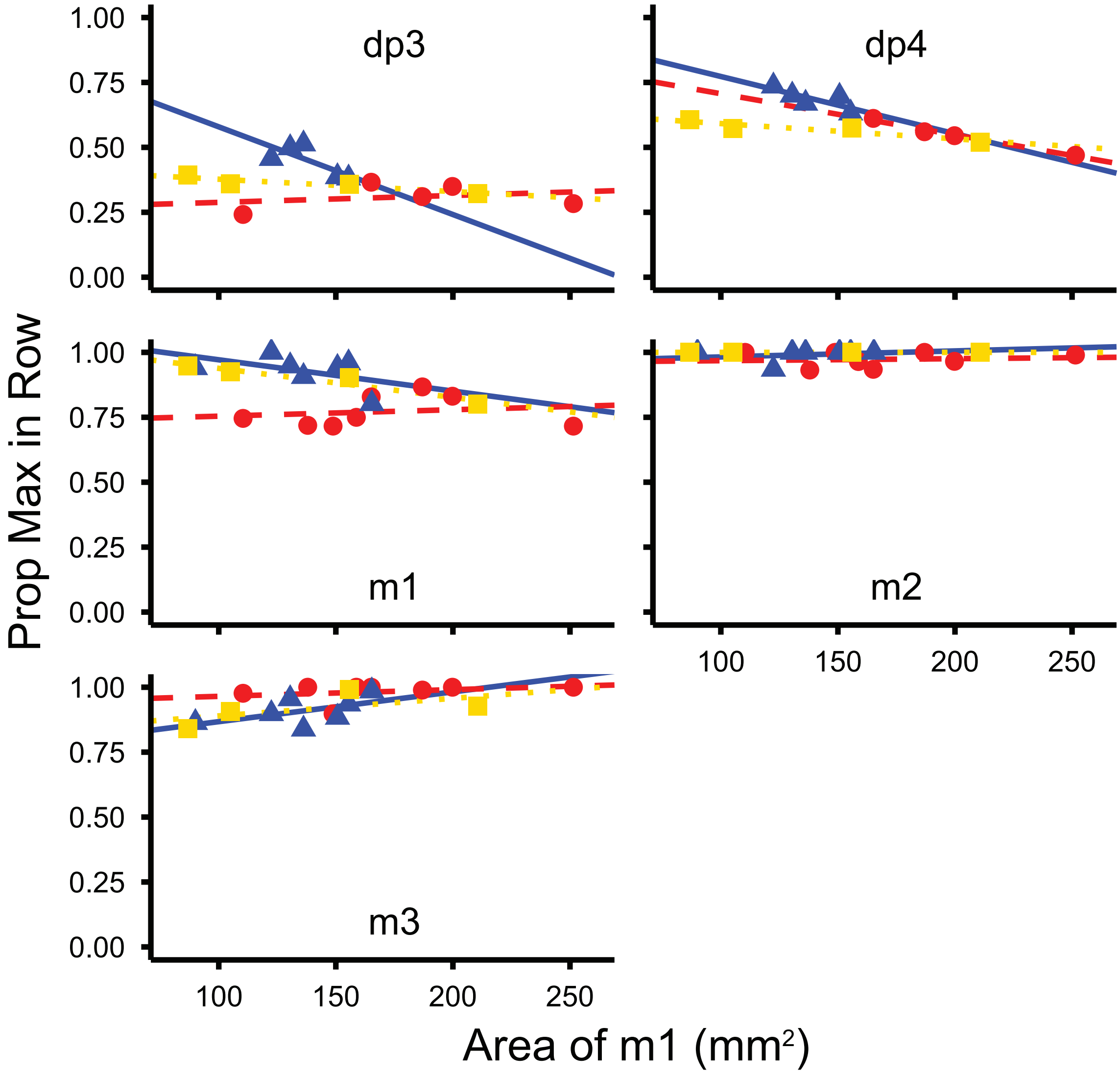

Extended Data Figure 4 | The proportional size of each tooth shows a tight relationship with absolute size of the first molar, with the relationship differing between *Homo* species, australopiths and great apes. Proportional size of each tooth (proportion of the largest tooth in the row) versus area of m1 (in square millimetres) for 15 hominin and 4 great ape species. Blue triangles and solid line, OLS regression for *Homo* species; red circles and dashed line, OLS for australopiths; yellow squares and dotted line, OLS for great apes.

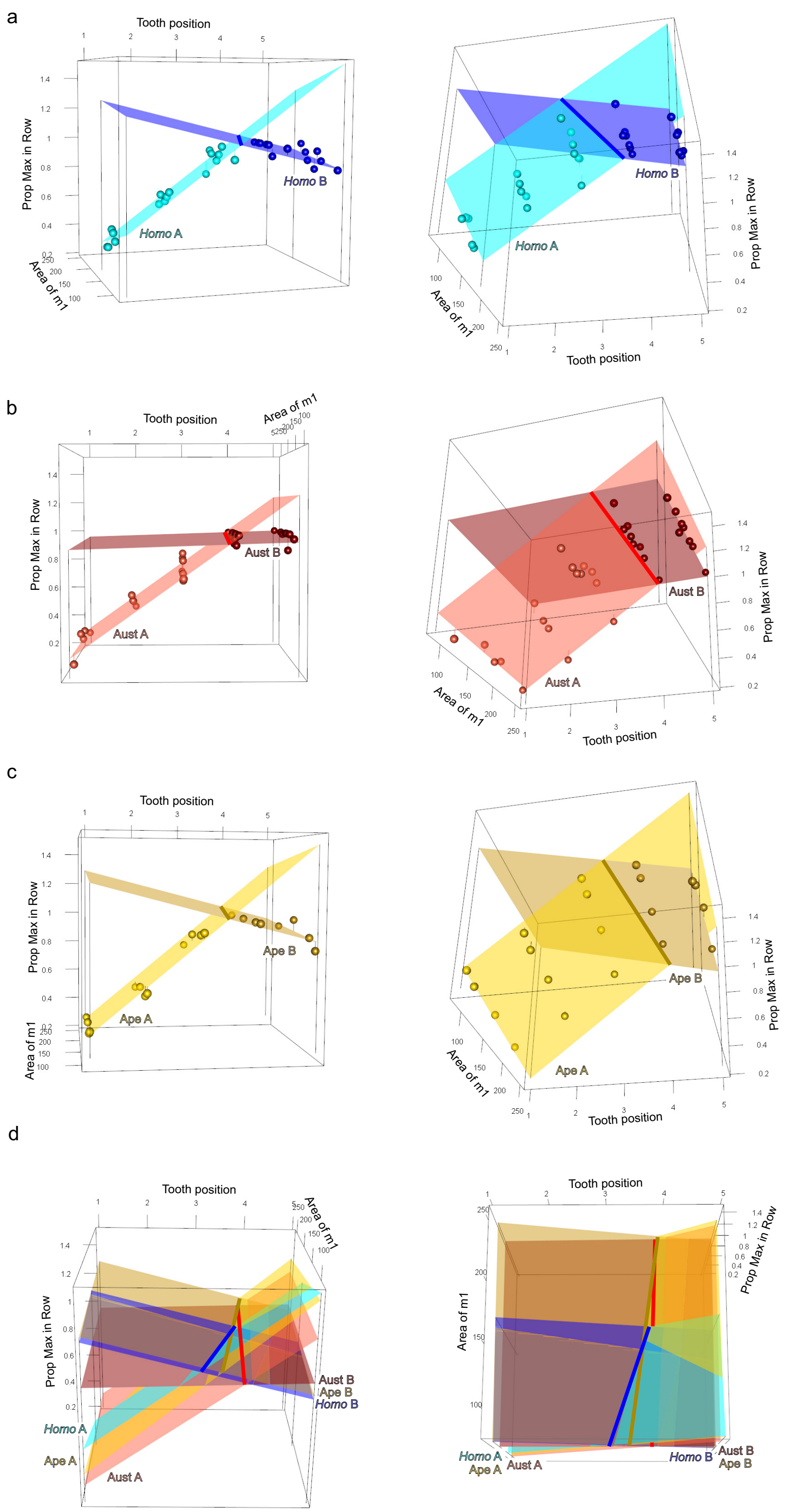

Extended Data Figure 5 | See next page for figure caption.

Extended Data Figure 5 | Tooth proportions of hominins are constrained by the inhibitory cascade and size of m1. Three-dimensional space of tooth position (horizontal axis, numbered 1–5 for dp3–m3), area of m1 (axis into page) and proportion of maximum in tooth row (vertical axis). The proportional sizes of all teeth lie on two planes in 3D space. For all groups, plane A is fitted to dp3–dp4–m1, and plane B to m2–m3. **a**, *Homo* species, plane A (cyan; $R^2 = 0.96$) formula: HomoAPropMaxinRow = 0.238 × ToothPos − 0.00166 × AreaM1 + 0.441. Plane B (blue; $R^2 = 0.62$) formula: HomoBPropMaxinRow = −0.0822 × ToothPos + 0.000690 × AreaM1 + 1.23. Thick blue line shows intersection of planes. **b**, Australopiths, plane A (light red; $R^2 = 0.93$) formula: AustAPropMaxinRow = 0.0810 × ToothPos + 0.230 × AreaM1 + 2.38×10^{-6}. Plane B (dark red; $R^2 = 0.07$) formula: AustBPropMaxinRow = 0.00963 × ToothPos + 0.000168 × AreaM1 + 0.906. Thick red line shows intersection of planes. **c**, Great apes, plane A (yellow; $R^2 = 0.98$) formula: ApeAPropMaxinRow = 0.268 × ToothPos − 0.0727 × AreaM1 + 0.173. plane B (light brown; $R^2 = 0.63$) formula: ApeBPropMaxinRow = −0.0837 × ToothPos + 0.000337 × AreaM1 + 1.29. While the R^2 values are substantially lower for the plane B regressions, the average deviations from plane B for *Homo* and australopiths are 0.026 and 0.022 respectively, which are lower than the equivalent values of 0.046 and 0.036 for plane A. Therefore, the low R^2 values do not reflect the close fit of the data to the planes. **d**, Comparison of *Homo*, australopith and great ape planes shows that the corresponding planes and intersections for the first two groups diverge at smaller m1 sizes. The great ape planes fall between those of the other two groups. See Supplementary Videos 1–4 for 3D rotating graph animations.

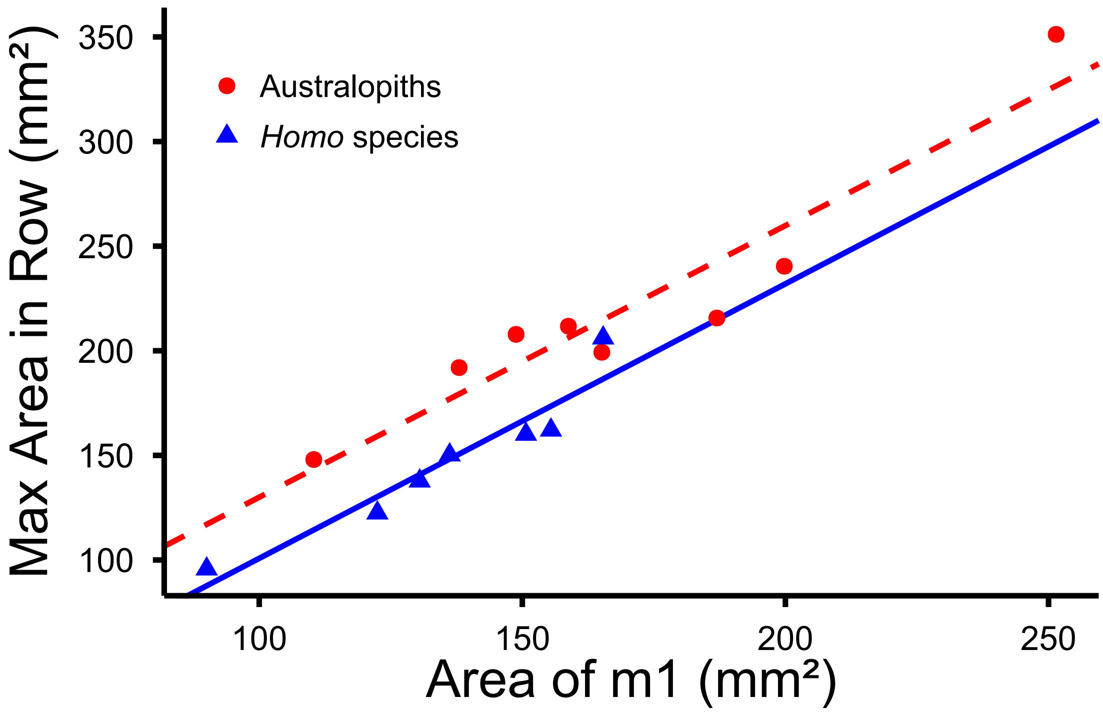

Extended Data Figure 6 | The size of the largest tooth in the row is closely related to the size of the m1 in hominins. OLS regressions. HomoMaxAreaInRow = 1.312 × AreaM1 − 30.44, $P = 0.001$, $R^2 = 0.90$; AustMaxAreaInRow = 1.298 × AreaM1 + 0.150, $P = 0.0003$, $R^2 = 0.90$.

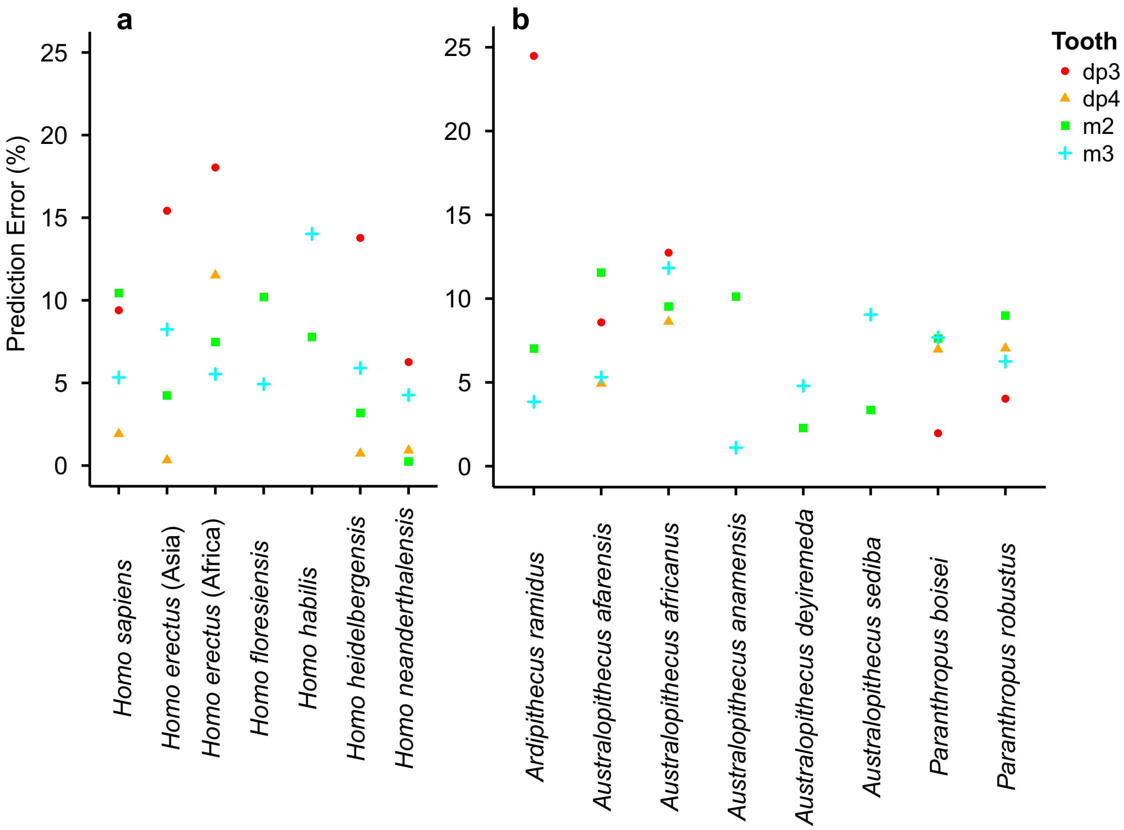

Extended Data Figure 7 | Percentage error in estimates of each tooth compared with the prediction surfaces in Fig. 2. Prediction surface is calculated so that m1 always has zero prediction error, therefore it is excluded from error calculations. **a**, *Homo* species; **b**, australopiths.

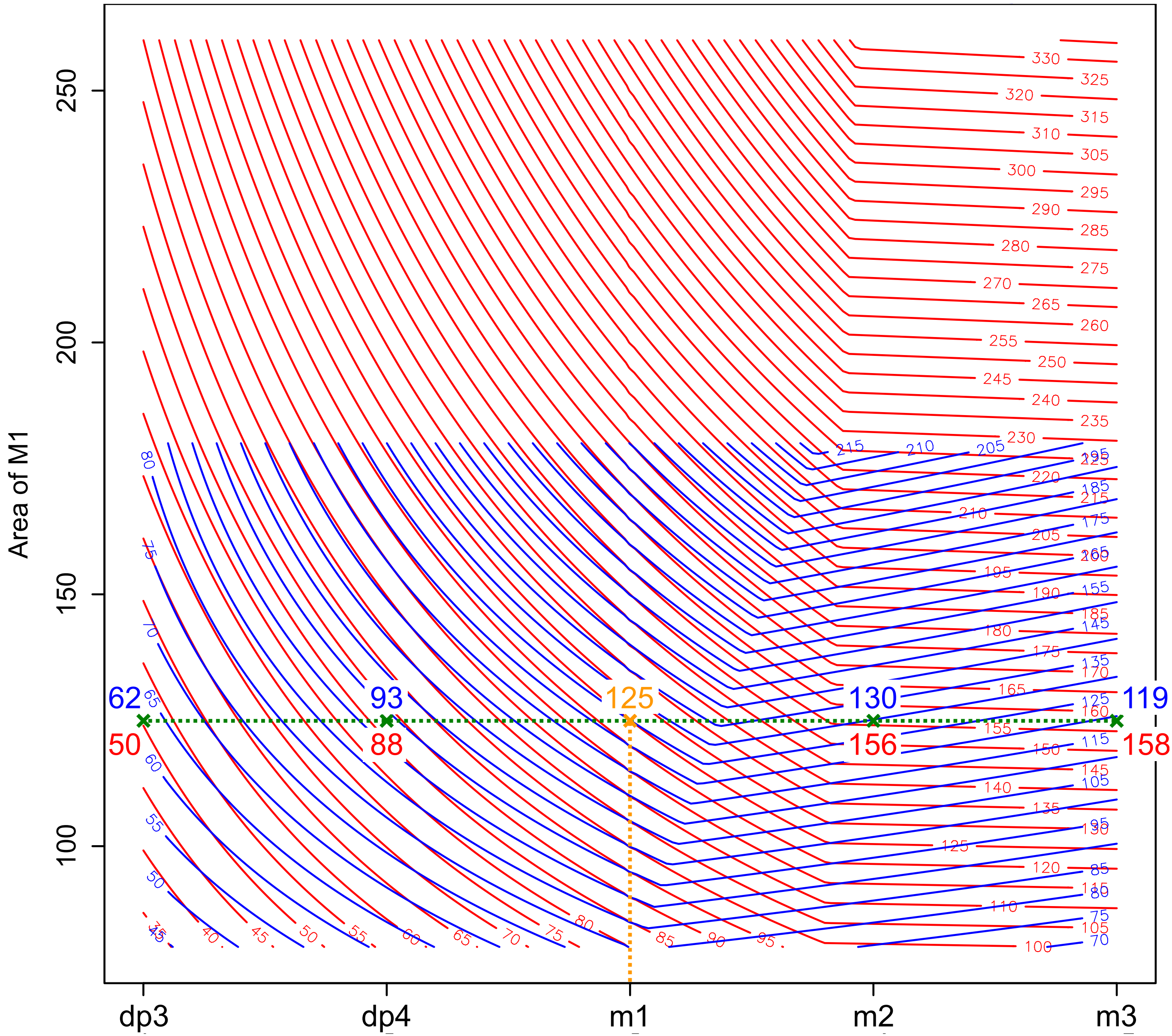

Extended Data Figure 8 | Detailed contour plot (contour step = 5 mm^2) for prediction surfaces of hominin tooth size. Area of m1 and areas on contour in mm^2. Blue contours are for *Homo* species, red for australopiths. From the mean size of one tooth position (for example, m1 at 125 mm^2), the mean sizes of the remaining four teeth in the row can be predicted by following the tooth position vertically (orange line) to meet the contour of the measured size, then moving horizontally to the other tooth positions (cyan line and crosses) to read off the sizes according to the contours. When mean m1 size is 125 mm^2, dp3, dp4, m2 and m3 are 62, 93, 130 and 199 mm^2 respectively for a *Homo* species and 50, 88, 156 and 158 mm^2 respectively for an australopith species.

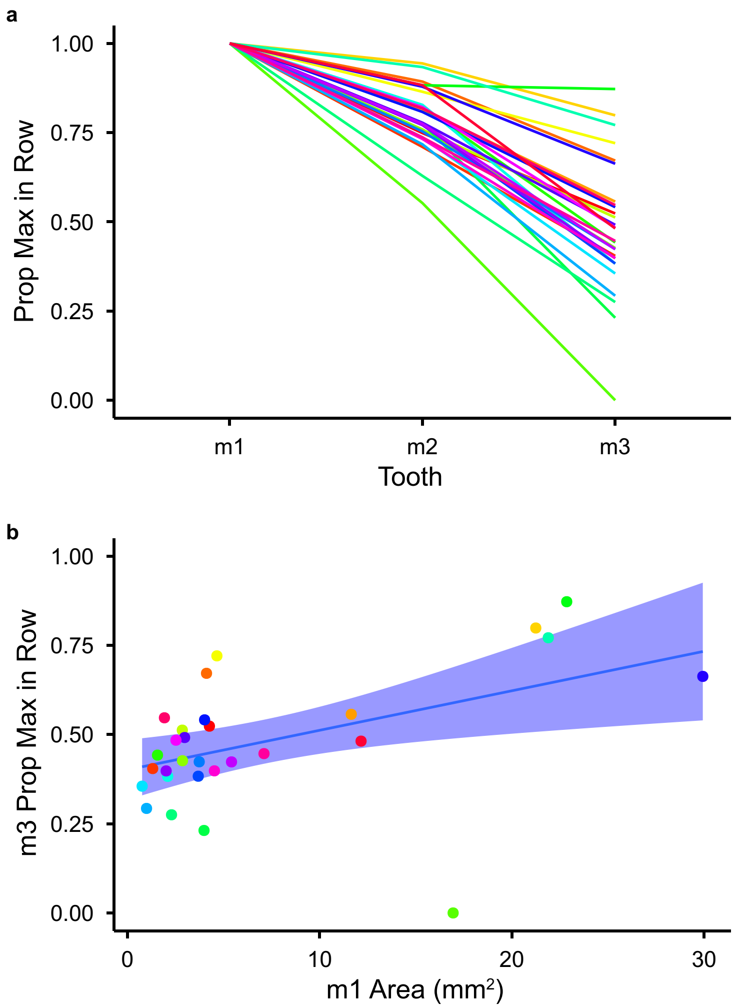

Extended Data Figure 9 | Slope of the inhibitory cascade in murines is weakly related to absolute size, unlike in hominins where there is a strong relationship. a, Relative sizes of molars for the 29 species of murine rodents in ref. 6. **b**, Relative size of third molar to first molar (m3/m1) plotted against absolute size of first molar (in square millimetres) shows a weak relationship (cf. Extended Data Fig. 4). Blue line and shaded area, OLS regression and 95% confidence interval.

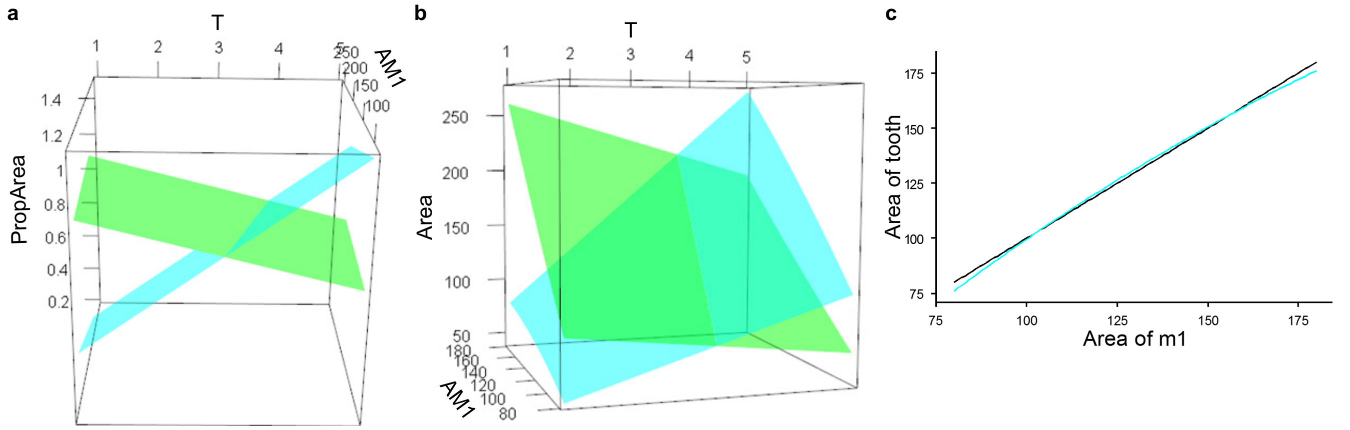

Extended Data Figure 10 | Planes and surfaces for equations of tooth position *T* (horizontal) versus area of m1 *AM1* (into page) versus proportion of area or area (vertical). **a**, Regression plane A (cyan) and plane B (green) with proportion of area PropArea as calculated in equations 2 and 3 in Supplementary Information. **b**, Surfaces AreaAH (cyan) and AreaBH (green) as calculated in equations 11 and 12 in Supplementary Information. The two regions that represent the data are plane A or AreaAH on the left of the intersection and plane B or AreaBH on the right of the intersection of the two planes or surfaces, respectively. **c**, Prediction of m1 area using formulae for AreaAH (cyan) when $T = 3$ compared with the expected 1:1 relationship (black) using equation 11 in the Supplementary Information. If the cyan formula were standardized by the expected value (black), the standardized surface will correctly predict m1 size (equation 17 in the Supplementary Information).

doi:10.1038/nature16971

Adult restoration of *Shank3* expression rescues selective autistic-like phenotypes

Yuan Mei[1]*, Patricia Monteiro[1,2,3]*, Yang Zhou[1], Jin-Ah Kim[1], Xian Gao[1,4], Zhanyan Fu[1,3] & Guoping Feng[1,3]

Because autism spectrum disorders are neurodevelopmental disorders and patients typically display symptoms before the age of three[1], one of the key questions in autism research is whether the pathology is reversible in adults. Here we investigate the developmental requirement of *Shank3* in mice, a prominent monogenic autism gene that is estimated to contribute to approximately 1% of all autism spectrum disorder cases[2–6]. SHANK3 is a postsynaptic scaffold protein that regulates synaptic development, function and plasticity by orchestrating the assembly of postsynaptic density macromolecular signalling complex[7–9]. Disruptions of the *Shank3* gene in mouse models have resulted in synaptic defects and autistic-like behaviours including anxiety, social interaction deficits, and repetitive behaviour[10–13]. We generated a novel *Shank3* conditional knock-in mouse model, and show that re-expression of the *Shank3* gene in adult mice led to improvements in synaptic protein composition, spine density and neural function in the striatum. We also provide behavioural evidence that certain behavioural abnormalities including social interaction deficit and repetitive grooming behaviour could be rescued, while anxiety and motor coordination deficit could not be recovered in adulthood. Together, these results reveal the profound effect of post-developmental activation of *Shank3* expression on neural function, and demonstrate a certain degree of continued plasticity in the adult diseased brain.

SHANK3 (also known as ProSAP2) protein is a major scaffolding protein at the excitatory synapse, coordinating the recruitment of many postsynaptic signalling molecules[14,15]. Previous work has shown that germline deletion of *Shank3* in mice disrupts the protein composition at the postsynaptic density (PSD), reduces neurotransmission efficiency and leads to autistic-like behaviour[10–13].

To address whether adult reversal of physiological and behavioural abnormalities in *Shank3* mutant mice is possible, we adopted a genetic method that allows for inducible *Shank3* expression. Because *Shank3* duplication is linked to attention deficit hyperactivity disorder and bipolar disorder[5,6,16], it is crucial to keep *Shank3* expression within its physiological concentrations to avoid potential confounds. Thus, we generated a novel *Shank3* conditional knock-in mouse by using the Cre-dependent genetic switch (FLEx) strategy[17], which enables the conditional manipulation of the *Shank3* gene at its endogenous genomic locus.

We genetically targeted the PDZ domain owing to its role in assembling the scaffold complex in the PSD[14,15] (Fig. 1a and Extended Data Fig. 1). In the absence of Cre, the *Shank3*$^{fx/fx}$ mice function as *Shank3* knockout (KO) mice, and result in the deletion of most major isoforms of SHANK3 including the putative α, β and γ bands (Fig. 1b). Similar to abnormalities previously reported on *Shank3* knockout mice[10–13], these *Shank3*$^{fx/fx}$ mice showed significant deficits in exploratory behaviour (Fig. 1c), anxiety (Fig. 1e) and motor coordination (Fig. 1d), and displayed open wound lesions that suggested repetitive grooming behaviour[12,18]. In addition, they showed impaired neurotransmission in the dorsal striatum (Fig. 1f, g). These novel *Shank3*$^{fx/fx}$ mice thus recapitulate autistic-like phenotypes, enabling us to investigate the possibility of reversing those deficits in adulthood.

To achieve temporal control of *Shank3* expression, we crossed the *Shank3*$^{fx/fx}$ mice to an inducible CAGGS-CreER mouse line[19] that activates global Cre function after tamoxifen treatment (Extended Data Fig. 1d). When the *Shank3*$^{fx/fx}$:*CreER*$^{+/-}$ mice reached 2–4.5 months, we used oral gavage to deliver tamoxifen to ensure efficient Cre-mediated gene restoration (Fig. 2a). All experiments were performed on the following three groups: *Shank3*$^{+/+}$:*CreER*$^{+/-}$ mice

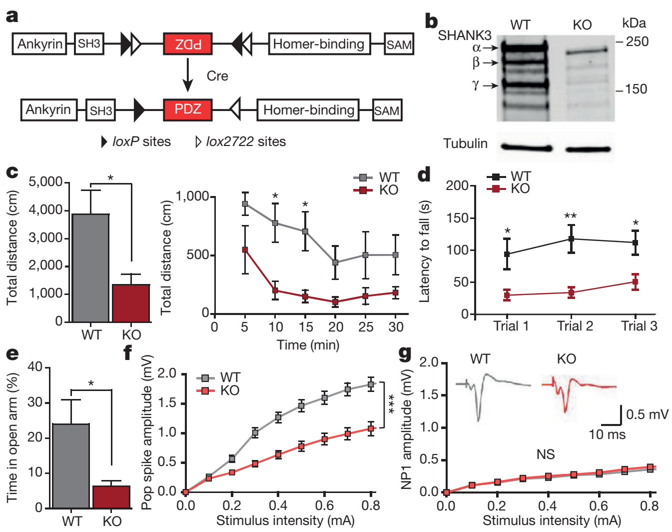

Figure 1 | *Shank3*$^{fx/fx}$ mice have deficits in neurotransmission and behaviour. a, Domain structure of SHANK3 protein, with FLExed PDZ domain inverted, which can be re-oriented in the presence of Cre. **b**, Western blot showing SHANK3 expression in striatal PSD from wild-type (WT) and *Shank3*$^{fx/fx}$ (KO) mice. **c**, KO mice show decreased total distance travelled in the open-field test compared to WT mice. **d**, KO mice show impaired motor coordination in the rotarod test. **e**, KO mice spend less time in the open arm during the elevated zero maze test. **f**, KO mice show a decreased pop spike amplitude in extracellular field recordings in the striatum. **g**, Normal relationship of stimulation intensity to the negative peak 1 (NP1) amplitude (action potential component), suggesting unaltered presynaptic function; insets show representative traces. $*P<0.05$, $**P<0.01$, $***P<0.001$ (two-tailed *t*-test (**c**, left, **e**) and two-way repeated measures analysis of variance (ANOVA) with Bonferroni post-hoc test (**c**, right, **d**, **f**, **g**)). Data are mean ± s.e.m. (all behaviour data from $n=6$ WT and $n=7$ KO mice; electrophysiology data from $n=9$ slices; 3 mice per genotype). See Supplementary Fig. 1 for gel source data.

[1]McGovern Institute for Brain Research, Department of Brain and Cognitive Sciences, Massachusetts Institute of Technology, Cambridge, Massachusetts 02139, USA. [2]PhD Programme in Experimental Biology and Biomedicine (PDBEB), Center for Neuroscience and Cell Biology, University of Coimbra, 3004-517 Coimbra, Portugal. [3]Stanley Center for Psychiatric Research, Broad Institute of MIT and Harvard, Cambridge, Masachusetts 02142, USA. [4]Key Laboratory of Brain Functional Genomics (Ministry of Education & Science and Technology Commission of Shanghai Municipality), Institute of Cognitive Neuroscience, School of Psychology and Cognitve Science, East China Normal University, Shanghai 200062, China.
*These authors contributed equally to this work.

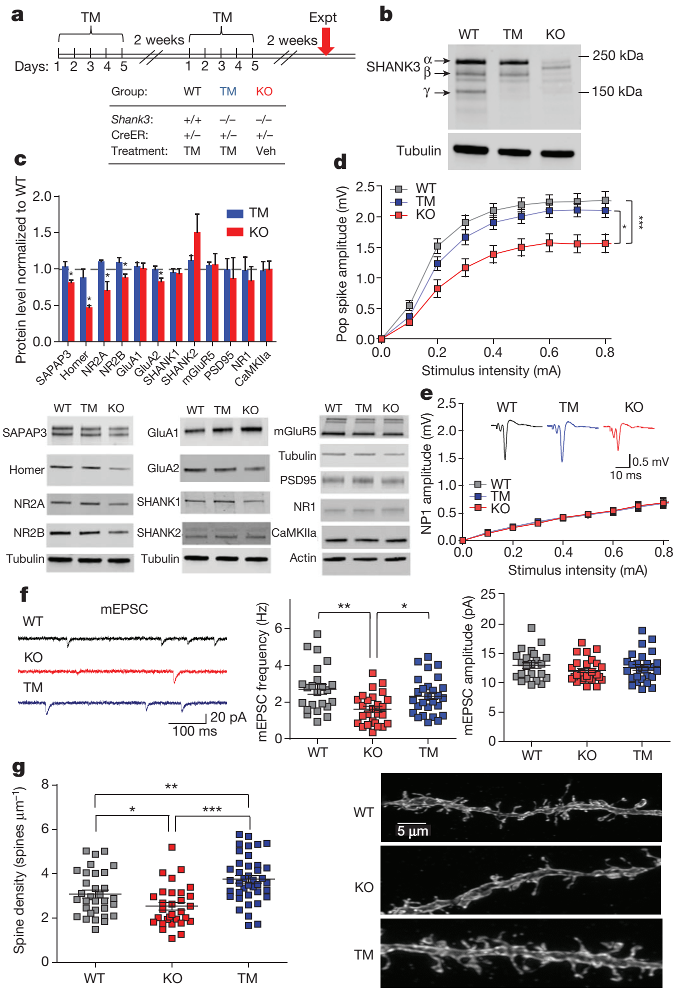

Figure 2 | Rescue of PSD proteins and striatal neurotransmission. **a**, Experimental groups and TM feeding scheme. Expt, experiment; veh, vehicle. **b**, Western blot from striatal synaptosome preparation after tamoxifen feeding shows restoration of most SHANK3 isoforms. **c**, Western blots of striatal synaptosomal fractions (bottom); PSD protein levels in KO mice are restored to WT levels in the TM group (top). **d**, Striatal field response in KO mice was rescued in TM mice. **e**, Representative traces for WT, KO and TM mice. Indistinguishable relationship of stimulation intensity to the NP1 amplitude among groups suggests unaltered presynaptic function. **f**, Rescued mESPC frequency in the striatum in the TM compared to KO mice. **g**, Increased spine density in the TM compared to KO mice, while spine density in the KO mice is lower than that of the WT. $*P<0.05$, $**P<0.01$, $***P<0.001$ (Student's two-tailed *t*-test (**c**), two-way repeated measures ANOVA with Bonferroni post-hoc test (**d**, **e**), one-way ANOVA with Bonferroni post-hoc test (**f**), one-way ANOVA with Newman–Keuls multiple comparison post-hoc test (**g**)). Data are mean ± s.e.m. (**c**: $n=3$ WT, $n=4$ TM and $n=3$ KO; each sample represents combined striatal tissue from 2 mice; **d** and **e**: $n=12$ slices from 4 WT, 4 TM and 4 KO mice; **f**: $n=23$ WT, $n=26$ KO and $n=27$ TM cells; **g**: $n=32$ WT, $n=30$ KO and $n=40$ TM dendritic segments). See Supplementary Fig. 1 for gel source data.

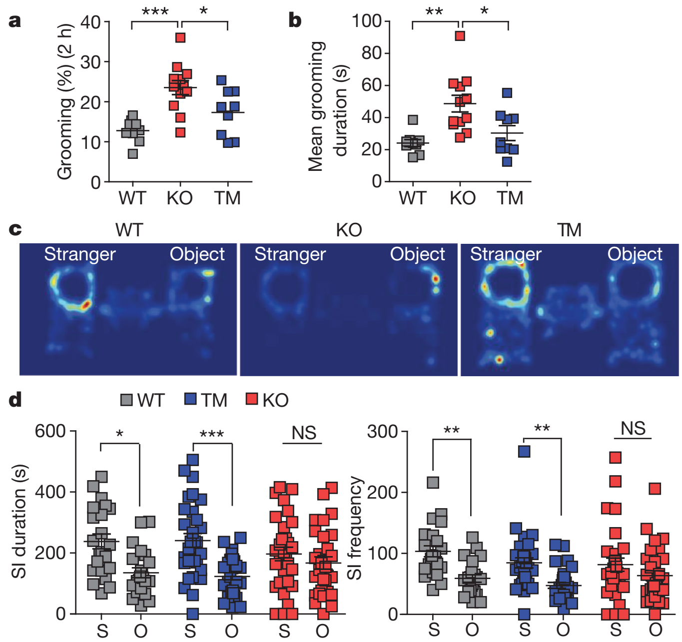

Figure 3 | Adult *Shank3* expression rescued repetitive grooming and social interaction. **a**, **b**, Significantly reduced repetitive grooming behaviour in TM compared to KO mice. **c**, Representative heat maps from the social interaction test for all groups. **d**, Unlike WT mice, KO mice showed no preference for social interaction (SI) with a stranger (S) mouse rather than a novel object (O); this behaviour is rescued in the TM group. $*P<0.05$, $**P<0.01$, $***P<0.001$ (one-way repeated measures ANOVA with Bonferroni post-hoc test (**a**, **b**, **d**, left), Kruskal–Wallis test with Dunn's multiple comparison test owing to non-normal distribution (**d**, right)). Data are mean ± s.e.m. (**a** and **b**: $n=9$ WT, $n=9$ TM and $n=12$ KO mice; **d**: $n=22$ WT, $n=30$ TM and $n=30$ KO mice).

treated with tamoxifen (wild type, WT), *Shank3*$^{fx/fx}$:*CreER*$^{+/-}$ mice treated with tamoxifen (TM), and *Shank3*$^{fx/fx}$:*CreER*$^{+/-}$ mice treated with corn oil vehicle (KO). Synaptosomal preparations showed that tamoxifen treatment restored the expression of most major SHANK3 isoforms, including the α and β isoforms, to the wild-type level at synapses (Fig. 2b).

Because SHANK3 is the only SHANK protein family member highly enriched in the striatum, a region strongly implicated in certain behaviours associated with autism[12,18], mechanistic characterizations were primarily carried out on striatal neurons. We found that the synaptic concentrations of scaffold proteins SAPAP3, Homer1b/c and glutamate receptor subunits NR2A, NR2B and GluA2 were significantly reduced in KO striatal synaptosomal preparations. However, in the TM condition, the synaptic levels of these postsynaptic proteins were significantly increased compared to those in the KO mice, reaching comparable levels to the WT (Fig. 2c). This molecular alteration shows for the first time, to our knowledge, that restoring *Shank3* expression in the adult brain can efficiently recruit major scaffolding and signalling proteins to the synapse and assemble the PSD protein network even after the developmental period.

To investigate whether there were functional changes parallel to molecular repair at synapses, we examined striatal physiology. As expected, the KO mice showed significantly reduced field population spikes. However, the reduced field responses were rescued to WT levels in the TM condition (Fig. 2d, e). We then performed whole-cell recordings and found that the KO mice had reduced miniature excitatory postsynaptic current (mEPSC) frequency compared to WT mice. Notably, mEPSC frequency was rescued in the TM condition to comparable levels of the WT group (Fig. 2f). We also measured the paired-pulse ratio, the AMPAR/NMDAR ratio (α-amino-3-hydroxy-5-methyl-4-isoxazole propionic acid receptor/*N*-methyl-D-aspartate receptor) (Extended Data Figs 2 and 3), and NR2B (also known as GRIN2B)/total NMDAR ratio (Extended Data Fig. 2c). We found no differences across genotypes. Overall, these results suggest that a primary defect of striatal physiology in KO mice is the reduced mEPSC frequency, and this defect can be improved by restoring SHANK3 expression in adulthood.

Previous studies have shown that *Shank3* manipulation can lead to significant changes in the total spine density[6,12]. It is, however, unclear whether post-developmental *Shank3* expression can also affect spine structure. To address this, we used systemic viral injection to sparsely label neurons with green fluorescdent protein (GFP) in the WT, KO

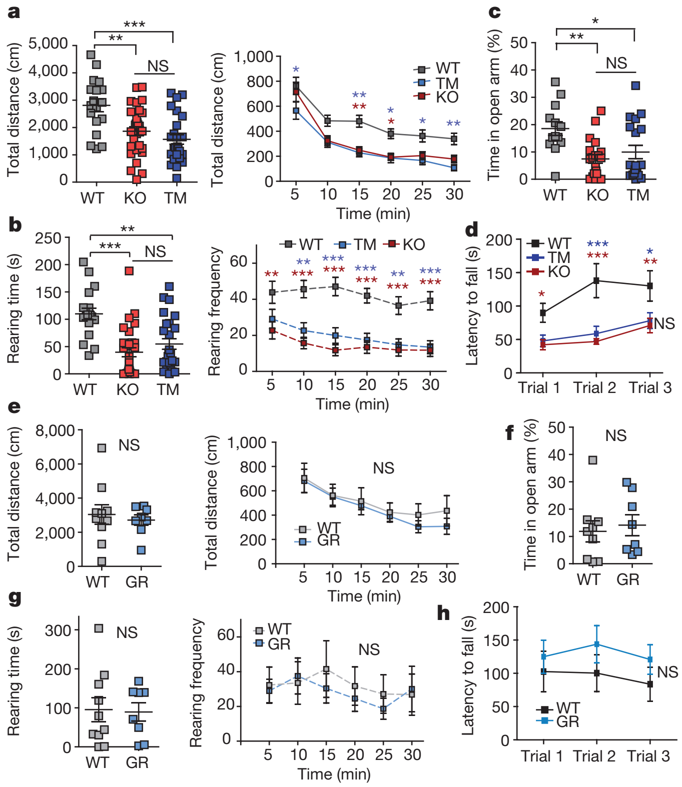

Figure 4 | Restoring *Shank3* expression in adulthood did not rescue anxiety and rotarod deficits. a, **b**, Open-field tests indicated that SHANK3 re-expression in adults (TM) does not rescue reduced locomotion and reduced rearing (axiogenic behaviour) in KO mice. NS, not significant. **c**, KO mice spend less time exploring the open arm during the elevated zero maze test; this behaviour is also not rescued in TM group. **d**, Motor coordination measurement from rotarod is not rescued in TM group. **e**–**h**, Germline rescued (GR) *Shank3*$^{fx/fx}$ mice show that all above parameters for open-field, elevated zero maze and rotarod tests can be rescued if *Shank3* expression is restored at the germ-cell stage. $^*P < 0.05$, $^{**}P < 0.01$, $^{***}P < 0.001$ (one-way ANOVA (**a**, left, **c**), Kruskal–Wallis test with Dunn's multiple comparisons (**b**, left), two-tailed *t*-test (**e**, left, **f**, **g**, left); two-way repeated measures ANOVA with Bonferroni post-hoc test (**a**, right, **b**, right, **d**, **e**, right, **g**, right, **h**). Data are mean ± s.e.m. (**a**–**c**: $n = 18$ WT, $n = 25$ TM and $n = 27$ KO mice; **d**: $n = 13$ WT, $n = 19$ TM and $n = 21$ KO mice; **e**–**h**: $n = 10$ WT and $n = 8$ GR mice).

and TM mice and analysed their dendritic spines in the dorsal striatum. Similar to our previous report on *Shank3B* (a *Shank3* isoform) KO mice[12], we observed a significant reduction of medium spiny neuron (MSN) spine density in the KO compared to WT mice. Surprisingly, the total spine density was significantly increased in the TM-treated mice compared to the KO mice (Fig. 2g). To our knowledge, this is the first indication that the ability of *Shank3* to promote spine formation or maintenance is not restricted to any developmentally critical period, highlighting the continued structural plasticity in the adult striatum. Interestingly, the spine density in the TM condition is significantly higher than that of the WT. One possibility for this phenomenon is that adult *Shank3* expression induces dendritic spines that may not be pruned and regulated by the same processes that occur in development.

We next tested how adult SHANK3 expression may affect behavioural abnormalities. Because striatal defects have been strongly linked to repetitive and compulsive behaviours[20,21], and *Shank3* KO mice show signs of overgrooming[12], we filmed WT, TM and KO mice after treatment, and quantified their grooming time. The results indicated that while there was a significant increase in the percentage of time spent grooming in the KO mice compared to WT mice, TM mice exhibited a significantly reduced grooming time (Fig. 3a, b). In addition, during the tamoxifen treatment, we noticed that some *Shank3*$^{fx/fx}$:*CreER*$^{+/-}$ mice that had initially developed lesions began to heal and regrow their lost fur, providing further support that the repetitive/excessive grooming phenotype is reversible in the *Shank3*$^{fx/fx}$ mice.

One of the defining features of autism is the impairment in social interaction. Thus, we used a modified three-chamber assay to probe voluntary social interaction[12,13,22]. After habituating to the three-chamber box, the test mice were given a choice of interacting with either a novel object or a stranger mouse. We found that although WT mice demonstrated a strong preference for the stranger mouse compared with the novel object, KO mice displayed no such preference (Fig. 3c, d). Notably, we found that TM mice behaved similarly to the WT controls in that they showed a strong preference for the stranger mouse in both the duration and frequency of the interaction (Fig. 3c, d). These data show that, similar to the repetitive grooming behaviour, the social interaction deficit can also be rescued in adulthood. Currently, the neurobiological mechanisms of social deficits of autism spectrum disorder are not well understood. Although ventral striatum has been associated with social interaction[23], we did not observe differences in the measurements of mEPSCs, the AMPAR/NMDAR ratio or the paired-pulse ratio in the ventral striatum/nucleus accumbens across genotypes (Extended Data Fig. 4).

Encouraged by the rescue of repetitive grooming and social deficits, we ran a range of other tests to assess the extent of behavioural rescue. In contrast to the social and grooming behaviours, adult *Shank3* re-expression has minimal effect on reduced locomotion, anxiety-like behaviour and motor coordination deficits (Fig. 4). In the open-field test, TM mice showed no significant difference from the KO mice in exploratory behaviour (Fig. 4a) and anxiety-like behaviour including rearing time and rearing frequency (Fig. 4b). This result was further corroborated by our observations from the elevated zero maze test (Fig. 4c). In addition, we found no significant recovery in the motor coordination deficit (Fig. 4d).

Because the cortex and cerebellum have been linked to anxiety and motor coordination, we assessed the mechanistic changes in these brain regions[24,25]. In both regions, SHANK3 expression was restored to the WT level in TM mice (Extended Data Figs 5 and 6). However, we found minimal differences across the genotypes (Extended Data Figs 5–7). Thus, the circuit mechanisms of anxiety and motor coordination deficits in the *Shank3* KO mice may involve other brain regions or could be the collective consequence of connectivity deficits across many brain regions.

To address whether the lack of rescue in these behaviour phenotypes is indeed due to missing SHANK3 expression during development, we crossed *Shank3*$^{fx/fx}$ mice to β-actin-Cre mice, enabling germline restoration of *Shank3*. The germline rescue mice showed no significant differences in striatal physiology (Extended Data Figs 4 and 8), exploratory behaviour (Fig. 4e), anxiety (Fig. 4f, g) or motor coordination (Fig. 4h) compared to their wild-type littermates, indicating that restoring *Shank3* expression at the germ-cell stage can restore all behavioural phenotypes. Together, these data strongly suggest that there are certain developmental defects that are irreversible by adult re-expression of *Shank3*.

To test whether there is a developmental window for rescuing anxiety and motor deficits, we treated postnatal day (P) 20–21 mice with tamoxifen to induce *Shank3* expression efficiently (Extended Data Fig. 9a), and assayed their behaviours in adulthood (Extended Data Figs 9 and 10). As previously reported[26], we observed that the treatment of young mice with tamoxifen leads to some toxicity including reduced body weights in the wild-type mice, and affected their motor coordination compared to the KO mice fed with corn oil (Extended Data Fig. 10d). However, even with the TM toxicity, we found that on the rotarod, the developmentally treated TM mice performed significantly better than their KO counterparts (Extended Data Fig. 10a, b). The P20–P21-treated TM mice also showed significantly reduced anxiety on the elevated zero maze compared to the KO mice (Extended Data Fig. 9f). Overall, these behavioural results show that earlier intervention

yields more behavioural improvement than adult treatment, further supporting the developmental origin of the behavioural abnormalities that are irreversible in adults.

We have shown that in the adult mouse brain, *Shank3* expression can increase dendritic spine density, restore the PSD protein composition, and improve striatal neurotransmission. Although adult gene rescue characterizations have been performed on other autism genes[27,28], this is the first report, to our knowledge, to show selective rescue in specifically autism-related behavioural phenotypes. Notably, we also demonstrated that the behavioural deficits that are irreversible in the adult can be improved by early postnatal intervention. Our results highlight the unique behavioural effect of SHANK3 expression after development, and underscore the surprising extent of continued neural plasticity in the adult brain.

Online Content Methods, along with any additional Extended Data display items and Source Data, are available in the online version of the paper; references unique to these sections appear only in the online paper.

Received 5 January 2015; accepted 05 January 2016.
Published online 17 February 2016.

1. Amaral, D., Geschwind, D. & Dawson, G. *Autism Spectrum Disorders* 1st edn (Oxford Univ. Press, 2011).
2. Gauthier, J. *et al.* Novel *de novo* SHANK3 mutation in autistic patients. *Am. J. Med. Genet. B. Neuropsychiatr. Genet.* **150B,** 421–424 (2009).
3. El-Fishawy, P. & State, M. W. The genetics of autism: key issues, recent findings, and clinical implications. *Psychiatr. Clin. North Am.* **33,** 83–105 (2010).
4. Leblond, C. S. *et al.* Meta-analysis of *SHANK* mutations in autism spectrum disorders: a gradient of severity in cognitive impairments. *PLoS Genet.* **10,** e1004580 (2014).
5. Moessner, R. *et al.* Contribution of *SHANK3* mutations to autism spectrum disorder. *Am. J. Hum. Genet.* **81,** 1289–1297 (2007).
6. Durand, C. M. *et al.* Mutations in the gene encoding the synaptic scaffolding protein SHANK3 are associated with autism spectrum disorders. *Nature Genet.* **39,** 25–27 (2007).
7. Ebert, D. H. & Greenberg, M. E. Activity-dependent neuronal signalling and autism spectrum disorder. *Nature* **493,** 327–337 (2013).
8. Kim, E. *et al.* GKAP, a novel synaptic protein that interacts with the guanylate kinase- like domain of the PSD-95/SAP90 family of channel clustering molecules. *J. Cell Biol.* **136,** 669–678 (1997).
9. Takeuchi, M. *et al.* SAPAPs. A family of PSD-95/SAP90-associated proteins localized at postsynaptic density. *J. Biol. Chem.* **272,** 11943–11951 (1997).
10. Wang, X. *et al.* Synaptic dysfunction and abnormal behaviors in mice lacking major isoforms of *Shank3*. *Hum. Mol. Genet.* **20,** 3093–3108 (2011).
11. Bozdagi, O. *et al.* Haploinsufficiency of the autism-associated *Shank3* gene leads to deficits in synaptic function, social interaction, and social communication. *Mol. Autism* **1,** 15 (2010).
12. Peça, J. *et al.* *Shank3* mutant mice display autistic-like behaviours and striatal dysfunction. *Nature* **472,** 437–442 (2011).
13. Yang, M. *et al.* Reduced excitatory neurotransmission and mild autism-relevant phenotypes in adolescent *Shank3* null mutant mice. *J. Neurosci.* **32,** 6525–6541 (2012).
14. Sheng, M. & Kim, E. The Shank family of scaffold proteins. *J. Cell Sci.* **113,** 1851–1856 (2000).
15. Boeckers, T. M. *et al.* Proline-rich synapse-associated proteins ProSAP1 and ProSAP2 interact with synaptic proteins of the SAPAP/GKAP family. *Biochem. Biophys. Res. Commun.* **264,** 247–252 (1999).
16. Han, K. *et al.* SHANK3 overexpression causes manic-like behaviour with unique pharmacogenetic properties. *Nature* **503,** 72–77 (2013).
17. Schnütgen, F. *et al.* A directional strategy for monitoring Cre-mediated recombination at the cellular level in the mouse. *Nature Biotechnol.* **21,** 562–565 (2003).
18. Karayannis, T. *et al.* Cntnap4 differentially contributes to GABAergic and dopaminergic synaptic transmission. *Nature* **511,** 236–240 (2014).
19. Guo, C., Yang, W. & Lobe, C. G. A Cre recombinase transgene with mosaic, widespread tamoxifen-inducible action. *Genesis* **32,** 8–18 (2002).
20. Rothwell, P. E. *et al.* Autism-associated neuroligin-3 mutations commonly impair striatal circuits to boost repetitive behaviors. *Cell* **158,** 198–212 (2014).
21. Welch, J. M. *et al.* Cortico-striatal synaptic defects and OCD-like behaviours in Sapap3-mutant mice. *Nature* **448,** 894–900 (2007).
22. Chao, H.-T. *et al.* Dysfunction in GABA signalling mediates autism-like stereotypies and Rett syndrome phenotypes. *Nature* **468,** 263–269 (2010).
23. Dölen, G. *et al.* Social reward requires coordinated activity of nucleus accumbens oxytocin and serotonin. *Nature* **501,** 179–184 (2013).
24. Gross, C. *et al.* Serotonin1A receptor acts during development to establish normal anxiety-like behaviour in the adult. *Nature* **416,** 396–400 (2002).
25. De Zeeuw, C. I. & Ten Brinke, M. M. Motor learning and the cerebellum. *Cold Spring Harb. Perspect. Biol.* **7,** a021683 (2015).
26. Poirier, M. C. & Schild, L. J. The genotoxicity of tamoxifen: extent and consequences, Kona, Hawaii, January 23, 2003. *Mutagenesis* **18,** 395–399 (2003).
27. Guy, J., Gan, J., Selfridge, J., Cobb, S. & Bird, A. Reversal of neurological defects in a mouse model of Rett syndrome. *Science* **315,** 1143–1147 (2007).
28. Clement, J. P. *et al.* Pathogenic SYNGAP1 mutations impair cognitive development by disrupting maturation of dendritic spine synapses. *Cell* **151,** 709–723 (2012).

Supplementary Information is available in the online version of the paper.

Acknowledgements We thank T. Dalia, A. Lim, S. Feng, K. Han, W. Stockton, H. Zaniewski and B. Clear for technical support. We thank Q. Zhang for designing the pAAV-hSYN1-EGFP-P2A-EGFPf-WPRE-HGHpA construct. We thank all members of the Feng laboratory for their support and discussions. Y.M. would like to thank T. Littleton, Y. Lin and K. Tye. P.M. would like to thank C. Duarte and the late S. Chaterjee, and acknowledge support from the 'Programa Doutoral em Biologia Experimental e Biomedicina' (CNC, Coimbra, Portugal). This work was funded by the National Science Foundation Graduate Fellowship and Integrative Neuronal Systems to Y.M.; the Stanley Center for Psychiatric Research at the Broad Institute of MIT and Harvard and a doctoral fellowship from the Portuguese Foundation for Science and Technology to P.M. (SFRH/BD/33894/2009). Y.Z. is supported by postdoc fellowships from the Simons Center for the Social Brain at MIT, Nancy Lurie Marks Family Foundation and Shenzhen Overseas Innovation Team Project (no. KQTD20140630180249366). X.G. was supported by the Stanley Center for Psychiatric Research at the Broad Institute of MIT and Harvard and a graduate fellowship from China Scholarship Council. Z.F. is supported by Stanley Center for Psychiatric Research at Broad Institute of MIT and Harvard and NARSAD Young Investigator Grant from the Brain & Behavior Research Foundation. Research in the Feng laboratory is supported by the Poitras Center for Affective Disorders Research at MIT, Stanley Center for Psychiatric Research at Broad Institute of MIT and Harvard, National Institute of Health (NIMH R01MH097104), Nancy Lurie Marks Family Foundation, Simons Foundation Autism Research Initiative (SFARI) and Simons Center for the Social Brain at MIT.

Author Contributions Y.M., P.M. and G.F. designed the experiments and wrote the paper. Y.M., P.M., Y.Z., J.-A.K., X.G. and Z.F. performed the experiments and analysed the data. Y.M., P.M., Y.Z., J.-A.K., X.G. and Z.F. interpreted the results.

Author Information Reprints and permissions information is available at www.nature.com/reprints. The authors declare no competing financial interests. Readers are welcome to comment on the online version of the paper. Correspondence and requests for materials should be addressed to G.F. (fengg@mit.edu).

METHODS

Generation of *Shank3* conditional knock-in (*fx/fx*) mice. The *Shank3*$^{fx/fx}$ targeting vector was designed by inverting the PDZ domain (exons 13–16) and flanking it with the FLEx cassette, which is composed of one pair of *loxP* sites staggered with one pair of *lox2722* sites. *Shank3*$^{fx/fx}$ conditional knock-in mice were generated by homologous recombination in R1 embryonic stem cells and implanting the correctly targeted cells into C57 blastocysts using standard procedures. Correct locus insertion of the targeting construct into the genomic DNA was determined by PCR genotyping using two primers End_F (5′-GGCAGACTCCACACAGTTCCTG-3′) and LoxR (5′-GTATCCTATACGAAGTTATTCCGGGTCGAC-3′). Subsequent mouse genotyping was determined by PCR of mouse tail or ear DNA using three primers. For the WT allele, primer FuncF2 (5′-CGTTTGACACACATAAGCACC-3′) and primer FuncFlipR4 (5′-CTCCACCTAGCTGAATTTCCC-3′) were used to produce a band of 340 base pairs (bp). For the knockout (Fx) allele, primer FuncF2 (5′-CGTTTGACACACATAAGCACC-3′) and primer Gen_Flx_R1 (5′-GCTGACATCACATTGCTGCC-3′) were used to produce a band of 481 bp. For the rescue allele, primer FuncF2 (5′-CGTTTGACACACATAAGCACC-3′) and primer FuncFlipR4 (5′-CTCCACCTAGCTGAATTTCCC-3′) were used to produce a band of 408 bp.

Chimaeric males were crossed to C57BL/6J females from Jackson Labs. The F_1 hybrids were crossed with C57BL/6J β-actin Flp to remove the neomycin cassette. All progeny were bred onto the pure C57BL/6J (Jackson Labs) for at least two generations before being bred onto a mixed background with 129S1/SvlmJ (Jackson Labs). Heterozygotes were initially bred with heterozygotes to produce experimental animals. All germline *Shank3*$^{fx/fx}$ (KO) and germline rescue (GR) mice along with their respective wild-type littermates were produced by breeding heterozygotes with heterozygotes. For the adult *Shank3* rescue experiments, the *Shank3* conditional knock-in line was crossed with CAGGS-CreER[19]. To produce enough animals for all necessary experiments, breeding strategy was switched to heterozygotes crossed with homozygotes and homozygotes crossed with homozygotes for all conditions (*Shank3*$^{fx/+}$:*CreER*$^{+/-}$ bred with *Shank3*$^{fx/fx}$:*CreER*$^{-/-}$; *Shank3*$^{fx/fx}$:*CreER*$^{+/-}$ bred with *Shank3*$^{fx/fx}$:*CreER*$^{-/-}$; *Shank3*$^{+/+}$:*CreER*$^{+/-}$ bred with *Shank3*$^{+/+}$:*CreER*$^{-/-}$; *Shank3*$^{+/-}$:*CreER*$^{+/-}$ bred with *Shank3*$^{+/+}$:*CreER*$^{-/-}$). It should be noted that all animals in the rescue condition were produced from the same litters as the animals in the knockout condition. The animals were randomly assigned to different conditions. No computerized randomization program was used.

Animals were housed by genotype at a constant 23 °C in a 12-h light/dark cycle (lights on at 07:00, lights off at 19:00) with ad libitum food and water. Rescue treatment, that is tamoxifen feeding, was initiated on mice at 2–4.5 months. All electrophysiological and behavioural experiments were done at least 6 weeks after treatment in adult mice with the experimenter being blinded to the genotypes. Only age-matched male mice were used for behavioural assays. All experimental procedures were inspected and approved by the MIT Committee on Animal Care.

Open-field test. An automated Omnitech Digiscan apparatus (AccuScan Instruments) was used to assess spontaneous locomotion as previously described[21]. Anxiety-like behaviours were assessed with the following parameters: time spent rearing and frequency of rearing. Locomotion was evaluated by the total distance travelled. The first 30 min were evaluated for all parameters. Statistical analysis was done using one-way ANOVA with Bonferroni multiple comparison tests.

Elevated zero maze test. An elevated zero maze was illuminated such that the open arm was lit by 60 Lx, and the dark arm was lit by 10–20 Lx. Animals were habituated with 10–20 Lx for at least 1 h before the test. The animal was introduced into the closed arm and allowed to explore the maze freely for 5 min, and this was filmed. An observer blinded to the genotype performed analysis using the automated tracking software Noldus Ethovision. Anxiety-like behaviour was assessed as the percentage of time spent by the animal in the open arm during the 5-min interval. Statistical analysis was done using one-way ANOVA with Bonferroni multiple comparison tests.

Rotarod test. Animals were placed on a rotarod apparatus (Med Associates) that accelerates 4–40 r.p.m. for 5 min. Each animal was tested for three trials with 1–2 h between trials in a single day. All trials were filmed. Latency to fall was manually analysed for each trial using Noldus Observer software by an observer blinded to genotypes. The change in the latency to fall over the course of three trails indicates the quality of motor coordination. Statistical analysis was done using two-way repeated measures ANOVA with Bonferroni post-hoc tests.

Grooming. Animals were individually placed into a new cage and allowed to habituate. Grooming behaviour was filmed for 2 h from 19:00 to 21:00 with red light (2 Lx). An observer blinded to the genotype manually quantified grooming behaviour using Noldus Observer. All instances of face-wiping, scratching/rubbing of head and ears, and full-body grooming were counted as grooming behaviour. Statistical analysis was done using one-way ANOVA with Bonferroni multiple comparison tests.

Social interaction test. A modified version of the three-chamber social interaction assay was used as previously described[12,13,22]. Only age-matched males were used for all tests. S129 males were used as stranger mice and were habituated to the test chamber for three sessions (20 min each), 1 or 2 days before the behavioural assay. On the day of the test, both test and stranger animals were habituated to the test room for at least 1 h before the start of the assay. The left and right chambers of the three-chamber apparatus were both lit by 4–6 Lx during the test session. Each test animal was first placed into the centre chamber with open access to both the left and right chamber, each of which contained an empty wired cup placed upside down. This allowed the animal to habituate to not only the social apparatus, but also to the cups that will eventually contain the stranger mice. After 15 min of habituation, the test animal was moved back to the centre chamber briefly before the next session. During the social phase, an age-matched stranger mouse was placed randomly into one of the two side chambers while a novel object was placed into the other side chamber. The test animal was allowed to explore the social apparatus freely and demonstrate whether it prefers to interact with the novel object or novel mouse. This social phase was also for 15 min. The placement of the stranger mouse and the object was alternated between test mice to eliminate any confounds due to chamber bias. Time spent by the test animal in close proximity (∼5 cm) to the cup containing either the stranger or the object was calculated. Analysis was done by an observer blinded to the genotype on Noldus Ethovision. One-way ANOVA with Bonferroni post-hoc test was used for statistical analysis.

Tamoxifen preparation and feeding. Tamoxifen (Sigma, T5648) was dissolved in corn oil at 20 mg ml^{-1} by vortexing. Freshly prepared tamoxifen was protected from light by aluminium foil and kept for 2–3 days at room temperature. Animal feeding needles from Harvard Apparatus (52-4025) were used for oral gavage. To avoid toxicity of tamoxifen, the following dosages were used for adult animals: mice at 17–21 g body weight were fed 5 mg day^{-1}; mice at 22–25 g body weight were fed 6 mg day^{-1}; mice at 26–29 g body weight were fed 7 mg day^{-1}; mice at 30–35 g body weight were fed 8 mg day^{-1}.

The adult animals were fed for 5 consecutive days followed by 2 weeks of rest. The animals were then fed for 5 more consecutive days followed by another 2 weeks of rest. Corn oil was used as a control. The mice fed with tamoxifen and with corn oil were housed separately to avoid contamination.

For induction of SHANK3 expression in P20–P21 animals, mice that weighed 7–9 g received 0.1 ml tamoxifen or corn oil per day for 2–3 consecutive days. Mice that weighed 10–12 g received 0.15 ml tamoxifen or coil per day for 2–3 consecutive days.

Western blot. PSD and synaptosomal fractions of the striatum, cortex and cerebellum were prepared as previously described[21]. Purified fractions were separated on SDS–PAGE and quantified using Odyssey Licor. β-Actin and tubulin were used as loading controls. Specific primary antibody for SAPAP3 was prepared as previously described[21]. Commercial antibodies used include SHANK3 (Santa Cruz, SC-30193), GluR1 (Millipore, MAB2263), GluR2 (Neuromab, 75-002), NR1 (BD Biosciences, 556308), NR2A (Millipore, 07-632), NR2B (Millipore, 05-920), Homer1 (Chemicon, AB5877, Synaptic Systems, 160022), Homer3 (Synaptic Systems, 160303), mGLUR5 (Abcam, ab76316), CaMKIIa (Millipore, 05-532), SHANK1 (Synaptic Systems, 162002), SHANK2 (Cell Signaling, 12218S), β-actin (Sigma, A5441) and tubulin (Sigma, T5168). Statistical analysis was done using two-tailed Student's *t*-tests.

Dendritic spine analysis. Age-matched male mice from WT ($n=5$), KO ($n=4$, 1 had to be euthanized owing to lesion development) and TM ($n=5$) conditions at 6–12 months old were used. The pAAV-hSYN1-EGFP-P2A-EGFPf-WPRE-HGHpA construct was cloned and sent for commercial viral packaging by Upenn Viral Core with serotype 2/9. Farnesylated GFP (GFPf) was previously shown to target the membrane[29]. To achieve sparse labelling, ∼8–30 μl of this virus with titre of 4.04×10^{13} genome copies (GC) ml^{-1} was injected through the retro-orbital route into each mouse. Three weeks after viral injection, the mice were transcardially perfused with 4% paraformaldehyde and sectioned into 200-μm slices. Immunohistochemistry was performed by staining the slices with an anti-GFP antibody (Invitrogen, A11122) for 48 h and 24 h of secondary antibody incubation. The stained slices were then surrounded by a 240-μm depth spacer (Electron Microscopy Sciences) and mounted with Vectashield Mounting Media.

Confocal images were taken with a ×60 objective of the dorsal striatum. Spine count on intact neurons began 30–40 μm away from the soma and was extended for 10–60 μm from the origin. Spine density was analysed automatically by Neuron Studio. All virus injections, imaging and software analysis were done with the experimenter blinded to the mouse genotypes. Statistical analysis was done using one-way ANOVA, Newman–Keuls post-hoc test.

Electrophysiology slices, dorsal and ventral striatum. Acute striatal slices were prepared from 3–7-month-old age-matched mice. Animals were anaesthetized by avertin intraperitoneal injection (tribromoethanol, 20 mg ml^{-1}, 0.5 mg g^{-1} body weight) and transcardially perfused with ice-cold oxygenated NMDG-based

cutting aCSF solution (mM): 92 *N*-methyl-D-glucamine (NMDG), 2.5 KCl, 1.20 NaH_4PO_4, 30 $NaHCO_3$, 20 HEPES, 25 glucose, 2 thiourea, 5 Na-ascorbate, 3 Na-pyruvate, 0.5 $CaCl_2$ and 10 $MgSO_4$ (~300 mOsm, 7.2–7.4 pH). After decapitation, brains were removed for sectioning in the same ice-cold cutting aCSF using a Vibratome 1200S (Leica Microsystems). For all dorsal striatal recordings, 300-μm coronal slices were prepared, unless otherwise stated (Extended Data Fig. 3). For all nucleus accumbens (NAc) core recordings, 300-μm parasagittal slices were prepared and NAc core was identified by the presence of anterior commissure. Slices were recovered in the same cutting aCSF solution at 32 °C for 12 min and transferred to room-temperature carbogenated regular aCSF (mM): 119 NaCl, 2.5 KCl, 1.2 NaH_2PO_4, 24 $NaHCO_3$, 12.5 glucose, 2 $MgSO_4.7H_2O$ and 2 $CaCl_2.2H_2O$ (~300 mOsm, 7.2–7.4 pH). Slices were allowed to recover at least ≥ 1 h and transferred to a recording chamber (RC-27L, Warner Instruments) before recordings. Stimulations were performed using a platinum iridium concentric bipolar electrode (CBAPC75, FHC). For dorsolateral striatum coronal slices, electrode was placed at the corpus callosum to mainly stimulate corticostriatal axons. For dorsolateral striatum parasagittal slices, stimulating electrode was placed at the cortex between layer V and VI. For ventral striatum parasagittal slices, electrode was placed dorsally to the anterior commissure at the border between NAc core and the cortex. Afferents were stimulated with 0.1 ms stimulation step (Isoflex, AMPI) delivered at 0.05 Hz frequency (unless otherwise stated). Slices were visualized under IR-DIC (infrared-differential interference contrast) using a BX-51WI microscope (Olympus). All slice preparations, recordings and data analysis were performed with experimenter blinded to the genotypes.

Medial prefrontal cortex. Acute brain slices were prepared from 3–7-month-old mice as follows. In brief, mice were deeply anaesthetized by intraperitoneal injection of avertin solution (20 mg ml^{-1}, 0.5 mg g^{-1} body weight) and then transcardially perfused with 20 ml of carbogenated (95% O_2, 5% CO_2) ice-cold cutting solution with the composition (in mM): 105 NMDG, 105 HCl, 2.5 KCl, 1.2 NaH_2PO_4, 26 $NaHCO_3$, 25 glucose, 10 $MgSO_4$, 0.5 $CaCl_2$, 1 L-ascorbic acid, 3 sodium pyruvate and 2 thiourea (pH 7.4, with osmolarity of 300–310 mOsm). The brains were rapidly removed and placed in ice-cold and oxygenated cutting solution. Coronal slices (300 μm) were sliced using Leica VT1200S (Leica Microsystems) and then transferred to recovery chamber at 32 °C with carbogenated cutting solution for 8 min, followed by transferring to holding chamber containing aCSF that contained (mM): 119 NaCl, 2.3 KCl, 1.0 NaH_2PO_4, 26 $NaHCO_3$, 11 glucose, 1.3 $MgSO_4$ and 2.5 $CaCl_2$ (pH was adjusted to 7.4 with HCl, with osmolarity of 300–310 mOsm) at room temperature. Slices were allowed to recover for at least 2 h in holding chamber before recording and used for experiment typically between 3 and 7 h after slicing. Layer 5 pyramidal cells with a prominent apical dendrite were visually identified with a microscope equipped with IR-DIC optics (BX-51WI, Olympus) mainly by location, shape and pClampex online membrane test parameters.

Extracellular field recordings. Slices were prepared from a daily group of mice containing all the three genotypes/treatments on randomized order, and recordings were obtained at room temperature with carbogenated regular aCSF (~2 ml min^{-1} rate). Borosilicate glass recording microelectrodes (King Precision Glass) were pulled on a P-97 horizontal puller (Sutter Instruments) and backfilled with 2 M NaCl. Recording electrode was placed ~400 μm away from stimulating electrode and field population-spike was evoked by a 0.1 ms stimulation step (Isoflex, AMPI) delivered at 0.05 Hz frequency. Input–output functions were generated through consecutive rounds from 0.1–1.0 mA in 0.1 mA increments (triplicate measurements per stimulation intensity). Three components were resolved in the recording traces: stimulation artefact, negative peak 1 (NP1, presynaptic fibre volley) and field population spike. Amplitude for each component was determined by the average peak amplitude from triplicated measurements per stimulation intensity. Data were amplified using a MultiClamp 700B and sampled at 10 kHz using a Digidata 1440A acquisition system. Analysis was performed blinded to genotype using pCLAMP 10 software (Axon Instruments/Molecular Devices).

Whole-cell recordings. Borosilicate glass recording microelectrodes (King Precision Glass) were pulled on a P-97 horizontal puller (Sutter Instruments) and backfilled with CsGlu (mM): 110 CsOH, 110 D-gluconic acid, 15 KCl, 4 NaCl, 5 TEA-Cl, 20 HEPES, 0.2 EGTA, 5 lidocaine *N*-ethyl chloride, 4 MgATP and 0.3 NaGTP. Internal pH was adjusted to ~7.3 with KOH and osmolarity adjusted to ~300 mOsm with K_2SO_4. Typical internal resistance was around 3–5 MΩ. MSNs were visually identified based on their shape, size and location under IR-DIC, using a BX-51WI microscope (Olympus). After seal rupture and internal equilibrium (5 min to allow proper dialysis of Cs^+ internal), cells were recorded with series-resistance values <20 MΩ (recording traces were excluded for data analysis if series resistance changed by >20%). All voltage clamp traces were recorded in the presence of 50 μM picrotoxin (Tocris) with theoretical liquid junction potential not corrected for. Signals were filtered at 2 kHz, digitized at 10 kHz and data acquired using a MultiClamp 700B amplifier and a Digidata 1440A. All analyses were performed blinded to the genotype. Grubb's test was used to remove single outliers.

mEPSCs. Slices were perfused with room temperature carbogenated regular aCSF at a rate of approximately 2 ml min^{-1}. Voltage clamp traces were recorded at holding potential −70 mV in the presence of 50 μM picrotoxin (Tocris), 50 μM DL-AP5 (DL-2-amino-5-phosphonovaleric acid, Abcam) and 1 μM tetrodotoxin (Tocris). Analysis of mEPSCs was performed using pCLAMP10 (Axon Instruments, Molecular Devices) and Minianalysis software (Synaptosoft) by manually clicking of individual events.

Paired-pulse ratios. Slices were perfused with carbogenated regular aCSF at ~30 °C, ~2 ml min^{-1} rate. Stimulus intensity was set to evoke 150–400 pA EPSCs at holding potential −70 mV. Two EPSCs (inter-stimulus interval of 50 ms) were evoked for 10 consecutive traces. The paired-pulse ratio was calculated by dividing the second EPSC peak amplitude by the first one.

AMPAR/NMDAR ratios. Slices were perfused with carbogenated regular aCSF at ~30 °C, ~2 ml min^{-1} rate. Stimulus intensity was set to evoke 150–400 pA EPSCs at holding potential −70 mV. An average EPSC was obtained (~10 traces) at −70 mV and then at +40 mV. The AMPAR/NMDAR ratio was calculated as the ratio of the average EPSC peak amplitude at −70 mV (AMPAR EPSC) to the average amplitude of the EPSC recorded at +40 mV, 50 ms after afferent stimulation. For pharmacologically isolated AMPAR/NMDAR ratios, dual-component evoked EPSCs at +40 mV was recorded before and after DL-AP5 bath application (50 μM, Abcam). NMDAR EPSC was obtained by digitally subtracting the average EPSC amplitude after DL-AP5 application (AMPAR EPSC). For NR2B/total NMDAR ratio, dual-component evoked EPSC at +40 mV was recorded before and after ifenprodil bath application (3 μM, NR2B antagonist, Tocris) and ifenprodil blockable fraction was defined as NR2B EPSCs. DL-AP5 (50 μM) was then applied to block all NMDARs for measuring total NMDAR EPSCs. The fraction of NR2B containing NMDAR EPSCs is presented as the percentage of the total NMDAR EPSCs (NR2B/total NMDAR ratio = ifenprodil sensitive current divided by DL-AP5 sensitive current).

Statistical analyses. All statistical analyses were performed using Prism (GraphPad Software). All data sets were analysed using D'Agostino–Pearson omnibus test and Shapiro–Wilk test for normality. Data sets with normal distributions were analysed for significance using either unpaired Student's two-tailed *t*-test or ANOVA measures with multiple comparison post-hoc test, using $*P < 0.05$, $**P < 0.01$, $***P < 0.001$; all data presented as mean ± s.e.m. Data sets with non-normal distributions were analysed using Kruskal–Wallis test with adjustments for multiple comparisons. On the basis of previously published SHANK3 models[10–13], we chose similar sample sizes for all experiments performed. All behaviour test results for the tamoxifen-treated cohorts are the combination of at least two different large animal cohorts that showed the same results. All electrophysiological, biochemical and morphological data were obtained by counterbalancing experimental conditions with controls. Further details on particular statistical analyses can be found on the respective figures/results section for each data set.

29. Hancock, J. F., Cadwallader, K., Paterson, H. & Marshall, C. J. A CAAX or a CAAL motif and a second signal are sufficient for plasma-membrane targeting of ras proteins. *EMBO J.* **10,** 4033–4039 (1991).

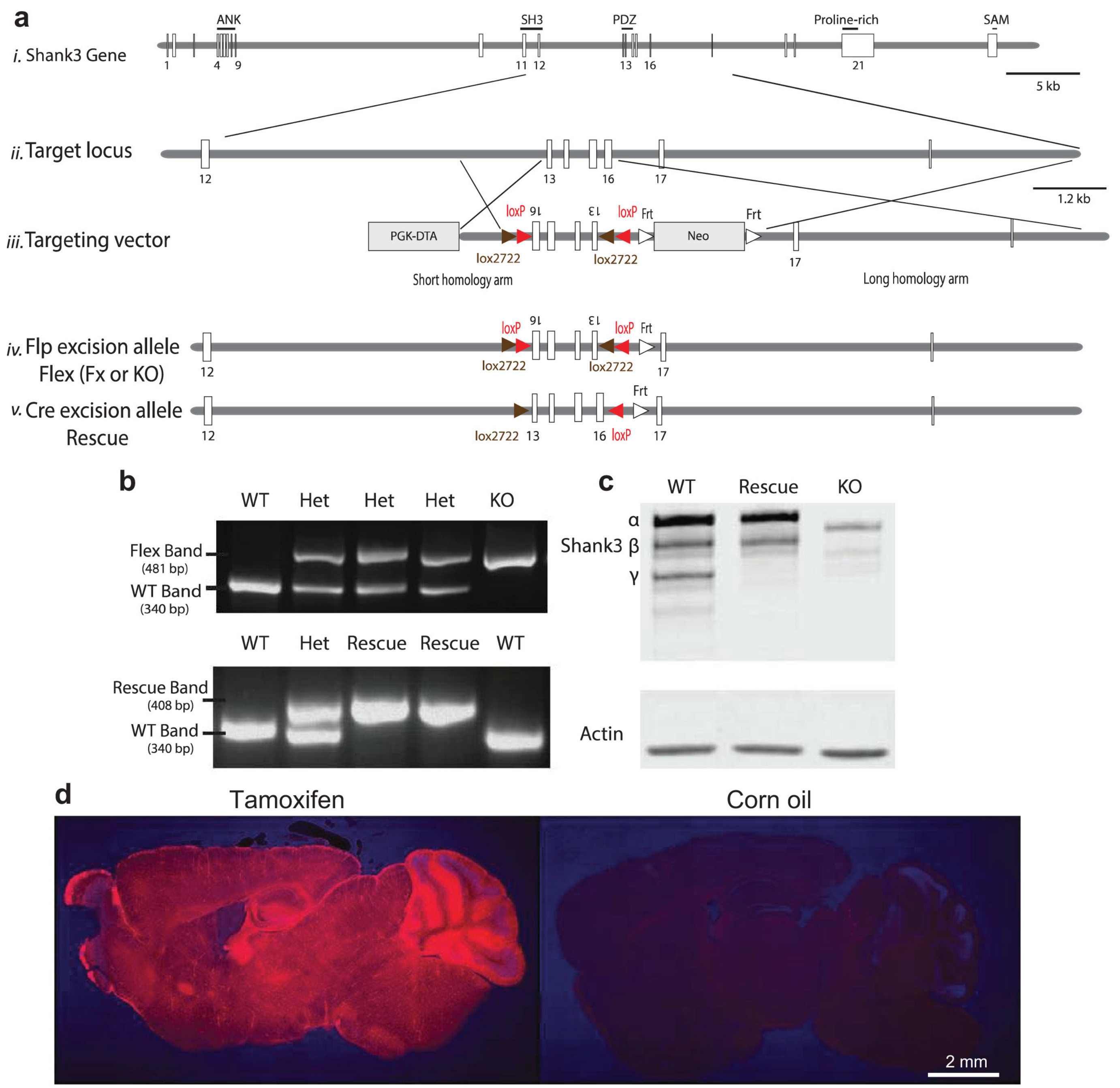

Extended Data Figure 1 | Generation of *Shank3* conditional knock-in mice. a, **i–ii**, Schematic of the *Shank3* gene and the target locus. **a**, **iii**, Targeted exons 13–16. **a**, **iv**, Neo-cassette excision via breeding with germline Flp mice. **a**, **v**, Exons 13–16 re-inversion via Cre-expressing mice. **b**, PCR genotyping showing the bands for Fx (knockout), rescue and WT. **c**, Western blot showing rescue of *Shank3* expression upon germline Cre recombination, with the exception of the putative SHANK3 γ isoform. This is probably due to the disruption of a putative intronic promoter by the introduction of the *loxP* sites. **d**, Tamoxifen-inducible Cre strategy leads to broad reporter expression. Sagittal sections from pCAGGS-CreER$^{+/-}$:Rosa-floxstop-tdTomato$^{+/-}$ mice after feeding with tamoxifen (left) or corn oil (right). Results show widespread induction of tdTomato reporter expression after tamoxifen-induced Cre activation, but not in the absence of Cre activity (corn oil feeding); the pCAGGS promoter consists of the CMV early enhancer with chicken β-actin promoter[19]. See Supplementary Fig. 1 for gel source data.

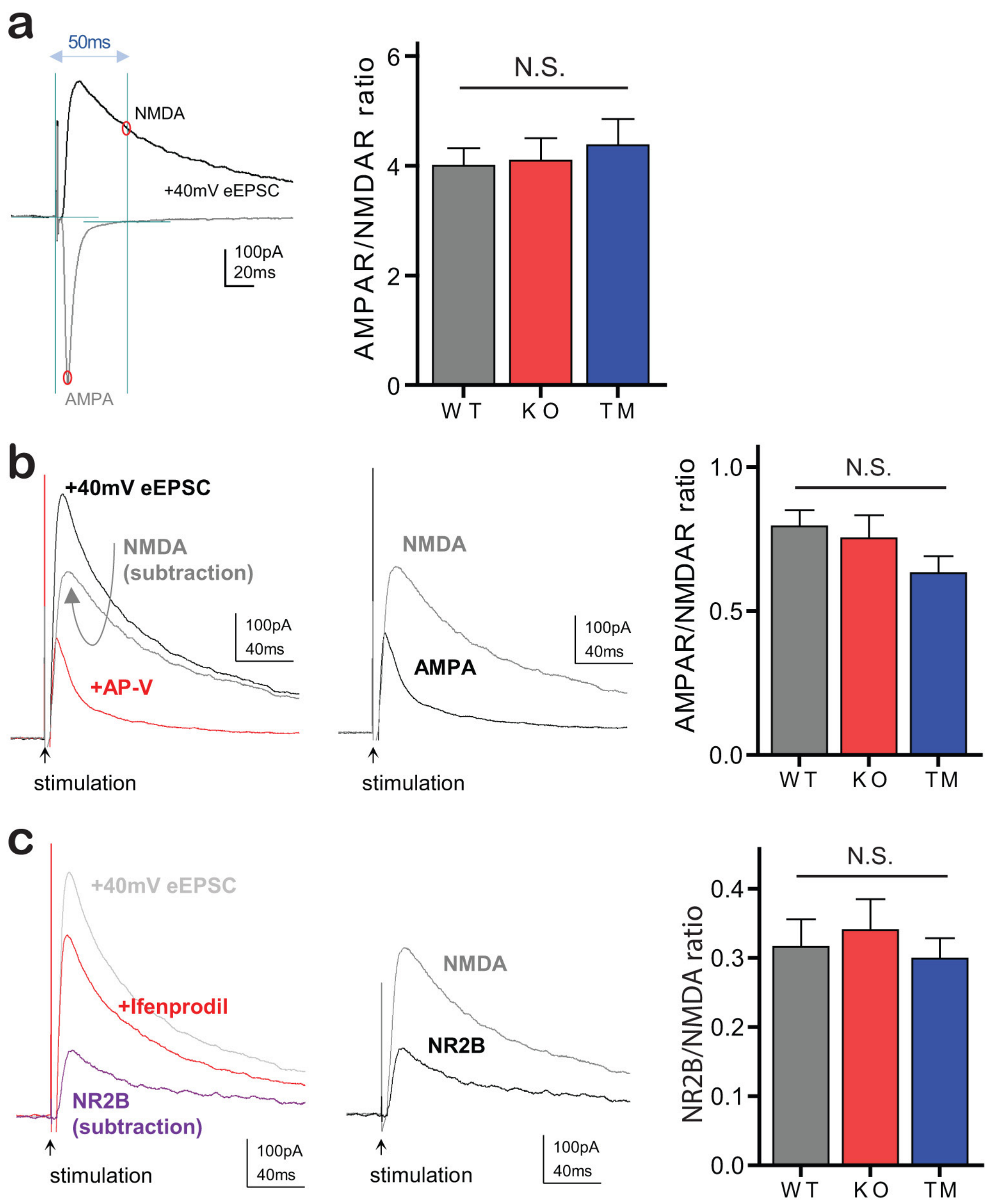

Extended Data Figure 2 | Additional measurements of dorsal striatum synaptic function in TM rescue. a, Representative traces (left) and bar graph (right) for the AMPAR/NMDAR ratio in WT, KO and TM groups ($n = 30$ WT, $n = 33$ KO and $n = 33$ TM MSNs). AMPAR/NMDAR ratio calculated as the ratio of the EPSC peak amplitude at −70 mV (AMPAR EPSC) to the amplitude of the EPSC recorded at +40 mV, 50 ms after afferent stimulation. **b**, Representative traces (left) and bar graph (right) for pharmacologically isolated AMPAR/NMDAR ratio ($n = 20$ WT, $n = 20$ KO and $n = 23$ TM MSNs). Dual-component evoked EPSC at +40 mV recorded before and after AP5 bath application. **c**, Representative traces (left) and bar graph (right) for the NR2B/NMDAR ratio in WT, KO and TM groups ($n = 16$ WT, $n = 16$ KO and $n = 22$ TM MSNs). Dual-component evoked EPSC at +40 mV recorded before and after ifenprodil bath application. N.S., not significant (Kruskal–Wallis test, with Dunn's multiple comparison test (**a**), one-way ANOVA with Bonferroni post-hoc test (**b**, **c**)). Data are mean ± s.e.m.

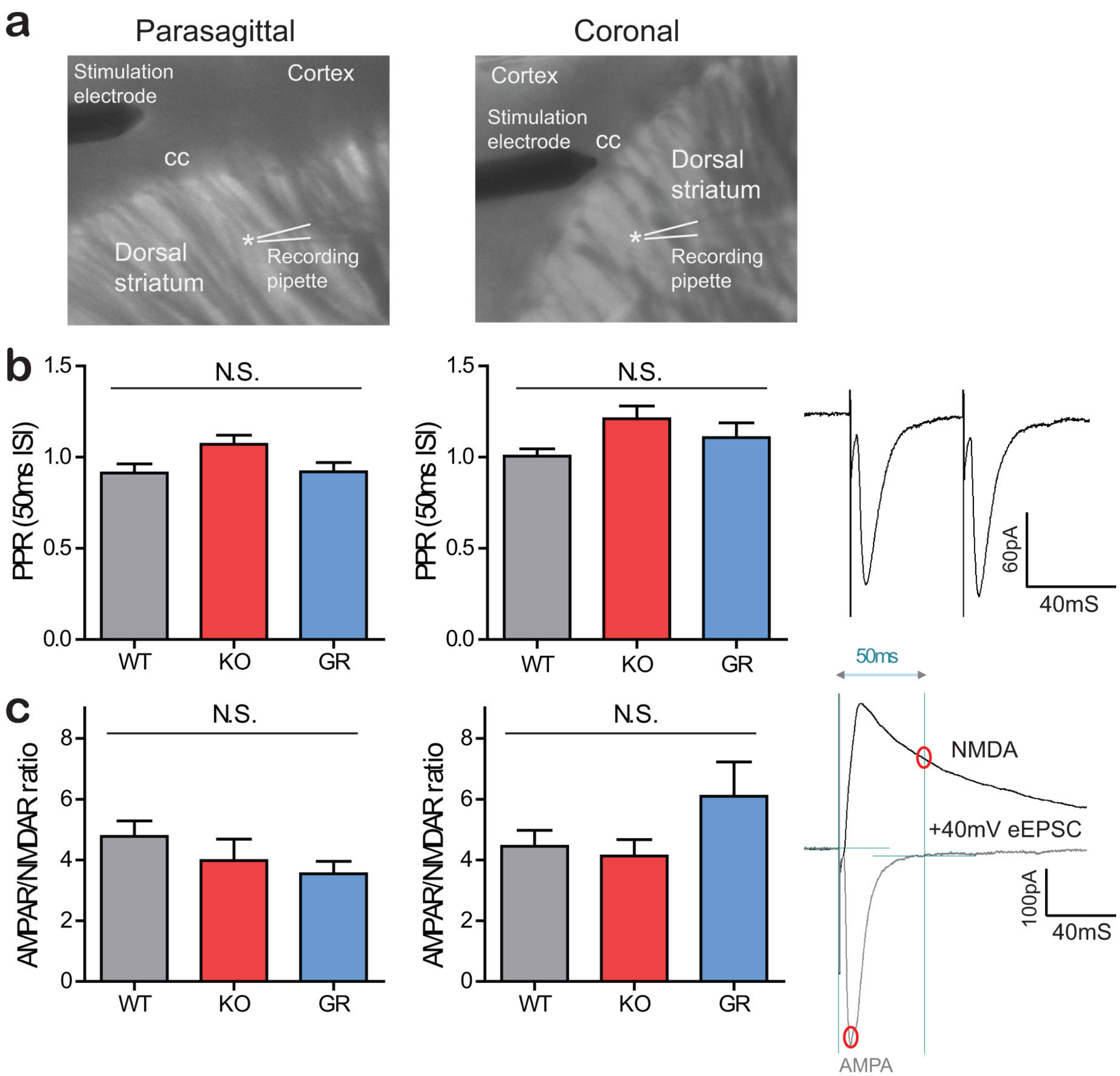

Extended Data Figure 3 | Additional measurements of synaptic function in dorsal striatum by cortical and corpus callosum evoked stimulation. a, IR-DIC images showing representative placement of the stimulation electrode in the cortex (left) or corpus callosum (cc; right) to evoke EPSCs in dorsal striatum, using parasagittal (left) and coronal (right) slices. **b**, Representative traces (right) and summary bar graphs for the paired-pulse ratios (PPR) of evoked EPSCs in dorsal striatum MSNs, showing similar magnitude in parasagittal (left; $n=23$ WT , $n=20$ KO and $n=20$ TM MSNs) and coronal (right; $n=9$ WT, $n=11$ KO and $n=10$ TM MSNs) slices. One-way ANOVA with Bonferroni post-hoc test. **c**, Representative traces (right) and summary bar graphs of AMPAR/NMDAR ratios evoked in parasagittal (left; $n=17$ WT, $n=15$ KO and $n=16$ TM MSNs) and coronal (right; $n=20$ WT, $n=16$ KO and $n=15$ TM MSNs) slices from all three genotypes. AMPAR/NMDAR ratio calculated as the ratio of the EPSC peak amplitude at −70 mV (AMPAR EPSC) to the amplitude of the EPSC recorded at +40 mV, 50 ms after afferent stimulation (**c**, right). Kruskal–Wallis test, with Dunn's multiple comparison test. Data are mean ± s.e.m.

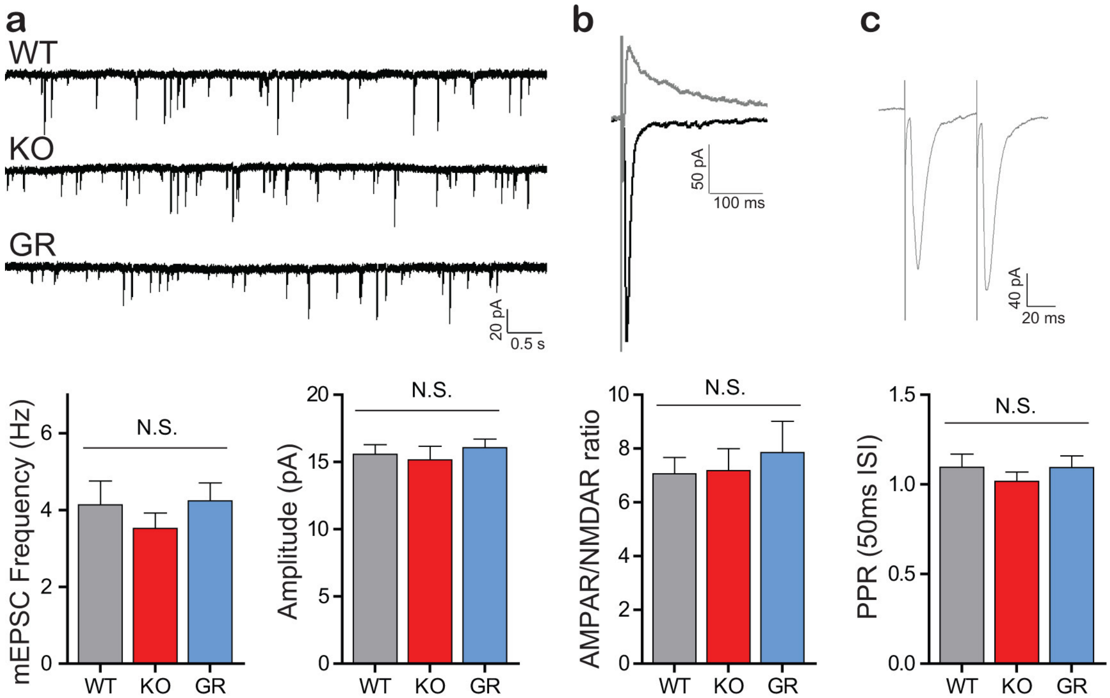

Extended Data Figure 4 | Whole-cell measurements of excitatory synaptic function in nucleus accumbens. a, Representative traces (top) and summary bar graphs (bottom) of mEPSCs in nucleus accumbens (NAc) MSNs ($n = 22$ WT, $n = 16$ KO and $n = 18$ GR MSNs). **b**, Representative traces (top) and summary bar graph (bottom) of the AMPAR/NMDAR ratio in NAc MSNs. The AMPAR/NMDAR ratio was calculated as the ratio of the EPSC peak amplitude at −70 mV (AMPAR EPSC) to the amplitude of the EPSC recorded at +40 mV, 50 ms after afferent stimulation ($n = 19$ WT, $n = 16$ KO and $n = 15$ GR MSNs). **c**, Representative traces (top) and summary bar graph (bottom) of paired-pulse ratios in NAc MSNs ($n = 25$ WT, $n = 22$ KO and $n = 19$ GR MSNs). One-way ANOVA Bonferroni post-hoc test (**a**, **c**), Kruskal–Wallis test, with Dunn's multiple comparison test (**b**). Data are mean ± s.e.m.

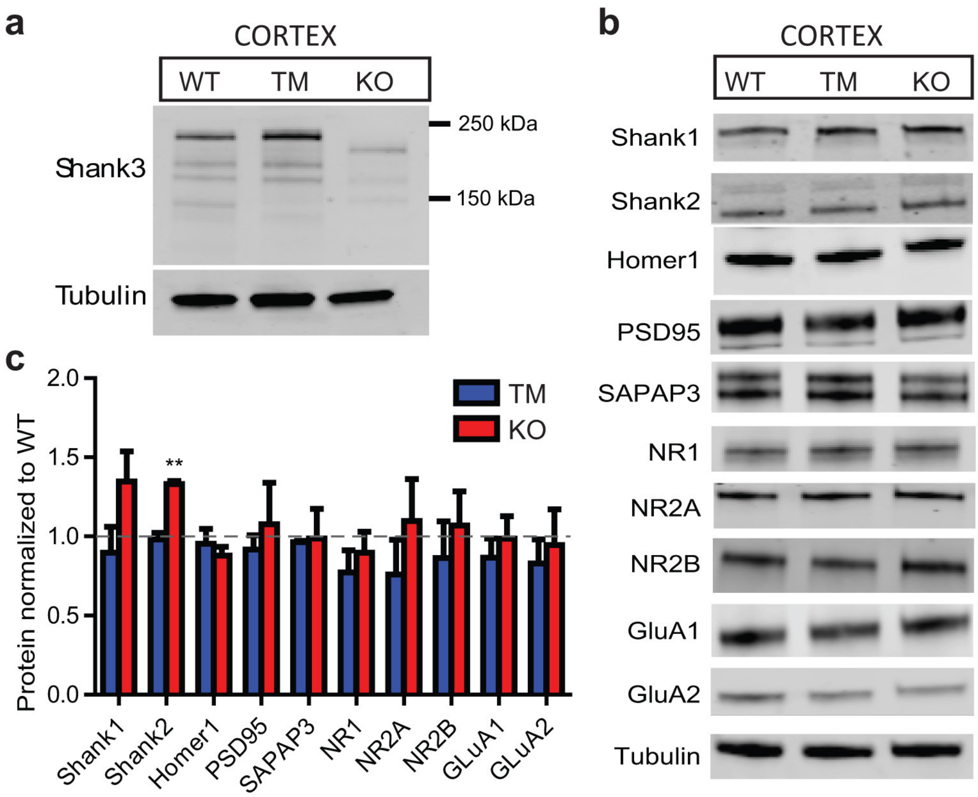

Extended Data Figure 5 | Western blots of synaptosomal preparations from the cortex of the adult treated mice show minimal difference across genotypes. a, Representative western blot of SHANK3 in the cortex of adult WT, KO and TM mice, showing that most major SHANK3 isoforms are restored in the TM mice. **b**, Representative western blots of synaptic proteins including scaffolding proteins and neurotransmitter receptors in the adult cortex across genotypes. **c**, Quantification of multiple synaptic proteins in the cortex of the adult treated mice. All data, $n = 3$ WT, $n = 3$ TM and $n = 3$ KO mice; each sample is from tissue taken from two animals. Student's two-tailed unpaired t-test. Data are mean ± s.e.m. See Supplementary Fig. 1 for gel source data.

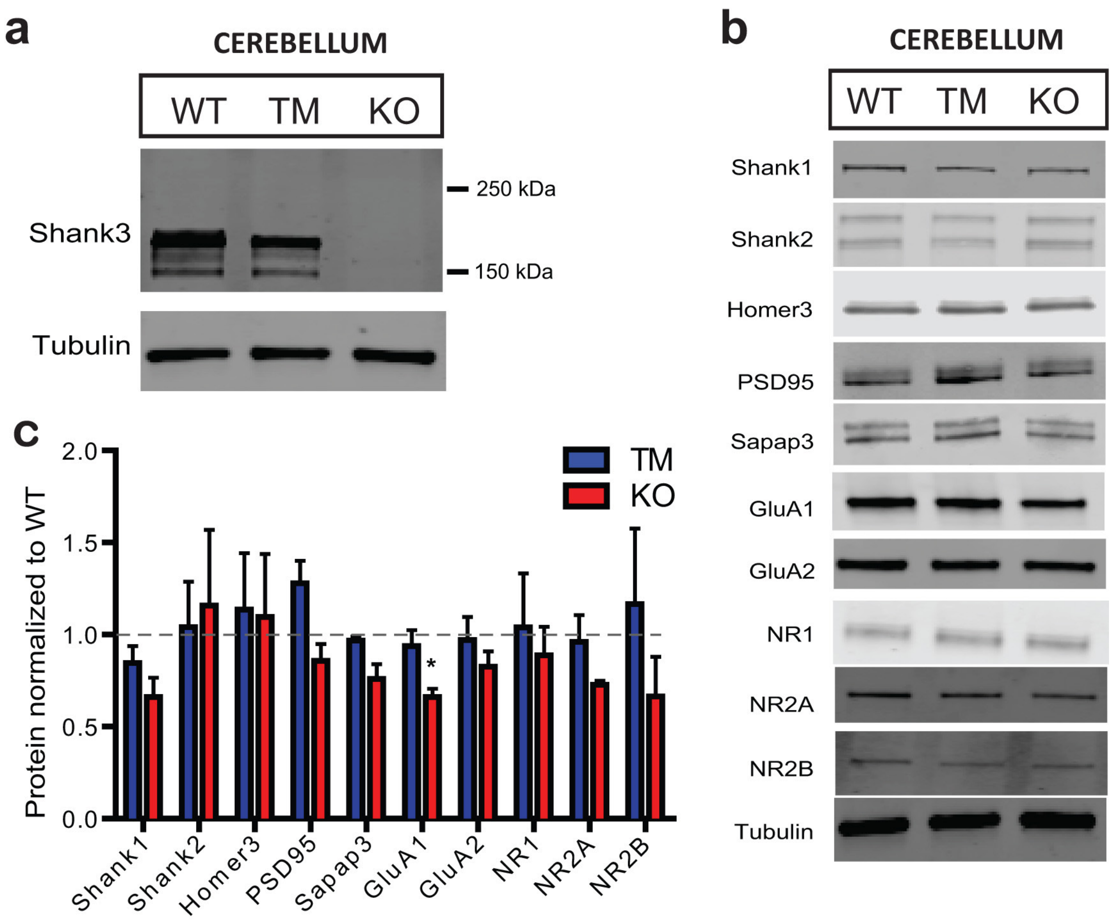

Extended Data Figure 6 | Western blots of synaptosomal preparations from the cerebellum of the adult treated mice show minimal difference across genotypes. a, Representative western blot of SHANK3 in the cerebellum of the adult mice treated with TM, showing that SHANK3 isoforms are restored in the TM mice. **b**, Representative western blots of synaptic proteins in the adult cerebellum across genotypes. **c**, Quantification of multiple synaptic proteins in the cerebellum of the adult treated mice. All data, $n = 3$ WT, $n = 3$ TM and $n = 3$ KO mice; each sample is from tissue taken from a single animal. Student's two-tailed unpaired t-test. Data are as mean ± s.e.m. See Supplementary Fig. 1 for gel source data.

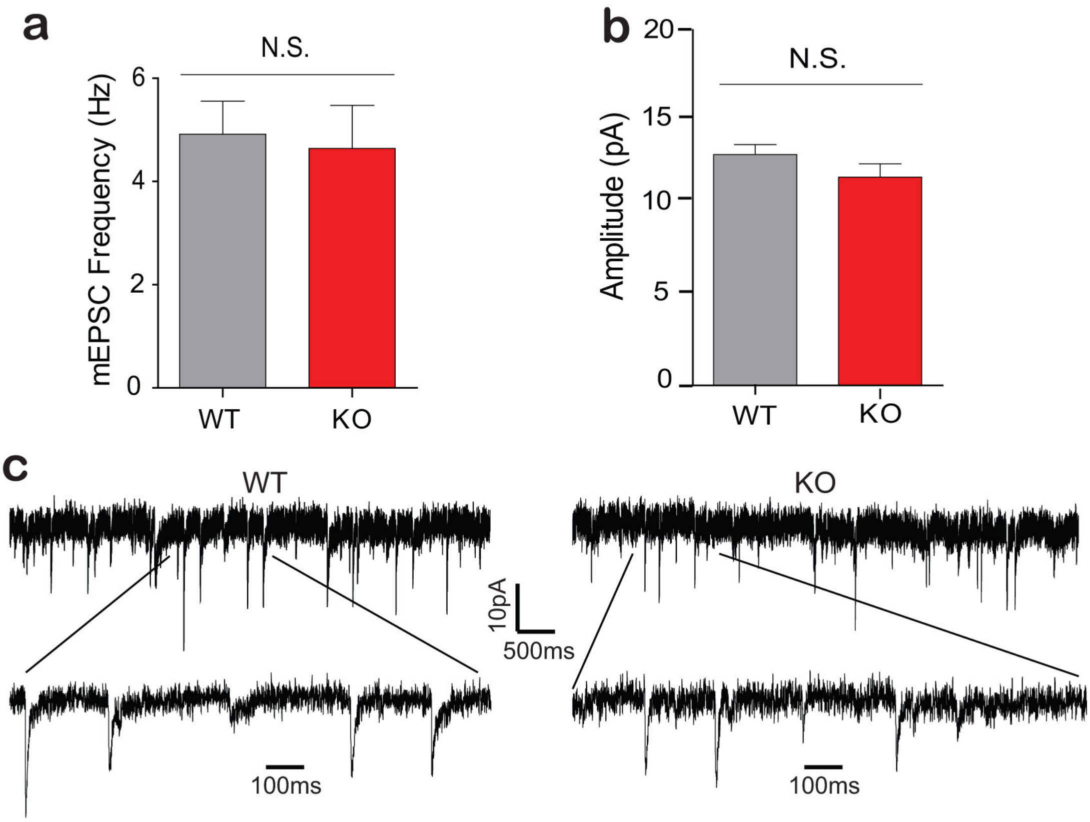

Extended Data Figure 7 | Whole-cell measurements of excitatory synaptic function in the cortex. a, **b**, Summary bar graphs of mEPSC frequency (**a**) and amplitude (**b**) in the prefrontal cortex of the adult WT and KO mice ($n = 13$ WT and $n = 10$ KO cells; Student's two-tailed unpaired t-test). Data are mean ± s.e.m. **c**, Representative traces from mEPSC recordings in the adult prefrontal cortex of the WT and KO mice.

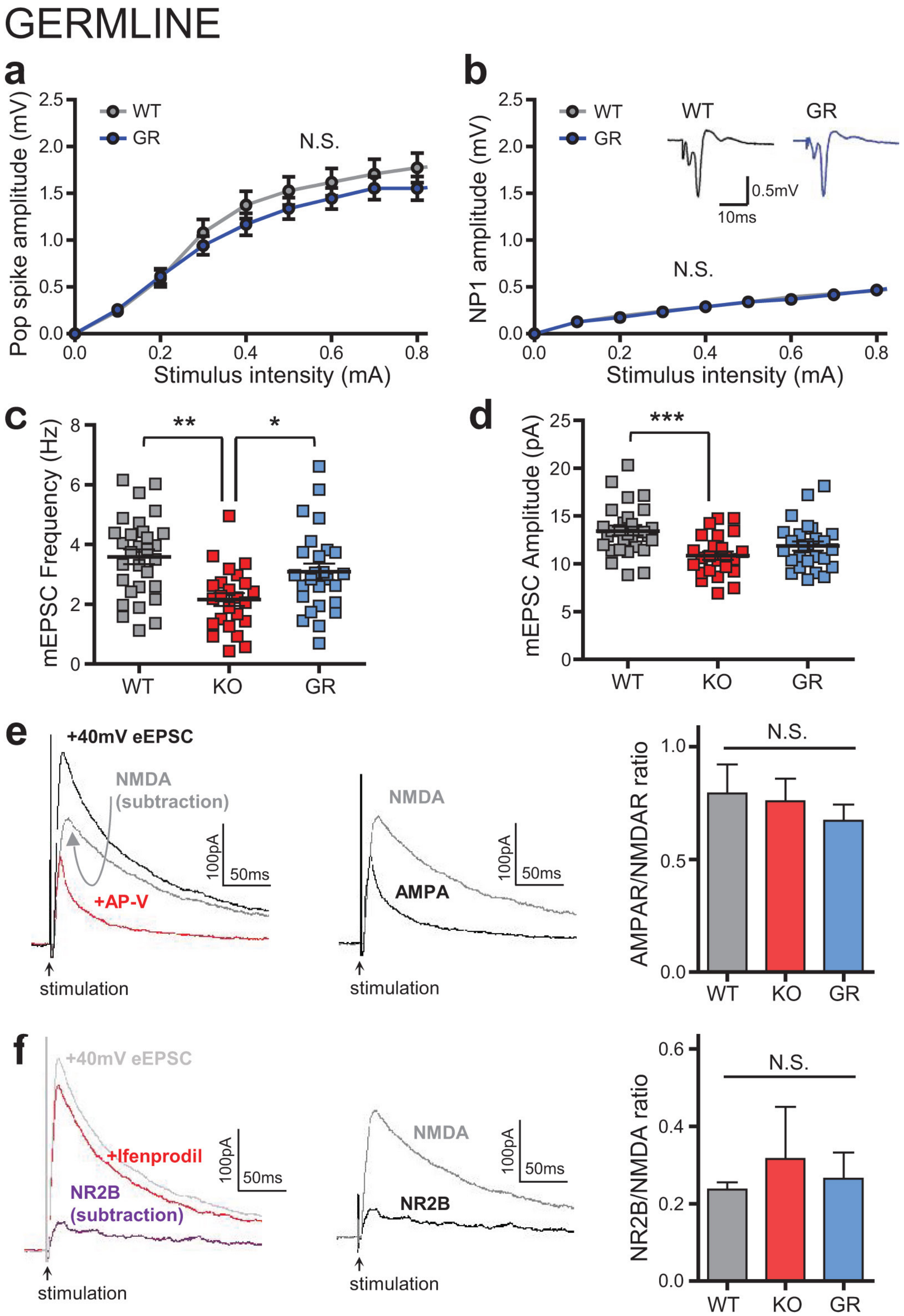

Extended Data Figure 8 | Electrophysiological measurements in the dorsal striatum of germline rescue mice. a, **b**, Normal pop spike amplitude (**a**) and NP1 (**b**) in germline rescued mice (insets show representative field traces). **c**, **d**, Reduced mEPSC frequency in KO compared to WT and GR mice (**c**). A reduction in mEPSC peak current amplitude is observed between KO and WT group only (**d**) ($n = 30$ WT, $n = 24$ KO and $n = 26$ GR MSNs). **e**, Representative traces (left) and bar graph (right) for the pharmacologically isolated AMPAR/NMDAR ratio ($n = 9$ WT, $n = 9$ KO and $n = 8$ GR MSNs). Dual-component evoked EPSC at +40 mV recorded before and after DL-AP5 bath application. **f**, Representative traces (left) and bar graph (right) for NR2B/NMDAR ratio in WT, KO and GR groups ($n = 6$ WT, $n = 5$ KO and $n = 7$ GR MSNs). Dual-component evoked EPSC at +40 mV recorded before and after ifenprodil bath application. *$P < 0.05$; **$P < 0.01$; ***$P < 0.001$ (two-way (**a**, **b**) and one-way (**c**–**f**) ANOVA with Bonferroni post-hoc test). Data are mean ± s.e.m.

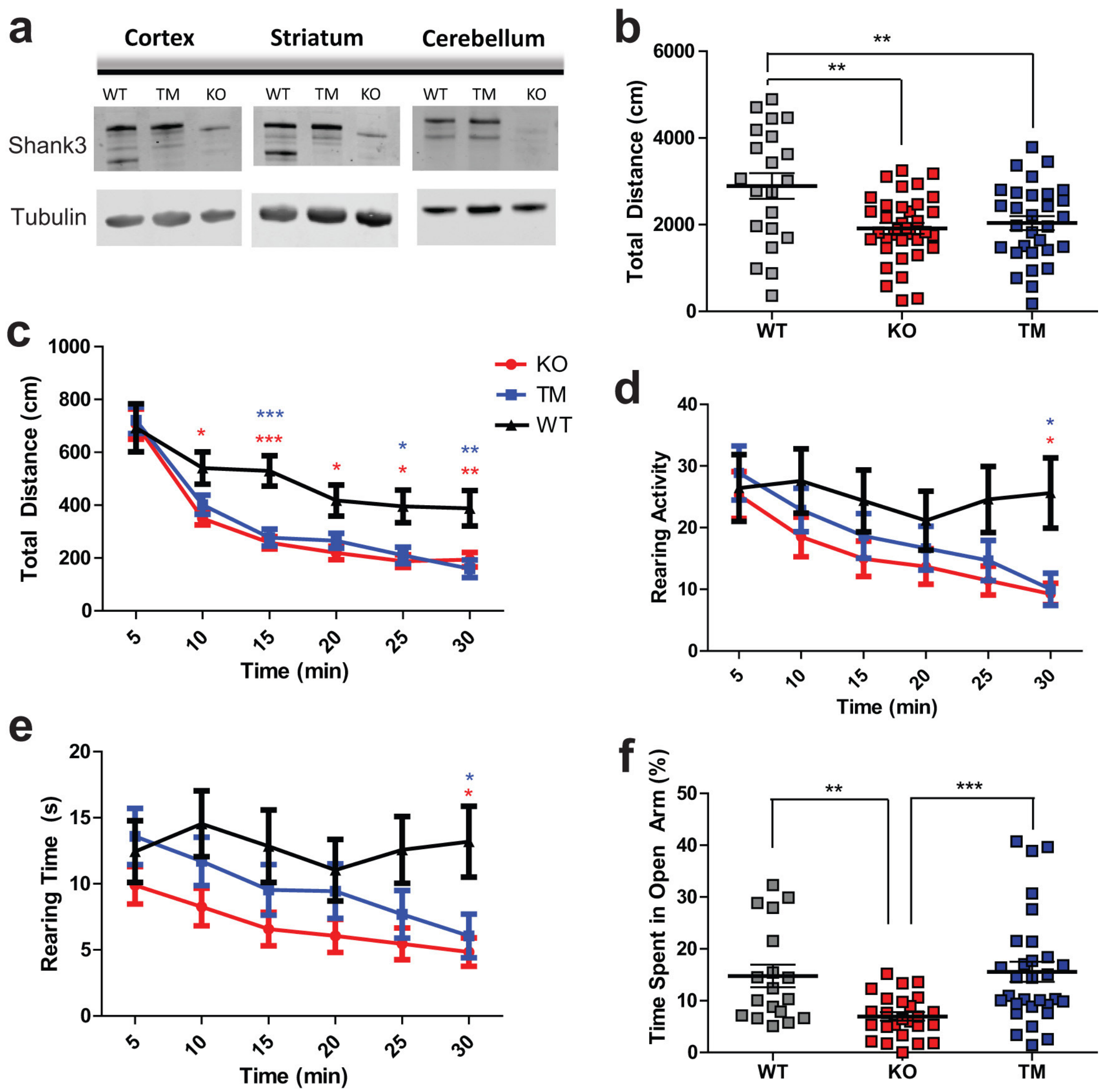

Extended Data Figure 9 | Expression of SHANK3 at P20–P21 rescues some behavioural measurements. a, Representative western blots showing efficient SHANK3 re-expression in the cortex, striatum and cerebellum in mice that were treated with tamoxifen at P20–P21. **b**, The total distance travelled as measured by the open-field test was not improved in the TM condition compared to the KO condition. One-way ANOVA with Bonferroni post-hoc test. **c**, The open-field total distance plotted across 5-min time bins, showing that there is no difference between KO and TM conditions across time. **d**, Rearing activity measured by open-field plotted across time, showing that the TM mice perform in between the WT and KO mice for most of the 30-min test. **e**, Rearing time measured by open-field test plotted across time, also showing the intermediate performance of TM mice between that of WT and KO mice (**b**–**e**: $n = 21$ WT, $n = 36$ KO and $n = 30$ TM mice; two-way ANOVA with Bonferroni post-hoc test). **f**, Activity on the zero maze indicates that the TM condition shows significantly reduced anxiety compared to that of the KO condition ($n = 18$ WT, $n = 25$ KO and $n = 30$ TM mice; outliers were removed using Iglewicz and Hoaglin's test (two-sided); Kruskal–Wallis test, Dunn's multiple comparison test). Data are mean ± s.e.m. See Supplementary Fig. 1 for gel source data.

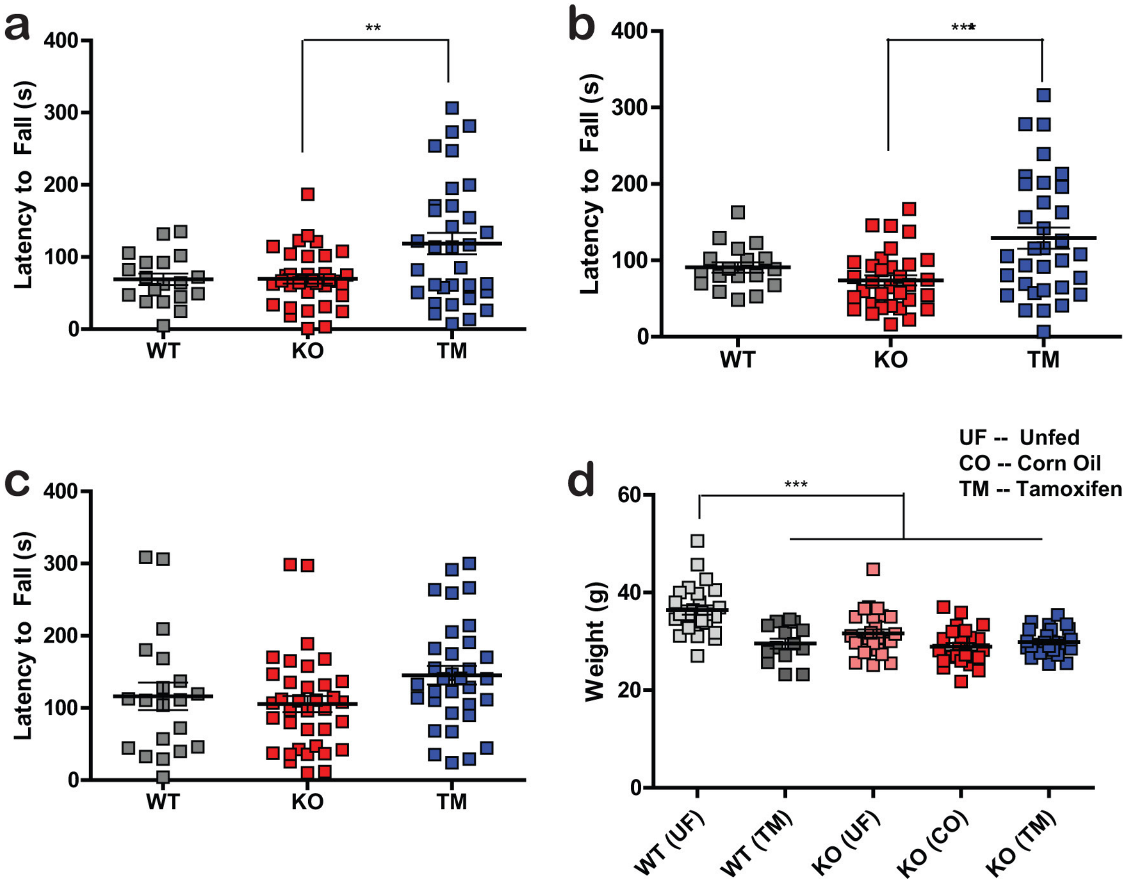

Extended Data Figure 10 | Expression of SHANK3 at P20–P21 improves motor coordination. a, Summary data from trial 1 of the accelerating rotarod test on mice treated with TM at P20–P21 ($n = 19$ WT, $n = 35$ KO and $n = 33$ TM mice). **b**, Summary data from trial 2 of the same rotarod test on mice treated at P20–P21 ($n = 18$ WT, $n = 33$ KO and $n = 33$ TM mice). **c**, Summary data from trial 3 of the rotarod on mice treated at P20–P21 ($n = 20$ WT, $n = 36$ KO and $n = 33$ TM mice). Outliers in **a**–**c** were removed using Iglewicz and Hoaglin's robust outlier test. One-way ANOVA with Bonferroni post-hoc test. **d**, Body weight from WT and KO mice that were unfed (UF) and mice that were fed with either corn oil or TM ($n = 28$ WT (UF), $n = 14$ WT (TM), $n = 27$ KO (UF), $n = 25$ KO (CO) and $n = 26$ KO (TM)). One-way ANOVA with Bonferroni post-hoc test. Data are mean ± s.e.m.

LETTER

doi:10.1038/nature16963

Inhibiting fungal multidrug resistance by disrupting an activator–Mediator interaction

Joy L. Nishikawa[1,2], Andras Boeszoermenyi[3], Luis A. Vale-Silva[4], Riccardo Torelli[5], Brunella Posteraro[6], Yoo-Jin Sohn[1,2], Fei Ji[7,8], Vladimir Gelev[9], Dominique Sanglard[4], Maurizio Sanguinetti[5], Ruslan I. Sadreyev[7,10], Goutam Mukherjee[11,12], Jayaram Bhyravabhotla[11,12,13], Sara J. Buhrlage[3,14], Nathanael S. Gray[3,14], Gerhard Wagner[3], Anders M. Näär[1,2] & Haribabu Arthanari[3]

Eukaryotic transcription activators stimulate the expression of specific sets of target genes through recruitment of co-activators such as the RNA polymerase II-interacting Mediator complex[1,2]. Aberrant function of transcription activators has been implicated in several diseases. However, therapeutic targeting efforts have been hampered by a lack of detailed molecular knowledge of the mechanisms of gene activation by disease-associated transcription activators. We previously identified an activator-targeted three-helix bundle KIX domain in the human MED15 Mediator subunit that is structurally conserved in Gal11/Med15 Mediator subunits in fungi[3,4]. The Gal11/Med15 KIX domain engages pleiotropic drug resistance transcription factor (Pdr1) orthologues, which are key regulators of the multidrug resistance pathway in *Saccharomyces cerevisiae* and in the clinically important human pathogen *Candida glabrata*[5,6]. The prevalence of *C. glabrata* is rising, partly owing to its low intrinsic susceptibility to azoles, the most widely used antifungal agent[7,8]. Drug-resistant clinical isolates of *C. glabrata* most commonly contain point mutations in Pdr1 that render it constitutively active[9–14], suggesting that this transcriptional activation pathway represents a linchpin in *C. glabrata* multidrug resistance. Here we perform sequential biochemical and *in vivo* high-throughput screens to identify small-molecule inhibitors of the interaction of the *C. glabrata* Pdr1 activation domain with the *C. glabrata* Gal11A KIX domain. The lead compound (iKIX1) inhibits Pdr1-dependent gene activation and re-sensitizes drug-resistant *C. glabrata* to azole antifungals *in vitro* and in animal models for disseminated and urinary tract *C. glabrata* infection. Determining the NMR structure of the *C. glabrata* Gal11A KIX domain provides a detailed understanding of the molecular mechanism of Pdr1 gene activation and multidrug resistance inhibition by iKIX1. We have demonstrated the feasibility of small-molecule targeting of a transcription factor-binding site in Mediator as a novel therapeutic strategy in fungal infectious disease.

On the basis of our previous findings that deletion of the KIX domain of *S. cerevisiae GAL11* or *C. glabrata GAL11A* abrogates Pdr1-dependent transcriptional responses and xenobiotic tolerance we hypothesized that the *C. glabrata* Pdr1–*C. glabrata* Gal11A (*Cg*Pdr1–*Cg*Gal11A) interaction interface might serve as a promising target for novel anti-multidrug resistance compounds[3]. A fluorescently tagged *Cg*Pdr1 activation domain (AD) was used in an *in vitro* fluorescence polarization screen[15] of ~140,000 chemically diverse compounds to identify small molecules that block the interaction between the *Cg*Gal11A KIX domain and the *Cg*Pdr1 AD (Extended Data Fig. 1). On the basis of the high degree of conservation between *S. cerevisiae* and *C. glabrata*, we followed up the top hits from the fluorescence polarization screen with an azole growth inhibition screen in *S. cerevisiae* to

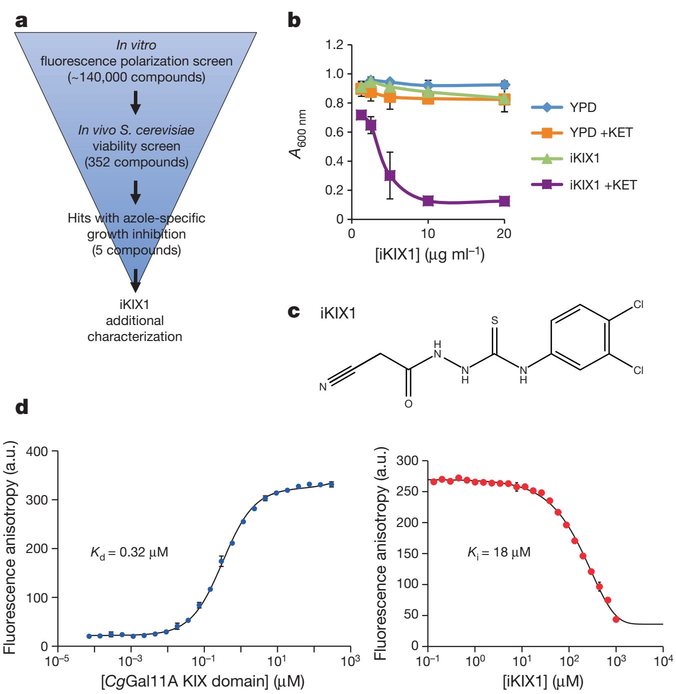

Figure 1 | Discovery of inhibitors of the *Cg*Gal11A KIX-*Cg*Pdr1AD interaction. **a**, Schematic of the screening process. **b**, iKIX1 inhibits cell growth in a concentration-dependent manner in the presence of 5 μM ketoconazole (KET); error bars represent means ± s.d. from duplicate plates. **c**, iKIX1 structure. **d**, Fluorescence polarization titration curve showing the interaction of *Cg*Gal11A KIX domain with *Cg*Pdr1 AD30 fitted to a dissociation constant (K_d) value of 319.7 nM ± 9.5 nM (left). iKIX1 competes out *Cg*Pdr1 AD30 with an half-maximum inhibitory concentration (IC_{50}) value of 190.2 μM ± 4.1 μM (right). The measured K_d and IC_{50} values were used to calculate an apparent inhibition constant (K_i) value of 18.1 μM for iKIX1. Data represent mean of two replicates and standard error from the fit is shown.

[1]Massachusetts General Hospital Cancer Center, Charlestown, Massachusetts 02129, USA. [2]Department of Cell Biology, Harvard Medical School, Boston, Massachusetts 02115, USA. [3]Department of Biological Chemistry and Molecular Pharmacology, Harvard Medical School, Boston, Massachusetts 02115, USA. [4]Institute of Microbiology, University Hospital Lausanne and University Hospital Center, Lausanne CH-1011, Switzerland. [5]Institute of Microbiology, Università Cattolica del Sacro Cuore, Rome 00168, Italy. [6]Institute of Public Health, Università Cattolica del Sacro Cuore, Rome 00168, Italy. [7]Department of Molecular Biology, Massachusetts General Hospital, Boston, Massachusetts 02114, USA. [8]Department of Genetics, Harvard Medical School, Boston, Massachusetts 02115, USA. [9]Faculty of Chemistry and Pharmacy, Sofia University, Sofia 1164, Bulgaria. [10]Department of Pathology, Massachusetts General Hospital and Harvard Medical School, Boston, Massachusetts 02114, USA. [11]Department of Chemistry, Indian Institute of Technology Delhi, Hauz Khas, New Delhi 110016, India. [12]Supercomputing Facility for Bioinformatics & Computational Biology, Indian Institute of Technology Delhi, Hauz Khas, New Delhi 110016, India. [13]Kusuma School of Biological Sciences, Indian Institute of Technology Delhi, Hauz Khas, New Delhi 110016, India. [14]Dana-Farber Cancer Institute, Boston, Massachusetts 02215, USA.

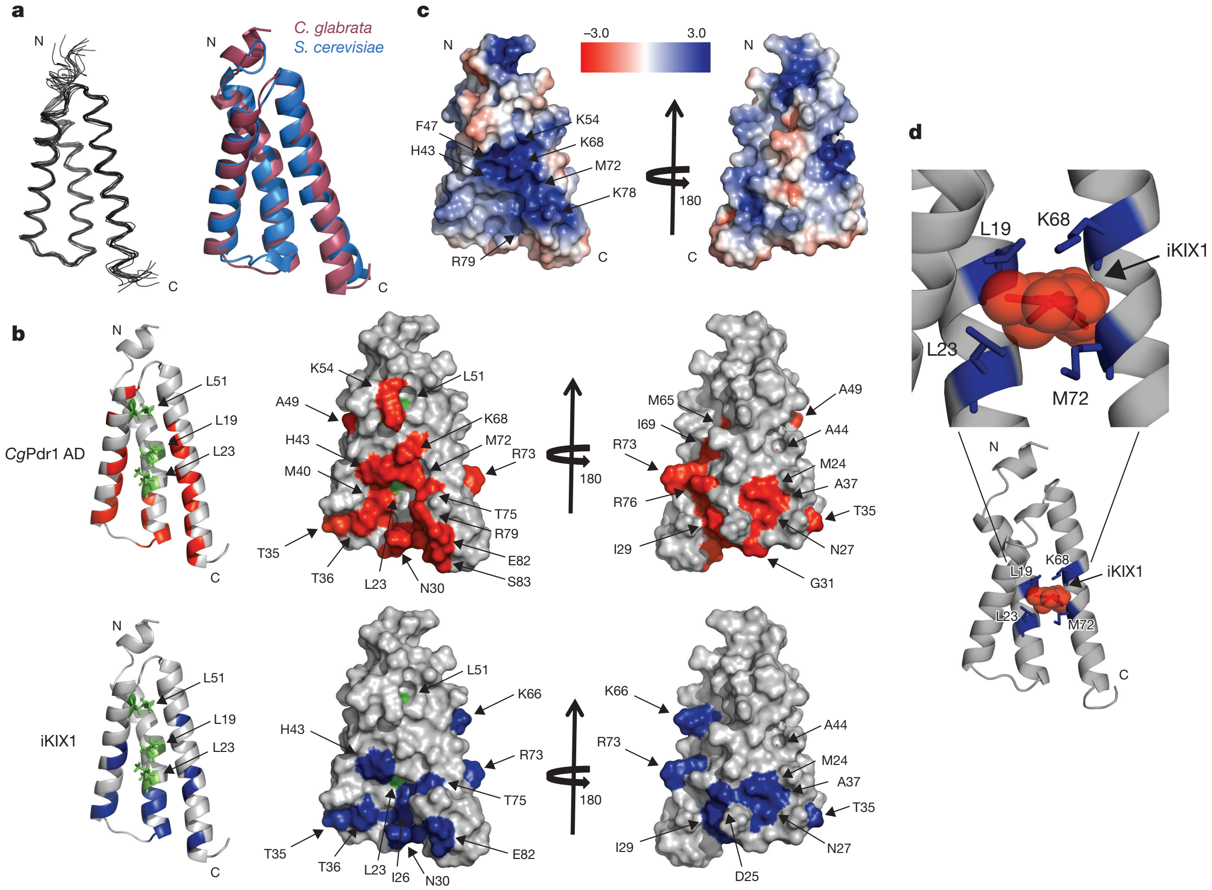

Figure 2 | Elucidation of the *Cg*Gal11A KIX domain structure; *Cg*Pdr1 AD and iKIX1 bind to a similar interface on the *Cg*Gal11A KIX domain. a, Backbone representation of the 10 lowest energy NMR structures of *Cg*Gal11A KIX domain; backbone r.m.s.d. ~ 0.7 Å, left. Overlay of *Cg*Gal11A (purple) and *S. cerevisiae* Gal11/Med15 (blue) KIX domains, with an overall r.m.s.d. of 2.0 Å (ref. 25), right. **b**, Chemical shift perturbations (CSPs) on the *Cg*Gal11A KIX domain in the presence of *Cg*Pdr1 AD (red) or iKIX1 (blue). Residues coloured in red or blue indicate a chemical shift perturbation greater than 2 s.d. Residues highlighted in green (L19, L23 and L51) represent important CSPs in the side-chain methyl groups of an ILV labelled sample. **c**, The iKIX1 and *Cg*Pdr1 AD target the hydrophobic groove on the *Cg*Gal11A KIX domain, which is surrounded by a basic patch. Residues H43, K54, K68, K78, R79, F47 and M72 present a positive electrostatic surface enclosing the binding interface. **d**, iKIX1 docked to the *Cg*Gal11A KIX domain. iKIX1 is depicted as red sticks and spheres. Residues near the binding site of iKIX1 are depicted as blue sticks. The methyl resonances of L19 and L23 experience considerable CSP upon addition of iKIX1.

identify hits with *in vivo* efficacy (Fig. 1a). We identified 5 compounds that reproducibly inhibited growth in a concentration-dependent manner only in the presence of ketoconazole (Extended Data Fig. 1). The most potent compound is referred to as iKIX1 (Fig. 1b, c). *In vitro* binding studies revealed that the K_d of the *Cg*Pdr1 AD for the *Cg*Gal11A KIX domain is 0.32 μM and the apparent K_i for iKIX1 is 18 μM (Fig. 1d).

To facilitate the elucidation of the mechanism of action of iKIX1, we determined the high-resolution solution structure of the *Cg*Gal11A KIX domain with a backbone root mean square deviation (r.m.s.d.) of 0.7 Å (Fig. 2 and Extended Data Table 1; PDB ID 4D7X). The *Cg*Gal11A KIX domain has 51% sequence identity and 61% similarity with the *S. cerevisiae* Gal11/Med15 KIX domain[3] with an overall r.m.s.d. of 2.0 Å (Fig. 2a and Extended Data Fig. 2c). The *Cg*Gal11A KIX domain forms a three-helix bundle harbouring an extensively hydrophobic core and a short helix at the N terminus (Fig. 2a). We determined interaction interfaces of the *Cg*Gal11A KIX domain with the *Cg*Pdr1 AD and iKIX1 (Fig. 2b) by chemical shift perturbation (CSP) analysis. The *Cg*Pdr1 AD and iKIX1 target the same large hydrophobic groove harboured by the three helices. Residues from all three helices constitute the interaction interface, and titration of an isoleucine, leucine, valine (ILV)-methyl labelled *Cg*Gal11A KIX domain reveals large CSPs on the three leucines (L19, L23 and L51) upon addition of *Cg*Pdr1 AD and iKIX1 (Extended Data Fig. 2b). The basic interaction interface on the KIX domain complements the acidic residues of *Cg*Pdr1 AD (Fig. 2c). Residues of the *Cg*Gal11A KIX domain that interact with *Cg*Pdr1 AD and iKIX1 overlap strongly, suggesting direct competitive binding as the mechanism of inhibition. Docking of iKIX1 to the *Cg*Gal11A KIX domain suggests extensive hydrogen bonding and hydrophobic interactions between iKIX1 and KIX domain residues (Fig. 2d and Extended Data Fig. 2a), matching the interaction interface mapped by CSP analysis.

To assess the *in vivo* effects of iKIX1 on Pdr1-dependent transcription, we initially used a strain in which the two *S. cerevisiae PDR1* orthologues (*ScPDR1* and *ScPDR3*) are deleted and which carries a plasmid expressing *CgPDR1*[3], and a heterologous luciferase gene driven by 3 pleiotropic drug response elements (PDREs). Luciferase activity was strongly induced by ketoconazole treatment; iKIX1 co-treatment was able to block this induction in a concentration-dependent manner (Fig. 3a).

A chromatin immunoprecipitation (ChIP) assay was used to examine Gal11/Med15 recruitment to Pdr1-regulated target genes in *S. cerevisiae* after iKIX1 treatment. Gal11/Med15 was rapidly recruited to the promoters of the Pdr1 target genes *PDR5* and *SNQ2* after ketoconazole addition; in contrast, ketoconazole-induced recruitment of Gal11/Med15 was abrogated when the cells were pre-treated with iKIX1 (Fig. 3b, Extended Data Fig. 3a). iKIX1 did not impede the constitutive occupancy of Pdr1 at the same Pdr1-regulated target genes (Extended Data Fig. 3b). Consistent with the ChIP data, iKIX1 strongly inhibited

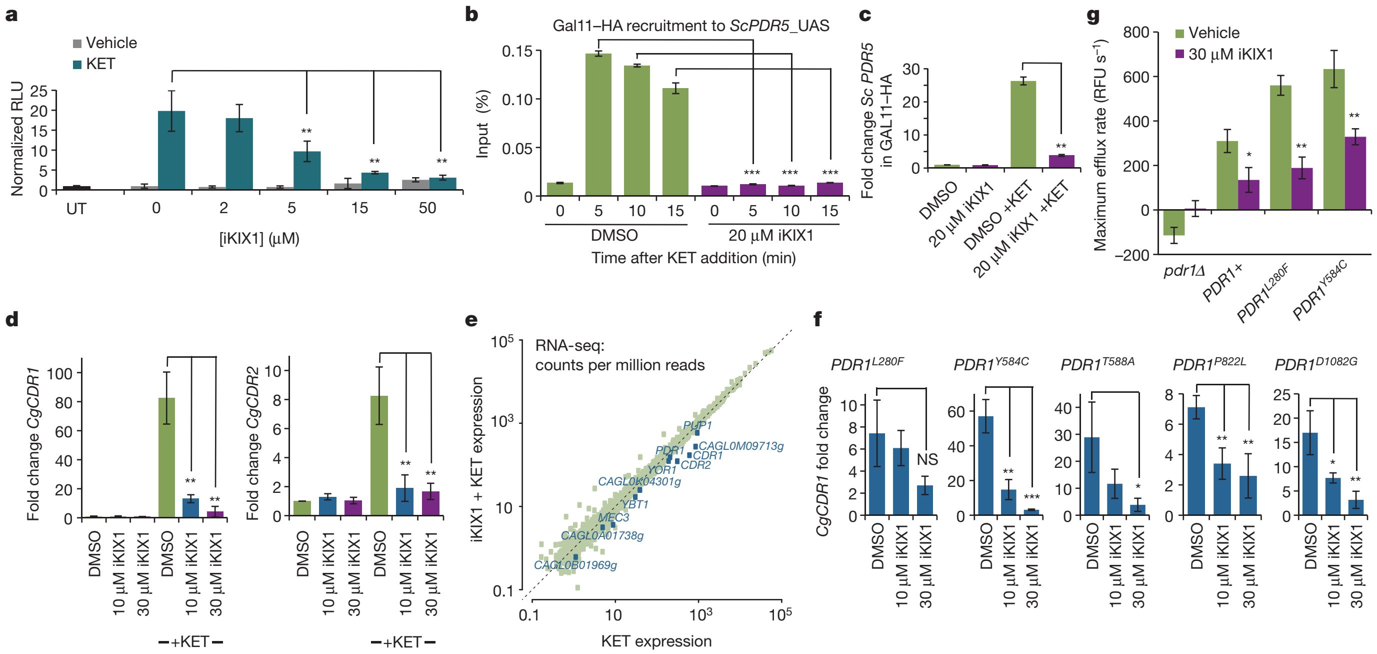

Figure 3 | iKIX1 blocks Gal11/Med15 recruitment and upregulation of Pdr1 target genes. a, iKIX1 inhibits ketoconazole-induced upregulation of luciferase activity in a dose-responsive manner in a *S. cerevisiae pdr1Δpdr3Δ* strain containing plasmid-borne *CgPDR1* and 3XPDRE-luciferase. UT, untreated control; $^{**}P < 0.001$. **b**, **c**, iKIX1 prevents the ketoconazole-induced recruitment of Gal11/Med15/Mediator to the upstream activating sequences (UAS) of the PDRE-regulated promoter *ScPDR5* (**b**), and *ScPDR5* induction (**c**). Representative experiment from two biological replicates (ChIP DNA and RNA from same experiment) is shown. Error bars indicate s.d. of technical replicates; $^{***}P < 0.00001$, $^{**}P < 0.0005$ by two-tailed Student's *t*-test. **d**, iKIX1 inhibits ketoconazole-induced transcriptional upregulation of *CgCDR1* and *CgCDR2* in a *CgPDR1* wild-type strain (SFY114). $^{**}P < 0.005$. **e**, RNA-seq analysis of a *C. glabrata* SFY114 (*PDR1* wild-type) strain pre-treated with iKIX1 or vehicle alone then induced with ketoconazole (iKIX1 + KET and KET, respectively). **f**, iKIX1 inhibits xenobiotic-induced *Cg*Pdr1 transcription in *Cg*Pdr1 gain-of-function mutants (amino acid changes indicated). Samples shown were induced with ketoconazole. $^{*}P < 0.05$ and $^{**}P < 0.01$ as compared to dimethylsulfoxide (DMSO) + ketoconazole control. **g**, iKIX1 inhibits rhodamine 6 G efflux in *C. glabrata* as compared to vehicle control. $^{*}P < 0.05$, $^{**}P < 0.005$ as compared to DMSO + ketoconazole control. **a**, **d**, **e**–**g**, Data represent the means of three biological replicates. Two-tailed Student's *t*-test used to determine *P* values; error bars represent means ±s.d.

azole-induced transcription of *Sc*Pdr1 target genes (Fig. 3c, Extended Data Fig. 3a, c).

Next, we determined the effect of iKIX1 on the transcription of *C. glabrata* Pdr1-regulated genes involved in drug efflux and multidrug resistance (*CgCDR1*, *CgCDR2* and *CgYOR1*). *Cg*Pdr1 targets were strongly upregulated after ketoconazole treatment[10,12]. However, pre-treatment with iKIX1 reduced target gene induction in a durable and concentration-dependent manner (Fig. 3d and Extended Data Fig. 4a, b). Treatment with iKIX1 alone did not significantly affect Pdr1-target gene induction (Extended Data Fig. 4c, d).

Next-generation RNA sequencing (RNA-seq) was employed to query the genome-wide effects of iKIX1 and azole treatments alone and in combination on the transcriptome in both *S. cerevisiae* and in *C. glabrata*. In accord with previous reports[10,16], azole treatment upregulates Pdr1-dependent genes in both yeasts, such as the drug efflux pumps *ScPDR5* and *CgCDR1* (Supplementary Tables 1 and 2). Combined azole and iKIX1 treatment strongly blunted expression of many azole-activated and Pdr1-dependent genes in both *S. cerevisiae* and *C. glabrata* (Fig. 3e, Extended Data Fig. 3d and Supplementary Tables 1 and 2), consistent with prior data and the proposed mechanism of action of iKIX1. iKIX1 alone affected very different sets of genes in *S. cerevisiae* and *C. glabrata* (Supplementary Tables 1–3). Treatment of *S. cerevisiae* and *C. glabrata* cells with iKIX1 did not significantly alter the expression of *PDR1* or *GAL11/MED15* after azole treatment (Extended Data Fig. 3e). Together, these findings suggest that the primary mechanism of synergistic antifungal effects of iKIX1 with azoles is through blocking the azole-stimulated and Pdr1-dependent drug efflux pathway.

To ascertain iKIX1 efficacy in azole-resistant *C. glabrata* strains, we examined the effects of iKIX1 on *Cg*Pdr1 target gene expression in a set of isogenic strains with gain-of-function *CgPDR1* mutations originally identified in azole-resistant *C. glabrata* clinical isolates[9]. iKIX1 reduced azole-induced transcription of *Cg*Pdr1 target genes (for example, *CgCDR1*) in a concentration-dependent manner in all strains tested (Fig. 3f and Extended Data Fig. 4d).

To investigate whether these transcriptional effects translated to functional effects on drug efflux rates, we used the fluorescent compound rhodamine 6 G, a substrate of the *Cg*Cdr1 efflux pump[17,18]. Maximum efflux rates were significantly decreased in *PDR1* wild-type or gain-of-function strains pre-treated with iKIX1, as compared to vehicle control (Fig. 3g and Extended Data Fig. 5).

Owing to its ability to reduce efflux pump gene expression and pump activity, we predicted that iKIX1 could restore azole-sensitivity to *CgPDR1* gain-of-function mutant strains. Isogenic *C. glabrata* strains with wild-type or single gain-of-function alterations across *Cg*Pdr1 (Fig. 4a) were tested for their sensitivity to fluconazole or ketoconazole on gradient plates with increasing concentrations of iKIX1 or vehicle. As expected, a *CgPDR1* wild-type strain was sensitive to both fluconazole and ketoconazole, whereas *CgPDR1* gain-of-function mutant strains grew robustly in the presence of azoles. iKIX1 restored azole-sensitivity to *PDR1* gain-of-function mutant strains in a concentration-dependent manner (Fig. 4b). *CgPDR1* wild-type strains also exhibited increased growth inhibition in the presence of both iKIX1 and azole versus single agents alone (Extended Data Fig. 6a, b).

On the basis of the strong combination effect of azoles and iKIX1 in the *CgPDR1*^{L280F} mutant we focused follow-up studies on this mutant strain. To investigate whether azoles and iKIX1 act in a synergistic or additive manner in *CgPDR1* wild-type and *CgPDR1*^{L280F} mutant strains, we assessed growth in checkerboard assays with ketoconazole and iKIX1. In the wild-type *CgPDR1* strain, the combination

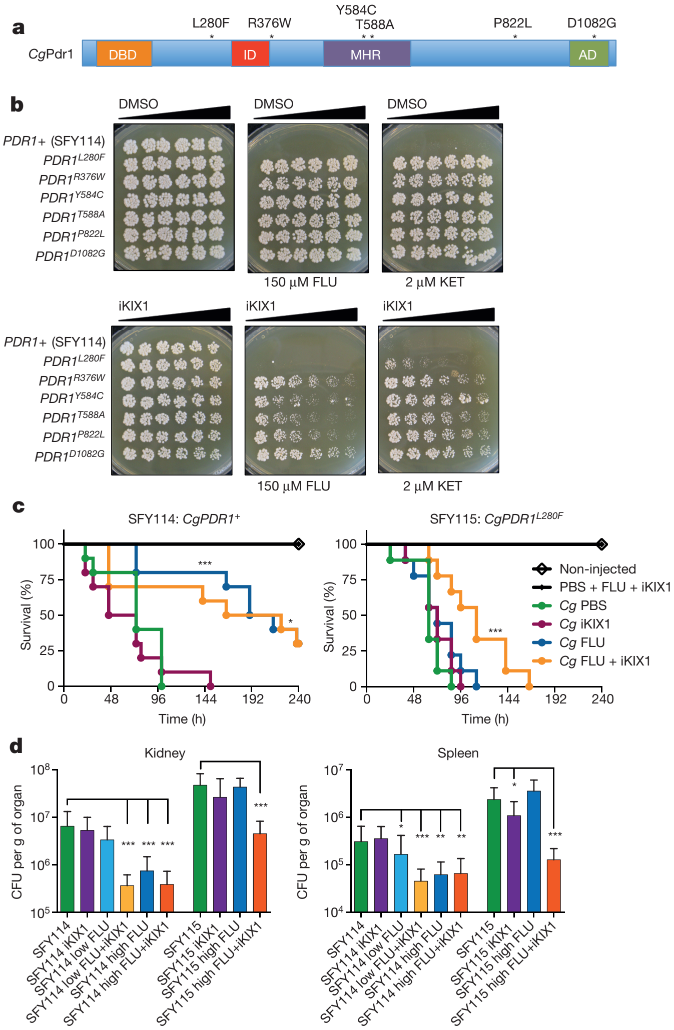

Figure 4 | iKIX1 as a co-therapeutic in models of *C. glabrata* disseminated disease. a, Schematic showing *Cg*Pdr1 gain-of-function alterations in relation to putative functional domains. DBD, DNA-binding domain; ID, inhibitory domain; MHR, middle homology region; AD, activation domain. **b**, iKIX1 restores the efficacy of azoles towards *CgPDR1* gain-of-function mutants. Plates contained increasing concentrations of vehicle control (DMSO) or iKIX1 to 150 μM in the absence or presence of fluconazole (FLU) or ketoconazole (KET). **c**, iKIX1 in combination with fluconazole but not fluconazole alone significantly extended survival of *G. mellonella* larvae injected with $CgPDR1^{L280F}$ (SFY115, $n = 9$). For SFY114, $n = 10$. $^*P < 0.05$, $^{***}P < 0.001$ as compared to PBS vehicle control. Statistical differences measured using a log-rank (Mantel–Cox) test. **d**, iKIX1 combination treatment with 25 mg kg^{-1} fluconazole (low FLU) reduces fungal tissue burden in the kidney or spleen of mice injected with *CgPDR1* wild-type (SFY114); iKIX1 in combination with 100 mg kg^{-1} fluconazole (high FLU) reduces fungal tissue burden in the kidney or spleen of mice injected with $CgPDR1^{L280F}$ (SFY115). $n = 5$ mice for each treatment condition; $^*P < 0.05$, $^{**}P < 0.005$ and $^{***}P < 0.0001$ as compared to no treatment. Statistical differences measured using a Wilcoxon rank-sum test; error bars represent means ±s.d.

of ketoconazole and iKIX1 was additive (Extended Data Fig. 6c). However, the $CgPDR1^{L280F}$ mutant exhibited synergistic growth inhibition with iKIX1 and ketoconazole combination treatment, with combination indices <1 (Extended Data Fig. 6d), in concordance with the spot-plating assay.

We carried out a limited analysis exploring the chemical space around the iKIX1 scaffold using commercial and custom synthesized iKIX1 analogues, identifying several compounds that lost activity in all assays; one analogue (A2) is shown in Extended Data Fig. 7a–d. This example, together with data from iKIX1 analogues and the docked structure of iKIX1 to the *Cg*Gal11A KIX domain, supports a model where iKIX1 engages the core of the KIX domain using an array of hydrophobic and hydrogen-bond contacts.

We used two metazoan model systems to evaluate the potential utility of iKIX1 as a co-therapeutic with fluconazole to treat disseminated *C. glabrata* infection. The larvae of the moth *Galleria mellonella* has been used as a model to test the pathogenicity of a wide variety of human pathogens[19]. We used a *G. mellonella* survival assay to determine the virulence of *C. glabrata PDR1* wild-type or $PDR1^{L280F}$ strains in the presence of fluconazole, iKIX1, or a combination of the two (Fig. 4c). Larvae were injected with *C. glabrata* and a single injection of fluconazole (50 mg kg^{-1}), iKIX1 (25 mg kg^{-1}), a combination of the two, or vehicle; survival was monitored every 24 h. *G. mellonella* injected with wild-type *CgPDR1* was sensitive to fluconazole alone, and exhibited no significant alterations in survival with a fluconazole-iKIX1 combination. However, in *G. mellonella* larvae injected with a $CgPDR1^{L280F}$ strain, whereas the single agents fluconazole or iKIX1 did not significantly increase survival compared to vehicle, co-treatment with iKIX1 and fluconazole significantly increased survival ($P < 0.001$).

Prior to mammalian studies, we sought to evaluate the potential toxicity of iKIX1 in mammalian cells (Extended Data Fig. 7e, f). Human HepG2 cells treated with iKIX1 revealed toxicity only at high concentrations of iKIX1 ($IC_{50} \approx 100\,\mu M$). iKIX1 had no effect on the transcription of SREBP-target genes at concentrations up to 100 μM, indicating its specificity for the fungal Gal11/Med15 KIX domain[4]. We also assessed the *in vitro* stability and *in vivo* mouse pharmacokinetics of iKIX1 and found that iKIX1 exhibited favourable drug-like properties and *in vivo* exposure in these studies (Extended Data Fig. 8 g, h).

To evaluate the therapeutic potential of iKIX1 and azole antifungal co-therapy in a mammalian model, we initially turned to an established mouse model of disseminated fungal disease[11]. Mice were inoculated with *C. glabrata* by tail-vein injection and were dosed peritoneally once-daily with 100 mg kg^{-1} fluconazole (high FLU), 100 mg kg^{-1} iKIX1, a combination of the two, or vehicle alone. After 7 days, mice injected with a *CgPDR1* wild-type strain exhibited significantly reduced tissue fungal burden in the kidney and spleen following fluconazole treatment alone; iKIX1 co-treatment did not result in further reductions (Fig. 4d). In contrast, in mice injected with the azole-resistant $CgPDR1^{L280F}$ strain, only co-treatment with iKIX1 and fluconazole resulted in significant (~tenfold) reductions in fungal burdens in the kidney and spleen ($P < 0.0001$) (Fig. 4d). Similar results were observed with the clinically isolated $CgPDR1^{+}$ and $CgPDR1^{L280F}$ strains DSY562 and DSY565 (Extended Data Fig. 8a). Consistent with previous studies[9], the fungal burden in mice infected with the $CgPDR1^{L280F}$ strain was higher than those infected with wild-type Cg*PDR1* strains, suggesting that *PDR1* mutant strains may be more virulent *in vivo*. Similar but less pronounced results were found in mice injected with a $CgPDR1^{P822L}$ strain (Extended Data Fig. 8b). When mice were injected with a *CgPDR1* wild-type strain and dosed with 25 mg kg^{-1} fluconazole (low FLU) alone or in combination with iKIX1, fluconazole alone poorly reduced tissue burden, whereas combination treatment resulted in significant (~tenfold) reductions in fungal burdens in both organs ($P < 0.0001$) (Fig. 4d). These results suggest that iKIX1 combination treatment with azole may be therapeutically desirable even in the absence of *CgPDR1* gain-of-function mutations. Mice infected with a *Cgpdr1* null strain were more sensitive to iKIX1 alone; unlike mice infected with $CgPDR1^{+}$ or $CgPDR1^{L280F}$ strains, low doses of iKIX1 did not further reduce fungal burden in *Cgpdr1* null infections (Extended Data Fig. 8c, d).

CgPDR1 gain-of-function mutations are also known to control adherence to host cells[20]. As previously observed[20], a $PDR1^{L280F}$ mutant increased relative adherence to epithelial cells as compared to a *PDR1* wild-type strain. Strikingly, iKIX1 treatment alone reduced adherence to levels similar to a *PDR1* wild-type strain (Extended Data Fig. 8e). Ketoconazole alone or co-treatment with iKIX1 also reduced relative adherence to levels comparable to a *PDR1* wild-type strain. To assess

the role of iKIX1 in modulating adhesion in an infection model, we turned to a mouse model of urinary tract infection[21]. In both the bladder and kidney, iKIX1 alone was sufficient to decrease fungal load after infection with either a *PDR1* wild-type strain or a *PDR1*^{L280F} strain (Extended Data Fig. 8f), suggesting that iKIX1 may indeed modulate adhesion.

The proportion of azole-resistant *C. glabrata* (up to 20% in the US) and the emergence of multidrug resistance (approximately 40% of echinocandin-resistant isolates are azole-resistant) shows the need for novel treatments that can target these resistant populations[22,23]. Our results demonstrate that small-molecule disruption of the interaction between the *Cg*Gal11A KIX domain and the *Cg*Pdr1 activation domain is a therapeutically tractable method for resensitizing azole-resistant *C. glabrata* to standard azole antifungal treatment (Extended Data Fig. 9).

Online Content Methods, along with any additional Extended Data display items and Source Data, are available in the online version of the paper; references unique to these sections appear only in the online paper.

Received 15 December 2014; accepted 29 December 2015.
Published online 17 February 2016.

1. Conaway, R. C. & Conaway, J. W. Function and regulation of the Mediator complex. *Curr. Opin. Genet. Dev.* **21,** 225–230 (2011).
2. Poss, Z. C., Ebmeier, C. C. & Taatjes, D. J. The Mediator complex and transcription regulation. *Crit. Rev. Biochem. Mol. Biol.* **48,** 575–608 (2013).
3. Thakur, J. K. *et al.* A nuclear receptor-like pathway regulating multidrug resistance in fungi. *Nature* **452,** 604–609 (2008).
4. Yang, F. *et al.* An ARC/Mediator subunit required for SREBP control of cholesterol and lipid homeostasis. *Nature* **442,** 700–704 (2006).
5. Paul, S. & Moye-Rowley, W. S. Multidrug resistance in fungi: regulation of transporter-encoding gene expression. *Front. Physiol.* **5,** 143 (2014).
6. Prasad, R. & Goffeau, A. Yeast ATP-binding cassette transporters conferring multidrug resistance. *Annu. Rev. Microbiol.* **66,** 39–63 (2012).
7. Pfaller, M. A. *et al.* Variation in susceptibility of bloodstream isolates of *Candida glabrata* to fluconazole according to patient age and geographic location in the United States in 2001 to 2007. *J. Clin. Microbiol.* **47,** 3185–3190 (2009).
8. Pfaller, M. A., Messer, S. A., Moet, G. J., Jones, R. N. & Castanheira, M. *Candida* bloodstream infections: comparison of species distribution and resistance to echinocandin and azole antifungal agents in Intensive Care Unit (ICU) and non-ICU settings in the SENTRY Antimicrobial Surveillance Program (2008–2009). *Int. J. Antimicrob. Agents* **38,** 65–69 (2011).
9. Ferrari, S. *et al.* Gain of function mutations in CgPDR1 of *Candida glabrata* not only mediate antifungal resistance but also enhance virulence. *PLoS Pathog.* **5,** e1000268 (2009).
10. Ferrari, S., Sanguinetti, M., Torelli, R., Posteraro, B. & Sanglard, D. Contribution of CgPDR1-regulated genes in enhanced virulence of azole-resistant *Candida glabrata*. *PLoS One* **6,** e17589 (2011).
11. Silva, L. V. *et al.* Milbemycins: more than efflux inhibitors for fungal pathogens. *Antimicrob. Agents Chemother.* **57,** 873–886 (2013).
12. Vermitsky, J. P. *et al.* Pdr1 regulates multidrug resistance in *Candida glabrata*: gene disruption and genome-wide expression studies. *Mol. Microbiol.* **61,** 704–722 (2006).
13. Sanguinetti, M. *et al.* Mechanisms of azole resistance in clinical isolates of *Candida glabrata* collected during a hospital survey of antifungal resistance. *Antimicrob. Agents Chemother.* **49,** 668–679 (2005).
14. Caudle, K. E. *et al.* Genomewide expression profile analysis of the *Candida glabrata* Pdr1 regulon. *Eukaryot. Cell* **10,** 373–383 (2010).
15. Roehrl, M. H., Wang, J. Y. & Wagner, G. A general framework for development and data analysis of competitive high-throughput screens for small-molecule inhibitors of protein-protein interactions by fluorescence polarization. *Biochemistry* **43,** 16056–16066 (2004).
16. DeRisi, J. *et al.* Genome microarray analysis of transcriptional activation in multidrug resistance yeast mutants. *FEBS Lett.* **470,** 156–160 (2000).
17. Sanglard, D., Ischer, F., Calabrese, D., Majcherczyk, P. A. & Bille, J. The ATP binding cassette transporter gene CgCDR1 from *Candida glabrata* is involved in the resistance of clinical isolates to azole antifungal agents. *Antimicrob. Agents Chemother.* **43,** 2753–2765 (1999).
18. Silva, L. V. *et al.* Milbemycins: more than efflux inhibitors for fungal pathogens. *Antimicrob. Agents Chemother.* **57,** 873–886 (2012).
19. Arvanitis, M., Glavis-Bloom, J. & Mylonakis, E. Invertebrate models of fungal infection. *Biochim. Biophys. Acta* **1832,** 1378–1383 (2013).
20. Vale-Silva, L., Ischer, F., Leibundgut-Landmann, S. & Sanglard, D. Gain-of-function mutations in PDR1, a regulator of antifungal drug resistance in *Candida glabrata*, control adherence to host cells. *Infect. Immun.* **81,** 1709–1720 (2013).
21. Chen, Y. L. *et al.* Convergent evolution of calcineurin pathway roles in thermotolerance and virulence in *Candida glabrata. G3* **2,** 675–691 (2012).
22. Farmakiotis, D., Tarrand, J. J. & Kontoyiannis, D. P. Drug-resistant *Candida glabrata* infection in cancer patients. *Emerg. Infect. Dis.* **20,** 1833–1840 (2014).
23. Pfaller, M. A. *et al.* Frequency of decreased susceptibility and resistance to echinocandins among fluconazole-resistant bloodstream isolates of *Candida glabrata*. *J. Clin. Microbiol.* **50,** 1199–1203 (2011).
24. Robert, X. & Gouet, P. Deciphering key features in protein structures with the new ENDscript server. *Nucleic Acids Res.* **42,** W320–W324 (2014).
25. EUCAST definitive document EDef 7.1: method for the determination of broth dilution MICs of antifungal agents for fermentative yeasts. *Clin. Microbiol. Infect.* **14,** 398–405 (2008).
26. Krissinel, E. & Henrick, K. Secondary-structure matching (SSM), a new tool for fast protein structure alignment in three dimensions. *Acta Crystallogr. D* **60,** 2256–2268 (2004).

Supplementary Information is available in the online version of the paper.

Acknowledgements We are grateful to P. Coote, E. Papadopoulos, R. Oh and R. E. Luna for helpful discussions and advice with data analysis and manuscript preparation. We acknowledge the ICCB-Longwood Screening Facility at Harvard Medical School for assistance with the high-throughput screens and access to the compound libraries, and the MGH Next Gen sequencing core for RNA-seq library construction. Mouse plasma and microsomal stability experiments were carried out at the Scripps Research Institute and iKIX1 pharmacokinetic parameters were assessed by Sai Life Sciences Limited. We acknowledge support from the National Institute of Health (grants GM047467 to G.W. and A.M.N. and EB002026 to G.W.). J.L.N. was supported by an NSERC fellowship.

Author Contributions J.L.N., A.B., G.W., A.M.N. and H.A. conceived and designed the studies. A.B. and H.A. performed experiments relating to protein structure, small molecule screening and small molecule-protein interaction and data analysis. J.B. and G.M. performed the docking and free energy calculations. V.G., S.J.B. and N.S.G. designed the synthesis for iKIX1 and its analogues. J.L.N. performed the *in vivo* small molecule screen, luciferase, ChIP, transcription, efflux, spot plating, combination index and mammalian cell culture (HepG2) experiments. Y.-J.S. performed transcription and efflux experiments. J.L.N. prepared samples for RNA-seq analysis; bioinformatic analysis was carried out by F.J. and R.I.S.; L.A.V.-S. and D.S. designed and performed moth survival and adhesion assays. R.T., B.P. and M.S. designed and executed mouse fungal burden and UTI model studies. J.L.N., A.B., G.W., A.M.N. and H.A. wrote the manuscript with input from the team.

Author Information Coordinates and NMR resonance assignments have been deposited in the Protein Data Bank (PDB code 4D7X) and Biological Magnetic Resonance Data Bank (BMRB code 25372). RNA-seq data have been deposited in the Gene Expression Omnibus (GEO) under accession GSE74361. Reprints and permissions information is available at www.nature.com/reprints. The authors declare no competing financial interests. Readers are welcome to comment on the online version of the paper. Correspondence and requests for materials should be addressed to G.W. (gerhard_wagner@hms.harvard.edu), or A.M.N. (naar@helix.mgh.harvard.edu) or H.A. (hari_arthanari@hms.harvard.edu).

Library name	Number of molecules
Biomol ICCB Known Bioactives3	430
Ninds Custom Collection 2	1,040
Prestwick 1 Collection	1,120
Asinex 1	12,378
ChemBridge 3	10,560
ChemDiv 4	14,677
Enamine 2	26,576
Life Chemicals 1	3,893
Maybridge 5	3,212
ChemDiv 3	16,544
Maybridge 1	8,800
ChemDiv 6	44,000
Total number of molecules	143,280

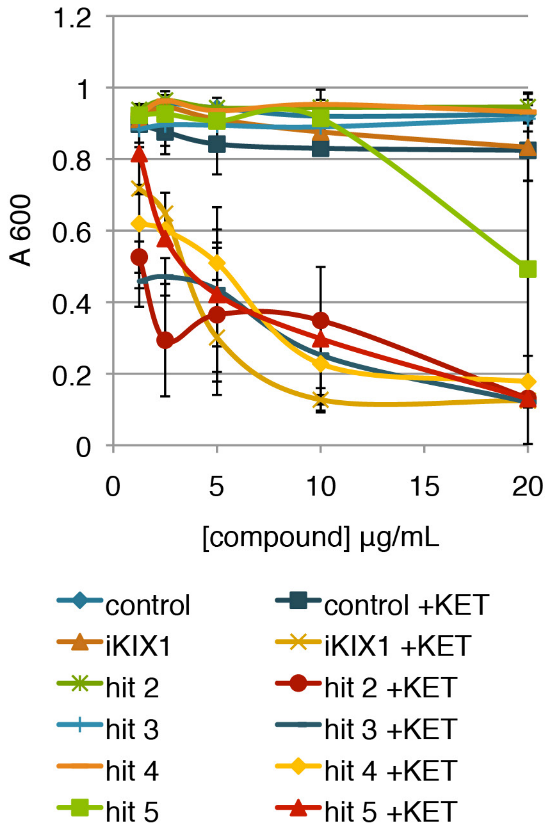

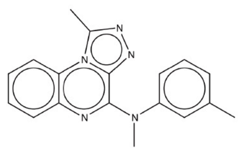

hit 2

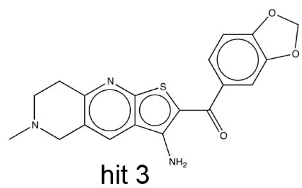

hit 3

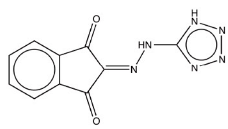

hit 4

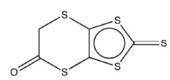

hit 5

Extended Data Figure 1 | List of compound libraries screened and top hits from the secondary *in vivo* viability screen. Left, table of compound libraries that were screened using a fluorescence polarization assay at the Institute of Chemistry & Cell Biology (ICCB) facility at Harvard Medical School. Right, an *S. cerevisiae* viability screen identifies small molecules that preferentially inhibit growth of *S. cerevisiae* in a concentration-dependent manner in the presence of 5 µM ketoconazole. Top hits from the screen are shown; $A_{600\ nm}$ values are the average of values from duplicate plates. Error bars denote mean ± s.d.

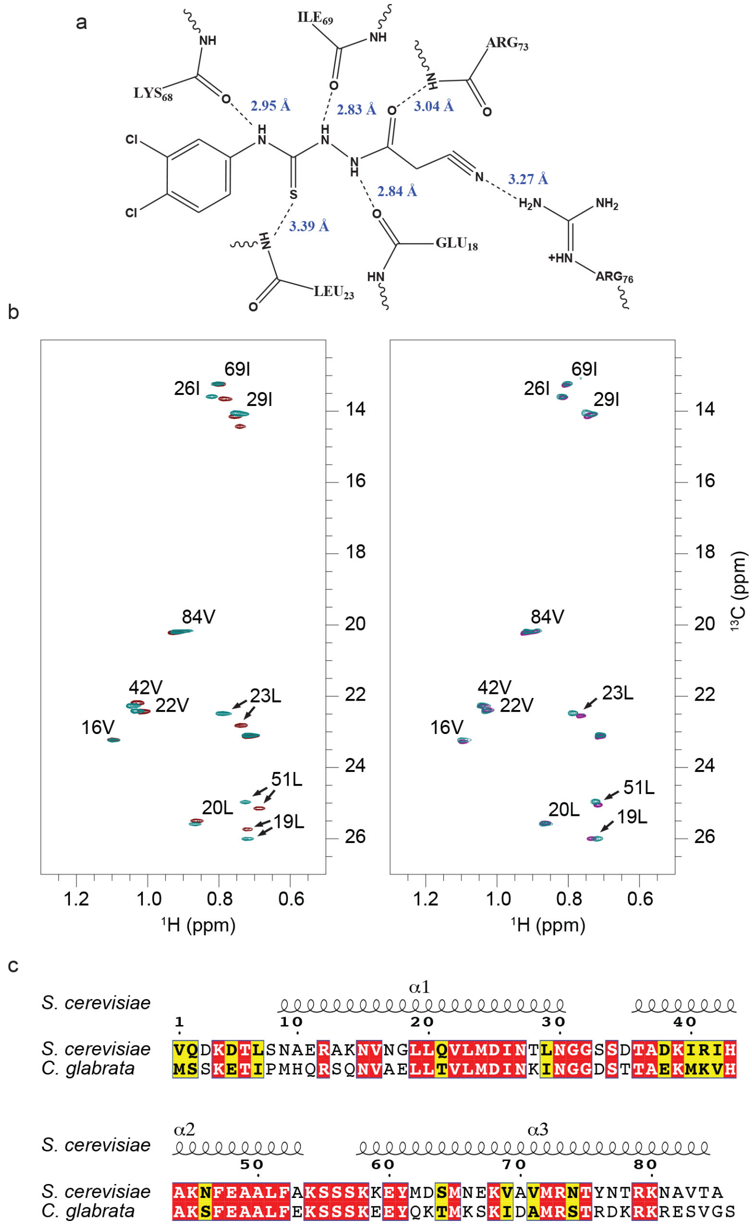

Extended Data Figure 2 | Mapping the interaction interface of iKIX1 and *Cg*Pdr1 AD on the *Cg*Gal11A KIX domain and molecular details of iKIX1 interaction with the *Cg*Gal11A KIX domain based on targeted docking. a, 2-dimensional representation of the H-bonding network between the *Cg*Gal11A KIX domain and iKIX1 based on docking studies. **b**, Chemical shift perturbations (CSPs) of ILV methyl resonances. Left, ^{1}H-^{13}C heteronuclear single quantum coherence (HSQC) spectrum showing ILV methyl resonances of *Cg*Gal11A KIX domain in presence (brown) and absence (teal) of *Cg*Pdr1 AD (twofold excess). Right, ^{1}H-^{13}C HSQC spectrum showing ILV methyl resonances of *Cg*Gal11A KIX domain in presence (purple) and in absence (teal) of iKIX1 (fourfold excess). Three leucines (L19, L23, L51) show significant CSPs in both spectra. **c**, Sequence alignment of the *C. glabrata* Gal11A and *S. cerevisiae* Gal11/Med15 KIX domains[24].

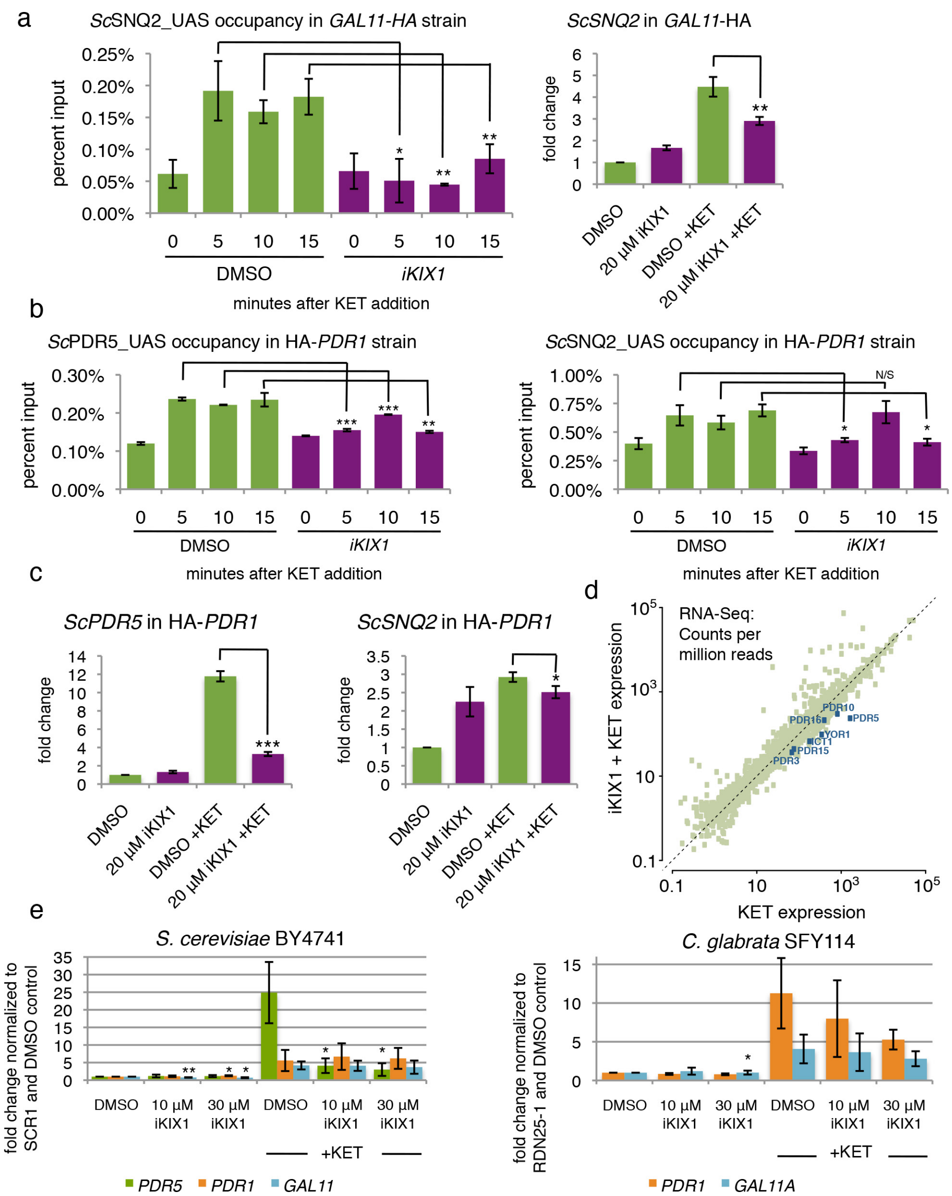

Extended Data Figure 3 | iKIX1 blocks Gal11/Med15 recruitment and upregulation of Pdr1 target genes. a, iKIX1 prevents the ketoconazole-induced recruitment of *Sc*Gal11/Med15/Mediator to the upstream activating sequences (UAS) of the PDRE-regulated promoter *ScSNQ2* and transcriptional upregulation of *ScSNQ2*. **b**, Haemagglutinin (HA)–tagged Pdr1 occupies PDRE-regulated promoters of *ScPDR5* and *ScSNQ2* in the presence of 20 µM iKIX1 or vehicle (DMSO) control before and following ketoconazole addition. **c**, 20 µM iKIX1 inhibits ketoconazole-induced upregulation of *Sc*Pdr1 target genes *ScPDR5* and *ScSNQ2* in the HA–Pdr1 strain. RNA was harvested concurrently with representative chromatin immunoprecipitation experiment shown in **b** at $t = 0$ min (DMSO, 20 µM iKIX1) and $t = 15$ min after ketoconazole induction (DMSO + KET, 20 µM iKIX1 + KET). Transcripts are normalized to *ScSCR1* and un-induced DMSO control. **a**–**c**, Representative experiment from two biological replicates is shown. Error bars represent mean ±s.d. of technical replicates; **P* < 0.05, ***P* < 0.01 and ****P* < 0.001 as calculated by two-tailed Student's *t*-test. **d**, RNA-seq analysis of a wild-type *S. cerevisiae* strain (BY4741) pre-treated with iKIX1 or vehicle alone then induced with ketoconazole (iKIX1 + KET and KET, respectively) demonstrate a blunted induction of Pdr1 target genes following iKIX1 pre-treatment. Data represent means of three biological replicates. **e**, iKIX1 pre-treatment does not significantly alter the transcript levels of *PDR1* or *GAL11/GAL11A* in *S. cerevisiae* or *C. glabrata* after azole induction. Cells were pre-incubated with vehicle (DMSO) or iKIX1 and then induced with 40 µM ketoconazole (+KET) for 15 min before harvest. Average value of three biological replicates is shown and error bars represent mean ±s.d.; **P* < 0.05, ***P* < 0.001 as compared to DMSO or DMSO+KET control, calculated by two-tailed Student's *t*-test.

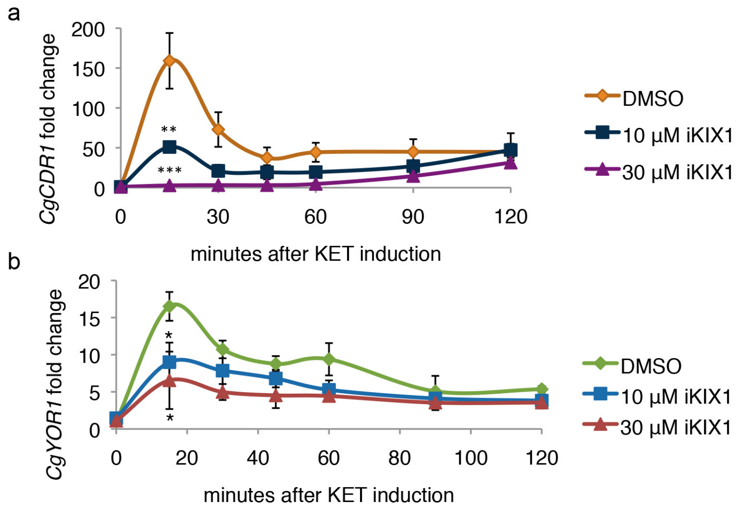

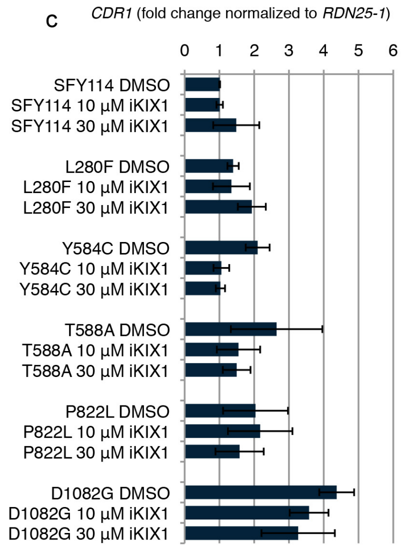

d

	average *CDR1* delta Cp, no KET	standard deviation, no KET	average *CDR1* delta Cp, +KET	standard deviation, + KET
SFY114 (+) DMSO	16.00	0.32	10.59	0.18
SFY114 (+) 10 μM iKIX1	15.99	0.22	11.79	0.71
SFY114 (+) 30 μM iKIX1	15.57	0.57	13.78	0.40
L280F DMSO	15.59	0.52	13.26	0.39
L280F 10 μM iKIX1	15.69	0.33	13.40	0.58
L280F 30 μM iKIX1	15.11	0.33	14.68	0.28
Y584C DMSO	15.10	0.35	10.35	0.21
Y584C 10 μM iKIX1	16.09	0.17	12.36	0.36
Y584C 30 μM iKIX1	16.14	0.20	14.51	0.19
T588A DMSO	14.64	0.85	11.30	0.55
T588A 10 μM iKIX1	15.52	0.34	12.60	0.52
T588A 30 μM iKIX1	15.49	0.36	14.57	0.76
P822L DMSO	15.05	0.70	13.13	0.33
P822L 10 μM iKIX1	15.06	0.44	14.35	0.30
P822L 30 μM iKIX1	15.57	0.57	14.91	0.63
D1082G DMSO	13.89	0.13	11.96	0.37
D1082G 10 μM iKIX1	14.15	0.26	13.05	0.35
D1082G 30 μM iKIX1	14.37	0.41	14.52	0.48

Extended Data Figure 4 | iKIX1 pre-treatment durably represses azole-induced *Cg*Pdr1-dependent transcription but not basal levels of *Cg*Pdr1-dependent transcripts. a, b, With iKIX1 pre-treatment, *Cg*Pdr1-dependent transcription of **(a)** *CgCDR1* and **(b)** *CgYOR1* remains repressed 120 min after ketoconazole induction. SFY114 (*PDR1* wild-type) cells were pre-incubated with vehicle (DMSO) or iKIX1 and then induced with 40 μM ketoconazole (+KET). Transcript levels were assessed by quantitative RT–PCR before and for 120 min following ketoconazole induction. Transcript levels are normalized to *CgRDN25-1* and un-induced vehicle control (DMSO) at $t = 0$. **c**, iKIX1 treatment alone does not have significant effects on *Cg*Pdr1 target gene induction either in the presence of wild-type (SFY114) or gain-of-function mutant *CgPDR1* (amino acid alterations indicated). **d**, Table of average *CgCDR1* delta Cp values ($Cp_{CgCDR1} - Cp_{CgRDN25\text{-}1}$) and corresponding standard deviation for quantitative real-time PCR experiments shown in Fig. 3 f and Extended Data Fig. 4c. **a**–**d**, For all panels of Extended Data Fig. 4, average value of three biological replicates is shown and error bars represent ±s.d.; $*P < 0.05$, $**P < 0.01$, and $***P < 0.005$ as compared to vehicle + ketoconazole control. P values calculated using two-tailed Student's t-test.

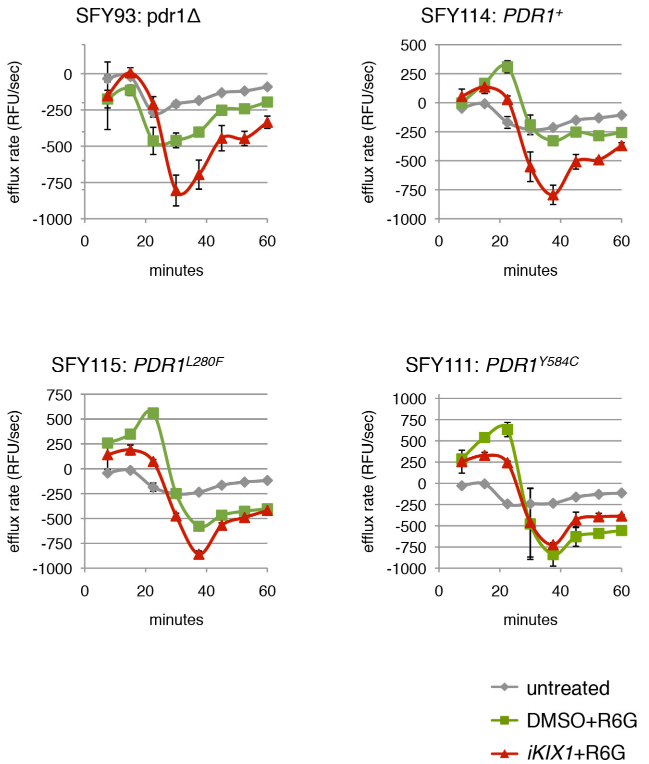

Extended Data Figure 5 | iKIX1 inhibits efflux of rhodamine 6 G in *PDR1* wild-type, *PDR1*^{L280F} and *PDR1*^{Y584C} strains. Data points indicate mean of three biological replicates and error bars represent mean ±s.d.

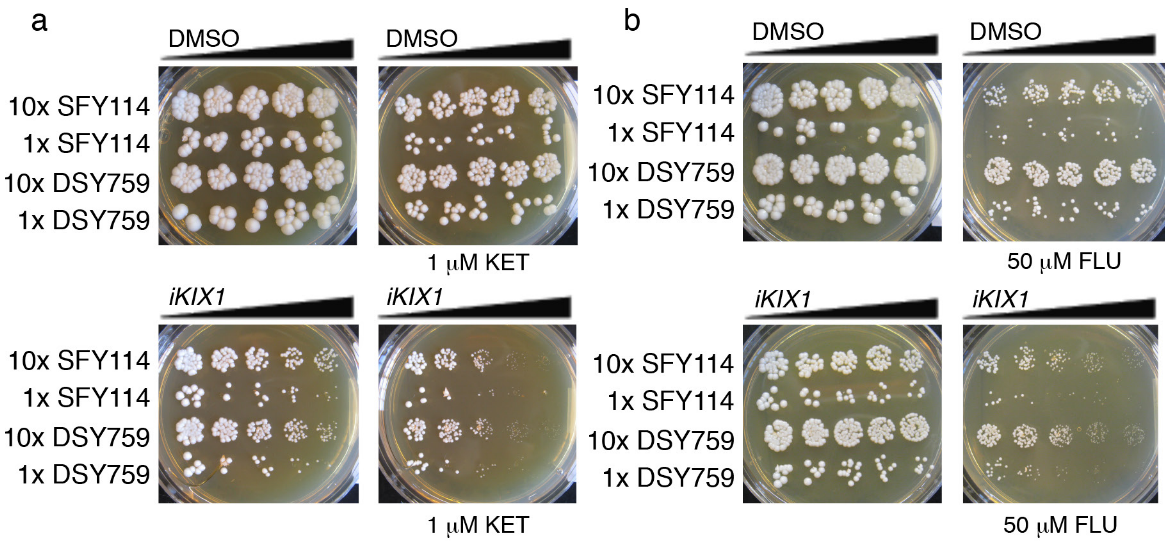

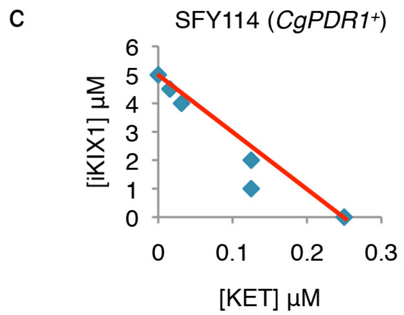

IC50 KET (μM)	IC50 *iKIX1* (μM)	CI
0	5	1.00
0.015625	4.5	0.96
0.03125	4	0.93
0.125	2	0.90
0.125	1	0.70
0.25	0	1.00

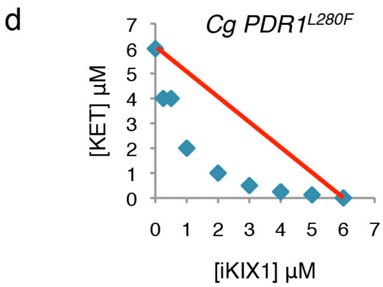

IC50 KET (μM)	IC50 *iKIX1* (μM)	CI
-	6	N/A
0.125	5	0.85
0.25	4	0.71
0.5	3	0.58
1	2	0.50
2	1	0.50
4	0.5	0.75
4	0.25	0.71
6	-	N/A

Extended Data Figure 6 | iKIX1 increases the sensitivity of *Cg* strains bearing wild-type *CgPDR1* to azole treatment and synergistically enhances azole sensitivity in a *CgPDR1*^{L280F} mutant strain. a, **b**, Two strains bearing wild-type Cg*PDR1* alleles (SFY114, DSY759) were plated at concentrations differing by tenfold (10×, 1×) on plates containing increasing concentrations of iKIX1 to 300 μM in the presence or absence of 1 μM ketoconazole (**a**) or iKIX1 to 250 μM in the presence or absence of 50 μM fluconazole (**b**). **c**, iKIX1 and ketoconazole have additive effects on the growth of a *CgPDR1* wild-type strain. **d**, iKIX1 and ketoconazole synergistically inhibit the growth of the *CgPDR1*^{L280F} mutant. **c**, **d**, The EUCAST broth microdilution method[25] was used to assess the effects of iKIX1 and ketoconazole combination treatment. Growth, as assessed by $A_{540\ nm}$, was normalized to no drug control. All combination indices (CI) for the *CgPDR1*^{L280F} mutant were less than 1, indicating synergy. A representative of three biological replicates is shown and the red line indicates a combination index of 1.

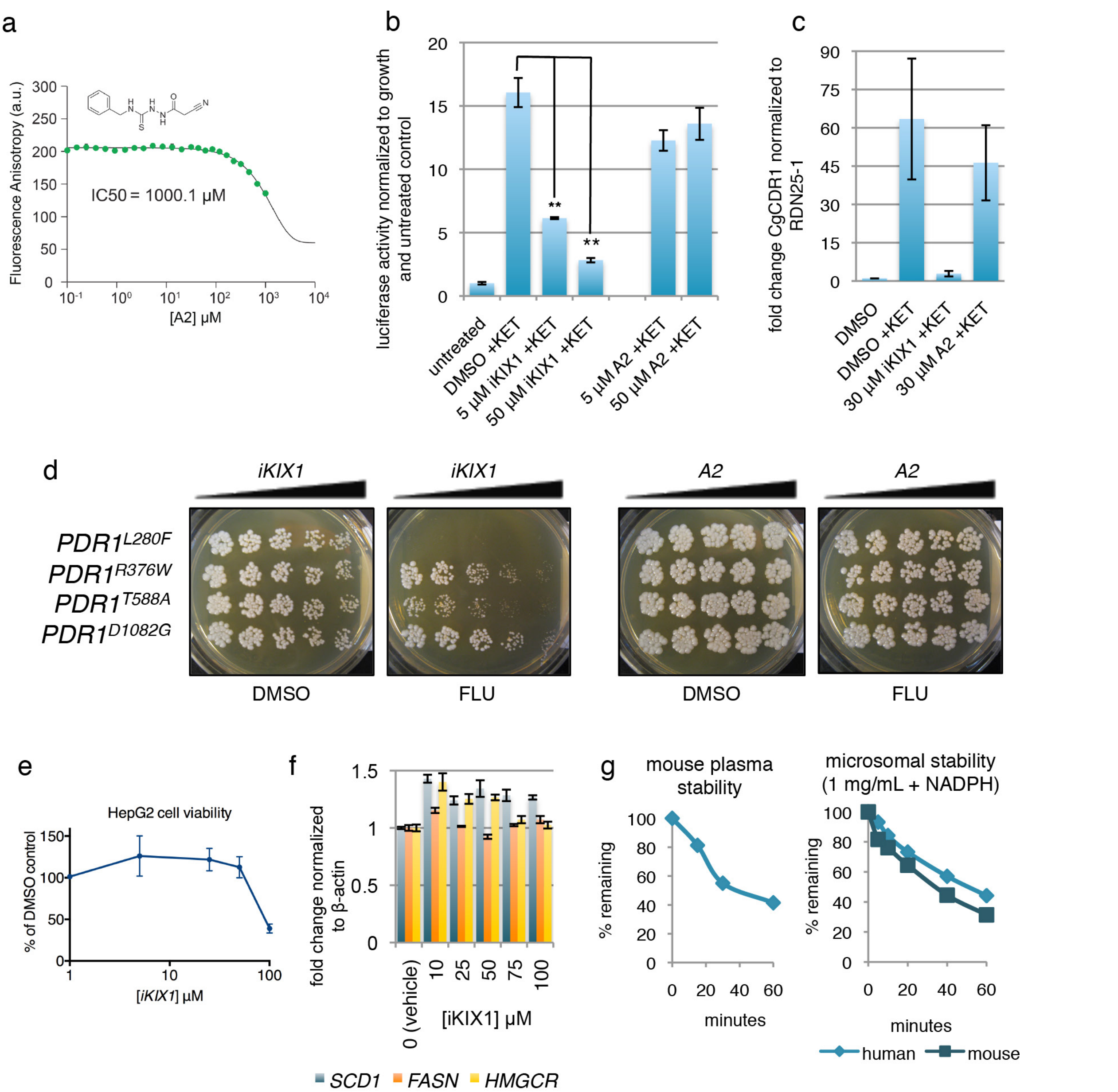

h

Route	Dose (mg/kg)	T_{max} (h)	C_0/C_{max} (ng/mL)	AUC_{last} (hr·ng/mL)	AUC_{INF} (hr·ng/mL)	$T_{1/2}$ (h)	Cl (mL/min/kg)	V_{ss} (L/kg)	F (%)
i.v.	2	-	12674.51	1502.00	1521.92	5.93	21.90	2.23	-
p.o.	10	0.25	336.59	455.95	456.05	-	-	-	6

Extended Data Figure 7 | iKIX1 exhibits favourable drug-like properties and an inactive analogue highlights the importance of the electron withdrawing chloride groups on the aromatic ring of iKIX1. a–d, A structurally similar iKIX1 analogue (*A2*) lacking electron-withdrawing groups increases the IC_{50} in the fluorescence polarization assay (**a**) and abolishes activity in the *S. cerevisiae* luciferase reporter assay (**b**), repression of *CgCDR1* expression (**c**), and synergistic *C. glabrata* cell growth inhibition with azoles (**d**). Error bars in **b**, **c** indicate mean ±s.d. of technical replicates (reads/real-time PCR reactions, respectively). $^{**}P < 0.005$; statistical differences calculated using two-tailed Student's *t*-test. **e**, iKIX1 inhibits viability of HepG2 cells at concentrations >50 µM. The mean of 3 biological replicates is shown; error bars represent means ±s.d. **f**, iKIX1 exhibits no effect on transcription of SREBP-target genes in HepG2 cells at concentrations up to 100 µM. Biological duplicates were assessed; representative experiment is shown and error bars represent means ±s.d. of technical (real-time PCR) replicates. **g**, Mouse plasma stability of iKIX1 and mouse and human microsomal stability of iKIX1, $n = 1$. **h**, *In vivo* pharmacokinetic parameters of iKIX1, $n = 3$ mice per time point.

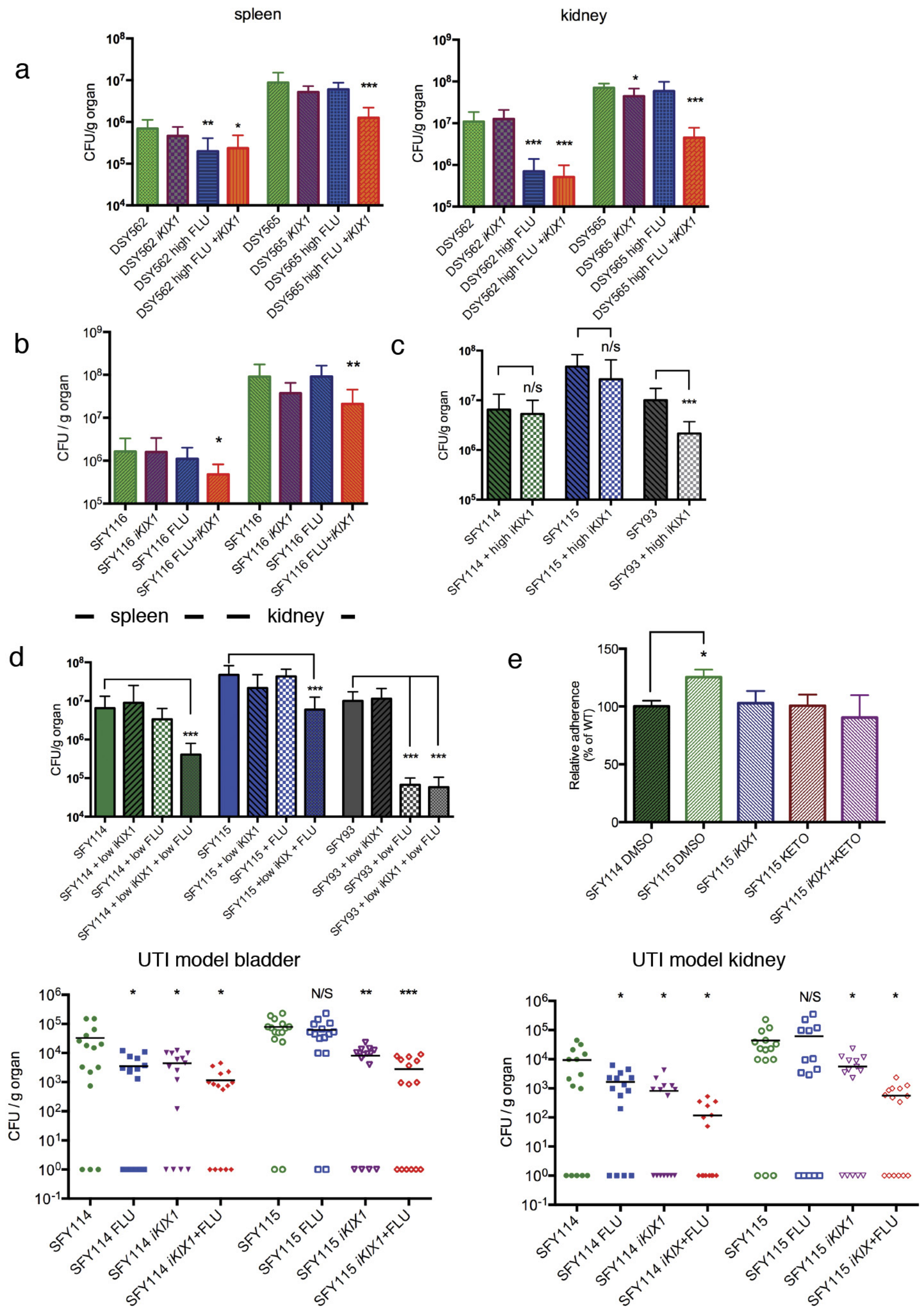

Extended Data Figure 8 | iKIX1-fluconazole combination treatment reduces fungal tissue burden by *CgPDR1*$^{+}$ or *CgPDR1* gain-of-function mutant strains in disseminated disease models; iKIX1 alone reduces adherence and fungal burden in a UTI model. a, Clinical isolates DSY562/DSY565 (azole sensitive and *PDR1*^{L280F} azole-resistant strains, respectively) behave similarly to SFY114/SFY115 (isogenic *PDR1*$^{+}$ and *PDR1*^{L280F} strains, shown in Fig. 4d) in the mouse infection model. $n = 10$ mice for each treatment condition; $*P < 0.01$, $**P < 0.005$ and $***P < 0.0001$. **b**, iKIX1 combination treatment with fluconazole reduces fungal tissue burdens in the spleen or kidney of mice injected with *C. glabrata PDR1*^{P822L} (SFY116). $n = 5$ mice for each treatment condition; $**P < 0.01$ and $*P < 0.05$. **c**, 100 mg kg^{-1} day^{-1} iKIX1 (high iKIX1) treatment of mice infected with SFY93 (*pdr1Δ*) significantly reduces fungal burden in a mouse infection model (colony forming units (CFU) per g of kidney) alone as compared to SFY114 (*PDR1*$^{+}$) or SFY115 (*PDR1*^{L280F}). $n = 10$ mice for each treatment condition; $*P < 0.01$, $**P < 0.005$, $***P < 0.0001$. **d**, Mice infected with SFY114 (*PDR1*$^{+}$), SFY115 (*PDR1*^{L280F}) or SFY93 (*pdr1Δ*) were treated with low (10 mg kg^{-1} day^{-1}) iKIX1, low fluconazole (low FLU; 25 mg kg^{-1} day^{-1}), fluconazole at 100 mg kg^{-1} day^{-1} or combination with the two. iKIX1 did not confer additional reductions in CFU per g of kidney with SFY93 infection. $n = 10$ mice for each treatment condition. $***P < 0.0005$. **e**, iKIX1 and ketoconazole reduce adherence of *CgPDR1*^{L280F} (SFY115) to CHO-Lec2 cells. Adherence is normalized to SFY114 DMSO control; each column represents the average of 4 biological replicates. $*P < 0.05$ as compared to SFY114 DMSO control. **f**, iKIX1 (100 mg kg^{-1} day^{-1}) or fluconazole significantly reduces fungal burden in the bladder and kidney in a urinary tract infection model in mice. $n = 15$ mice were infected in each group and points at 0 $\log_{10}$ CFU per g of organ fell below the detection limit of the method (50 CFU per g of organ). $*P < 0.05$, $**P < 0.005$. **a–f**, Statistical differences were measured using a Mann–Whitney/Wilcoxon rank-sum test as compared to no treatment control; error bars represent means ±s.d.

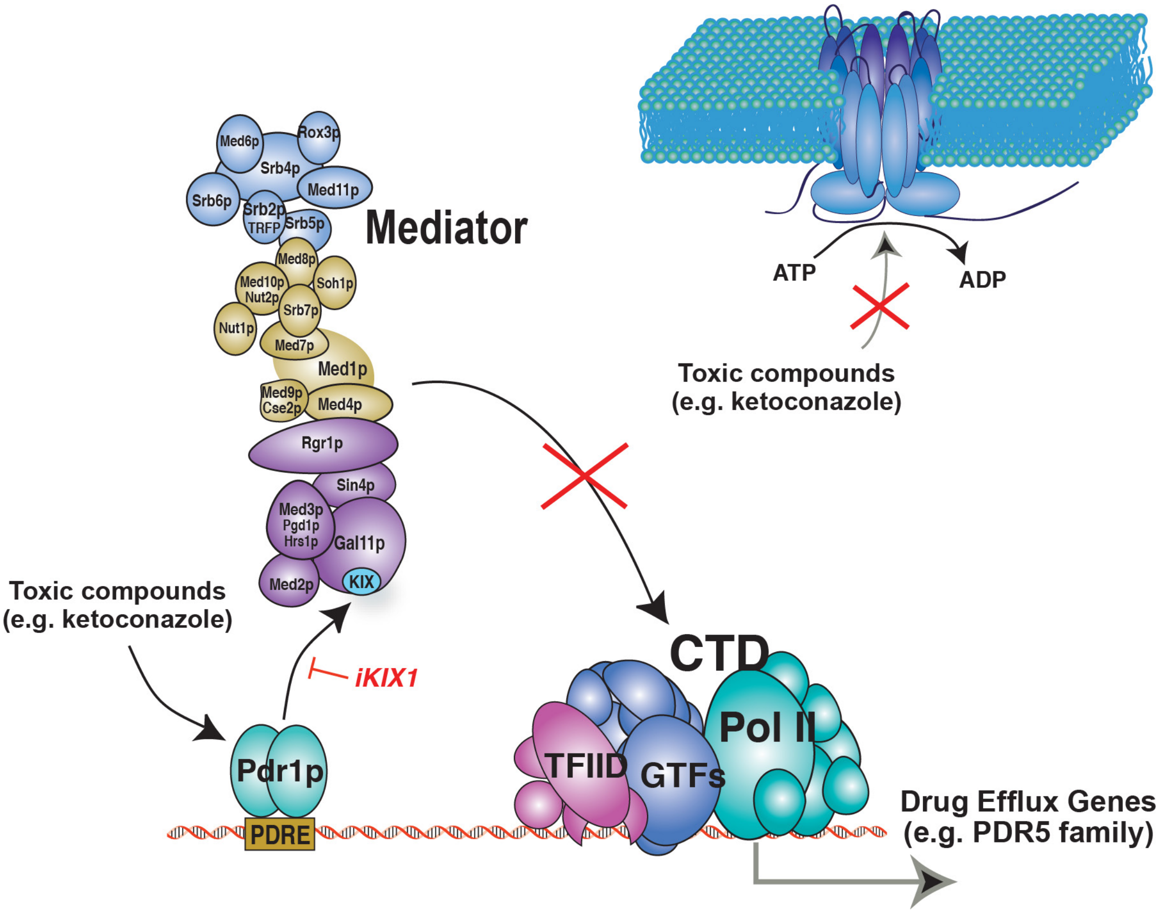

Extended Data Figure 9 | Model of iKIX1 function. iKIX1 functions as a co-therapeutic in combination with an azole, blocking the azole-induced recruitment of Gal11/Med15-Mediator to Pdr1 target genes upon azole-treatment and preventing the upregulation of Pdr1 target genes, including those which encode drug efflux pumps. This figure has been adapted from ref. 3.

Extended Data Table 1 | Summary of quality statistics for the ensemble of 10 structures calculated with AMBER explicit water refinement and list of experimental restraints

	Protein
NMR distance and dihedral constraints	
Distance constraints	
Total NOE	1718
Intra-residue	602
Inter-residue	1116
Sequential (|i-j| = 1)	517
Medium-range (|i-j| ≤ 4)	488
Long-range (|i-j| ≥ 5)	111
Hydrogen bonds	0
Total dihedral angle restraints	158
phi	79
psi	79
Structure statistics	
Violations (mean and s.d.)	
Distance constraints (Å)	0.083 ± 0.039
Dihedral angle constraints (°)	2.407 ± 0.357
Max. dihedral angle violation (°)	10.267
Max. distance constraint violation (Å)	0.248
Deviations from idealized geometry	
Bond lengths (Å)	0.013
Bond angles (°)	1.9
Average pairwise r.m.s.d.** (Å)	
Heavy	1.1
Backbone	0.7

**Pairwise r.m.s.d. was calculated among ordered residues (3-83) of 10 refined structures.

doi:10.1038/nature16982

Tumour-specific proline vulnerability uncovered by differential ribosome codon reading

Fabricio Loayza-Puch[1]*, Koos Rooijers[1]*, Levi C. M. Buil[2], Jelle Zijlstra[1], Joachim F. Oude Vrielink[1], Rui Lopes[1], Alejandro Pineiro Ugalde[1], Pieter van Breugel[1], Ingrid Hofland[3], Jelle Wesseling[4], Olaf van Tellingen[2], Axel Bex[5] & Reuven Agami[1,6]

Tumour growth and metabolic adaptation may restrict the availability of certain amino acids for protein synthesis. It has recently been shown that certain types of cancer cells depend on glycine, glutamine, leucine and serine metabolism to proliferate and survive[1–4]. In addition, successful therapies using L-asparaginase-induced asparagine deprivation have been developed for acute lymphoblastic leukaemia[5]. However, a tailored detection system for measuring restrictive amino acids in each tumour is currently not available. Here we harness ribosome profiling[6] for sensing restrictive amino acids, and develop diricore, a procedure for differential ribosome measurements of codon reading. We first demonstrate the functionality and constraints of diricore using metabolic inhibitors and nutrient deprivation assays. Notably, treatment with L-asparaginase elicited both specific diricore signals at asparagine codons and high levels of asparagine synthetase (ASNS). We then applied diricore to kidney cancer and discover signals indicating restrictive proline. As for asparagine, this observation was linked to high levels of PYCR1, a key enzyme in proline production[7], suggesting a compensatory mechanism allowing tumour expansion. Indeed, PYCR1 is induced by shortage of proline precursors, and its suppression attenuated kidney cancer cell proliferation when proline was limiting. High PYCR1 is frequently observed in invasive breast carcinoma. In an *in vivo* model system of this tumour, we also uncover signals indicating restrictive proline. We further show that CRISPR-mediated knockout of PYCR1 impedes tumorigenic growth in this system. Thus, diricore has the potential to reveal unknown amino acid deficiencies, vulnerabilities that can be used to target key metabolic pathways for cancer treatment.

In previous work we used ribosome profiling to map changes in translation of wild-type and disease-triggering mutant mitochondria[8]. A mitochondrial disease-promoting tryptophan transfer RNA (tRNA) mutation elicited specific pausing of mitochondrial ribosomes at tryptophan codons and enrichment of ribosome-protected fragments (RPFs) covering these sites. We hypothesized that also in the cytosol global occupancy of ribosome positions could be used as a cellular detector of alterations in the availability of amino acid for protein synthesis. To examine this issue we constructed a protocol to measure differential ribosome codon reading (diricore), which is based on ribosome profiling measurements. We performed two complementary analyses, subsequence and 5′-end density (Fig. 1a). The positions 9, 12 and 15 from the 5′-end of the RPFs correspond to the E (exit), P (peptide bond), and A (tRNA recruitment and reading codon) sites of the ribosome[9].

To evaluate our approach we first examined ribosome profiling performed on yeast treated with 3-amino-1,2,4-triazole (3-AT), an inhibitor of histidine synthesis[10]. As expected, subsequence analysis resulted in strong signals in the two histidine-codons at the reading codon (position 15, Fig. 1b). RPF density analysis of histidine codons, but not control phenylalanine, showed a vast increase at position 15 (Fig. 1c). Out-of-frame and randomization analyses indicated a significant and robust signal (Fig. 1b and Extended Data Fig. 1a). Second, we tested harringtonine, an agent that immobilizes initiating ribosomes and depletes elongating ones[11,12], in human cells. As expected, diricore detected a significant and robust increased signal only at the initiator ATG codon (Fig. 1d, e and Extended Data Fig. 1b). This signal was at the P-site (position 12), coinciding with harringtonine's function in blocking elongation. Third, we analysed by diricore the response of cancer cells to asparagine deprivation using L-asparaginase treatment. This uncovered a specific signal at asparagine codons in the treated cells (Fig. 1f), which was highly reproducible and statistically significant (Extended Data Fig. 2a, b). Out-of-frame and randomization analyses showed that only asparagine codons at position 15 give a true signal, excluding bias in the data (Extended Data Figs 2c and 1c). Interestingly, in response to L-asparaginase the expression of the enzyme responsible for asparagine synthesis in the cells (ASNS) increased ~fourfold (Fig. 1g, Extended Data Fig. 2d), providing evidence for a feedback loop activated in response to asparagine deprivation. To verify the asparagine-specific signal by diricore we performed tRNA-aminoacylation measurements[13] (Extended Data Fig. 2e). This analysis indicated a significant increase in the non-aminoacylated forms of the asparagine (Asn)-tRNAs GTT and ATT, but not of the controls leucine (Leu)-tRNA CAG and valine (Val)-tRNA TAC (Fig. 1h). As the total levels of Asn-tRNAs did not change following asparaginase treatment (Extended Data Fig. 2f), our results link asparagine availability with Asn-tRNA-aminoacylation and the emergence of asparagine codon signals in diricore. Altogether, we provide here evidence indicating that diricore is able to detect specific signals of amino acid deficiencies.

Next, we tested diricore in conditions of vast global translation changes using basal and luminal breast cancer cell lines (MDA-MB-231 and Hs587T, and T47D and MCF7, respectively). While basal cells are highly sensitive to glutamine deprivation, luminal cells are relatively resistant owing to sustained control of translation elongation by maintaining inhibitory phosphorylation at threonine 56 of the key elongation factor eEF2 (refs 14, 15 and Fig. 2a, b). Following glutamine deprivation, diricore revealed markedly reduced signals in the initiator-ATG codon position 12 of the basal cells, while little signal was observed in the luminal ones (Fig. 2c). In contrast, diricore signals at glutamine codons appeared only in the deprived luminal cells.

[1]Division of Biological Stress Response, The Netherlands Cancer Institute, Plesmanlaan 121, 1066 CX Amsterdam, The Netherlands. [2]Department of Bio-Pharmacology/ Mouse Cancer Clinic, The Netherlands Cancer Institute, Plesmanlaan 121, 1066 CX Amsterdam, The Netherlands. [3]Core Facility Molecular Pathology and Biobanking, The Netherlands Cancer Institute, Plesmanlaan 121, 1066 CX Amsterdam, The Netherlands. [4]Molecular Pathology, The Netherlands Cancer Institute, Plesmanlaan 121, 1066 CX Amsterdam, The Netherlands. [5]Division of Surgical Oncology, Department of Urology The Netherlands Cancer Institute, Plesmanlaan 121, 1066 CX Amsterdam, The Netherlands. [6]Department of Genetics, Erasmus University Medical Center, Wytemaweg 80, 3015 CN Rotterdam, The Netherlands.
*These authors contributed equally to this work.

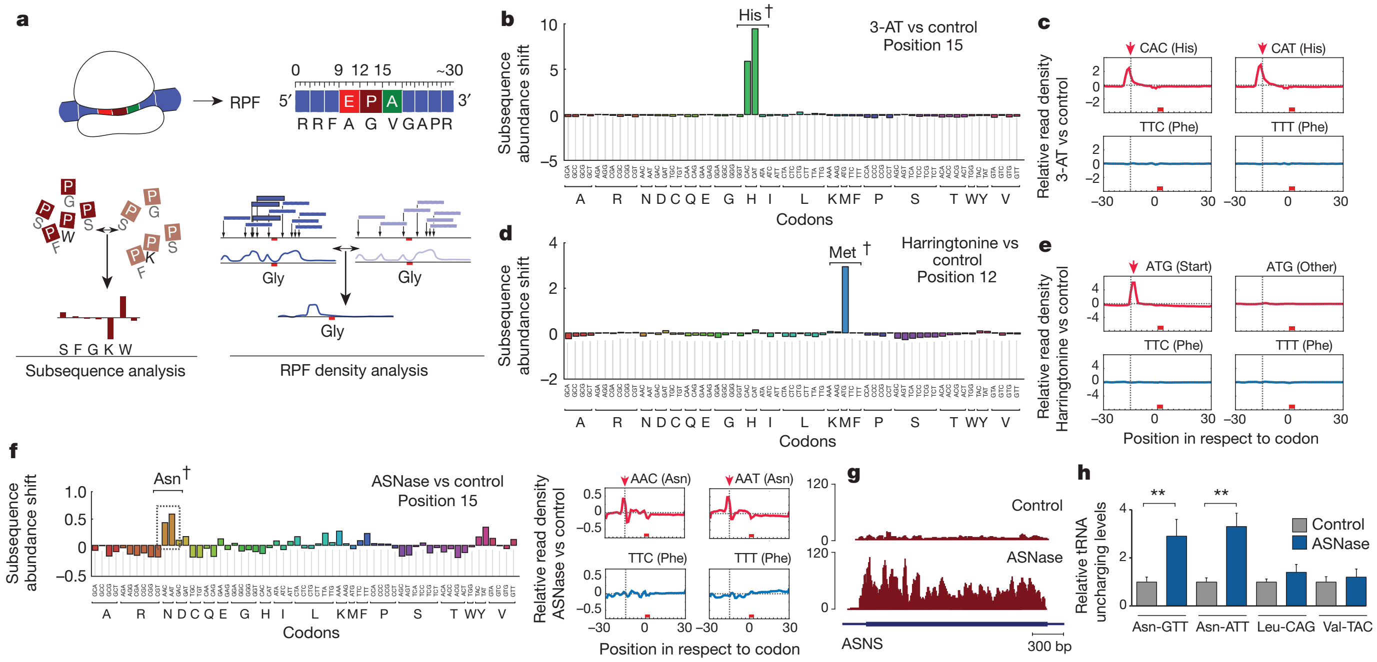

Figure 1 | Ribosome positions as readout for amino acid availability for protein synthesis. a, A scheme of the protocol for differential ribosome codon reading (diricore). Subsequence analysis examined the codons at 9, 12 and 15 nucleotides from the 5′-ends of RPFs. RPF density analysis examined every instance of a codon throughout the transcriptome to inspect the local RPF 5′-end density surrounding that codon. While the latter makes use of all RPFs, subsequence analysis takes into account only those that are in frame with the coding sequence. A detailed overview is available in Extended Data Fig. 1g, h. **b**, **c**, Diricore analysis of data obtained from ref. 10 of yeast cells treated with 3-amino-1,2,4-triazole (3-AT), an inhibitor of His production. †$P < 1 \times 10^{-300}$ for CAC and CAT His-codons by out of frame analysis. **d**, **e**, Diricore analysis of the SUM1315 cells treated with harringtonine, an inhibitor of initiation of translation[11,12]. †$P < 1 \times 10^{-250}$ for the ATG codon by out of frame analysis. **f**, Diricore analysis of PC3 cells treated for 48 h with L-asparaginase (ASNase). †$P = 1.05 \times 10^{-5}$ for AAT and $P = 1.11 \times 10^{-4}$ for AAC Asn-codons by out of frame analysis. **g**, Ribosome profiling analysis shows overexpression of the *ASNS* gene, a key component in the synthesis of asparagine. **h**, Analysis of the relative levels of non-aminoacylated tRNAs in PC3 cells treated for 48 h with L-asparaginase. For **h**, error bars represent s.d.; $n = 3$ independent biological replicates; $^{**}P < 0.01$ by Student's *t*-test.

Thus, diricore signals at the initiator-ATG codon can be used to estimate global changes in translation, and specific codon signals appear in conditions where strong global inhibition of translation had not arisen.

Next, we examined whether diricore could detect restrictive amino acids in cancer. We obtained directly from surgery a kidney with clear cell renal cell carcinoma (ccRCC), and sampled two normal and four tumour tissues for ribosome profiling (Extended Data Fig. 3a). Quality control of the ribosome profiling indicated high and comparable quality of all samples, and gene expression analysis verified ccRCC (Extended Data Fig. 3b–d). Notably, diricore analysis comparing tumour to normal tissues revealed two consistent, statistically significant, and robust signals in methionine and proline codons (Fig. 3a and Extended Data Figs 4a, b and 1d). Control comparisons showed no signal, and other codons (for example, alanine) were either not consistent in all tumours or did not show signal in the 5′ density plots (Extended Data Fig. 4c, d).

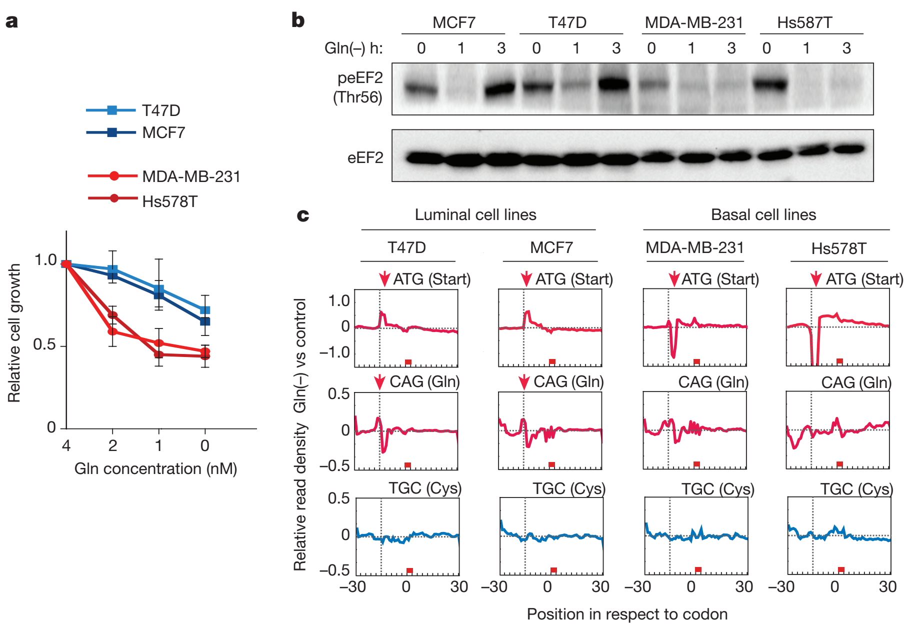

Figure 2 | Estimation of global changes in translation and specific codon signals by diricore. a, Normalized cell growth of the indicated breast cancer cell lines at different concentrations of glutamine. Measurements were taken 48 h after plating. peEF2, phosphorylated eEF2. **b**, Immunoblot analysis of cells grown in complete media or under glutamine starvation for the indicated times. **c**, Diricore analysis of cell lines deprived of glutamine for 48 h. For **a**, values represent the mean of three independent biological replicates; error bars represent s.d. Cutoff for RPF density shift plots in **c** was 25 reads per window.

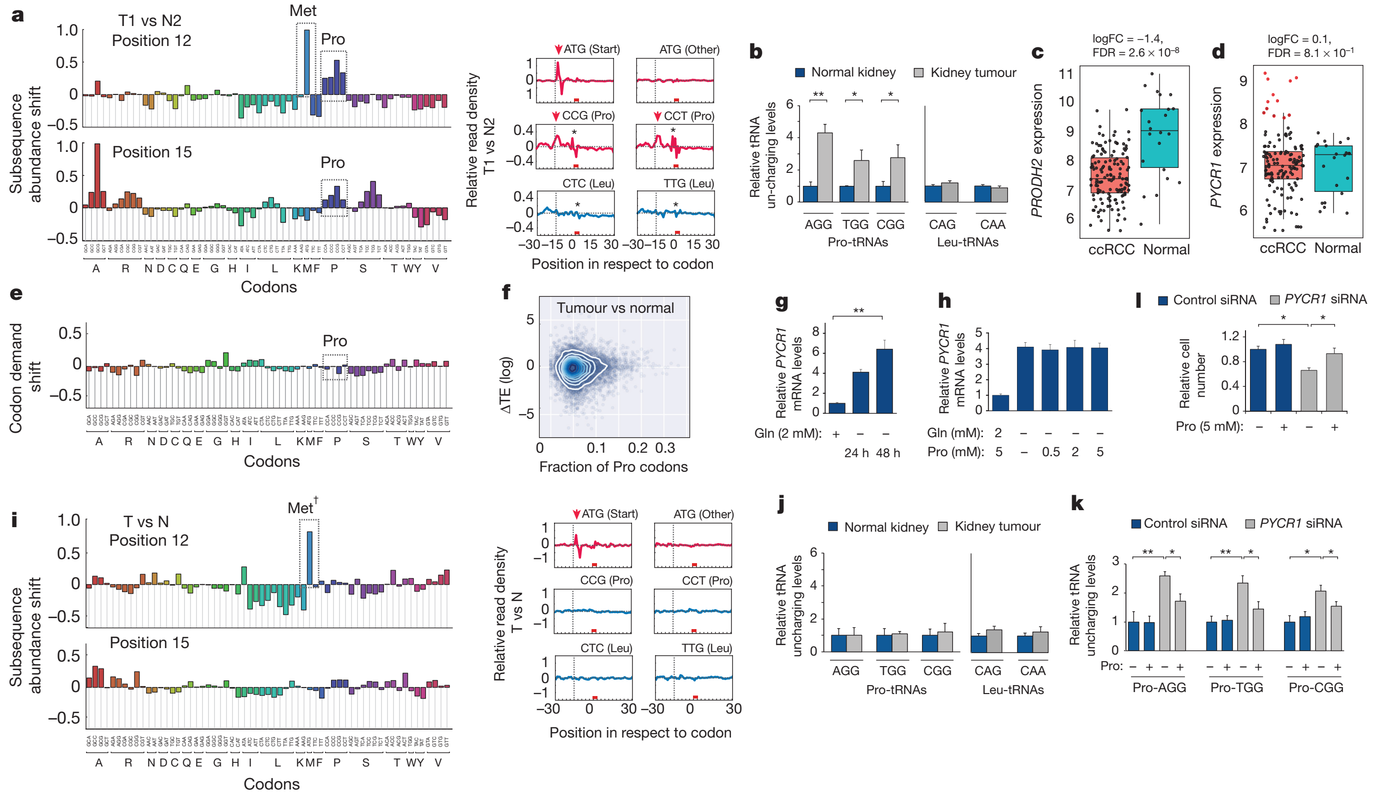

Figure 3 | Diricore detects limitations in proline availability in ccRCC. **a**, Samples were subjected to diricore analysis. Shown is the comparison tumour 1 versus normal 2 (T1 vs N2), while in Extended Data Fig. 4a additional comparisons are shown. Highlighted are the tumour-specific signals at the methionine and proline codons. Combined statistical analysis of all T vs N comparisons is shown in Extended Data Fig. 4b. Asterisk in the right panels marks an artificial signal from a 5′ bias in the ligation/amplification step. **b**, Tumour and normal kidney tissue were subjected to Pro-tRNA and control Leu-tRNAs aminoacylation analysis. **c**, Expression analysis of *PRODH2* in ccRCC tumours. Differential expression test was done comparing ccRCC to normal samples using the R-package limma. **d**, Expression analysis shows high *PYCR1* levels in ~4% of tumours (marked red). **e**, Global change in codon abundance (codon demand) was performed by calculating the relative number of proline codons in the normal and tumour sections using RNA-seq data from the same samples as in **a**. **f**, Analysis of translational efficiency changes (ΔTE) vs proline codon content of genes. **g**, The ccRCC A498 cell line was deprived of glutamine for 24 and 48 h, and *PYCR1* mRNA levels were measured by reverse transcription followed by quantitative PCR (qRT–PCR) and normalized to *GAPDH*. **h**, A498 cells were depleted from glutamine, and then supplemented with proline in the indicated concentrations. *PYCR1* levels were measured by qRT–PCR and normalized to *GAPDH* mRNA. **i**, Diricore analysis of a second ccRCC tumour. †$P < 3.4 \times 10^{-8}$ for the ATG codon by out of frame analysis. **j**, Pro-tRNA and control Leu-tRNA aminoacylation analysis of tumour and normal tissues. **k**, Pro-tRNA aminoacylation analysis was performed with the 786-O ccRCC cell line subjected to proline deprivation and PYCR1 knockdown using short interfering RNA (siRNA), as indicated. **l**, The same experimental setup as in **k**. Cells were counted 72 h after treatment to assess proliferation. For **c** and **d**, The box indicates the 25th/50th/75th percentiles (bottom/middle/top bar), the extent of the whiskers indicate the most extreme values that are within 1.5 times the IQR (inter-quartile range) of the hinge (as per R package ggplot2/geom_boxplot). For **b**, **g**, **h**, **l**, **j**, and **k** error bars represent s.d.; $n = 3$ independent biological replicates; $*P < 0.05$; $**P < 0.01$ by Student's *t*-test. Cutoff for RPF density shift plots in **i** was 15 reads per window.

Intriguingly, the strong signal in methionine originated solely from the initiator-ATG codon, suggesting global alteration in translation rates (Fig. 3a and Extended Data Fig. 4b). The position of the peak (P-site) suggests that increased translation initiation rate in the tumour is the underlying mechanism. A relative increase in initiation of translation, in conditions when the initiation to elongation step becomes rate limiting, would generate relatively more ribosomes with the initiator-ATG codon at their P-site. Supporting evidence for this scenario is the strong elevation of phospho-4EBP1, a canonical marker of initiation of translation, in the tumour compared to normal tissue (Extended Data Fig. 5a). Also the strong depletion of the signal at the P-site of the initiator-ATG following short inhibition of mTOR (an upstream kinase of 4EBP) or nutrient starvation supports this notion (Extended Data Fig. 5b). Thus, diricore identified a signal at the initiator-ATG codon that suggests enhanced global translation initiation in the tumour.

In contrast to the initiator-ATG, the signal in proline codons appeared at both positions A and P sites, suggesting limiting availability of proline (Pro)-tRNA for protein synthesis (Fig. 3a). The relative higher level of non-aminoacylated, but not total Pro-tRNAs in the tumour compared with normal tissue supports this suggestion (Fig. 3b, Extended Data Fig. 4e). Intriguingly, like L-asparaginase treatment (Fig. 1g), gene expression analysis of proline metabolic enzymes revealed vast upregulation of PYCR1, a key enzyme that catalyses the last step in proline synthesis[7], and also strong downregulation of the proline catabolic enzymes PRODH2 and ALDH4A1 (Extended Data Fig. 3d). While loss of PRODH2 expression is commonly seen in kidney tumours[16], PYCR1 activation is infrequent (Fig. 3c, d). We confirmed upregulation of PYCR1 in this tumour by immunohistochemistry (Extended Data Fig. 5a). The proline signal in diricore and the changes in proline metabolic genes suggest a compensatory feedback mechanism in the kidney cancer cells to enable proliferation in conditions of relative proline shortage. Intriguingly, two other PYCR1-high kidney tumours showed similar diricore proline pattern and increased Pro-tRNA non-aminoacylation (Extended Data Fig. 6), strengthening the link between high PYCR1 and proline shortage.

Proline deficiency in the tumour cells can be a result of increased proline demand or decreased proline production, for example due to lack of proline precursors. Codon demand measurements revealed no global increase in the tumours, even when analysis was restricted to differentially expressed genes or those exported extracellularly,

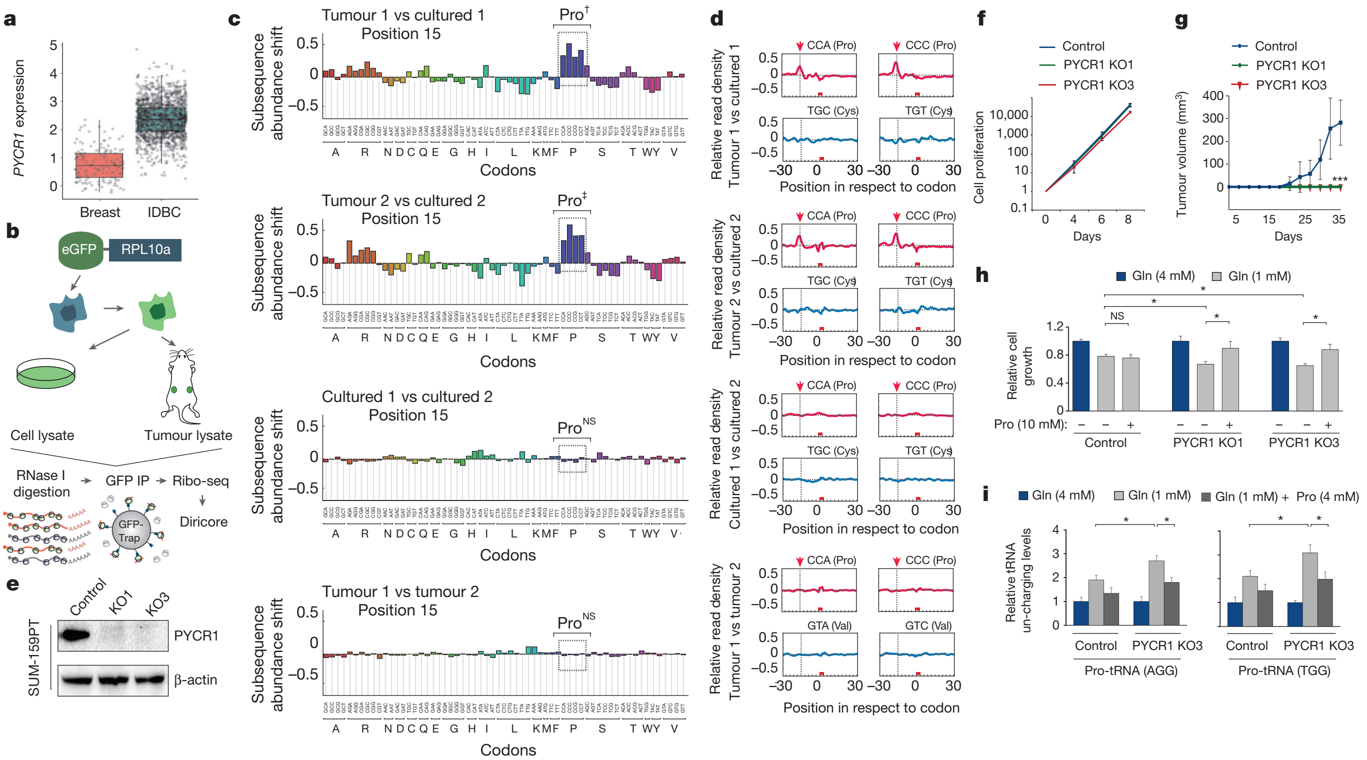

Figure 4 | Diricore uncovers tumour-specific proline vulnerability. **a**, PYCR1 expression analysis in invasive ductal breast carcinoma (IDBC) compared to normal breast. The box indicates the 25th/50th/75th percentiles (bottom/middle/top bar), the extent of the whiskers indicates the most extreme values that are within 1.5 times the interquartile range (IQR) of the hinge (as per R package ggplot2/geom_boxplot). **b**, Schematic diagram showing the generation of cancer cell lines expressing the eGFP–RPL10a fusion protein, the isolation of GFP-tagged ribosomes from tumours and cells in culture by immunoprecipitation (IP), and the experimental design. Ribo-seq denotes ribosome profiling. **c**, **d**, Diricore analysis of tumours derived from eGFP–RPL10a-expressing SUM159PT cells. †Out-of-frame analysis $P < 3.15 \times 10^{-5}$, $P < 3.13 \times 10^{-3}$, $P < 5.31 \times 10^{-2}$, and $P < 1.8 \times 10^{-1}$ for the CCC, CCT, CCA and CCG Pro codons, respectively. ‡Out of frame analysis $P < 3.9 \times 10^{-5}$, $P < 9.4 \times 10^{-3}$, $P < 1.17 \times 10^{-2}$, and $P < 1.0 \times 10^{-1}$ for the CCC, CCT, CCA and CCG Pro codons, respectively. NS, not significant by out-of-frame analysis. **e**, Immunoblot analysis of SUM159PT cell clones expressing CRISPR-Cas9 with either a non-targeting (control) or two independent single-guide RNAs (sgRNAs) against PYCR1 (knockout, KO). **f**, **g**, The same SUM159PT clones as in **e** were propagated either *in vitro* or *in vivo,* and cell proliferation and tumour volume ($n = 6$) were monitored in time. **h**, The same SUM159PT cell clones as in **e** were deprived of glutamine and grown with additional proline, as indicated. The number of cells was counted 48 h after treatment. **i**, Analysis of the relative levels of non-aminoacylated tRNAs was performed with the same cell clones as in **e** deprived of glutamine for 18 h. Error bars represent s.d.; $n = 3$ independent biological replicates; $*P < 0.05$, $***P < 0.001$ by Student's *t*-test. For **g**, *n* refers to the number of xenografts per condition. NS, non significant. Cutoff for subsequence shift plots in **c** was 50 reads per gene.

or when rate of translation was considered (Fig. 3e, f and Extended Data Fig. 5c). We therefore investigated the regulatory events leading to PYCR1 activation, rationalizing that this can be a clue to the proline deficiency. Particularly, we asked whether limiting amount of glutamine, the precursor of proline (Extended Data Fig. 3d), or low proline levels, is causal to activation of PYCR1. We selected A498, a ccRCC cell line with moderate PYCR1 expression (Extended Data Fig. 5d), depleted glutamine, and measured *PYCR1* messenger RNA levels. This analysis revealed a strong and significant activation of PYCR1, but not its paralogues, following glutamine deprivation (Fig. 3g and Extended Data Fig. 5e). However, addition of proline to the glutamine-depleted cells did not attenuate PYCR1 activation (Fig. 3h), suggesting PYCR1 responsiveness to a precursor substrate in the metabolic pathway from glutamine to proline.

Interestingly, when we examined an additional ccRCC tumour by diricore, a specific, significant and robust signal was identified in the initiator-ATG, which resembled the signal observed in the first tumour, but not at proline codons (Fig. 3i and Extended Data Fig. 1e). Also in this tumour, the signal in the initiator-ATG correlated with global activation of translation initiation (Extended Data Fig. 5f). In contrast, the lack of proline signal suggested sufficient proline. Indeed, this tumour presented no increase in non-aminoacylated Pro-tRNA levels, no change in total Pro-tRNA levels, and no upregulation of PYCR1 or any other related gene (Fig. 3j and Extended Data Figs 4f and 5f, g). Immunohistochemistry with CD31, a marker for blood vessels, revealed higher vascularity of this tumour compared with the first, providing a potential evidence for efficient nutrient supply and an explanation for the lack of diricore proline signal (Extended Data Fig. 5h).

Next, we tested whether interference with the proline/PYCR1 regulatory pathway can affect cellular proliferation, and used 786-O, a ccRCC cell line with high PYCR1 (Extended Data Fig. 5d), suggestive of proline shortage vulnerability. We knocked down PYCR1, and cultured cells in medium containing dialysed serum with or without proline to mimic proline shortage (Extended Data Fig. 5i). Indeed, PYCR1 knockdown increased non-aminoacylated Pro-tRNA levels, and addition of proline attenuated this effect (Fig. 3k). Notably, PYCR1 knockdown reduced proliferation, which was negated by proline addition (Fig. 3l), supporting the assumption that interfering with intracellular proline production attenuates proliferation when proline availability is limiting.

High PYCR1 is commonly observed in invasive ductal breast carcinoma (IDBC, Fig. 4a), possibly indicating proline shortage when grown *in vivo*. To test this hypothesis, we generated SUM159PT/eGFP–RPL10a, a PYCR1-high IDBC cell line (Extended Data Fig. 7a) expressing enhanced green fluorescent protein (eGFP)-tagged ribosomal protein RPL10a. As expected[17], eGFP–RPL10a protein was incorporated into polysomes to be used for ribosome-isolation using anti-GFP antibodies (Extended Data Fig. 7b, c). Quality control

experiments indicated very similar profiles as the protocol we routinely use for ribosome profiling (Extended Data Fig. 7d, e), enabling us to apply diricore to tumours grown *in vivo*. We then either transplanted SUM159PT/eGFP–RPL10a cells into immuno-compromised mice, or cultured them *ex vivo* (Fig. 4b). Following expansion, cells and tumours were harvested for immunoprecipitation and diricore analysis. Intriguingly, comparing tumours with cultured cells indicated specific signals in all four proline codons position 15, three of which were significant (Fig. 4c, d). Randomization analysis confirmed robust signal (Extended Data Fig. 1f). Control comparisons produced no signal, and an independently repeated experiment produced similar results (Extended Data Fig. 8a and b). These results indicate that limiting levels of proline are experienced by SUM159PT during tumorigenic development in mice.

As diricore signals in proline were linked to PYCR1 expression levels, we interrogated the impact of PYCR1-loss on tumour development using two PYCR1 knockouts (KO) and one control SUM159PT monoclonal cell lines (Fig. 4e). Interestingly, while PYCR1-KO cells proliferated normally *ex vivo* (Fig. 4f), their capacity to expand *in vivo* was diminished (Fig. 4g and Extended Data Fig. 9a). To further link proline deficiency and cell growth, we cultured these cell lines in medium with limiting amounts of glutamine, the major precursor of proline. While control cells were only relatively mildly affected by glutamine deprivation, PYCR1-KO cells showed a greater sensitivity (Fig. 4h). Importantly, proline addition improved proliferation of PYCR1-KO, but not control, cells following glutamine deprivation. We confirmed increased non-aminoacylation of Pro-tRNAs following glutamine deprivation, augmentation of this effect in PYCR1-KO cells, and its attenuation following proline addition (Fig. 4i). Thus, in growth limiting cellular environments, such as glutamine deprivation and expansion *in vivo*, PYCR1 expression is required for extensive proline production to maintain tumorigenic growth (Extended Data Fig. 10).

Altogether we show that ribosome profiling can sense amino acid shortages in cells and tumours. Although approaches to directly measure amino acids in tumours and bodily fluids exist, they are unlikely to yield biologically meaningful results as tumour demand, energy requirement, and genetic makeup can differ greatly. Our experiments uncovered proline codon signals in tumours. Proline signals in translation can be caused by the unique and constrained shape of proline[18,19] which is resolved by the translation factor eIF5A[20,21]. However, the increased levels of eIF5A in kidney tumours regardless of their proline signature, and the lack of a higher signal at poly-proline motifs (Extended Data Fig. 9b, c), disfavour such a possibility. In contrast, tRNA-aminoacylation assays indicated proline shortage as the cause of the proline signal. The link we uncovered between proline codon signals and elevated proline production pathway indicated compensatory mechanism and vulnerability for tumour expansion. Indeed, reducing cellular proline production impaired tumorigenic growth, providing indications for the usage of ribosome profiling for detecting tumour vulnerabilities and for rational targeting proline for cancer therapy.

Online Content Methods, along with any additional Extended Data display items and Source Data, are available in the online version of the paper; references unique to these sections appear only in the online paper.

Received 24 August 2015; accepted 8 January 2016.
Published online 15 February 2016.

1. Jain, M. *et al.* Metabolite profiling identifies a key role for glycine in rapid cancer cell proliferation. *Science* **336,** 1040–1044 (2012).
2. Maddocks, O. D. *et al.* Serine starvation induces stress and p53-dependent metabolic remodelling in cancer cells. *Nature* **493,** 542–546 (2013).
3. Sheen, J. H., Zoncu, R., Kim, D. & Sabatini, D. M. Defective regulation of autophagy upon leucine deprivation reveals a targetable liability of human melanoma cells *in vitro* and *in vivo*. *Cancer Cell* **19,** 613–628 (2011).
4. Son, J. *et al.* Glutamine supports pancreatic cancer growth through a KRAS-regulated metabolic pathway. *Nature* **496,** 101–105 (2013).
5. Richards, N. G. & Kilberg, M. S. Asparagine synthetase chemotherapy. *Annu. Rev. Biochem.* **75,** 629–654 (2006).
6. Ingolia, N. T., Ghaemmaghami, S., Newman, J. R. & Weissman, J. S. Genome-wide analysis *in vivo* of translation with nucleotide resolution using ribosome profiling. *Science* **324,** 218–223 (2009).
7. De Ingeniis, J. *et al.* Functional specialization in proline biosynthesis of melanoma. *PLoS One* **7,** e45190 (2012).
8. Rooijers, K., Loayza-Puch, F., Nijtmans, L. G. & Agami, R. Ribosome profiling reveals features of normal and disease-associated mitochondrial translation. *Nat. Commun.* **4,** 2886 (2013).
9. Bazzini, A. A. *et al.* Identification of small ORFs in vertebrates using ribosome footprinting and evolutionary conservation. *EMBO J.* **33,** 981–993 (2014).
10. Guydosh, N. R. & Green, R. Dom34 rescues ribosomes in 3′ untranslated regions. *Cell* **156,** 950–962 (2014).
11. Fresno, M., Carrasco, L. & Vazquez, D. Initiation of the polypeptide chain by reticulocyte cell-free systems. Survey of different inhibitors of translation. *Eur. J. Biochem.* **68,** 355–364 (1976).
12. Ingolia, N. T., Lareau, L. F. & Weissman, J. S. Ribosome profiling of mouse embryonic stem cells reveals the complexity and dynamics of mammalian proteomes. *Cell* **147,** 789–802 (2011).
13. Zaborske, J. M. *et al.* Genome-wide analysis of tRNA charging and activation of the eIF2 kinase Gcn2p. *J. Biol. Chem.* **284,** 25254–25267 (2009).
14. Singh, B. *et al.* Selection of metastatic breast cancer cells based on adaptability of their metabolic state. *PLoS One* **7,** e36510 (2012).
15. Leprivier, G. *et al.* The eEF2 kinase confers resistance to nutrient deprivation by blocking translation elongation. *Cell* **153,** 1064–1079 (2013).
16. Dalgliesh, G. L. *et al.* Systematic sequencing of renal carcinoma reveals inactivation of histone modifying genes. *Nature* **463,** 360–363 (2010).
17. Heiman, M. *et al.* A translational profiling approach for the molecular characterization of CNS cell types. *Cell* **135,** 738–748 (2008).
18. Artieri, C. G. & Fraser, H. B. Accounting for biases in riboprofiling data indicates a major role for proline in stalling translation. *Genome Res.* **24,** 2011–2021 (2014).
19. Sabi, R. & Tuller, T. A comparative genomics study on the effect of individual amino acids on ribosome stalling. *BMC Genomics* **16** (Suppl. 10), S5 (2015).
20. Doerfel, L. K. *et al.* EF-P is essential for rapid synthesis of proteins containing consecutive proline residues. *Science* **339,** 85–88 (2013).
21. Gutierrez, E. *et al.* eIF5A promotes translation of polyproline motifs. *Mol. Cell* **51,** 35–45 (2013).

Supplementary Information is available in the online version of the paper.

Acknowledgements We thank R. Kerkhoven, R. Kluin and M. Nieuwland from the NKI-AVL Genomics Core Facility for assistance with deep-sequencing experiments, P. Snaebjornsson for valuable help with the pathology studies, and K. Verhoef for advice. We acknowledge the assistance of the NKI-AVL core facilities of Radionuclides Centre, Flow Cytometry, Molecular Pathology, and Biobanking (CFMPB). We thank R. Elkon for technical assistance, and all the members of the Agami group for valuable discussions. This work was supported by funds from the Human Frontier Science Program (LT000640/2013) to A.P.U, and the European Research Council (ERC-PoC EEG-CEC / EU665317), the Netherlands Organization for Scientific Research (NWO-VICI 918.11.601), and the Dutch Cancer Society (KWF NKI-2013-5814) to R.A.

Author Contributions F.L.-P., K.R., and R.A. conceived the project, designed all the experiments, and wrote the manuscript. F.L.-P. and J.Z. performed ribosome profiling and most of the experiments on the study. K.R. developed the diricore analysis and performed all the bioinformatic studies. L.C.M.B. and O.v.T. performed the *in vivo* studies. J.F.O.V. and P.v.B. prepared the plasmid constructs and established cell line models. R.L. designed and established the PYCR1 knockout models. A.P.U. prepared RNA-seq libraries. I.H. and J.W. performed the pathological studies. A.B. performed the nephrectomies on kidney cancer patients.

Author Information Data were deposed in GEO with accession code GSE59821. Reprints and permissions information is available at www.nature.com/reprints. The authors declare no competing financial interests. Readers are welcome to comment on the online version of the paper. Correspondence and requests for materials should be addressed to R.A. (r.agami@nki.nl).

METHODS

Cell culture. SUM1315MO2 cells were cultured in DMEM/F12 1:1 medium supplemented with 5% fetal bovine serum (FBS), EGF (10 ng ml^{-1}), and insulin (5 μg ml^{-1}) in 5% CO_2 at 37 °C. SUM159PT cells were cultured in DMEM/F12 1:1 medium supplemented with 5% FBS, insulin (5 μg ml^{-1}), and hydrocortisone (1 μg ml^{-1}). PC3, 786-O, and A498 cells were cultured in RPMI medium supplemented with 10% FBS. The breast cancer cell lines MCF7, T47D, MDA-MB-231, and Hs578T were cultured in DMEM medium supplemented with 10% FBS. All cell lines were obtained from ATCC, except for SUM159PT and SUM1315MO2, which were obtained from Asterand Bioscience. Cell lines were regularly tested for Mycoplasma contamination. Cell lines were authenticated by expression analysis based on RNA-seq and/or ribosome profiling. For glutamine starvation experiments, cells were cultured for 48 h in glutamine-free DMEM supplemented with 10% of dialysed FBS.

siRNAs against PYCR1 were purchased from Life Technologies (PYCR1 siRNA catalogue number 4390824, ID s194735; Negative control siRNA catalogue number 4390844). Cells were transfected using Dharmafect I reagent (Dharmacon) following the manufacturer's instructions.

Immunoblotting. Immunoblots were performed as described previously[8]. The following antibodies and dilutions were used, anti-GFP (Santa Cruz Biotechnology, sc-8339, 1:1,000), anti-RPL10a (Santa Cruz Biotechnology, sc-100827, 1:1,000), anti-RPS6 (Cell Signaling Technology, 2217, 1:1,000), anti-RPL13a (Cell Signaling Technology, 2765, 1:1,000), anti-PYCR1 (Proteintech, 13108-1-AP, 1:1,000).

Immunohistochemistry. Immunohistochemistry of the FFPE tumour samples was performed on a BenchMark Ultra autostainer (Ventana Medical Systems). Briefly, paraffin sections were cut at 3 μm, heated at 75 °C for 28 min and deparaffinized in the instrument with EZ prep solution (Ventana Medical Systems). Heat-induced antigen retrieval was carried out using Cell Conditioning 1 (CC1, Ventana Medical Systems) for respectively 32, 36 and 64 min at 95 °C (CD31, phospho-4E-BP1 and PYCR1). CD31 was detected using clone JC/70A (1:300 dilution, 32 min room temperature, ThermoScientific), Phospho-4E-BP1 with clone 236B4 (1:750 dilution, 1 h room temperature , Cell Signaling), and PYCR1 using a polyclonal antibody (1:4,000 dilution, 1 h room temperature , ProteinTech). Bound phospho-4E-BP1 was detected using the UltraView Universal DAB Detection Kit (Ventana Medical Systems), while detection for CD31 and PYCR1 was visualized using the OptiView DAB Detection Kit (Ventana Medical Systems). Slides were counterstained with haematoxylin.

Ribosome profiling (Ribo-seq). Libraries from cultured cells were prepared as described previously[22]. For ribosome profiling from tissue, samples were snap frozen after surgical removal and lysed mechanically using a tissue homogenizer in the presence of ice- cold lysis buffer (20 mM Tris-HCl, pH 7.8, 100 mM KCl, 10 mM MgCl2, 1% Triton X-100, 2 mM DTT, 100 μg ml^{-1} cycloheximide, 1× EDTA-free Complete protease inhibitors). Lysates were centrifuged at 5,000 r.p.m. and the supernatant was digested with 2 U μl^{-1} of RNase I (Life Technologies) for 45 min at room temperature. Resulting monosomes were purified, RNA was isolated, and ribosome profiling libraries were prepared as described previously. Studies with patient material were approved by the Medical Ethical Committee of The Netherlands Cancer Institute. An informed consent was obtained from all the subjects.

eGFP–RPL10a immunoprecipitation. SUM-159 eGFP–RPL10a cells were treated with cycloheximide at a final concentration of 10 μg ml^{-1}for 5 min. Cells were washed with cold PBS, scraped, and pelleted. Cell pellet was lysed in 1 ml of NP40 lysis buffer (20 mM Tris-HCl, pH 7.8, 10 mM MgCl2, 150 mM KCl, 1% NP40, 2 mM DTT, 1× Complete protease Inhibitors, 100 ug ml^{-1} CHX) for 15 min, centrifuged for 10 min at 1,300*g* and 1 ml of supernatant was recovered. For tumours, each sample was lysed in 1 ml of NP40 lysis buffer in a tissue homogenizer. Tumour lysate was centrifuged at 1,300*g* for 10 min and the supernatant was recovered. 85 μl per condition of GFP-Trap_M beads (Chromotek) were washed for 3 times in 1 ml of NP40 lysis buffer, resuspended in 3 ml of NP40 lysis buffer. 1 ml of cleared lysate (cell line or tumour) was added to the beads and digested with RNase I (100 U μl^{-1}) for 1 h at room temperature under constant rotation. Beads were washed 3 times with 1 ml of NP40 Lysis buffer and 3 times with NP40 wash buffer (20 mM Tris-HCl pH 7.8, 10 mM $MgCl_2$, 350 mM KCl, 1% NP40, 2 mM DTT, 1× Complete protease Inhibitors, 100 μg ml^{-1} CHX). Beads were resuspended in 300 μl of lysis buffer with 1% SDS and 15 μl of PCR-grade proteinase K (Roche) and incubated for 1 h at 45 °C. Supernatant was recovered and resuspended in TriSure. RNA was isolated and libraries prepared according to the ribosome profiling protocol.

tRNA aminoacylation. Cells were harvested in cold PBS, centrifuged, and resuspended in 0.3 M sodium acetate/acetic acid (NaOAc/HOAc) (pH 4.5). Total RNA was isolated using acetate-saturated phenol/$CHCl_3$ (pH 4.5). Precipitated RNA was resuspended in 10 mM NaOAc/HOAc (pH 4.5). Samples were split in two, one half (2 μg) was oxidized with 50 mM $NaIO_4$ in 100 mM NaOAc/HOAc (pH 4.5) for 15 min and the other half (2 μg) was incubated in 50 mM NaCl in 100 mM NaOAc/HOAc (pH 4.5) for 15 min. Samples were quenched with glucose 100 mM for 5 min at room temperature, purified in G50 columns (GE Healthcare), and then precipitated with ethanol. tRNAs were deacylated in 50 mM Tris-HCl (pH 9) for 30 min at 37 °C. RNA was precipitated and then ligated to the 3′adaptor (5′-/5rApp/TGGAATTCTCGGGTGCCAAGG/3ddC/-3′) using T4 RNA ligase 2 (NEB) for 2 h at 37 °C. Relative aminoacylation levels were calculated by qRT–PCR using tRNA specific primers.

Reverse primer, GCCTTGGCACCCGAGAATTCCA; Pro-tRNA(AGG) primer, GGCTCGTTGGTCTAGGGGTATG; Pro-tRNA(TGG) primer, CAGAACTAT AGGAATTGAACCTA; Pro-tRNA(CGG) primer, GTTGGTCTAGGGGTATGAT TCTCGCTTC; Leu-tRNA(CAA) primer, GTCAGGATGGCCGAGTGGTCTA; Leu-tRNA (CAG) primer, GTCAGGATGGCCGAGCGGTCTA; Val-tRNA (TAC) primer, GGTTCCATAGTGTAGTGGTTAT; Asn-tRNA(GTT) primer, GTCTCTGTGGCGCAATCGGT.

Real-time PCR. 1 μg of total RNA was reverse transcribed using the SuperScript III first-strand synthesis system (Life Technologies) following the manufacturer's instructions. Real-time PCR was performed using the SensiFAST SYBR real time PCR kit (Bioline).

The following primer sequences were used, *PYCR1* forward primer, CATG ACCAACACTCCAGTCG; *PYCR1* reverse primer, CCTTGGAAGTCCCATC TTCA; *PYCR2* forward primer, ATAGCCAGCTCCCCAGAAAT; *PYCR2* reverse primer, CTCCACAGAGCTGATGGTGA; *PYCRL* forward primer, GCCTCATCAGAGCAGGAAAA; *PYCRL* reverse primer, CACGGACACCAA GATGTGTT; *GAPDH* forward primer, ACCCAGAAGACTGTGGATGG; *GAPDH* reverse primer, TCTAGACGGCAGGTCAGGTC.

Deep sequencing data preprocessing and alignment. Adaptor sequences were trimmed from raw ribosome profiling data using cutadapt[23]. Sequences shorter than 20 bp after adaptor trimming were discarded. rRNA and tRNA sequences were filtered by alignment to indices of rRNA and tRNA sequences respectively, using bowtie2[24] and default parameters. A rRNA index was constructed from GENCODE v19 annotations, transcript types "rRNA", "Mt_rRNA" and "rRNA_pseudogene", supplemented with UCSC repeats of class "rRNA" (table "rmsk"). The tRNA index was constructed from sequences obtained from GtRNAdb[25] at 5 September 2012. The remaining (unmapped) reads were aligned to GRCh37/hg19 using TopHat2[26] and GENCODE v19/BASIC[27] transcript coordinates (parameters "-N 2 -m 1–no-novel-juncs–no-novel-index–no-coverage-search–segment-length 25"). In subsequent analyses, only primary alignments with mapping quality of 10 or greater were considered. Ribosome profiling and RNA-seq data followed the same pipeline, with the exception of adaptor trimming, which was only performed on ribosome profiling data. Data presented in this manuscript is available with GEO accession number GSE59821.

Subsequence analysis. In summary, subsequence shift analysis compares RPF codon occupancy frequencies between samples, in a gene-level normalized manner (to exclude gene expression differences as cause for differences in observed codon frequencies).

Specifically, gene IDs and reading frames were assigned to RPFs, using GENCODE v19/BASIC. RPFs not within a valid CDS (taking into account the 15-nucleotide 5′-overhang of RPFs), RPFs with ambiguous gene ID and RPFs with ambiguous reading frame were excluded. The remaining RPFs were used to count, for the different positions (12 and 15 nucleotides from 5′-end), the frequencies of all codons, for all genes in the transcriptome. Within-gene frequencies were calculated by dividing the observed counts by the total counts for that gene. Normalized codon frequencies were averaged over all genes that had at least *n* counts in both the condition and control samples (*n* is 100 for all figures, unless otherwise specified). Shifts were calculated from these normalized and averaged frequencies per codon as: (condition – reference)/reference. That is, per codon shifts were calculated relative to the control. To test for significant differential codon occupancy at the amino acid level, we used the subsequence shifts between control and conditions over the replicates. We used a linear mixed model (R package 'lme4') with fixed effects over the 20 amino acids and random effects over the codons. This supplied us with *t*-values and *P*-values. We used Benjamini–Hochberg multiple testing correction (R function 'p.adjust', method "fdr") to extract adjusted *P*-values. For schematic representation of the method see (Extended Data Fig. 1g).

Code availability. Code is available upon request.

RPF density analysis. Codon-regions of 61 nucleotides width around designated codons along the transcriptome (as annotated by GENCODE v19/BASIC) were identified (using transcript coordinates; that is, codon-regions were all supported by exons). Overlapping transcript annotations were used, and overlapping regions were retained, but regions with identical genomic coordinates were collapsed. Codon-regions that could not be extended to 61 nucleotides (due to being near the 5′ or 3′ ends of transcripts) were discarded.

5′ ends of RPFs were counted for each codon-region. For a comparison between two samples, only codon-regions where the total number of counts was at least n in both samples were taken into consideration (n was 50 for all figures, unless otherwise specified. n was lowered in some data sets to include at least 1,000 windows for common codons). For each sample and each codon-region, the normalized 5′ end RPF density was calculated by dividing over the total number of counts within that region, and multiplying by the width of the codon-region, so the average density within each codon region is equal to 1. The normalized densities were convolved using a rectangular window of width 3 and height 1/3. The mean density over the codon-regions was taken and the difference in the mean densities between the samples yielded to the density shift.

Out-of-frame analysis. We performed out-of-frame analysis to ensure that the signals we observed in the cases where we have no replicate samples (3-AT main text Fig. 1b, harringtonine main text Fig. 1d, second ccRCC tumour from main text Fig. 3i) are robust and significant. A background distribution of values was generated using −1/+1 nucleotide. Shifts from the analysed codon. From this background distribution we excluded values implicitly caused by real signal (for example, for harringtonine, which causes a signal at ATG in the 12th position, we used the nucleotide triplets observed in the 11th and 13th position, but excluded NAT and TGN at the 11th and 13th position, respectively). We then used this background distribution to measure the significance of the diricore signal in the original (+0) position using Z-tests (we ensured that values in the background distribution were approximately normally distributed using visual inspection of q-q plots, the Anderson–Darling test and the Shapiro–Wilk test).

Diricore analysis of randomized data sets. Aligned reads were displaced by −5 to +5 nucleotides. Since alignments are done against the genome transcript coordinates/introns were taken into account and reads were effectively displaced along the transcript. In case of inconsistent transcript isoforms, leading to ambiguous location after displacement, reads were discarded (this occurred with less than 1% of the reads). For every sample, three independent randomizations were performed. Only reads in the CDS and in-frame with the CDS (before displacement) were taken into account (for details, see Methods section Subsequence analysis). For further diricore analysis, we used all reads post displacement, with all other methods identical (see sections Subsequence analysis and RPF density analysis).

Normalized abundances and translational efficiencies. Gene-wise counts were performed using annotations from GENCODE v19/BASIC and HTSeq. Counts were normalized by correction for the total library sizes using trimmed-mean of M-values (TMM) normalization, supplied by the R-package 'edgeR'. Translational efficiencies were calculated as the ratio of (normalized abundance determined by ribosome profiling)/(normalized abundance determined by RNA-seq).

GSEA. To obtain a RankedList as input for GSEA[28], gene-wise counts (generated using GENCODE v19/BASIC and HTseq) were normalized using edgeR's[29] TMM normalization. Predictive fold-changes were obtained using edgeR's predFC routine with a prior count of 3. Ensembl/GENCODE gene IDs were converted to Entrez gene IDs using a look-up table obtained from Ensembl MartView. Fold-changes of genes that mapped to a single Entrez gene ID were averaged. In GSEA, the predictive fold-changes were used a scores. The gene sets analysed contained all MSigDB/C2 (v4.0) gene sets. Default settings were used, with the exception that 10,000 permutations were used to estimate the significance of enrichments.

Codon demand calculations. Codon demand was calculated by calculation of the absolute abundances of each codon in the transcriptome, as determined by RNA-seq. Reads per gene ID were counted using GENCODE v19/BASIC annotations and HTSeq. Gene-wise abundances were normalized by the total library sizes. Per-gene isoform abundances were estimated using MISO[30]. The total numbers of codons present per transcript were calculated using the CDS annotations. Shifts in codon demand were calculated relative to the reference, that is, the shifts were calculated as (condition − reference)/ reference.

Processing of yeast data. Yeast ribosome profiling data of cells treated with 3-AT[10] was obtained from GEO (samples GSM1279568 and GSM1279579). Adaptor sequences were trimmed using cutadapt[24]. Sequences shorter than 20 bp after adaptor trimming were discarded. rRNA and tRNA sequences were filtered by alignment to indices of rRNA and tRNA sequences respectively. A rRNA index was constructed from Ensembl annotations (EF4.69), transcript type "rRNA"). Similarly, a tRNA index was constructed from Ensembl annotations (EF4.69), transcript type "tRNA"). Remaining (unmapped) reads were aligned to the yeast genome (EF4.69) using corresponding Ensembl transcript annotations and TopHat2[26] (using parameters "-N 2 -m 1–no-novel-juncs–no-novel-index–no-coverage-search–segment-length 25"). In subsequent analyses, only primary alignments with mapping quality of 10 or greater were considered.

Animal studies. The Animal Ethics Committee of The Netherlands Cancer Institute approved all the experiments in this study. 5–7-week-old, female NOD-SCID IL2Rg null (Charles River) were used in all the experiments. 5×10^6 cells were injected in the fat pads and tumour growth was measured over time. Experiments in Fig. 4 were repeated twice at independent times. The values reported represent the mean of 6 xenografts. Measurements were taken every 3–5 days and tumour volume was estimated by $0.5 \times W \times W \times L$, where W is the width and L is the length of the tumour. None of the experiments exceeded the limit of the maximum tumour allowed by the NKI institutional guidelines. Maximum tumour size allowed was 1,000 cubic millimetres. Distributions were assumed to follow a Student's t distribution. No animals were excluded from the analysis and they were assigned to groups by simple randomization. Experiments were not conducted blind. No statistical methods were used to predetermine sample size.

CRISPR-cas9-mediated knockout. PYCR1 was targeted using the lenti-CRISPR-V2 and sgRNAs to TCTCCGGACAGCATGAGCGT (KO1) and CTTCATCGGCGCTGGCCAGC (KO3) sites.

22. Loayza-Puch, F. *et al.* p53 induces transcriptional and translational programs to suppress cell proliferation and growth. *Genome Biol.* **14,** R32 (2013).
23. Martin, M. Cutadapt removes adapter sequences from high-throughput sequencing reads. *EMBnet.journal* **17,** 10–12 (2011).
24. Langmead, B. & Salzberg, S. L. Fast gapped-read alignment with Bowtie 2. *Nature Methods* **9,** 357–359 (2012).
25. Chan, P. P. & Lowe, T. M. GtRNAdb: a database of transfer RNA genes detected in genomic sequence. *Nucleic Acids Res.* **37,** D93–D97 (2009).
26. Kim, D. *et al.* TopHat2: accurate alignment of transcriptomes in the presence of insertions, deletions and gene fusions. *Genome Biol.* **14,** R36 (2013).
27. Harrow, J. *et al.* GENCODE: the reference human genome annotation for The ENCODE Project. *Genome Res.* **22,** 1760–1774 (2012).
28. Subramanian, A. *et al.* Gene set enrichment analysis: a knowledge-based approach for interpreting genome-wide expression profiles. *Proc. Natl Acad. Sci. USA* **102,** 15545–15550 (2005).
29. Robinson, M. D., McCarthy, D. J. & Smyth, G. K. edgeR: a Bioconductor package for differential expression analysis of digital gene expression data. *Bioinformatics* **26,** 139–140 (2010).
30. Katz, Y., Wang, E. T., Airoldi, E. M. & Burge, C. B. Analysis and design of RNA sequencing experiments for identifying isoform regulation. *Nature Methods* **7,** 1009–1015 (2010).

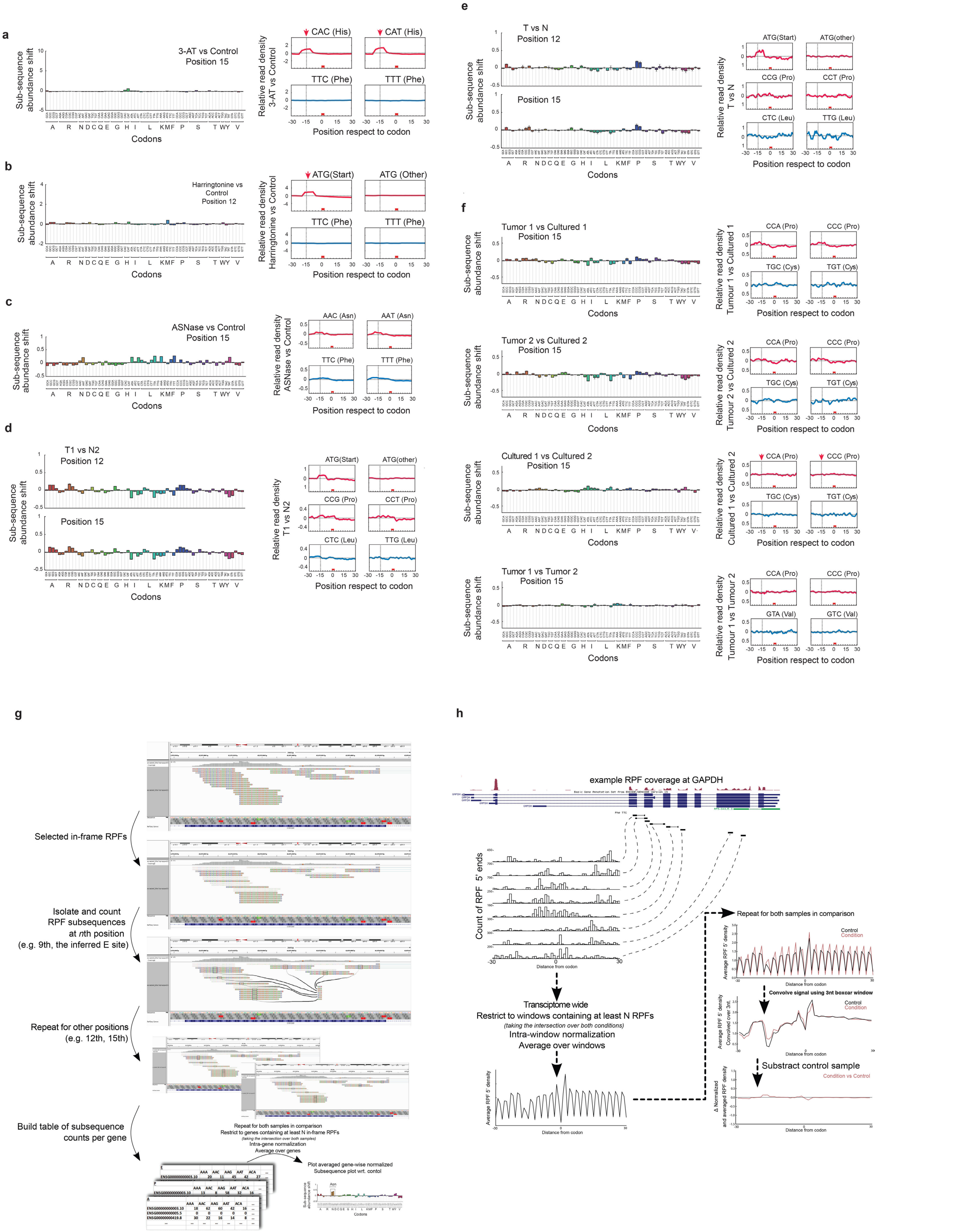

Extended Data Figure 1 | Robustness analysis. Diricore analysis was performed on data sets where the reads were displaced −5/+5 nucleotides randomly, for details see material and methods section. For each panel we present RPF density analyses to the right (note the randomization of the signal at −5 to +5 nucleotides) and to the left subsequence analyses following the randomization process. **a** refers to Fig. 1b, c; **b** refers to Fig. 1d, e; **c** refers to Fig. 1f; **d** refers to Fig. 3a; **e** refers to Fig. 3i; **f** refers to Fig. 4c. **g**, **h**, Illustrative overviews of the diricore method.

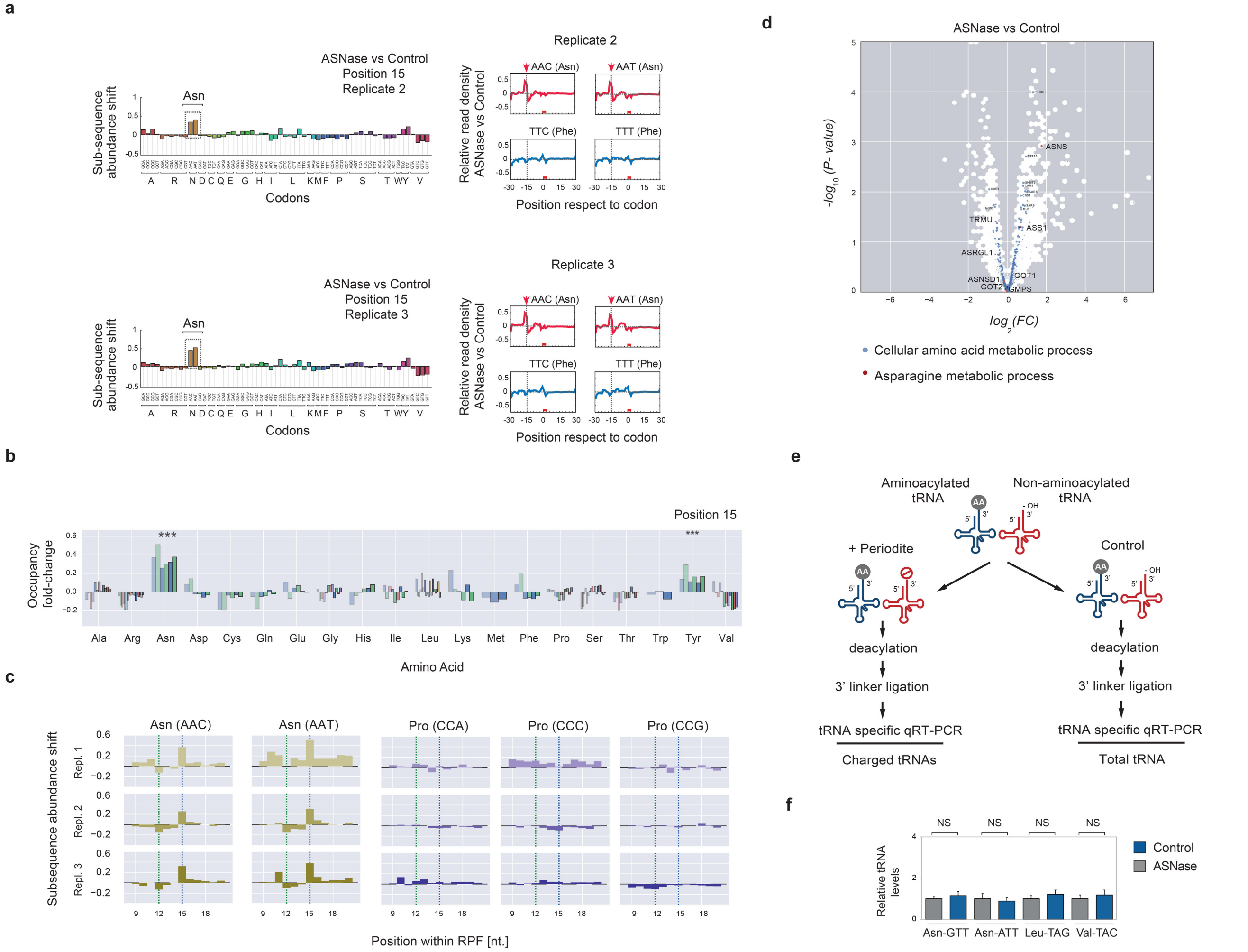

Extended Data Figure 2 | Supporting evidence for the asparagine signal in diricore. a, Diricore analysis of PC3 cells treated for 48 h with L-asparaginase reveals a specific signal in asparagine codons at position 15, two replicates are shown. **b**, Subsequence shift data from Fig. 1f, and **a**, in which significant shifts at the amino-acid level are displayed (***FDR ≤ 0.001). **c**, Subsequence shift at in-frame and out-of-frame positions (8–21 nucleotides from RPF 5′-ends). **d**, Volcano plot showing gene expression changes (as determined by ribosome profiling) upon ASNase treatment. The horizontal axis shows log-fold-changes, while the vertical axis shows the statistical significance of the differential expression. Blue dots indicate genes annotated with GO term "cellular amino acid metabolic process" (GO:0006520), while red dots indicate genes annotated with GO term "asparagine metabolic process" (GO:0006528). **e**, Schematic diagram of a protocol based on Zaborske *et al.*[13], to compare aminoacylated and non-aminoacylated tRNAs by qRT–PCR. **f**, Relative total tRNA levels from Fig. 1h, Leu-CAG tRNA was used to normalize the values. The error bars in **f** represent s.d.; $n = 3$ independent biological replicates; NS, non significant by Student's *t*-test.

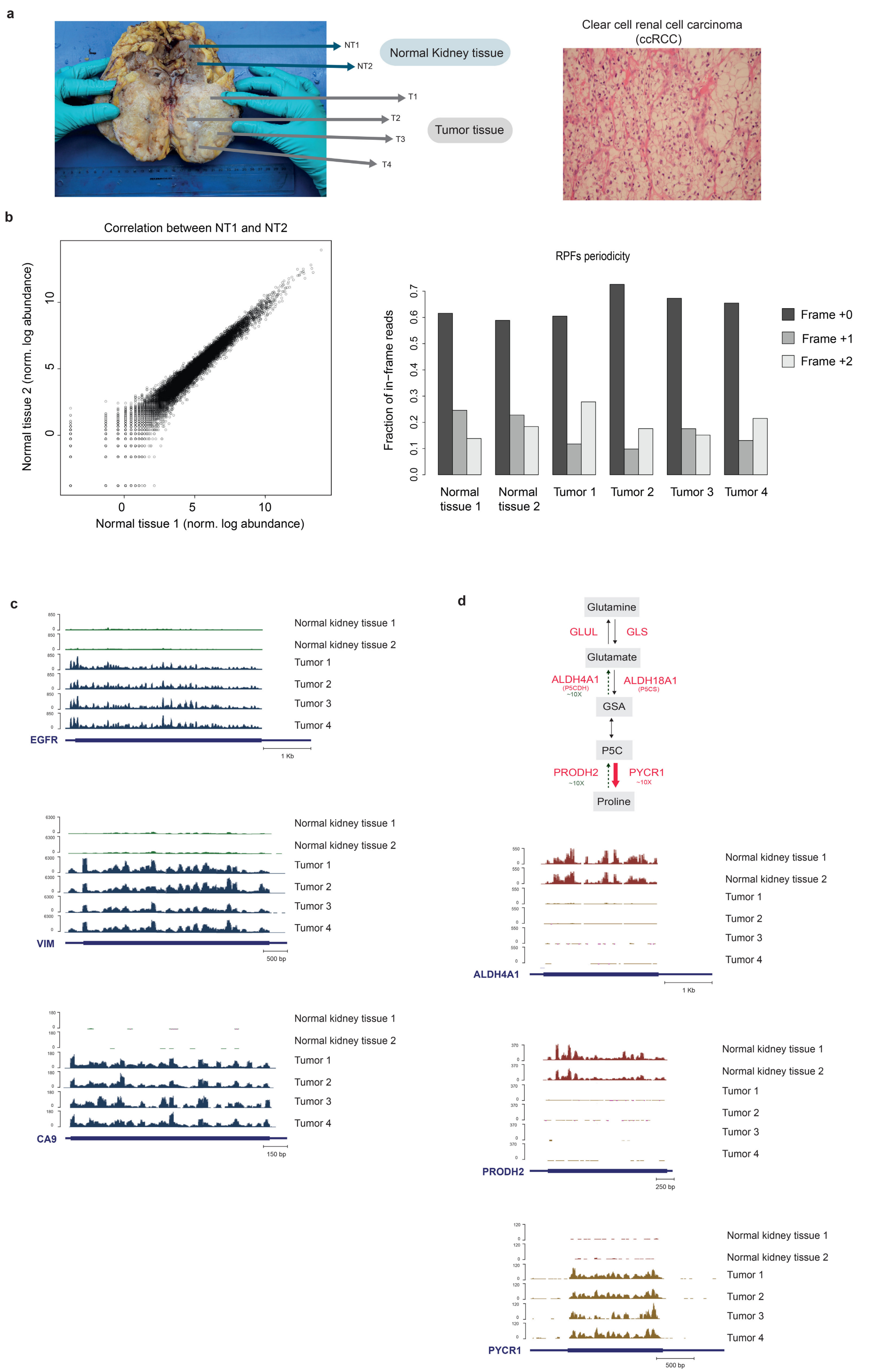

Extended Data Figure 3 | Quality control of ribosome profiling from tumour and normal ccRCC tissue, and gene expression analysis of key ccRCC tumour markers. a, Left, gross presentation of ccRCC. Depicted areas indicate normal and tumour tissue. Arrows indicate regions where the samples were taken. Right, representative microscopic images of tumour sections stained with haematoxylin and eosin (H&E). Pathological analysis confirmed a clear cell renal cell carcinoma (ccRCC). **b**, Quality control of the Ribo-seq data obtained from Normal and Tumour tissues. Left, correlation of Ribo-seq data from independent samples. Right, RPF periodicity from all the samples. **c**, Gene expression analysis by Ribo-seq confirms high level of *EGFR*, *VIM*, and *CA9* in the tumour samples compared with the normal tissues, as was reported for renal cell carcinomas (Cancer Genome Atlas Research, 2013). **d**, Schematic diagram of the proline synthesis pathway (upper panel). Changes in gene expression in the proline synthesis pathway based on Ribo-seq.

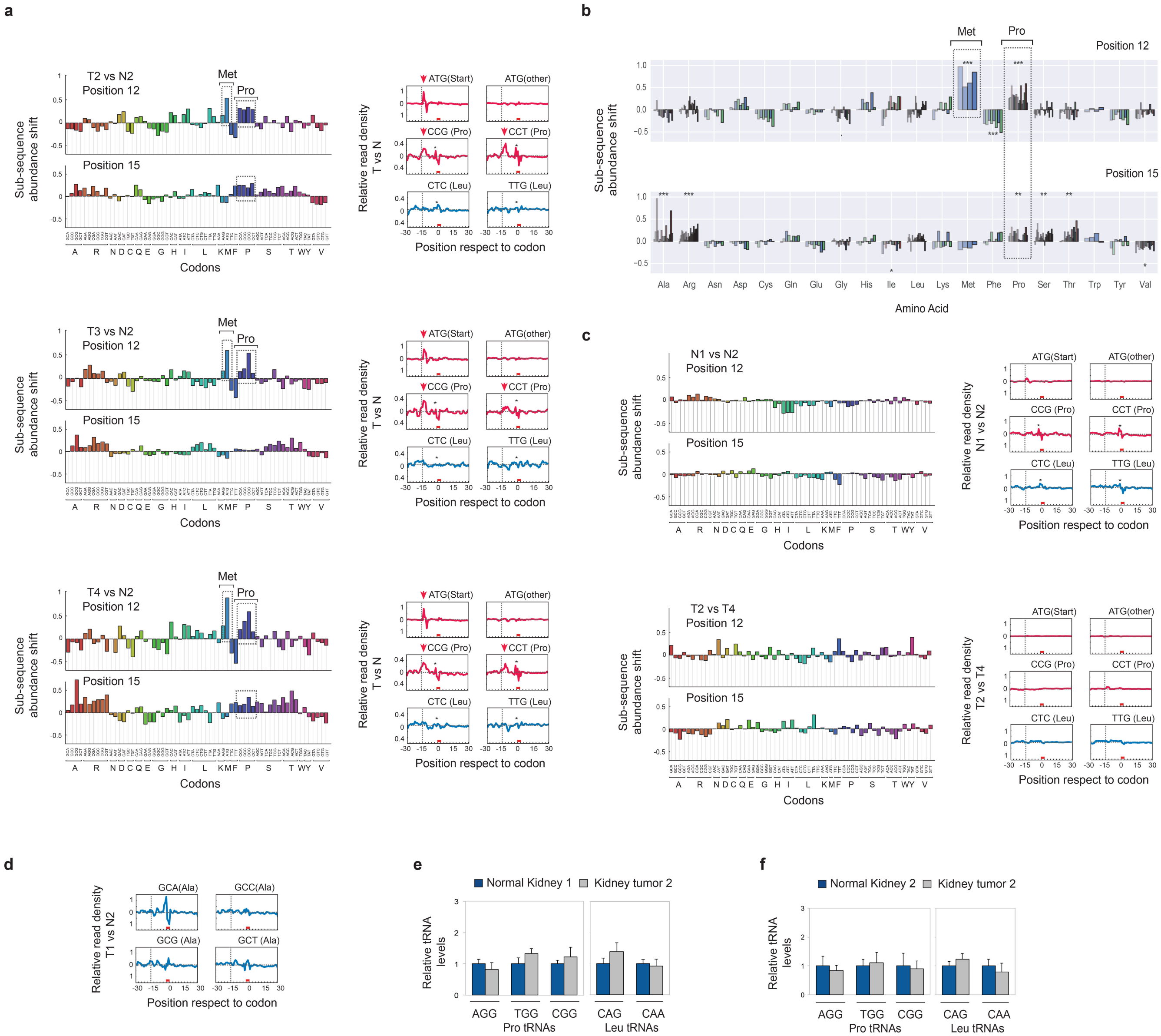

Extended Data Figure 4 | Diricore analysis of additional tissue samples of ccRCC tumour 1, and a combined statistical analysis of signals at positions 12 and 15. a, Diricore analysis as in Fig. 3a. **b**, Subsequence shifts calculated by counting codon occurrences in specific positions within RPFs, normalized within and averaged over genes, with respect to untreated controls. A mixed linear model, in which amino acids are fixed effects and codons are random effects, is used to test for deviating shifts at the amino acid level (***FDR ≤ 0.001, **FDR ≤ 0.01, *FDR ≤ 0.1). **c**, Diricore analysis between samples N1 and N2 from normal kidney (upper panel) and between samples T2 and T4 (lower panel). **d**, Diricore analysis between samples T1 and N2 does not show a consistent signal at Ala codons. **e**, **f**, Relative total tRNA levels from Fig. 3b, j, respectively. Leu-CAG tRNA was used to normalize the values. For **e** and **f**, error bars represent s.d.; $n = 3$ independent biological replicates.

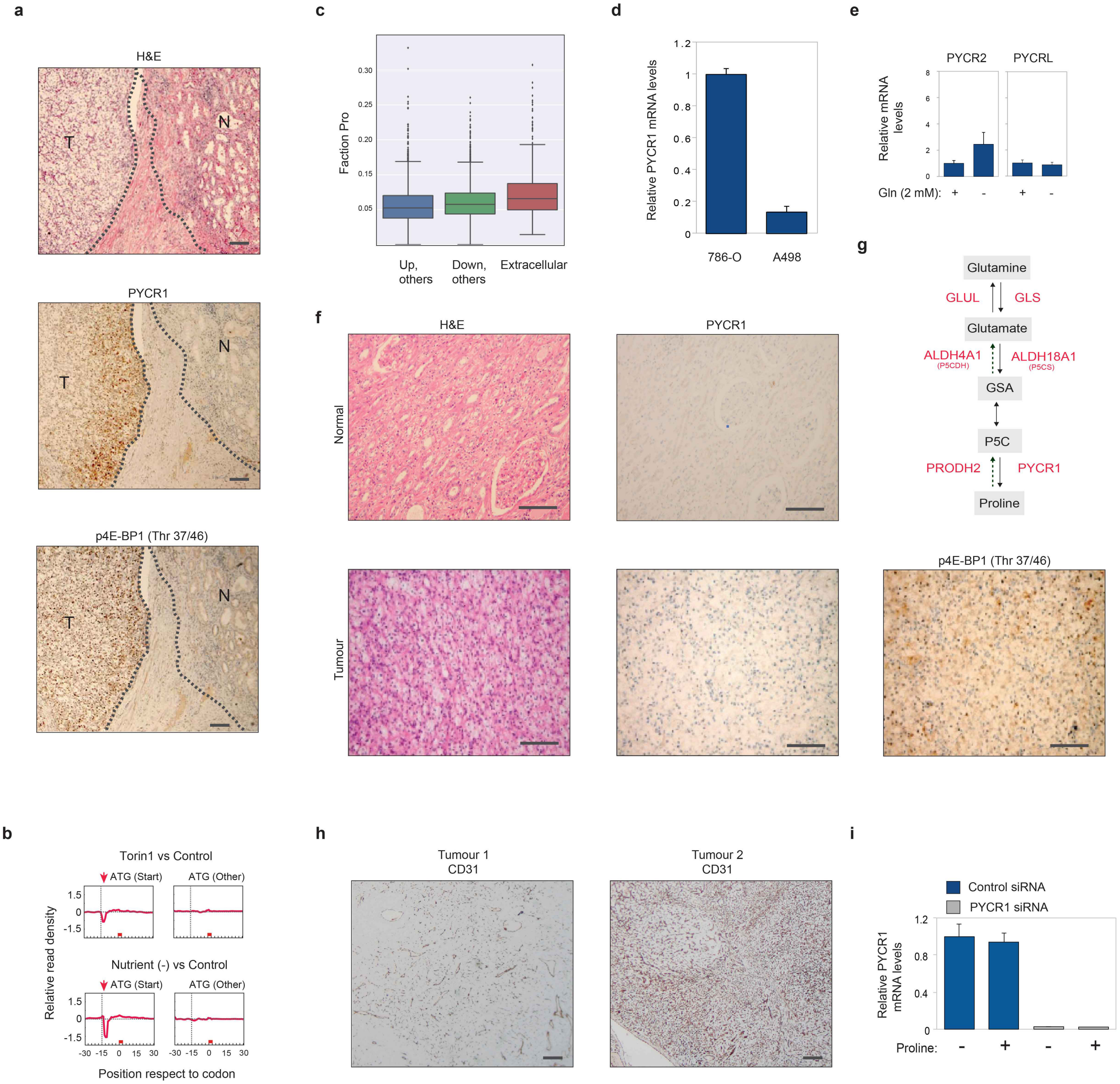

Extended Data Figure 5 | Supporting evidence for global stimulation of translation in ccRCC tumours in study. a, Immunohistochemistry performed on a section containing tumour and normal tissues (T and N, respectively) using anti-p4EBP1 threonine 37/46 and anti-PYCR1 antibodies. **b**, Diricore analysis of MCF10a cells treated with either Torin 1 or deprived of nutrients for 2 h. Methionine codons at the Start and CDS are shown. **c**, Proline codons content was interrogated using RNA-seq data from the tumour presented in Fig. 3. The analysis was performed with a subset of genes significantly (FDR < 0.05) altered in the tumour compared with normal tissue (up or down). The box indicates the 25th/50th/75th percentiles (bottom/middle/top bar), the extent of the whiskers indicate the most extreme values that are within 1.5 times the IQR (inter-quartile range) of the hinge (as per R package ggplot2/geom_boxplot). **d**, qRT–PCR analysis of the relative expression of PYCR1 in 786-O and A498 ccRCC cell lines. **e**, qRT–PCR analysis of the relative expression of PYCR2 and PYCRL in the A498 ccRCC cell line after 48 h of glutamine deprivation. **f**, Immunohistochemistry analysis detects high levels of p4EBP1 threonine 37/46 but no PYCR1 signal. **g**, A scheme of the common tumour changes in gene expression. In particular, while down regulation of PRODH2 and ALDH4A1 was clearly observed, no strong activation of PYCR1 was noted. **h**, Immunohistochemistry analysis using anti-CD31 antibodies. **i**, Knockdown of PYCR1 in 786-O cells expressing high levels of PYCR1 (**d**), expression is normalized to *GAPDH* mRNA. Error bars represent s.d.; scale bar, 100 μm.

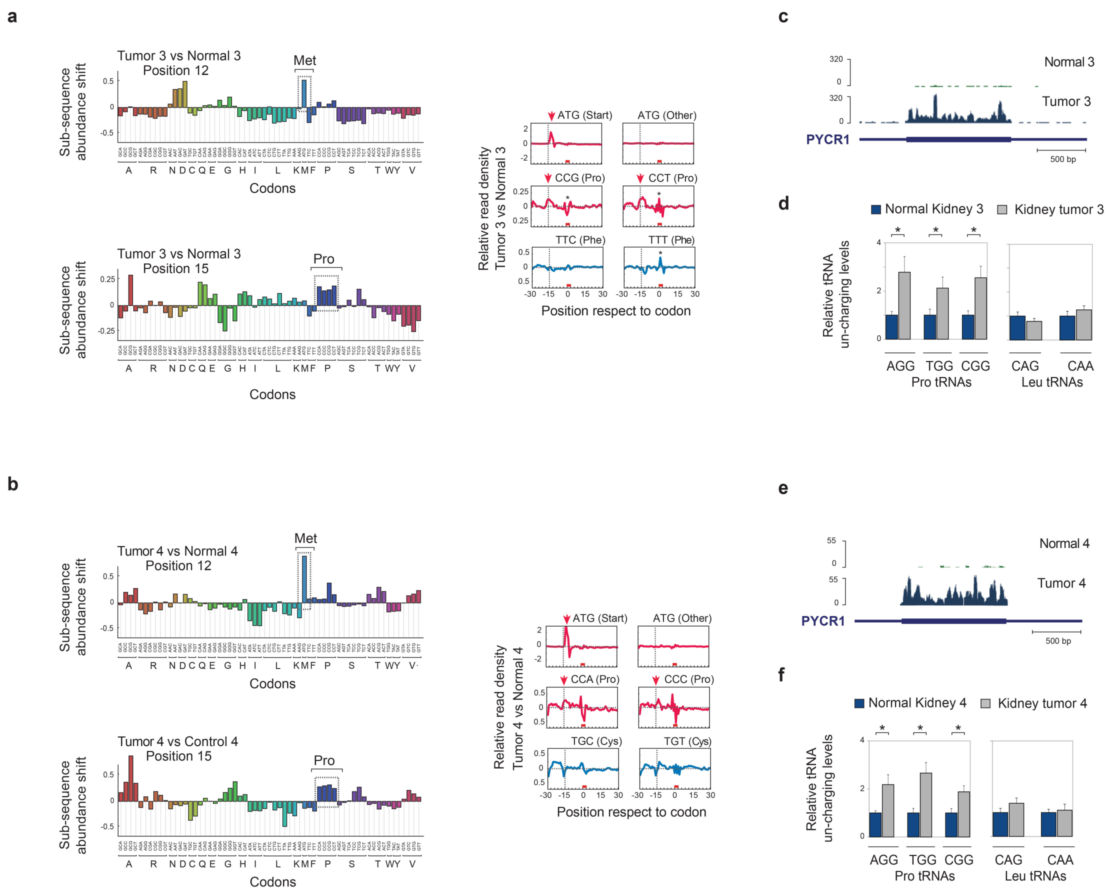

Extended Data Figure 6 | Supporting evidence for the link between the proline signals in diricore and high PYCR1 expression level. **a**, **b**, Two additional ccRCC and normal samples were subjected to diricore analysis. Tumour specific signals at the methionine and proline codons are highlighted. **c**, **e**, Gene expression analysis based on Ribo-seq shows that the selected tumours express high levels of PYCR1. **d**, **f**, Analysis of the relative levels of non-aminoacylated tRNAs in ccRCC tumours. For **d** and **f**, error bars represent s.d.; $n = 3$ independent biological replicates; $n = 3$ independent biological replicates; $*P < 0.05$ by Student's t-test. Cutoff for subsequence shift plots in this figure was 25 reads per gene. Cutoff for RPF density shift plots in this figure was 25 reads per window.

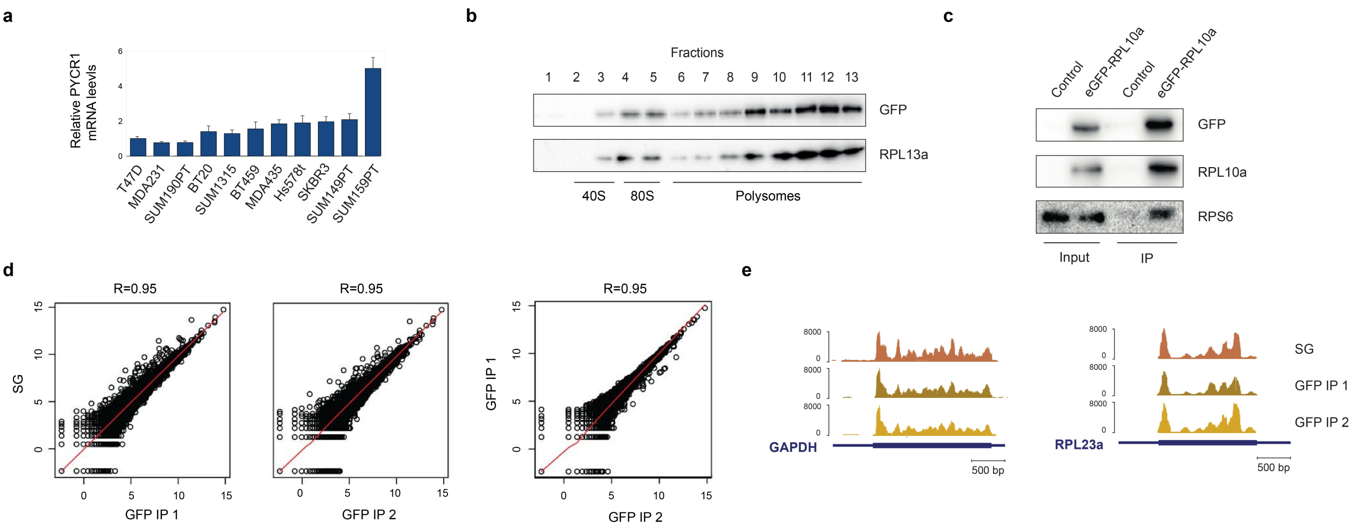

Extended Data Figure 7 | Usage of eGFP–RPL10a fusion protein for ribosome profiling in a high PYCR1 expressing ccRCC cell line. **a**, *PYCR1* mRNA levels measured by qRT–PCR in a panel of breast cancer cell lines. Values were normalized to *GAPDH* mRNA. **b**, Immunoblot analysis from sucrose gradients shows the incorporation of the eGFP–RPL10a fusion protein in polysomes. **c**, Immunoprecipitation experiments with beads coated with antibodies against GFP followed by western blot analysis in SUM159PT cells expressing eGFP–RPL10a. **d**, Correlations between independent Ribo-seq experiments where ribosomes where purified by sucrose gradients (SG) or by GFP immunoprecipitation. MCF7 eGFP–RPL10a cells were used in this experiment. **e**, RPF reads profiles from Ribo-seq experiments generated from sucrose gradients or GFP immunoprecipitation. Error bars represent s.d.

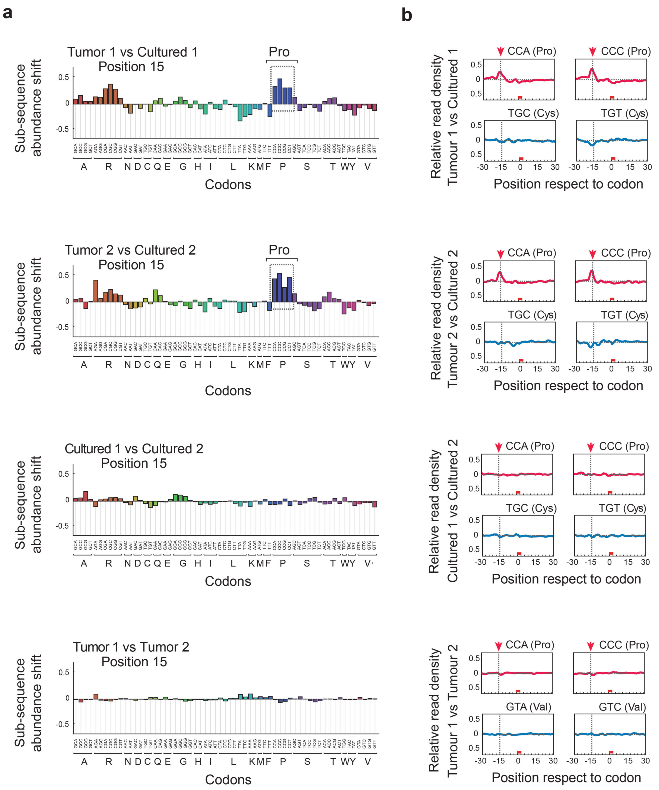

Extended Data Figure 8 | Additional tumour vs cultured eGFP–RPL10a-expressing SUM159PT conditions. a, b, Diricore analysis of an independent experiment of tumours derived from eGFP–RPL10a-expressing SUM159PT. A specific signal in proline codons at position 15 is observed.

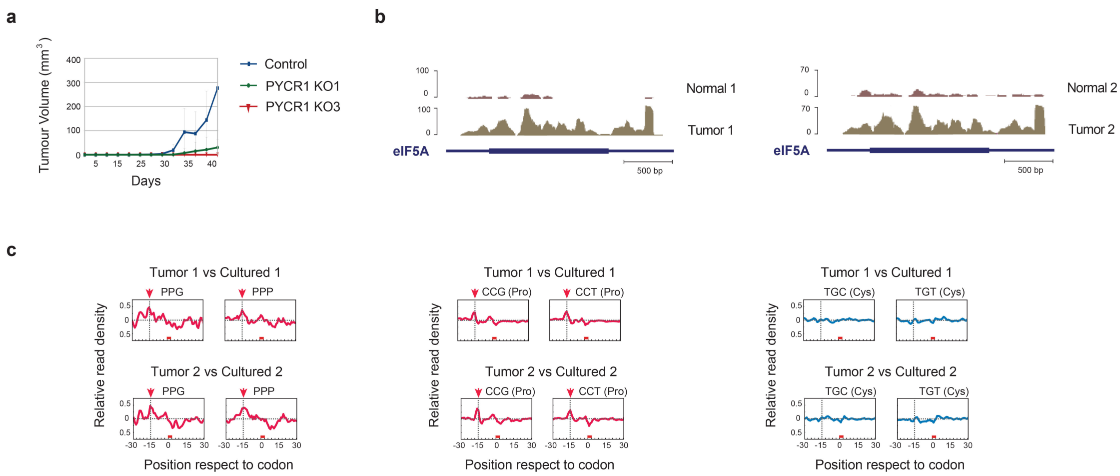

Extended Data Figure 9 | Additional data supporting a role for proline production pathway in tumour growth *in vivo*. a, Tumour volume of clonally derived SUM159PT cells expressing a non-targeting sgRNA (control) or two independent sgRNAs against PYCR1 (KO). **b**, Gene expression analysis by RNA-seq shows high levels of eiF5A in the tumour samples compared to normal tissues. **c**, RPF density shift plots at amino acid motifs PPG and PPP (left panels) on the *in vivo* ribosome profiling data set of Fig. 4c, d. The first nucleotide of the first codon of the motif is located at the 0-position. RPF density shift plots at proline and cysteine codons are shown in the middle and right panels, respectively. For the PPG and PPP motifs the cutoff of RPFs per window was lowered to 10 (from the usual 50) in order to compensate for the fewer windows with sufficient coverage. $n = 6$. Error bars represent s.d.; n refers to the number of xenografts per condition.

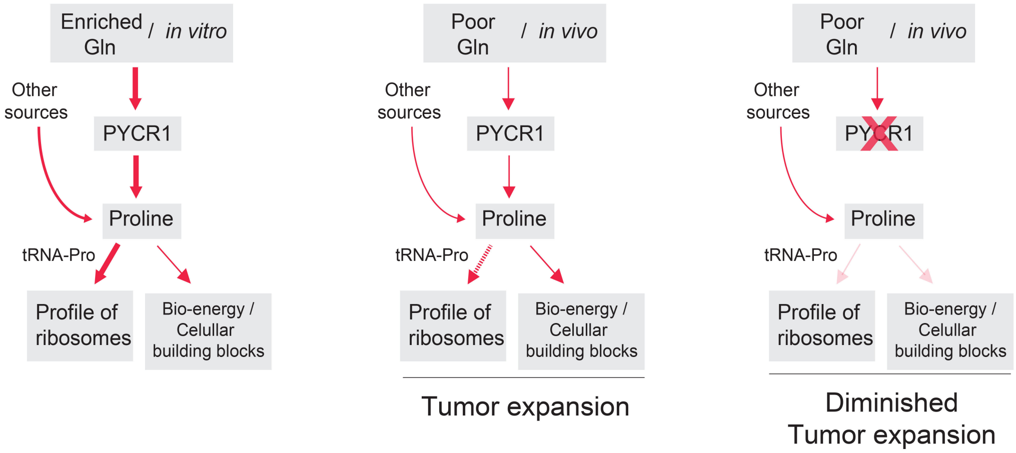

Extended Data Figure 10 | A schematic diagram modelling our findings.

doi:10.1038/nature16970

Epithelial tricellular junctions act as interphase cell shape sensors to orient mitosis

Floris Bosveld[1], Olga Markova[1], Boris Guirao[1], Charlotte Martin[1]†, Zhimin Wang[1], Anaëlle Pierre[2], Maria Balakireva[1], Isabelle Gaugue[1], Anna Ainslie[1]†, Nicolas Christophorou[1]†, David K. Lubensky[1,3], Nicolas Minc[2] & Yohanns Bellaïche[1]

The orientation of cell division along the long axis of the interphase cell—the century-old Hertwig's rule—has profound roles in tissue proliferation, morphogenesis, architecture and mechanics[1,2]. In epithelial tissues, the shape of the interphase cell is influenced by cell adhesion, mechanical stress, neighbour topology, and planar polarity pathways[3–12]. At mitosis, epithelial cells usually adopt a rounded shape to ensure faithful chromosome segregation and to promote morphogenesis[1]. The mechanisms underlying interphase cell shape sensing in tissues are therefore unknown. Here we show that in *Drosophila* epithelia, tricellular junctions (TCJs) localize force generators, pulling on astral microtubules and orienting cell division via the Dynein-associated protein Mud independently of the classical Pins/Gα_i pathway. Moreover, as cells round up during mitosis, TCJs serve as spatial landmarks, encoding information about interphase cell shape anisotropy to orient division in the rounded mitotic cell. Finally, experimental and simulation data show that shape and mechanical strain sensing by the TCJs emerge from a general geometric property of TCJ distributions in epithelial tissues. Thus, in addition to their function as epithelial barrier structures, TCJs serve as polarity cues promoting geometry and mechanical sensing in epithelial tissues.

To understand how rounded mitotic cells tend to align their spindle along their interphase shape long axis, we deciphered the mechanisms of spindle orientation in the *Drosophila* pupal notum epithelium. Within this tissue, more than ten thousand cells divide[13], and, as in many epithelial tissues, the division of rounded mitotic cells takes place in the plane of the tissue and is influenced by their interphase cell shape (Extended Data Fig. 1a, b). One possibility is that Pins (vertebrate LGN) or Gα_i polarization orients division as found in single cells in culture or during asymmetric divisions[14]. However, Pins and Gα_i were homogenous around the cortex (Extended Data Fig. 1c, d). In contrast, the distribution of the Dynein-associated protein Mud (vertebrate NuMA) suggested a role in orienting the spindle according to the interphase cell shape. GFP–Mud (Mud tagged with green fluorescent protein) was localized at the spindle poles and unexpectedly was also enriched at TCJs where at least three cells meet (Fig. 1a, Extended Data Fig. 1e, h and Supplementary Video 1). Accordingly, in this tissue and other pupal or larval epithelial tissue GFP–Mud or endogenous Mud co-localized with Gliotactin (Gli), a septate TCJ marker[15] (Fig. 1b and Extended Data Fig. 1i–o). Furthermore, we established that in G2 phase GFP–Mud localizes at TCJs where it persists through mitosis (Extended Data Fig. 2). The TCJ localization of Mud was independent of Pins and Gα_i in both interphase and mitotic cells (Fig. 1c–e and not shown). Accordingly, GFP–Mud lacking the Pins binding domain (GFP–Mud∆Pins) localizes at TCJs (Fig. 1c). Whereas Mud loss of function did not affect Gli localization, loss of Gli led to a reduction of GFP–Mud localization at the TCJs (Fig. 1d, e and Extended Data Fig. 3a). Likewise, loss of function of the Discs-large (Dlg) septate junction protein, which is necessary for Gli localization[15] caused the disappearance of both Gli and GFP–Mud from the TCJs (Fig. 1d, e and Extended Data Fig. 3b–d). Collectively, our results show that independently of the Pins/Gα_i pathway, epithelial mitotic cells harbour a cortical TCJ Mud distribution inherited from interphase.

Since astral microtubules contacted ChFP–Mud (Mud tagged with cherry fluorescent protein) patches at TCJ (Extended Data Fig. 4a and Supplementary Video 2), we asked whether TCJs recruit or activate force generators to orient the spindle. Following experiments in *Caenorhabditis elegans* zygotes[16], we developed a laser ablation assay to estimate the relative magnitude and the direction of mechanical forces exerted by astral microtubules on the centrosome within tissue (Extended Data Figs 4b and 5). Astral microtubule ablation in wild-type cells caused the centrosomes to recoil away from the ablation site, suggesting that microtubules predominantly exert pulling forces on spindle poles (Fig. 2a, b and Supplementary Video 3). The loss of Mud or Dynein minus-end-directed motor activity led to a reduction in centrosome recoil upon microtubule ablation (Fig. 2b). In agreement with the role of Gli and Dlg in promoting TCJ Mud localization, centrosome recoil velocities upon microtubule ablation were also reduced in *Gli* and *dlg* mutant cells (Fig. 2b). Together, these results indicate that TCJs control the pulling forces exerted by astral microtubules on the spindle via Mud and Dynein activities.

We then investigated whether the Mud distribution at TCJs accounts for the torque exerted by microtubules on the spindle to dictate its orientation. To this end, we adapted a mechanical model predicting the spindle orientation according to cell shape[17,18]. In this model, developed to describe isolated and non-epithelial cells which do not round up at mitosis, the pulling forces exerted by astral microtubules scale with microtubule length and, as a consequence, the model predicts the preferred spindle orientation along the long axis of the cell (Fig. 2c). To account for the contribution of Mud to microtubule pulling forces in epithelia, we modified the model to assume that astral microtubules instead pull with a force proportional to the cortical GFP–Mud intensity and independent of microtubule length (Fig. 2d). We then measured the metaphase distribution of cortical GFP–Mud and cell shapes to compare the predictions based on GFP–Mud intensity and cell shape models for cells in metaphase (Fig. 2e). Notably, the model based on GFP–Mud distribution along the cortex predicted spindle orientation and its predictions were significantly better than the ones based on the metaphase cell shape (Fig. 2f–h, Extended Data Fig. 6a–i and Supplementary Table 1). In agreement with the fact that Pins does not regulate Mud localization at TCJs, spindle orientation predictions were similar in wild-type and *pins* mutant tissues (Extended Data Fig. 7). To test the contribution of Mud-dependent microtubule pulling forces to spindle orientation further, we characterized a GFP–Mud mutant deleted of its coiled-coil domain (GFP–Mud∆CC, Extended Data Fig. 8). GFP–Mud∆CC co-localizes with Gli in wild-type or *mud*

[1]Polarity, Division and Morphogenesis Team, Institut Curie, CNRS UMR 3215, INSERM U934, 26 rue d'Ulm, 75248 Paris Cedex 05, France. [2]Institut Jacques Monod, CNRS UMR7592 15 rue Hélène Brion, 75205 Paris Cedex 13, France. [3]Department of Physics, University of Michigan, Ann Arbor, Michigan 48109-1040, USA. †Present addresses: Institut Curie, CNRS UMR 3348, Université Paris Sud, Bâtiment 110, 91405 Orsay, France (C.M.); INRA, Institut Jean-Pierre Bourgin, UMR 1318, ERL CNRS 3559, Saclay Plant Sciences, RD10, Versailles, France (N.C.); The Francis Crick Institute, Lincoln's Inn Fields Laboratory, 44 Lincoln's Inn Fields, London WC2A 3LY, UK (A.A.).

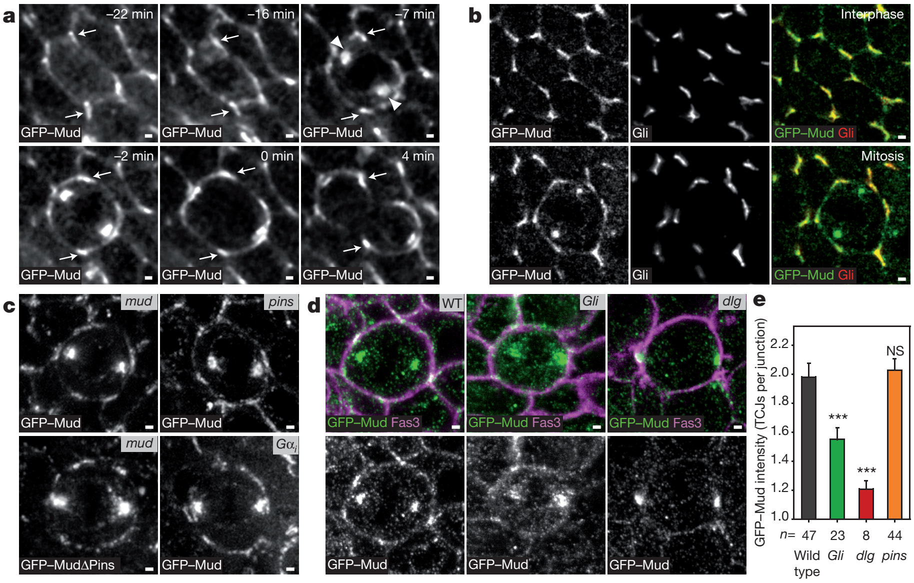

Figure 1 | Mud localizes at TCJs. a, GFP–Mud from interphase to telophase ($t = 0$ min, anaphase). GFP–Mud at TCJs (arrows), spindle poles (arrowheads). $n = 21$ cells. **b**, GFP–Mud and Gli co-localization in interphase (top, $n = 54$ cells) and metaphase (bottom, $n = 8$ cells). **c**, GFP–Mud localization in *mud* ($n = 15$), *pins* ($n = 22$), $G\alpha_i$ ($n = 5$) cells and GFP–MudΔPins in *mud* cells ($n = 18$). **d**, **e**, GFP–Mud distribution (**d**, images representative of quantifications shown in **e**) and TCJ intensities (**e**) in wild-type (WT), *Gli*, *dlg* and *pins* cells (mean ± s.e.m.). Fas3, cell contours. Student's *t*-test; NS, not significant; $***P < 0.0005$. Scale bars, 1 μm (**a**–**d**).

tissues, but GFP–MudΔCC cannot restore astral pulling forces in *mud* tissue (Fig. 2i–k). Whereas the GFP–MudΔCC cortical localization predicted spindle orientation in wild-type tissue (Extended Data Fig. 8d), planar mitotic spindles were not oriented according to the distribution of GFP–MudΔCC in *mud* tissue (Fig. 2l). Collectively, these findings indicate that TCJs via Mud define the distribution of microtubule pulling forces, specifying the spindle orientation in epithelial tissues.

Our finding that in metaphase the Mud distribution at TCJs is a better predictor of spindle orientation than is cell shape argues against a model where incomplete cell rounding ensures interphase cell shape 'memorization'. We therefore hypothesized that the

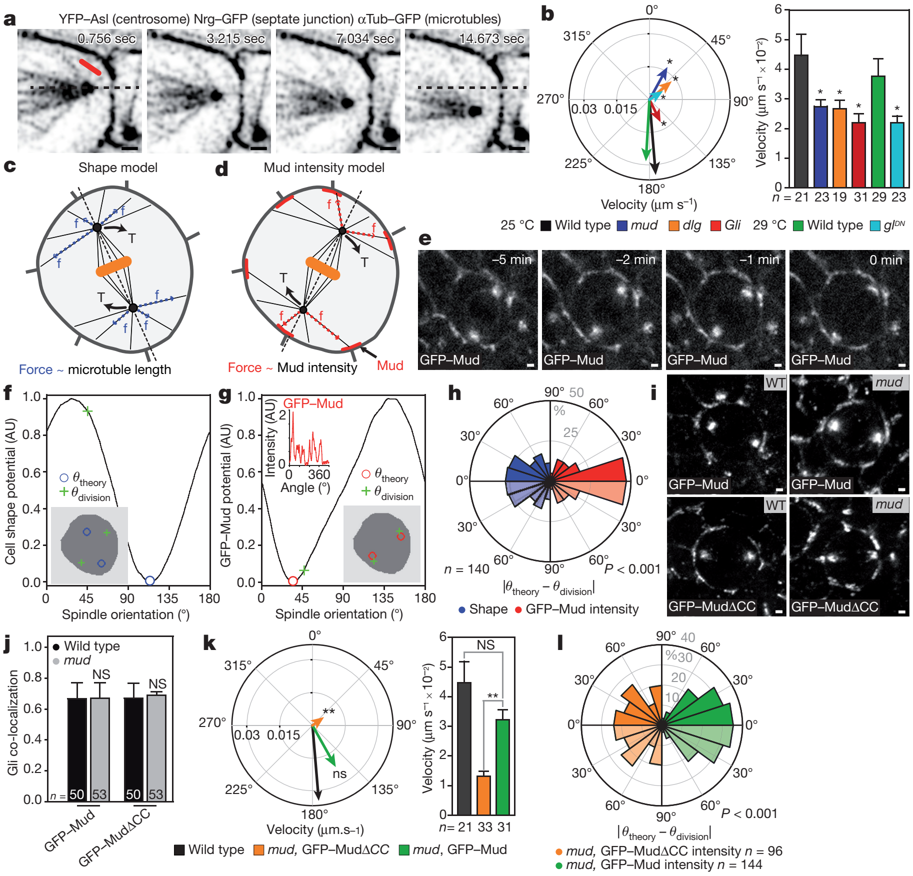

Figure 2 | TCJs regulate Mud-dependent microtubule pulling forces to orient divisions. a, Ablation of astral microtubules (red line), $n = 21$ cells quantified in **b**. **b**, Mean centrosome velocity relative to microtubule ablation site (left), mean velocity amplitude after ablation (mean ± s.e.m., right) in wild-type, *mud*, *dlg* and *Gli* cells at 25 °C and in wild-type and gl^{DN} cells at 29 °C. Student's *t*-test; $*P < 0.05$. Orientations in *mud*, *dlg* and gl^{DN} differ from wild type (Watson's U^2 test; $P < 0.01$). **c**, **d**, Cell shape (**c**) and Mud intensity (**d**) models: pulling forces scale with microtubule length (blue arrows) or Mud cortical intensity (red arrows) to exert a torque (T, arrows). **e**–**g**, Experimental spindle orientation (green cross) and predictions based on cell shape (blue circles, **f**) or GFP–Mud intensity (red circles, **g**) potentials at $t = -1$ min for cell in **e** ($n = 121$ cells). AU, arbitrary units; WT, wild type. **h**, Difference between theoretically predicted (θ_{theory}) (blue, shape; red, GFP–Mud intensity) and experimental (θ_{division}) spindle orientation. Data are duplicated in a lighter colour relative to 0° line in this and subsequent plots. Kolmogorov–Smirnov test (*P* value). **i**, Localizations of GFP–Mud in wild-type ($n = 54$) and *mud* ($n = 15$) cells as well as GFP–MudΔCC in wild-type ($n = 18$) and *mud* ($n = 67$) cells. **j**, Quantifications (mean ± s.e.m.) of GFP–Mud or GFP–MudΔCC co-localization with Gli in wild-type and *mud* cells. Student's *t*-test; NS, not significant. **k**, Mean centrosome velocity relative to microtubule ablation (left), mean velocity amplitude after ablation (mean ± s.e.m., right) in wild-type and in *mud* tissues expressing GFP–Mud or GFP–MudΔCC. Student's *t*-test; $**P < 0.005$. Orientation in *mud*, *GFP–MudΔCC* differs from wild type (Watson's U^2 test, $P < 0.001$). **l**, Difference between θ_{theory} (from cortical GFP intensity) and θ_{division} in *mud* cells expressing GFP–MudΔCC or GFP–Mud. GFP–Mud in *mud* and wild-type (**h**, red) tissue are similar ($P = 0.12$). Kolmogorov–Smirnov test (*P* values). Scale bars, 1 μm (**a**, **e**, **i**).

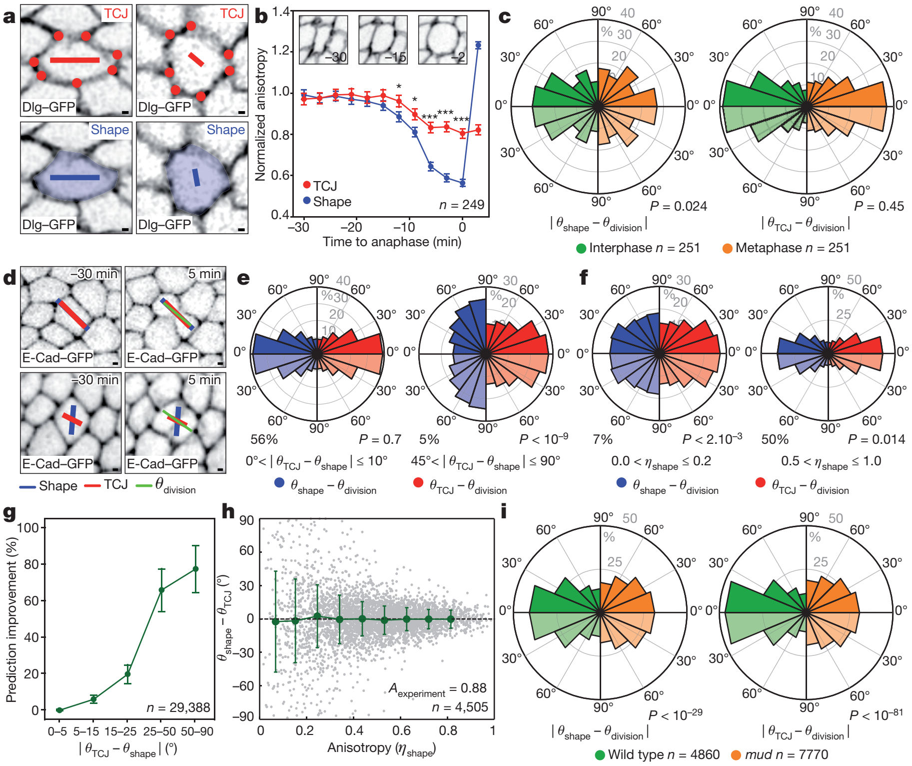

Figure 3 | TCJ distribution accounts for division orientation along the interphase cell shape. **a**, TCJ (red dots) bipolarity and cell shape (blue) anisotropies η and orientations θ represented by the length and orientation of red and blue bars. **b**, η_{TCJ} and η_{shape} from interphase to anaphase (mean $\pm$ s.e.m.). Insets, time-lapse images of a cell from interphase to mitotic rounding ($n = 249$ cells). Student's t-test; $*P < 0.05$, $***P < 0.0005$. **c**, Difference between experimental ($\theta_{division}$) and predicted division orientations by the average (-20 to -10 min interphase, -4 to -3 min metaphase) cell long axis (θ_{shape}) (left) or TCJ bipolarity (θ_{TCJ}) (right). Kolmogorov–Smirnov test (P values). **d**, Top, θ_{shape} and θ_{TCJ} align with $\theta_{division}$. Bottom, only θ_{TCJ} aligns with $\theta_{division}$. Time-lapse images of 2 cells out of the 29,388 cells analysed. **e**, **f**, Difference between experimental ($\theta_{division}$) and predicted division orientations based on interphase TCJ bipolarity (θ_{TCJ}) or cell long axis (θ_{shape}) for $|\theta_{TCJ} - \theta_{shape}|$ intervals (**e**) and indicated η_{shape} intervals (**f**). Kolmogorov–Smirnov test (P values), percentage of 29,388 cells. **g**, TCJ bipolarity (θ_{TCJ}) prediction improvement over cell long axis (θ_{shape}) versus $|\theta_{TCJ} - \theta_{shape}|$. Mean $\pm$ s.e.m. of three movies for a total of $n = 29{,}388$ cells analysed. **h**, Differences (green bars, mean $\pm$ s.d.) between θ_{shape} and θ_{TCJ} versus η_{shape}. 4,505 cells (grey dots) randomly picked from the 29,388 cells analysed. Correlation coefficient $A_{experiment} = 0.88$. **i**, Difference between experimental ($\theta_{division}$) and predicted division orientations based on interphase cell long axis (θ_{shape}) (left) or TCJ bipolarity (θ_{TCJ}) (right) in wild-type and *mud* cells. Kolmogorov–Smirnov test (P values). Scale bars, 1 μm (**a**, **d**).

interphase TCJ distribution might account for the Hertwig rule in tissues. Since our theoretical analysis indicated that spindle orientation is mainly dictated by the anisotropy of the TCJ distribution (Extended Data Fig. 6h, i), we introduced a TCJ bipolarity quantity characterized by an anisotropy (η_{TCJ}) and orientation (θ_{TCJ}) to describe the TCJ angular distribution in a given cell (Fig. 3a and Extended Data Fig. 6j). The TCJ bipolarity anisotropy and orientation can be similar to or distinct from the cell shape anisotropy (or elongation, η_{shape}) and long-axis orientation (θ_{shape} ; Fig. 3a). We found that the anisotropy of TCJ bipolarity decreases much less than cell shape anisotropy during mitotic cell rounding (Fig. 3b). Also, division orientation predictions based on the TCJ distribution, unlike those based on cell shape, were similar in interphase and mitosis (Fig. 3c). These findings support the notion that TCJ bipolarity is a persistent marker of the interphase cell elongation axis during mitotic rounding. We then measured each cell's average shape (θ_{shape}) and TCJ bipolarity (θ_{TCJ}) from 60 to 30 minutes before mitosis (from late G2 interphase to before mitotic rounding) as well as its division orientation ($\theta_{division}$). Apart from cases where TCJ and shape orientation are aligned ($|\theta_{TCJ} - \theta_{shape}| < 10°$), TCJ gives better division orientation predictions than cell shape does, and this improvement increases as the difference between shape and TCJ orientation increases (Fig. 3d, e, g and Extended Data Fig. 9a). This finding applies for both rounded cells (low η_{shape}) and elongated cells (high η_{shape}) (Extended Data Fig. 9b, c) and thus raises the question of why cells tend to divide according to their interphase cell long axis. The distribution of the angular difference between TCJ and shape orientation is broad in rounded cells (low η_{shape}) but narrow in elongated cells (high η_{shape}) (Fig. 3h). Accordingly, cell shape does not predict the cell division axis in rounded cells, and as cell shape anisotropy increases, the predictions based on cell shape agree more and more with the predictions based on TCJ bipolarity (Fig. 3f, g and Extended Data Fig. 9b, c). Hence, in rounded cells TCJ bipolarity and cell shape orientations may be misaligned and division orientation follows TCJ bipolarity, whereas in elongated cells TCJ bipolarity and cell shape orientations are aligned in most cases, and the TCJ distribution ensures that cell division occurs along the former interphase cell long axis. Lastly, cell division orientation along the interphase cell long axis and TCJ distribution was strongly reduced in *mud* mutant tissue (Fig. 3i and Extended Data Fig. 5f, g). Altogether, we propose that TCJs, via Mud, constitute the dominant mechanism of division orientation along the interphase cell long axis.

Why are the orientations of cell long axes and TCJ distributions aligned? This can be understood by picturing regular hexagonal cells, which are then pulled. The cell elongation leads to the alignments of cell shape and TCJ bipolarity orientations with the pulling direction (Fig. 4a). Computer simulation can then be used to model the disordered case of epithelial cells whose shapes depend on adhesion and cortical tension[19]. The simulations reproduce the alignment between cell shape long axis and TCJ bipolarity orientations as cell shape anisotropy increases, as well as the average alignment of the TCJ bipolarity and mechanical strain orientation (Fig. 4b, c, Extended Data Fig. 10d and Supplementary Video 4). Therefore, generic properties of epithelial cells, adhesion and cortical tension, are sufficient to reproduce the alignment of TCJ bipolarity and cell shape as their anisotropy increases. Furthermore, in agreement with the fact that global mechanical stress tends to elongate cells[8,12], the alignment of TCJ bipolarity with mechanical stress increases as tissue stress anisotropy increases, thus accounting for orientation of divisions along the global mechanical stress direction (Fig. 4d and Extended Data Fig. 10c). Our findings indicate that the alignment of TCJ distribution with cell elongation and mechanical stress axis is a core geometric property of epithelial tissues and accounts for a role of TCJs as spatial landmarks that provide the information needed for cell shape and mechanical strain orientation sensing.

Altogether our findings provide evidence that TCJs can serve as built-in interphase shape sensors to orient division when the interphase cell shape is well defined. This mechanism is distinct from others

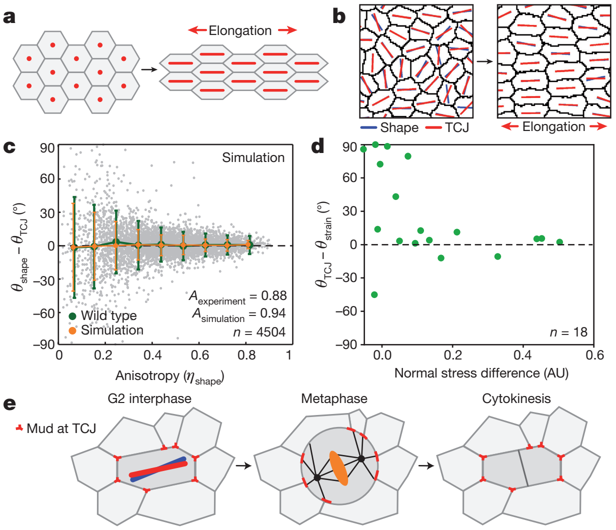

Figure 4 | TCJ alignment with shape is a core geometric property. **a**, **b**, Regular hexagonal cells (**a**) and simulated cell lattice (**b**) before and after elongation. **c**, Differences (mean ± s.d.) between θ_{shape} and θ_{TCJ} versus η_{shape} for 4,504 simulated cells (grey dots) and 4,505 experimental cells (Fig. 3h). $A_{simulation} = 0.94$. **d**, Difference between θ_{TCJ} and principal strain axis (θ_{strain}) versus normal stress differences. AU, arbitrary units; n, ablation number. **e**, Upon mitotic rounding, Mud interphase localization is maintained at TCJs orienting the spindle along the interphase cell long axis.

involving extracellular matrix retraction fibres or signalling[17,20–23]. It accounts for the integration of two properties of epithelial division: orientation along the interphase cell shape and mitotic rounding (Fig. 4e). The packing of tissue promotes contacts between three (or more) cells and the formation of TCJs. TCJs are implicated in epithelial barrier function[24,25] and are the sites of enrichment of several proteins including adhesion molecules, cytoskeleton regulators and Hippo pathway components[25–29]. The alignment of TCJs with cell shape or mechanical strain being a geometrical property of epithelia, TCJs might therefore provide epithelial cells with an axial polarity (or bipolarity) to couple cell shape and tissue mechanics with adhesion, cytoskeleton organization and signalling.

Online Content Methods, along with any additional Extended Data display items and Source Data, are available in the online version of the paper; references unique to these sections appear only in the online paper.

Received 11 October 2015; accepted 5 January 2016.
Published online 17 February 2016.

1. Cadart, C., Zlotek-Zlotkiewicz, E., Le Berre, M., Piel, M. & Matthews, H. K. Exploring the function of cell shape and size during mitosis. *Dev. Cell* **29,** 159–169 (2014).
2. Hertwig, O. Das Problem der Befruchtung und der Isotropie des Eies, eine Theory der Vererbung. *Jenaische Zeitschrift fuer Naturwissenschaft.* (1884).
3. Baena-López, L. A., Baonza, A. & García-Bellido, A. The orientation of cell divisions determines the shape of *Drosophila* organs. *Curr. Biol.* **15,** 1640–1644 (2005).
4. Saburi, S. *et al.* Loss of Fat4 disrupts PCP signaling and oriented cell division and leads to cystic kidney disease. *Nature Genet.* **40,** 1010–1015 (2008).
5. Aigouy, B. *et al.* Cell flow reorients the axis of planar polarity in the wing epithelium of *Drosophila*. *Cell* **142,** 773–786 (2010).
6. Gibson, W. T. *et al.* Control of the mitotic cleavage plane by local epithelial topology. *Cell* **144,** 427–438 (2011).
7. Mao, Y. *et al.* Planar polarization of the atypical myosin Dachs orients cell divisions in *Drosophila*. *Genes Dev.* **25,** 131–136 (2011).
8. Campinho, P. *et al.* Tension-oriented cell divisions limit anisotropic tissue tension in epithelial spreading during zebrafish epiboly. *Nature Cell Biol.* **15,** 1405–1414 (2013).
9. LeGoff, L., Rouault, H. & Lecuit, T. A global pattern of mechanical stress polarizes cell divisions and cell shape in the growing *Drosophila* wing disc. *Development* **140,** 4051–4059 (2013).
10. Mao, Y. *et al.* Differential proliferation rates generate patterns of mechanical tension that orient tissue growth. *EMBO J.* **32,** 2790–2803 (2013).
11. Xiong, F. *et al.* Interplay of cell shape and division orientation promotes robust morphogenesis of developing epithelia. *Cell* **159,** 415–427 (2014).
12. Wyatt, T. P. *et al.* Emergence of homeostatic epithelial packing and stress dissipation through divisions oriented along the long cell axis. *Proc. Natl Acad. Sci. USA* **112,** 5726–5731 (2015).
13. Bosveld, F. *et al.* Mechanical control of morphogenesis by Fat/Dachsous/Four-jointed planar cell polarity pathway. *Science* **336,** 724–727 (2012).
14. Kotak, S. & Gönczy, P. Mechanisms of spindle positioning: cortical force generators in the limelight. *Curr. Opin. Cell Biol.* **25,** 741–748 (2013).
15. Schulte, J. *et al.* Gliotactin and Discs large form a protein complex at the tricellular junction of polarized epithelial cells in *Drosophila*. *J. Cell Sci.* **119,** 4391–4401 (2006).
16. Grill, S. W., Gönczy, P., Stelzer, E. H. & Hyman, A. A. Polarity controls forces governing asymmetric spindle positioning in the *Caenorhabditis elegans* embryo. *Nature* **409,** 630–633 (2001).
17. Théry, M., Jiménez-Dalmaroni, A., Racine, V., Bornens, M. & Jülicher, F. Experimental and theoretical study of mitotic spindle orientation. *Nature* **447,** 493–496 (2007).
18. Minc, N., Burgess, D. & Chang, F. Influence of cell geometry on division-plane positioning. *Cell* **144,** 414–426 (2011).
19. Morelli, L. G., Uriu, K., Ares, S. & Oates, A. C. Computational approaches to developmental patterning. *Science* **336,** 187–191 (2012).
20. Fink, J. *et al.* External forces control mitotic spindle positioning. *Nature Cell Biol.* **13,** 771–778 (2011).
21. Kwon, M., Bagonis, M., Danuser, G. & Pellman, D. Direct microtubule-binding by myosin-10 orients centrosomes toward retraction fibers and subcortical actin clouds. *Dev. Cell* **34,** 323–337 (2015).
22. Tamada, M. & Zallen, J. A. Square cell packing in the *Drosophila* embryo through spatiotemporally regulated EGF receptor signaling. *Dev. Cell* **35,** 151–161 (2015).
23. Machicoane, M. *et al.* SLK-dependent activation of ERMs controls LGN-NuMA localization and spindle orientation. *J. Cell Biol.* **205,** 791–799 (2014).
24. Byri, S. *et al.* The triple-repeat protein anakonda controls epithelial tricellular junction formation in *Drosophila*. *Dev. Cell* **33,** 535–548 (2015).
25. Furuse, M., Izumi, Y., Oda, Y., Higashi, T. & Iwamoto, N. Molecular organization of tricellular tight junctions. *Tissue Barriers* **2,** e28960 (2014).
26. Lye, C. M., Naylor, H. W. & Sanson, B. Subcellular localisations of the CPTI collection of YFP-tagged proteins in *Drosophila* embryos. *Development* **141,** 4006–4017 (2014).
27. Rauskolb, C., Pan, G., Reddy, B. V., Oh, H. & Irvine, K. D. Zyxin links fat signaling to the hippo pathway. *PLoS Biol.* **9,** e1000624 (2011).
28. Sawyer, J. K., Harris, N. J., Slep, K. C., Gaul, U. & Peifer, M. The *Drosophila* afadin homologue Canoe regulates linkage of the actin cytoskeleton to adherens junctions during apical constriction. *J. Cell Biol.* **186,** 57–73 (2009).
29. Oda, Y., Otani, T., Ikenouchi, J. & Furuse, M. Tricellulin regulates junctional tension of epithelial cells at tricellular contacts through Cdc42. *J. Cell Sci.* **127,** 4201–4212 (2014).

Supplementary Information is available in the online version of the paper.

Acknowledgements We thank V. Auld, A. Bardin, R. Basto, B. Edgar, S. Luschnig, F. Schweisguth, the Bloomington Stock Center and Developmental Studies Hybridoma Bank for reagents; M. Manil-Ségalen, S. Rigaud. T. Piolot and I. Bonnet for input and data analyses; the Developmental Biology Curie imaging facility (PICT-IBiSA@BDD); F. Graner, A. Guichet, S. Herszterg, J.-L. Maître, M. Piel and M. Thery for comments; CePoDro ANR, MorphoDro ERC Advanced, ARC (SL220130607097), Curie Mayent-Rothschild, Labex DEEP, NSF DMR1056456 and ICAM grants for funding.

Author Contributions F.B., N.M. and Y.B. designed the project. F.B., M.B., A.A. and N.C. performed experiments. C.M., Z.W. and I.G. produced reagents. O.M., B.G., A.P. and N.M. developed methods and scripts for data analysis. O.M. performed simulations. F.B., O.M., B.G., A.P., N.M. and Y.B. analysed the data. D.K.L. and N.M. developed theoretical models. F.B., O.M., D.K.L., N.M. and Y.B. wrote the manuscript.

Author Information Reprints and permissions information is available at www.nature.com/reprints. The authors declare no competing financial interests. Readers are welcome to comment on the online version of the paper. Correspondence and requests for materials should be addressed to F.B. (floris.bosveld@curie.fr) or Y.B. (yohanns.bellaiche@curie.fr).

METHODS

Fly stocks and genetics. *Drosophila melanogaster* stocks and associated references are listed in Supplementary Table 2. Flies were crossed and experiments were performed at 25 °C unless specified otherwise. Male or female pupae were used. Experiments using the temperature-sensitive allele of p150/Glued, *D82glued*[30] were performed as previously described for temperature-controlled experiments in the *Drosophila* pupa[13]. Loss-of-function, gain-of-function and dual-coloured-patches experiments were carried out using the FLP/FRT or the MARCM techniques[31–33]. Somatic clones were induced in the second instar larval stage by heat shock (20 min at 37 °C for FRT19A and FRT40A, 1 h at 37 °C for FRT42D) and analysed 3–4 days after clone induction in 12–20 h after pupa formation (hAPF) pupae. The analyses of dlg^{m52} loss-of-function clones were performed in small clones (3 days after induction) to avoid apical–basal polarity defects[34].

Molecular biology. To create the GFP–Mud or ChFP–Mud transgenes under the control of Mud endogenous promoter, we used recombineering[35,36] to introduce a GFP or ChFP tag at the ATG of the *mud* open reading frame in the CH322-147E14 BAC genomic clone (BACPAC Resources Center). This BAC clone contains ~19.5 kb of X chromosome genomic region including ~3.3 kb upstream of the *mud* mRNA 5′ and 5.4 kb downstream of the *mud* 3′ mRNA and thus most of the coding regions of genes proximal and distal to *mud* locus.

First a galK cassette, amplified with primers F (5′-CATACATATACGGGCGCACACACACCCATAAAAACGCACAAAAATTCGCACCTGTTGACAATTAATCATCGGCA-3′) and R (5′-GATTTACATACCCACTGGAGTAGGACCTTGCGCCAGCTGCGCGTGTCCATTCAGCACTGTCCTGCTCCTT-3′) (underlined bases indicate galK sequences), was inserted via recombination at the N terminus of the *mud* open reading frame. After positive selection, the galK cassette was replaced with a GFP tag, primers F (5′-CATACATATACGGGCGCACACACACCCATAAAAACGCACAAAAATTCGCAATGGTGAGCAA GGGCGA GGA-3′) and R (5′-GATTTACATACCCACTGGAGTAGGACCTTGCGCCAGCTGCGCGTGTCCATCTTGTACAGCTCGTC CATGC-3′) (underscored letters for GFP sequences) or with a ChFP tag, primers F (5′-CATACATATACGGGCGCACACACACCCATAAAAACGCACAAAAATTCGCAATGGTG AGCAAGGGCGAGGAGGATAACATG-3′) and R (5′-GATTT ACATACCCACTGGAGTAGGACCTTGCGCCAGCTGCGCG TGTCCATCTTGTACAGCTCGTCCATGCCGCCGGTGGA-3′) (underscored letters for ChFP sequences) via recombination and negative selection for galK[37]. The attB-P[acman-GFP-Mud]-CmR-BW was integrated into the PBac{y[+]-attP-9A}VK00030 landing site at 50E1, PBac{y[+]-attP-9A}VK00031 landing site at 62E1 and PBac{y[+]-attP-9A}VK00033 landing site at 65B2. The attB-P[acman-ChFP-Mud]-CmR-BW was integrated into the PBac{y[+]-attP-9A}VK00030 landing site at 50E1, PBac{y[+]-attP-9A}VK00031.

Deletions within the GFP–Mud genomic region were created by recombineering using a neomycin resistance cassette flanked by *loxP* sites[38], which were amplified by PCR (see below), at the amino acid positions shown in Extended Data Fig. 8a. Upon neomycin selection, the cassette was removed by Cre-mediated recombination[38] leaving behind a 78 bp *loxP* site sequence. The following primers were used for PCR: MudΔCH: F (5′-CATACATATACGGGCGCACACACACCCATAAAAACGCACAAAAATTCGCAGGCCTGGTGATG ATGGCGGGATC-3′) and R (5′-CTGCTGGGAAGACATGGGCTGACTGAGGTCGAAACCCCTTGTCG GTAAACTCAGAAGAACTCGTCAAG AAGGCG-3′, Note that the MudΔCH is not tagged with GFP); GFP–MudΔCC: F (5′-GGCTGTTGACGCGCGAATATCTTAGCCAGGCGATCGCCAACGTTGCAGTTCGTTCCTTGTATACGGCGGAGGTGACGCGCATGAAGGAGAAGCAGGAACG-3′) and R (5′-CGTTCCTGCTTCTCCTTCATGCGCGTCACCTCCGCCGTATACAAGGAACGAACTGCAACGTTGGCGATCGC CTGGCTAAGATATTCGCGCGTCAACAGCC-3′); GFP–MudΔPins: F (5′-CCGTTTCGTCCAGTTCGTCGGCGCCGAA CGATGACTGGCAGCCCTTCAAGCGCCACTCCGGCTCCCAGATAAC-3′) and R (5′-CTTACTTTGAGATCTTCGTCCTGGCTGCCCAAATCATATTGGGCAGCATAACT AGTGGATCCCCT CGAGGGACC TAATAAC-3′) and GFP–MudΔTM: F (5′-AATTCACACAACTGGTGGCCGCCTCTTGCAGTAATATCACTACGACTAGCTAGAAGCGGCAACGAAAGCAATGGGAAACGCACAAATCTTGCTGATGATC-3′) and R (5′-GATCATCAGCAAGATTTGTGCGTTTCCCATTGCTTTCGTTGCCGCTTCTAGCTAGTCGTAGTGATATTACTGCAAGAGGCGGCCACCAGTTGTGTGAATT-3′).

The MudΔCH, GFP–MudΔPins, GFP–MudΔCC and GFP–MudΔTM BAC constructs were integrated at the (PBac{y[+]-attP-9A}VK00030 landing site at 50E1 and at the PBac{y[+]-attP-9A}VK00033 landing site at 65B2.

A deletion of the C-terminal domain of Mud including the Pins and microtubule binding domains (MudΔC) (see Extended Data Fig. 8a) was created using the CRISPR/Cas9 system[39] at the endogenous *mud* locus. Two sgRNAs (upstream targeting sequence; 5′-CATCCAGTCTA ACCAGGCGGAGG-3′ and downstream targeting sequence: 5′-AGATGAGGCGCCGGTCATGTTGG-3′) were inserted into pU6B-sgRNA-short[40] and co-injected with purified ssODN 5′-GGCTGCTTCTCGCTTCCAACCAAGAGTTGGAAGAACTAAATTCCATCCAGTCTAACCAGGT-Δ-GACCGGCGCCTCATCTTGTACAGTCTATTCGATCGGCAGTG TGCACATGCAGC CGCTGC-3′ (Δ denotes position of the deletion) in the *vas-Cas9* line[41]. Resulting F1 flies were screened for germline transmission of the deletion by single fly PCR. The F2 progeny was sequenced to confirm the deletion of the C terminus domain.

Immunohistochemistry and fixed tissue imaging. Pupae were dissected and fixed as previously described[42]. Primary antibodies were: rabbit anti-Gα_i (1:500, provided by J. A. Knoblich), rabbit anti-Mud (aa375-549) (1:1,000 (ref. 43), mouse anti-Gli (1:250 (ref. 44), mouse anti-Dlg (1:1,000, DSHB, 4F3), mouse anti-FasIII (1:50, DSHB, 7G10), guinea-pig anti-Cora (1:2,000 (ref. 45), rabbit anti-GFP (1:2,000, Molecular Probes). Fluorescent secondary antibodies were: Alexa-488 goat-anti-rabbit IgG (1:500, Molecular Probes), Cy2, Cy3 and Cy5 donkey-anti-mouse IgGs (1:500, Jackson ImmunoResearch). Images were collected with confocal microscopes (LSM710NLO or LSM780, Carl Zeiss). All images are maximum projections of a *z*-stack unless otherwise indicated.

Live imaging. Pupae were prepared for live imaging as described previously[46]. Samples were imaged at 25 °C or 29 °C with either an inverted confocal spinning disk microscope from Nikon or Zeiss using either 40× NA1.3 OIL DIC H/N2 WD0.2 PL FLUOR, 60× NA1.4 OIL DIC N2 PL APO VC, 63× NA1.4 OIL DICII PL APO or 100× NA1.4 OIL DIC N2 PL APO VC objectives and either a CoolSNAP HQ2 (Photometrics), an EMCCD Evolve (Photometrics) or a CMOS (Hamamtsu) camera. Live images of FUCCI and GFP–Mud were acquired using a confocal microscope (LSM780, Carl Zeiss) and 63× NA1.4 OIL DICII PL APO objective. To improve signal-to-noise ratio, videos and images for display and segmentation were either deconvolved using Huygens software (Scientific Volume Imaging) or denoised using Safir software[47]. Average projections of raw *z*-stack images were used for intensity measurements.

Unless specified otherwise, all experiments on dividing cells were performed during the first round of cell divisions in the notum tissue (12–20 hAPF). In the analyses (unless mentioned otherwise), the time (t) equals 0 was set at anaphase onset defined by the initial cell elongation and/or centrosome movements towards the cortex.

Photobleaching of GFP–Mud or GFP–MudΔCC in neighbouring cells. Since the cortical GFP–Mud or GFP–MudΔCC signals at the TCJ has contributions from both the dividing cell and its neighbouring cells, we performed prediction of spindle orientation based on GFP–Mud or GFP–MudΔCC intensity upon photobleaching of GFP–Mud or GFP–MudΔCC in the neighbouring cells, the residual GFP–Mud or GFP–MudΔCC signal reflecting more faithfully the distribution of GFP–Mud or GFP–MudΔCC at the TCJ in the dividing cells. Having found by fluorescence recovery after photobleaching (FRAP) that GFP–Mud turnover at TCJs is on the order of tens of seconds ($t_{1/2} = 21 \pm 7$ s, $n = 28$, data not shown), a region of approximately two cell diameters was photobleached (491 nm laser at 100% power, 12 iterations) around a dividing cell, which was identified by the accumulation of GFP–Mud or GFP–MudΔCC at the spindle poles. Following photobleaching of GFP–Mud or GFP–MudΔCC in neighbouring cells, confocal *z*-stacks of 14 slices (0.5 μm per slice) were acquired every 1 min. Cells were used for predictions of mitotic spindle orientation when their anaphase onset ($t = 0$) occurred at least 4 min after photobleaching ensuring that the GFP–Mud or GFP–MudΔCC signal are mainly contributed by the dividing cells.

Segmentation and tracking of cells during tissue development. To record cell division orientation, cell shape and TCJ bipolarity during development, maximal projected images of multiscale time-lapse videos of pupa notum tissue labelled with either E-Cad–GFP (16–28 *z*-stacks 0.5 μm per slice, 0.322 μm per pixel, 5 min per acquisition, labelling of the apical adherens junctions) or Dlg–GFP (20 *z*-stacks 0.5 μm per slice, 0.205 μm per pixel, 3 min per acquisition, labelling of the septate junctions) were segmented and cell divisions were tracked as in refs 13,48.

GFP–Mud kymograph from interphase to mitosis. To generate the kymograph of the GFP–Mud signal around the cell contour from interphase to anaphase, the cell contour was manually segmented using the GFP–Mud signal. The GFP–Mud intensity of the fluorescence signal was recorded as a function of the angle θ of each contour pixel around the centre of mass and then plotted as a line for each time point.

Laser ablations of astral microtubules and estimation of cortical forces. Laser ablation of astral microtubules were performed in cells labelled with Jupiter–GFP or αTub–GFP (microtubule markers) and Sas-4–RFP, Spd-2–RFP or YFP-Asl (centrosome markers) as well as Dlg–GFP or Nrg–GFP (septate junction markers). Images were captured using a two-photon laser-scanning microscope (LSM710 NLO, Carl Zeiss) equipped with a 63× NA1.4 OIL DICII PL APO objective (digital zoom 3×) in single-photon bidirectional scan mode lasting $\delta t = 756$ ms. The astral

microtubules of mitotic spindles, which were parallel to the plane of the epithelial tissue were severed (t_3) using the Ti:Sapphire laser (Mai Tai DeepSee, Spectra Physics) at 890 nm with <100 fs pulses with a 80 MHz repetition rate typically set at 60% power.

To measure the recoil velocity (amplitude and orientation) of the centrosomes upon astral microtubule ablation, all spindles were registered horizontally with the ablated astral microtubules at the top right and the centrosome positioned at the origin. Centrosome movements were then manually tracked. The velocity (amplitude and orientation) was measured between t_2 and t_{20}.

Image quantifications and GFP–Mud and GFP–MudΔCC localization analyses. To measure and compare the TCJ accumulation of GFP–Mud in wild-type, *pins*, *Gli* and *dlg* cells (Fig. 1e), confocal *z*-stack average projections at the level of the septate junction (labelled by FasIII, Cora, PH–ChFP or mRFP) were generated using ImageJ from fixed (*pins* and *dlg*) or live (wild-type and *Gli*) tissues harbouring wild-type, *Gli*, *dlg* and *pins* mutant cells. Using FasIII, Cora, PH–ChFP or mRFP labelling, the positions of the TCJs in each cell were manually determined. The FasIII, Cora, PH–ChFP or mRFP labelling were used to draw a mask (5 pixels wide) delineating the cell outline at the level of the mitotic spindle (as determined by GFP–Mud localization at the spindle poles) of (pro)metaphase cells. Following background subtraction, the mean intensity at TCJs (10° over each TCJ) was divided by the mean intensity along the rest of the cell outline to obtain the accumulation at TCJs. Significance was determined using Student's *t*-test.

To compare the GFP–Mud or GFP–MudΔCC distributions at TCJ in wild-type, *pins* and *mud* tissues (Fig. 2j or Extended Data Fig. 7b), their co-localization with Gli was quantitatively compared as follows. Confocal *z*-stack average projections at the level of the septate junction of fixed (pro)metaphase cells (as determined by DAPI staining) expressing either GFP–Mud or GFP–MudΔCC and labelled with Gli and Coracle (Cora, a septate junction marker) were generated using ImageJ. Using the Cora staining, a mask 5 pixels wide was manually drawn to measure the raw fluorescent intensity profiles of GFP–Mud or GFP–MudΔCC and Gli in (pro)metaphase cells (as determined by DAPI staining) which were normalized by their total fluorescence intensity upon subtraction of the background intensity. The co-localization factor (*C*, vertical axis Fig. 2j and Extended Data Fig. 7b) between GFP–Mud or GFP–MudΔCC and Gli was then determined by calculating the area between the GFP–Mud or GFP–MudΔCC and Gli normalized intensity curves.

$$C = 1 - \frac{1}{2}\int_0^{2\pi} |\mathrm{GFP}(\theta) - \mathrm{Gli}(\theta)|\,\mathrm{d}\theta$$

C equals 1 if the two proteins perfectly co-localize and equals 0 if the two proteins do not co-localize. The comparisons of the distribution of GFP–Mud, GFP–MudΔCC in wild-type and *mud* tissues were performed blind (Fig. 2j). Significance was determined using Student's *t*-test.

Measurement of apical–basal (AB) angle of the spindle α_{AB}. The AB orientations of the mitotic spindle (α_{AB}) in the different experimental conditions were determined by measuring the orientation of the centrosomes (marked by Spd-2–RFP, Sas-4–RFP or Sas-4–GFP) relative to the plane of the epithelial tissue (labelled by αTub–GFP, Jupiter–GFP or RFP–αTub) using a custom ImageJ plugin. Statistical significance was assessed using the Kolmogorov–Smirnov test.

Analyses of cell rounding and mitotic spindle prediction from interphase cell shape and TCJ bipolarity. The analyses of cell rounding from $t = -60$ min to cytokinesis was performed using Dlg–GFP. The mitotic spindle being positioned at the level of the septate junction (Extended Data Fig. 1g-i), the segmentation of Dlg–GFP cortical signal recapitulates cell shape changes at the level of the spindle and the distributions of TCJ where GFP–Mud is enriched in interphase and mitosis. Owing to the spreading of the Dlg–GFP cortical signal along the lateral domain of the cell, the accurate segmentation of the cortical Dlg–GFP signal was achieved by manual correction of each individual cell. This can only be performed on a limited number of cells during their cell cycle ($n = 249$ cells from 2 distinct videos, 3 min temporal resolution).

In order to compare the prediction based on cell shape long axis versus TCJ bipolarity, a very large number of segmented cells are needed. We therefore used E-Cad–GFP time-lapse videos (5 min temporal resolution) since the segmentation of the E-Cad–GFP signal can be readily automated and accurate segmentation of cell shapes and TCJ positions can be achieved for a very large number of cells. Quantifications shown in Fig. 3e–g and Extended Data Fig. 9 were obtained from 29,388 cells analysed from 3 distinct videos.

To compare the prediction based on cell shape long axis versus TCJ bipolarity in wild-type (6 videos, $n = 4{,}860$ cells) and *mud* (8 videos, $n = 7{,}770$ cells) mutant tissue, predictions were performed in a specific region of the tissue were spindle misorientation along the AB is very weak (Extended Data Fig. 5f, g).

Upon Dlg–GFP signal or E-Cad–GFP signal segmentation and cell tracking, the following measurements were determined using Matlab.

(i) The experimental cell division orientation ($\theta_{\mathrm{division}}$) was determined as the orthogonal of the interface between the two daughter cells upon cytokinesis. $\theta_{\mathrm{division}}$, which correlates very well with cell division orientation measured by the positions of the two centrosomes at metaphase ($R = 0.91$, $n = 127$ cells, data not shown) as established using time-lapse videos of E-Cad–GFP- and Spd-2–mRFP (centrosome marker)-labelled epithelial tissue.

(ii) To characterize cell shape elongation (η_{shape}) and cell shape long axis orientation (θ_{shape}), each cell region was used to construct its inertia matrix.

$$S = \frac{1}{n_{\mathrm{pix}}}\sum_{p=1}^{n_{\mathrm{pix}}} \overrightarrow{r_p} \otimes \overrightarrow{r_p} = \frac{1}{n_{\mathrm{pix}}}\sum_{p=1}^{n_{\mathrm{pix}}} \begin{pmatrix} x_p^2 & y_p x_p \\ x_p y_p & y_p^2 \end{pmatrix}$$

where n_{pix} is the number of pixels in the cell and $\overrightarrow{r_p} = (x_p, y_p)$ are the vectors pointing from the barycentre of the cell to each pixel of the cell, p. Its eigenvalues λ_S, Λ_S, with $0 < \lambda_S < \Lambda_S$, have the dimensions of a squared distance. Its eigenvector associated to Λ_S defines the direction of the cell's long-axis (θ_{shape}). The cell shape anisotropy was defined as a dimensionless number, which ranged from 0 for a cell perfectly circular, to 1 for an infinitely stretched cell: $\eta_{\mathrm{shape}} = 1 - \lambda_S / \Lambda_S$.

(iii) To characterize the anisotropy (η_{TCJ}) and orientation of the TCJ (θ_{TCJ}) angular distribution, we built the 'TCJ bipolarity' matrix V:

$$V = \sum_{v=1}^{n_{\mathrm{TCJ}}} \overrightarrow{u_v} \otimes \overrightarrow{u_v}$$

where n_{TCJ} is the number of TCJs in the cell and the $\overrightarrow{u_v}$ are the unit vectors pointing from the barycentre of the cell to each cell TCJ, v (that is, $\overrightarrow{u_v} = \overrightarrow{r_v} / |\overrightarrow{r_v}|$) (Extended Data Fig. 6j). Its eigenvalues $\lambda_{\mathrm{TCJ}}, \Lambda_{\mathrm{TCJ}}$, with $0 < \lambda_{\mathrm{TCJ}} < \Lambda_{\mathrm{TCJ}}$, are dimensionless numbers. Its eigenvector associated to Λ_{TCJ} defines the direction of the long axis of the TCJ bipolarity (θ_{TCJ}). The TCJ distribution anisotropy was defined as a dimensionless number, ranging from 0 for TCJ uniformly distributed around the cell, to 1 for the theoretical case of TCJ split in two groups diametrically opposed: $\eta_{\mathrm{TCJ}} = 1 - \lambda_{\mathrm{TCJ}} / \Lambda_{\mathrm{TCJ}}$.

Note that unlike the cell inertia S that is calculated using all the pixels making up the cell, the TCJ bipolarity V solely uses the unit vectors $\overrightarrow{u_v}$ pointing from the cell centre to each cell TCJ. By doing so, the TCJ bipolarity disentangles the characterization of the TCJ distribution from cell shape measurement, and any correlation observed between the two quantities is not due a shape bias in the TCJ bipolarity measurement. In the example shown in Extended Data Fig. 6j, although the two cells have different shape anisotropies, they share the same set of $\overrightarrow{u_v}$ vectors and have therefore the same TCJ bipolarity.

Both cell shape anisotropy and TCJ anisotropy were normalized to their respective averages over all the cells in the tissue. The cell shape and TCJ distribution anisotropies are represented with bars whose directions give the direction of their respective anisotropies and whose length is proportional to the magnitude of the normalized anisotropy.

To compare the orientations of the cell shape long axis or the TCJ bipolarity axis with the cell division orientation, the cell shape and TCJ distribution tensors S and V were averaged during late interphase from 60 to 30 min before the end of cytokinesis. The orientations $\tilde{\theta}_{\mathrm{shape}}$ and $\tilde{\theta}_{\mathrm{TCJ}}$ of the resulting averaged tensors were then compared to the experimental cell division orientation, $\theta_{\mathrm{divison}}$.

The improvement of spindle orientation prediction is calculated as $\left(\frac{N_{\mathrm{TCJ}}}{N_S} - 1\right) \times 100$. N_S is the number of cells for which $|\theta_{\mathrm{divison}} - \tilde{\theta}_{\mathrm{shape}}| \le 15°$, and N_{TCJ} is the number of cells for which $|\theta_{\mathrm{division}} - \tilde{\theta}_{\mathrm{TCJ}}| \le 15°$. The mean improvement and its standard deviation were calculated using the improvement values from three different videos. Similar improvement values are found when determining N_S and N_{TCJ} for $|\theta_{\mathrm{division}} - \tilde{\theta}_{\mathrm{shape}}|$ and $|\theta_{\mathrm{division}} - \tilde{\theta}_{\mathrm{TCJ}}|$ below 5°, 10°, 20° or 25°.

The correlation coefficient A between TCJ bipolarity and cell long axis orientation is calculated as

$$A = \frac{2\sum_{i=1}^{N} \eta_i cos^2(\Delta\theta_i)}{\sum_{i=1}^{N} \eta_i} - 1$$

where N is the total number of cells analysed. For each cell, $\Delta\theta_i$ equals $\theta_{\mathrm{TCJ}} - \theta_{\mathrm{shape}}$ and η_i is the cell shape anisotropy. The correlation coefficient A ranged from -1 for complete anti-correlation to 1 for complete correlation. In between, a homogeneous distribution indicating an absence of correlation led to $A = 0$. The correlation coefficient was calculated over all 4,504 simulated cells or over an equal number of experimental cells randomly picked ($n = 4{,}505$) among the 29,388 cells analysed in Fig. 3e–g and Extended Data Fig. 9.

As cell division is symmetric in size in the *Drosophila* notum we have focused on the anisotropy and the orientation of the distribution of the TCJ (bipolarity). The analysis of the asymmetry of TCJ distribution in epithelial tissue where epithelial cells undergo unequal size distribution might provide insights on how unequal daughter cells are generated in epithelial tissue.

Numerical simulations. We used numerical simulations based on the cellular Potts model, which is particularly relevant in biology to describe variable cell shape, size, packing and irregular fluctuating interfaces of cells[48–50]. We consider a 2D square lattice. Each pixel *i* has an integer index σ_i The *m*th cell is defined as the domain consisting of all pixels with the same index value $\sigma_i = m$. The number of pixels that cell has defines its cell area. A cell shape changes when one of its pixels is attributed to another cell. Here, the evolution is driven by the minimization of a total energy E, which has three physical ingredients: interfacial energy, area constraints and an external force applied to the patch of cells. Since the calculations are performed on a lattice, we have

$$E = \Lambda \sum_{i,j} [\, 1 - \delta(\sigma_i, \sigma_j)] + \gamma \sum_{m} (A_m - A_0)^2 + k \sum_{i} (x_i - x_0)$$

The first term represents the contribution of the energy of the interfaces between the cells. Minimizing this term leads to perimeter minimization (δ is the Kronecker symbol and Λ is interfacial energy). The second term keeps each cell area A_m close to its predefined target value A_0 (γ is the compressibility). The balance between this term and the preceding one simulates a tissue relaxing towards mechanical equilibrium. The third term describes an energy gradient[51,52], that is, an elastic force field, which pulls on the tissue in opposite directions (k is an elastic constant and x_0 is the x position of the centre of the simulated field).

The algorithm to minimize E uses Monte Carlo sampling and the Metropolis algorithm, as follows. We randomly draw (without replacement) a lattice pixel and one of its eight neighbouring pixels. If both pixels belong to different cells, we try to copy the state of the neighbouring pixel to the first one. If the copying decreases E, we accept it, and if it increases E, we accept it with probability $P = e^{-\Delta E/T}$, where $\Delta E = E_{\text{after}} - E_{\text{before}}$. The prefactor T is a fluctuation (random copying) allowance. Because all energy parameters are scalable with T, we can fix it without loss of generality; for numerical convenience, we choose numbers on the order of 10^3. We define one Monte Carlo time step (MCS) as the number of random drawings equal to the number of lattice pixels. We ran simulations during 600 MCS to reach a tissue shape that no longer evolves (initial image). We then applied a constant bulk force that stretched a tissue and ran the simulations for 600 MCS (final image). To obtain a large range of cell anisotropies in the simulations we used simulations with an elastic constant, $k = [0; 0.5; 1; 2; 3; 4; 5; 10]$ For each value of k, 5 simulations (with about 170 cells in each simulation) were run. Using the initial and final images, the tissue elongation along the direction of stretching was calculated for each simulation as the relative increase in distances between landmarks. On the final image, the segmented cell contours were used to determine the tensors V (TCJ bipolarity) and S (inertia matrix) for each cell as well as their averages over all cells in the simulation.

Mechanical stress estimation and TCJ bipolarity orientation. To compare the mechanical stress and TCJ bipolarity orientations as a function of the normal mechanical stress difference ($\sigma_{yy} - \sigma_{xx}$), we used $\sigma_{yy} - \sigma_{xx}$ experimental values of the estimated mechanical stress obtained up to a prefactor by Bonnet *et al.*[53] measured from 12 hAPF to 28 hAPF in the medial region of the scutellum, where the mechanical stress is oriented along the medial–lateral axis ($\sigma_{xy} = 0$ and $\theta_{\text{stress}} = 0$). The experimental orientation of mechanical stress for each ablation was compared to the average TCJ bipolarity orientation determined using the segmented cell outlines of the E-Cad–GFP cells within the rim of ablated cells (Extended Data Fig. 10a, b).

Predictions of spindle orientation based on experimental Mud distribution and cell shape. For predictions of the mitotic spindle orientation based on GFP–Mud or GFP–MudΔCC signals (hereafter referred to as Mud fluorescence signal) in wild-type and *mud* tissues, average intensity (2–4 μm) projections centred around the plane of the centrosomes were generated using a custom ImageJ plugin for the $t = -2$ min and $t = -1$ min frames ($t = 0$ corresponding to the anaphase onset). A 5-pixel mask that does not overlap with the GFP–Mud or GFP–MudΔCC centrosome signal was drawn around the cortex to determine, using a Matlab script, the shape of the dividing cell as well as the cortical Mud signal profiles. The experimental orientation of the mitotic spindle and the positions of the two centrosomes were manually determined using the GFP–Mud or GFP–MudΔCC accumulation at the spindle poles (Fig. 2e,i).

The model predicting spindle orientation from cell shape is similar to the one used in refs 8,18. The model based on Mud fluorescence signal is adapted from this previous model and inputs the distribution of cortical intensity of GFP–Mud or GFP–MudΔCC obtained from a fluorescence image in a mitotic cell[17,18]. This intensity computed around the cell contour is renormalized, so that the sum of intensities around each treated cell is the same. For each cell, we aimed to compute the global torque T generated as a function of the spindle orientation angle θ (Fig. 2d, g). For each possible spindle orientation θ, (θ varying from 0 to π) we generate two asters of N microtubules nucleated at a constant angular density ρ from centrosomes placed at a distance $\pm L/2$ from the spindle centre along the axis θ. Both L, which represents the spindle length, and the spindle centre are computed from the experimental position of the two centrosomes (Fig. 2e). A microtubule projecting at an angle ϕ with respect to the spindle contacts the cortex at a given location with a GFP–Mud or GFP–MudΔCC concentration C_{mud} and is assumed to pull on the spindle pole it is connected to with a force $f[C_{\text{mud}}(\theta, \phi)]$ that scales with C_{mud}: $f[C_{\text{mud}}(\theta, \phi)] \sim (C_{\text{mud}})^{\alpha}$, with the exponent α representing putative nonlinearity in how Mud may influence astral microtubule pulling forces. This yields a torque, $\tau(\theta, \phi)$, at the spindle centre projected along the z axis:

$$\tau(\theta, \phi) = \frac{L}{2} f[C_{\text{mud}}(\theta, \phi)] \sin(\phi)$$

The resultant total torque $T(\theta)$ generated by the two asters is then obtained by summing the projected torques over all microtubules:

$$T(\theta) = \frac{L}{2} \int_{-\frac{\Phi}{2}}^{\frac{\Phi}{2}} f[C_{\text{mud}}(\theta, \phi)] \sin(\phi) \rho \, d\phi$$

where Φ is the total angular width of the aster. Initial tests of the model showed that, above a certain threshold, the number of microtubules N (or equivalently the angular density: $\rho = N/\Phi$), does not materially impact axis definition (Extended Data Fig. 6c–f). Thus, in the model, we keep N as a silent parameter, by normalizing the total torque with N. The stable theoretical axis orientation, θ_{theory} can be identified from the minima of the potential $U(\theta)$ computed as a primitive of $T(\theta)$, and compared with the experimental division axis θ_{division} (Fig. 2f–h and Extended Data Fig. 6g).

The quality of the prediction was computed based on the magnitude of the angular deviation between the model and the experiments, $|\theta_{\text{theory}} - \theta_{\text{division}}|$. Overall, the model based on the Mud distribution accounts for observed spindle orientation, with a mean angular deviation magnitude of 27.7° ± 11.9° ($n = 140$ cells). The shape-based model applied to these same cells predicted a higher mean deviation magnitude of 37.6° ± 12.3° ($n = 140$ cells). An open question is why the model based on Mud distribution predicts spindle orientation within only 27.7° For comparison, a previous model applied to dividing sea urchin eggs of various shapes made predictions within 15.6°. Although we cannot fully preclude the existence of Mud-independent secondary systems that contribute to spindle orientation, it is important to outline the structural differences in models and biological systems that could explain these differences. One first difference is that the Mud model infers a fluorescence signal distribution which could be in part affected by the imaging itself, yielding variations in Mud signal peak heights or widths which do not reflect the actual force field. In agreement with this, the same model run with cells where the neighbours are not photobleached makes predictions within 32.4° ($n = 241$ cells, data not shown). Another probably more important difference is that in *Drosophila* epithelial cells the spindles move with a time-scale close to mitosis duration (data not shown). By contrast, in large cells like zygotes and blastomeres, division axes are stably set for tens of minutes with negligible movement and rotation of the spindles[18,54]. Although the lack of a standardized Mud distribution precludes us from computing the effective temperature of the system, the difference in spindle movements suggests that the noise in the *Drosophila* epithelial system studied is much larger than in the other cell types previously analysed.

Predictions of spindle orientation at the tissue scale based on TCJ anisotropy. In order to study spindle orientation across the entire tissue, we used the bipolarity axis of the TCJ distribution in each cell as a proxy for a prediction based on the full Mud protein distribution (see Fig. 3 and the discussion of the tensor V above). This quantity has the advantages that it relies only on a marker (E-Cad–GFP or Dlg–GFP) that can be reliably imaged over the necessary length and time scales and that the predicted spindle orientations can be computed in a reasonable time, even for tens of thousands of cells. In this section, we show how the bipolarity axis arises naturally as an approximation to a more detailed description that explicitly calculates forces and torques.

We begin by examining in general terms how a cortical force distribution translates into a potential $U(\theta)$ governing the spindle orientation. In the context of this analytic formulation, we assume that the rounded, mitotic cells are approximately circles with radius R and centre coinciding with the centre of the spindle. Points on the cortex can then be labelled by their angle with the

positive x axis. If the spindle makes an angle θ with the positive x axis, then a microtubule projecting from one of the spindle poles at an angle ϕ to the spindle contacts the cortex at an angle $\beta = \theta + \psi$ to the positive x axis, where ψ satisfies $\cot(\phi) = \cot(\psi) - \epsilon / \sin(\psi)$ with $\epsilon = L / 2R$. (Extended Data Fig. 6h). With this relation, one can translate the integral (see above) over ϕ giving the net torque into an integral over the circle of the form

$$T(\theta) = \frac{\rho L}{2} \int_{-\pi}^{\pi} [f(\beta) + f(\beta + \pi)] \tilde{\tau}(\beta - \theta) \, \mathrm{d}\beta$$

Similarly, the potential can be written as

$$U(\theta) = \frac{\rho L}{2} \int_{-\pi}^{\pi} [f(\beta) + f(\beta + \pi)] \tilde{u}(\beta - \theta) \, \mathrm{d}\beta$$

Here, we have suppressed the explicit dependence of the force f on C_{mud}, and the kernel $\tilde{u}(\psi)$ is a 2π-periodic function given, for $-\pi < \psi \leq \pi$, by

$$\tilde{u}(\psi) = \begin{cases} \dfrac{\epsilon - \cos(\psi)}{\sqrt{1 + \epsilon^2 - 2\epsilon \cos(\psi)}}, |\psi| < \Psi \\ \dfrac{\epsilon - \cos(\Psi)}{\sqrt{1 + \epsilon^2 - 2\epsilon \cos(\Psi)}}, |\psi| \geq \Psi \end{cases},$$

where Ψ is related to Φ as $\cot(\Phi / 2) = \cot(\Psi) - \epsilon / \sin(\Psi)$.

Importantly, $\tilde{u}(\psi)$ is hence a symmetric function whose magnitude peaks at $\psi = 0$. That is, within our model the net effect of the microtubules is to act as a linear filter that smooths out the cortical Mud distribution without otherwise altering it. We therefore expect that the spindle should generally prefer to orient itself towards the direction of highest Mud concentration but that it is more sensitive to relatively wide, broad peaks of Mud than to the fine details of a rapidly varying Mud distribution. This idea can be expressed more formally by Fourier transforming the periodic functions U, f and $\tilde{u}$. With $U(\theta) = \sum_n U_n \exp(in\theta)$, and similarly for f and $\tilde{u}$, we have $U_n = \rho L f_n \tilde{u}_n$ for n even and $U_n = 0$ for n odd. The magnitudes of the coefficients $\tilde{u}_n$ are plotted in Extended Data Fig. 6i. As expected, the filter decreases the importance of components with higher n relative to the dominant $n = 2$ mode. Thus, the orientation of the $n = 2$ mode of the force distribution $f(\beta)$ gives the natural, leading approximation to the location of the minimum of $U(\theta)$. For forces centred on the TCJs (where the Mud concentration is highest), the $n = 2$ mode of the TCJ distribution similarly gives the natural proxy for f_2 and thus for the orientation of the mitotic spindle. Moreover, the orientation of this bipolar mode can be computed far more efficiently than can the location of the global minimum of a potential including all Fourier modes. Indeed, it is a standard result that this orientation corresponds with the anisotropy axis of the second rank tensor V defined previously. This makes it especially appropriate for use in our tissue-scale calculations.

Statistics. No statistical methods were used to predetermine sample size. Sample sizes vary in each experiment. Statistical significances of protein distribution and velocity amplitude were assessed using Student's t-test, the distribution normalities were checked using Kolmogorov–Smirnov test. In cases where the variances were different, significance was assessed using the unequal variance t-test. The angular distribution of velocity was assessed using Watson's U^2 test for circular data. GFP–Mud localization at TCJ and GFP–Mud or GFP–MudΔCC co-localization with Gli in the different mutant backgrounds were analysed blindly. Kolmogorov–Smirnov tests were used to analyse differences in α_{AB} spindle orientations and differences in division orientation. P values greater than 0.05 are indicated as not significant in figure legends or graphs. Predictions of division orientation based on GFP–Mud or GFP–MudΔCC in *mud* or wild-type tissues were performed blindly. Experiments were not randomized and every experiment was repeated at least three independent times.

Code availability. Matlab code used to segment and track cells has been previously published[13]. Matlab code used to determine division orientation, cell shape and TCJ bipolarity upon cell segmentation and tracking are available upon request.

30. Allen, M. J. *et al.* Targeted expression of truncated glued disrupts giant fiber synapse formation in *Drosophila*. *J. Neurosci.* **19,** 9374–9384 (1999).
31. Herszterg, S., Leibfried, A., Bosveld, F., Martin, C. & Bellaiche, Y. Interplay between the dividing cell and its neighbors regulates adherens junction formation during cytokinesis in epithelial tissue. *Dev. Cell* **24,** 256–270 (2013).
32. Xu, T. & Rubin, G. M. Analysis of genetic mosaics in developing and adult *Drosophila* tissues. *Development* **117,** 1223–1237 (1993).
33. Lee, T. & Luo, L. Mosaic analysis with a repressible cell marker for studies of gene function in neuronal morphogenesis. *Neuron* **22,** 451–461 (1999).
34. Nakajima, Y., Meyer, E. J., Kroesen, A., McKinney, S. A. & Gibson, M. C. Epithelial junctions maintain tissue architecture by directing planar spindle orientation. *Nature* **500,** 359–362 (2013).
35. Venken, K. J., He, Y., Hoskins, R. A. & Bellen, H. J. P[acman]: a BAC transgenic platform for targeted insertion of large DNA fragments in *D. melanogaster*. *Science* **314,** 1747–1751 (2006).
36. Venken, K. J. *et al.* Versatile P[acman] BAC libraries for transgenesis studies in *Drosophila melanogaster*. *Nature Methods* **6,** 431–434 (2009).
37. Warming, S., Costantino, N., Court, D. L., Jenkins, N. A. & Copeland, N. G. Simple and highly efficient BAC recombineering using galK selection. *Nucleic Acids Res.* **33,** e36 (2005).
38. Venken, K. J. *et al.* Recombineering-mediated tagging of *Drosophila* genomic constructs for *in vivo* localization and acute protein inactivation. *Nucleic Acids Res.* **36,** e114 (2008).
39. Gratz, S. J. *et al.* Genome engineering of *Drosophila* with the CRISPR RNA-guided Cas9 nuclease. *Genetics* **194,** 1029–1035 (2013).
40. Ren, X. *et al.* Optimized gene editing technology for *Drosophila melanogaster* using germ line-specific Cas9. *Proc. Natl Acad. Sci. USA* **110,** 19012–19017 (2013).
41. Gratz, S. J. *et al.* Highly specific and efficient CRISPR/Cas9-catalyzed homology-directed repair in *Drosophila*. *Genetics* **196,** 961–971 (2014).
42. Ségalen, M. *et al.* The Fz-Dsh planar cell polarity pathway induces oriented cell division via Mud/NuMA in *Drosophila* and zebrafish. *Dev. Cell* **19,** 740–752 (2010).
43. Yu, J. X., Guan, Z. & Nash, H. A. The mushroom body defect gene product is an essential component of the meiosis II spindle apparatus in *Drosophila* oocytes. *Genetics* **173,** 243–253 (2006).
44. Auld, V. J., Fetter, R. D., Broadie, K. & Goodman, C. S. Gliotactin, a novel transmembrane protein on peripheral glia, is required to form the blood-nerve barrier in *Drosophila*. *Cell* **81,** 757–767 (1995).
45. Lamb, R. S., Ward, R. E., Schweizer, L. & Fehon, R. G. *Drosophila* coracle, a member of the protein 4.1 superfamily, has essential structural functions in the septate junctions and developmental functions in embryonic and adult epithelial cells. *Mol. Biol. Cell* **9,** 3505–3519 (1998).
46. David, N. B. *et al.* *Drosophila* Ric-8 regulates Galphai cortical localization to promote Galphai-dependent planar orientation of the mitotic spindle during asymmetric cell division. *Nature Cell Biol.* **7,** 1083–1090 (2005).
47. Boulanger, J. *et al.* Patch-based nonlocal functional for denoising fluorescence microscopy image sequences. *IEEE Trans. Med. Imaging* **29,** 442–454 (2010).
48. Bardet, P. L. *et al.* PTEN controls junction lengthening and stability during cell rearrangement in epithelial tissue. *Dev. Cell* **25,** 534–546 (2013).
49. Käfer, J., Hayashi, T., Marée, A. F., Carthew, R. W. & Graner, F. Cell adhesion and cortex contractility determine cell patterning in the *Drosophila* retina. *Proc. Natl Acad. Sci. USA* **104,** 18549–18554 (2007).
50. Graner, F. & Glazier, J. Simulation of biological cell sorting using a two-dimensional extended Potts model. *Phys. Rev. Lett.* **69,** 2013–2016 (1992).
51. Jiang, Y., Swart, P. J., Saxena, A. & Asipauskas, M. & Glazier, J. A. Hysteresis and avalanches in two-dimensional foam rheology simulations. *Phys. Rev. E Stat. Phys. Plasmas Fluids Relat. Interdiscip. Topics* **59,** 5819–5832 (1999).
52. Raufaste, C., Dollet, B., Cox, S., Jiang, Y. & Graner, F. Yield drag in a two-dimensional foam flow around a circular obstacle: effect of liquid fraction. *Eur. Phys. J. E. Soft Matter* **23,** 217–228 (2007).
53. Bonnet, I. *et al. Mechanical state, material properties and continuous description of an epithelial tissue. J. R. Soc. Interface* **9,** 2614–2623 (2012).
54. Wühr, M., Tan, E. S., Parker, S. K., Detrich, H. W. & Mitchison, T. J. A model for cleavage plane determination in early amphibian and fish embryos. *Curr. Biol.* **20,** 2040–2045 (2010).
55. Zielke, N. *et al.* Fly-FUCCI: a versatile tool for studying cell proliferation in complex tissues. *Cell Rep.* **7,** 588–598 (2014).
56. Bergstralh, D. T., Lovegrove, H. E. & St Johnston, D. Discs large links spindle orientation to apical-basal polarity in *Drosophila* epithelia. *Curr. Biol.* **23,** 1707–1712 (2013).
57. Morin, X. & Bellaïche, Y. Mitotic spindle orientation in asymmetric and symmetric cell divisions during animal development. *Dev. Cell* **21,** 102–119 (2011).
58. Bowman, S. K., Neumüller, R. A., Novatchkova, M., Du, Q. & Knoblich, J. A. The *Drosophila* NuMA homolog Mud regulates spindle orientation in asymmetric cell division. *Dev. Cell* **10,** 731–742 (2006).
59. Izumi, Y., Ohta, N., Hisata, K., Raabe, T. & Matsuzaki, F. *Drosophila* Pins-binding protein Mud regulates spindle-polarity coupling and centrosome organization. *Nature Cell Biol.* **8,** 586–593 (2006).
60. Siller, K. H., Cabernard, C. & Doe, C. Q. The NuMA-related Mud protein binds Pins and regulates spindle orientation in *Drosophila* neuroblasts. *Nature Cell Biol.* **8,** 594–600 (2006).

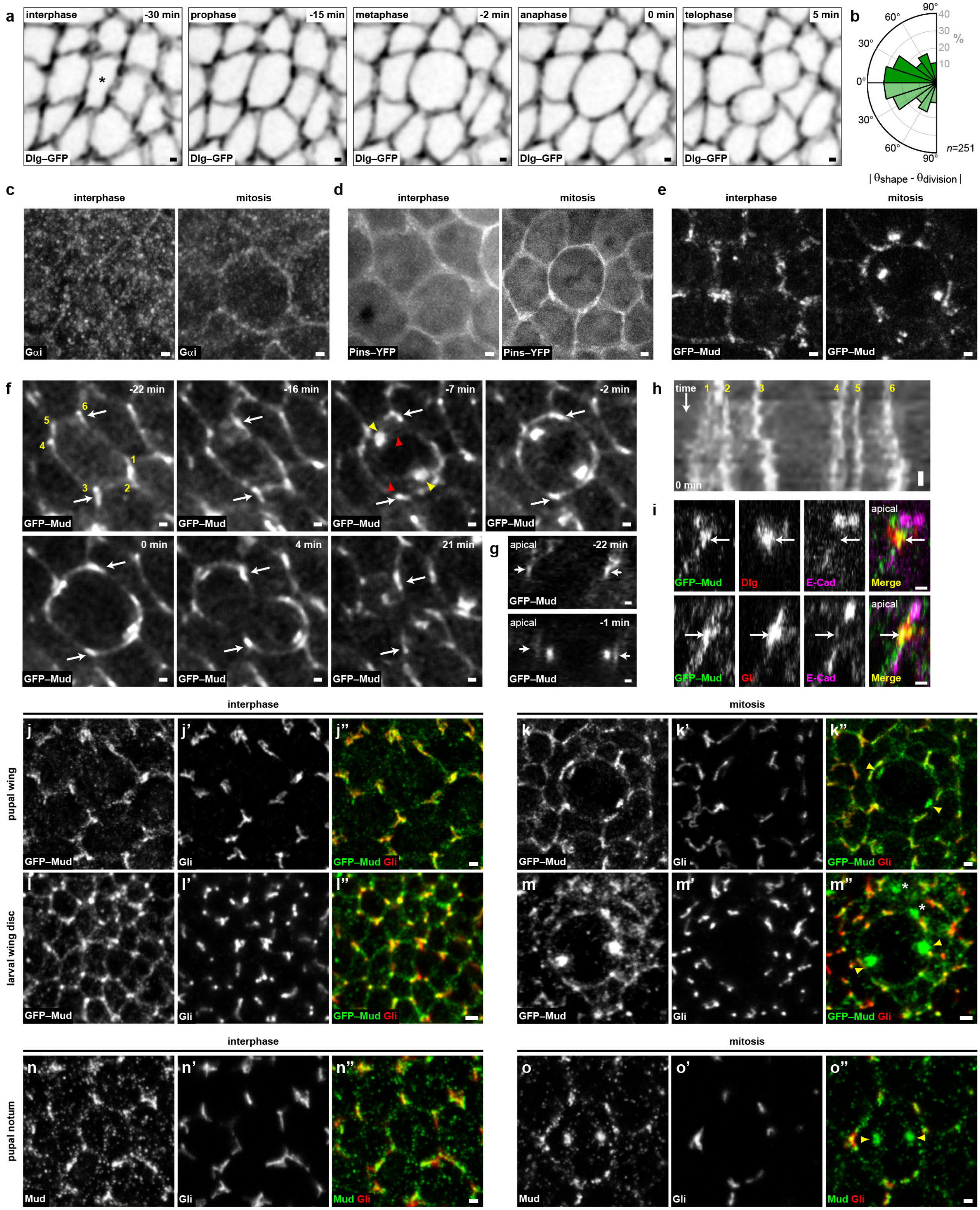

Extended Data Figure 1 | See next page for figure caption.

Extended Data Figure 1 | Mud, Pins, Gα_i and Gli localization during symmetric epithelial cell division in the *Drosophila* notum. **a**, **b**, Within the *Drosophila* pupal notum tissue cells divide according to their intephasic cell shape long axis, thereby following the 130-year-old Hertwig rule. However, upon entry into mitosis cells round up (the cell shown in **a**, −15 to −2 min and Fig. 3b). **a**, Time-lapse images of Dlg–GFP in a dividing cell (out of 249 cells quantified in **b**) in the pupal notum tissue illustrating cell rounding during mitosis (the same cell is shown as inset in Fig. 3b). Prior to mitosis (−30 min) the cell (marked by asterisk) is clearly elongated and divides according to its interphasic cell shape (5 min). Upon entry into mitosis (−15 min) the cell rounds up and reaches a minimal anisotropy just before anaphase (−2 min, see also Fig. 3b). **b**, Rose plot of the difference between the experimental ($\theta_{\mathrm{division}}$) and predicted division orientations by the average (60–30 min before mitosis) interphase cell long axis (θ_{shape}). The data are duplicated relative to 0° line (light green). Number of cells (n) analysed is indicated. **c**–**e**, Gα_i localization in fixed epithelial dorsal thorax tissue (**c**), Pins–YFP localization in *pins* mutant tissue (**d**) and GFP–Mud localization (**e**) showing cells in G2 interphase (left) and mitosis (right). Gα_i is hardly detected at the cell cortex in G2 phase and is mostly homogenously distributed around the cortex during mitosis. Pins–YFP is homogenously distributed around the cell cortex in both interphase and mitotic cells. In mitosis Pins–YFP also weakly localizes at the mitotic spindle. GFP–Mud localizes at TCJs during interphase and mitosis (see also **f**). $n = 24$ cells (**c**, left); $n = 19$ cells (**c**, right); $n = 80$ cells (**d**, left); $n = 12$ cells (**d**, right); $n = 111$ cells (**e**, left) and 54 cells (**e**, right). **f**, GFP–Mud time-lapse images from G2 interphase to telophase ($n = 21$ cells). White arrows, GFP–Mud at TCJs (numbered at $t = -22$ min). Red and yellow arrowheads, GFP–Mud on the spindle and its poles, respectively. The same panels −22 min to 4 min are shown in Fig. 1a. See also Supplementary Video 1. **g**, Apical–basal (AB) sections of the cell in **f** at $t = -22$ min (top) and $t = -1$ min (bottom). White arrows, GFP–Mud at TCJs. $n = 21$ cells. **h**, GFP–Mud kymograph along the cortex (x axis) from $t = -22$ to $t = 0$ min of the cell in **f**. TCJs numbered as in **f**. The kymograph shows that during mitotic rounding GFP–Mud spread only modestly along the cortex of the dividing cell. $n = 21$ cells. **i**, AB sections of GFP–Mud, adherens junction marker E-Cad and septate junction marker Dlg (top, $n = 16$ cells) or septate TCJ marker Gli (bottom, $n = 30$ cells). **j**–**m**, Localizations of GFP–Mud (white in **j**–**m** and green in **j′′**–**m′′**) and Gli (white in **j′**–**m′** and red in **j′′**–**m′′**) in fixed pupal wing (**j**, **k**) and larval wing disc (**l**, **m**) tissues. GFP–Mud co-localizes with Gli at TCJs in G2 interphase and mitotic cells in both the pupal wing and larval wing disc epithelium. Asterisks mark Mud punctate structures present on the nuclear envelope of early G1 cells. Yellow arrows indicate GFP–Mud on the spindle poles. $n = 20$ cells (**j**, **j′′**); $n = 5$ cells (**k**, **k′′**); $n = 63$ cells (**l**, **l′′**) and $n = 12$ cells (**m**–**m′′**). **n**, **o**, Localizations of Mud (white in **n**, **o** and green in **n′′**, **o′′**) and Gli (white in **n′**, **o′** and red in **n′′**, **o′′**) detected by antibody staining in G2 interphase and mitotic cells in the pupal dorsal thorax tissue. As observed for GFP–Mud (Fig. 1b and Extended data Fig. 1j–m), the endogenous Mud is enriched at TCJ where it co-localizes with Gli in G2 interphase and mitotic cells. Yellow arrows indicate Mud on the spindle poles. $n = 37$ cells (**n**, **n′′**) and $n = 21$ cells (**o**, **o′′**). Scale bars, 1 μm (**a**, **c**, **d**–**g**, **i**, **j**, **k**, **l**, **m**, **n**, **o**), 3 min (**h**).

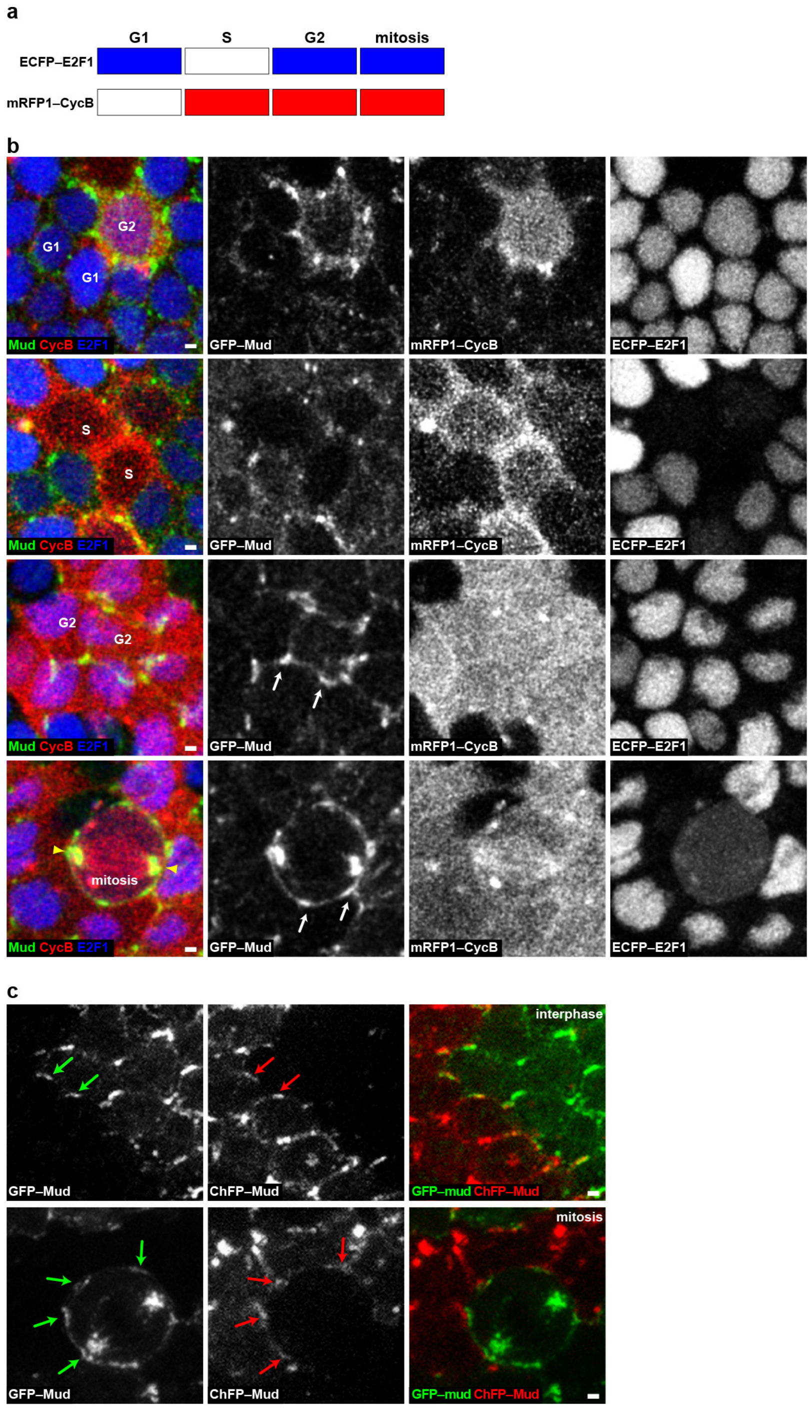

Extended Data Figure 2 | GFP–Mud localizes at TCJ from G2 interphase to mitosis. a, Scheme depicting the accumulation of the *Drosophila* FUCCI reporters during the cell cycle. ECFP–E2F1 accumulates during G1 phase, G2 phase and mitosis, whereas mRFP1–CycB accumulates during S phase, G2 phase and mitosis[55]. **b**, Localization of GFP–Mud (green left column and white in the second column panels), mRFP1–CycB (red in the left column and white in the third column panels) and ECFP–E2F1 (blue in the left column and white in the right column panels) in epithelial cells of the pupal notum tissue. Confocal sections at the level of septate junctions are shown. Cells in G1 ($n = 21$), S ($n = 6$), G2 ($n = 35$) phases and mitosis ($n = 6$) are indicated in the left panels. During both G1 and S phase (upper two rows of panels), GFP–Mud is weakly localized at the nuclear envelope membrane, weakly localized at the cortex and at the apically localized centrioles (not shown). During G2 phase GFP–Mud becomes prominently localized at the TCJ (one cell in the first row of panels and two cells in the third row of panels). Arrows indicate examples of TCJ GFP–Mud accumulation. During mitosis GFP–Mud remains localized at the TCJ and accumulates on the spindle and the spindle pole (bottom row panels). Similar results were obtained on fixed tissue for which the cell cycle phases were determined using the PCNA S-phase marker and the nucleus size to distinguish cells in G1 or G2 interphases (not shown). **c**, GFP–Mud (green arrows) and ChFP–Mud (red arrows) in adjacent tissue patches in G2 ($n = 31$) and mitotic ($n = 8$) cells. The FLP/FRT system was used to generate adjacent groups of cells labelled with either GFP–Mud or ChFP–Mud. By analysing the distribution of GFP–Mud in dividing cells adjacent to ChFP–Mud interphasic cells, we found that GFP–Mud was localized at the TCJs of the dividing cell from G2 through mitosis. Scale bars, 1 μm.

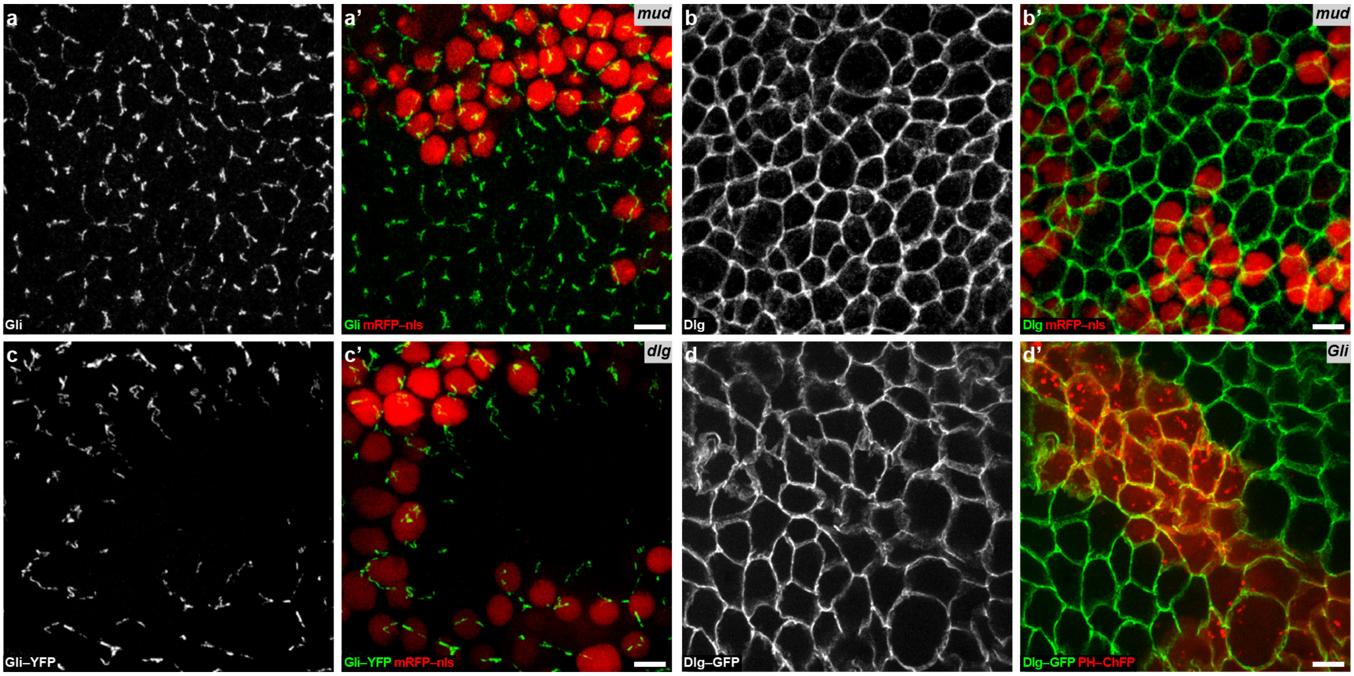

Extended Data Figure 3 | Regulation of Dlg, Gli and Mud localization in epithelial tissue. **a**, **b**, Localizations of Gli (white in **a** and green in **a′**, $n = 2$ clones) and Dlg (white in **b** and green in **b′**, $n = 3$ clones) in fixed notum tissues harbouring *mud* clones (identified by loss of mRFP–nls, red in **a′**–**b′**). The loss of Mud function does not modify the Gli and Dlg localizations at septate junctions. **c**, Localization of Gli–YFP (white in **c** and green in **c′**) in live notum tissue harbouring a clone of *dlg* (identified by the loss of mRFP–nls, red in **c′**, $n = 13$ clones). The loss of Dlg function results in a loss of Gli localization at TCJs. **d**, Localization of Dlg–GFP (white in **d** and green in **d′**) in live epithelial dorsal thorax tissue harbouring a *Gli* clone (identified by expression of PH–ChFP, red in **d′**, $n = 5$ clones). The loss of Gli function does not affect the distribution of Dlg–GFP at the septate junctions. Scale bars, 5 μm.

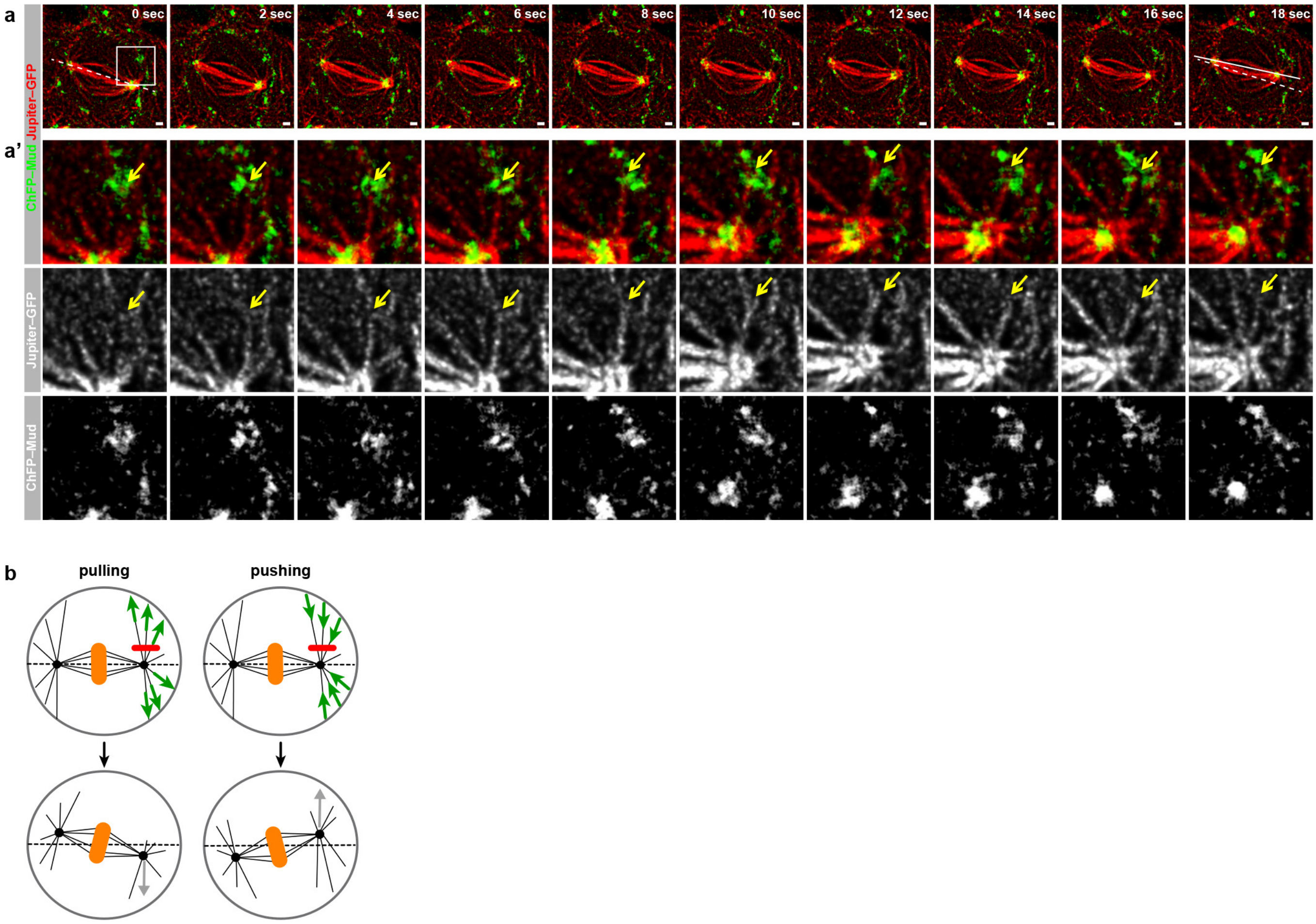

Extended Data Figure 4 | Astral microtubules contact Mud at the TCJ. a, **a′**, Time-lapse images of ChFP–Mud (green in **a** and top panels of **a′**, white in bottom panel of **a′**) and of Jupiter–GFP (red in **a** and top panels of **a′**, white in middle panel of **a′**) in dividing cells ($n = 11$) in the *Drosophila* pupal notum tissue. The panels in **a′** are magnifications of the boxed region in **a**. Yellow arrow indicates an astral microtubule that contacts ChFP–Mud at the cortex and shortens concomitant to the spindle pole movement towards the TCJ and spindle rotation. The dashed line corresponds to the initial spindle orientation and the solid lines correspond to its orientation at the final time point (see Supplementary Video 2). Similar results were obtained in cells expressing GFP–Mud and αTub–RFP to label the microtubules (data not shown). **b**, Schematic of the laser-ablation assay used to estimate the origin and magnitude of forces on astral microtubules required for spindle orientation in the *Drosophila* pupal dorsal thorax epithelium. Upon ablation (red lines, top), pulling forces (green arrows, left column) or pushing forces (green arrows, right column) yield recoil away (grey arrow, left column) or towards the ablation site (grey arrow, right column), respectively. Scale bars, 1 μm.

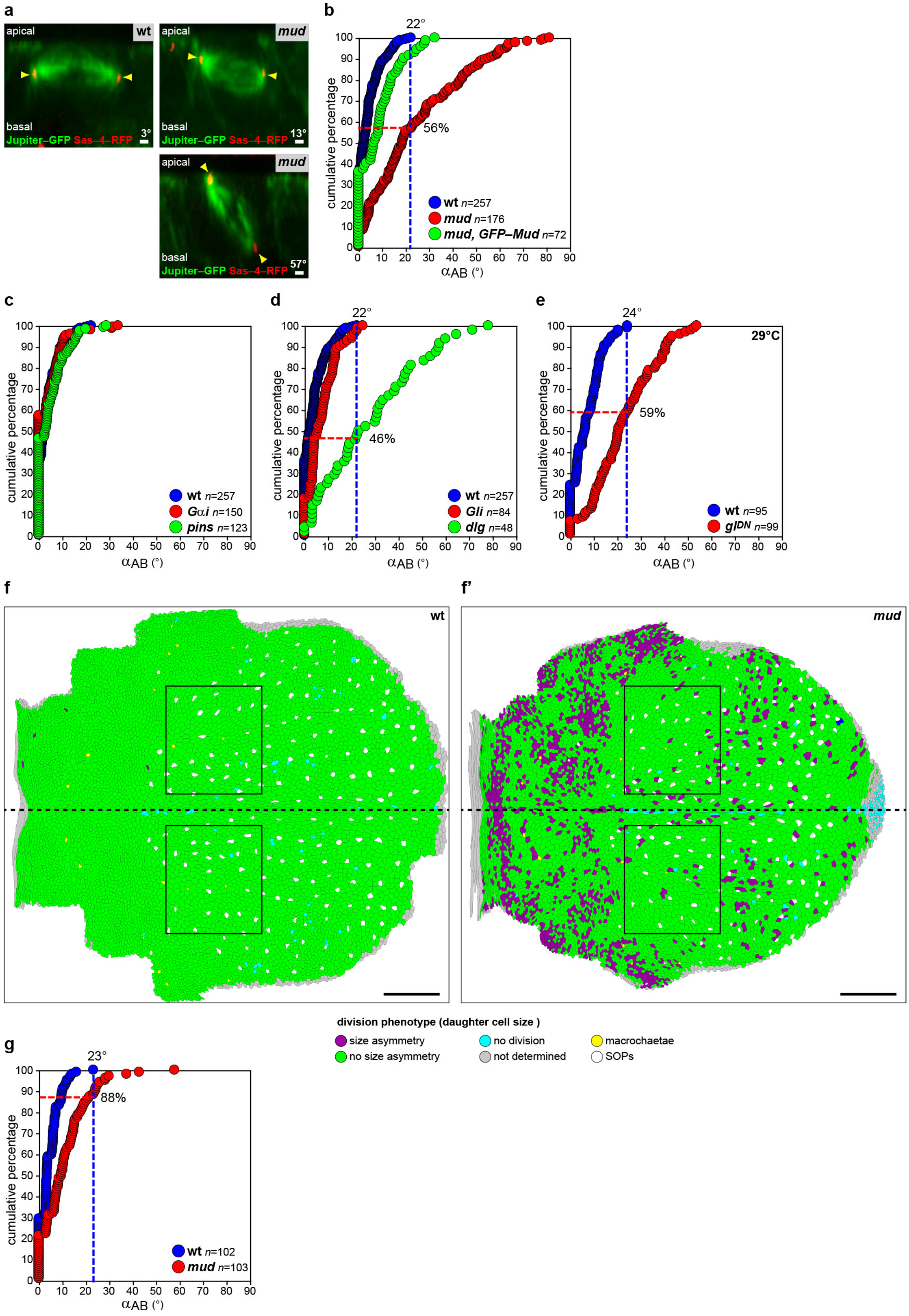

Extended Data Figure 5 | See next page for figure caption.

Extended Data Figure 5 | A large proportion of mitotic spindles remain planar in the absence of Mud, Dlg and Dynein function. Loss of Mud activity is known to induce defects in mitotic spindle orientation relative to the apical–basal axis (AB) of the cell[31,34,56]. Nonetheless, in *mud*, *dlg*, *dynein* (gl^{DN}) mutant cells around 50% of the epithelial cell divide with an AB angle (α_{AB}) in the range of the wild-type tissue (**a**–**e**). Since a large proportion of the spindles remain within the plane of the tissue, all analyses reported in the manuscript were performed on cell divisions that occurred within the plane of the tissue. Furthermore, in a central region of the tissue (box in **f** and **f′**), 88% of the divisions in *mud* tissue occur with an α_{AB} in the range of the wild-type tissue (**g**). This region was analysed to compare TCJ bipolarity and cell-shape-based predictions of division orientation in wild-type and *mud* tissue (Fig. 3h). **a**, AB views of a dividing epithelial cell in wild-type (left panel, out of 257 cells quantified in **b**) or *mud* (right panels, out of 176 cells quantified in **b**) tissue. The spindle is labelled using Jupiter–GFP (green) and the centrosomes using Sas-4–RFP (red). α_{AB} varies from 0° (spindle parallel to the plane of the tissue) to 90° (spindle perpendicular to the plane of the tissue). **b**, Quantification of α_{AB} in wild-type, *mud* and in *mud* tissue expressing GFP–Mud (*mud*, *GFP–Mud*). In wild-type tissue, α_{AB} varies between 0 and 22° (blue dashed line). In *mud* tissue, 56% of cells divide with a α_{AB} angle lower than 22° (dashed red lines). The expression of GFP–Mud in *mud* tissue rescues the spindle AB orientation phenotype caused by Mud loss of function. Numbers of cells (n) for each genotype are indicated. The distribution of angles in *mud* tissue is significantly different from wild type ($P < 1 \times 10^{-4}$), and is restored in *mud*, *GFP–mud* ($P < 1 \times 10^{-4}$). P values, Kolmogorov–Smirnov test. **c**, Quantification of α_{AB} in wild-type, $G\alpha_i$ and *pins*. The loss of either $G\alpha_i$ or Pins function does not affect the orientation of the spindle relative to the plane of tissue ($P > 0.3$) in agreement with our findings that Mud localization at TCJs is independent of Pins and $G\alpha_i$. The analysis in *pins* tissue confirmed previously published findings[46]. Number of cells (n) are indicated. P values, Kolmogorov–Smirnov test. **d**, **e**, Quantification of α_{AB} in wild-type, *Gli* and *dlg* tissues at 25 °C (**d**) and in wild-type and gl^{DN} tissues at 29 °C (**e**). Gli loss of function does not affect α_{AB} orientation, whereas 46% of the *dlg* cells ($P < 1 \times 10^{-4}$) and 59% of the gl^{DN} cells ($P < 1 \times 10^{-4}$) divide with α_{AB} lower than 22° and 24°, respectively. Numbers of cells (n) are indicated. P values, Kolmogorov–Smirnov test. **f**, **f′**, Identification of a region of the notum where AB orientation of the spindle is not affected in *mud* mutant tissue. Defects in AB orientation of the mitotic spindle result in size asymmetry of the two daughter cells[57]. Therefore daughter cell size was initially used as a proxy for the magnitude of spindle misorientation along the AB axis in *mud* tissue. The maps of daughter cell size asymmetry in wild-type (**f**) and *mud* (**f′**) tissues (green, no size asymmetry; purple, strong size asymmetry) revealed that a region (highlighted by the black box, **f**, **f′**) in the *mud* notum tissue exhibits almost no defects in daughter cell size asymmetry. Accordingly the quantification of spindle AB orientation within the region in wild-type and *mud* tissue revealed that 88% of the cells of the region divide within the range of the wild-type cells (see **g**). Anterior is to the right and the dashed back line indicates the midline. Colour coding: purple, daughter cells with strong size asymmetry; green, daughter cells with normal size symmetry; cyan, cells for which no division was detected; grey, cells which left the field of view and were not analysed; yellow, macrocheatae; white, sensory organ precursors (SOPs). **g**, Quantification of α_{AB} in wild-type and *mud* tissue in the boxed regions in **f** and **f′** was performed as in **b**–**e**. Numbers of cells (n) for each genotype are indicated. Scale bars, 1 μm (**a**), 100 μm (**f**, **f′**).

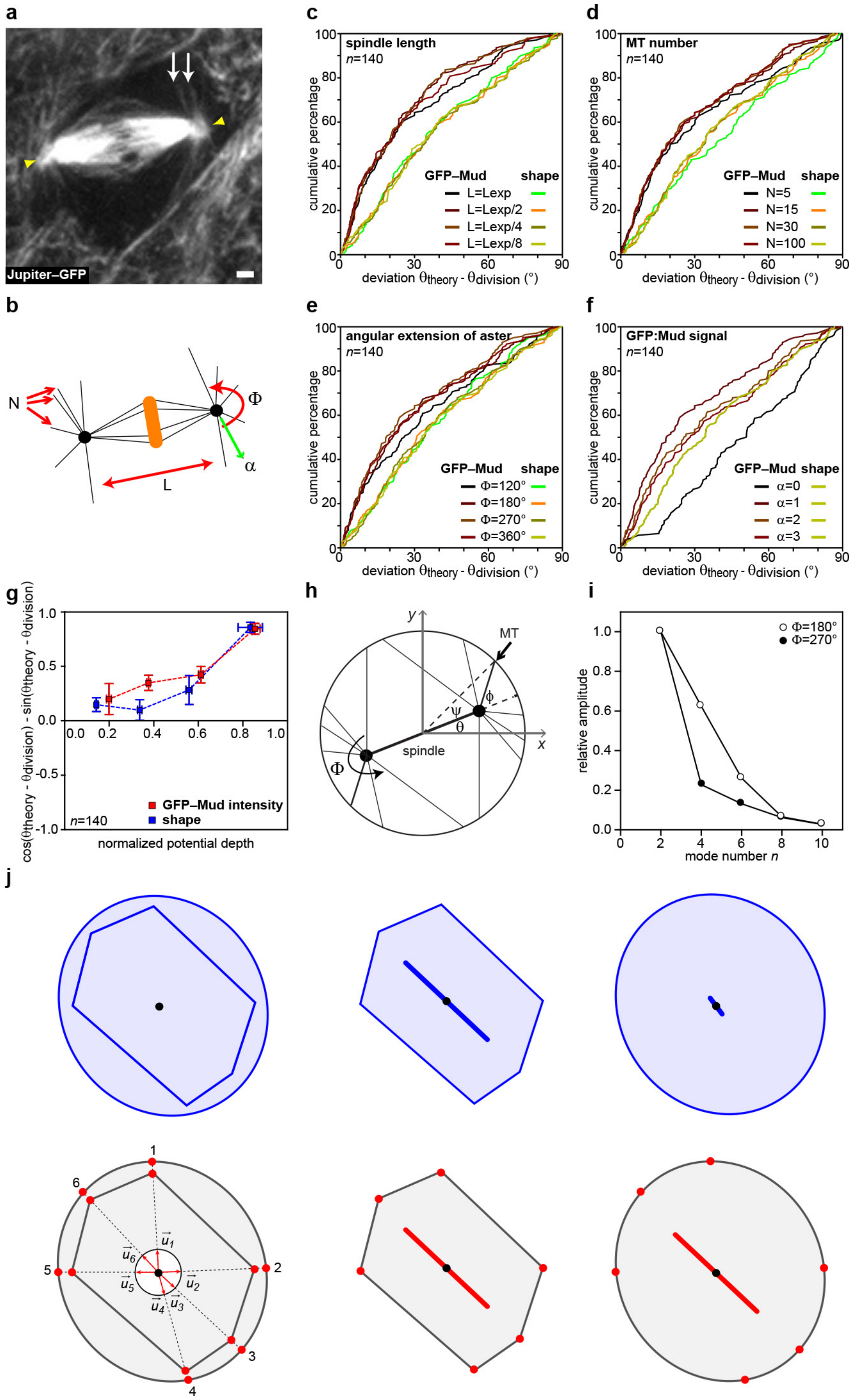

Extended Data Figure 6 | See next page for figure caption.

Extended Data Figure 6 | Spindle orientation modelling. a, Mitotic cell in the *Drosophila* pupal notum labelled with Jupiter–GFP to label microtubules ($n = 23$ cells). White arrows indicate astral microtubules. Yellow arrowheads indicate spindle poles. Scale bar, 1 μm.
b, Representation of the different parameters that were varied for the predictions based on the GFP–Mud cortical intensity and shape model to estimate their contribution. L, length of the mitotic spindle; N, number of astral microtubules; Φ, the angle covered by the astral microtubules; and α, the GFP–Mud intensity scaling factor. See also Supplementary Table 1.
c–f, Cumulative plots of the differences between the theoretical spindle orientation (θ_{theory}) and the experimental spindle orientation (θ_{division}) angles in GFP–Mud-expressing cells (same cells as in Fig. 2h) for different spindle lengths (**c**), microtubule number (**d**), angular extension of astral microtubules (**e**) and different scaling factor between the GFP–Mud intensity and mechanical pulling force (**f**). The GFP–Mud model predictions are mostly independent of spindle length, the number of astral microtubules, the angle covered by the astral microtubules or the scaling factor between GFP–Mud intensity and microtubule pulling force.
g, Dependence of model prediction on shape or GFP–Mud effective potential depth (±s.e.m.). The y axis quantitates the difference between the theoretical angle (θ_{theory}) and experimental angle (θ_{division}) (1, aligned; -1, perpendicular). A larger potential depth corresponds to more deformed cells for the shape model, and to a sharp and anisotropic GFP–Mud distribution for the cortical model. Model predictions improve with potential depth, suggesting the model can capture the effect of GFP–Mud distributions in a dose-dependent manner. $n = 140$ cells. **h**, Definitions of the angles used in the analytical calculation of the contribution of different harmonics to the potential $U(\theta)$. The spindle (heavy black line) makes an angle θ with the positive x axis. An astral microtubule (thin black line indicated by the black arrow) projects to the cortex (circle) at an angle ϕ with respect to the spindle. The same microtubule contacts the cortex an angle $\beta = \psi + \theta$ above the positive x axis. **i**, Normalized magnitudes $|\tilde{u}_n| / |\tilde{u}_2|$ of the Fourier coefficients of the kernel $\tilde{u}(\psi)$ for n even. The magnitudes $|\tilde{u}_n|$ drop off substantially with increasing n, indicating that for many purposes it should be sufficient to approximate the function U by its lowest, $n = 2$ mode. To calculate numerical values for the Fourier coefficients, we took the average of the normalized spindle length $\epsilon = L / 2R$ or the $n = 140$ cells analysed in this paper, obtaining $\overline{\epsilon} \approx 0.76 \pm 0.03$; because it is difficult to precisely estimate Φ from the available data, coefficients are shown for $\Phi = 180°$ and $270°$ in agreement with the astral microtubule distribution observed in **a**. **j**, Schematic illustrating the difference between cell shape and cell TCJ bipolarity measurements. An elongated cell and a rounded cell are overlaid (left panels) and shown side-by-side (middle and right panels). In this example, although the two cells have distinct shapes, they have the same TCJ bipolarity. The upper panels illustrate the measurement of cell shape, which uses all the pixels making up the cell (blue bars). The lower panels illustrate the measurement of TCJ bipolarity (red bars), which is solely based on the angular distribution of the TCJs (red dots), only using the unit vectors $\overrightarrow{\mathbf{u}_v}$ pointing from the cell centre (black dot) to each cell TCJ. The TCJ bipolarity therefore characterizes TCJ distribution independently of cell shape, and a correlation observed between the two quantities is not due to a shape bias in the TCJ bipolarity measurement.

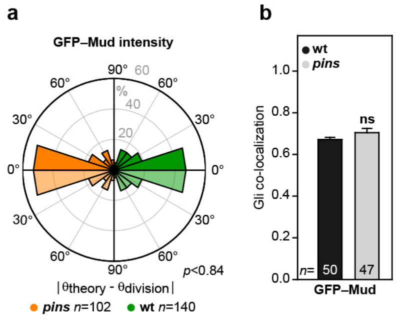

Extended Data Figure 7 | Pins does not contribute to Mud-dependent epithelial cell division orientation. a, Rose plots of the difference between the theoretically predicted (θ_{theory}) and the experimental division (θ_{division}) orientation of the mitotic spindle in *pins* tissue (orange, left rose plot) and wild-type tissue (green, right) based on the GFP–Mud intensity. To facilitate the comparison between the left and the right rose plots, the data are duplicated relative to 0° line (light orange and light green). Number of cells (n) analysed is indicated. P values, Kolmogorov–Smirnov test. **b**, Quantifications of the co-localization of GFP–Mud with Gli in *pins* in metaphase cells (mean ± s.e.m.). Number of cells (n) analysed is indicated. ns, not significant (Student's t-test).

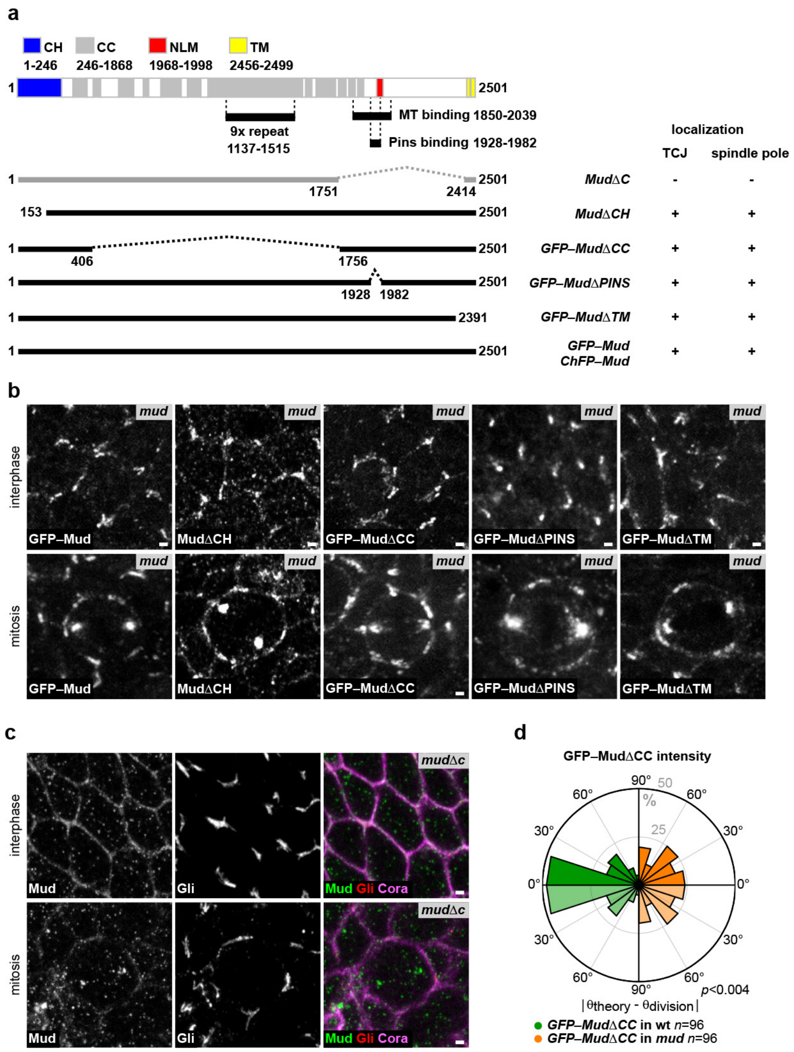

Extended Data Figure 8 | Structure–function analyses of the Mud protein in epithelial cells. a, Diagram of the domains of the Mud protein: putative actin binding calponin homology domain (CH, amino acids 1–246, blue), coiled-coil domain (CC, amino acids 246–1,868, grey), conserved Numa/Lin-5/Mud domain (NLM, amino acids 1,968–1,998, red), putative transmembrane domain (TM, amino acids 2,456–2,499, yellow), 9× repeat domain (amino acids 1,137–1,515), microtubule-binding domain (MT, amino acids 1,850–2,039) and Pins binding domain (amino acids 1,928–1,982)[58–60]. GFP- or ChFP-tagged deletion constructs and the MudΔCH constructs were generated by BAC recombineering (see Methods for details). The MudΔC allele was generated at the *mud* locus using a CRISPR/Cas9 approach (see Methods for details). For each mutant allele, its localization at the TJCs and its localization at the spindle pole are indicated. **b**, Localization of the GFP–Mud, MudΔCH, GFP–MudΔCC, GFP–MudΔPins, GFP–MudΔTM and in G2 interphase and mitotic *mud* epithelial cells. GFP–Mud, GFP–MudΔCC, GFP–MudΔPins, GFP–MudΔTM proteins were imaged in living tissue, whereas MudΔCH was localized on fixed tissue using Mud antibodies. GFP–Mud ($n = 56$), MudΔCH ($n = 33$), GFP–MudΔCC ($n = 165$), GFP–MudΔPins ($n = 42$) and GFP–MudΔTM ($n = 67$) interphase cells. GFP–Mud ($n = 15$), MudΔCH ($n = 4$), GFP–MudΔCC ($n = 67$), GFP–MudΔPins ($n = 18$) and GFP–MudΔTM ($n = 11$) mitotic cells. **c**, Localization of the MudΔC protein (white in the left panels, green in the right panels), Gli (white in the panels in the middle and red in panels at the right) and Cora (magenta in the right panels) in fixed G2 interphase ($n = 71$) and mitotic ($n = 6$) cells. The MudΔC protein is not enriched at TJCs and its localization at the spindle pole is strongly reduced. **d**, Rose plots of the difference between the theoretically predicted (θ_{theory}) and experimental ($\theta_{division}$) spindle orientation angles in wild-type (left rose plot, green) and *mud* (right rose plot, orange) tissues based on the distribution of GFP–MudΔCC. The right rose plot is identical to the one shown in Fig. 2l. To facilitate the comparison between the left and the right rose plots, the data are duplicated relative to 0° line (light green and light orange). Number of cells (n) analysed is indicated. P values, Kolmogorov–Smirnov test. Scale bars, 1 μm.

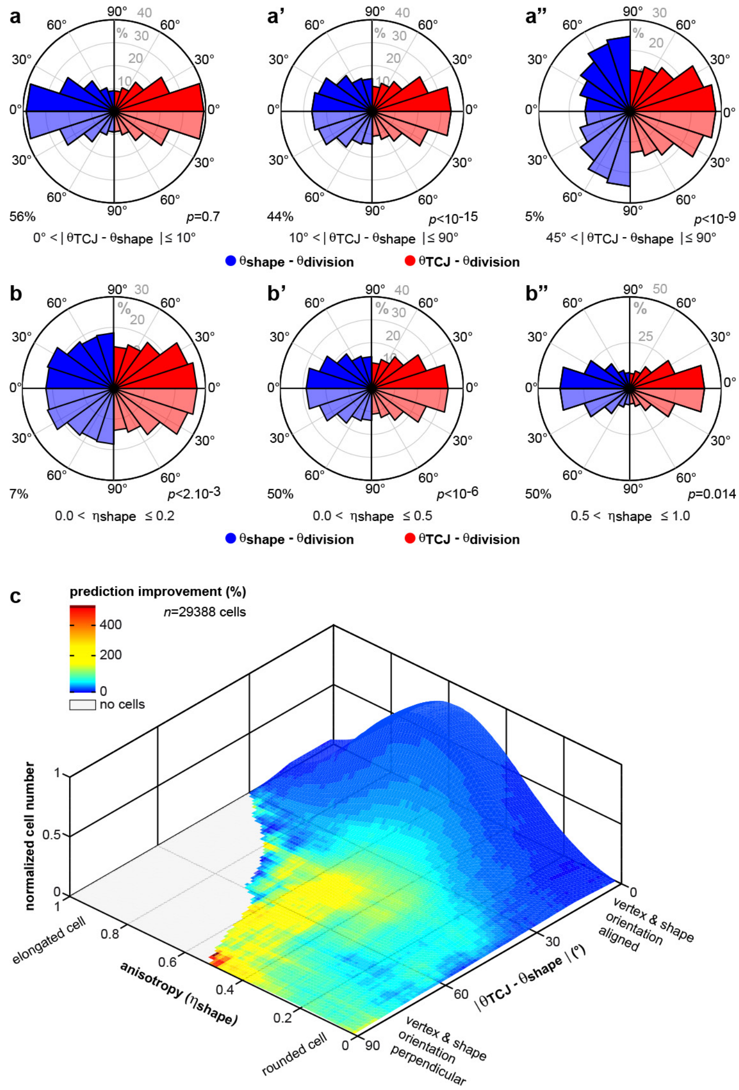

Extended Data Figure 9 | Predicting cell division based on TCJ distribution. a, **a′′**, Rose plots of the magnitude of the difference between experimental ($\theta_{\mathrm{division}}$) and predicted division orientations by the average (60–30 min before mitosis) interphase TCJ bipolarity (θ_{TCJ}) or cell long axis (θ_{shape}) in cells for the indicated $|\theta_{\mathrm{TCJ}} - \theta_{\mathrm{shape}}|$ intervals. To facilitate the comparison between the left and the right rose plots, the data are duplicated relative to 0° line (light blue and light red). Kolmogorov–Smirnov test (P values), percentage of total cells ($n = 29{,}388$). Panels **b** and **b′′** are identical to panel **e** in Fig. 3. **b**, **b′′**, Rose plots of the magnitude of the difference between experimental ($\theta_{\mathrm{division}}$) and predicted division orientations by the average (60–30 min before mitosis) interphase TCJ bipolarity (θ_{TCJ}) or cell long axis (θ_{shape}) for the indicated η_{shape} intervals. To facilitate the comparison between the left and the right rose plots, the data are duplicated relative to 0° line (light blue and light red). Kolmogorov–Smirnov test (P values), percentage of total cells ($n = 29{,}388$). Panels **c** and **c′′** are identical to panel **f** in Fig. 3. **c**, Plot of the spindle orientation prediction improvements (colour-coded from dark blue to red) based on TCJ bipolarity over those based on cell shape versus the magnitude of their angular difference ($|\theta_{\mathrm{TCJ}} - \theta_{\mathrm{shape}}|$) and the cell shape anisotropy (η_{shape}). The plot height is the normalized cell number in each domain of the plot (29,883 cells were analysed in total). As $|\theta_{\mathrm{TCJ}} - \theta_{\mathrm{shape}}|$ increases, the TCJ bipolarity predictions improve over cell shape prediction for both rounded (low η_{shape}) and elongated cells (high η_{shape}). Whereas the rounded cells are characterized by an even distribution along the $|\theta_{\mathrm{TCJ}} - \theta_{\mathrm{shape}}|$ axis, the elongated cells are mainly characterized by a strongly skewed distribution towards low $|\theta_{\mathrm{TCJ}} - \theta_{\mathrm{shape}}|$.

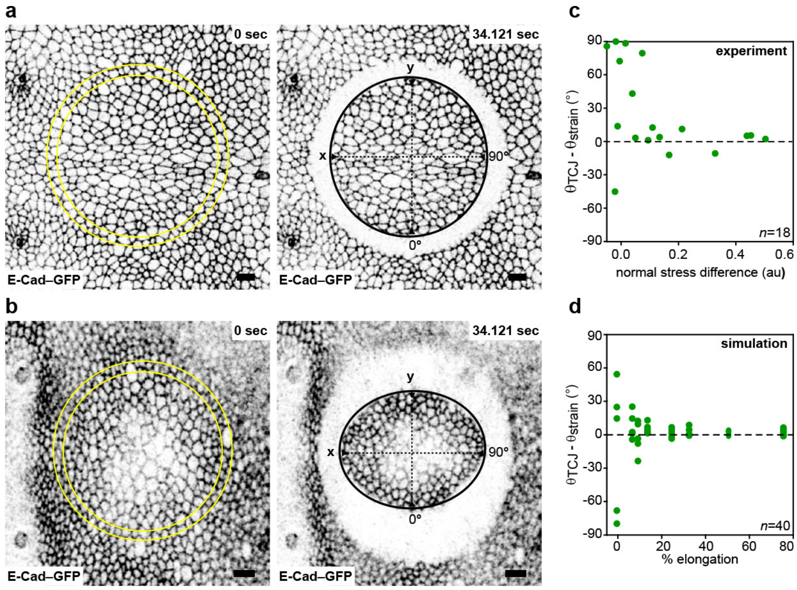

Extended Data Figure 10 | TCJ bipolarity aligns with mechanical stress. **a, b**, Images of the scutellum tissue before and after ablation (ablated region in yellow) in early and late pupa characterized by small isotropic stress (**a**) and high anisotropic stress (**b**). Tissue stress was estimated by determining the initial recoiled velocity upon circular ablation in the x and y directions[53]. First and last images of two time-lapse movies out of the 18 quantified in **c** are shown. Scale bars, 10 μm. **c**, Plot of the difference between the orientation of TCJ bipolarity (θ_{TCJ}) and principal strain axis (θ_{strain}) as a function of normal stress differences ($\sigma_{yy} - \sigma_{xx}$, note that $\sigma_{xy} = 0$) as estimated up to a prefactor by circular laser ablation. Number of ablations (n) analysed is indicated. The same plot is shown in Fig. 4d. **d**, Plot of the difference between the orientation of TCJ bipolarity (θ_{TCJ}) and the orientation of strain (θ_{strain}) as a function of the percentage of cell elongation applied to a simulated cell lattice. When cell elongation increases TCJ bipolarity orientation becomes aligned with the direction of cell elongation. Number of simulations (n) analysed is indicated.

doi:10.1038/nature16995

Structural basis for promiscuous PAM recognition in type I–E Cascade from *E. coli*

Robert P. Hayes[1], Yibei Xiao[1], Fran Ding[1], Paul B. G. van Erp[4], Kanagalaghatta Rajashankar[2], Scott Bailey[3], Blake Wiedenheft[4] & Ailong Ke[1]

Clustered regularly interspaced short palindromic repeats (CRISPRs) and the *cas* (CRISPR-associated) operon form an RNA-based adaptive immune system against foreign genetic elements in prokaryotes[1]. Type I accounts for 95% of CRISPR systems, and has been used to control gene expression and cell fate[2,3]. During CRISPR RNA (crRNA)-guided interference, Cascade (CRISPR-associated complex for antiviral defence) facilitates the crRNA-guided invasion of double-stranded DNA for complementary base-pairing with the target DNA strand while displacing the non-target strand, forming an R-loop[4,5]. Cas3, which has nuclease and helicase activities, is subsequently recruited to degrade two DNA strands[4,6,7]. A protospacer adjacent motif (PAM) sequence flanking target DNA is crucial for self versus foreign discrimination[4,8–16]. Here we present the 2.45 Å crystal structure of *Escherichia coli* Cascade bound to a foreign double-stranded DNA target. The 5′-ATG PAM is recognized in duplex form, from the minor groove side, by three structural features in the Cascade Cse1 subunit. The promiscuity inherent to minor groove DNA recognition rationalizes the observation that a single Cascade complex can respond to several distinct PAM sequences. Optimal PAM recognition coincides with wedge insertion, initiating directional target DNA strand unwinding to allow segmented base-pairing with crRNA. The non-target strand is guided along a parallel path 25 Å apart, and the R-loop structure is further stabilized by locking this strand behind the Cse2 dimer. These observations provide the structural basis for understanding the PAM-dependent directional R-loop formation process[17,18].

Differentiating ‘self’ from ‘non-self’ is crucial in CRISPR systems, as foreign target sequences (protospacers) are identical to sequences recorded in the host CRISPR locus (spacers). In type I and II CRISPR systems, foreign DNA detection relies on protein-mediated PAM recognition[4,8–16]. Whereas PAM recognition in Cas9-based type II systems has been attributed to major groove DNA contact[19,20], it remains unclear whether Cascade recognizes PAM in the major or minor groove[12], in single-stranded or double-stranded form[4,21]. The promiscuity in PAM recognition also remains unexplained. Five PAM sequences (5′-ATG, AAG, AGG, GAG and TAG reading from the non-target strand) can trigger robust CRISPR interference by *E. coli* Cascade[4,11,21,22]. Crystal structures of *E. coli* Cascade in free and single-stranded DNA (ssDNA)-bound forms revealed multiple conformational states and insights about the crRNA-guided ssDNA recognition mechanism[21,23,24]; however, the mechanisms for double-stranded DNA (dsDNA) entry, PAM recognition, and R-loop formation remain poorly defined.

To understand PAM-dependent foreign DNA recognition, we determined the 2.45 Å crystal structure of *E. coli* Cascade bound to dsDNA that forms a partial R-loop (Fig. 1a–c and Extended Data Fig. 1); such DNA substrates are known to bind *Thermobifida fusca* type I–E Cascade and to recruit Cas3 specifically[25]. Our structure agrees well with the cryo-electron microscopy (cryoEM) reconstruction of the full R-loop–Cascade complex, underlining its validity in explaining R-loop formation[21] (Extended Data Fig. 2 and Supplementary Video 1). Comparison with high-resolution crystal structures suggests that R-loop formation requires both the sliding of Cse1-CTD (carboxy-terminal domain)–Cse2.1–Cse2.2, as seen in the ssDNA-bound Cascade structure, and the engagement of Cse1-NTD (amino-terminal domain), as seen in the free Cascade structure[21,23,24] (Extended Data Fig. 3 and Supplementary Videos 2 and 3). In addition, a localized conformational change, only observed in this R-loop-bound structure, occurs near the putative Cas3-binding site[21]; this may have a role in Cas3 recruitment (Extended Data Fig. 4). dsDNA enters Cascade between Cas7.5 and Cas7.6, contacted by the lysine-rich helices[16,26] (Fig. 1d, e and Extended Data Fig. 5). DNA bifurcates underneath PAM. The entire target DNA strand flips to form the segmented DNA–crRNA duplex[27]. The 10-nucleotide non-target strand is guided to a parallel path 25 Å apart by sequence-nonspecific contacts, an active mechanism to stabilize the R-loop (Fig. 1d, e). Modelling dsDNA beyond PAM projects it across the Cse1-CTD without severe steric clashes (Fig. 1f), illustrating a possible PAM-searching scenario[21].

The 5′-ATG PAM sequence is recognized by Cse1 in the double-stranded form, from the minor groove side (Fig. 2a, b). This mode of recognition strongly biases towards the target DNA strand, which rationalizes previous observations that mismatched PAMs could be tolerated, provided that the target strand sequence was optimal[4,21]. PAM recognition requires three structural features in Cse1: a glutamine wedge, a glycine loop and a lysine finger (Fig. 2a, b). Only C_{T-1}–G_{NT-1} is tolerated at the −1 position (PAM−1) in *E. coli*[5,21], although recent analyses revealed spacer-dependent tolerance of alternative base pairs at PAM−1 (ref. 28). In our structure (Fig. 2a–d), the amide of Ala355 in the glutamine wedge donates a H-bond to O2 of C_{T-1}, specifying a pyrimidine in the target strand. The carbonyl of Gly157 in the glycine loop accepts a water-mediated H-bond from N2 of G_{NT-1}. G_{NT-1}-to-inosine substitution suggests that this contact only provides minor discrimination against A_{NT-1} (Extended Data Fig. 6a). The affinity of Cascade for different PAM−1 base-pair combinations correlates well with the structural observation that a target strand pyrimidine is strongly specified (Extended Data Fig. 6b). The tenfold differences in the dissociation constant (K_d) values, however, do not support an absolute C_{T-1}–G_{NT-1} specification at PAM−1. Indeed, Cas3 can cleave alternative PAM−1 targets, provided that the Cascade concentration is above the corresponding K_d value (Extended Data Fig. 6c). These results echo the recent finding in suggesting that the PAM−1 readout is further complicated by the Cascade/Cas3 expression level and spacer content[28].

Importantly, PAM recognition coincides with insertion of a glutamine wedge into dsDNA underneath PAM (Fig. 2a, d). The tip

[1]Department of Molecular Biology and Genetics, Cornell University, 253 Biotechnology Building, Ithaca, New York 14853, USA. [2]Department of Chemistry and Chemical Biology, Cornell University, NE-CAT, Advanced Photon Source, Argonne National Laboratory, Argonne, Illinois 60439, USA. [3]Department of Biochemistry and Molecular Biology, Johns Hopkins University, Bloomberg School of Public Health, Baltimore, Maryland 21205, USA. [4]Department of Microbiology and Immunology, Montana State University, Bozeman, Montana 59717, USA.

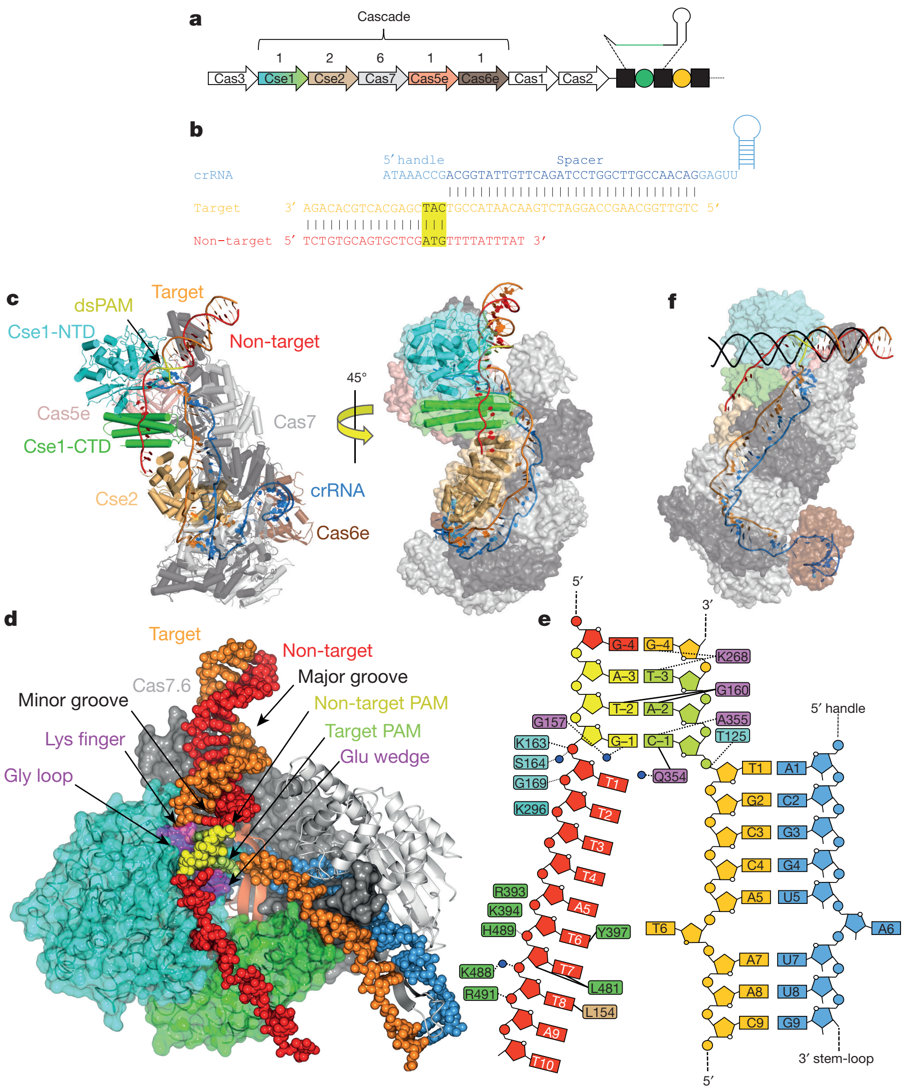

Figure 1 | Foreign-DNA-bound Cascade structure. **a**, Arrangement of I–E CRISPR-*cas* locus in the *E. coli* K12 genome. Colour schemes are preserved throughout all figures. **b**, **c**, Nucleic acid sequences (**b**) and overall views (**c**) of the foreign-DNA-bound Cascade structure. **d**, Entry of dsDNA between Cas7.5 and Cas7.6, PAM recognition by three structural elements in Cse1-NTD (magenta), and the partial R-loop underneath PAM. **e**, Schematic of Cascade–DNA contacts around PAM regions. Hydrogen bonds and electrostatic contacts are shown as dashed lines, hydrophobic interactions as solid lines, and water molecules as blue circles. **f**, Modelling of Cascade sampling B-form dsDNA for PAM.

residue Gln354 stacks underneath C_{T-1} and, together with Asn353, sterically displaces the first two protospacer nucleotides in the target strand, forcing them to rotate outwards. Given its strategic location, it is rather surprising that this wedge is not highly conserved in sequence (Extended Data Fig. 7). Indeed, tip residue substitutions (Gln354Ala, Asn353Ala and Gln354Ala/Asn353Ala) barely affect DNA binding. By contrast, trimming this wedge (NNQAS352–356/GG) reduced DNA binding 100-fold, suggesting that the wedge functions by a steric interference mechanism to nucleate the target strand displacement upon PAM recognition (Fig. 2e, f). A serine-to-phosphate 'lock' is essential in initiating the target strand flipping in Cas9 (ref. 19). Thr125 is in a similar location in our structure but contacts the +1 bridging oxygen instead, and the Thr125Ala substitution had a negligible defect (Fig. 2e).

Recognition at PAM−2 is promiscuous. Only G_{T-2}–C_{NT-2} is rejected at this position; the other three combinations lead to efficient interference[22]. Here the glycine-loop residues (159–161) assume a lip-like structure, introduce DNA bending at A_{T-2}–T_{NT-2}, and 'bite' onto the PAM−1 base pair in conjunction with the glutamine wedge underneath; T_{NT-2} retreats backwards and tilts upwards (Fig. 2b, d). The rim of the glycine loop explores shape-complementarity to A_{T-2}, and donates a weak H-bond to N3 of A_{T-2}. Gly160Ala substitution disrupts the shape complementarity, and reduces Cascade binding affinity by ~100-fold and Cas3 cleavage to baseline levels (Fig. 2e, f). Rejection of G_{T-2}–C_{NT-2} at PAM−2 is rationalized by the fact that the N2 amine of G_{T-2} would introduce steric clashes against the glycine loop; whereas T_{T-2}–A_{NT-2} or C_{T-2}–G_{NT-2} would not, based on modelling (Extended Data Fig. 8a). Indeed, removal of this amine by inosine substitution largely rescued the DNA-binding defect, confirming that the N2 of G_{T-2} is the anti-determinant for PAM−2 specificity (Extended Data Fig. 8b). An equivalent glycine-rich loop is present in all known Cse1 structures; they probably have a similar minor groove DNA recognition function (Extended Data Fig. 7).

PAM−3 is typically specified as a pyrimidine$_{T}$–purine$_{NT}$ pair by Cascade[4,11,21]. 5′-TAG PAM also leads to interference, but G_{T-3}–C_{NT-3} containing PAMs fail to[22,28]. Here a favourable electrostatic interaction from a lysine finger (Lys268) to O2 of T_{T-3} is observed, underlying the strong preference for pyrimidine at this position (Fig. 2b, d). Lys268Ala mutation reduced Cascade binding and Cas3 cleavage by >8-fold and >10-fold, respectively, emphasizing its positive contribution to PAM−3 recognition (Fig. 2e, f). Interestingly, the Lys268Ala mutant still retained wild-type level discrimination against 5′-CTG PAM (Extended Data Fig. 8c). G_{T-3}-to-inosine substitution ultimately proved that the N2 of G_{T-3} also serves as a strong anti-determinant

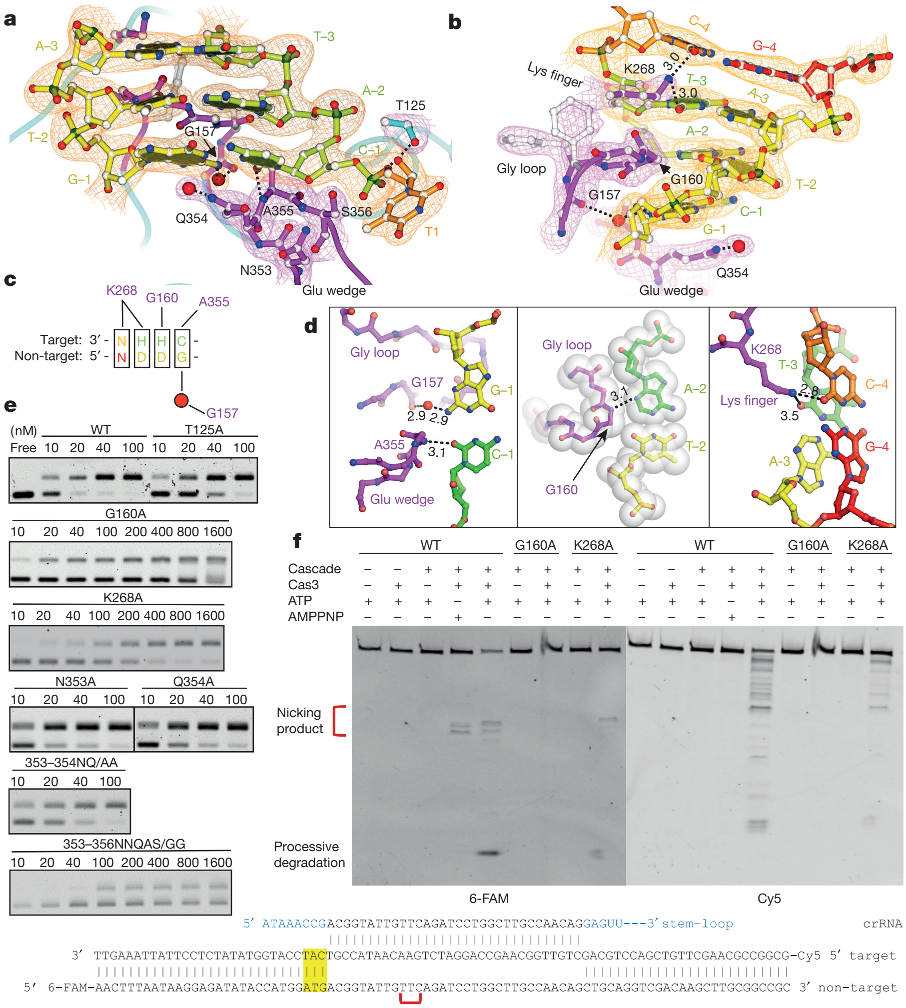

Figure 2 | PAM recognition by Cse1 subunit of Cascade. a, **b**, Detailed views featuring PAM recognition by the glutamine wedge (and its involvement in target DNA strand displacement), glycine loop, and lysine finger of Cse1. The $2F_o - F_c$ electron density map is shown at 1.5σ. **c**, Summarization of the five interference PAMs in *E. coli* type I-E CRISPR system, with the observed Cascade contacts marked. **d**, Top-down views of PAM recognition at each base pair. Left, stringent recognition of PAM−1. Middle, shape complementarity to PAM−2. Right, Electrostatic contacts to PAM−3 and −4. **e**, **f**, Mutagenesis assayed by Cascade-binding (electrophoretic mobility shift assay, EMSA) (**e**) and Cas3-mediated DNA cleavage (**f**) to evaluate the observed PAM contacts. WT, wild type. Experiments were done in triplicate and representative results are shown. Uncropped gels are shown in Supplementary Fig. 1.

in the rejection of G_{T-3}-containing PAMs (Extended Data Fig. 8d). Interestingly, Lys268 makes an electrostatic interaction to C_{T-4} (Fig. 2b, d), indicating certain level of sequence discrimination at PAM−4 as well.

Detailed structure dissection also helps to rationalize the self-avoidance mechanism. All spacers in *E. coli* CRISPR loci are 'protected' by a 5′-CCG PAM. This PAM is the combination of the least-preferred nucleotides at each position (3′-$G_{T-3}G_{T-2}C_{T-1}$), which would strongly disfavour Cascade-mediated R-loop formation, despite a perfect spacer match.

The non-target strand is guided sequence-nonspecifically along the Cascade surface, 20–25 Å away from the target strand (Fig. 3a). The sugar phosphates of nucleotides 1–3 are contacted by Lys163, Gly169 and Lys296 of Cse1-NTD, nucleotides 6–9 by a string of positive charges (Arg393/Lys394/Lys488/His489/Arg491) across Cse1-CTD (Fig. 3a). The redundant interactions were not disrupted by a point mutation (Tyr397Ala). A double mutant (488–489KH/AA) neutralizing a positive patch, however, led to a fourfold binding defect (Fig. 3b). The tenth/last nucleotide rests at an intersection between Cse1-CTD and Cse2.1. To investigate whether the following non-target residues travels on the surface or backside of the Cse2 dimer, we further determined a 3.2 Å structure in which the non-target protospacer is 22 nucleotides longer. Although most of the additional residues remain unresolved, density clearly reveals that the non-target strand residues take the downward trench route towards the backside of the Cse2.1 dimer, attracted by the favourable electrostatic environment therein (Fig. 3c–e). Non-target strand sequestration probably corresponds to the extra 'locking' step after most R-loop forms, as a mechanism to prevent the R-loop collapse[17].

In summary, our structural analysis provides important insights about the PAM-dependent directional R-loop formation[17] (Fig. 4). Recognition of an interference PAM by Cascade coincides with the wedge-mediated displacement of the first two target strand nucleotides, initiating DNA unwinding. Directional DNA melting ensures the ordered guidance of the non-target DNA strand ~25 Å away from the target strand, as a mechanism to stabilize the seed bubble. Further R-loop propagation leads to non-target strand sequestration behind the Cse2 dimer, locking the R-loop in place. Conformational changes accompany the process and reorganize the Cse1 surface, paving the way for Cas3 binding. The active guidance of the non-target DNA strand is a theme not observed in Cas9–DNA structures[19,20]. It rationalizes the observation that the Cascade-bound R-loop is considerably more stable than that of Cas9 (ref. 17). Besides 5 interference PAMs, 21 other PAMs stimulate 'primed adaptation' in *E. coli*[22], in which Cascade and Cas3 actively recruit the Cas1/Cas2 spacer acquisition complex[29,30]. Priming PAMs may lead to suboptimal Cascade contacts

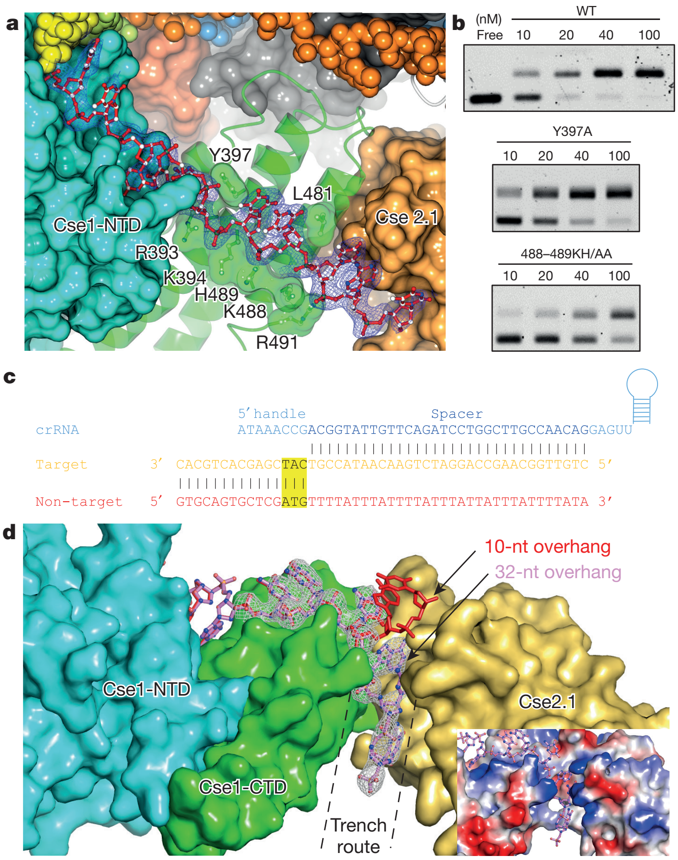

Figure 3 | Active guidance of the non-target DNA strand by Cascade. **a**, Sequence-nonspecific electrostatic contacts guide the 10-nucleotide non-target strand (red sticks) protospacer along the Cse1-NTD surface (cyan), and across a binding site on Cse1-CTD (green). Tyr397 and Leu481 from Cse1-CTD further interdigitate between di-nucleotide stacks. **b**, EMSA evaluating non-target contacts by Cascade. Experiments were done in triplicate and representative results are shown. **c**, **d**, Nucleic acid sequence (**c**) and zoomed-in view of the 3.2 Å structure (**d**) of Cascade programmed with a 22-nucleotide (nt) longer non-target strand. The $2F_o - F_c$ electron density map at 1.0σ clearly reveals that the longer non-target DNA strand takes the trench route. Inset illustrates the favourable electrostatic surface. Uncropped gels are shown in Supplementary Fig. 1.

and non-canonical R-loops. Such R-loops are difficult to form and may not be completely unwound[18], requiring higher Cascade concentration[30] and favourable DNA torque[17]. They also fail to recruit Cas3 directly[30], which may indicate that the non-target DNA strand is misguided, as Cas3 recruitment is contingent upon non-target strand contact as well[25]. Overall, these results will facilitate future studies to better understand the interference and primed adaptation mechanisms in type I CRISPR-Cas systems.

Online Content Methods, along with any additional Extended Data display items and Source Data, are available in the online version of the paper; references unique to these sections appear only in the online paper.

Received 5 November 2015; accepted 14 January 2016.
Published online 10 February 2016.

1. van der Oost, J., Westra, E. R., Jackson, R. N. & Wiedenheft, B. Unravelling the structural and mechanistic basis of CRISPR-Cas systems. *Nature Rev. Microbiol.* **12,** 479–492 (2014).
2. Luo, M. L., Mullis, A. S., Leenay, R. T. & Beisel, C. L. Repurposing endogenous type I CRISPR-Cas systems for programmable gene repression. *Nucleic Acids Res.* **43,** 674–681 (2015).
3. Caliando, B. J. & Voigt, C. A. Targeted DNA degradation using a CRISPR device stably carried in the host genome. *Nature Commun.* **6,** 6989 (2015).
4. Westra, E. R. *et al.* CRISPR immunity relies on the consecutive binding and degradation of negatively supercoiled invader DNA by Cascade and Cas3. *Mol. Cell* **46,** 595–605 (2012).

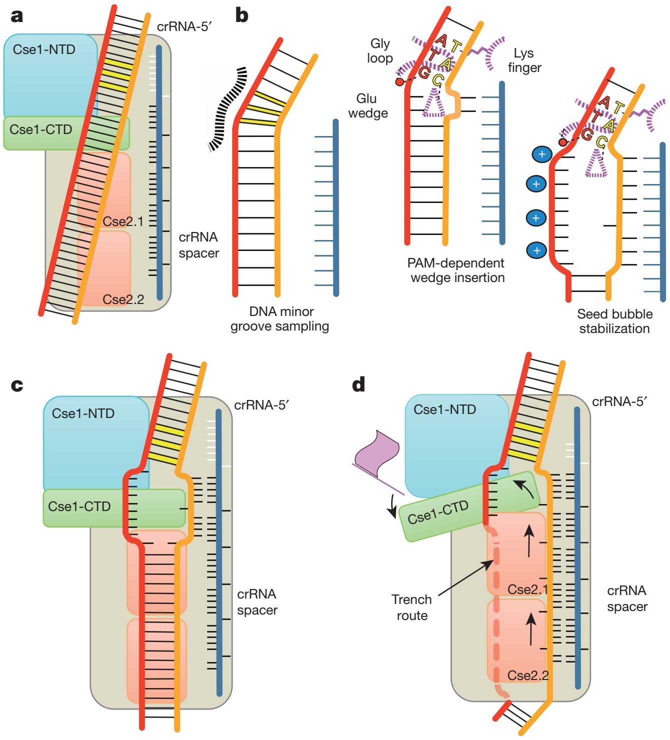

Figure 4 | Model for PAM-dependent directional R-loop formation in type I CRISPR-Cas system. **a**, Cascade samples dsDNA minor groove for various sequence combinations (yellow sticks). **b**, Left, interference and priming PAMs lead to longer dwell time and local DNA bending. Middle, interference PAMs allow optimal minor groove interaction, which is coupled with the glutamine wedge insertion and disruption of the first two base pairs of protospacer. Right, directional DNA melting leads to segmented DNA–crRNA duplex formation at the target strand side and favourable sugar phosphate contacts at the non-target side, stabilizing the seed bubble. **c**, Further DNA unwinding leads to non-target strand sequestration to the backside of Cse2 dimer, locking the R-loop in place. **d**, R-loop formation is accompanied by a pivoting motion in Cse1-CTD and a sliding motion in the Cse2 dimer. Local rearrangement occurs in Cse1 (depicted as a flag), licensing Cas3 recruitment.

5. Jore, M. M. *et al.* Structural basis for CRISPR RNA-guided DNA recognition by Cascade. *Nature Struct. Mol. Biol.* **18,** 529–536 (2011).
6. Brouns, S. J. *et al.* Small CRISPR RNAs guide antiviral defense in prokaryotes. *Science* **321,** 960–964 (2008).
7. Wiedenheft, B. *et al.* Structures of the RNA-guided surveillance complex from a bacterial immune system. *Nature* **477,** 486–489 (2011).
8. Westra, E. R. *et al.* Type I-E CRISPR-Cas systems discriminate target from non-target DNA through base pairing-independent PAM recognition. *PLoS Genet.* **9,** e1003742 (2013).
9. Marraffini, L. A. & Sontheimer, E. J. Self versus non-self discrimination during CRISPR RNA-directed immunity. *Nature* **463,** 568–571 (2010).
10. Mojica, F. J., Díez-Villaseñor, C., Garcia-Martinez, J. & Almendros, C. Short motif sequences determine the targets of the prokaryotic CRISPR defence system. *Microbiology* **155,** 733–740 (2009).
11. Mulepati, S. & Bailey, S. *In vitro* reconstitution of an *Escherichia coli* RNA-guided immune system reveals unidirectional, ATP-dependent degradation of DNA target. *J. Biol. Chem.* **288,** 22184–22192 (2013).
12. Rollins, M. F., Schuman, J. T., Paulus, K., Bukhari, H. S. & Wiedenheft, B. Mechanism of foreign DNA recognition by a CRISPR RNA-guided surveillance complex from *Pseudomonas aeruginosa*. *Nucleic Acids Res.* **43,** 2216–2222 (2015).
13. Sashital, D. G., Wiedenheft, B. & Doudna, J. A. Mechanism of foreign DNA selection in a bacterial adaptive immune system. *Mol. Cell* **46,** 606–615 (2012).
14. Sinkunas, T. *et al.* *In vitro* reconstitution of Cascade-mediated CRISPR immunity in *Streptococcus thermophilus*. *EMBO J.* **32,** 385–394 (2013).
15. Sternberg, S. H., Redding, S., Jinek, M., Greene, E. C. & Doudna, J. A. DNA interrogation by the CRISPR RNA-guided endonuclease Cas9. *Nature* **507,** 62–67 (2014).
16. van Erp, P. B. *et al.* Mechanism of CRISPR-RNA guided recognition of DNA targets in *Escherichia coli*. *Nucleic Acids Res.* **43,** 8381–8391 (2015).
17. Rutkauskas, M. *et al.* Directional R-loop formation by the CRISPR-Cas surveillance complex cascade provides efficient off-target site rejection. *Cell Rep.* **10,** 1534–1543 (2015).

18. Blosser, T. R. *et al.* Two distinct DNA binding modes guide dual roles of a CRISPR-Cas protein complex. *Mol. Cell* **58,** 60–70 (2015).
19. Anders, C., Niewoehner, O., Duerst, A. & Jinek, M. Structural basis of PAM-dependent target DNA recognition by the Cas9 endonuclease. *Nature* **513,** 569–573 (2014).
20. Nishimasu, H. *et al.* Crystal Structure of *Staphylococcus aureus* Cas9. *Cell* **162,** 1113–1126 (2015).
21. Hochstrasser, M. L. *et al.* CasA mediates Cas3-catalyzed target degradation during CRISPR RNA-guided interference. *Proc. Natl Acad. Sci. USA* **111,** 6618–6623 (2014).
22. Fineran, P. C. *et al.* Degenerate target sites mediate rapid primed CRISPR adaptation. *Proc. Natl Acad. Sci. USA* **111,** E1629–E1638 (2014).
23. Zhao, H. *et al.* Crystal structure of the RNA-guided immune surveillance Cascade complex in *Escherichia coli*. *Nature* **515,** 147–150 (2014).
24. Jackson, R. N. *et al.* Crystal structure of the CRISPR RNA-guided surveillance complex from *Escherichia coli*. *Science* **345,** 1473–1479 (2014).
25. Huo, Y. *et al.* Structures of CRISPR Cas3 offer mechanistic insights into Cascade-activated DNA unwinding and degradation. *Nature Struct. Mol. Biol.* **21,** 771–777 (2014).
26. Jackson, R. N. *et al.* Crystal structure of the CRISPR RNA-guided surveillance complex from *Escherichia coli*. *Science* **345,** 1473–1479 (2014).
27. Mulepati, S., Heroux, A. & Bailey, S. Crystal structure of a CRISPR RNA-guided surveillance complex bound to a ssDNA target. *Science* **345,** 1479–1484 (2014).
28. Xue, C. *et al.* CRISPR interference and priming varies with individual spacer sequences. *Nucleic Acids Res.* **43,** 10831–10847 (2015).
29. Datsenko, K. A. *et al.* Molecular memory of prior infections activates the CRISPR/Cas adaptive bacterial immunity system. *Nature Commun.* **3,** 945 (2012).
30. Redding, S. *et al.* Surveillance and processing of foreign DNA by the *Escherichia coli* CRISPR-Cas system. *Cell* **163,** 854–865 (2015).

Supplementary Information is available in the online version of the paper.

Acknowledgements This work is supported by National Institutes of Health (NIH) grants GM102543 and GM086766 to A.K., GM097330 to S.B. and GM108888 to B.W. NE-CAT beamlines were supported by NIH grants P41 GM103403 and S10 RR029205. We thank G. Feigenson and J. Mallon for technical help, and I. Finkelstein, I. Price and A. Dolan for discussions.

Author Contributions R.P.H. and A.K. designed the research, R.P.H. determined the structure and performed biochemical analyses, Y.X., F.D. and P.B.G.vE. contributed to biochemical analysis, K.R. assisted with diffraction data collection and processing, and B.W. and S.B. contributed to assay setup. R.P.H., B.W. and A.K. wrote the manuscript.

Author Information The structure factors and coordinates for Cascade–partial-R-loop structures with 10-nucleotide and 35-nucleotide non-target protospacer have been deposited in the Protein Data Bank (PDB) under accession numbers 5H9F and 5H9E, respectively. Reprints and permissions information is available at www.nature.com/reprints. The authors declare no competing financial interests. Readers are welcome to comment on the online version of the paper. Correspondence and requests for materials should be addressed to A.K. (ak425@cornell.edu).

METHODS

No statistical methods were used to predetermine sample size. The experiments were not randomized, and investigators were not blinded to allocation during experiments and outcome assessment.

Expression and purification of Cascade, the Cascade–dsDNA complex and Cas3. Sequence information for primers and the synthetic CRISPR expression cassette can be found in Extended Data Table 1. Cascade expression was similar to ref. 26. In brief, *cse1* was PCR amplified from *E. coli* K12 genomic DNA and cloned into the pRSF-Duet-ORF1 vector (Kan^R), between NcoI and NotI restriction sites (Extended Data Table 1). The *cse2-cas7-cas5e-cas6e* sub-operon was cloned into pET52b (Amp^R) between NcoI and NotI; as a Precission cleavable His_6 fusion at the N terminus of *cse2*. The pre-crRNA expression cassette was synthesized by Life Technologies and cloned into the pHSG-398 vector (Cam^R) (Extended Data Table 1). *E. coli* BL21 (DE3) star cells containing the three plasmids were grown in LB medium at 37 °C to $A_{600\,nm}$ of 0.6. Cascade expression was induced by the addition of 0.5 mM isopropyl-β-D-1-thiogalactopyranoside (IPTG) and cells were further cultured at 20 °C for 12 h.

The cells were disrupted by sonication in buffer A (50 mM Tris, pH 8.0, 20 mM imidazole and 300 mM NaCl), loaded to Ni-NTA column, and eluted with buffer A supplemented with 300 mM imidazole. The His_6 tag was cleaved by Precision protease, and back-adsorbed with a second Ni-NTA column binding step. Cascade was concentrated and buffer exchanged into buffer B (20 mM Tris, pH 7.5, 150 mM NaCl and 2 mM DTT), and further purified on Superdex 200 prep grade column (GE healthcare). Free-Cascade containing fractions were pooled, concentrated to 15 mg ml^{-1}, flash-frozen, and stored at −80 °C.

The Cascade–dsDNA complex was prepared by mixing free-Cascade with dsDNA R-loop mimicking substrate. DNA substrates were chemically synthesized from IDT (Extended Data Table 1). The non-target strand was annealed with the target strand at a 1.5:1 molar ratio. The resulting R-loop mimicking substrate was mixed with Cascade at a 2:1 molar ratio, incubated at room temperature for 30 min, and re-purified on Superdex 200. Cascade–dsDNA complex fractions were pooled and used in crystallization trials. The Cascade–dsDNA complex containing the 32-nucleotide non-target strand overhang was also obtained using the above protocol, except that the His tag was not cleaved. Cascade mutants were constructed with site-directed mutagenesis, and purified using the same method as free-Cascade, except that the N-terminal His_6 tag was left intact. Cascade integrity was checked using SDS–PAGE (Extended Data Fig. 4b).

The Cas3 gene was amplified from *E. coli* K12 genomic DNA and cloned between BamHI and XhoI into the pET28a-SUMO plasmid. *E. coli* BL21 (DE3) star cells were grown in LB medium at 20 °C to $A_{600\,nm}$ of 0.3, induced with 0.2 mM IPTG, and further cultured at 20 °C for 12 h. The Ni-NTA and SEC purification procedures were similar to the procedure mentioned above. The monomeric SUMO-Cas3 fractions were pooled, concentrated to 2 mg ml^{-1}, flash-frozen and stored at −80 °C until usage in biochemical assays.

Crystallization and structure determination of Cascade–partial-R-loop complex. Cascade complex crystals were grown using the hanging drop vapour-diffusion method by mixing 2 μl of purified Cascade–dsDNA complex (15 mg ml^{-1}) with 2 μl of mother liquor (1.6 M Na/K-phosphate, pH 6.2) at 18 °C. Initial crystals appeared after 2 weeks and grew to full size after ~6 weeks. Crystals were cryoprotected in motherliquor supplemented with 20% ethylene glycol and flash frozen in liquid nitrogen. Diffraction data were collected at Advanced Photon Source NECAT beamline 24-ID-C and were processed with HKL2000 (ref. 31). The structure was solved by molecular replacement with PDB accession 4QYZ as the search model. Iterative model building and refinement was conducted with COOT[32] and PHENIX[33]. A summary of the diffraction and refinement statistics can be found in Extended Data Table 2. The Ramachandran plot for the Cascade–dsDNA 10-nucleotide overhang structure indicated 96.65% of residues in the favoured region, 3.10% allowed, and 0.25% outliers. The Ramachandran plot for the Cascade–dsDNA 32-nucleotide overhang structure indicated 94.56% of residues in the favoured region, 4.81% allowed, and 0.63% outliers. Figures were generated using PyMOL (The PyMOL Molecular Graphics System, version 1.3r1, Schrödinger, LLC) and CCP4mg (ref. 34).

EMSA. Fluorescent dsDNA target substrates were generated for biochemical assays. The crRNA-matching targets with varied PAMs were cloned into pCDF-Duet between the PstI and NcoI sites Extended Data Table 1. The dsDNA1 and dsDNA2 substrates were PCR amplified from the plasmid using the indicated fluorescent oligonucleotides (5′ 6-FAM for the non-target strand and 5′ Cy5 for the target strand). The dsDNA3 substrates were prepared by oligonucleotide annealing. All dsDNA substrates were subsequently gel-purified. The dsDNA1 substrate (5′ATG-PAM) was used for all main-text EMSA and Cas3 cleavage assays. The dsDNA2 substrates were used for the experiments shown in Extended Data Figs 6b, c and 8c. The dsDNA3 substrates were used in the experiments shown in Extended Data Figs 6a and 8b, d. DNA binding was conducted in 20 mM Tris, pH 7.5, 150 mM NaCl and 5% glycerol. The dsDNA substrate concentration was held constant at 3 nM and Cascade concentration was titrated as indicated. The Cascade and dsDNA were incubated at 37 °C for 30 min in 20 mM Tris, pH 7.5, 150 mM NaCl and 5% glycerol. EMSA was carried out at 4 °C on 2% agarose gels. Fluorescent signals were scanned using a Typhoon 9200 scanner. The EMSA gels shown in the main and Extended Data figures are representative results, out of triplicated experiments. The raw, uncropped source data can be found in Supplementary Fig. 1.

Cascade-mediated Cas3 DNA cleavage assay. Cascade-R-loops were pre-formed by mixing 40 nM Cascade or Cascade mutants with 6 nM fluorescent dsDNA target in binding buffer (5 mM HEPES, pH 7.5 and 60 mM KCl) at 37 °C for 30 min. Cascade-R-loops were then mixed with 500 nM SUMO-Cas3 in DNA cleavage RXN buffer (5 mM HEPES, pH 7.5, 60 mM KCl, 10 mM $MgCl_2$ and 10 μM $CoCl_2$). Either 2 mM ATP or 2 mM AMPPNP was added and the reaction was incubated at 37 °C for 30 min. Cy5 and 6-FAM fluorescent signals were recorded by Typhoon 9200 scanner. The wild-type *E. coli* Cascade specifically nicked the non-target DNA strand ~10–12 nucleotides into the R-loop region in the presence of a non-hydrolysable ATP analogue, AMPPNP. Addition of ATP triggered processive degradation of the non-target DNA strand and distributive degradation of the target strand upstream of the R-loop. These results are consistent with previous studies[11,21]. Uncropped gels are shown in Supplementary Fig. 1.

31. Otwinowski, Z. & Minor, W. Processing of X-ray diffraction data collected in oscillation mode. *Methods Enzymol.* **276,** 307–326 (1997).
32. Emsley, P. & Cowtan, K. Coot: model-building tools for molecular graphics. *Acta Crystallogr. D* **60,** 2126–2132 (2004).
33. Adams, P. D. *et al.* PHENIX: a comprehensive Python-based system for macromolecular structure solution. *Acta Crystallogr. D* **66,** 213–221 (2010).
34. Collaborative Computational Project, Number 4. The *CCP4* suite: programs for protein crystallography. *Acta Crystallogr. D* **50,** 760–763 (1994).

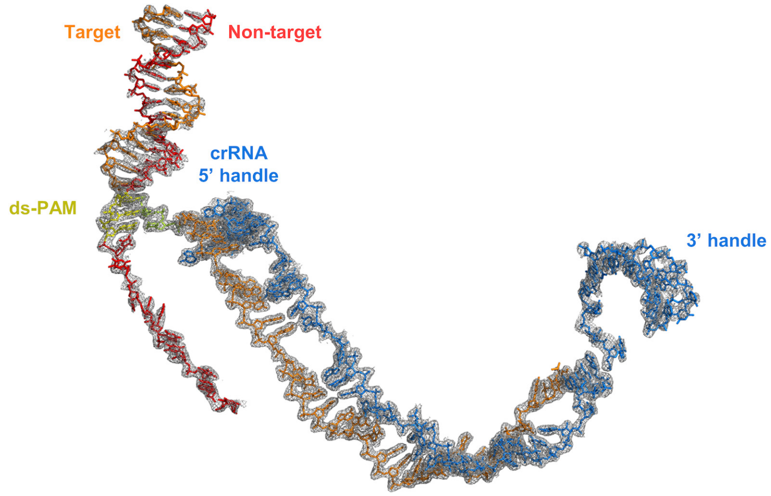

Extended Data Figure 1 | Electron density of nucleic acids in Cascade–dsDNA complex structure. $2F_o - F_c$ electron density map (1.0σ). Nucleic acid strands are shown as sticks and coloured as previously indicated.

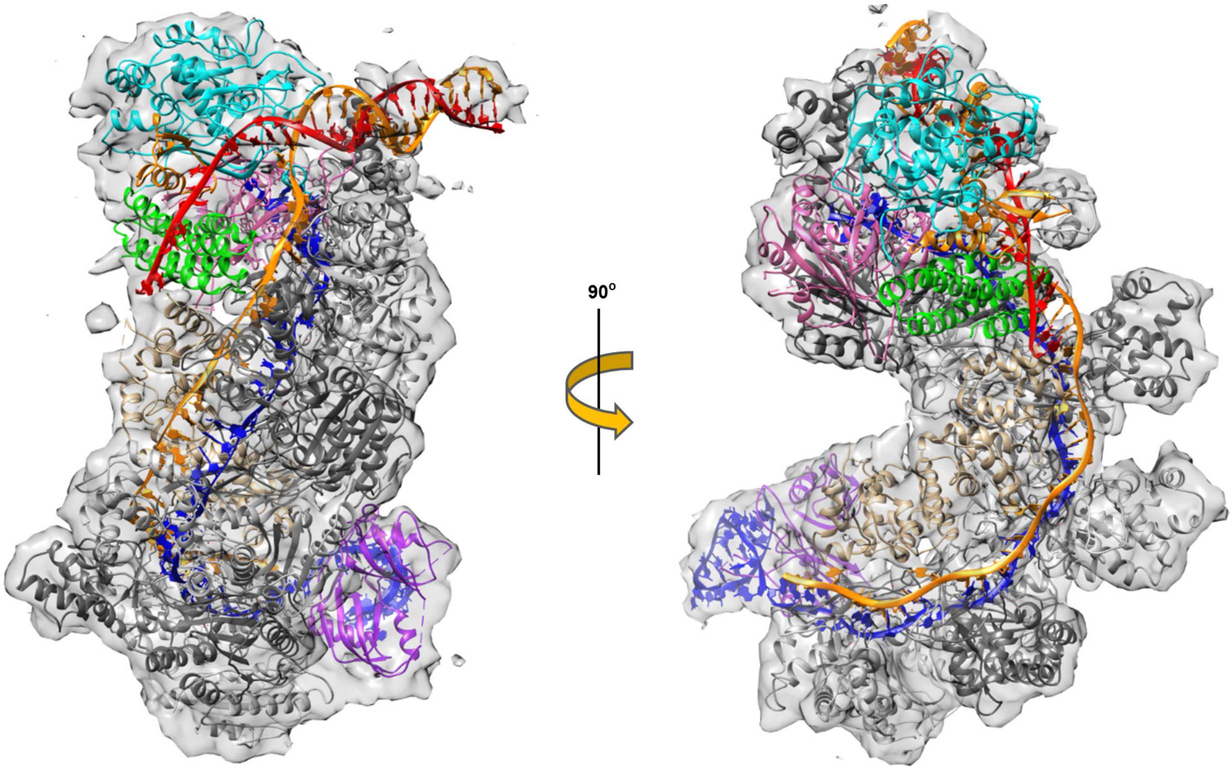

Extended Data Figure 2 | Comparison between the Cascade–partial-R-loop crystal structure and the Cascade–full-R-loop EM reconstruction. Rigid body docking of the partial-R-loop–Cascade crystal structure into the EM reconstruction (EMD-5929) of the full R-loop–Cascade illustrates a similar overall conformation, with a correlation value of 0.83.

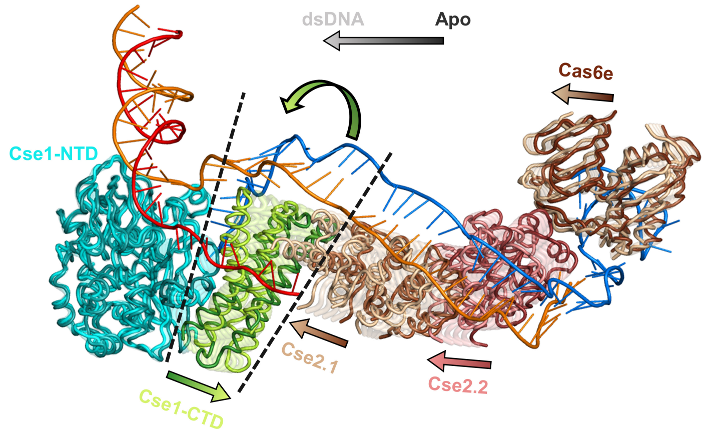

Extended Data Figure 3 | Conformational changes in Cascade upon partial R-loop formation. Comparison of free (PDB 4TVX; in a darker shade) and partial R-loop-bound (this study, in lighter shade) Cascade. Arrows indicate the direction of the movement. The CTD of Cse1 pivots 30° about a hinge at the Cse1 NTD–CTD interface. The amplified motion at the tip of the Cse1-CTD slides with the Cse2 dimer ∼12 Å relative to the Cas7 scaffold, and protrudes upwards into the R-loop. Cse1-NTD remains in the docked position, stabilized by the clamping of Cse1 L1 loop onto the exposed tri-nucleotide motif on crRNA 5′-handle.

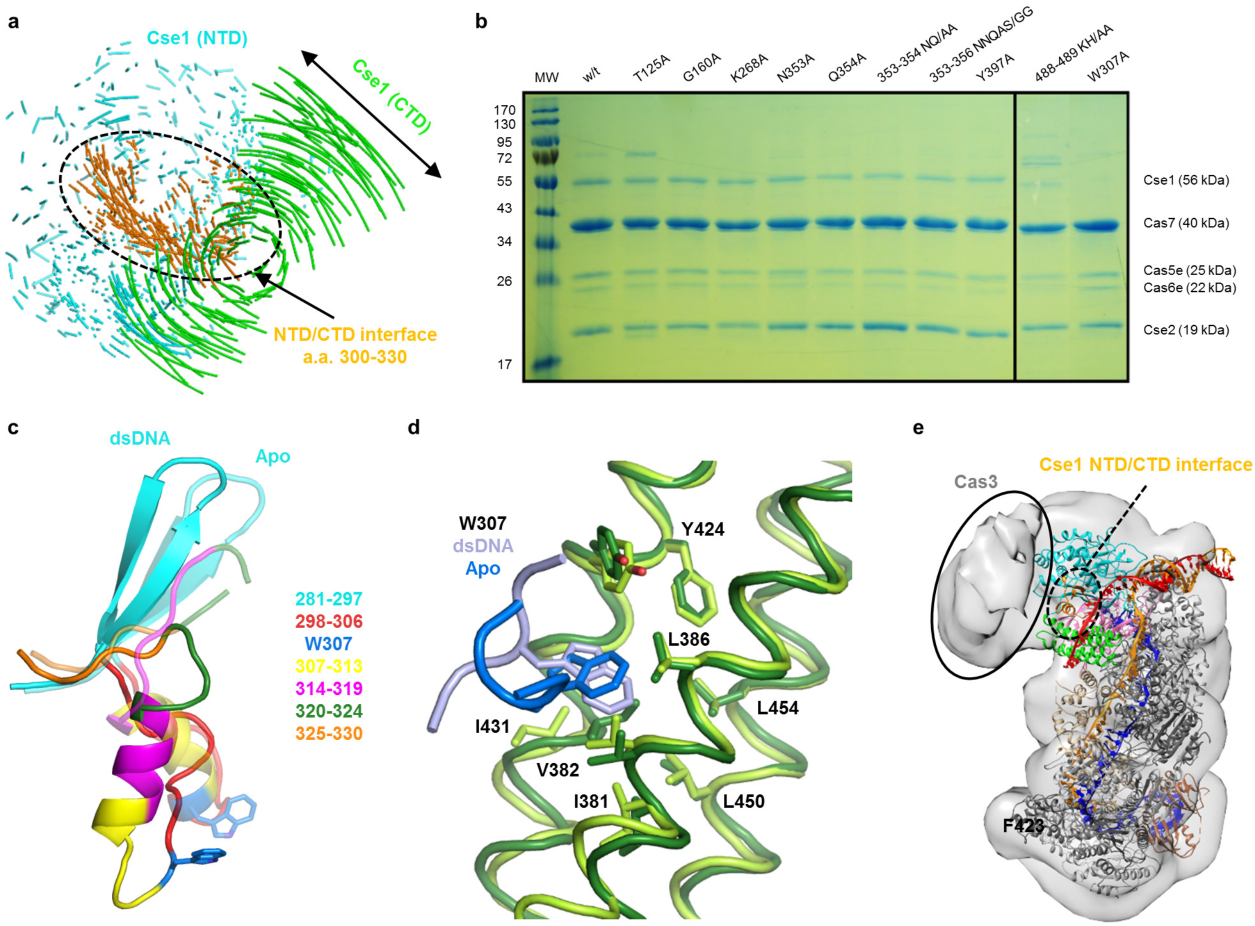

Extended Data Figure 4 | Local conformational rearrangement in Cse1 at the proposed Cas3-binding site. a, Vector map showing global and local conformational changes in Cse1. Cse1-NTD (in cyan) undergoes moderate movement. Cse1-CTD (in green) swings about a pivoting point (Trp307) as part of the global conformational changes, The Cse1 NTD–CTD interface (in orange) undergoes considerable local conformational rearrangement upon partial R-loop formation. **b**, SDS–PAGE of wild-type and mutant Cascades used in mutagenesis. All mutants contained stoichiometric amounts of Cse1, except Trp307Ala, in which Cse1 failed to assemble. Uncropped gels are shown in Supplementary Fig. 1. **c**, Detailed structure rearrangement at Cse1 NTD–CTD interface, involving amino acids 300–326. Different colours are used to differentiate structural elements (amino acid numbers tabulated to the right). Partial R-loop-bound and free Cascade structures are rendered in solid and semi-transparent cartoons, respectively. **d**, Trp307 from Cse1-NTD rotates inside a hydrophobic socket at Cse1-CTD during the conformational change (free-Cascade-CTD rendered in a darker shade of green). Disruption of this interaction (Trp307Ala) caused Cse1 dissociation from Cascade. **e**, Docking of our structure into the cryoEM reconstruction of the crosslinked Cascade–dsDNA–Cas3 complex (EMD-5930). Cas3 density and the location of the local rearrangement in Cse1 are circled to highlight their proximity.

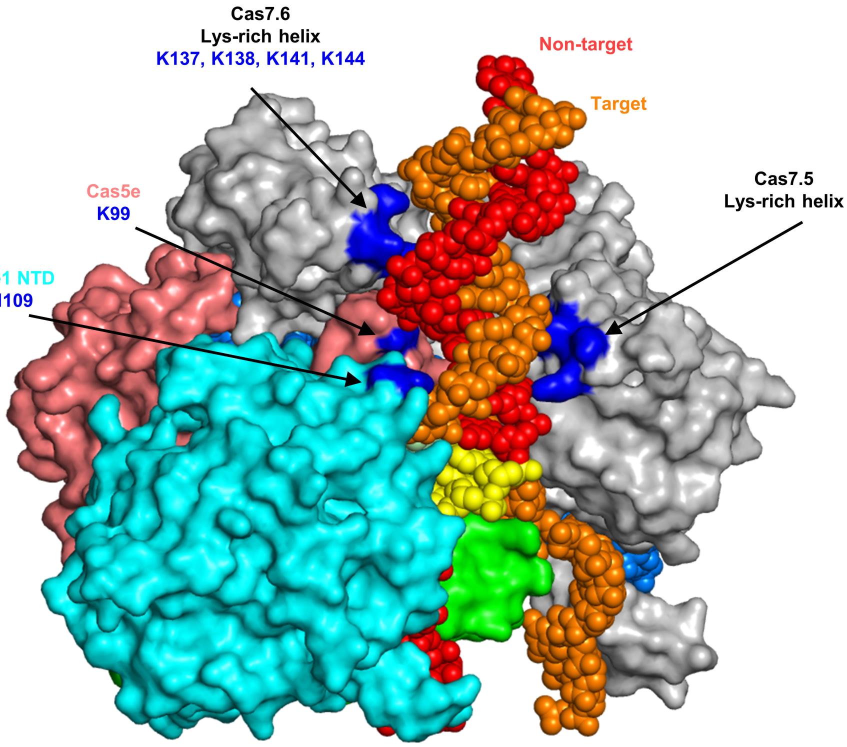

Extended Data Figure 5 | Guided entry of dsDNA into Cascade. A series of positively charged residues from Cas7.5, Cas7.6, Cas5e and Cse1 (dark blue surfaces) guide the dsDNA into Cascade and towards PAM recognition elements in Cse1-NTD.

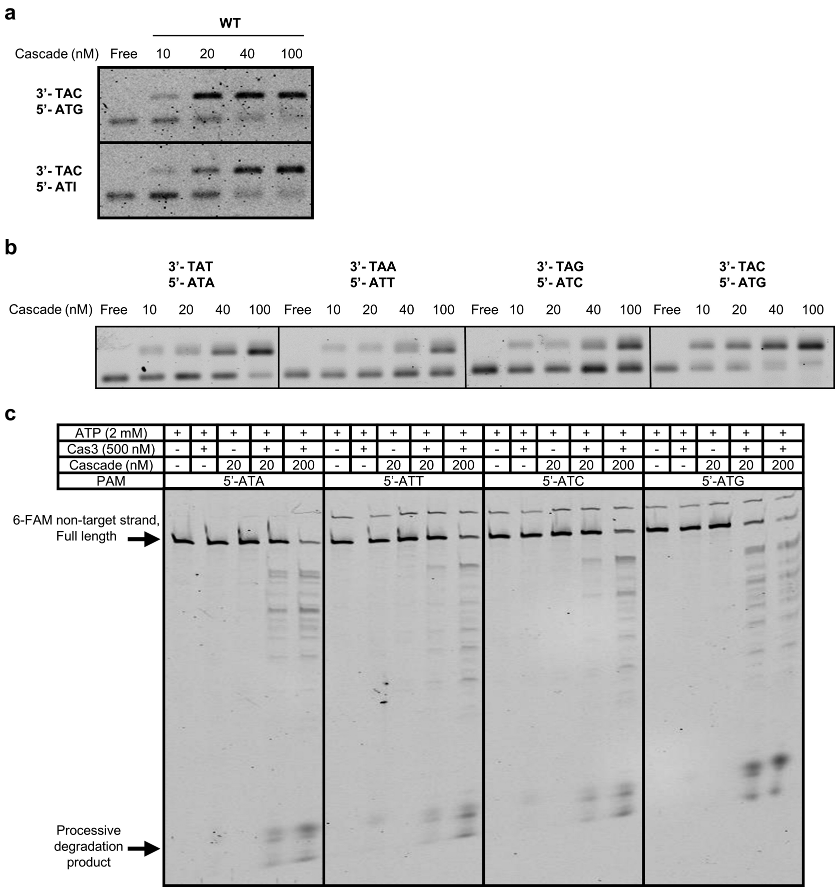

Extended Data Figure 6 | Influence of PAM−1 base-pair composition on Cascade binding affinity and Cas3 cleavage efficiency. a, Inosine substitution of G_{NT-1} led to a mild twofold binding defect, suggesting that the N2 amine of G_{NT-1} is a minor determinant of specificity. **b**, Binding K_d values of *E. coli* Cascade for all four base-pair combinations at PAM−1. K_d values for 5′-ATG, ATA, ATC and ATT PAMs were determined to be ~10, 20, 40 and 100 nM, respectively. **c**, Cas3 cleavage efficiency was governed by the Cascade affinity for the corresponding PAM-containing target (5′-ATG > ATA >> ATT ≈ ATC). Cascade concentration above the K_d led to efficient Cas3 cleavage. Experiments were done in triplicate and representative results are shown. Uncropped gels are shown in Supplementary Fig. 1.

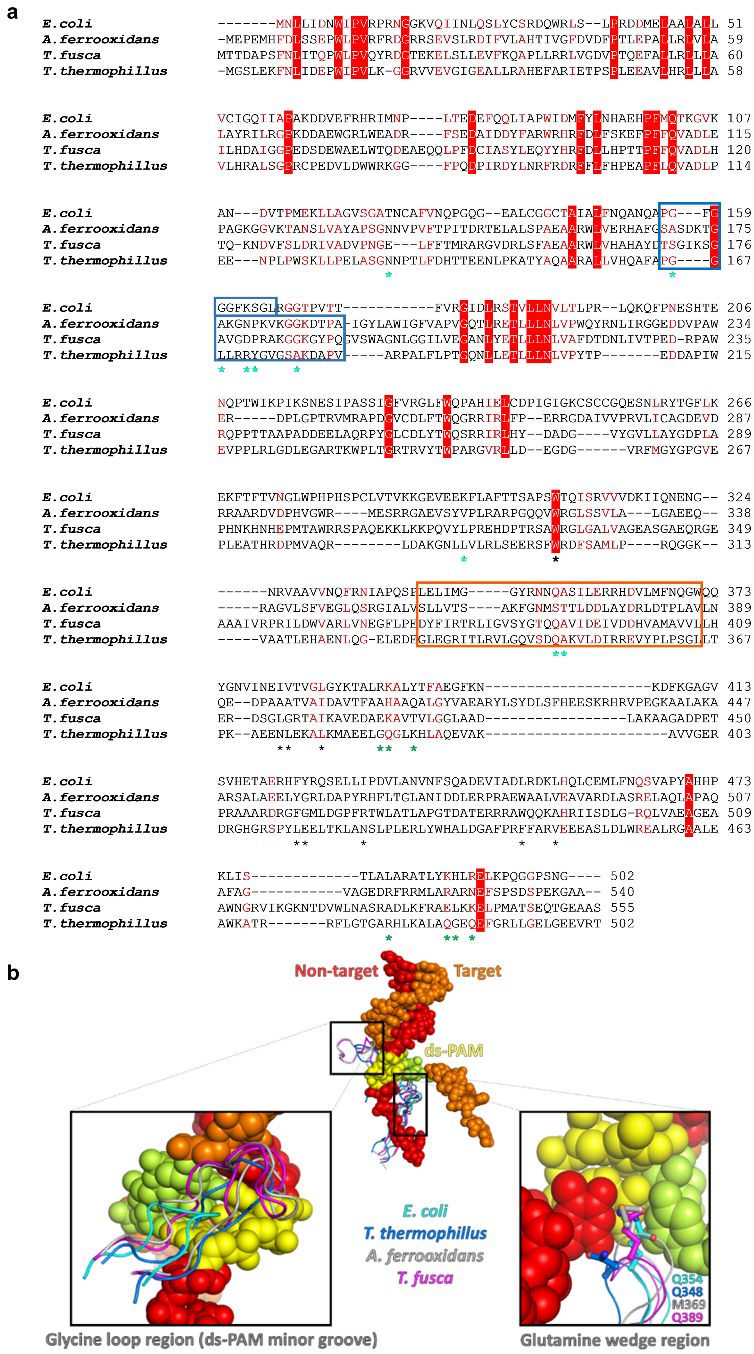

Extended Data Figure 7 | Conservation of PAM recognition elements. **a**, Sequence alignment of Cse1 proteins with known structures. Identical residues are highlighted in red, conserved residues in red text. DNA-contacting residues in the Cse1-NTD and -CTD are marked by cyan and green asterisks, respectively. The glycine loop and glutamine wedge are in blue and orange boxes, respectively. Residues mediating the Trp307 ball-and-socket interaction are marked with black asterisks. **b**, Structural alignment of Cse1 PAM recognition elements. Apo Cse1 from *T. Thermus thermophilus* (PDB 4AN8), *Acidithiobacillus ferrooxidans* (PDB 4H3T) and *T. fusca* (PDB 3WVO) were superimposed with the Cse1 in our partial R-loop-forming *E. coli* Cascade structure. Despite sequence variation, a glycine-rich loop is present in each Cse1 structure, and probably has a similar function to recognize PAM from the minor groove (left inset). The glutamine-wedge protrusion is highly conserved in 3D. Each wedge features a long side chain at the tip (right inset), which probably stacks underneath PAM in a similar fashion.

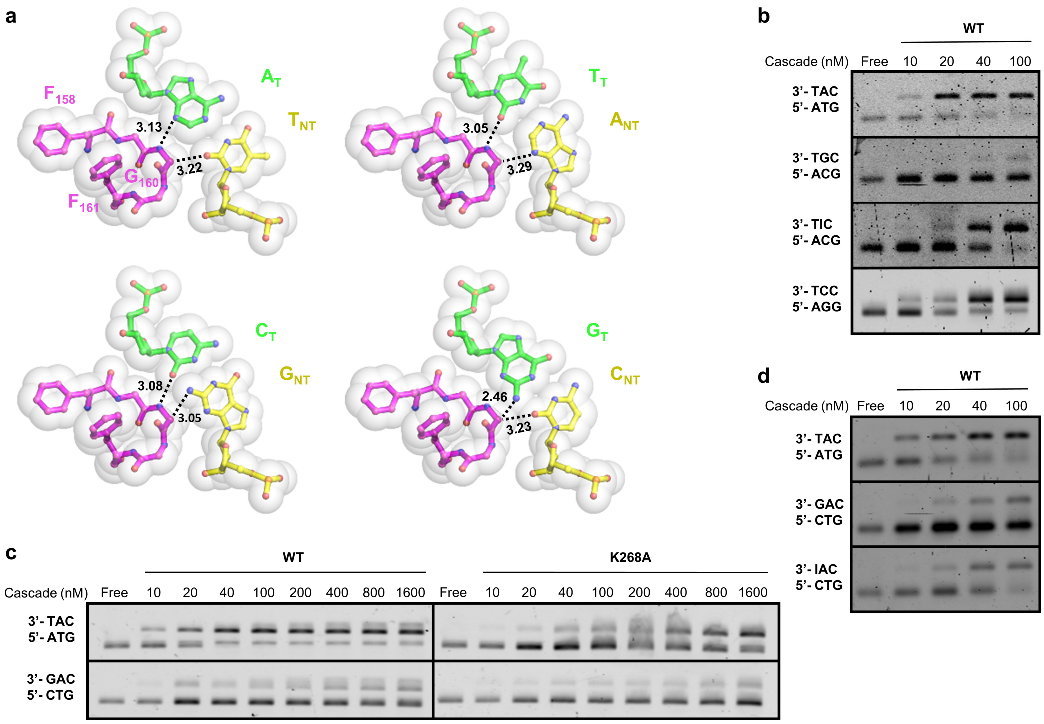

Extended Data Figure 8 | Rationalization of PAM−2 and PAM−3 specificity using nucleotide substitution and modelling. a, Modelling of alternative base pairs at PAM−2 suggests that only the N2 amine of G_{T-2} would cause steric clashes with C_α of Gly160 (bottom right quadrant), this amine therefore may serve as the anti-determinant for the rejection of G_T–C_{NT} at PAM−2. **b**, EMSAs demonstrating that removal of this amine in inosine substitution rescued the Cascade binding defect. **c**, Whereas Lys268Ala contained reduced affinity for the correct PAM, it still possessed strong discrimination against G_T–C_{NT} at PAM−3 (5′-CTG), suggesting the further presence of a mechanism to reject G_{T-3}. **d**, Inosine substitution of G_{T-3} restored the Cascade binding K_d to ~40 nM, leading to the conclusion that the N2 amine of G_{T-3} is a minor determinant of specificity. Experiments were done in triplicate and representative results are shown. Uncropped gels are shown in Supplementary Fig. 1.

Extended Data Table 1 | Oligonucleotides used in this study

Oligonucleotide	Sequence (5'-3')	Notes
Cse1 (forward)	GCGCGCCATGGCTAATTTGCTTATTGATAACTGGATCC	NcoI + Cse1 fragment (pRSF-Duet ORF1)
Cse1 (reverse)	GGCCCGCGGCCGCTCAGCCATTTGATGGCCCTCC	Cse1 fragment +NotI (pRSF-Duet ORF1)
Cse2-Cas7-Cas5e-Cas6e (forward)	GCGCGGGTACCAGATGGCTGATGAAATTGATGCA	KpnI + Cse2-Cas7-Cas5e-Cas6e fragment (pET52b)
Cse2-Cas7-Cas5e-Cas6e (reverse)	CGCGCGCGGCCGCTCACAGTGGAGCCAAAGATAG	Cse2-Cas7-Cas5e-Cas6e fragment + NotI (pET-52b)
Cse2-Cas7-Cas5e-Cas6e (forward)	GCGCGCCATGGGTCATCACCACCATCATCACGGTGCACTTGAAGTCCTCTTTC	NcoI + 6XHIS + Precission (pET-52b)
R-loop mimic (target strand)	CTGTTGGCAAGCCAGGATCTGAACAATACCGTCATCGAGCACTGCACAGA	
R-loop mimic (non-target strand)	TCTGTGCAGTGCTCGATGTTTTATTTAT	
SUMO-Cas3 (forward)	GCGCCGCGGATCCATGGAACCTTTTAAATATATATGCCAT	BamHI + Cas3 fragment (pET28b-SUMO vector)
SUMO-Cas3 (reverse)	GCGCCGCCTCGAGTTATTTGGGATTTGCAGGGAT	Cas3 fragment + XhoI (pET28b-SUMO vector)
Target plasmid construction (non-target strand)	CATGGATGACGGTATTGTTCAGATCCTGGCTTGCCAACAGCTGCA	NcoI overhang + Target sequence + PstI overhang (pCDF-Duet1) PAM altered as indicated in text
Target plasmid construction (target strand)	GCTGTTGGCAAGCCAGGATCTGAACAATACCGTCATC	PstI + non-target sequence + NcoI (pCDF-Duet1) PAM altered as indicated in text.
dsDNA1 Fluorescent ATG PAM substrate (forward)	AACTTTAATAAGGAGATATACCATGGATG	5'- 6-FAM label, PCR product used in main text EMSA and Cas3 cleavage assays.
dsDNA1 Fluorescent ATG PAM substrate (reverse)	GCGGCCGCAAGCTTGTC	5'- Cy5 label, PCR product used in main text EMSA and Cas3 cleavage assays.
dsDNA2 Fluorescent substrate (forward)	TAATACGACTCACTATAGGG	T7 Forward 5'-6-FAM label. Used with dsDNA1 (reverse) primer to amplify set of 5'-ATA, ATT, ATC, ATG, AGG and CTG PAM substrates from target plasmids.
dsDNA3 (non-target strand)	AGATATACATGGATGACGGTATTGTTCAGATCCTGGCTTGCCAACAGCTGCAGGTCGACA	5' 6-FAM or HEX label, PAM altered (base mutation or inosine substitution) as indicated in text.
dsDNA3 (target strand)	TGTCGACCTGCAGCTGTTGGCAAGCCAGGATCTGAACAATACCGTCATCCATGTATATCT	PAM altered (base mutation or inosine substitution) as indicated in text.
crRNA expression cassette	GCGCCGGGAATTCCCTGCATTAGGTAATACGACTCACTATAGGGAGTTCCCCGCGCCAGCGGGGATAAACC GACGGTATTGTTCAGATCCTGGCTTGCCAACAGGAGTTCCCCGCGCCAGCGGGGATAAACCGACGGTATTG TTCAGATCCTGGCTTGCCAACAGGAGTTCCCCGCGCCAGCGGGGATAAACCGACGGTATTGTTCAGATCCTG GCTTGCCAACAGGAGTTCCCCGCGCCAGCGGGGATAAACCGACGGTATTGTTCAGATCCTGGCTTGCCAAC AGGAGTTCCCCGCGCCAGCGGGGATAAACCGACGGTATTGTTCAGATCCTGGCTTGCCAACAGGAGTTCCC CGCGCCAGCGGGGATAAACCGACGGTATTGTTCAGATCCTGGCTTGCCAACAGGAGTTCCCCGCGCCAGCG GGGATTTTGCCCTAGCATAACCCCTTGGGGCCTCTAAACGGGTCTTGAGGGGTTTTTTGGACCGGATCCCCG	The crRNA expression cassette containing six identical repeat-spacer units was de novo synthesized and inserted to the pHSG-398 vector. The T7 promoter, T7 terminator, and the repeats are highlighted green, red, and yellow, respectively.

Extended Data Table 2 | Data collection and refinement statistics

	Cascade-dsDNA	Cascade-dsDNA (32-nt non-target spacer)
Data collection		
Space group	P 2 2_1 2_1	P 2 2_1 2_1
Cell dimensions		
a, b, c (Å)	92.98, 150.06, 400.55	92.81, 149.83, 404.10
α, β, γ (°)	90, 90, 90	90, 90, 90
Resolution (Å)	50.0-2.45 (2.49-2.45)	50.0-3.20 (3.26-3.21)*
R_{merge}	0.169 (1.288)	0.265 (1.066)
R_{pim}	0.050 (0.531)	0.143 (0.667)
$I / \sigma I$	12.9 (1.1)	5.8 (1.5)
Completeness (%)	99.7 (97.2)	96.8 (84.1)
Redundancy	12.1 (6.5)	3.6 (3.0)
CC(1/2)	0.997 (0.496)	0.967 (0.422)
Refinement		
Resolution (Å)	50.0-2.45	50.0-3.21
No. reflections	205,381	90,215
R_{work} / R_{free}	0.2058 / 0.2327	0.2087 / 0.2470
No. atoms		
Macromolecule	27896	27237
Ligand/ion	1 (Zn)	1 (Zn)
Water	1051	0
B-factors		
Macromolecule	53.60	62.10
Ligand/ion	51.90	61.50
Water	45.90	N/A
R.m.s. deviations		
Bond lengths (Å)	0.013	0.018
Bond angles (°)	0.840	1.010

*One crystal was used for each structure.
*Values in parentheses are for highest-resolution shell.

CORRECTIONS & AMENDMENTS

CORRIGENDUM

doi:10.1038/nature16074

Corrigendum: NLRP10 is a NOD-like receptor essential to initiate adaptive immunity by dendritic cells

Stephanie C. Eisenbarth, Adam Williams, Oscar R. Colegio, Hailong Meng, Till Strowig, Anthony Rongvaux, Jorge Henao-Mejia, Christoph A. Thaiss, Sophie Joly, David G. Gonzalez, Lan Xu, Lauren A. Zenewicz, Ann M. Haberman, Eran Elinav, Steven H. Kleinstein, Fayyaz S. Sutterwala & Richard A. Flavell

Nature **484,** 510–513 (2012); doi:10.1038/nature11012

In this Letter, we reported that NLRP10-deficient mice had no defect in inflammasome function in macrophages or dendritic cells (DCs). Instead, a loss of T-cell-dependent immune responses was seen in these mice secondary to a defect in DC migration. We have since noticed a change in the phenotype of the NLRP10-knockout mice involving DC migration, after backcrossing them onto backgrounds such as FVB or BALB/c (see Supplementary Methods). We used whole-exome sequencing of these mice to determine whether loss of a different gene accounted for the observed phenotype. Six homozygous mutations/indels were found (sequence deposited in NCBI Sequence Read Archive under accession SRR1792904); one was a homozygous point mutation in the *Dock8* gene (Fig. 1a). DOCK8 is a guanine nucleotide exchange factor that has been shown to regulate the GTPase CDC42 in mouse DCs, and biallelic mutations in humans cause a severe immunodeficiency syndrome (OMIM 611432)[1,2]. This point mutation results in a premature stop codon in the second to last exon, and we believe results in nonsense-mediated decay of *Dock8* messenger RNA (Fig. 1b). *Dock8* mRNA is significantly reduced in DCs from the original *Nlrp10*$^{-/-}$ strain, but is restored when the mice are bred onto other wild-type backgrounds (Fig. 1c). The Bruce4 embryonic stem cells used to generate the NLRP10-deficient mice do not contain the mutation after sequencing (see Fig. 1a for primers and nucleotide change). It may have arisen spontaneously as a natural mutation early during the intercrossing of the knockout mice, and became fixed in our colony before the original phenotype analysis. From a previous proteomic screen, we identified DOCK8 as a candidate molecule involved in the loss of coordinated DC movement[3]. We tested whether this point mutation accounted for the loss of DC migration *in vivo* and adaptive immune responses. When mice were bred to isolate the NLRP10 deficiency, we found that DC migration was independent of NLRP10 (Fig. 1d). However, some aspects of the phenotype originally reported were maintained. For example, isolated NLRP10 loss does not result in enhanced NLRP3 inflammasome activation[3]. In addition, aberrant *Gdpd3* upregulation was due to *Nlrp10* loss and was not affected by the *Dock8* gene[3]. Notably, spontaneous *Dock* gene loss of function has been reported in many unrelated knockout mouse strains. For example, *Dock2* loss was recently reported in ASC-knockout mice[4,5]. In addition, *Dock2* mutations have been found in a subset of IRF5-deficient strains[6]. These separate instances suggest that the *Dock* gene family is prone to mutation, whether because of the large size (average of 275 kb across the 11 family members) or something more specific to these genes themselves, and that these mutations are readily discovered owing to the induction of a profound phenotype. Regardless of the aetiology of the mutations, these cases highlight the need for continual evaluation of genetic stability of inbred mouse strains, especially those expanded by sibling matings, as is common practice in many animal facilities. In addition, to limit accumulation of mutations in inbred strains as seen in our mice from the exome sequencing, periodically obtaining new breeding stock from founder lines or cryopreserved embryos from early generations has been recommended[7]. The original mouse phenotype reported in our Letter is correct and highly reproducible, but the conclusions must be reinterpreted in light of this new finding. We conclude that (1) DC migration is dependent on DOCK8 and not NLRP10; (2) NLRP10 deficiency is associated with aberrantly upregulated GDPD3; and (3) NLRP10 deletion does not alter NLRP3 inflammasome activity. We regret any confusion that this may have caused.

1. Zhang, Q. *et al.* Combined immunodeficiency associated with DOCK8 mutations. *N. Engl. J. Med.* **361,** 2046–2055 (2009).
2. Harada, Y. *et al.* DOCK8 is a Cdc42 activator critical for interstitial dendritic cell migration during immune responses. *Blood* **119,** 4451–4461 (2012).
3. Krishnaswamy, J. K. *et al.* Coincidental loss of DOCK8 function in NLRP10-deficient and C3H/HeJ mice results in defective dendritic cell migration. *Proc. Natl Acad. Sci. USA* **112,** 3056–3061 (2015).
4. Ippagunta, S. K. *et al.* Addendum: defective Dock2 expression in a subset of ASC-deficient mouse lines. *Nature Immunol.* **13,** 701–702 (2012).
5. Ippagunta, S. K. *et al.* The inflammasome adaptor ASC regulates the function of adaptive immune cells by controlling Dock2-mediated Rac activation and actin polymerization. *Nature Immunol.* **12,** 1010–1016 (2011).
6. Purtha, W. E., Swiecki, M., Colonna, M., Diamond, M. S. & Bhattacharya, D. Spontaneous mutation of the *Dock2* gene in *Irf5*$^{-/-}$ mice complicates interpretation of type I interferon production and antibody responses. *Proc. Natl Acad. Sci. USA* **109,** E898–E904 (2012).
7. Taft, R. A., Davisson, M. & Wiles, M. V. Know thy mouse. *Trends Genet.* **22,** 649–653 (2006).

Supplementary Information is available in the online version of the Corrigendum.

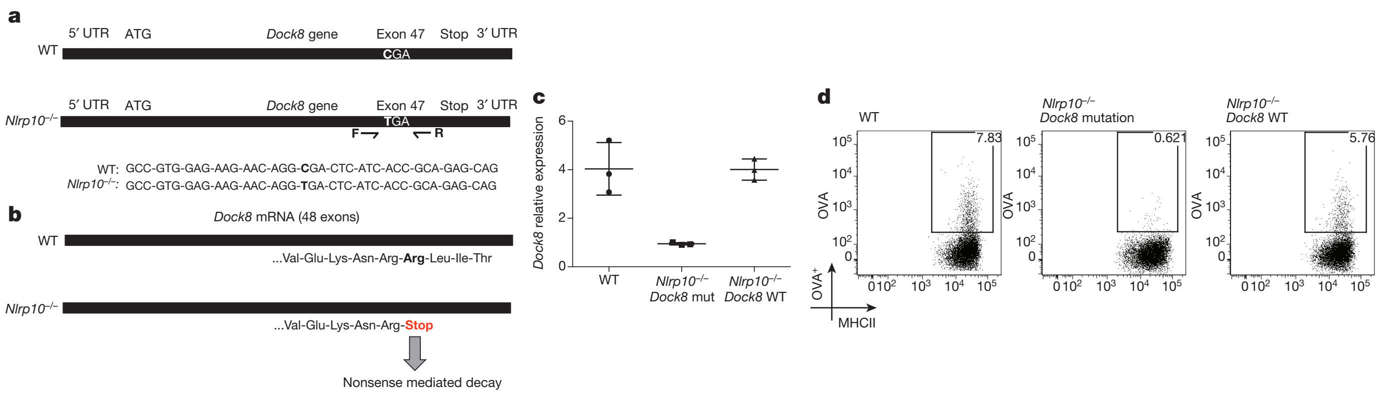

Figure 1 | NLRP10-deficient mice contain a *Dock8* point mutation resulting in failed DC migration. a, *Dock8* gene structure, highlighting homozygous point mutation in exon 47 in NLRP10-knockout mice. **b**, Resulting coding changes in DOCK8 induced by point mutation in **a**. **c**, Unstimulated bone-marrow-derived DCs from the original NLRP10-deficient mice with a *Dock8* mutation had significantly reduced *Dock8* mRNA. When the *Dock8* mutation was corrected through breeding, DCs from NLRP10-deficient mice showed no alteration in *Dock8* mRNA (relative to *Hprt*). **d**, *In vivo* DC migration to inguinal lymph nodes (see Supplementary Methods).

POLAR SCIENCE Antarctic expeditions, and the women who lead them **p.507**

JOB INTERVIEWS How to learn from past mistakes **go.nature.com/icl6ft**

NATUREJOBS For the latest career listings and advice **www.naturejobs.com**

PW ILLUSTRATION/GETTY

ACTIVISM

Frustrated postdocs rise up

US postdoctoral researchers struggle with pay and career prospects. But some groups are fighting back.

BY PAUL SMAGLIK

The tribulations of US postdoctoral researchers — low stipends, spotty benefits, uneven training and hazy career prospects — have received plenty of airtime in the past few years. But efforts to combat these woes have been achingly slow. Frustrated that recommendations by universities, policymakers and other stakeholders are not quickly bearing fruit, grass-roots and advocacy groups are trying to address some of the problems on their own.

High-level reports have noted the problems for more than a decade. The US National Academy of Sciences (NAS) outlined the hardships faced by science and engineering postdocs in 2000, and its 2014 follow-up report noted that the issues persist and have begun to bleed into other disciplines. A study in the *Proceedings of the National Academy of Sciences* (*PNAS*) that same year found that the US research enterprise prepares most of its postdocs and graduate students for tenure-track positions that only 20% of them are likely to secure (B. Alberts *et al. Proc. Natl Acad. Sci. USA* **111,** 5773–5777; 2014). The reports have called for measures such as higher stipends, set training periods and broader career training.

"There's a frustration with constantly talking about it and constantly writing about it," says Gary McDowell, a developmental-biology postdoc at Tufts University in Boston, Massachusetts, and a member of Future of Research (FOR), a Boston-based group that is working to improve postdoc pay and benefits. Other organizations are fighting their own battles. A postdoc group at Stanford University in California helped to push for higher stipends there. Another group at the University of California, San Francisco (UCSF), expanded an internship programme to allow postdocs in addition to graduate students. And a New York University (NYU) group launched an effort to battle isolation among its postdocs, who are scattered throughout the metropolitan region, and provide them with professional networking and collaboration opportunities.

Postdocs stand to gain much by becoming active in such local and regional organized groups — including developing skills that may help with their career (see 'Activism pays off'). Change can happen much more quickly at local levels. And postdocs don't have to wait for a national level, universal solution that may never materialize. "I feel that there's a lot more hope," says McDowell.

Money, for many postdocs, is the number-one issue. The Stanford University Postdoctoral Association (SURPAS) has already made independent strides in this arena. Last year, it negotiated for higher stipends and, in October, it won a minimum level of US$50,000 a year for all 2,000 Stanford postdocs, regardless of their funding source, and a higher rate for those with more than 3 years in the position. That rate is 17% higher than the US National Research Service Awards minimum of $42,840.

SURPAS has also helped Stanford postdocs to defray their commuting expenses. Faculty members and staff have historically received free rail commuter passes, but Stanford postdocs had not been entitled to that benefit. In 2012 and 2013 polls, SURPAS found that many were upset about commuting outlays. With support from faculty and staff allies, it secured a pilot programme in 2014 to extend the free rail pass to postdocs: Stanford postdocs previously spent up to $2,100 a year on train commutes; now they spend $190. Stanford administrative offices are evaluating the pilot programme for renewal this year.

Other organizations focus on training that prepares postdocs for jobs beyond academia, because reports continue to document the dearth of jobs in the sector. Postdocs need time away from the bench to learn career-related skills, but they often can't get it, even when their host universities offer such programmes for graduate students. Such was the case at UCSF, where postdocs had been ineligible for career-exploration internships. P-Value, a UCSF-based postdoc-advocacy group that formed in 2014, changed that.

After a forum last March to discuss career training, members united to request that UCSF support short, flexible internships for postdocs in fields such as intellectual property and technology transfer. The university administration agreed to sponsor campus-based internships and created a pilot that launched last September and has drawn half a dozen participants so far. One of them, Jessica Lao, teaches a biochemistry class at San Francisco State University under the programme. A postdoc at UCSF's medical school, she decided to explore a career in teaching and wanted classroom experience. The course requires up to six hours a week of lecture and office time, and more for preparation, but her lab head has been supportive of her need for time away from the bench, she says. "He understands that it's essential."

Katherine Thompson-Peer, co-chair of P-Value, attributes the success of the pilot to building it on an existing scheme, rather than trying to create a new one. She is optimistic that UCSF will formalize the programme when the pilot period ends.

These regional efforts are spreading nationally as local organizations seek to link with and support their counterparts elsewhere. SURPAS has created a postdoc advocacy plan for adaptation by other groups. FOR has extended into New York and Chicago, Illinois. Along with providing mutual advocacy, this expansion can also boost potential research connections. FOR New York's regular meetings and other events, for example, have helped members from different disciplines to form bonds and identify common research interests. The group organized and presented an interdisciplinary research symposium last year that included sessions on career issues and research policy. "This is quite an achievement," says FOR member Rodoniki Athanasiadou. "Historically, postdocs in different departments at NYU have not interacted scientifically."

Postdoc-advocacy groups have also triumphed together in another battle. The paucity of concrete data about employment trends for post-postdocs has plagued trainees for decades and stymies their career-planning efforts. Some groups are gathering their own data by tracking alumni.

At a national level, postdoc groups have been pressuring the US National Science Foundation to collect these data. Those efforts led last year to the creation of a website by the authors of the *PNAS* and NAS reports that aims to collect and organize such data. The web page also hosts suggestions to improve postdocs' training and funding, among other issues. Jessica Polka, a postdoc at Harvard Medical School in Boston, Massachusetts, says that the site provides a 'bottom-up' way for groups such as FOR to directly address top biomedical policymakers. She is a member of FOR Boston and of the site's steering committee.

Thompson-Peer, for one, says that she is delighted to have the opportunity to contribute to the national dialogue. The voices of postdoc organizations are growing stronger, she says, and postdocs have far more leverage as members of a collective group than they do individually. "We cannot make these structural changes on our own," she says. ■

Paul Smaglik *is a freelance writer in Milwaukee, Wisconsin.*

ACTIVISM PAYS OFF

Postdocs who help colleagues also help themselves

Postdocs are drawn to grass-roots activism to create better training conditions for themselves and their peers. In doing so, they can pick up and polish skills such as negotiation, time management, communication and leadership that aid their own career development.

Amita Bansal, a postdoc at the University of Pennsylvania in Philadelphia and member of the Penn Biomedical Postdoctoral Council, learned all of those skills when she developed a programme to help foreign national postdocs integrate into the Penn postdoc community. To get ideas for events, she reached out to fellow postdocs who were foreign nationals. And she had to negotiate with university leadership to get approval for the programme, which, she says, can draw up to 100 attendees depending on the type of session or topic. "I've learned how academic structure and administrative hierarchy work," she says.

The planning aspect of the programme — inviting and setting up speakers, arranging sponsorship and securing venues — has forced her to hone her organizational skills. Although sessions take place after working hours, she sets aside an hour or so daily for tasks that must be done during the daytime and spends time in the evening and on weekends on others, such as e-mails and text messages.

"Time management is extremely crucial," she says.

That same skill has also played a major role in Rodoniki Athanasiadou's advocacy efforts. The New York University postdoc formed a regional branch of the postdoc corps Future of Research (FOR) and co-organized and presented a day-long seminar for the branch last year. Like Bansal, she has learned to fit in e-mails and phone calls around her benchwork.

Advocacy efforts can teach postdocs to tailor their message. Jessica Polka, a postdoc at Harvard Medical School in Boston, Massachusetts, is active in the Boston-area FOR group and is a member of a national-level steering committee that is gathering information on postdoc problems and employment. In these roles she works with university administration, heads and members of postdoc organizations and national policy leaders, and has learned to adapt her messages to appeal to each. "Speaking about topics other than science has helped me communicate more effectively," Polka says.

Jessica Polka leads a FOR meeting in Boston.

LIPOFSKY.COM

J. T. Neal, a postdoc at Stanford University School of Medicine in California and a member of the Stanford University Postdoctoral Association, has noticed a similar benefit from his work to negotiate postdoc stipends with the university.

"The whole process taught me about identifying each party's points of conflict and working collaboratively to address them," he says. "And I learned to be patient, as the pace of change in institutions of higher learning can be glacial."

For both Polka and her fellow FOR member Gerry McDowell, a postdoc at Tufts University in Boston, their advocacy efforts have also opened potential career paths beyond research. "I am now more aware of the super-important work in policy and communications," Polka says. "I would be very happy in either of these areas." P.S.

COLUMN

Changes on the ice

Diverse faces are appearing on a frozen continent, says **Robin Bell**.

KEVIN EMERY

Geologist Christine Siddoway maps faults in Marie Byrd Land, West Antarctica.

To measure gravity from the sky, you need a calm day and a steady aircraft. Often, the instruments involved do not need much tending to, even when flying at low altitude over the frozen Weddell Sea off the Antarctic Peninsula. As a graduate student in 1986, I was lucky: my experiments mostly worked well. In moments of peace, I could sneak to a window in the aircraft's belly.

As my equipment collected data that would reveal the hidden sea bed, I would spend hours watching the sea below. My fellow scientists and I were far from any place that a wheeled US Navy P-3 Orion aircraft could safely land. The polar ice, floating and flowing, was beautiful. Leopard seals looked like slugs from 150 metres up. They gathered around the large tabular icebergs where our pilots planned to ditch if our plane lost an engine.

During these expeditions, I avoided stories of polar explorers such as Shackleton, Scott and Amundsen. It seemed impossible to relate to these all-male teams. The other graduate student on the trip was also a woman, geophysicist Carol Raymond. She now co-leads NASA's Dawn mission, which is orbiting the protoplanet Ceres. We wore paratrooper boots and helmets like the rest of the team, and were still mistaken for secretaries. Both of us experienced what would today be considered harassment. As students, we dared not utter a word. Such behaviour by male colleagues was considered part of the job, or the woman's fault.

"We wore paratrooper boots and helmets, and were still mistaken for secretaries."

Role models were few and far between back then. There were no female Earth-science faculty at Columbia University in New York where I did my PhD and work today. Marine geologist Marie Tharp, who was the first to map the mid-ocean ridge, would occasionally appear on campus. Deep in mourning for her life partner and collaborator, who had died in a submersible at the bottom of the Atlantic Ocean, she had little time for students such as Carol and me. Outside Columbia, we looked to geophysicist Marcia McNutt, who was said to file her nails on the fantails of research ships before tossing dynamite overboard to blast through the ice.

But just as geophysicists' instruments have captured changes in the ice sheets, we are seeing changes in the scientific establishment. Women now routinely lead expeditions. Institutions take harassment seriously. The rising generation of scientists is unwilling to accept the hostility that drove many of my friends from science. Female scientists are speaking up; they are being heard, and they are getting work done.

These days, when I look out of the aircraft that carries an imaging system built by my research group, I still see ice — flowing, folding and rotating in its many beautiful forms. But if I close my eyes, I do not picture the frost-encrusted beards of an all-male expedition.

FEMALE FACES

I see palaeoclimatologist Dorthe Dahl-Jensen on the Greenland ice sheet, sheltering in a tiny tent while running a winch that drags an instrument through a borehole. She has drilled ice cores in Greenland and Antarctica to assemble spectacular records of the changing climate.

I see geologist Christine Siddoway, who is trying to figure out how the Antarctic continent tore off from New Zealand. She once spent a sleepless night in her camp as hurricane-force winds lifted snowmobiles into the air and shredded tents.

I see microbiologist Jill Mikucki, with a satellite phone glued to her ear, leading an international team to study ecosystems under the ice.

And I see so many more: glaciologist Helen Fricker, installing Global Positioning System base stations on the Amery Ice Shelf in Antarctica; Indrani Das, who was drawn by the beauty of snow to leave astrophysics; and Adrienne Block, whose PhD dissertation took her to a remote camp in East Antarctica. It brings me great joy to see so many women among the ranks of polar scientists.

Last November, my team was deployed to Antarctica to launch a programme called ROSETTA-Ice. We used gravity to map the Ross Ice Shelf and to uncover its tectonics, an idea that Siddoway and I thought of more than a decade ago. The fieldwork was led by Kirsty Tinto; I met her eight years ago at McMurdo Station, the main US base in Antarctica. I had been lost in logistics — how to get my team safely atop the ice sheet, along with the fuel — when Tinto walked down the hall that serves as the main street of that small science town. The young geophysicist had just returned from weeks on the ice. Her laughter and confidence caught my eye: she fit my idea of what a scientist should look like.

Now, I don't have to shut my eyes to see scientists in all shapes, sizes, nationalities and genders. It is this rich array that buoys me as I watch the ice sheet shift. ■

Robin Bell *is a research professor at the Lamont–Doherty Earth Observatory of Columbia University in Palisades, New York.*

DUCK, DUCK, DUCK

It's no game.

BY SAMANTHA MURRAY

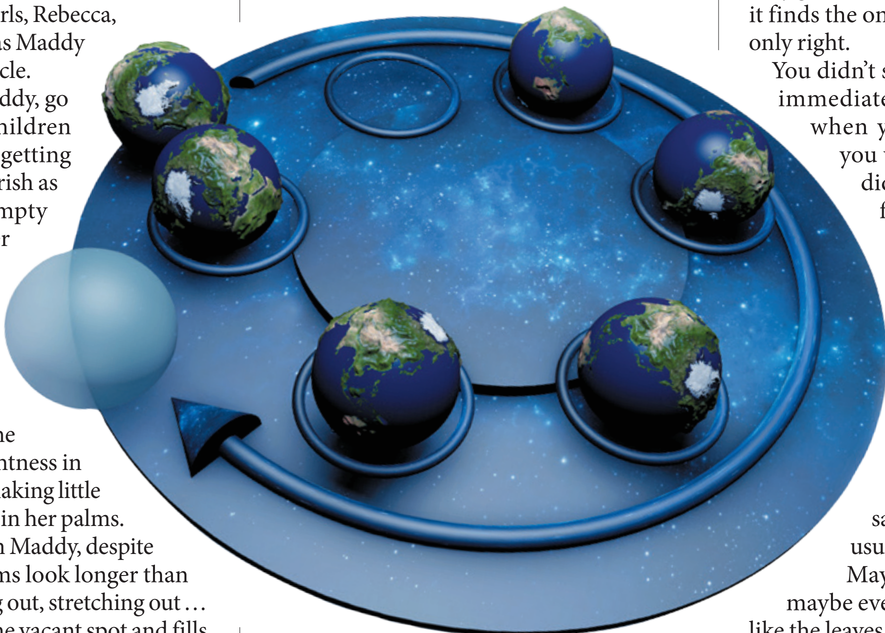

"Duck, duck, duck," says Maddy, touching each head in the circle with a perfunctory authority. "Duck, duck," she pauses almost imperceptibly at the curly blonde head in front of her, "alien."

The owner of the curls, Rebecca, scrambles to her feet as Maddy tears off round the circle.

"Go Maddy, go Maddy, go Maddy," the other children screech, their voices getting higher and more feverish as Maddy passes the empty space and starts on her second lap around. No one cheers for the little blonde girl. No one wants the alien to win.

"Go Maddy," yells Candice, along with the others, feeling the tightness in her chest, her hands making little crescent moon marks in her palms. The alien is gaining on Maddy, despite her head-start. Its arms look longer than they should stretching out, stretching out … as Maddy skids into the vacant spot and fills it with her warm panting body. The circle is complete again.

Rebecca stops. Her face is red and there is a little bit of spit at the corner of her mouth. Then she smiles and starts walking, a slow measured gait.

"Duck," she says. "Duck, duck, duck."

The teachers don't like this game, Candice knows, but they don't cross over the expanse of bitumen to the grassed area that skirts the oval where the kids play it at recess time. Everyone plays it now, the climbing frames are desolate in the sun and the skipping ropes and footballs are left in the sports cupboards.

The teachers don't like the game, probably because they don't like to talk about the aliens at all. Candice's mother doesn't talk about them either, her eyes went all shifty and she got a worried crease in her forehead the one and only time Candice brought it up. She switches off the news when Candice is around, but Candice knows anyway. The kids all know.

The first sign of turning into an alien is that your eyes start to look like glass, all reflective and shiny and hard. And you are cold, cold, cold, because something different is happening to your blood. The last, and final, sign is that you start to go transparent, so that you can see your veins and bones and intestines and gross things through your skin. Candice doesn't know what happens after that, she knows that they quarantine you and stick you with needles and probably try to get you to tell them where the other aliens are and what plans they have for invading Earth.

Candice looks towards the teacher on duty, standing near the classroom under the shade of a large box tree, every green leaf glinting. Candice doesn't wear a watch, but all of the kids know by some kind of internal instinct that recess time is nearly over. The game has picked up an added urgency. A dark-haired girl from the grade below Candice trips on her way round the circle and only just avoids the alien. She looks like she is going to cry.

When the siren goes all of the kids will scatter like ash to the wind, helter-skeltering back to the school buildings. If you are stuck being the alien at that point you will have to be the alien all day. No one will want to sit next to the alien, or pass notes to it, or walk home with it. Even the teachers can somehow detect the stench of alien and will respond to it with a distaste that is almost, almost, but not quite, concealed.

Candice knows that the aliens have an '*R* nought' of exactly one. She doesn't know where she heard that, but she knows what it means. It means an alien will always pass it on to just one person. An alien might have contact with many people, but it will only go "duck" and "duck" and "duck", until it finds the one person who is exactly and only right.

You didn't show that you were an alien immediately. There would be a time when you were still yourself but you were really an alien but you didn't know it. Maybe you just felt colder inside, cold, cold like her Dad's hands when he'd clutched her when he picked her up on Friday because it was his weekend with her.

He'd been cold and his eyes had been glinty and distracted all weekend, and when he'd dropped her at school Candice had felt all sad and lost although she didn't usually, usually it was fine.

Maybe you would feel cold and maybe everything would look sharper like the leaves on the box tree even from so far away, and maybe your blood wouldn't go in hot spurts anymore, but instead be cool and steady like cooled lava — dark and intricate, swirled and ropey.

"Duck," says Gracie, who used to be Candice's best friend last year.

Candice looks back to see the teacher looking at her wrist. She can see the little lines cross-hatched in the skin below her eyes, and the beads of sweat to the side of her nose, even though the teacher is all the way over near the classroom.

"Duck," says Gracie, her footsteps approaching, and were they slowing, just a little?

I don't want to be the alien, thinks Candice. *I don't want to be the alien, I don't want to be the alien.*

"Duck," says Gracie. ■

ILLUSTRATION BY JACEY

Samantha Murray *is a writer, actor, mathematician and mother. Not particularly in that order. Her fiction has been seen in* Lightspeed (Women Destroy Science Fiction!), Flash Fiction Online, Daily Science Fiction *and* Writers of the Future, Vol. 31, *among others.*

➲ NATURE.COM
Follow Futures:
@NatureFutures
go.nature.com/mtoodm